IntechOpen

Infrared Spectroscopy

Life and Biomedical Sciences

Edited by Theophile Theophanides

INFRARED SPECTROSCOPY – LIFE AND BIOMEDICAL SCIENCES

Edited by **Theophile Theophanides**

Infrared Spectroscopy - Life and Biomedical Sciences
http://dx.doi.org/10.5772/2655
Edited by Theophile Theophanides

Contributors

Milica Pojić, Jiang Yinlai, Shuoyu Wang, Renpeng Tan, Kenji Ishida, Masakatsu Fujie, Takeshi Ando, M. S. Mohy Eldin, Shu Morioka, Shouhei Koyama, Kazuki Yanagisawa, Brett Wedding, Hitoshi Kaneko, Hiroyuki Ito, Takashi Okada, M.D., Toru Yoshikawa, Kenji Nomura, Shuji Honjo, Rienk Van Grondelle, Kenichi Kuriyama, Masahito Mihara, Ichiro Miyai, Maria Margarida Figueiredo, José António Gamelas, Gabriela Martins, Haiqing Yang, Abdul M. Mouazen, Shaul Mordechai, Masayoshi Nagai, Keiko Tagai, Sadaki Takata, Takatsune Kumada, Vasiliki Dritsa, Taeko Ogawa, Michio Nomura, Barbara Engelhardt, Alexander Gersten, Dov Heimer, Jacquelin Perle, Amir Raz, Robert Fried, Theophanides Theophile

Notice

First published in Croatia, 2012 by INTECH d.o.o.
eBook (PDF) Published by IN TECH d.o.o.
Place and year of publication of eBook (PDF): Rijeka, 2019.
IntechOpen is the global imprint of IN TECH d.o.o.
Printed in Croatia

Legal deposit, Croatia: National and University Library in Zagreb

Additional hard and PDF copies can be obtained from orders@intechopen.com

Infrared Spectroscopy - Life and Biomedical Sciences
Edited by Theophile Theophanides

p. cm.

ISBN 978-953-51-0538-1

eBook (PDF) ISBN 978-953-51-4298-0

Meet the editor

Professor Theophile Theophanides was born in Platamon, Kavala, Greece and is known from his ground-breaking research in the field of Metal Coordination Chemistry and Infrared Spectroscopy. In particular his research focus has been in the areas of life metal ions, bioinorganic chemistry and in his pioneering work in anti-tumor drugs, such as cis-Platinum, commonly employed in chemotherapy. He has authored over 250 peer-reviewed scientific publications in international journals, penned numerous articles and book chapters and served on the board of many Scientific Associations and Committees. He has been honored many times for his research. He is an Honorary Professor of the University of Montreal and the National Technical University of Athens, Doctor Honoris Causa of the University of Reims and Silver Medalist of the National French Academy of Medicine for his outstanding work on magnesium research. Additionally, he has received medals from Universities, Media and other Associations for his research and communications on Environmental and Public Health issues.

Contents

Preface

In this book one finds the applications of Infrared Spectroscopy to Life and Biomedical Sciences. It contains three sections and 20 chapters.

The three sections are:

Brain Activity and Clinical Research The 10 chapters that are included in this section skillfully describe the application of MIRS and NIRS to such new areas of research in medicine like management of patients in neonatal intensive care, effects of sleep dept on cognitive performance in humans, neurorehabilitation, brain activity, social relations, non invasive measurements, cortical activation, brain oxygenation and haemodynamic activation.

The second section, **Cereals, Fruits and Plants** includes 4 chapters. In this section one can find applications of MIRS and NIRS in food industry and research, in quality control of wheat, in farms in order to predict the amounts of nitrogen and carbon at a farm scale, for assessing avocado quality control and in research to determine, for example the structure and dynamics of carotenoid and chlorophyll triplets in photosynthetic light-harvesting complexes.

Finally, the third and last section of this book, **Biomedical Applications** contains 6 chapters of MIRS and NIRS on medical applications, such as the role of β-antagonists on the structure of human bone, characterization of bone-based graft materials , brain computer interface in rehabilitation a review of FT-IR on medical applications, biomedical research in cells and biopolymer modifications for biomedical applications.

This book of Infrared Spectroscopy on Life and Biomedical Sciences is a state-of-the art publication in research and technology of FT-IR as applied to medicine.

Theophile Theophanides
National Technical University of Athens, Chemical Engineering Department,
Radiation Chemistry and Biospectroscopy, Zografou Campus, Zografou, Athens
Greece

Introductory Chapter

Introduction to Infrared Spectroscopy in Life and Biomedical Sciences

Theophile Theophanides
National Technical University of Athens, Chemical Engineering Department, Radiation Chemistry and Biospectroscopy, Zografou Campus, Zografou, Athens Greece

1. Introduction

By 1950 IR spectroscopy was applied to more complicated molecules such as proteins by Elliot and Ambrose [1]. The studies showed that IR spectroscopy could also be used to study complex biological molecules, such as proteins, DNA and membranes and thus, IR could be also used as a powerful tool in biosciences [2, 3].

The FT-IR spectra of very complex biological or biomedical systems, such as, atheromatic plaques and carotids were studied and characterized as it will be shown in chapters of this book. From the interpretation of the spectra and the chemistry insights very interesting and significant conclusions could be reached on the healthy state of these systems. It is found that FT-IR can be used for diagnostic purposes for several diseases. Characteristic absorption bands of proteins, amide bands, O-P-O vibrations of DNA or phospholipids, disulfide groups, e.t.c. can be very significant and give new information on the state of these molecules.

Furthermore, with the addition of micro-FT-IR spectrometers one can obtain IR spectra of tissue cells, blood samples, bones and cancerous breast tissues [4-7]. Samples in solution can also be measured accurately. The spectra of substances can be compared with a store of thousands of reference spectra. IR spectroscopy is useful for identifying and characterizing substances and confirming their identity since the IR spectrum is the "fingerprint" of a substance.

Therefore, IR has also a forensic purpose and is used to analyze substances, such as, alcohol, drugs, fibers, hair, blood and paints [8-12].In the sections that are given in the book the reader will find numerous examples of such applications.

2. References

[1] Elliot and E. Ambrose, Nature, Structure of Synthetic Polypeptides 165, 921 (1950)
[2] D.L.Woernley, Infrared Absorption Curves for Normal and Neoplastic Tissues and Related Biological Substances, Current Research, Vol. 12, , 1950 , 516p
[3] T. Theophanides, J. Anastassopoulou and N. Fotopoulos, *Fifth International Conference on the Spectroscopy of Biological Molecules*, Kluwer Academic Publishers, Dodrecht, 1991,409p

[4] J. Anastassopoulou, E. Boukaki, C. Conti, P. Ferraris, E.Giorgini, C. Rubini, S. Sabbatini, T. Theophanides, G. Tosi, Microimaging FT-IR spectroscopy on pathological breast tissues, *Vibrational Spectroscopy*, 51 (2009)270-275

[5] Conti, P. Ferraris, E. Giorgini, C. Rubini, S. Sabbatini, G. Tosi, J. Anastassopoulou, P. Arapantoni, E. Boukaki, S FT-IR, T. Theophanides, C. Valavanis, FT-IR Microimaging Spectroscopy:Discrimination between healthy and neoplastic human colon tissues , J. Mol Struc. 881 (2008) 46-51.

[6] M. Petra, J. Anastassopoulou, T. Theologis & T. Theophanides, Synchrotron micro-FT-IR spectroscopic evaluation of normal paediatric human bone, *J. Mol Structure*, 78 (2005) 101

[7] P. Kolovou and J. Anastassopoulou, "Synchrotron FT-IR spectroscopy of human bones. The effect of aging". Brilliant Light in Life and Material Sciences, Eds. V. Tsakanov and H. Wiedemann, Springer, 2007 267-272p.

[8] Conti, P. Ferraris, E. Giorgini, C. Rubini, S. Sabbatini, G. Tosi, J. Anastassopoulou, P. Arapantoni, E. Boukaki, S FT-IR, T. Theophanides, C. Valavanis, FT-IR Microimaging Spectroscopy:Discrimination between healthy and neoplastic human colon tissues , J. Mol Struc. 881 (2008) 46-51.

[9] T. Theophanides, *Infrared and Raman Spectra of Biological Molecules*, NATO Advanced Study Institute, D. Reidel Publishing Co. Dodrecht, 1978,372p.

[10] T. Theophanides, C. Sandorfy) *Spectroscopy of Biological Molecules*, NATO Advanced Study Institute, D. Reidel Publishing Co. Dodrecht, 1984 , 646p

[11] T. Theophanides *Fourier Transform Infrared Spectroscopy*, D. Reidel Publishing Co. Dodrecht, 1984.

[12] T. Theophanides, *Inorganic Bioactivators*, NATO Advanced Study Institute, D. Reidel Publishing Co. Dodrecht, 1989, 415p

Section 1

Brain Activity and Clinical Research

1

Use of Near-Infrared Spectroscopy in the Management of Patients in Neonatal Intensive Care Units – An Example of Implementation of a New Technology

Barbara Engelhardt and Maria Gillam-Krakauer
Vanderbilt University, Nashville, TN
USA

1. Introduction

Near-infrared spectroscopy (NIRS) is a spectroscopic technique which uses the NIR region of the electromagnetic spectrum to gain information about natural samples through their absorption of NIR light. This method is used in several branches of science. In medicine, it was first used in adult patients, who were placed on by-pass during cardiac surgery to follow cerebral oxygenation, cerebral rSO2 (rSO2-c,) and thereby perfusion and metabolism of the brain. Its many other possibilities soon became apparent. Although the brain remains the main organ of interest in patients of all ages, other tissues are being studied as well. Aside from cardiac surgery clinicians in specialties such as sports medicine, plastic surgery (to assess flap viability), and neonatology apply NIRS in clinical settings. (Feng et al., 2001)

By the late 1980's the first studies on monitoring of regional oxygenation in the neonatal brain were published. (Delpy et al., 1987; Edwards et al., 1988) In 2004 on average one new article on NIRS was published in Pub Med every day. (Ferrari et at, 2004) Monitoring of vital signs in the ICUs has scientific and patient care related goals. One may be able to gain better understanding of physiology and be alerted to changes in patient status to be able to respond immediately.

The vulnerability of the neonate, especially of the newborn brain, to changes in oxygenation is an ever present concern as it is linked to long-term outcome. For that reason neonatologists are obligated to find ways to monitor their patients to be ahead of evolving pathology and avoid the severe impact of negative events.

As early as 1999 the NINDS and NIH hosted a workshop for experts in the fields of neurology and neonatology to discuss the use of NIRS for cerebral monitoring in infants. The panel determined that the best NIRS instrument should be selected and used in longitudinal, blinded studies. Obtained data would need to be compared with short term, intermediate and long term outcomes. The questions the panel suggested to investigate were the predictive value of NIRS and its usefulness in leading to timely interventions and prevention of long term injury. (www.ninds.nih.gov/news_andevents/proceedings/

nirswkshop1999.htm) Once NIRS monitors became commercially available a few animal and many clinical trials were conducted. The clinical investigations were for the most part small, brief observational prospective studies. Also NIRS was introduced into daily practice by others at that time, years before normative data and validation studies had been obtained.

There is great potential to use the NIRS technology in the neonatal intensive care unit (NICU) since it is a portable, continuous, non-invasive bedside monitoring technique. Following the development of small and skin friendly sensors and FDA approval of some NIRS monitors for use in neonates, both research and clinical use of NIRS in the NICU increased exponentially. The number of research projects over the last 5-10 years is large. However, the trials, while dealing with questions important to understanding physiology and clinical care in the NICU, are small and almost exclusively conducted at single centers. Often no more than 10-20 patients are being followed. Very large NIRS related studies enrolled 40-90 patients. Many of the observations reported are of brief sampling periods, sometimes being no more than spot samples.

This chapter is a limited overview for non-clinicians such as engineers and science students, or clinicians who want to learn about a medical application of NIRS. The recent introduction of the NIRS technology into neonatal medicine is used as an example of how a new device came into use into use in the clinical setting over the last decade. Main areas of clinical use and supporting studies will be mentioned. Limitations of NIRS technology and controversies as well as future directions will be addressed. With the abundance of available literature this chapter cannot claim to be a reference. This is an exciting and rapidly advancing field with new studies published even as this article was sent to press. This chapter will demonstrate how a new technology is adopted into medical care, in this case the NICU.

1.1 Materials

Pub Med and Google have been queried regarding NIRS in NICUs, abdominal/splanchnic, cerebral and renal measurements, utility, and of NIRS use as prognosticator.

1.2 Technology and measurements

The principle of how NIRS works in humans was excellently summarized by Cohn:

Near-infrared spectroscopy has been used as a tool to determine the redox state of light-absorbing molecules. This technology is based on the Beer-Lambert Law, which states that light transmission through a solution with a dissolved solute decreases exponentially as the concentration of the solute increases. In mammalian tissue, only three compounds change their spectra when oxygenated: cytochrome *aa3*, myoglobin, and hemoglobin. Because the absorption spectra of oxyhemoglobin and deoxyhemoglobin differ, their relative concentrations within tissue change with oxygenation, and the relative concentrations of the types of hemoglobin can be determined. Because NIRS measurements are taken without regard to systole or diastole, and because only 20% of blood volume is intra-arterial, spectroscopic measurements are primarily indicative of the venous oxyhemoglobin concentration. In the near infrared region (700 –1,000 nm), light transmits through skin, bone, and muscle without attenuation. (Cohn et al., 2003) There are several FDA approved

NIRS monitors with somewhat different technology and algorithms available commercially (Wolf & Greisen, 2009) to measure the venous weighted regional oxygen saturation (rSO2) or tissue oxygenation index (TOI).

Due to the small size and the thin covering layers of tissue of both term and preterm neonates, r-SO2/TOI measurements at a depth of 2-3 cm can reach brain, kidney, gut/ splanchnic circulation, liver and muscle. The access to these critical organs promises valuable physiologic information through monitoring by NIRS. Measurements of several sites can be recorded simultaneously. (Hoffman et al., 2003; McNeill et al., 2010, 2011)

NIRS measurements are organ specific and regional (rSO2), reflecting perfusion and metabolism by non-invasive measurement in real-time. They are not temperature, pulsatility or flow dependent. Thus they may offer advantages over traditional measures of perfusion such as capillary refill, blood pressure, and urine output, lactate, venous and arterial O2 which tend to alert the clinician once the disease process is further progressed. R-SO2 measurements cannot stand alone. While they may often be the first sign of change, they need to be interpreted in the context of other measurements such as mean arterial blood pressure (MABP), pulse oximetry (O2sat), blood gases, additionally in the research setting with measurements of cerebral blood flow (CBF) and cerebral blood volume (CBV). Evaluation of the link between the venous weighted NIRS readings and peripheral pulse oximetry, a measure of arterial O2, gives insight into oxygen supply and demand. Using a simple equation, the fractional extraction of oxygen (FTOE = SaO2-rSO2/SaO2) oxygen consumption can be calculated and oxygen supply can be assessed. (Lemmers et al., 2006)

1.3 Validation

NIRS was implemented by many enthusiastic clinicians without a vast body of previous research evidence. This phenomenon may be representative of an era of limited funding for larger studies linked with the promise of a non-invasive "safe" monitoring technology.

Before human application the initial research applying NIRS to measure rSO2 technology in the medical field occurred in the laboratory: One of the first examples of validation used a phantom brain model in which O2, N2, and CO2 content of a blood perfusate could be altered during measurements. The results correlated with findings in animal models. (Kurth et al., 1995) Later NIRS was further validated for the neonatologist in a newborn piglet model. The carotid, renal and mesenteric arteries were occluded and reperfused. These interventions led to rapid, simultaneous changes in rSO2 of the affected end-organs. (Wider, 2009) Furthermore, there have been validations in patients during intensive care, extra-corporeal membrane oxygenation (ECMO) and cardiac surgery by comparing central blood samples with NIRS values. (Abdul-Khaliq et al., 2002; Benni et al., 2005; Nagdyman et al., 2004; Rais-Bahrami K et al, 2006; Weiss, 2005) Menke found reproducibility to be good as well. (Menke et al., 2003). The accuracy of data is impacted by light scattering, hemoglobin concentration and chromophores such as melanin and bilirubin. In the presence of a thicker overlying tissue layer, such as severe subcutaneous edema or excess subcutaneous fat, it may be impossible for the NIR light beam to reach the target organ. In the newborn modest changes in weight have a small effect on abdominal measurements while changes in hemoglobin over the first weeks of life can change measurements by 30-50%. (Ferrari et al.,

2004; Madsen et al., 2000; McNeill et al., 2010, 2011; Wassenaar et al., 2005) NIRS measurements may differ between probes. (Sorensen et al., 2008)

1.4 Safety and feasibility

Commercially available sensors for neonates have become well tolerated due to smaller size and being lined with a skin friendly adhesive. To provide further skin protection in extremely premature patients probes can be attached to a light-permeable skin barrier without interference with measurements. (McNeill et al., 2010, 2011)

1.5 Monitoring

Organs which can be monitored in neonates are brain, kidney, gut, liver and muscle. This chapter will comment on the most commonly used sites– the brain, kidney and gut.

2. Cerebral NIRS

The neonatal period is a unique time in life as the infant undergoes dramatic physiologic changes during transition from intra- to extra-uterine life, which involve hemodynamics and affect oxygenation, reflected in rSO2. Due to its vulnerability the neonatal central nervous system is the main area of interest for measurements of oxygenation. The majority of articles written on the clinical use of NIRS in neonates include reports on cerebral measurements (c-rSO2 or cerebral Tissue Oxygenation Index (TOI)).

2.1 Effect of gestational and postnatal age

The largest body of research investigates cerebral NIRS values. Reports regarding effects of gestational age (pre-term, term, post-term) and postnatal/chronologic age on NIRS values are conflicting.

In a study by McNeill, which was blinded to caregivers and sampled from birth for a maximum of 21 days, baseline rSO2 for preterm infants (gestational age of 29-34 weeks) differed from established pediatric norms, while values for term neonates in the first days of life did not (McNeill et al., 2010, 2011). The observation by McNeill (McNeill et al., 2010, 2011) that cerebral NIRS decreases over time are supported by Roche-Labarbe's findings following weekly spot samples during the first 6 weeks obtained with a different study protocol and different NIRS equipment. (Roche-Labarbe et al., 2010, 2011) Both observations contradict Lemmers' study in which twice daily 60 minute sampling periods found no observed change. (Lemmers et al., 2006)

Naulears found an increase in cerebral oxygenation in premature infants during the first three days. In this study sampling periods were 30 min. NIRS recordings occurred with a different instrument. (Naulaers et al., 2002) Meek's earlier report from 1998 in ventilated babies used NIRS and found an increase in cerebral blood flow over time. (Meek et al., 1998)

A study measuring rSO2-c in transition after delivery found by minute 3 that rSO2 increased and reached a plateau by minute 7. (Urlesberger et al., 2010)

More recently, Takami followed cerebral TOI in extremely low birth weight infants (ELBWs) at 3-6h followed by samples every 6h up to 72h. He observed a decrease in measurements until 12h, then an increase that correlated with similar changes in SVC flow. (Takami et al., 2010).

When reviewing this literature regarding the contradicting study results, possible explanations present themselves: Patient populations are not identical. Protocols vary from study to study. Different sampling times may play an important role in influencing results, especially when spot samples versus long-term continuous data were collected. If studies were not blinded, care giving and subsequently observations might have been influenced. The use of different monitors and probes and probe placement may further lead to different results. Studies were small and data inconclusive. There was some agreement regarding abnormally low values being linked to poor outcome. (Dullenkopf et al., 2003; Sorensen et al., 2008; van Bel et al., 2008; Wolf & Greisen, 2009, also see cerebral hypoxia)

2.2 Variability

Variability is the change in percent of rSO2 away from a calculated baseline. It can be followed over time to know how much time the rSO2 was above or below baseline. The baseline differs from patient to patient. Variability is an area of interest and needs further investigation: Cerebral daily variability is small. Large changes (>20%) off the baseline would raise concern for acute clinical change. (McNeill et al., 2010, 2011) Change in variability may be an indicator of infection (Yanowitz et al., 2006). The change in baseline over the first weeks of life, which is observed in preterm infants, may represent ongoing developmental maturation independent of feeding status. (McNeill et al., 2010, 2011)

2.3 Peripheral blood pressure and oxygenation, impact on autoregulation

In the research setting cerebral blood flow and blood volume measurements, oxy- and deoxy hemoglobin and fractional extraction of oxygen (FTOE) as well as blood gas samples from central catheters added to detailed understanding of physiology.

Adequate O2 delivery to the brain tissue is most critical. Assessment of O2 delivery and consumption help understand clinical scenarios and their underlying pathophysiology: At the bed side this evaluation can occur by following changes in cerebral rSO2, changes in BP, oxygenation and peripheral blood gases. The below clinical scenarios for monitoring are amongst the more common:

Cerebral autoregulation is a homeostatic phenomenon controlled by the main capacitance vessels in the cerebral circulation. Through dilatation and constriction of these vessels cerebral blood flow and cerebral rSO2 or TOI are maintained at a steady level over a range of changing mean arterial blood pressures (MABP). This range is narrower in neonates, particularly in preterm infants. Cerebral pressure-passivity or loss of autoregulation is associated with low gestational age, low birth weight and systemic hypotension in a large study of 90 patients. (Soul et al., 2007)

If rSO2 or TOI changes correlate with the wave form of MABP autoregulation is lost. Swings in peripheral perfusion will be mirrored in cerebral blood flow and regional saturation readings. This phenomenon, when profound, carries an increased risk for intra-ventricular hemorrhage (IVH) and peri-ventricular leucomalacia (PVL) in preterm infants and generally a poor prognosis for neurodevelopment outcome. The more swings or changes in mean arterial pressure (MAP) and NIRS coincide and mirror each other, the more the waves are in concordance. Several studies link concordance with a more unfavorable prognosis and a higher likelihood of death. (Caicedo et al., 2011; DeSmet et al., 2010; Greisen & Borch, 2001;

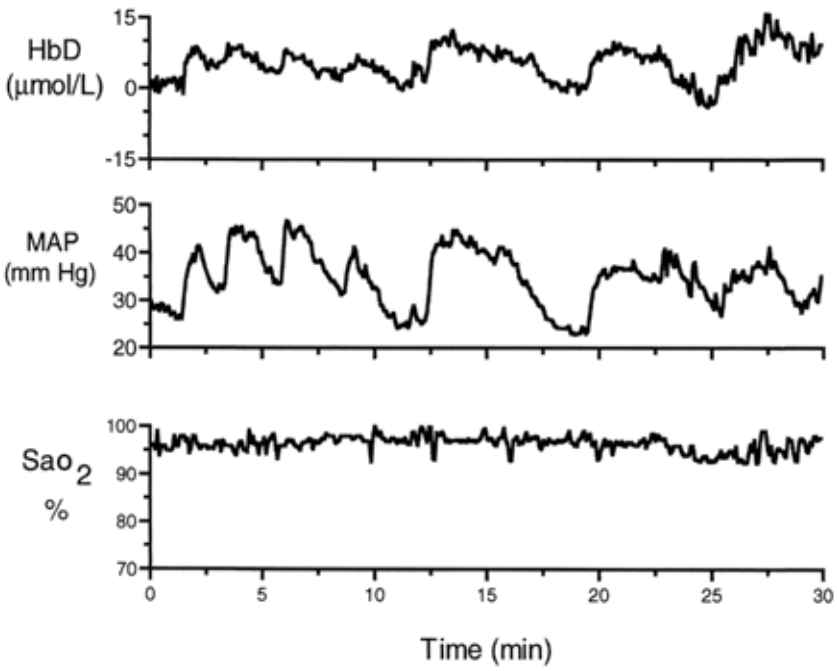

Fig. 1a. Example 1: Patient with loss of autoregulation and concordance of MAP and NIRS measurement of intravascular oxygenation (HbD). This patient had an unfavorable outcome.

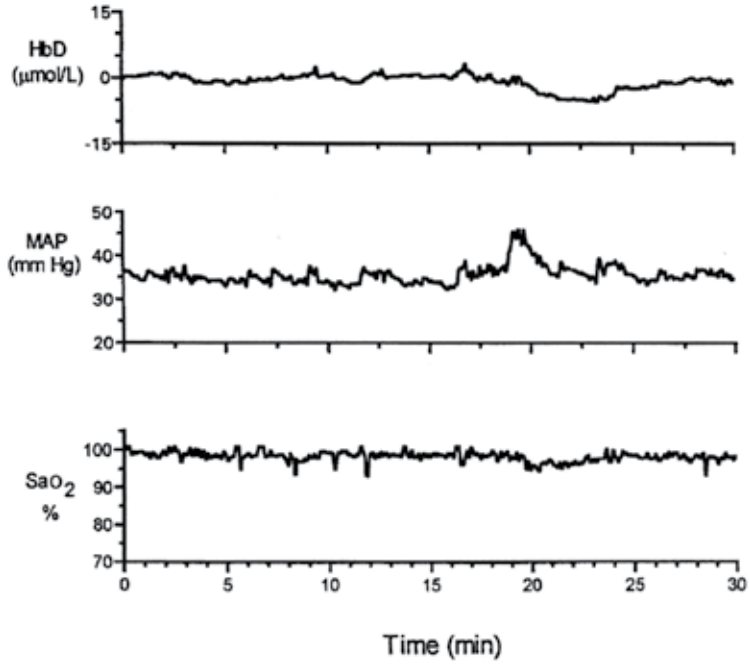

Fig. 1b. Example 2: Maintenance of autoregulation (Tsuji, 2000)

Hahn et al., 2010; Lemmers et al., 2006; Morren et al., 2003; Munro et al., 2004, 2005; O'Leary et al., 2009; Seri, 2006; Tsuji et al., 2000; Wong et al., 2008) In a recent study 23 infants with a mean gestational age of 26.7 +/-1.4 weeks were observed with NIRS. They were found to have periods of loss of cerebral autoregulation which were more profound with lower, longer lasting MABPs. There was no correlation with head ultrasound (HUS) findings as measure of short term outcome. (Gilmore et al., 2011)

A study followed changes in cerebral NIRS in ventilated preterm infants and found frequent periods of loss of autoregulation. (Lemmers et al., 2006). Vanderhaegen stresses the important contribution of pCO2 to cerebral blood flow, which may possibly override autoregulation. (Vanderhaegen et al., 2010) Hoffmann manipulated pCO2 in neonates undergoing cardiac surgery to improve cerebral blood flow. (Hoffman et al., 2005) According to another study by Vanderhaegen in 11 ELBWS blood glucose may play a role in influencing oxygenation. (Kurth et al., 1995)

2.4 Cerebral hypoxia

Cerebral hypoxia is a feared event as it translates to long-term morbidity and mortality. There is not enough data available linking a specific duration of hypoxia and levels of rSO2 or TOI while in the NICU with outcomes. There are no absolute numbers as reference in the human neonate. A piglet study from 2007 demonstrated changes seen on brain autopsy 72h after the animal spent 30 min. with rSO2-c of <40%. (Hou et al., 2007) It is not certain whether observations of concerning low levels of r-SO2/TOI in cardiac patients (Dullenkopf et al., 2003; Sorensen et al., 2008; van Bel et al., 2008; Wolf & Greisen, 2009) apply to infants with other diagnoses.

2.5 Cerebral hyperoxia

Cerebral hyperoxia in the critically ill neonate may occur by 2 mechanisms: either as hyper-oxygenation during the reperfusion phase of severe hypoxic ischemic encephalopathy most commonly occurring in neonates after perinatal birth depression or from decreased brain metabolism as seen in critical patients when blood flow is uncoupled from O2 (Toet, 2006; Wolf & Greisen, 2009). Either scenario is concerning for a poor long-term prognosis. The overall clinical situation needs to be taken into consideration as cerebral rSO2 in well preterm neonates has also been reported to be high in the first days of life. (Sorensen et al., 2009).

3. Renal NIRS

Renal rSO2 is higher than cerebral rSO2. McNeill reported that trends in cerebral and renal NIRS during the first 21 days of life mirror each other. Short-term and long-term variability of r-SO2 is small. Saturation changes exceeding >20% from baseline would be reason for concern and may indicate compromised perfusion. Several investigators report use in patients with shock or during surgery. Measurements of the renal rSO2 give insight into peripheral perfusion in general and into renal end-organ function. Using renal rSO2 in conjunction with cerebral rSO2 has been reported to give more and sometimes earlier insights into evolving pathology such as shock. (Cohn et al., 2003; Hoffman et al., 2003, 2004) See figure 2.

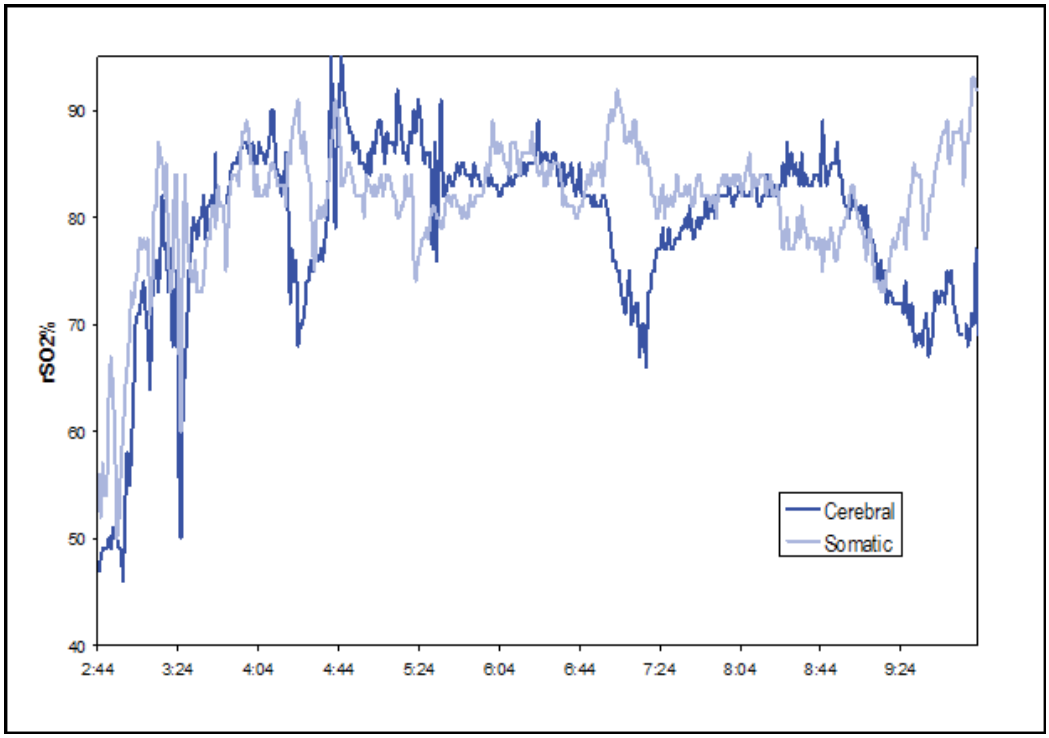

Fig. 2. Two-site NIRS trends from a patient undergoing resuscitation from hypovolemic/septic shock. Early aggressive resuscitation with fluid and epinephrine to normal regional rSO2 values restored urine output. The effect of changes in pCO2 on cerebral blood flow are evident at 0700. The mirror changes in cerebral and somatic rSO2 suggest that total cardiac output was relatively limited but that the distribution changed.(Hoffman et al., 2007)

4. Splanchnic (gut) NIRS

Monitoring the GI tract as opposed to monitoring the brain or kidneys is more complex since the gut is a hollow or gas and stool filled, moving structure, in close proximity of stomach and bladder, which could affect its position and functioning. Proper probe placement may therefore be a challenge. In addition movements of the baby and pull on electrodes are more likely. A recent small study by Gillam-Krakauer et al. using Doppler confirmed that splanchnic NIRS reflects bloodflow to the small intestine. (Gillam-Krakauer et al., 2011)

McNeill's study of splanchnic/abdominal rSO2 in healthy preterm infants between day 0 and day 21 found that baseline changed over time. Overall abdominal rSO2 values were significantly lower than cerebral and renal values. The baseline increased over time. When comparing patients born at 32 and 33 weeks to those born at 29 and 30 weeks gestation, higher weekly means were observed in the 2nd week of life in the older group. (McNeill et al., 2010, 2011)

These changes too may indicate regional developmental maturation. For abdominal rSO2 long- and short-term variability is much higher and exceeds 20%. It may be associated with

clinical and caregiving events and warrants further investigation/characterization. (McNeill et al., 2010, 2011)

Cortez found higher splanchnic rSO2-s and variability to be associated with a healthy gut, whereas infants with necrotizing enterocolitis, a condition of devastating bowel inflammation, had low splanchnic rSO2s and decreased variability. (Cortez et al., 2010, 2011)

5. Clinical events observed with NIRS

To further demonstrate the extent of topics and studies, examples of some clinical scenarios are listed. Referenced articles date back to 2000. The articles quoted are found in the bibliography. They are representative of the scope of interest.

5.1 Unstable neonates

Respiratory distress (Lemmers et al., 2006; Meek et al., 1998)

ECMO (Benni et al., 2005; Rais-Bahrami et al., 2006)

Pediatric Surgery (Dotta et al., 2005)

Cardiac disease pre-, intra, post op (Abdul-Khaliq et al., 2002; Hoffman et al., 2003; Johnson, 2009; Kurth et al., 2001; Li et al., 2008; Redlin et al., 2008; Seri, 2006)

Patent Ductus Arteriosus (Hüning et a., 2008; Keating et al., 2010; Lemmers et al., 2008, 2010; Meier et al., 2006; Underwood et al., 2006, 2007; Vanderhaegen et al., 2008; Zaramella et al., 2006)

CNS abnormalities HIE, PVL, PIH (Caicedo et al., 2011; De Smet et al., 2010; Morren et al., 2003; Munro et al., 2004, 2005; Wolf & Greisen, 2009; Wong et al., 2008)

Greisen & Borch , 2001; Hou et al. 2007; O'Leary et al., 2009; Sorensen & Greisen, 2009; Toet, 2006; van Bel F et al., 2008; Vanderhaegen et al., 2009, 2010; Weiss, 2005; Verhaen et al. , 2010; Wolf & Greisen , 2009)

Mechanical Ventilation (Noone et al., 2003; van Alfen-van der Velden et al., 2006; Verhagen et al., 2010)

Apnea (Payer et al., 2003; Yamamota et al., 2003)

Intensive Care (Limperopoulos et al., 2008)

Resuscitation (Baerts et al., 2010, 2011; Fuchs , 2011)

5.2 Care giving

Delivery room (Baenziger et al. ; Urlesberger et al., 2010)

Feedings (Baserga et al., 2003; Dave et al., 2008, 2009)

Blood transfusion (Bailey et al., 2010; Dani et al., 2010; Hess, 2010; van Hoften et al., 2010) *

Head ultrasound (van Alfen-van der Velden et al., 2008, 2009)

Kangaroo care (Begum et al., 2008)

Endotracheal tube suctioning (Kohlhauser et al., 2000)

CPAP (Dani et al., 2007; van den Berg et al.,2009, 2010; Zaramella et al., 2006)

Blood draws from umbilical artery catheters (Bray et al., 2003; Hüning et al., 2007; Roll et al., 2006; Schulz et al., 2003) **

Stimuli, Pain (Bartocci et al., 2001, 2006; Holsti et al., 2011; Liao et al., 2010; Ozawa et al., 2010, 2011; Slater et al., 2007)

Posture/Position (Ancora et al., 2009, 2010; Pichler et al., 2001)

NIRS/EEG (van den Berg et al., 2009, 2010)

5.3 Medications

Caffeine (Tracy et al., 2010)

Dopamine (Wong et al., 2009)

Epinephrine (Pellicer et al., 2005)

Ibuprofen (Bray et al. 2003; Naulaers et al., 2005)

Indomethacin (Dave et al., 2008, 2009; Keating et al., 2010)

Morphine/Midozalam (van Alfen-van der Velden et al., 2006)

Propofol (Vanderhaegen et al.,2009, 2010)

Surfactant (Fahnenstich et al., 1991; van den Berg et al., 2009, 2010)

***Blood transfusions** too are a routine part of NICU care. 3 studies found increases in rSO2-c following transfusion, in addition 2 of the authors reported increase in splanchnic oxygenation and lastly one of the studies found increased renal rSO2 as well. These findings are overall encouraging. Dani however questions whether the increases in rSO2 are reflecting benefits or administration of a pro-oxidant. Another author is attempting to identify the need for transfusion by calculating splanchnic-cerebral oxygen ratios. Infants with low ratios pre-transfusion are more likely to improve post-transfusion. (Bailey et al., 2010 ; Dani et al., 2010; Hess, 2010; van Hoften et al., 2010)

****Blood draws from umbilical artery catheters** decrease rSO2-c. Two reports conflict on whether volume or a rapid draw causes the decrease in rSO2. (Roll et al., 2006; Schulz et al., 2003)

6. Conclusions

NIRS is a fascinating technology with impressive potential. The opportunities to learn more about physiology and effects of therapy through monitoring with NIRS are limitless.

The literature reporting about NIRS in the clinical setting of the NICU is abundant. However published supporting scientific evidence for the use of NIRS in neonatology has limitations. There are no large multi-center collaborative studies. The advent of NIRS has

been affected by coinciding with the era of limited research funding for large clinical studies.

Studies are largely observational either observing a group of patients over time or following changes caused by therapeutic interventions (ECMO, heart surgery, transfusion, medications). Studies for the most part are small in patient numbers and short in time of observation. Study protocols observing the same phenomenon are often distinctly different from each other. Devices used may differ from trial to trial as well. All this can contribute to differences in study results. Due to the differences in study design meta-analysis, as an opportunity to obtain more robust results from a large number of trials and patients, may not be an option. Cerebral NIRS measurements are the most researched and incorporated into daily care. There is some consensus regarding critical lower limits of cerebral oxygenation (Wolf & Greisen, 2009; Wider, 2009). In addition the patient is accepted as his own control, using the NIRS monitor as a trend monitor. (van Bel et al., 2008).

For the future of NIRS monitoring in the NICU, it may be necessary for another NIH panel to be called to review the existing evidence obtained since the initial group met in 1999 and devise a hopefully low budget strategy to validate NIRS in the NICU further. Larger, randomized trials will be needed. Blinding would not be useful unless normative data is obtained. Unblinded studies would allow interventions based on NIRS measurements and observe possible benefits. An anecdotal example was a rotated ECMO cannula that led to a steep decrease in cerebral r-SO2 with all other vital signs remaining unchanged. The caregivers responded immediately avoiding adverse consequences. Greisen in a paper from November 2011 estimates one needs to study 4000 infants with cerebral oximetry to have the power to detect the reduction of a clinically relevant endpoint, such as death or neurodevelopmental handicap, by 20%. (Greisen et al., 2011)

In the meantime, NIRS monitors could be further improved to make interpretation of data easier:

While the information gained is tempting, interpretation of data takes experience. NIRS does not stand alone. It needs to be viewed in context of other occurring physiologic changes. Recently data collection and interpretation has been made easier and more precise by the increasing ability to synchronize collection of different data points and thus link NIRS observations, possibly from multiple channels, with vital signs, EEG, interventions, medications, stimulation and care giving events. At this point this technology is not generally available.

Eventually more channels to measure greater than 3 sites, allowing for more than one cerebral site plus somatic sites, may be needed.

Once norms are established for cerebral, renal and splanchnic sites, normal limits at each site for different gestational and postnatal ages could be indicated on the monitor. Alarms could signal when a patient's rSO2-c is outside the normal range. Variability could be reported both by percent change and change over time, also possibly in reference to gestational age for the observed organ. Incorporation of the ability for the monitor to calculate physiologic equations like FTOE or cerebral blood flow could give more value to NIRS monitoring.

Will those changes improve life and care in the NICU for patients and staff? Perhaps. Possibly clinicians find themselves confronted by unexpected physiology and new problems

to solve. Now it is time to prove benefits of using the NIRS technology by decreasing adverse events in day-to-day patient care and improving outcome.

Greisen summarized the current situation in an article published recently:

> *"On the one hand, cerebral oximetry can potentially become inexpensive as it is based on technology that can be mass produced. Also, the probe may be miniaturized and integrated with the electronics into a soft 'plaster' that may stick to the skin of the head of tiny infants and need little attention. Solid evidence of benefit to patients will create a large market. Evidence of benefit of an instrument using public domain technology can serve as a platform for healthy competition on user-friendliness and price. On the other hand, what will happen if the clinical use of cerebral oximetry is not developed in a rational, evidence-based format? Then it may become another randomly applied expensive technology. Cerebral oximetry will be supported by anecdotal evidence, expert opinion, active branding and marketing. The consequences include unnecessary disturbances and risks to a very vulnerable group of patients and depletion of scarce healthcare resources".*
>
> (Greisen et al., 2011)

In closing, this chapter is not a manual for patient management. It demonstrated the implementation of a new tool as well as the temptations and hurdles faced by investigators and clinicians using a new promising device, which the author herself understands from both observation and personal experience.

7. Acknowledgment

We would like to thank Michelle Carretero for her help with the preparation of this chapter.

8. References

Abdul-Khaliq H et al. 2002 Cerebral oxygen monitoring during neonatal cardiopulmonary bypass and deep hypothermic circulatory arrest. *Thorac Card Surg* 50; 77-81

Ancora G, Maranella E, Aceti A, Pierantoni L, Grandi S, Corvaglia L, FaldellaG. Effect of posture on brain hemodynamics in preterm newborns not mechanically ventilated. Neonatology. 2010; 97(3):212-7. Epub 2009 Oct 29.

Baenziger O, Stolkin F, Keel M, von Siebenthal K, Fauchere JC, Das Kundu S, Dietz V, Bucher HU, Wolf M. The influence of the timing of cord clamping on postnatal cerebral oxygenation in preterm neonates: a randomized, controlled trial.

Baerts W, Lemmers PM, van Bel F. Cerebral oxygenation and oxygen extraction in the preterm infant during desaturation: effects of increasing FiO(2) to assist recovery. Neonatology. 2011; 99(1):65-72. Epub 2010 Jul 15.

Bailey SM, Hendricks-Muñoz KD, Wells JT, Mally P. Packed red blood cell transfusion increases regional cerebral and splanchnic tissue oxygen saturation in anemic symptomatic preterm infants. Am J Perinatol. 2010 Jun;27(6):445-53. Epub 2010 Jan 22.

Bartocci M, Bergqvist LL, Lagercrantz H, Anand KJ. Pain activates cortical areas in the preterm newborn brain. Pain. 2006 May;122(1-2):109-17. Epub 2006 Mar 13.

Bartocci M, Winberg J, Papendieck G, Mustica T, Serra G, Lagercrantz H. Cerebral hemodynamic response to unpleasant odors in the preterm newborn measured by near-infrared spectroscopy. Pediatr Res. 2001 Sep; 50(3):324- 30.

Baserga MC, Gregory GA, Sola A. Cerebrovascular response in small preterm infants during routine nursery gavage feedings. Biol Neonate. 2003;83(1):12-8.

Begum EA, Bonno M, Ohtani N, Yamashita S, Tanaka S, Yamamoto H, Kawai M, Komada Y. Cerebral oxygenation responses during kangaroo care in low birth weight infants. BMC Pediatr. 2008 Nov 7;8:51.

Benni PB, Chen B, Dykes FD, Wagoner SF, Heard M, Tanner,AJ, Young TL, Rais-Bahrami K, Rivera O, Short BL. *Validation of the CAS neonatal NIRS system by monitoring vv-ECMO patients: preliminary results.* Adv Exp Med Biol. 2005;566:195-201.

Bray M, Stucchi I, Fumagalli M, Pugni L, Ramenghi L, Agosti M, Mosca F. Blood withdrawal and infusion via umbilical catheters: effect on cerebral perfusion and influence of ibuprofen. Biol Neonate. 2003;84(3):187-93.

Caicedo A, De Smet D, Vanderhaegen J, Naulaers G, Wolf M, Lemmers P, Van Bel F, Ameye L, Van Huffel S. Impaired cerebral autoregulation using near-infrared spectroscopy and its relation to clinical outcomes in premature infants. Adv Exp Med Biol. 2011; 701:233-9

Cantagrel S, Cloarec S, Suc AL, Chamboux C, Tessier V, Saliba E, Laugier J. Consequences of pulmonary inflations (sighs) on cerebral haemodynamics in neonates ventilated by high-frequency oscillation. Acta Paediatr. 1999 Sep;88(9):1004-8.

Cohn SM et al. NIRS in resuscitation. J Trauma 2003:54;S199-S202.

Cortez J, Gupta M, Amaram A, Pizzino J, Sawhney M, Sood BG. Noninvasive evaluation of splanchnic tissue oxygenation using near-infrared spectroscopy in preterm neonates. J Matern Fetal Neonatal Med. 2011 Apr; 24(4):574-82. Epub 2010 Sep 9

Dani C et al. 2007 Brain haemodynamic effects of nasal CPAP in preterm infants of less than 30 weeks gestation. Acta Pediatrica ISSN 0803-5253n.pdf

Dani C, Bertini G, Pezzati M, Pratesi S, Filippi L, Tronchin M, Rubaltelli FF. Brain hemodynamic effects of doxapram in preterm infants. Biol Neonate. 2006;89(2):69-74. Epub 2005 Sep 12.

Dani C, Pratesi S, Fontanelli G, Barp J, Bertini G. Blood transfusions increase cerebral, splanchnic, and renal oxygenation in anemic preterm infants. Transfusion. 2010 Jun; 50(6):1220-6. Epub 2010 Jan 22

Dave V, Brion LP, Campbell DE, Scheiner M, Raab C, Nafday SM. Splanchnic tissue oxygenation, but not brain tissue oxygenation, increases after feeds in stable preterm neonates tolerating full bolus orogastric feeding. J Perinatol. 2009 Mar;29(3):213-8. Epub 2008 Nov 20

Dave V, Brion LP, Campbell DE, Scheiner M, Raab C, Nafday SM. Splanchnic tissue oxygenation, but not brain tissue oxygenation, increases after feeds in stable preterm neonates tolerating full bolus orogastric feeding. J Perinatol. 2009 Mar;29(3):213-8. Epub 2008 Nov 20.

De Smet D, Jacobs J, Ameye L, Vanderhaegen J, Naulaers G, Lemmers P, van Bel F, Wolf M, Van Huffel S. The partial coherence method for assessment of impaired cerebral autoregulation using near-infrared spectroscopy: potential and limitations. Adv Exp Med Biol. 2010; 662:219-24.

Delpy DT, Cope MC, Cady EB, Wyatt JS, Hamilton PA, Hope PL, Wray S, Reynolds EO. Cerebral monitoring in newborn infants by magnetic resonance and near infrared spectroscopy. Scand J Clin Lab Invest Suppl. 1987;188:9-17.

Dotta A et al. 2005 Effects of surgical repair of congenital diaphragmatic hernia on cerebral hemodynamics evaluated by NIRS. J Ped Surg 40; 1748-1752

Dullenkopf A et al. 2003 measurement of cerebral oxygenation state in anesthetized children using the INVOS 5100 cerebral oximeter. Ped Anesth 13; 384-391.pdf

Dullenkopf A et al. 2003 measurement of cerebral oxygenation state in anesthetized children using the INVOS 5100 cerebral oximeter. Ped Anesth 13; 384-391

Edwards AD, Wyatt JS, Richardson C, Delpy DT, Cope M, Reynolds EO. Cotside measurement of cerebral blood flow in ill newborn infants by near infrared spectroscopy. Lancet. 1988 Oct 1;2(8614):770-1.

Elwell CE, Henty JR, Leung TS, Austin T, Meek JH, Delpy DT, Wyatt JS. Measurement of CMRO2 in neonates undergoing intensive care using near infrared spectroscopy. Adv Exp Med Biol. 2005;566:263-8.

Fahnenstich H et al Relative changes in oxyhemoglobin, deoxyhemoglobin and intracranial blood volume during surfactant replacement therapy in infants with respiratory distress syndrome. Dev Pharmacol Ther. 1991; 17(3-4):150-3.

Feng W et al. 2001 Influence of overlying tissue and probe geometry on the sensitivity of a NIR tissue oximeter. Physiol Measures 22; 201-208.pdf

Ferrari M et al. 2004 Principles, techniques and limitations of NIRS. Can J Appl Physiol 29; 463-487.

Fuchs E, 2011 Brain oxygenation monitoring during neonatal resuscitation of very low birth weight infants, Journal of Perinatology advance online publication 18 August 2011; doi: 10.1038/jp.2011.110

Gilmore MM, Stone BS, Shepard JA, Czosnyka M, Easley RB, Brady KM·Relationship between cerebrovascular dysautoregulation and arterial blood pressure in the premature infant. *Journal of Perinatology* (2011) 31, 722–729; doi:10.1038/jp.2011.17; published online 3 March 2011

Gillam-Krakauer M. et al Abdominal Near-Infrared Spectroscopy Measurements Correlate with Superior Mesenteric Artery Doppler Ultrasound in Very Preterm Infants, PAS 2011, E-PAS20111421.216

Greisen G, Borch K. White matter injury in the preterm neonate: the role of perfusion. *Dev Neurosci* 2001; 23: 209–212.2005

Greisen G et al , Has the time come to use near-infrared spectroscopy as a routine clinical tool in preterm infants undergoing intensive care? Phil. Trans. R. Soc. *A* (2011) 369, 4440–4451 doi:10.1098/rsta.2011.0261

Hahn GH, Christensen KB, Leung TS, Greisen G. Precision of coherence analysis to detect cerebral autoregulation by near-infrared spectroscopy in preterm infants. J Biomed Opt. 2010 May-Jun; 15(3):037002.

Hess JR. Seeing red. Transfusion. 2010 Jun;50(6):1170-2. [Link to PubMed for fulltext: PMID: 20598099.

Hoffman GM et al. 2003 Two-site NIRS transcutaneous oximetry as a non-invasive indicator of mixed venous oxygen saturation in cardiac neonates. Anesthesiology 99; A1393

Hoffman GM et al. 2004.NIRS-Derived Somatic and Cerebral Saturation Difference Provides Non-Invasive Real-Time Hemodynamic Assessment of Cardiogenic Shock and Riskof Anaerobic Metabolism Anesthesiology 2004; 101: A1448

Hoffman GM et al.2007 NONINVASIVE MONITORING OF CARDIAC OUTPUT: BENEFITS OFNIRS TECHNOLOGY Congenital CardToday - Cardiac Output 0607

Hoffman GM et al. 2005 Differential effects of carbon dioxide tension on cerebral and somatic oxygenation assessed by NIRS. Anesthesiology 103; A1374.

Holsti L, Grunau RE, Shany E. Assessing pain in preterm infants in the neonatal intensive care unit: moving to a 'brain-oriented' approach. Pain Manag. 2011 Mar 1; 1(2):171-179

Hou X et al. 2007 Research on the relationship between brain anoxia at different regional oxygen saturations and brain damage using NIRS. Physiol Measures 28; 1251-1265

Hüning BM, Asfour B, König S, Hess N, Roll C. Cerebral blood volume changes during closure by surgery of patent ductus arteriosus. Arch Dis Child Fetal Neonatal Ed. 2008 Jul;93(4):F261-4. Epub 2008 Feb 5.

Hüning BM, Horsch S, Roll C. Blood sampling via umbilical vein catheters decreases cerebral oxygenation and blood volume in preterm infants. Acta Paediatr. 2007 Nov;96(11):1617-21.

Johnson BA 2009 Near-Infrared Spectroscopy in Neonates Before

Keating P, Verhagen E, van Hoften J, ter Horst H, Bos AF. Effect of indomethacin infused over 30 minutes on cerebral fractional tissue oxygen extraction in preterm newborns with a patent ductus arteriosus. Neonatology.2010;98(3):232-7. Epub 2010 Apr 13

Kohlhauser C et al. 2000 Effects of Endotracheal Suctioning on NIRS - Ped Pulmon 29; 270-275

Kurth CD et al. 1995 A dynamic phantom brain model for NIRS. Phys Med Biol 40; 2079-2092.

Kurth CD et al. 2001 Cerebral oxygen saturation before congenital heart surgery. Ann Thorac Surg 72; 187-192

Lemmers PM, Molenschot MC, Evens J, Toet MC, van Bel F. Is cerebral oxygen supply compromised in preterm infants undergoing surgical closure for patent ductus arteriosus? Arch Dis Child Fetal Neonatal Ed. 2010 Nov;95(6):F429-34. Epub 2010 Jun 28.

Lemmers PM, Toet M, van Schelven LJ, van Bel F. Cerebral oxygenation and cerebral oxygen extraction in the preterm infant: the impact of respiratory distress syndrome. Exp Brain Res. 2006 Aug; 173(3):458-67. Epub 2006 Feb 28

Lemmers PM, Toet MC, van Bel F. Impact of patent ductus arteriosus and subsequent therapy with indomethacin on cerebral oxygenation in preterm infants. Pediatrics. 2008 Jan;121(1):142-7

Lemmers PM, van Bel F. Left-to-right differences of regional cerebral oxygen saturation and oxygen extraction in preterm infants during the first days of life. Pediatr Res. 2009 Feb;65(2):226-30

Lemmers PMA, Toet M, van Schelven LJ, van Bel F. Cerebral oxygenation and cerebral oxygen extraction in the preterm infant: the impact of respiratory distress syndrome. *Exp Brain Res* 2006; 173: 458–467.

Li J, Zhang G, Holtby H, Guerguerian AM, Cai S, Humpl T, Caldarone CA, Redington AN, Van Arsdell GS. The influence of systemic hemodynamics and oxygen transport on cerebral oxygen saturation in neonates after the Norwood procedure. J Thorac Cardiovasc Surg. 2008 Jan;135(1):83-90, 90.e1-2.

Liao SM, Gregg NM, White BR, Zeff BW, Bjerkaas KA, Inder TE, Culver JP. Neonatal hemodynamic response to visual cortex activity: high-density near-infrared spectroscopy study. J Biomed Opt. 2010 Mar-Apr;15(2):026010

Limperopoulos C, Gauvreau KK, O'Leary H, Moore M, Bassan H, Eichenwald EC, Soul JS, Ringer SA, Di Salvo DN, du Plessis AJ. Cerebral hemodynamic changes during intensive care of preterm infants. Pediatrics. 2008 Nov;122(5):e1006-13. Epub 2008 Oct 17.

Madsen PL et al. 2000 Interference of Cerebral NIR in patients with Icterus Anesth and Analgesia 90 489-93.pdf

McNeill S, Gatenby JC, McElroy S, Engelhardt B. Normal cerebral, renal and abdominal regional oxygen saturations using near-infrared spectroscopy in preterm infants. J Perinatol. 2011 Jan; 31(1):51-7. Epub 2010 Jun 10.

McQuillen PS, Nishimoto MS, Bottrell CL, Fineman LD, Hamrick SE, Glidden DV, Azakie A, Adatia I, Miller SP. Regional and central venous oxygen saturation monitoring following pediatric cardiac surgery: concordance and association with clinical variables. Pediatr Crit Care Med. 2007 Mar;8(2):154-60.

Meek JH, Tyszczuk L, Elwell CE, Wyatt JS. Cerebral blood flow increases over the first three days of life in extremely preterm neonates. Arch Dis Child Fetal Neonatal Ed. 1998 Jan; 78(1):F33-7

Meier SD, Eble BK, Stapleton GE, Morales DL, Chang AC, Andropoulos DB. Mesenteric oxyhemoglobin desaturation improves with patent ductus arteriosus ligation. J Perinatol. 2006 Sep;26(9):562-4.

Meier SD, Eble BK, Stapleton GE, Morales DL, Chang AC, Andropoulos DB. Mesenteric oxyhemoglobin desaturation improves with patent ductus arteriosus ligation. J Perinatol. 2006 Sep; 26(9):562-4.

Menke J et al. 2003 Reproducability of NIRS in neonates - Biol Neonate 83; 6-11

Morren G, Naulaers G, Lemmerling P, Van Huffel S, Casaer P, Devlieger H. Quantitation of the concordance between cerebral intravascular oxygenation and mean arterial blood pressure for the detection of impaired autoregulation. Adv Exp Med Biol. 2003;510:403-8.

Mott AR, Alomrani A, Tortoriello TA, Perles Z, East DL, Stayer SA. Changes in cerebral saturation profile in response to mechanical ventilation alterations in infants with bidirectional superior cavopulmonary connection. Pediatr Crit Care Med. 2006 Jul;7(4):346-50.

Munro MJ, Walker AM, Barfield CP. Hypotensive extremely low birth weight infants have reduced cerebral blood flow. Pediatrics. 2004 Dec;114(6):1591-6. Erratum in: Pediatrics. 2005 Jun;115(6):1794-5

Nagdyman N, Fleck T, Barth S, Abdul-Khaliq H, Stiller B, Ewert P, Huebler M, Kuppe H, Lange PE. Relation of cerebral tissue oxygenation index to central venous oxygen saturation in children. Intensive Care Med. 2004 Mar;30(3):468-71. Epub 2004 Jan 13

Naulaers G, Delanghe G, Allegaert K, Debeer A, Cossey V, Vanhole C, Casaer P, Devlieger H, Van Overmeire B. Ibuprofen and cerebral oxygenation and circulation. Arch Dis Child Fetal Neonatal Ed. 2005 Jan; 90(1):F75-6.

Naulaers G, Morren G, Van Huffel S, Casaer P, Devliegar H. Cerebral tissue oxygenation index in very premature infants. *Arch Dis Child Fetal Neonatal Ed* 2002; 87: F189–F192.

Noone MA, Sellwood M, Meek JH, Wyatt JS. Postnatal adaptation of cerebral blood flow using near infrared spectroscopy in extremely preterm infants undergoing high-frequency oscillatory ventilation. Acta Paediatr. 2003 Sep;92(9):1079-84.

O'Leary H, Gregas MC, Limperopoulos C, Zaretskaya I, Bassan H, Soul JS, Di Salvo DN, du Plessis AJ. Elevated cerebral pressure passivity is associated with prematurity-related intracranial hemorrhage. Pediatrics. 2009 Jul;124(1):302-9.

Ozawa M, Kanda K, Hirata M, Kusakawa I, Suzuki C. Influence of repeated painful procedures on prefrontal cortical pain responses in newborns. Acta Paediatr. 2011 Feb; 100(2):198-203. doi: 10.1111/j.1651-2227.2010.02022.x. Epub 2010 Oct 8.

Palliation of Hypoplastic Left Heart Syndrome Ann Thorac Surg 2009;87:571–9)

Payer C, Urlesberger B, Pauger M, Müller W. Apnea associated with hypoxia in preterm infants: impact on cerebral blood volume. Brain Dev. 2003 Jan;25(1):25-31.

Pellicer A, Valverde E, Elorza MD, Madero R, Gayá F, Quero J, Cabañas F. Cardiovascular support for low birth weight infants and cerebral hemodynamics: a randomized, blinded, clinical trial. Pediatrics. 2005 Jun;115(6):1501-12.

Pichler G, Schmölzer G, Müller W, Urlesberger B. Body position-dependent changes in cerebral hemodynamics during apnea in preterm infants. Brain Dev. 2001 Oct;23(6):395-400.

Pichler G, Urlesberger B, Schmölzer G, Müller W. Effect of tilting on cerebral haemodynamics in preterm infants with periventricular leucencephalomalacia. Acta Paediatr. 2004 Jan; 93(1):70-5.

Pichler G, van Boetzelar MC, Müller W, Urlesberger B. Effect of tilting on cerebral hemodynamics in preterm and term infants. Biol Neonate. 2001;80(3):179-85.

Rais-Bahrami K et al. 2006 Validation of a noninvasive neonatal cerebral oximeter in venous-venous ECMO patients. J Perinatol 26 628-635

Redlin M, Koster A, Huebler M, Boettcher W, Nagdyman N, Hetzer R, Kuppe H, Kuebler WM. Regional differences in tissue oxygenation during cardiopulmonary bypass for correction of congenital heart disease in neonates and small infants: relevance of near-infrared spectroscopy. J Thorac Cardiovasc Surg. 2008 Oct;136(4):962-7.

Roche-Labarbe N, Carp SA, Surova A, Patel M, Boas DA, Grant PE, Franceschini MA. Noninvasive optical measures of CBV, StO(2), CBF index, and rCMRO(2) in human premature neonates' brains in the first six weeks of life. Hum Brain Mapp. 2010 Mar; 31(3):341-52. Erratum in: Hum Brain Mapp. 2011 Jul; 32(7):1179.

Roll C, Hüning B, Käunicke M, Krug J, Horsch S. Umbilical artery catheter blood sampling volume and velocity: impact on cerebral blood volume and oxygenation in very-low-birthweight infants. Acta Paediatr. 2006 Jan;95(1):68-73.

Schrod L, Walter J. Effect of head-up body tilt position on autonomic function and cerebral oxygenation in preterm infants. Biol Neonate. 2002;81(4):255-9.

Schulz G, Keller E, Haensse D, Arlettaz R, Bucher HU, Fauchère JC. Slow blood sampling from an umbilical artery catheter prevents a decrease in cerebral oxygenation in the preterm newborn. Pediatrics. 2003 Jan;111(1):e73-6.

Seri I. Management of hypotension and low systemic blood flow in the very low birth weight neonate during the first postnatal week. *Journal of Perinatology* (2006) 26, S8–S13.

Slater R, Cantarella A, Gallella S, Worley A, Boyd S, Meek J, Fitzgerald M. Cortical pain responses in human infants. J Neurosci. 2006 Apr 5;26(14):3662-6.

Slater R, Fitzgerald M, Meek J. Can cortical responses following noxious stimulation inform us about pain processing in neonates? Semin Perinatol. 2007 Oct;31(5):298-302. Review.

Sorensen LC, Greisen G. The brains of very preterm newborns in clinically stable condition may be hyperoxygenated. Pediatrics. 2009 Nov;124(5):e958-63. Epub 2009 Oct 19.

Sorensen LC, Leung TS, Greisen G. Comparison of cerebral oxygen saturation in premature infants by near-infrared spatially resolved spectroscopy: observations on probe-dependent bias. J Biomed Opt. 2008 Nov-Dec; 13(6):064013

Soul JS, Hammer PE, Tsuji M, Saul JP, Bassan H, Limperopoulos C, Disalvo DN, Moore M, Akins P, Ringer S, Volpe JJ, Trachtenberg F, du Plessis AJ. Fluctuating pressure-passivity is common in the cerebral circulation of sick premature infants. Pediatr Res. 2007 Apr;61(4):467-73.

Takami T, Sunohara D, Kondo A, Mizukaki N, Suganami Y, Takei Y, Miyajima T, Hoshika A. Changes in cerebral perfusion in extremely LBW infants during the first 72 h after birth. Pediatr Res. 2010 Nov; 68(5):435-9.

Tobias JD. Cerebral oximetry using near-infrared spectroscopy aids in the diagnosis of interrupted aortic arch. J Intensive Care Med. 2008 Sep-Oct;23(5):335-7.

Toet Mona C. Cerebral Oxygenation and Electrical Activity After Birth Asphyxia: Their Relation to Outcome *Pediatrics* 2006; 117;333-339

Tracy MB, Klimek J, Hinder M, Ponnampalam G, Tracy SK. Does caffeine impair cerebral oxygenation and blood flow velocity in preterm infants? Acta Paediatr. 2010 Sep; 99(9):1319-23. doi: 10.1111/j.1651-2227.2010.01828.x.

Tsuji M 2000 Cerebral intravascular oxygenation correlates with mean arterial pressure in critically ill premature infants. Pediatrics 106; 625-632.

Underwood MA, Milstein JM, Sherman MP. Near-infrared spectroscopy as a screening tool for patent ductus arteriosus in extremely low birth weight infants. Neonatology. 2007;91(2):134-9. Epub 2006 Nov 20.

Urlesberger B J et al. Regional Oxygen Saturation of the Brain and Peripheral Tissue during Birth Transition of Term Infants Pediatrics 2010 epub[1].

van Alfen-van der Velden AA, Claessen VP, Hopman JC, Klaessens JH, Sengers RC, Liem KD. Changes in cerebral oxygenation and hemodynamics during cranial ultrasound in preterm infants. Brain Dev. 2009 Jun;31(6):427-34. Epub 2008 Oct 5.

van Alfen-van der Velden AA, Hopman JC, Klaessens JH, Feuth T, Sengers RC, Liem KD. Effects of midazolam and morphine on cerebral oxygenation and hemodynamics in ventilated premature infants. Biol Neonate. 2006;90(3):197-202. Epub 2006 May 22.

van Bel F et al. 2008 Monitoring Neonatal Regional Cerebral Oxygen Saturation in Clinical Practice: Value and Pitfalls. Neonatology 2008; 94:237–244 DOI: 10.1159/000151642

van den Berg E, Lemmers PM, Toet MC, Klaessens JH, van Bel F. Effect of the "InSurE" procedure on cerebral oxygenation and electrical brain activity of the preterm infant. Arch Dis Child Fetal Neonatal Ed. 2010 Jan;95(1):F53-8. Epub 2009 Aug 13.

van Hoften JC, Verhagen EA, Keating P, ter Horst HJ, Bos AF. Cerebral tissue oxygen saturation and extraction in preterm infants before and after blood transfusion. Arch Dis Child Fetal Neonatal Ed. 2010 Sep; 95(5):F352-8. Epub 2010 May 13

Vanderhaegen J, De Smet D, Meyns B, Van De Velde M, Van Huffel S, Naulaers G. Surgical closure of the patent ductus arteriosus and its effect on the cerebral tissue oxygenation. Acta Paediatr. 2008 Dec;97(12):1640-4. Epub 2008 Sep 11.

Vanderhaegen J, Naulaers G, Van Huffel S, Vanhole C, Allegaert K. Cerebral and systemic hemodynamic effects of intravenous bolus administration of propofol in neonates. Neonatology. 2010 Jun;98(1):57-63. Epub 2009 Dec 24.

Vanderhaegen J, Naulaers G, Vanhole C, De Smet D, Van Huffel S, Vanhaesebrouck S, Devlieger H. The effect of changes in tPCO2 on the fractional tissue oxygen extraction--as measured by near-infrared spectroscopy--in neonates during the first days of life. Eur J Paediatr Neurol. 2009 Mar;13(2):128-34. Epub 2008 Jul 10.

Vanderhaegen J, Vanhaesebrouck S, Vanhole C, Casaer P, Naulaers G. The effect of glycaemia on the cerebral oxygenation in very low birthweight infants as measured by near-infrared spectroscopy. Adv Exp Med Biol. 2010;662:461-6.

Verhagen EA, Keating P, ter Horst HJ, Martijn A, Bos AF. Cerebral oxygen saturation and extraction in preterm infants with transient periventricular echodensities. Pediatrics. 2009 Jul;124(1):294-301

Verhagen EA, Ter Horst HJ, Keating P, Martijn A, Van Braeckel KN, Bos AF. Cerebral oxygenation in preterm infants with germinal matrix-intraventricular hemorrhages. Stroke. 2010 Dec; 41(12):2901-7. Epub 2010 Oct 21.

www.ninds.nih.gov/news_and_events/proceedings/nirsworkshop1999.htm

Wassenaar EB et al. 2005 Reliability of NIRS in people with dark skin pigmentation. J Clin Monitoring and Computing 19; 195-199.pdf

Weiss M 2005 NIRS Cerebral Oxygenation Reading in Neonates and Infants and SvO2 - Ped Anesth 15; 102-109.pdf(Validation)

Wider M. Hemodynamic Management and Regional Hemoglobin Oxygen Saturation (rSO2) of the Brain, Kidney and Gut, Neonatal Intensive Care, Vol. 22 No. 5, September 2009

Wolf M, Greisen G. Advances in near-infrared spectroscopy to study the brain of the preterm and term neonate. Clin Perinatol. 2009 Dec; 36(4):807-34

Wolf M, Greisen G. Advances in near-infrared spectroscopy to study the brain of the preterm and term neonate. Clin Perinatol. 2009 Dec;36(4):807-34, vi. Review.

Wong FY, Barfield CP, Horne RS, Walker AM. Dopamine therapy promotes cerebral flow-metabolism coupling in preterm infants. Intensive Care Med. 2009 Oct;35(10):1777-82. Epub 2009 Aug 1.

Wong FY, Leung TS, Austin T, Wilkinson M, Meek JH, Wyatt JS, Walker AM. Impaired autoregulation in preterm infants identified by using spatially resolved spectroscopy. Pediatrics. 2008 Mar;121(3):e604-11. Epub 2008 Feb 4

Yamamoto A, Yokoyama N, Yonetani M, Uetani Y, Nakamura H, Nakao H. Evaluation of change of cerebral circulation by SpO2 in preterm infants with apneic episodes using near infrared spectroscopy. Pediatr Int. 2003 Dec; 45(6):661-4.

Yanowitz TD, Potter DM, Bowen A, Baker RW, Roberts JM. Variability in cerebral oxygen delivery is reduced in premature neonates exposed to chorioamnionitis. Pediatr Res. 2006 Feb;59(2):299-304.

Zaramella P, Freato F, Grazzina N, Saraceni E, Vianello A, Chiandetti L. Does helmet CPAP reduce cerebral blood flow and volume by comparison with Infant Flow driver CPAP in preterm neonates? Intensive Care Med. 2006 Oct;32(10):1613-9. Epub 2006 Aug 1.

Zaramella P, Freato F, Quaresima V, Ferrari M, Bartocci M, Rubino M, Falcon E, Chiandetti L. Surgical closure of patent ductus arteriosus reduces the cerebral tissue oxygenation index in preterm infants: a near-infrared spectroscopy and Doppler study. Pediatr Int. 2006 Jun;48(3):305-12.

2

Effects of Sleep Debt on Cognitive Performance and Prefrontal Activity in Humans

Kenichi Kuriyama and Motoyasu Honma
Department of Adult Mental Health,
National Institute of Mental Health,
National Center of Neurology and Psychiatry
Japan

1. Introduction

Functional neuroimaging is universally recognized to be a remarkably effective modality for exploring precise brain function. Functional magnetic resonance imaging (fMRI) and positron-emission tomography (PET) are among the most widely used neuroimaging techniques; however, their invasiveness in terms of, for example, exposure to high magnetic fields or radiation, or restriction of body movement during the examination, makes their application difficult in infants, children, and some subjects with an atypical condition.

Near infrared spectroscopy (NIRS), on the other hand, is an alternative neuroimaging modality that is suitable for use with most individuals due to its non-invasive nature. It measures local cortical activity during brain activation. Although NIRS has several limitations compared with fMRI and PET, it is an appropriate and feasible method to use with infants, children, and other subjects such as those who suffer from loss of sleep. Naturally, sleep loss raises some problems related to the subject keeping still yet awake during the examination, but otherwise is a good option. The effects of sleep loss on local cortical activities associated with certain cognitive functioning as assessed by NIRS are the topic of this chapter.

2. Utilization of NIRS for functional brain imaging

Information processing in the brain occurs via two different systems, a neuroelectric transmission system and an energy-supplying system to neurons (Guiou et al., 2005). Nutrient arteries around the neurons supply them with blood containing the oxygen and glucose necessary for neural activity. Thus, changes in the ratio of oxygenated hemoglobin (oxy-Hb) to deoxygenated hemoglobin (deoxy-Hb) due to increased blood flow for such activity should be observable in tissues adjacent to the activated neurons. This relationship between neural activity and subsequent changes in cerebral blood flow is known as neurovascular coupling (Guiou et al., 2005; Rasmussen et al., 2009).

Similar to fMRI and PET, NIRS indirectly measures local cortical activity in vivo by measuring the differential concentration between oxy- and deoxy-Hb in the blood vessels. Specifically, it measures the difference in the absorption rate of near-infrared light by oxy-

and deoxy-Hb, and the scalp and skull are high permeable to near-infrared light (Obrig et al., 2000). When such light is locally irradiated from an irradiation probe, it diffuses in the cerebral tissue up to a depth of 20-30 mm. A detection probe located 30 mm from the irradiation probe can detect the light diffusely reflected by the oxy- or deoxy-Hb, making it possible to estimate local changes in oxy-, deoxy- and total-Hb concentrations (Ferrari et al., 2004). For high-resolution detection of oxy- and deoxy-Hb concentrations, multiple channels of wavelengths (2 or 3) of near-infrared light (700-1000 nm) are usually simultaneously irradiated and detected.

NIRS has been widely used for several years in medical and biological studies of the brain. Although NIRS uses an accessible, non-invasive neuroimaging device, it should be applied to measure local cerebral metabolic rate of oxygen consumption with consideration given to its strong and weak points, which are listed in Table 1.

Strengths (compared with MRI or PET)
• **inexpensive**
• **high portability**
• **easy-to-use approach**
• **high tolerance to body movements**
• **high temporal resolution (10 Hz or less)**
• **high tolerance to long-time measurements**
• **utility regardless of subject's posture**
• **independence of a specific measurement setting**
Weaknesses (compared with MRI or PET)
• **low spatial resolution**
• **difficulty in strict identification of anatomic locations**
• **narrow range of measurement (only cortical surface)**
• **relative quantitation (not absolute quantitation)**

Table 1. Strengths and weaknesses of NIRS

3. Effects of sleep loss on cognition

Although what constitutes sufficient quality and quantity of sleep per day remains a subject of debate due to its the wide interindividual variability and age-related differences, it has been elucidated that sleep loss deteriorates various cognitive functions, whether due to partial or total sleep deprivation and chronic or acute sleep disturbance. Loss of sleep also impairs the activities of various cerebral regions or neural networks associated with ongoing cognitive performance. A recent study in rats suggested that sleep loss often elicits periods of local sleep, in which some neurons often go 'offline' briefly in one cortical area but not in another during long periods of wakefulness (Vyazovskiy, 2011). Several basic cognitive functions are vulnerable to sleep loss in humans. These include simple response speed (Buysse et al., 2005; Frey et al., 2004; Koslowsky & Babkoff, 1992), psychomotor vigilance (Blatter et al., 2005; Doran et al., 2001; Drake et al., 2001; Van Dongen et al., 2003), mental arithmetic (Frey et al., 2004; Stenuit & Kerkhofs, 2008; Van Dongen et al., 2003;), response inhibition (Drummond et al., 2006; Stenuit & Kerkhofs, 2008), problem solving (Killgore et al., 2008; Nilsson et al., 2005), and short-time perception (Soshi et al., 2010). However, the

performance of executive functions, one of the higher cognitive functions that includes divided attention (Drake et al., 2001; Frey et al., 2004; Lim & Dings, 2010; Stenuit & Kerkhofs, 2008) and working memory (Bartel et al., 2004; Binks et al., 1999; Choo et al., 2005; Frey et al., 2004; Lim & Dings, 2010; Tucker et al., 2010; Wimmer et al., 1992) varies among studies; some report a significant effect of sleep loss (Bartel et al., 2004; Choo et al., 2005; Drake et al., 2001; Frey et al., 2004; Stenuit & Kerkhofs, 2008), while others report no such effect (Binks et al., 1999; Lim & Dings, 2010; Tucker et al., 2010; Wimmer et al., 1992).A discrepancy has also been seen in the influence of sleep loss has on behavioral performance versus its influence on neural activity; functional neuroimaging has revealed that sleep loss deteriorates not behavioral performance but neural activity (Choo et al., 2005). Such a discrepancy could point to a difference in neural substrates between basic and higher cognitive functions and/or possible personal differences in vulnerability of executive functions to sleep loss. We describe here two of our studies conducted using NIRS in order to explore the influence of sleep loss on basic and higher cognition associated with the frontal functions mentioned above.

4. Influence of sleep loss due to total deprivation of a night's sleep on time perception

4.1 Short-time perception

When elapsed time is comparatively brief (within several minutes), humans can typically perceive the passage of time accurately without referring to an artificial time keeping device such as a wristwatch (Ivry, 1996; Rammsayer, 1999; Treisman, 1963). Human short-time perception is modulated by a robust neural basis consisting of subcortical structures, such as the cerebellum and basal ganglia, together with the right prefrontal cortex (Harrington et al., 1998; Pouthas et al., 1999). Moreover, a circadian pacemaker located in the suprachiasmatic nucleus of the hypothalamus, which is driven by a self-sustaining oscillator with a period of about 24 h and provides the time of day, participates in short-time perception (Aschoff, 1998; Ashoff & Daan, 1997; Kuriyama et al., 2003). As such, short-time perception is not independent of the influence of the circadian pacemaker; under a condition where zeitgebers are strictly controlled, short-time perception fluctuates on around a 24-h cycle and correlates with circadian markers such as core body temperature and melatonin, and consequently shows diurnal variation (Kuriyama et al., 2005). It has been confirmed that short-time perception shortens from morning into night, and is prolonged again from night to the next morning under a 30-h constant routine (Kuriyama et al., 2005; see Fig. 1). For sleep deprivation on the other hand, it has been reported that there is less diurnal variation

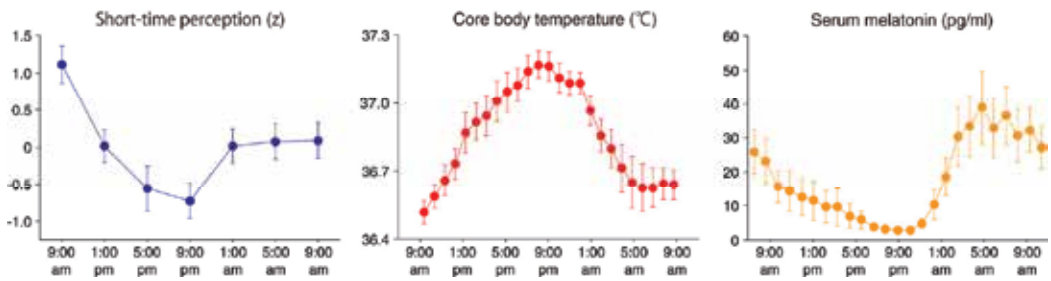

Fig. 1. Diurnal fluctuation of short-time perception

in short-time perception as it is dissociated from endogenous circadian markers (Kuriyama et al., 2005; Soshi et al., 2010). This may be because short-time perception is modulated by the prefrontal cortex (PFC) along with subcortical structures including the circadian pacemaker; it is well known that the PFC is vulnerable to sleep loss, and this vulnerability presumably disturbs short-time perception (Soshi et al., 2010). To elucidate this issue, Soshi et al. (2010) utilized NIRS because it neither produces pulse scanning noise nor requires severe restriction of the subject's body posture nor movements, and thus is unlikely to seriously influence the sleep-deprived condition. It is also suitable for monitoring the subject's condition while performing the experimental tasks.

4.2 Study design

Fourteen healthy male university students participated in a crossover design study conducted over a 4-day period. Subjects performed a 10-s time production (TP) task in sleep controlled (SC) and sleep deprived (SD) conditions, scheduled in random order with a 1-day interval (Fig. 4). On the first day (day 1) NIRS probes were attached to the surface of the scalp. The 15-min TP session in either the SC or SD condition started at 21:00. After the session, in the SC condition, subjects rested without sleep or exercise until 0:00 and then stayed in bed under complete darkness (> 0.1 lux) until 08:00 on day 2; in the SD condition, subjects stayed awake quietly under room light (100 lux) until 08:00 the next morning while being monitored by video. On day 2, the TP session started again at 09:00. All the experiments were performed at a time isolation facility, and the ambient temperature and humidity were maintained constant throughout the study.

TP tasks were arranged in an event-related design to detect the hemodynamic response for a single trial. TP sessions were conducted at 21:00 on day 1 and 09:00 on day 2, corresponding to the expected nadir and peak period of the diurnal variation of TP in subjects with a regular sleep-wake cycle. Each TP session consisted of 15 trials with 30-s inter-trial intervals. Subjects were asked to produce a 10-s interval and to begin and end each trial by pressing a key button (Kuriyama et al., 2003, 2005). Duration from the first to the second button presses was defined as the perceived time.

4.3 NIRS recording and data analysis

Regional hemodynamic changes in brain tissue were monitored throughout the TP sessions by a continuous wave-type NIRS system (FOIRE-3000; Shimazu Co., Tokyo, Japan; Fig. 2) which outputs near-infrared light at three wavelengths (780, 805 and 830 nm). All transmitted intensities of the three wavelengths were recorded every 130 ms at 22 channels in order to estimate concentration changes in oxy-Hb, deoxy-Hb, and total-Hb, based on the modified Beer-Lambert equation as a function of light absorbance of Hb and pathlength. A set of 3×5 probes were utilized, in which light detectors and emitters were alternately positioned at an equal distance of 30 mm. The 22 channels (see Fig. 3) covered the middle and superior PFC regions (BA9, 46, 10).

Oxy-Hb data was chosen to examine event-related responses in the PFC since it is an optimal index for changes in regional cerebral blood flow (Hoshi et al., 2001). We applied a high-pass filter to raw data, re-sampled at 10 Hz, using a low-cutoff frequency of 0.05 Hz. Smoothing was performed by the moving average method (boxcar filter) with a sliding time

Fig. 2. NIRStation FOIRE-3000 (Shimazu Co., Tokyo, Japan)

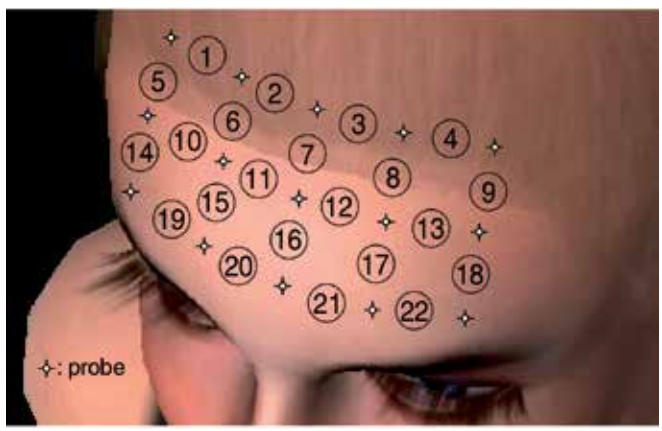

Fig. 3. Schematic layout of NIRS probes with recorded channels on the frontal region

window of 1.1 s. Data were normalized into z-scores to avoid the methodological ambiguity that changes in absolute values of Hb concentration for each recording channel would not be determined because the absolute path lengths of light through the cerebral cortex were not detectable. Concentration changes time-locked to trial onset were extracted from 5 s before to 27 s after the onset, covering a mean produced time of around 11 s and a mean rest interval of around 16 s. A total of 15 epochs were obtained for each experimental day (day 1 or day 2) in each condition (SC or SD). Before individual averaging, baselines were corrected with mean z-scores of 5 s before trial onset. Grand averaged concentration changes in the left anterior PFC (LAPFC) region, based on statistical analyses, were superimposed.

4.4 Effects of sleep loss on short-time perception

Behavioral data suggested that time perception fluctuates through the night to the morning in the SC condition; TP was significantly prolonged from night to the next morning. However, TP was not prolonged from night to the next morning in the SD condition (Fig. 4).

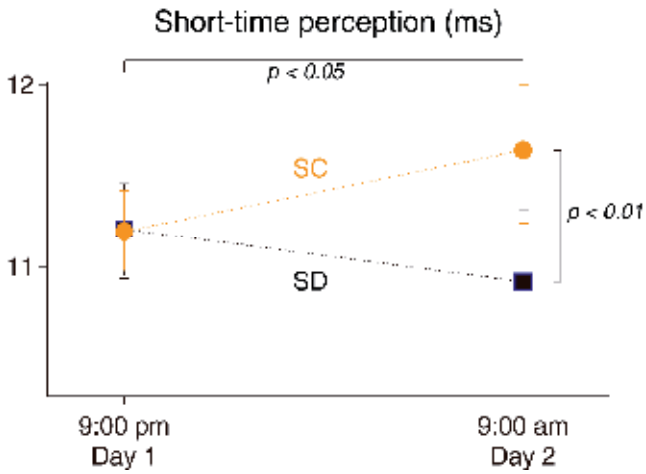

Fig. 4. Sleep deprivation attenuates short-time perception the following morning

It was previously shown that a short-time perception profile exhibits diurnal variation, reaching a peak (the longest produced time) around 09:00 and a nadir (the shortest produced time) around 21:00 with a regular sleep-wake cycle under experimental conditions (Kuriyama et al., 2005). Taken together, circadian oscillation in short-time perception under the SD condition is clearly attenuated.

4.5 Influence of the PFC's vulnerability to sleep loss on short-time perception

Oxy-Hb concentration measured by NIRS suggested that PFC activity in the SD condition, compared with that in the SC condition, was more enhanced in the left hemisphere on day 2. Moreover, enhanced oxy-Hb concentration changes on day 2 in the SD condition, compared with those in the SC condition, were observed in the LAPFC region of interest (ROI) at channels 17, 21, and 22 (Fig. 5).

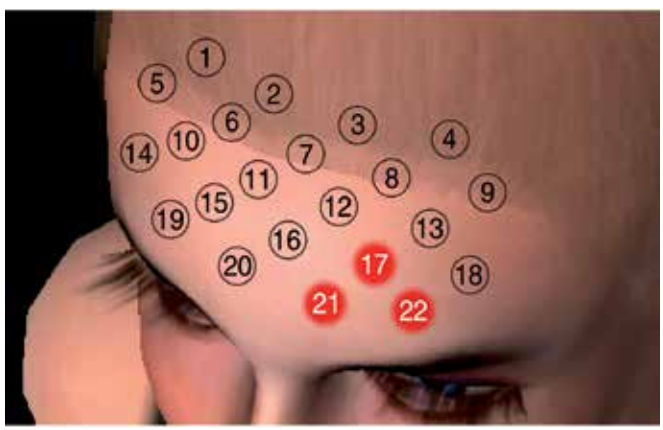

Fig. 5. Left anterior PFC activity during the TP task was enhanced after sleep deprivation

A functional correlation was observed between increased activation of the LAPFC after sleep deprivation and short-time perception, although unlike in previous studies

(Harrington et al., 1998; Pouthas et al., 1999) the present study failed to detect any significant changes in right PFC activity (Soshi et al., 2010). It has also been argued that increased activation of the PFC after sleep deprivation is associated with neural compensation for cognitive function, although TP on day 2 in the SD condition was different from that in the SC condition.

NIRS has a serious shortcoming in that it cannot determine whether or not a subcortical network including the cerebellum and the basal ganglia contributes to attenuating the diurnal fluctuation of short-time perception. If subcortical activities may be altered by sleep deprivation, attenuation of short-time perception possibly reflects subcortical vulnerability, and thus the PFC activity change is possibly only a byproduct.

A temporary decline in the diurnal variation of short-time perception may be important for surviving a crisis, such as in an emergency situation. Time perception in humans should be fundamentally synchronized to the physical state to allow for constant adaptation to the regularity of daily life; however, in times of severe stress, time perception must desynchronize from regular physical homeostasis and be shortened, to enable time expansion and presumably allow us to adopt suitable strategies for coping with the stressful environment by thinking and acting more rapidly than usual. In-depth consideration of the adaptive nature of the PFC function in humans (Duncan, 2001; Miller & Cohen, 2001) suggests that the PFC might play a switch-like role in short-time perception as a situation demands, helping us meet demands for adaptation.

5. Influence of sleep loss due to partial deprivation of a night's sleep on individual differences in working memory performance

5.1 Working memory performance

As already noted in Section 3 concerning the effects of sleep loss on cognition, a discrepancy in the effects that sleep loss has on behavioral performance compared with the effects it has on neural activity has been reported in relation to working memory performance; sleep loss does not deteriorate behavioral performance itself, but rather the neural activity associated with the behavior. Possible interindividual differences in the vulnerability to sleep loss of executive functions, which also play crucial roles in working memory processing, have also been suggested. We explored this issue in a second study using NIRS (Honma et al., 2010).

5.2 Study design

Fifty-five healthy university students (26 males, 29 females) participated in the study. Subjects, who regularly slept 7–9 h in a night, participated in an overnight experiment in a laboratory setting, starting at 22:00 on day 1 and finishing at 10:00 on day 2. Subjects were deprived an average of 2.32 h (29.5%) of sleep by experimental manipulation. Subjects retired to bed at 01:00 in the laboratory and were forcibly awakened at 07:00 am.

A visual *n*-back working memory (WM) task (Callicott et al., 1998, 1999; Gevins & Cutillo, 1993; Kuriyama et al., 2008) with two separate load levels was utilized. For the 0-back task (low-load WM task), subjects had to respond whenever a single-digit number appeared on a screen. For the 2-back task (high-load WM task), they had to press a button on the right when the single-digit number on the screen was identical to that which had appeared last

but one, otherwise to press the button on the left. Each level of task was run in blocks of 12+n stimuli and was conducted two times; thus, 24 responses were obtained at each load level. Average response times (RTs) and correct response rates (%CRs) were evaluated.

Alertness level was evaluated immediately before and after the experiment using the Stanford Sleepiness Scale (SSS; Hoddes et al., 1971). The SSS consists of a 7-point scale ranging from level 1 (feeling active, vital, alert, or wide awake) to level 7 (no longer fighting sleep). Subjects selected the most appropriate level to reflect their present state of alertness. To assess individual ability to overcome sleepiness during WM tasks, change in SSS level was individually calculated by subtracting the post-experiment SSS score from the pre-experiment SSS score.

5.3 NIRS recording and data analysis

Regional hemodynamic changes in brain tissue were monitored throughout the TP sessions by a continuous wave-type NIRS system (ETG-100, Hitachi Medical Co., Tokyo, Japan: Fig. 6), which outputs near-infrared light at two wavelengths (780 and 830 nm). Oxy- and deoxy-Hb concentrations were measured in a manner similar to the short-time perception study (Soshi et al., 2010) described in the preceding section [section 4.3].

Fig. 6. Optical Topography System ETG-100 (Hitachi Medical Co., Tokyo, Japan)

We analyzed oxy-Hb data as a reflection of event-related responses in the PFC. The continuous oxy-Hb data were filtered with band-pass frequencies in the range of 0.01–0.2 Hz and were standardized (z-score). Changes in oxy-Hb concentration time-locked to experimental blocks consisting of 12 trials were extracted for each experimental condition 1000 ms before the onset of the trial block (baseline) to 4400 ms after the onset (2400 ms for the 12-trial duration and 2000 ms for the post-trial interval). Baseline correction of the changes in oxy-Hb concentration was performed utilizing the mean z-scores of 1000 ms prior to the onset of the experimental blocks before individual averaging. Mean z-scores of the changes in oxy-Hb concentration during the 4400 ms period after the beginning of the trial block were utilized for subsequent statistical analysis.

5.4 Influence of the PFC's vulnerability to sleep loss on working memory performance

Twelve of the 55 subjects showed overnight decrements in alertness level as reflected by an increased SSS level (average: 1.41, SD: 0.41), while conversely 17 showed overnight decrements reflected by a decreased SSS level (average: 21.29, SD: 0.49), and 26 showed no change in alertness level. The change in alertness level was negatively correlated with RT on the 2-back task, but not on the 0-back task (Fig. 7), and the change in SSS was not correlated with %CR regardless of the task difficulty.

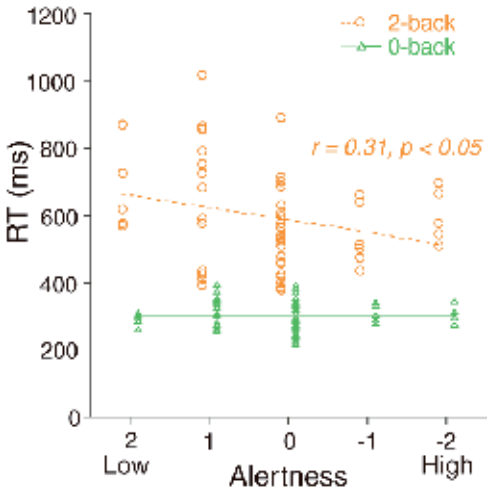

Fig. 7. Correlation of overnight change in alertness level with that in WM performance

Although the subjects had similar sleep-wake habits in daily life and they experienced the same restricted sleep duration on the experimental night, alertness was increased in some subjects but was decreased in others during the WM tasks. This suggests that subjects who improved their alertness—who may have better abilities to overcome sleepiness—showed better performance not on the low-load WM task but on the high-load WM task.

5.5 Relationship between the PFC's vulnerability to sleep loss and working memory processing difficulties

At every channel in the bilateral PFC region, differences in the change in oxy-Hb concentration between the 2- and 0-back tasks positively correlated with overnight change in alertness (Fig. 8), which is in line with previous neuroimaging studies using fMRI (Cohen et al., 1997; Owen et al., 1998) and PET (Owen et al., 1996; Sweeney et al., 1996). On the other hand, change in oxy-Hb concentration in the bilateral PFC region on the 2-back task for some channels (channels 5, 10, 13, and 18) positively correlated with overnight change in alertness (Fig. 9 left), while change on the 0-back task for some channels (channels 10 and 15) in the right PFC region negatively correlated with overnight change in alertness (Fig. 9 right).

The activity in the right prefrontal site corresponding to channel 10 showed an opposite pattern between the 2- and 0-back tasks (Fig. 10), suggesting the ability to conquer sleepiness. This ability might contribute to the function of providing sufficient activity to

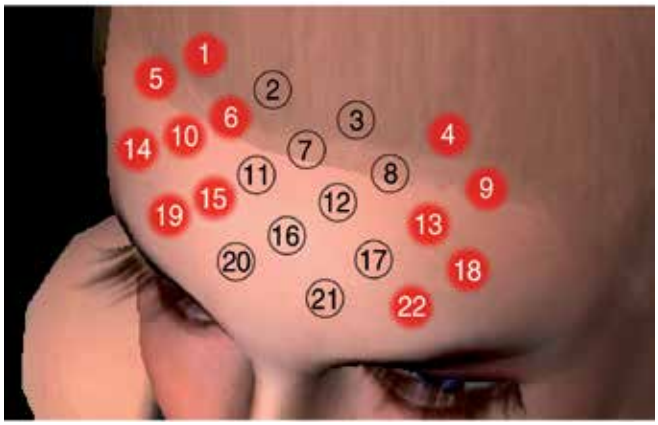

Fig. 8. Significant positive correlation between changes in oxy-Hb concentration and alertness for the difference between the 2- and 0-back tasks

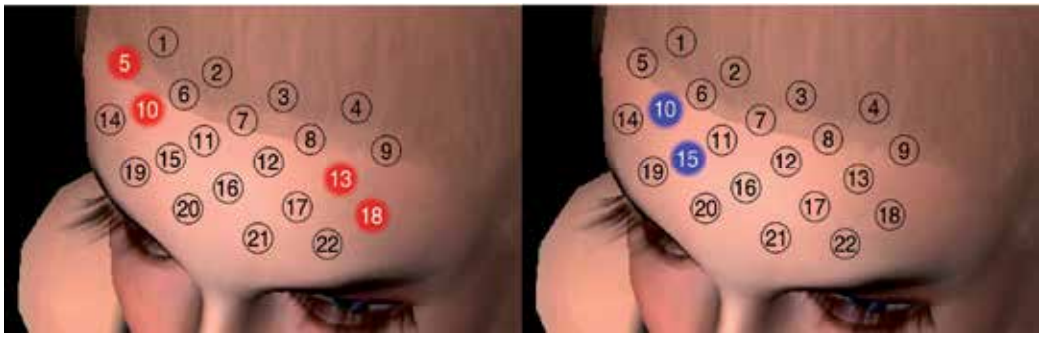

Fig. 9. Correlation between changes in oxy-Hb concentration and alertness on the 2-back task (left panel) and 0-back task (right panel)

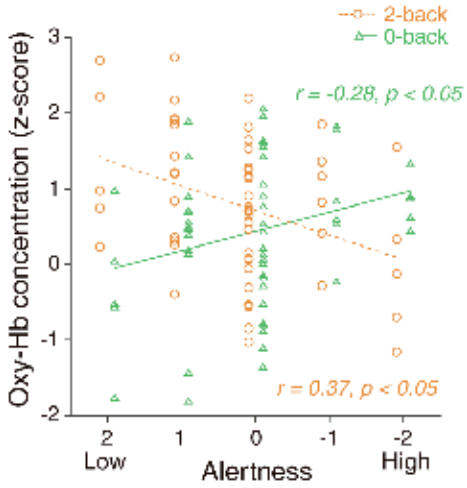

Fig. 10. Correlation between changes in oxy-Hb concentration and alertness on the 2- and 0-back tasks for channel 10

match the demands of a task. In other words, the cortical activity corresponding to channel 10 susceptibly escalates with changes in both alertness and cognitive load, thereby achieving better performance. This site in the right PFC might therefore be related to the ability to conquer sleepiness with cognitive performance.

5.6 Relation between individual differences in the ability to conquer sleepiness during working memory processing and personality traits

We next explored the relationship between activity in the right prefrontal site corresponding to channel 10 and individual personality traits. We assessed personality traits using the revised version of the Neuroticism-Extroversion-Openness Personality Inventory (NEO PI-R) and the Revised Temperament and Character Inventory (TCI, Version 9). NEO PI-R is a 240-item measure of the Five Factor Model: Neuroticism, Extraversion, Openness to experience, Agreeableness, and Conscientiousness (Costa & McCrae, 1995). The TCI, too, is a 240-item measure of the seven dimensions of personality traits: Novelty seeking, Harm avoidance, Reward dependence, Persistence, Self-directedness, Cooperativeness, and Self-transcendence (Cloninger, 1987). Both of these inventories are widely used in biological correlational research in a variety of fields, including psychiatric diagnosis (Cloninger, 1990; Frokjaer et al., 2008), behavior (Grucza et al., 2006; Saggino & Balsamo, 2003), genotyping (Cloninger, 2002; Strobel et al., 2003), and brain activities (Baeken et al., 2009; Villafuerte et al., 2011).

We identified several personality traits that correlated with a difference in activity change between the 2- and 0-back tasks at channel 10. For instance, Neuroticism on the NEO PI-R was positively correlated and Self-directedness on the TCI negatively correlated with a difference in change in oxy-Hb concentration between the two tasks (Yoshiike, Honma & Kuriyama, in preparation). This finding suggests that a stronger tendency for neuroticism and a weaker one for self-directedness may lead to successful performance under sleep loss conditions. Greater neuroticism is sometimes associated with psychiatric problems such as depression or anxiety (Strobel et al., 2003), which reflect poor stress coping mechanisms like avoidance (Andrews et al., 2010). However, within a healthy range, a trait of neuroticism may be beneficial to conquering sleepiness. Moreover, although the concept of self-directedness is based on the "power of will" (i.e., the ability to control oneself to serve the purpose of one's own will), greater self-directedness may, surprisingly, result in succumbing to sleepiness. Chronic insomniacs showed greater neuroticism (van de Laar et al., 2010) and less self-directedness (de Saint Hilaire et al., 2005), suggesting that problems in the right PFC might be associated with the symptoms of insomnia.

6. Conclusion

When the ROI is compatible with the strengths of NIRS, the technique is valuable for investigating human frontal functioning associated with deteriorated cognition caused by sleep loss. Indeed, our studies demonstrated that certain functional differences in the bilateral PFC under sleep loss conditions correspond to certain cognitive tasks.

We can sum up by saying the PFC mediates various cognitive functions, from basic functions such as simple response to stimulus and time perception to higher functions such as working memory including executive functions, to orchestrate perception, memory,

thought, and action in accordance with a given purpose (Halford et al., 2010). The findings discussed here clearly suggest a novel function for the PFC, that of controlling sleepiness and compensating brain function deteriorated by sleep loss.

NIRS is a developing technique and it is expected that its applications will increase to cover other cerebral regions in future and that further noise reductions will improve the technique further: it will undoubtedly provide invaluable information about human cognition and its neural substrates.

7. Acknowledgment

We are grateful to Kazuo Mishima and Takahiro Soshi for cooperating in our research concerning NIRS.

8. References

Andrews, R.M., Browne, A.L., Drummond, P.D., & Wood, F.M. (2010). The impact of personality and coping on the development of depressive symptoms in adult burns survivors. *Burns,* Vol.36, No.1, pp. 29-37, ISSN 0305-4179

Aschoff, J. (1998). Human perception of short and long time intervals: its correlation with body temperature and the duration of wake time. *Journal of Biological Rhythms,* Vol.13, No.5, pp. 437–442, ISSN 0748-7304

Ashoff, J., & Daan, S. (1997). Human time perception in temporal isolation: effects of illumination intensity. *Chronobiology International,* Vol.14, No.6, pp. 585–596, ISSN 0742-0528

Baeken, C., De Raedt, R., Ramsey, N., Van Schuerbeek, P., Hermes, D., Bossuyt, A., Leyman, L., Vanderhasselt, M.A., De Mey, J., & Luypaert, R. (2009). Amygdala responses to positively and negatively valenced baby faces in healthy female volunteers: influences of individual differences in harm avoidance. *Brain Research,* Vol.3, No.1296, pp. 94-103, ISSN 0006-8993

Bartel, P., Offermeier, W., Smith, F., & Becker, P. (2004). Attention and working memory in resident anaesthetists after night duty: group and individual effects. *Occupational and Environmental Medicine,* Vol.61, No.2, pp. 167-170, ISSN 1076-2752

Binks, P.G., Waters, W.F., & Hurry, M. (1999). Short-term total sleep deprivations does not selectively impair higher cortical functioning. *Sleep,* Vol.22, No.3, pp. 328-334, ISSN 0161-8105

Blatter, K., Graw, P., Münch, M., Knoblauch, V., Wirz-Justice, A., & Cajochen, C. (2006). Gender and age differences in psychomotor vigilance performance under differential sleep pressure conditions. *Behavioural Brain Research,* Vol.168, No.2, pp. 312-317, ISSN 0166-4328

Buysse, D.J., Monk, T.H., Carrier, J., & Begley, A. (2005). Circadian patterns of sleep, sleepiness, and performance in older and younger adults. *Sleep,* Vol.28, No.11, pp. 1365-1376, ISSN 0161-8105

Callicott, J.H., Mattay, V.S., Bertolino, A., Finn, K., Coppola, R., Frank, J.A., Goldberg, T.E., & Weinberger, D.R. (1999). Physiological characteristics of capacity constraints in working memory as revealed by functional MRI. *Cerebral Cortex,* Vol.9, No.1, pp. 20–26, ISSN 1047-3211

Callicott, J.H., Ramsey, N.F., Tallent, K., Bertolino, A., Knable, M.B., Coppola, R., Goldberg, T., van Gelderen, P., Mattay, V.S., Frank, J.A., Moonen, C.T., & Weinberger, D.R. (1998). Functional magnetic resonance imaging brain mapping in psychiatry: methodological issues illustrated in a study of working memory in schizophrenia. *Neuropsychopharmacology,* Vol.18, No.3, pp. 186–196, ISSN 0893-133X

Choo, W.C., Lee, W.W., Venkatraman, V., Sheu, F.S., & Chee, M.W. (2005). Dissociation of cortical regions modulated by both working memory load and sleep deprivation and by sleep deprivation alone. *Neuroimage,* Vol.25, No.2, pp. 579-587, ISSN 1053-8119

Cloninger, C.R. (1987). A systematic method for clinical description and classification of personality variants. A proposal. *Archives of General Psychiatry,* Vol.44, No.6, pp. 573-588, ISSN 0003-990X

Cloninger, C.R. (1990). Comorbidity of anxiety and depression. *Journal of Clinical Psychopharmacology,* Vol.10, No.3, Supplement, pp. 43S-46S, ISSN 0271-0749

Cloninger, C.R. (2002). The discovery of susceptibility genes for mental disorders. *Proceedings of the National Academy of Sciences of the United States of America,* Vol.99, No.21, pp. 13365-13367, ISSN 0027-8424

Cohen, J.D., Perlstein, W.M., Braver, T.S., Nystrom, L.E., Noll, D.C., Jonides, J., & Smith, E.E. (1997). Temporal dynamics of brain activation during a working memory task. *Nature,* Vol.386, No.6625, pp. 604-608, ISSN 0028-0836

Costa, P.T. Jr., & McCrae, R.R. (1995). Domains and facets: hierarchical personality assessment using the revised NEO personality inventory. *Journal of Personality Assessment,* Vol.64, No.1, pp. 21-50, ISSN 0022-3891

de Saint Hilaire, Z., Straub, J., & Pelissolo, A. (2005). Temperament and character in primary insomnia. *European Psychiatry,* Vol.20, No.2, pp. 188-192, ISSN 0924-9338

Doran, S.M., Van Dongen, H.P., & Dinges, D.F. (2001). Sustained attention performance during sleep deprivation: evidence of state instability. *Archives Italiennes de Biologie,* Vol.139, No.3, pp. 253-267, ISSN 0003-9829

Drake, C.L., Roehrs, T.A., Burduvali, E., Bonahoom, A., Rosekind, M., & Roth, T. (2001). Effects of rapid versus slow accumulation of eight hours of sleep loss. *Psychophysiology,* Vol.38, No.6, pp. 979-987, ISSN 0048-5772

Drummond, S.P., Paulus, M.P., & Tapert, S.F. (2006). Effects of two nights sleep deprivation and two nights recovery sleep on response inhibition. *Journal of Sleep Research,* Vol.15, No.3, pp. 261-265, ISSN 0962-1105

Duncan, J. (2001). An adaptive coding model of neural function in prefrontal cortex. *Nature Reviews Neuroscience,* Vol.2, No.11, pp. 820–829, ISSN 1471-003X

Ferrari, M., Mottola, L., & Quaresima, V. (2004). Principles, techniques, and limitations of near infrared spectroscopy. *Canadian Journal of Applied Physiology,* Vol.29, No.4, pp. 463-487, ISSN 8750-7587

Frey, D.J., Badia, P., & Wright, K.P. Jr. (2004). Inter- and intra-individual variability in performance near the circadian nadir during sleep deprivation. *Journal of Sleep Research,* Vol.13, No.4, pp. 305-315, ISSN 0962-1105

Frokjaer, V.G., Mortensen, E.L., Nielsen, F.A., Haugbol, S., Pinborg, L.H., Adams, K.H., Svarer, C., Hasselbalch, S.G., Holm, S., Paulson, O.B., & Knudsen, G.M. (2008). Frontolimbic serotonin 2A receptor binding in healthy subjects is associated with

personality risk factors for affective disorder. *Biological Psychiatry,* Vol.63, No.6, pp. 569-576, ISSN 0006-3223

Gevins, A., & Cutillo, B. (1993). Spatiotemporal dynamics of component processes in human working memory. *Electroencephalography and Clinical Neurophysiology,* Vol.87, No.3, pp. 128–143, ISSN 0013-4694

Grucza, R.A., Cloninger, C.R., Bucholz, K.K., Constantino, J.N., Schuckit, M.I., Dick, D.M., & Bierut, L.J. (2006). Novelty seeking as a moderator of familial risk for alcohol dependence. *Alcoholism, Clinical and Experimental Research,* Vol.30, No.7, pp. 1176-1183, ISSN 0145-6008

Guiou, M., Sheth, S., Nemoto, M., Walker, M., Pouratian, N., Ba, A., & Toga, A.W. (2005). Cortical spreading depression produces long-term disruption of activity-related changes in cerebral blood volume and neurovascular coupling. *Journal of Biomedical Optics,* Vol.10, No.1, pp. 11004, ISSN 1083- 3668

Halford, G.S., Wilson, W.H., & Phillips, S. (2010). Relational knowledge: the foundation of higher cognition. *Trends in Cognitive Sciences,* Vol.14, No.11, pp. 497-505, ISSN 1364-6613

Harrington, D.L., Haaland, K.Y., & Knight, R.T. (1998). Cortical networks underlying mechanisms of time perception. *The Journal of Neuroscience,* Vol.18, No.3, pp. 1085-1095, ISSN 0270-6474

Hoddes, E., Dement, W.C., & Zarcone, V. (1971). The history and use of the Stanford sleepiness scale. *Psychophysiology,* Vol.9, pp. 150, ISSN 1469-8986

Honma, M., Soshi, T., Kim, Y., & Kuriyama, K. (2010). Right prefrontal activity reflects the ability to overcome sleepiness during working memory tasks: a functional near-infrared spectroscopy study. *PLoS ONE,* Vol.5, No.9, pp. e12923, ISSN 1932-6203.

Hoshi, Y., Kobayashi, N., & Tamura, M. (2001). Interpretation of near-infrared spectroscopy signals: a study with a newly developed perfused rat brain model. *Journal of Applied Physiology,* Vol.90, No.5, pp. 1657–1662, ISSN 0021-8987

Ivry, R.B. (1996). The representation of temporal information in perception and motor control. *Current Opinion in Neurobiology,* Vol.6, No.6, pp. 851–857, ISSN 0959-4388

Killgore, W.D., Kahn-Greene, E.T., Lipizzi, E.L., Newman, R.A., Kamimori, G.H., & Balkin, T.J. (2008). Sleep deprivation reduces perceived emotional intelligence and constructive thinking skills. *Sleep Medicine,* Vol.9, No.5, pp. 517-526, ISSN 1389-9457

Koslowsky, M., & Babkoff, H. (1992). Meta-analysis of the relationship between total sleep deprivation and performance. *Chronobiology International,* Vol.9, No.2, pp. 132-136, ISSN 0742-0528

Kuriyama, K., Mishima, K., Suzuki, H., Aritake, S., & Uchiyama, M. (2008). Sleep accelerates the improvement in working memory performance. *The Journal of Neuroscience,* Vol.28, No.40, pp. 10145–10150, ISSN 0270-6474

Kuriyama, K., Uchiyama, M., Suzuki, H., Tagaya, H., Ozaki, A., Aritake, S., Kamei, Y., Nishikawa, T., & Takahashi, K. (2003). Circadian fluctuation of time perception in healthy human subjects. *Neuroscience Research,* Vol.46, No.1, pp. 23–31, ISSN 0168-0102

Kuriyama, K., Uchiyama, M., Suzuki, H., Tagaya, H., Ozaki, A., Aritake, S., Shibui, K., Xin, T., Lan, L., Kamei, Y., & Takahashi, K. (2005). Diurnal fluctuation of time

perception under 30-h sustained wakefulness. *Neuroscience Research,* Vol.53, No.2, pp. 123–128, ISSN 0168-0102

Lim, J., & Dinges, D.F. (2010). A meta-analysis of the impact of short-term sleep deprivation on cognitive variables. *Psychological Bulletin,* Vol.136, No.3, pp. 375-389, ISSN 0033-2909

Miller, E.K., & Cohen, J.D. (2001). An integrative theory of prefrontal cortex function. *Annual Review of Neuroscience,* Vol.24, pp. 167–202, ISSN 0147-006X

Nilsson, J.P., Söderström, M., Karlsson, A.U., Lekander, M., Akerstedt, T., Lindroth, N.E., & Axelsson, J. (2005). Less effective executive functioning after one night's sleep deprivation. *Journal of Sleep Research,* Vol.14, No.1, pp. 1-6, ISSN 0962-1105

Obrig, H., Neufang, M., Wenzel, R., Kohl, M., Steinbrink, J., Einhäupl, K., & Villringer, A. (2000). Spontaneous low frequency oscillations of cerebral hemodynamics and metabolism in human adults. *Neuroimage,* Vol.12, No.6, pp. 623-639, ISSN 1053-8119

Owen, A.M., Doyon, J., Petrides, M., & Evans, A.C. (1996). Planning and spatial working memory: a positron emission tomography study in humans. *European Journal of Neuroscience,* Vol.8, No.2, pp. 353-364, ISSN 0953-816X

Owen, A.M., Stern, C.E., Look, R.B., Tracey, I., Rosen, B.R., & Petrides, M. (1998). Functional organization of spatial and nonspatial working memory processing within the human lateral frontal cortex. *Proceedings of the National Academy of Sciences of the United States of America,* Vol.95, No.13, pp. 7721-7726, ISSN 0027-8424

Pouthas, V., Maquet, P., Garnero, L., Ferrandez, A.M., & Renault, B. (1999). Neural basis of time estimation: a PET and ERP study. *Electroencephalography and Clinical Neurophysiology Supplement,* Vol.50, pp. 598–603, ISSN 0424-8155

Rammsayer, T.H. (1999). Neuropharmacological evidence for different timing mechanisms in humans. *Quarterly Journal of Experimental Psychology Section B,* Vol.52, No.3, pp. 273–286, ISSN 0272-4995

Rasmussen, T., Holstein-Rathlou, N.H., & Lauritzen, M. (2009). Modeling neuro-vascular coupling in rat cerebellum: characterization of deviations from linearity. *Neuroimage,* Vol.45, No.1, pp. 96-108, ISSN 1053-8119

Saggino, A., & Balsamo, M. (2003). Relationship between WAIS-R intelligence and the five-factor model of personality in a normal elderly sample. *Psychological Reports,* Vol.92, No.3 (Part 2), pp. 1151-1161, ISSN 0033-2941

Soshi, T., Kuriyama, K., Aritake, S., Enomoto, M., Hida, A., Tamura, M., Kim, Y., & Mishima, K. (2010). Sleep deprivation influences diurnal variation of human time perception with prefrontal activity change: a functional near-infrared spectroscopy study. *PLoS ONE,* Vol.5, No.1, pp. e8395, ISSN 1932-6203

Stenuit, P., & Kerkhofs, M. (2008). Effects of sleep restriction on cognition in women. *Biological Psychology,* Vo.77, No.1, pp. 81-88, ISSN 0301-0511

Strobel, A., Gutknecht, L., Rothe, C., Reif, A., Mössner, R., Zeng, Y., Brocke, B., & Lesch, K.P. (2003). Allelic variation in 5-HT1A receptor expression is associated with anxiety- and depression-related personality traits. *Journal of Neural Transmission,* Vol.110, No.12, pp. 1445-1453, ISSN 0300-9564

Sweeney, J.A., Mintun, M.A., Kwee, S., Wiseman, M.B., Brown, D.L., Rosenberg, D.R., & Carl, J.R. (1996). Positron emission tomography study of voluntary saccadic eye movements and spatial working memory. *Journal of Neurophysiology,* Vol.75, No.1, pp.454-468, ISSN 0022-3077

Treisman, M. (1963). Temporal discrimination and the indifference interval. Implications for a model of the 'internal clock'. *Psychological Monographs,* Vol.77, No.13, pp. 1–31, ISSN 0016-6677

Tucker, A.M., Whitney, P., Belenky, G., Hinson, J.M., & Van Dongen, H.P. (2010). Effects of sleep deprivation on dissociated components of executive functioning. *Sleep,* Vol.33, No.1, 47-57, ISSN 0161-8105

van de Laar, M., Verbeek, I., Pevernagie, D., Aldenkamp, A., & Overeem, S. (2010). The role of personality traits in insomnia. *Sleep Medicine Reviews,* Vol.14, No.1, pp. 61-68, ISSN 1087-0792

Van Dongen, H.P., Maislin, G., Mullington, J.M., & Dinges, D.F. (2004). The cumulative cost of additional wakefulness: dose-response effects on neurobehavioral functions and sleep physiology from chronic sleep restriction and total sleep deprivation. *Sleep,* Vol.26, No.2, pp. 117-126, ISSN 0161-8105

Villafuerte, S., Heitzeg, M.M., Foley, S., Wendy Yau, W.Y., Majczenko, K., Zubieta, J.K., Zucker, R.A., & Burmeister, M. (2011). Impulsiveness and insula activation during reward anticipation are associated with genetic variants in GABRA2 in a family sample enriched for alcoholism. *Molecular Psychiatry,* in press, ISSN 1359-4184

Vyazovskiy, V.V., Olcese, U., Hanlon, E.C., Nir, Y., Cirelli, C., & Tononi, G. (2011). Local sleep in awake rats. *Nature,* Vol.472, No.7344, pp. 443-447, ISSN 0028-0836

Wimmer, F., Hoffmann, R.F., Bonato, R.A., & Moffitt, A.R. (1992). The effects of sleep deprivation on divergent thinking and attention processes. *Journal of Sleep Research,* Vo.1, No.4, pp. 223-230, ISSN 0962-1105

3

Applications of Near Infrared Spectroscopy in Neurorehabilitation

Masahito Mihara and Ichiro Miyai
Neurorehabilitation Research Institute, Morinomiya Hospital
Japan

1. Introduction

In developed countries, stroke is a major cause of acquired disability among adults. Although there is a considerable inter-subject variability, the time course of functional recovery assumes an exponential shape, with a faster recovery in the initial few weeks, followed by a slower recovery over the next few months (Jorgensen et al., 1999; Duncan et al., 2000). In the former phase, faster recovery is thought to be due to the reduction of parenchymal oedema or recanalization of the blood flow. The latter phase is believed to depend upon the adaptive plasticity of the brain, including unmasking or disinhibiting the potentially aberrant neural network, and vicariation of function (Ward & Frackowiak, 2004). Although there are many evidences for brain plasticity after stroke or brain injury, most of our knowledge is derived from animal experiments (Jenkins & Merzenich, 1987; Nudo et al., 1996). Direct investigation of functional reorganization after brain damage in humans has only recently become possible with advancements in non-invasive functional imaging techniques, such as positron emission tomography (PET) and functional MRI (fMRI). Among these functional neuroimaging techniques, functional near infrared spectroscopy (NIRS) has drawn attention from investigators in rehabilitation medicine since it is thought to be less constrained and more available for measurement during various tasks. In this chapter, we introduce the clinical applications of fNIRS in the field of rehabilitation medicine and I shall discuss the further possibilities for its application.

2. Application of functional NIRS in studies of human motor control

2.1 Principles of functional NIRS

Near infrared light, particularly that with a wavelength between 700 and 900 nm, can easily pass through biological tissues, including skin and skull bone, and be absorbed by biological chromophores such as haemoglobin, myoglobin, and cytochrome oxidase in the mitochondria. Because myoglobin concentration is much lower than haemoglobin concentrations in the brain tissue and a change in the redox state of cytochrome oxidase occurs only under severely hypoxic conditions, near infrared light is mainly absorbed by haemoglobin when used as a functional brain-imaging tool. The NIRS system with continuous waves, which is widely used in commercially available instruments, measures the transmitted intensity and calculates the relative changes in the haemoglobin concentration according to the modified Beer-Lambert law for highly scattering media

(MBLL) (Cope et al., 1988). If the light attenuation by scattering is considered constant, MBLL is denoted as follows:

$$\Delta A_{\lambda 1} = \left(\varepsilon_{\lambda 1}^{OxyHb} \cdot \Delta C^{OxyHb} + \varepsilon_{\lambda 1}^{DeoxyHb} \cdot \Delta C^{DeoxyHb}\right) \cdot L$$

Where ε_λ is the extinction coefficient at a given wavelength λ, L is the optical pathlength, and ΔC is the change in the concentration of each chromophore. If measurements with multiple wavelengths are performed simultaneously and optical pathlength is considered to be constant across the measurement, the product of the change in concentration of the chromophore and the optical pathlength can be calculated by solving the simultaneous equations. However, it should be noted that the precise optical pathlength is difficult to determine with the continuous-wave NIRS system. Therefore, calculated measurements are usually denoted in arbitrary units such as millimolar·millimetres (mM × mm) (Maki et al., 1995). It is generally accepted that the distribution of near infrared light paths between an illuminator-detector pair become 'banana-shaped' (Gratton et al., 1994), and that certain interoptode distances are needed for the propagation of near infrared light to the cerebral cortex. Commonly, a distance of 2 cm or more is used.

In the brain tissues, regional brain activation is accompanied by an increase in the regional blood flow (Fox & Raichle, 1986), and this regional blood flow increase is thought to exceed the regional oxygen consumption. Therefore, regional cortical activation results in a regional increase in the oxygenated haemoglobin (OxyHb) levels, with a decrease in the deoxygenated haemoglobin (DeoxyHb) levels. Similar to fMRI or PET, functional NIRS detects the task-related haemodynamic responses, that is, the task-related increase in the OxyHb signal and/or the task-related decrease in DeoxyHb.

2.2 Potential advantages and shortcomings of functional NIRS

There are several potential advantages of functional NIRS for investigating human brain activity. First, functional NIRS imposes less onerous constraints on its subjects. In a NIRS system, minor head and truncal motion is irrelevant, if a tight contact is maintained between the skull surface and optodes during measurement. Second, unlike other neuroimaging modalities, functional NIRS requires relatively small and simple equipment. Finally, the NIRS system is completely safe and non-invasive, since it uses only a low-power near infrared laser. It therefore enables us to investigate brain activation under natural conditions, such as at the bedside or while sitting on a chair, and measure cortical activation in the activities of daily life, such as standing and walking. Based on these characteristics, NIRS is thought to be a suitable neuroimaging tool for clinical investigation in fields such as paediatric neurology and rehabilitation medicine.

Despite these potential advantages, NIRS has several shortcomings as a functional neuroimaging tool. First, NIRS cannot measure activation in deep brain structures, including the basal ganglia, brainstem, and cerebellum. Secondly, NIRS has relatively poor spatial resolution (a few centimetres) and cannot provide any spatial information. Therefore, spatial registration should be made with other data, such as anatomical information from MRI scans and real-world coordinates derived from a 3-dimensional digitizer and other standard references (Okamoto et al., 2004). Third, with the continuous-wave NIRS system, we cannot measure the precise optical pathlength, and therefore cannot measure absolute

changes, but only relative changes, in the haemoglobin concentration. Finally, not only the brain tissue but also skin tissue beneath the optodes can affect NIRS signal changes. To avoid or cancel the effect of skin blood flow, several methodologies have been introduced (Kohno et al., 2007; Yamada et al., 2009), but there is no 'gold standard' for this problem. Therefore, researchers should be cautious about the contamination of these non-brain signals when interpreting NIRS measurements (Takahashi et al., 2011).

2.3 Application of NIRS to human gait control

Gait requires complex visuo-sensorimotor coordination. Like in other animals, human locomotion is controlled by multiple neural systems, hierarchically distributed throughout the central nervous system, including the spinal cord, brainstem, cerebellum, basal ganglia, and motor cortex (Grillner & Wallen, 2004). Although most studies of neuronal mechanisms of gait control were conducted with quadruped animals, a bipedal stance and gait are unique functions of humans. Therefore, functional imaging studies in humans are important for investigating the neural mechanisms of gait control. However, as stated above, it is difficult to study dynamic movements such as gait control with conventional neuroimaging techniques, and functional NIRS is a suitable tool for these studies.

2.3.1 Cortical activation of gait in healthy subjects

Using a multi-channel NIRS system, Miyai and colleagues reported cortical activation during human gait on a treadmill (Miyai et al., 2001). They used a custom-made plastic holder cap and a weight-balancing system to avoid excessive motion artifacts during the locomotor task, and they could measure the task-related haemoglobin signal changes from the frontoparietal skull surface (Fig. 1).

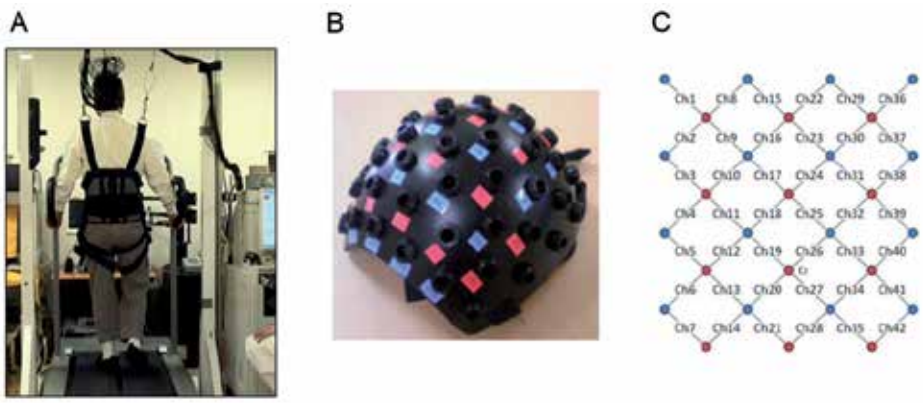

A: Subject performing a locomotor task on the treadmill. B: A custom-made plastic holder cap for fixing optode fibres. C: The schematic location of each optode and channel. Cz represents the vertex. Red and blue circles represent the light sources and detector fibres.

Fig. 1. Measurement of cortical activation during walking by using a functional NIRS system

In healthy subjects, the locomotor task on a treadmill evoked symmetrical activation in the medial sensorimotor cortex and supplementary motor area (Fig. 2). These findings were consistent with results from a study using single photon emission tomography (Fukuyama

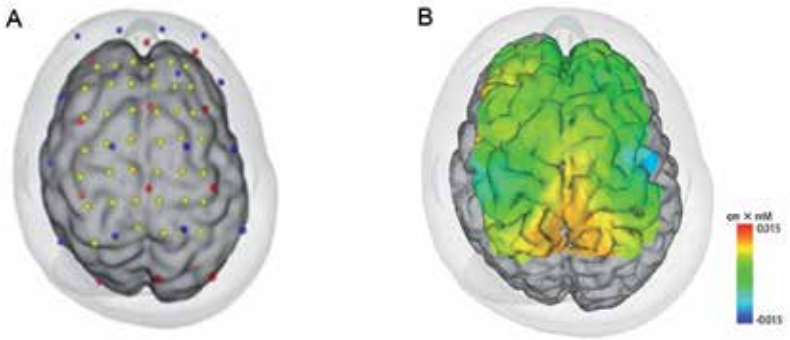

A: Optode locations on the skull surface (red and blue dots) and estimated cortical projection points of functional NIRS measurement (yellow dots) B: Cortical activation map based on OxyHb signal changes during 3-km/h gait on the treadmill. Data averaged from 3 repetitions of 30-s gait followed by 30-s rest periods.

Fig. 2. Cortical activation during gait in a healthy subject

et al., 1997). Furthermore, it was suggested that the different areas of the cerebral cortex play different roles in human gait control. During the locomotor task, cortical activation in the prefrontal cortex temporally increased during the acceleration phase of gait, and gradually decreased during walking at a stable speed (Suzuki et al., 2004). It was also revealed that cortical activation change was more prominent at higher locomotor speed in the prefrontal cortex, but cortical activation in the sensorimotor cortex was not associated with gait speed. Therefore, the prefrontal cortex was involved in the adaptation of gait speed, but the medial sensorimotor cortex was involved in stable gait.

2.3.2 Cortical activation of gait in stroke patients

Gait disturbance is a major consequence of stroke and is shown to greatly affect the ability to independently perform activities of daily living (ADL). Although it is assumed that functional reorganization of the central nervous system plays an important role in gait recovery after stroke, there is not enough evidence to associate cortical reorganization with gait recovery. Because the NIRS system is non-invasive and places fewer burdens on the patient, it is useful for repetitive measurement of the cortical activation of gait. In stroke patients, there are several reported cortical activation patterns. In hemispheric stroke patients with supratentorial lesions, activation in the motor-related cortex in the affected hemisphere increases with functional recovery. Particularly, the premotor cortex in the affected hemisphere appears to be essential (Miyai et al., 2002, 2003), as a previous observational study had suggested (Miyai et al., 1999). On the other hand, ataxic stroke patients with infratentorial lesions display a different activation pattern during gait. In ataxic stroke patients, activation in the medial sensorimotor cortex is not significantly changed compared to that in the healthy subjects. However, the prefrontal activation pattern differs, and ataxic patients show sustained activation in the prefrontal cortex (Fig. 3) (Mihara et al., 2007). As described above, prominent activation in the prefrontal cortex is reported in the acceleration phase of gait in healthy subjects, and is presumed to be involved in the adaptation of gait speed. Ataxic stroke patients exhibit increased postural sway, difficulty in multi-joint adjustment during locomotion, and reduced walking speed (Morton & Bastian,

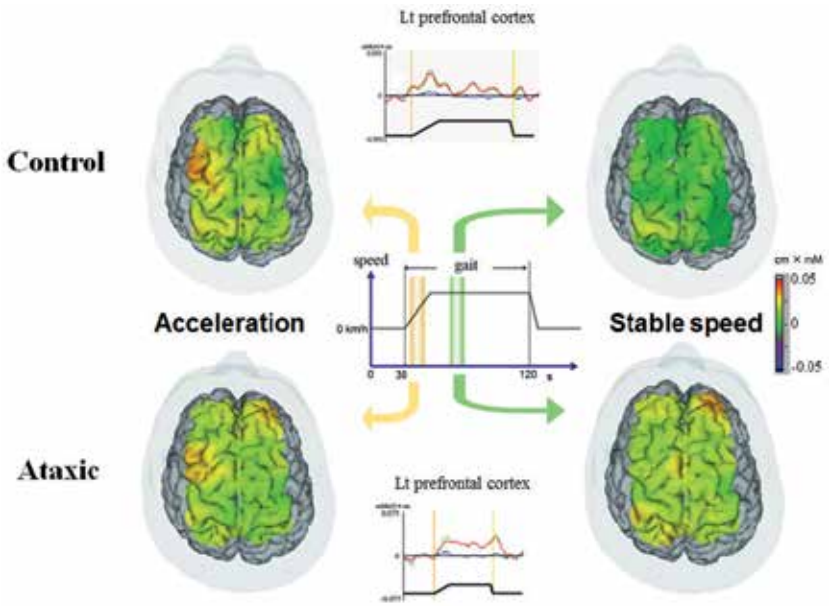

Cortical mapping results from healthy control subjects and ataxic stroke patients. In the acceleration phase, the cortical activation in both groups was consistent, but in the stable phase, cortical activation (particularly activation in the prefrontal cortex) was sustained in ataxic stroke patients but reduced in healthy control subjects. Raw data from the NIRS channel covering the left prefrontal cortex is also shown (red, blue, and green lines denote Oxy-, Deoxy-, and total-Hb signal changes, respectively).

Fig. 3. Gait-related cortical activation in the healthy and ataxic stroke patients

2004). Such a substantial variability of limb movements may require both more attention and more intention to control lower limb movements during gait. Thus, our findings are in accordance with the hypothesis that the impaired control of automated locomotion in ataxic patients is compensated by recruitment of the frontal cortices in the course of gait recovery, especially the prefrontal cortex.

2.3.3 Supposed mechanisms for the gait recovery after stroke

The abovementioned NIRS studies revealed the vital role of cortical reorganization in gait recovery after stroke, and that the cortical activation pattern could differ with the lesion location and size. One possible interpretation for these findings is that a widespread neural network is engaged in the locomotor control, and different regions regulate different aspects. Although both the infra- and supratentorial structures are thought to regulate locomotion through the putative central pattern generator in the spinal cord (Dimitrijevic et al., 1998), these contribute to different aspects of locomotor control. The infratentorial regions, including the reticular nuclei and the medial cerebellum, are regarded as the main structures for controlling automated locomotion and muscle tone during gait (Armstrong, 1988; Drew et al., 2004; Mori et al., 2004). In contrast, the supratentorial structures are predominantly involved in adjusting locomotor performance to an altered environment (Armstrong, 1988; Matsuyama et al., 2004; Takakusaki et al., 2004). For instance, studies using fMRI and PET report decreased the cortical activation during motor imaging of

automated locomotion, such as walking at a steady speed (Malouin et al., 2003; Jahn et al., 2004). These results indicate that the cortical demand for controlling gait is reduced during the steady phase of locomotion in control subjects, since the infratentorial structures engage in automated locomotion.

In patients with hemiparetic stroke and supratentorial lesion, it is assumed that the infratentorial locomotor centre, which engages in automated locomotion, is intact. Therefore, increased activation in the ipsilesional premotor cortex, which has ample connections to the brainstem and basal ganglia, is likely to compensate for the reduced regulatory output from the cerebral cortex. In contrast, automated locomotor control is impaired in ataxic stroke patients with infratentorial lesions. Thus, continuous monitoring and adjustment are needed, and this may result in sustained activation of the prefrontal cortex (Fig. 4).

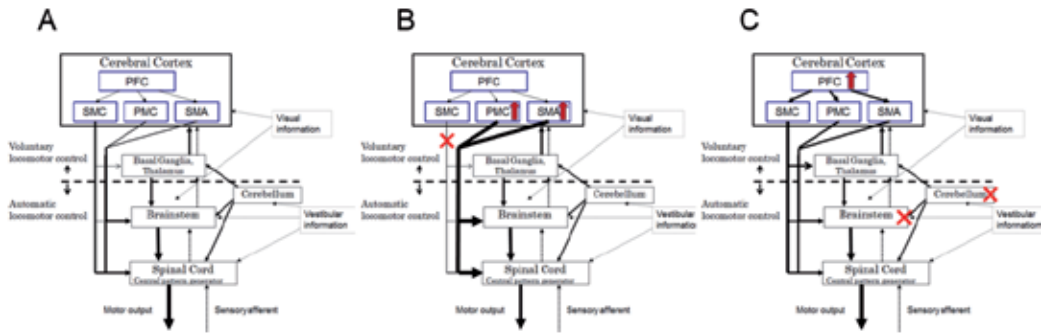

A: Neural network in central nervous system for locomotor control B: Assumed compensatory reorganization for gait recovery in supratentorial hemiparetic stroke C: Assumed compensatory reorganization for gait recovery after infratentorial ataxic stroke

Fig. 4. Suggested framework for locomotor recovery after stroke

2.4 Cortical activation associated with the maintenance of postural balance

Our habitual bipedal stance is highly advantageous because it enables us to maximize the dexterity of our hands, which is useful for developing tools. However, as a trade-off for this advantage, the unstable nature of bipedal standing increases the tendency to fall, leading to severe injuries such as limb fracture, joint dislocation, and head injury. A community-based study revealed that more than one-third of the people aged over 65 years fell at least once a year, and that proportion increased to 50% by the age of 80 years (O'Loughlin et al., 1993). To prevent falls and resultant disability in the elderly, it is essential to understand the neural mechanisms underlying bipedal standing. Accumulated results from studies in cats and other vertebrates (Armstrong, 1988; Drew et al., 2004) suggest that multiple automated and reflexive actions regulated by the subcortical structures contribute to balance control. However, since balance control in bipedal standing requires more complex and sophisticated sensorimotor coordination than quadruped standing, it is plausible that not only the subcortical structures but also the well-evolved cerebral cortices are involved in balance control during bipedal standing in humans (Nielsen, 2003). In line with this notion, recent studies suggest that the cerebral cortex is involved in human balance control (Dietz et al., 1984; Quant et al., 2005; Slobounov et al., 2005). Compared to conventional neuroimaging techniques, such as fMRI or

PET, functional NIRS is relatively robust against a subject's motion and seems to be suitable for investigating cortical involvement in postural control.

2.4.1 Cortical activation with postural perturbation in healthy subjects

Using functional NIRS, Mihara et al. reported the cortical activation associated with predictable and unpredictable postural perturbation (Mihara et al., 2008). During the experiment, subjects were asked to stand still on a platform, and postural perturbation was given by the brisk forward and backward translation of the platform (Fig.5). Oxy- and DeoxyHb signal changes were recorded from 50 channels on the frontoparietal skull surface with a sampling rate of 4 Hz.

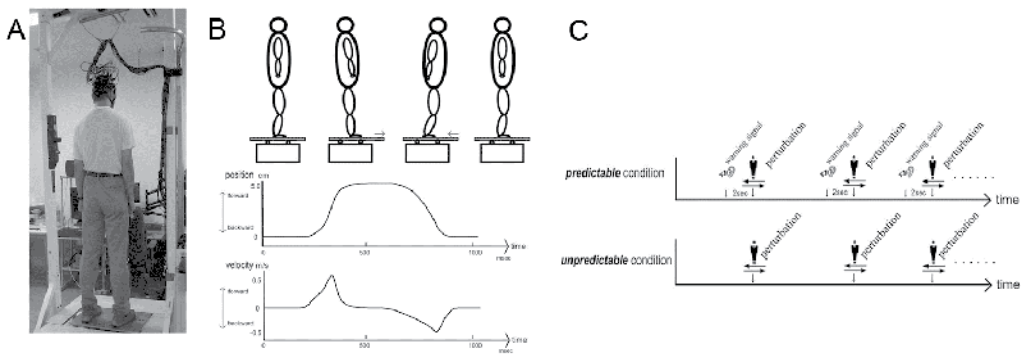

A: Experimental overview: Subjects are asked to stand on the custom-made platform with their feet shoulder-width apart. B: Schematic figure of platform movement. The middle and bottom row denote the time course of platform position and velocity. C: Task protocol in both conditions. Postural perturbations are given with randomised intervals. In the predictable condition, auditory warning signals are provided 2 s before the perturbation.

Fig. 5. Experimental setup for the measurement of cortical activation associated with postural perturbation.

Statistical analyses, using a general linear model with least squares estimation, revealed significant task-related OxyHb increase in the bilateral prefrontal cortex regardless of preceding warning cues. In the predictable condition, the supplementary motor area and the parietal association cortex were activated as well as the prefrontal cortex (Fig. 6).

Considering that results from previous studies imply attentional demands for postural control (Woollacott & Shumway-Cook, 2002), the prefrontal involvement suggests the recruitment of the attentional process for the maintenance of standing posture against postural perturbation. The supplementary motor area and the parietal association cortex, however, were more activated with the preceding warning cues, suggesting that these cortices are involved in voluntary postural control.

2.4.2 Possible application of functional NIRS as a surrogate marker for balance ability

Neurological disorders, including stroke, Parkinson's disease, and spinocerebellar ataxia, affect the balance ability and activity of daily living. In the field of rehabilitation medicine,

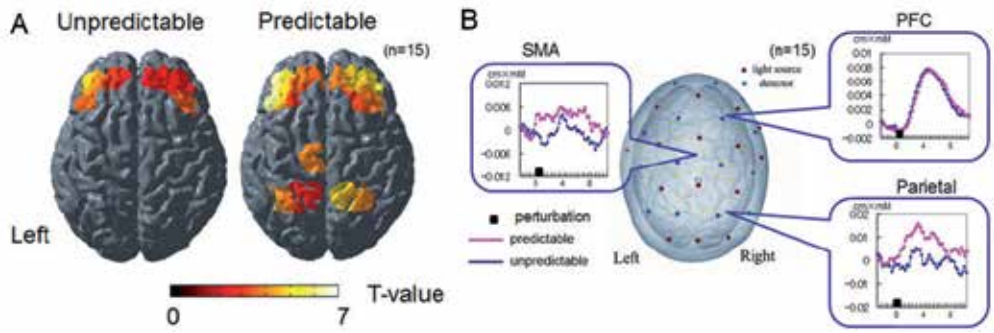

A: Cortical activation mapping based on task-related OxyHb signal increase. In the unpredictable condition, a task-related OxyHb signal increase is prominent in the bilateral prefrontal cortex (left). In the predictable condition, postural perturbation evoked task-related OxyHb signal increases in the supplementary motor area and parietal association cortex, as well as the bilateral prefrontal cortex (right). B: Timeline analyses of the OxyHb signal in both conditions.

SMA: supplementary motor area, PFC: prefrontal cortex

Fig. 6. Cortical activation associated with postural perturbation in healthy subjects.

balance impairment is one of the main targets for improvement. As described above, functional NIRS can monitor the activation of the cortical network, which is vital for postural control. Therefore, functional NIRS may possibly help objectively monitor balance recovery. Below, we present several cases in which we observe changes in cortical activation during functional recovery after inpatient rehabilitation.

A hemiplegic stroke patient with a subcortical lesion showed a similar cortical activation pattern change. Figure 7 shows the longitudinal change of cortical activation mapping associated with unpredicted postural perturbation. In a left hemiplegic patient, activation in the broad cortical area, including the bilateral prefrontal cortex, premotor cortex,

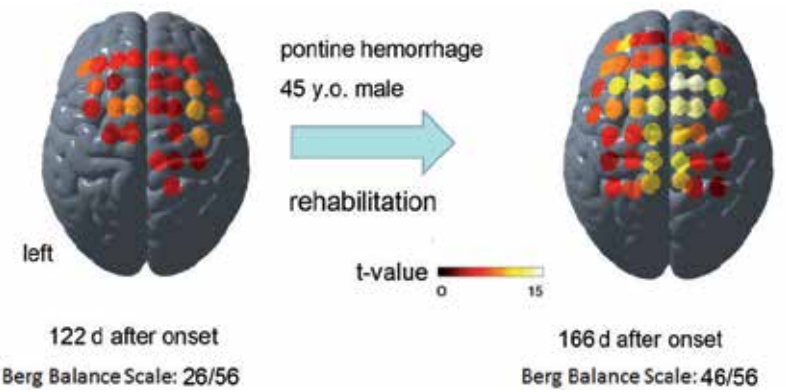

Cortical activation mapping based on task-related OxyHb signal increase associated with unpredictable postural perturbation. Cortical activation was increased after 40 d of inpatient rehabilitation.

Fig. 7. Cortical mapping change associated with postural perturbation in a patient with left hemiplegic stroke (45 years old).

supplementary motor area, and sensorimotor cortex, became evident as his balance ability recovered after inpatient rehabilitation. These results suggest that balance recovery is associated with cortical activation change, as is upper and lower limb recovery after stroke (Calautti & Baron, 2003; Ward et al., 2003; Luft et al., 2005; Enzinger et al., 2009).

Interestingly, not only stroke patients show functional recovery-associated cortical mapping pattern changes. Figure 8 shows cortical activation with postural perturbation in a 73-year-old male patient with Parkinson's disease. He exhibited postural instability and could not walk without assistance at admission, but after 4 weeks of inpatient rehabilitation and drug control, his condition improved and he became ambulant. Postural perturbation-related cortical activation was dramatically changed along with functional recovery. Cortical activation in the bilateral prefrontal, premotor, and supplementary motor areas was increased after inpatient rehabilitation. Considering the subcortical nature of Parkinson's disease, increased cortical activation may compensate for subcortical dysfunction, similar to gait in the ataxic stroke patients described above. Although there are several issues to be elucidated, these results imply that functional NIRS could be used as a surrogate marker for balance ability in patients with neurological disorders.

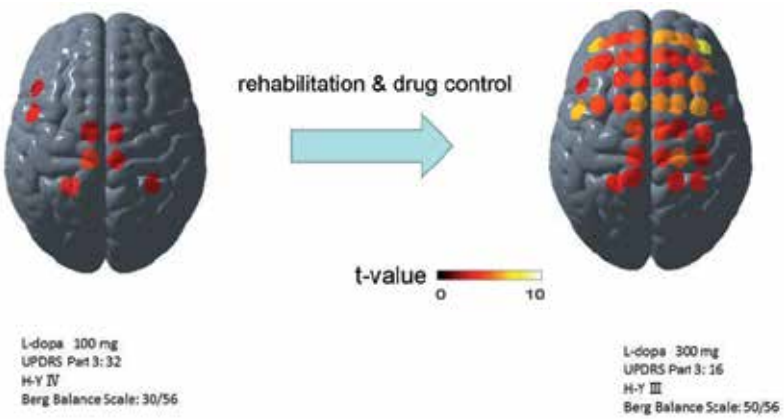

Cortical activation mapping based on the task-related OxyHb signal increase associated with unpredictable postural perturbation. Cortical activation increased along with the recovery of balance ability in a widespread cortical area, including the bilateral prefrontal, premotor, and supplementary motor areas.

Fig. 8. Cortical mapping change associated with postural perturbation in a patient with Parkinson's disease (73 years old).

2.5 Functional NIRS as a tool for motor learning studies

Motor learning is vital and essential process in acquiring motor skills in daily life, not only for the neurological patients, but also for healthy individuals. Motor learning comprises motor sequence learning and motor adaptation in experimental settings (Doyon & Benali, 2005). Motor sequence learning is assessed by the incremental acquisition of movements with repetition, while motor adaptation refers to the ability to compensate for environmental changes. To date, most human studies of motor sequence learning have used positron emission tomography (PET) or functional magnetic resonance imaging (fMRI) and

investigated the neural mechanisms underlying the learning of sequential movements of fingers or feet in a lying position. However, motor learning usually occurs under postural control since most movements are executed while subjects are sitting or standing in daily situations. As described above, because of less postural restriction, functional NIRS is considered suitable for investigating motor learning under normal daily circumstances.

Using functional NIRS, Hatakenaka et al. studied the cortical activation change during the pursuit rotor (PR) task in healthy subjects (Hatakenaka et al., 2007). A pursuit rotor (PR) is a tool to evaluate motor sequence learning by measuring the ability to keep a stylus on a rotating target. In the PR task, there is no need for precise control of finger movements, but it requires motor control of proximal parts of the upper extremity, including the shoulder and elbow, as well as postural control for sitting (Grafton et al., 1992).In this study, 18 right-handed healthy subjects performed 8 repetitions of 30-s PR tasks followed by 30-s rest periods. Gains of motor skill were evaluated by the contact time between the stylus and target. During 8 repetitions of the PR task, cortical activation in the frontoparietal cortices was evaluated with functional NIRS.

As shown in Figure 9, performance of the subjects improved with PR task repetition. A task-related OxyHb increase was observed in the sensorimotor cortex, prefrontal cortex, and premotor cortex. A task-related DeoxyHb decrease was also observed. Interestingly, the centre of the task-related OxyHb increase was observed in the pre-supplementary motor area initially, but it shifted caudally to the supplementary motor area with cycle repetitions (Fig. 9). These data suggest that the pre-supplementary motor area and the supplementary motor area play different roles in the motor skill learning process.

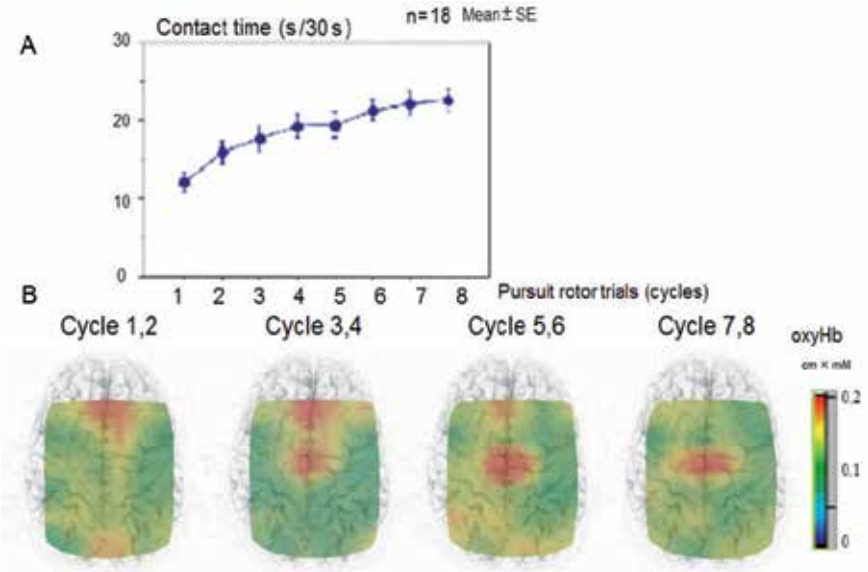

A: Cycle-by-cycle contact time during the pursuit rotor (PR) task in healthy right-handed subjects. B: Cortical activation mapping based on the task-related OxyHb signal increase associated with the PR task in a representative subject. A caudal shift of the centre of task-related cortical activation from the pre-supplementary motor area to the supplementary motor area was evident.

Fig. 9. Cortical mapping change associated with motor sequence learning.

Functional NIRS was also used in a study investigating the adaptation learning process. We investigated the cortical activation changes during the adaptation of reaching with robotic devices with 3-dimensional virtual reality (VR) system (Mihara et al., 2009), in which the limb coordination pattern is altered. Seven right-handed healthy subjects participated in this study. An upper limb training system, mediated by electro-rheological fluid actuators with 3° of free movement range, was used (Furusho et al., 2005). The subjects are given visual feedback of the position and the movement of the gripping handle of the robot arm, as the coloured ball (object) moves in the 3-dimensional VR space on the 13''monitor. The experiment consisted of 16 cycles of alternating 12-s rest and 8-s task periods. In the rest period, the floating target (Target) was fixed at the near lower left corner (the home position) of the VR space. In the reaching task period, the Target moved from the home position to the far upper right corner, and then returned to the home position in 8 s, and they asked the subject to follow the Target by moving the robot arm. The distance between the Object and the Target was indicated by the colour of the object. The mean distance in each cycle was calculated as a measure of performance. Cortical activation was measured as OxyHb signal change using 50-channel functional NIRS from the frontoparietal area, and the task-related cortical activation of each subject was modeled using 2 orthogonal covariates (Buchel et al., 1998). The first was the task covariate, modeled as a boxcar function in all task periods, and the second was the error covariate that comprised a boxcar function scaled by the mean distance. The error covariate was mean-corrected and orthogonalized with respect to the first covariate. Both covariates were convolved with the canonical haemodynamic response functions and used in a GLM analysis. Group analysis was performed using the random effects model.

The mean distance of 7 subjects gradually reduced with cycle repetitions, indicating that the subjects learned to adapt to the visuo-motor reaching task in the VR space. Group analysis of functional NIRS signals showed significant effects primarily in the bilateral prefrontal, bilateral premotor, and left primary sensorimotor areas. Significant negative correlations to the error covariate were also found in the left prefrontal and premotor areas (Fig. 10). Although a broad cortical network is involved in the visuo-motor adaption learning of the reaching task, the prefrontal and premotor areas may be involved in the early stages of the adaptation process.

2.6 Future directions of functional NIRS in the rehabilitation field

To improve the performance of the activities of daily life and to restore function in severely damaged patients with stroke or neurodegenerative disease, there has been much interest in developing brain–computer interface (BCI) technology (Dobkin, 2007; Daly & Wolpaw, 2008). The main purpose of BCI development is to substitute for lost neuromuscular output. For interactions between the brain and the outer environment, the BCI system must be able to detect brain signal, decode these signals, and output the appropriate information. Among several techniques for detecting brain activity, functional NIRS has attracted attention because of its portability and noninvasiveness. Although the clinical usage of BCI in the rehabilitation field is limited at this time, decoding techniques are improving with enthusiastic efforts from many groups. Sitaram et al. reported that right/left finger motor imagery could be classified with an average of 89% accuracy by applying a pattern recognition algorithm with hidden Markov Models to the multi-channel NIRS data

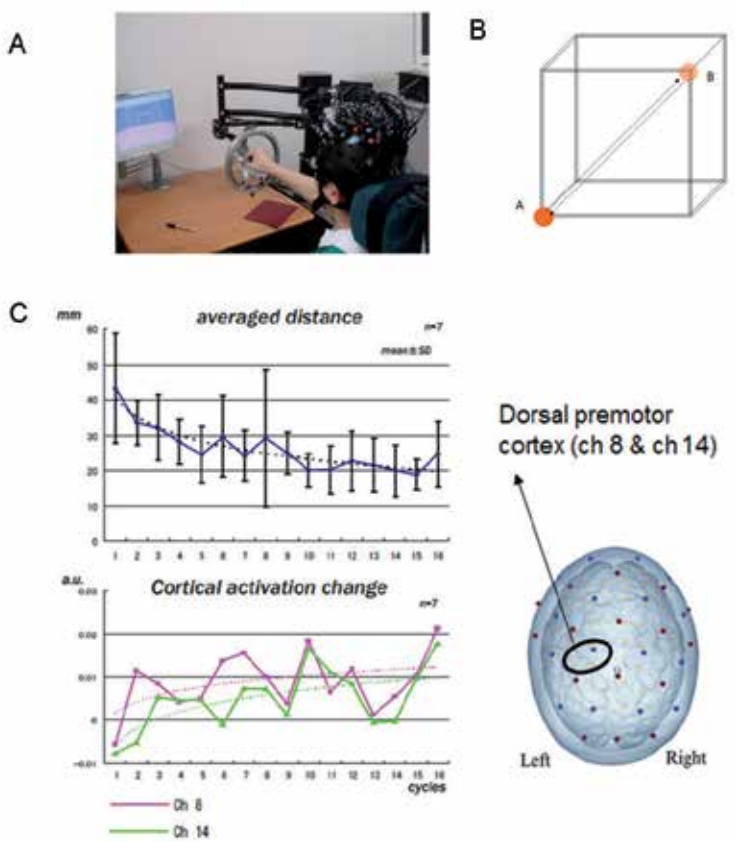

A: Experimental setting of the robotic rehabilitation system with functional NIRS. B: Reaching task with the robotic rehabilitation system. In a virtual reality space, subjects were asked to follow the target, which moves from the lower left corner to the upper right corner, and then back to the lower left corner in 8 s. C: Average distance from the handle position and the target, and cortical activation in the contralateral premotor cortex.

Fig. 10. Adaptation learning task with the 3-dimensional robotic rehabilitation system

(Sitaram et al., 2007). As another approach, the real-time analysis of the NIRS signal with an adaptive general linear model using Kalman filtering was also reported (Abdelnour & Huppert, 2009).

In addition, BCI could be used as a tool to augment cortical plasticity. Using electroencephalography signals, it has been shown that providing feedback of brain activity to the subjects can alter their brain activity itself. This technique, known as 'neurofeedback', has been investigated for several years and is already used in the clinical setting. It has been reported that real-time feedback of EEG activity enables voluntary regulation of cortical activation and attentional level (Delorme & Makeig, 2003), and this has been applied in the treatment of attention deficit and hyperactivity disorder (Fuchs et al., 2003) and epilepsy (Kotchoubey et al., 2001). Combined with the real-time signal processing technique described above, functional NIRS could be used as a neurofeedback system for enhancing cortical plasticity.

3. Conclusion

Functional NIRS is a unique tool as a neuroimaging modality. Despite several shortcomings, including difficulty in measuring haemoglobin oxygenation changes in deep brain structures and poor spatial resolution, it has characteristic advantages that can measure cortical activation in normal daily conditions. Functional NIRS could be used not only as a tool for measurement of cortical activation but also as a tool for treatment with further advancements in data analysis techniques.

4. References

Abdelnour, A. F. & Huppert, T. (2009).Real-time imaging of human brain function by near-infrared spectroscopy using an adaptive general linear model.*Neuroimage*, Vol.46,No. 1, pp 133-43

Armstrong, D. M. (1988).The supraspinal control of mammalian locomotion.*J Physiol*, Vol.405,, p 1-37

Buchel, C., Holmes, A. P., Rees, G. &Friston, K. J. (1998). Characterizing stimulus-response functions using nonlinear regressors in parametric fMRI experiments. *Neuroimage*, Vol.8,No. 2, pp 140-8

Calautti, C. & Baron, J. C. (2003). Functional neuroimaging studies of motor recovery after stroke in adults: a review. *Stroke*, Vol.34,No. 6, pp 1553-66

Cope, M., Delpy, D. T., Reynolds, E. O., Wray, S., Wyatt, J. & van der Zee, P. (1988). Methods of quantitating cerebral near infrared spectroscopy data.*AdvExp Med Biol*, Vol.222,, p 183-9

Daly, J. J. &Wolpaw, J. R. (2008). Brain-computer interfaces in neurological rehabilitation. *Lancet Neurol*, Vol.7,No. 11, pp 1032-43

Delorme, A. &Makeig, S. (2003). EEG changes accompanying learned regulation of 12-Hz EEG activity. *IEEE Trans Neural SystRehabilEng*, Vol.11,No. 2, pp 133-7

Dietz, V., Quintern, J. & Berger, W. (1984). Cerebral evoked potentials associated with the compensatory reactions following stance and gait perturbation. *NeurosciLett*, Vol.50,No. 1-3, pp 181-6

Dimitrijevic, M. R., Gerasimenko, Y. & Pinter, M. M. (1998). Evidence for a spinal central pattern generator in humans.*Ann N Y AcadSci*, Vol.860,, p 360-76

Dobkin, B. H. (2007). Brain-computer interface technology as a tool to augment plasticity and outcomes for neurological rehabilitation. *J Physiol*, Vol.579,No. 3, pp 637-42

Doyon, J. &Benali, H. (2005). Reorganization and plasticity in the adult brain during learning of motor skills.*CurrOpinNeurobiol*, Vol.15,No. 2, pp 161-7

Drew, T., Prentice, S. &Schepens, B. (2004). Cortical and brainstem control of locomotion. *Prog Brain Res*, Vol.143,, p 251-61

Duncan, P. W., Lai, S. M. & Keighley, J. (2000). Defining post-stroke recovery: implications for design and interpretation of drug trials. *Neuropharmacology*, Vol.39,No. 5, pp 835-41

Enzinger, C., Dawes, H., Johansen-Berg, H., Wade, D., Bogdanovic, M., Collett, J., Guy, C., Kischka, U., Ropele, S., Fazekas, F. & Matthews, P. M. (2009). Brain activity changes associated with treadmill training after stroke. *Stroke*, Vol.40,No. 7, pp 2460-7

Fox, P. T. &Raichle, M. E. (1986). Focal physiological uncoupling of cerebral blood flow and oxidative metabolism during somatosensory stimulation in human subjects. *ProcNatlAcadSci U S A*, Vol.83,No. 4, pp 1140-4

Fuchs, T., Birbaumer, N., Lutzenberger, W., Gruzelier, J. H. & Kaiser, J. (2003).Neurofeedback treatment for attention-deficit/hyperactivity disorder in children: a comparison with methylphenidate. *ApplPsychophysiol Biofeedback*, Vol.28,No. 1, pp 1-12

Fukuyama, H., Ouchi, Y., Matsuzaki, S., Nagahama, Y., Yamauchi, H., Ogawa, M., Kimura, J. &Shibasaki, H. (1997). Brain functional activity during gait in normal subjects: a SPECT study. *NeurosciLett*, Vol.228,No. 3, pp 183-6

Furusho, J., Koyanagi, K., Imada, Y., Fujii, Y., Nakanishi, K., Domen, K., Miyakoshi, K., Ryu, U., Takenaka, S. & Inoue, A. (2005). A 3-D Rehabilitation system for Upper Limbs. Developed in a 5-year NEDO Project and its Clinical Testing. *Proceedings of IEEE 9th International Conference on Rehabilitation Robotics*.

Grafton, S. T., Mazziotta, J. C., Presty, S., Friston, K. J., Frackowiak, R. S. & Phelps, M. E. (1992). Functional anatomy of human procedural learning determined with regional cerebral blood flow and PET. *J Neurosci*, Vol.12,No. 7, pp 2542-8

Gratton, G., Maier, J. S., Fabiani, M., Mantulin, W. W. &Gratton, E. (1994).Feasibility of intracranial near-infrared optical scanning.*Psychophysiology*, Vol.31,No. 2, pp 211-5

Grillner, S. &Wallen, P. (2004). Innate versus learned movements--a false dichotomdddy? *Prog Brain Res*, Vol.143,pp 3-12

Hatakenaka, M., Miyai, I., Mihara, M., Sakoda, S. & Kubota, K. (2007). Frontal regions involved in learning of motor skill--A functional NIRS study. *Neuroimage*, Vol.34,No. 1, pp 109-16

Jahn, K., Deutschlander, A., Stephan, T., Strupp, M., Wiesmann, M. & Brandt, T. (2004). Brain activation patterns during imagined stance and locomotion in functional magnetic resonance imaging. *Neuroimage*, Vol.22,No. 4, pp 1722-31

Jenkins, W. M. &Merzenich, M. M. (1987). Reorganization of neocortical representations after brain injury: a neurophysiological model of the bases of recovery from stroke. *Prog Brain Res*, Vol.71,, p 249-66

Jorgensen, H. S., Nakayama, H., Raaschou, H. O. & Olsen, T. S. (1999). Stroke. Neurologic and functional recovery the Copenhagen Stroke Study.*Phys Med RehabilClin N Am*, Vol.10,No. 4, pp 887-906

Kohno, S., Miyai, I., Seiyama, A., Oda, I., Ishikawa, A., Tsuneishi, S., Amita, T. & Shimizu, K. (2007).Removal of the skin blood flow artifact in functional near-infrared spectroscopic imaging data through independent component analysis.*J Biomed Opt*, Vol.12,No. 6, pp 062111

Kotchoubey, B., Strehl, U., Uhlmann, C., Holzapfel, S., Konig, M., Froscher, W., Blankenhorn, V. &Birbaumer, N. (2001). Modification of slow cortical potentials in patients with refractory epilepsy: a controlled outcome study. *Epilepsia*, Vol.42,No. 3, pp 406-16

Luft, A. R., Forrester, L., Macko, R. F., McCombe-Waller, S., Whitall, J., Villagra, F. & Hanley, D. F. (2005). Brain activation of lower extremity movement in chronically impaired stroke survivors. *Neuroimage*, Vol.26,No. 1, pp 184-94

Maki, A., Yamashita, Y., Ito, Y., Watanabe, E., Mayanagi, Y. & Koizumi, H. (1995).Spatial and temporal analysis of human motor activity using noninvasive NIR topography.*Med Phys*, Vol.22,No. 12, pp 1997-2005

Malouin, F., Richards, C. L., Jackson, P. L., Dumas, F. & Doyon, J. (2003). Brain activations during motor imagery of locomotor-related tasks: a PET study. *Hum Brain Mapp*, Vol.19,No. 1, pp 47-62

Matsuyama, K., Mori, F., Nakajima, K., Drew, T., Aoki, M. & Mori, S. (2004). Locomotor role of the corticoreticular-reticulospinal-spinal interneuronal system.*Prog Brain Res*, Vol.143,pp 239-49

Mihara, M., Miyai, I., Haraguchi, M., Kikuchi, T., Hatakenaka, M., Hattori, N. &Furusho, J. (2009). Cortical network involved in the adaptation learning of reaching using 3-dimensional robotic rehabilitation system: A functional near-infrared spectroscopic study. *Neuroimage*, Vol.47, Supplement 1, pp S170

Mihara, M., Miyai, I., Hatakenaka, M., Kubota, K. &Sakoda, S. (2007). Sustained prefrontal activation during ataxic gait: a compensatory mechanism for ataxic stroke? *Neuroimage*, Vol.37,No. 4, pp 1338-45

Mihara, M., Miyai, I., Hatakenaka, M., Kubota, K. &Sakoda, S. (2008). Role of the prefrontal cortex in human balance control.*Neuroimage*, Vol.43,No. 2, pp 329-36

Miyai, I., Suzuki, T., Kang, J., Kubota, K. & Volpe, B. T. (1999). Middle cerebral artery stroke that includes the premotor cortex reduces mobility outcome. *Stroke*, Vol.30,No. 7, pp 1380-3

Miyai, I., Tanabe, H. C., Sase, I., Eda, H., Oda, I., Konishi, I., Tsunazawa, Y., Suzuki, T., Yanagida, T. & Kubota, K. (2001). Cortical mapping of gait in humans: a near-infrared spectroscopic topography study. *Neuroimage*, Vol.14,No. 5, pp 1186-92

Miyai, I., Yagura, H., Hatakenaka, M., Oda, I., Konishi, I. & Kubota, K. (2003).Longitudinal optical imaging study for locomotor recovery after stroke.*Stroke*, Vol.34,No. 12, pp 2866-70

Miyai, I., Yagura, H., Oda, I., Konishi, I., Eda, H., Suzuki, T. & Kubota, K. (2002). Premotor cortex is involved in restoration of gait in stroke. *Ann Neurol*, Vol.52,No. 2, pp 188-94

Mori, S., Nakajima, K., Mori, F. & Matsuyama, K. (2004). Integration of multiple motor segments for the elaboration of locomotion: role of the fastigial nucleus of the cerebellum. *Prog Brain Res*, Vol.143,, p 341-51

Morton, S. M. & Bastian, A. J. (2004). Cerebellar control of balance and locomotion.*Neuroscientist*, Vol.10,No. 3, pp 247-59

Nielsen, J. B. (2003). How we walk: central control of muscle activity during human walking. *Neuroscientist*, Vol.9,No. 3, pp 195-204

Nudo, R. J., Wise, B. M., SiFuentes, F. & Milliken, G. W. (1996).Neural substrates for the effects of rehabilitative training on motor recovery after ischemic infarct.*Science*, Vol.272,No. 5269, pp 1791-4

O'Loughlin, J. L., Robitaille, Y., Boivin, J. F. &Suissa, S. (1993). Incidence of and risk factors for falls and injurious falls among the community-dwelling elderly.*Am J Epidemiol*, Vol.137,No. 3, pp 342-54

Okamoto, M., Dan, H., Sakamoto, K., Takeo, K., Shimizu, K., Kohno, S., Oda, I., Isobe, S., Suzuki, T., Kohyama, K. & Dan, I. (2004). Three-dimensional probabilistic

anatomical cranio-cerebral correlation via the international 10-20 system oriented for transcranial functional brain mapping. *Neuroimage*, Vol.21,No. 1, pp 99-111

Quant, S., Maki, B. E. &McIlroy, W. E. (2005).The association between later cortical potentials and later phases of postural reactions evoked by perturbations to upright stance.*NeurosciLett*, Vol.381,No. 3, pp 269-74

Sitaram, R., Zhang, H., Guan, C., Thulasidas, M., Hoshi, Y., Ishikawa, A., Shimizu, K. &Birbaumer, N. (2007). Temporal classification of multichannel near-infrared spectroscopy signals of motor imagery for developing a brain-computer interface. *Neuroimage*, Vol.34,No. 4, pp 1416-27

Slobounov, S., Hallett, M., Stanhope, S. &Shibasaki, H. (2005). Role of cerebral cortex in human postural control: an EEG study. *ClinNeurophysiol*, Vol.116,No. 2, pp 315-23

Suzuki, M., Miyai, I., Ono, T., Oda, I., Konishi, I., Kochiyama, T. & Kubota, K. (2004). Prefrontal and premotor cortices are involved in adapting walking and running speed on the treadmill: an optical imaging study. *Neuroimage*, Vol.23,No. 3, pp 1020-6

Takahashi, T., Takikawa, Y., Kawagoe, R., Shibuya, S., Iwano, T. & Kitazawa, S. (2011). Influence of skin blood flow on near-infrared spectroscopy signals measured on the forehead during a verbal fluency task. *Neuroimage*, Vol.57,No. 3, pp 991-1002

Takakusaki, K., Oohinata-Sugimoto, J., Saitoh, K. &Habaguchi, T. (2004). Role of basal ganglia-brainstem systems in the control of postural muscle tone and locomotion.*Prog Brain Res*, Vol.143,pp 231-7

Ward, N. &Frackowiak, R. (2004). The cerebral basis of functional recovery., In. *Human brain function*. F. K. Frackowiak RSJ, Frith CD, Dolan RJ, Price CJ, Zeki S, Ashburner J, Penny W. pp. 105-123, Academic press.San Diego

Ward, N. S., Brown, M. M., Thompson, A. J. &Frackowiak, R. S. (2003). Neural correlates of motor recovery after stroke: a longitudinal fMRI study. *Brain*, Vol.126,Pt 11, pp 2476-96

Woollacott, M. & Shumway-Cook, A. (2002). Attention and the control of posture and gait: a review of an emarging area of research. *Gait Posture*, Vol.16,pp1-14

Yamada, T., Umeyama, S. & Matsuda, K. (2009).Multidistanceprobe arrangement to eliminate artifacts in functional near-infrared spectroscopy. *Journal of Biomedical Optics*, Vol.14,No. 6, pp 064034

4

The Use of Near-Infrared Spectroscopy to Detect Differences in Brain Activation According to Different Experiences with Cosmetics

Masayoshi Nagai[1], Keiko Tagai[2], Sadaki Takata[2] and Takatsune Kumada[1]
[1]*National Institute of Advanced Industrial Science and Technology (AIST)*
[2]*Shiseido Co., Ltd.*
Japan

1. Introduction

1.1 Economic behavior and brain imaging

Human economic and purchasing behavior has been studied primarily with brain imaging techniques such as functional magnetic resonance imaging (fMRI). One common topic in this domain of investigation is the willingness to pay (WTP). An essential component of every marketplace transaction is a WTP calculation in which buyers calculate the maximum amount of money they are willing to pay in exchange for the object being sold. WTP decisions are related to activation in the (medial) orbitofrontal cortex (OFC) (Wallis & Miller, 2003; Padoa-Schioppa & Assad, 2006; Erk, Spitze, Wunderlich, Galley, & Walter, 2002; Rolls, 1996; Plassmann, O'Doherty, Rangel, 2007; Schoenbaum, Chiba, & Gallagher, 1998; Tremblay & Schultz, 1999; Roesch & Olson, 2004). Medial OFC activation is related to choice or preference in the absence of explicit attention to the products presented, suggesting that the WTP calculation occurs implicitly. These studies have been performed under both well-controlled experimental settings and artificial environments because of the restrictions involved in using fMRI techniques. Although fMRI offers advantages related to the spatial resolution of cognitive and deep-brain activities, it requires a high degree of patient restraint during measurements made in pediatric research settings.

1.2 Advantages of using near-infrared spectroscopy

Near-infrared spectroscopy (NIRS) is a relatively new imaging technique that is non-invasive, highly flexible, and requires less participant restraint and sedation; it also produces continuous real-time measurements (Baird, Kagan, Gaudette, Walz, Hershlag, & Boas, 2002; Endo, Nagai, Kumada, 2009; Kubota, Toichi, Shimizu, Mason, Findling, Yamamoto, & Calabresea, 2006; Matsuda & Hiraki, 2006; Otsuka, Nakato, Kanazawa, Yamaguchi, Watanabe, & Kakigi, 2007). The NIRS technique has been successfully used in investigations of the neural correlates of complex actions such as walking and running on a treadmill (Suzuki, Miyai, Ono, Oda, Konishi, Kochiyama, & Kubota, 2004), peeling an apple (Okamoto, Dan, Shimizu, Takeo,

Amita, Oda, Konishi, Sakamoto, Isobe, Suzuki, Kohyama, & Dan, 2004), demonstrating that NIRS can be applied to real-life situations involving actions and movements.

1.3 In-store buying experiences and brain imaging

Many different ways of trying articles/products at stores exist, including touching and listening to explanations offered by sales persons. However, the most effective ways to provide a good impression to customers or increase the chance that customers will purchase a given item remains unclear. Additionally, the association of the formation of an impression and buying behavior with brain activation has not been investigated. In actual situations, sales persons have a variety of ways to explain the features of articles to be sold. In the present study, we simulated a situation in which a customer (i.e., participant) and a sales person (i.e., confederate) interacted in five different ways.

1.4 Purpose of the study

The purpose of the current study was to investigate the relationship between different ways of learning about a cosmetic and brain activation and to examine the relationship between brain activation and impression formation and willingness-to-use decisions.

2. Method

2.1 Participants

Sixty women (age range: 25–39 years, average age: 30.6 years) participated in this experiment; the sample included 17 Japanese, 10 Chinese, 11 American, 11 German, and 11 Hispanic individuals. These classifications were based on nationality and place of residence. One left-handed subject (Hispanic) and two subjects (American and German) with a Japanese father or mother were excluded from the data analysis.

2.2 Apparatus

We used a multichannel NIRS system (ETG-4000, Hitachi Medical Corp., Tokyo, Japan) to measure brain activity. The NIRS unit was operated at near-infrared wavelengths of 695 and 830 nm and was used to measure temporal changes in concentrations of oxygenated hemoglobin (oxy-Hb), deoxygenated hemoglobin (deoxy-Hb), and total-hemoglobin. We used a pair of probe holders, each of which consisted of arrays measuring 4 × 4. Sixteen optodes (eight emitting and eight detecting) produced 24 channels for each probe. The distance between each emitting and corresponding detecting optode was 3.0 cm. The sampling rate at each channel was approximately 10 Hz.

The probes were placed on the frontal region of each hemisphere (Fig. 1). The Cz (international 10/20 system) was set to align with a line connecting between the positions at the superior/posterior corners of the arrays (i.e., the emitter for the right probe and the detector for the left probe), and the Fz was aligned with the middle of the two connecting lines between the positions at the superior/anterior corners of the arrays and between the positions at the superior/second-from-anterior intersections of the arrays. Because the participant's heads were not exactly the same size, the Fz positions of participants differed slightly. The position of each column of emitters or detectors in the array was parallel to the midline of the brain.

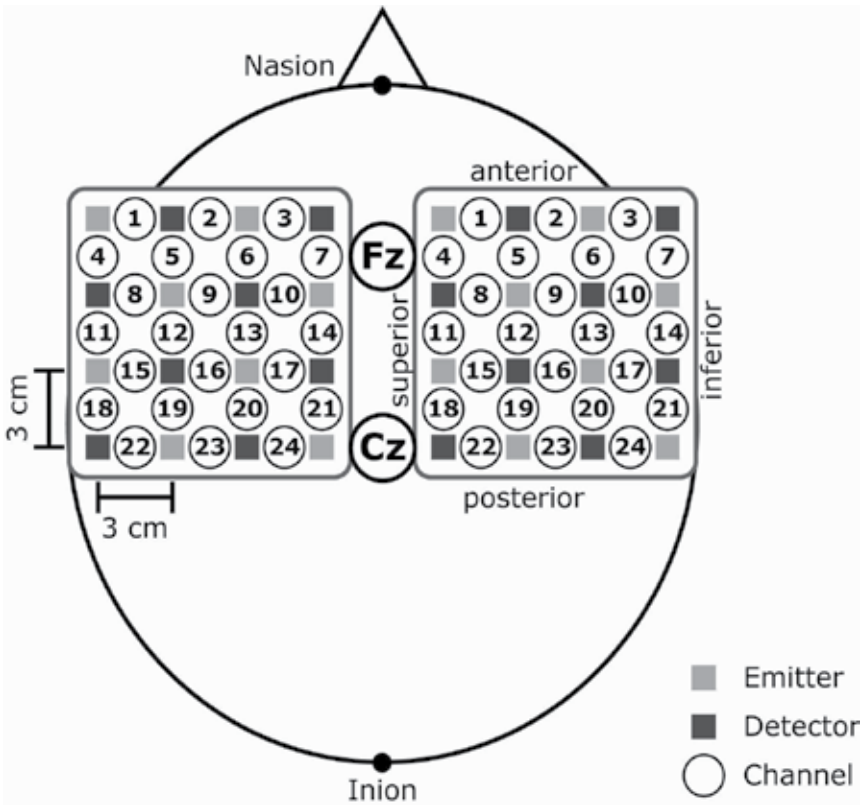

Fig. 1. Positions of optodes placed on the prefrontal regions of both hemispheres. The distance between each emitter (indicated by light gray squares) and the corresponding detector (indicated by dark gray squares) was 3 cm. These emitters and detectors were placed in probes with 4 × 4 arrays.

2.3 Stimuli, conditions, and task

The task involved gathering information about a cosmetic article (facial cream) in five different ways (verbal explanation, written explanation, application, smell, and touch) in an environment simulating a cosmetics counter (Fig. 2). The facial cream was in a gold jar without a label bearing the name of a particular product. Five simulation conditions were used. Under the explanation condition, the subjects were asked to understand the explanation about the facial cream provided by a sales person (i.e., a confederate). Under the written condition, the explanation was given by a sales person, but he or she used a text and pictures to provide information about the facial cream. Under the application condition, the subjects were required to apply the facial cream to the back of their left hand. Under the smell condition, they were required to smell the facial cream on their left hand. Under the touch condition, they were required to touch a jar of facial cream. The order of these five conditions corresponded to the sequence above, and each condition lasted 15 sec. A 5-sec preparation time and a 35-sec rest time were added for NIRS data recording (Fig. 3).

Fig. 2. Five different ways by which participants learned about a facial cream:
a) explanation, b) written, c) application, d) smell, and e) touch.

Fig. 3. Experimental schedule for NIRS recording

2.4 Subjective rating

After the NIRS measurements, subjects used a 100-point scale to rated the face cream with respect to 11 subjective reactions : 1, comfort; 2. relief; 3, conviction; 4, satisfaction; 5, understanding; 6, promise; 7, reliability; 8, likability; 9, willingness to use; 10. interest; and 11, appeal.

3. Results

3.1 NIRS data analysis

Trials that had movement artifacts, as reflected by steep changes in the time series of the oxy-Hb and deoxy-Hb concentrations, were removed from the analysis. After these data were eliminated, we focused on oxy-Hb concentrations as the index of brain activation. Many NIRS studies use changes in oxy-Hb concentrations as the primary foci of analyses (e.g., Matsuda & Hiraki, 2006; Otsuka, Nakato, Kanazawa, Yamaguchi, Watanabe, Kakigi, 2007) because these values are the most sensitive to changes in regional cerebral blood flow and are correlated with the blood-oxygen-level dependence (BOLD) signal (Hoshi, Kobayashi, & Tamura, 2001; Strangman, Culver, Thompson, & Boas, 2002).

Before starting the actual data analysis, the relative oxy-Hb concentrations at baseline (the line in the data repesenting oxy-Hb concentrations between the 5-sec preparation time and the last 5-sec rest time) were calculated, which reduced low–frequency noise. Moreover, if the calculated relative oxy-Hb concentration values included an artifact, such as alternating current noise due to the poor contact of the probe with the skin, data from that channel under all conditions were deleted.

Data from one channel of one subject are shown in Fig. 4. The horizontal axis shows time from the beginning of the task, and the vertical axis shows oxy-Hb changes. This subject's

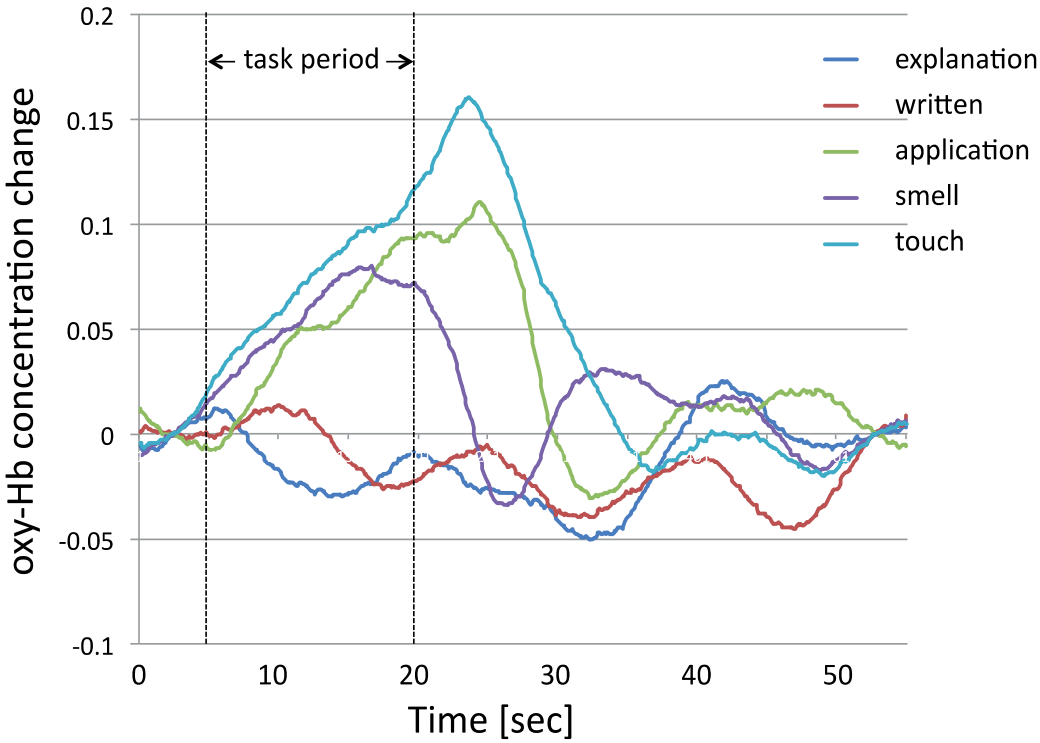

Fig. 4. An example of the time course of changes in the concentrations of oxy-hemoglobin (Hb) under the five conditions.

data show that the oxy-Hb concentration increased after task onset and decreased after offset under the application, smell, and touch conditions. The brain-activation level was defined as the integral value of the oxy-Hb concentration during the task (15 sec). The average and standard deviation of the activation levels were calculated for each channel across subjects. When the activation level at a channel was higher than the average ±2.5 standard deviations, that channel's data were deleted from analysis under all conditions.

3.2 Brain activation

We performed *t*-tests to compare the activation levels with zero. Figure 5 shows the significantly activated channels under the five different conditions. The left and right 48 circles represent channel loci. Red, orange, and yellow circles show that the *p*-values for the test were <0.01, 0.05, and 0.1, respectively. Following Okamoto, Dan, Sakamoto, Takeo, Shimizu, Kohno, Oda, Isobe, Suzuki, Kohyama, and Dan (2004), the channels were located in brain areas. One channel at the left frontal lobe was activated under the explanation condition. This channel is part of Broca's area, and its activation was due to the verbal explanation under the explanation condition. Under the written condition, the left and right superior frontal lobes, corresponding to the supplementary motor area, were activated. Under the written condition, participants needed to integrate the visual and auditory information on the form. These activated areas may have been related to integrated

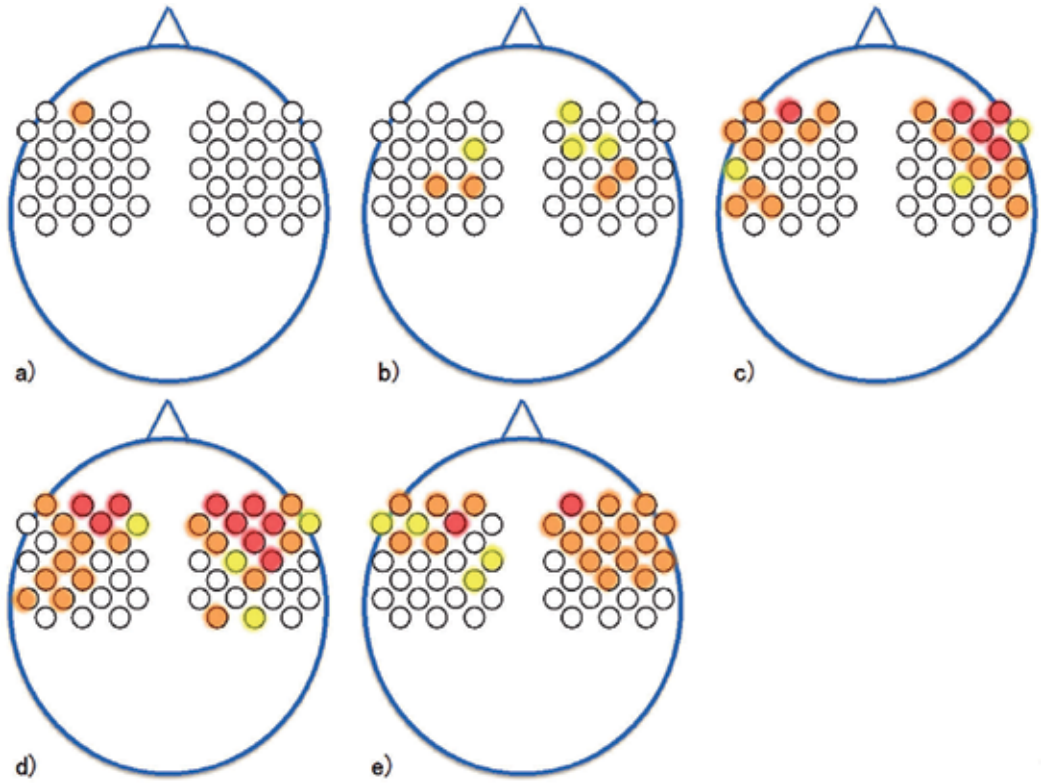

Fig. 5. Channels with statistically significant brain activation

processing. More channels and more areas were activated under the next three conditions than under the explanation and written conditions. Under the application condition, the left and right frontal and lateral lobes were activated. Under the smell condition, the strongest activation location shifted in the superior direction in the left hemisphere and activation in the right frontal area increased compared with that under the application condition. Moreover, activation in the lateral lobes was weakened compared with that under the application condition, and activation in the parietal lobes was also evident. Under the touch condition, activation in the left parietal lobe disappeared and activation in the right frontal lobe weakened compared with the results under the application condition. Under the latter three conditions, participants were required to perform motor actions and engage in sensory-information processing, which may have activated broader areas in the corresponding motor and sensory areas. These results indicate that different ways of considering a facial cream activated different brain areas.

3.3 Brain activation and subjective ratings

We analyzed the correlation between the subjective ratings and brain activation. The 11 subjective ratings were classified into two subtypes: "impressions" of the facial cream (1, comfort; 2, relief; 3, conviction; 4, satisfaction; 5, understanding; 6, promise; 7, reliability; 8, likability) and "willingness to use" (WTU) (9, willingness to use; 10, interest; 11, appeal.).

Figure 6 shows the channels showing statistically significant correlations with impression or WTU. Under the explanation condition, brain activation in the left inferior frontal lobe was correlated with impression and WTU. Under the written condition, brain activation in the left parietal lobe was correlated with impression, and that in the right superior frontal lobe was correlated with impression and WTU. Under the application condition, brain activation in the left superior frontal lobe and lateral lobe was correlated with impression, that in the right superior frontal lobe was correlated with impression, and that in the right parietal and lateral lobes was correlated with impression and WTU. Under the smell condition, brain activation in the left parietal lobe was correlated with impression and WTU, that in the right inferior frontal lobe was correlated with impression, and that in the right parietal lobe was correlated with impression and WTU. Under the touch condition, brain activation in the left parietal lobe was correlated with impression, and that in the right parietal lobe was correlated with impression and WTU.

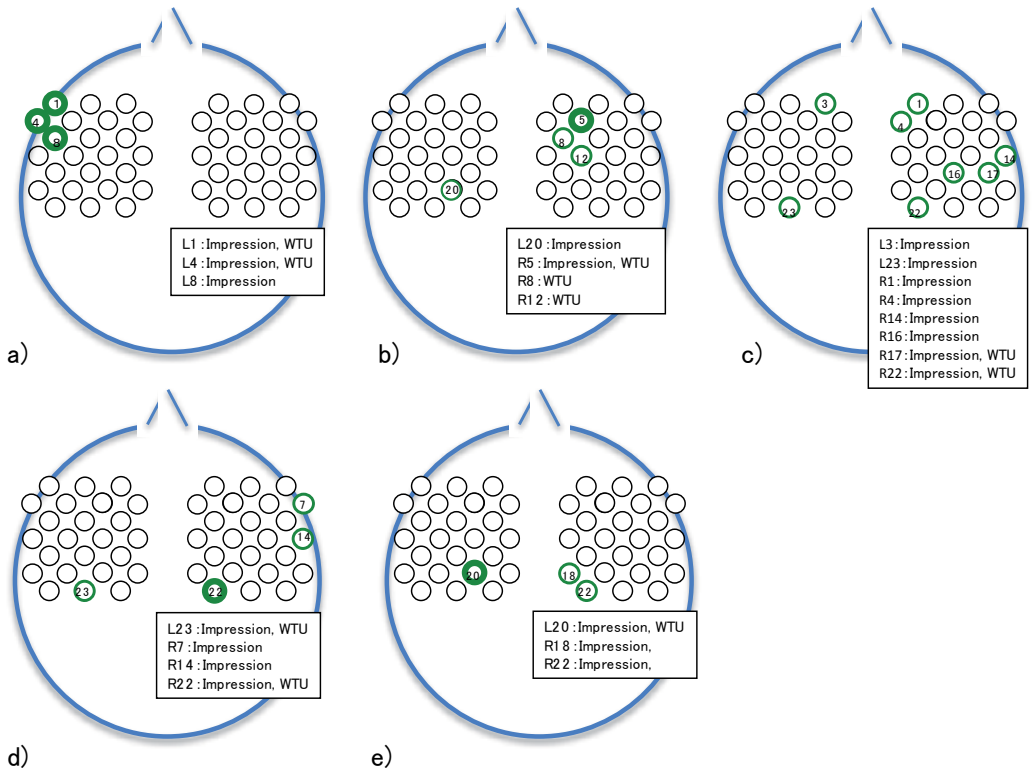

Fig. 6. Channels with statistically significant associations of brain activation with impression and WTU

3.4 Brain activation and subjective ratings

We analyzed the correlation between subjective ratings of the facial cream and brain activations using the dichotomy between impression and WTU described above.

We found the following relationships between brain activation and subjective ratings for impression and WTU. Under the explanation condition, brain activation in the left frontal

lobe was correlated with impression and WTU; under the written condition, brain activation in the right superior frontal lobe was correlated with impression and WTU. Under the application condition, brain activation in the right superior frontal and parietal areas were related to impression and WTU. Under the smell and touch conditions, activation in the left and right parietal lobes was related to impression and WTU.

3.5 Brain activation by subjective ratings and/or by task

Three different trends emerged from comparisons among areas showing statistically significant activation while the subjects performed tasks (Fig. 5). Statistically significant correlations related to subjective rating are shown in Figure 6. The first trend involved the statistically significant relationship between channels and brain activation during tasks but did not include a correlation with subjective ratings. Most channels followed this trend (86% of all channels). The second trend involved a statistically significant relationship between channel and brain activation during tasks and a significant correlation with subjective ratings. Only a few channels followed the second trend; one channel followed it under the written condition, two followed it under the smell condition, and five followed under the application condition. The third trend involved statistically non-significant relationships between channels and brain activation during a task but included significant correlations with subjective ratings. Thus, brain activations following the first and third trends showed stronger influences on subjective ratings.

4. Discussion

4.1 Summary of results

In the current experiment, participants learned about a facial cream in five different ways while their brain activity was monitored. They then rated their impressions and WTU the facial cream. The results suggested that different ways of learning about a facial cream activated different brain areas. Moreover, some channels showed a correlation between brain activation and subjective ratings.

4.2 Relationship with WTP

Many studies have suggested that WTP judgments are based on activation in the medial OFC. Because this area is not on the brain surface, it is difficult to monitor this activation with NIRS. We have shown that brain activation in the right superior frontal and the left and right parietal lobes was related to WTU. Because of the limitations of NIRS measurements, it is unclear whether the medial OFC was activated in the current experiments and related to WTU judgments.

4.3 Difference by race

Participants with different nationalities and different cultural backgrounds are expected to have different styles of thinking. A number of studies have suggested that people from different cultures have different cognitive processing styles (e.g., North Americans attend to focal objects more than do East Asians). Although these cultural differences may cause the correlations between brain activations and subjective ratings to differ among cultures, our

results indicate the operation of a common brain mechanism in this regard. However, culture may nonetheless influence impressions, WTU, WTB, and brain activation related to these judgments. The cultural differences involved in-store shopping behaviors need to be understood given that such differences carry important implications for both academic and commercial domains.

4.4 Advantage of NIRS for studying everyday situations

The participants in the current study moved their arms and hands to apply a facial cream and touched jar. These actions are not permitted in magnetic resonance imaging scanners, and they also cause strong electroencephalogram artifacts due to muscle potentials. Thus, brain monitoring with NIRS is the only acceptable technique to use in situations in which participants move with relative freedom.

5. Conclusion

The current study was to investigate the relationship between different ways of learning about a cosmetic and brain activations. In the current experiment, participants learned about a facial cream in five different ways while their brain activity was monitored, and then rated their impressions and WTU on the facial cream. The results suggested that different ways of learning about a facial cream activated different brain areas. Moreover, some channels showed a correlation between brain activation and subjective ratings.

6. References

Baird, A. A., Kagan, J., Gaudette, T., Walz, K. A., Hershlag, N., & Boas, D. A. (2002). Frontal lobe activation during object permanence: data from near-infrared spectroscopy. *Neuroimage,* 16:1120–5.

Endo, N., Nagai, M., & Kumada, T. (2009). Objective estimation of state of content understanding by near-infrared spectroscopy (NIRS). *Japanese Journal of Psychonomic Science, 28, 2–16.*

Erk, S., Spitzer, M., Wunderlich, A., Galley, L., & Walter, H. (2002) Cultural objects modulate reward circuitry. *NeuroReport,* 13:2499–2503

Hoshi, Y., Kobayashi, N., & Tamura, M. (2001). Interpretation of near-infrared spectroscopy signals: a study with a newly developed perfused rat brain model. *Journal of Applied Physiology*, 90, 1657–1662.

Kubota, Y., Toichi, M., Shimizu, M., Mason, R. A., Findling, R. L., Yamamoto, K., & Calabresea, J. R. (2006). Prefrontal hemodynamic activity predicts false memory—A near-infrared spectroscopy study. *Neuroimage*, 31, 1783-1789.

Matsuda, G., & Hiraki, K. (2006). Sustained decrease in oxygenated hemoglobin during video games in the dorsal prefrontal cortex: a NIRS study of children. *NeuroImage*, 29, 706–711.

Okamoto, M., Dan, H., Shimizu, K., Takeo, K., Amita, T., Oda, I., Konishi, I., Sakamoto, K., Isobe, S., Suzuki, T., Kohyama, K., and Dan, I. (2004). Multimodal assessment of cortical activation during apple peeling by NIRS and fMRI. *Neuroimage,* 21, 1275–1288.

Otsuka, Y., Nakato, E., Kanazawa, S., Yamaguchi, M. K., Watanabe, S., & Kakigi, R. (2007). Neural activation to upright and inverted faces in infants measured by near infrared spectroscopy. *NeuroImage*, 34, 399–406.

Padoa-Schioppa, C. & Assad, J. A. (2006). Neurons in the orbitofrontal cortex encode economic value. *Nature*, 441:223–226.

Plassmann, H., O'Doherty, J. & Rangel, A. (2007). Orbitofrontal cortex encodes willingness to pay in everyday economic transactions. Journal of Neuroscience. 27, 9984–9988.

Roesch, M. R. & Olson, C. R. (2004). Neuronal activity related to reward value and motivation in primate frontal cortex. *Science*, 304, 307–310.

Schoenbaum, G., Chiba, A.A. & Gallagher, M. (1998). Orbitofrontal cortex and basolateral amygdala encode expected outcomes during learning. *Nature Neuroscience*. 1, 155–159.

Shibata, H., Suzuki, M., & Gyoba, J. (2007). Cortical activity during the recognition of cooperative actions. *Neuroreport*, 7, 697–701.

Strangman, G., Culver, J. P., Thompson, J. H., & Boas, D. A. (2002). A quantitative comparison of simultaneous BOLD fMRI and NIRS recordings during functional brain activation. *NeuroImage*, 17, 719–731.

Suzuki, M., Miyai, I., Ono, T., Oda, I., Konishi, I., Kochiyama, T., & Kubota, K. (2004). Prefrontal and premotor cortices are involved in adapting walking and running speed on the treadmill: an optical imaging study. *Neuroimage, 23, 1020–1026.*

Tremblay L. & Schultz W. (1999) Relative reward preference in primate orbitofrontal cortex. *Nature*, 398, 704–708.

Wallis, J. D. & Miller, E. K. (2003) Neuronal activity in primate dorsolateral and orbital prefrontal cortex during performance of a reward preference task. *European Journal of Neuroscience,* 18, 2069–2081.

5

Using NIRS to Investigate Social Relationship in Empathic Process

Taeko Ogawa and Michio Nomura
Tokai Gakuin University and Kyoto University
Japan

1. Introduction

We perform appropriate social actions in the various scenes of everyday life. For example, we speculate about other people's intentions and feelings in order to understand them, or inhibit negative emotions such as anger toward them. Furthermore, we engage in altruistic behaviors out of consideration and empathy for unrelated others. Even for a person who we do not like, we can also be sensitive to his or her feelings and take the most suitable action that seems altruistic at the time. When we behave in such a prosocial way, how do we recognize ourself and others, regulate our emotions, and make decisions?

In this chapter, we first give an outline of the social neuroscience studies on empathy and perspective-taking that use brain imaging techniques. Next, we review a near-infrared spectroscopy (NIRS) study reported by Nomura, Ogawa, and Nomura (2010), and finally we explain how we can use NIRS to investigate psychological and social neuroscience issues.

1.1 Social cognition and social brain

The mental ability underlying prosocial behaviors involving interaction with others is called *social cognition*, and the neural network involved in the functions of social cognition is called *social brain* (Brothers, 1990). Although brain imaging and lesion studies have always been related to psychology, over the past two decades the social brain studies have demonstrated the neural mechanisms underlying social cognition, including self-other recognition, emotion, recognition of facial expression, detection of intentionality and eye-direction, imitation of action, and theory of mind; these studies have been conducted in such fields as cognitive neuroscience, comparative cognitive science, social psychology, and developmental psychology (e.g., Decety & Cacioppo, 2011). Social cognitive neuroscience is a relatively new field studying social cognition from the standpoint of cognitive neuroscience (Cacioppo & Bernston, 1992; Ochsner & Lieberman, 2001).

In this chapter, we focus on empathy to others as a theme of social cognition. After we review recent studies on empathy by the approach of social cognitive neuroscience (mainly using functional magnetic resonance imaging (fMRI)), we introduce a NIRS study in which we investigated perspective taking associated with social relationships in the empathic process. First, however, we briefly explain the principle of NIRS measurement.

1.2 Measurement of human brain activity by NIRS

In the field of brain science, fMRI and positron emission tomography (PET) have mainly been used to measure human brain activity since the 1990s. Coupled with the development of cognitive neuroscience, brain imaging techniques using NIRS have spread rapidly since the early 2000s.

When neural activity occurs in the human brain, regional cerebral blood flow increases in specific brain regions associated with the performance of a particular task. Therefore, hemoglobin concentration of blood increases in the regions. Capturing the change of hemoglobin concentrations enables us to identify the active regions in the brain. NIRS noninvasively monitors the hemodynamic change mediated by the change in hemoglobin concentration (advantages and disadvantages of NIRS in comparison with other devices are described in Section 3).

The NIRS device emits a near-infrared light from the surface of the head through optical fiber and detects the scattered and reflected light in the brain. The light of the near-infrared range, from 700 to 1,000 nm, has relatively high permeability in living tissue. The measurement uses the different absorbance characteristics between oxygenated hemoglobin (oxy-Hb) and deoxygenated hemoglobin (deoxy-Hb). Because the light path's length from the emitting position to the detecting position cannot be measured, absolute concentration changes of hemoglobin in the brain tissue cannot be determined. The relative concentration changes in oxy-Hb, deoxy-Hb, and total-Hb are calculated by using three wavelengths in the current NIRS devices according to the modified Beer-Lambert law (e.g., Hoshi & Tamura, 1993; Villinger & Chance, 1997).

Previous studies using brain imaging techniques of multi-channel NIRS clarified the neural mechanisms involved in various cognitive functions, such as motion perception of the human body (Shimada, Hiraki, Matsuda, & Oda, 2004), language processing (Herrmann, Ehlis, & Fallgatter, 2003; Noguchi, Takeuchi, & Sakai, 2000), emotion (Suzuki, Gyoba, & Sakuta, 2005), Stroop effect (Schroeter, Zysset, Kruggel, & Yves von Cramon, 2003), and Go-Nogo task (Herrmann, Plichta, Ehlis, & Fallgatter, 2005).

1.3 Neuroscience perspectives on empathy

1.3.1 Functional components of empathy

"Empathy" is understanding another person's internal state, including their thoughts and feelings, imaging the viewpoint of the other, and responding with compassion to the other's distress (e.g., Decety & Ickes, 2009; Preston & de Waal, 2002). The psychological construct of empathy that motivates prosocial behaviors is regulated by both a basic emotional contagion system (affective components) and a more advanced cognitive perspective taking system (cognitive components).

Emotion contagion occurs by the influence of others' emotions automatically without self-awareness (Hatfield, Rapson, & Le, 2009). On the other hand, cognitive perspective taking is the ability to understand the other's thoughts and feelings by imaging his or her viewpoint. In order to understand the other intentionally and consciously, cognitive empathy may modulate and control emotions depending on executive resources (i.e., higher cognitive functions including working memory, attention control, and memory retrieval).

Decety (2006) proposed a neuroscientific model corresponding to the conceptual model of empathy. This model consists of four major functional components: shared representation between the self and the other, mental flexibility to take the other's perspective, self-awareness, and emotion regulation. It is assumed that these four components dynamically interact to produce empathy.

The four components are related to brain functions according to Decety's model. Shared representation is related to fronto-parietal networks based on the shared circuits between perception-action, and self-awareness is related to the inferior parietal lobule and the anterior insula on the right side. Mental flexibility is related to the prefrontal cortex. Emotion regulation is involved in the interaction between prefrontal and anterior cingulated systems and subcortical emotion-generation systems.

1.3.2 Empathy and ventrolateral prefrontal cortex

According to the model of empathy (Decety, 2006) described above, it is hypothesized that the interaction between bottom-up processing and top-down processing produces empathy. Bottom-up processing begins by an input of perceived data (information from the outside world) and interprets the perceived data under the influence of the physical characteristics of the stimuli. When we meet an other person, we are resonant to the movements and emotions of that person by the perceptual input automatically and unconsciously. In other words, emotions are contagious, and this processing proceeds in a bottom-up fashion automatically. On the other hand, top-down processing is influenced by the context of the present situation and by knowledge from past experience that individuals use as stimuli. Consequently, in order to understand others from the viewpoint of the others, intentional and conscious mental efforts are required. These cognitive empathic processes modulate emotion regulation and perspective taking, depending on the executive functions for higher controlled processing of working memory, attention control, and memory retrieval.

Such higher cognitive-controlled functions are involved in the prefrontal cortex, including the ventrolateral prefrontal cortex (VLPFC). The right VLPFC is well known as a critical region for general inhibition and for regulating affective responses. The VLPFC also modulates the activity of the amygdala, which plays a key role in emotional appraisal and is related to detections of fear expression and eye-direction (Adolphs, Tranel, Damasio, & Damasio, 1994, 1995; Wicker, Michel, Henaff, & Decety, 1998). Therefore, the VLPFC is a critical area for the processing of emotional regulation via cortical-subcortical pathways (Batson, Early, & Salvarini, 1997).

1.3.3 "Pain network" which feels the pain of others

Previous studies on perspective taking have been reported in the brain imaging studies that deal with empathy for the physical pain of others (Decety & Grezes, 2006; Singer, Seymour, O'Doherty, Kaube, Dolan, & Frith 2004; Singer, Seymour, O'Doherty, Stephan, Dolan, & Frith, 2006). These studies found the existence of a "*pain network*" including the anterior cingulate cortex (ACC) and insula, which are involved in understanding the pain of others like one's own pain.

Singer et al. (2004) used fMRI to compare brain activities between two conditions: when participants felt pain in oneself, and when participants observed that their beloved partner,

who came to the laboratory with them, felt pain. In addition, the subjective empathic abilities of the participants were measured by questionnaires. The results show that the activated brain areas in common between the self condition (i.e., the participants themselves feel a pain) and the other condition (i.e., the participants observe their partners feeling a pain) were the bilateral anterior insula (AI), rostral anterior cingulate cortex (ACC), brainstem, and cerebellum. The activation levels of AI and ACC were significantly correlated positively with the empathic ability of individuals. These findings indicate that AI and ACC form the neural basis of understanding the emotions of one's own and others' pain and that the areas are related to emotion processing to evoke the empathic response to the pain of others.

Furthermore, Singer et al. (2006) reported evidence that the empathic response to the pain of others is affected by the social relationship with the other. Namely, a person shows strong empathy for the pain of a favorite person, whereas a person does not show empathy for the pain of non-favorite persons. More interestingly, the results indicate that males appear to feel pleasure in the pain of the non-favorite others.

In the experimental paradigm presented by Singer et al. (2006), participants played the Prisoner's Dilemma game in order to form a good or a bad impression of the opponent players (confederates) before measuring the brain activity by fMRI. In the game, one of two opponents made a cooperative and fair play toward the participants, whereas the other opponent made an uncooperative and unfair play. As a result, the participants came to like the fair opponent but came to dislike the unfair opponent. After the game, the brain activity was measured while the participants were observing the opponent receive a pain to the hand by electrical stimulation.

The results showed that activation in the pain network encompassing the AI and ACC was observed for fair opponents in both male and female participants. However, this activation was significantly reduced in males for pain given to the unfair opponents. At the same time, it was reported that the activity of the nucleus accumbens, known as a reward-related area, increased depending on the degree that the participant strongly desired revenge. This means that for males, the pain felt by the opponents who show unfair behavior brings them satisfaction in their revenge.

Nevertheless, even if they are disliked or unknown others, we can give them a helping hand when we encounter a situation in which the disliked or unknown other feels pain or distress, and we feel the need to help them from an ethical viewpoint. In order to clarify the neural mechanisms underlying such prosocial behaviors that suppress our own feelings, we must examine how the individual difference in perspective-taking ability influences not only the social relationships with the others but also influences the ability to evaluate the emotional states based on the social relationship.

Previous studies have demonstrated that emotion regulation processing is involved in the right VLPFC in relation to regulating or suppressing negative emotions caused by pain (Lieberman, Eisenberger, Crockett, Tom, Pfeifer, & Way, 2007; Wager, Davidson, Hughes, Lindquist, & Ochsner, 2008). In addition, it has also been reported that both self- and other-perspective taking are related to the activation of the pain network (Jackson, Brunet, Meltzoff, & Decety, 2006), and the activation of these areas increases depending on the degree of subjective empathic abilities as measured by questionnaires (Singer et al., 2004, 2006). Therefore, Nomura et al. (2010) focused on the mechanism of perspective taking in

the empathic process and investigated the individual differences in perspective taking and the neural responses evoked by the inhibition of emotions; this was done by analyzing the activation of VLPFC.

2. A NIRS study on perspective taking associated with social relationships by Nomura et al. (2010)

2.1 Purpose

Following the paradigm of Singer et al. (2006), after playing the Prisoner's Dilemma game to form a good or a bad impression of the opponents, the participants observed the opponents' facial expressions (happy, neutral, and angry) and evaluated the valence of each facial expression on a 7-point scale ranging from "pleasantness" to "unpleasantness." The participants observed the facial expressions under two perspective-taking conditions: self-perspective vs. other-perspective. The brain activity was measured by using NIRS while the participants were evaluating the facial expressions. The participants were divided into two groups according to the points of the Interpersonal Reactivity Index (IRI) that they completed after all experiments. The IRI measures the components of empathy, from which we took particular note of perspective taking (e.g., 'I sometimes try to understand my friends better by imagining how things look from their perspective.').

The prediction was that a higher unpleasant emotion would be produced in the self-perspective condition rather than in the other-perspective condition during observation of an unfair opponent, since negative emotions should arise automatically when the participants observe the facial expression of the unfair opponent. On the other hand, in the other-perspective condition with the unfair opponent, the participants should rate the facial expression from the viewpoint of the unfair opponent while inhibiting the negative emotions for the disliked opponent, especially for a happy expression. Therefore, it was expected that the activation would increase in the right VLPFC in the other-perspective condition.

Moreover, the right VLPFC might play an important role for individuals who have a high ability of perspective taking. The right VLPFC would likely have a greater impact on taking the other-perspective, since top-down control from the prefrontal cortex functions very well for individuals with a high ability of perspective taking than for individuals with a low ability of perspective taking.

2.2 Method

2.2.1 Participants

Thirty-seven healthy volunteers (18 females; mean age ± SD: 19.5 ± 3.4) were divided into two groups according to the perspective taking scale of a Japanese version of the IRI (Davis, 1983): 19 participants with a high perspective-taking ability (mean score 24.79 ± 1.76) and 18 participants with a low perspective-taking ability (mean score 18.83 ± 1.89).

2.2.2 Stimuli

Pictures of happy and anger facial expressions were made by a morphing technique, based on digitized grayscale images of 6 Japanese faces (3 men and 3 women) showing a neutral

facial expression. Participants in a pilot study rated each facial expression on a 5-level scale (0 = not at all to 4 = very intense) in terms of happiness and anger. The mean rating for the valence of the selected stimuli was 2.32 ± 0.73 for anger and 2.57 ± 0.89 for happiness. Furthermore, the intensity of each facial expression was rated and the rating scores for the intensity of all selected facial stimuli showing anger and happiness were 3.40 ± 0.92 and 3.15 ± 0.86, respectively.

2.2.3 Procedure

First, as an orienting task, the relationship between the participants and six opponent players (two fair, two unfair, and two neutral players) was manipulated through a sequential Prisoner's Dilemma game controlled by a computer program. In each trial, the participants decided whether they cooperate with the opponent or not. If both the participant and the opponent decide to cooperate, they each earn 10 points; if both defect, neither earns any points. If the participant cooperates and the opponent defects, the participants loses 40 points and the opponent earns 40 points, and vice versa. The cooperation rates throughout all trials for the fair opponent, the neutral opponent, and the unfair opponent were set in 80%, 50%, and 20%, respectively.

The opponent's facial expressions were presented on a PC screen after the participants decided their selection. When both the participant and the opponent cooperated, the opponent's expression became happy; when both defected, the opponent's expression became angry. When the participant cooperated and the opponent defected, the opponent's expression became happy, whereas when the participant defected and the opponent cooperated, the opponent's expression became angry. After playing with each opponent, the participants evaluated the opponent on a 7-point scale ranging from "cooperative" to "uncooperative" and "like" to "dislike."

After the orienting task, the participants performed a perspective-taking task with the NIRS device. A block design consisting of 12 blocks was used. The participants observed the facial expressions of the opponents under the two conditions of self-perspective and other's perspective. After a fixation point, the other's facial expression was shown for one second. The participants evaluated the valence of the facial expression on a 7-point scale from "pleasantness" to "unpleasantness" within two seconds.

2.2.4 NIRS data acquisition

A dual-channel NIRS unit (NIRO-200; Hamamatsu Photonics K.K., Hamamatsu, Japan) was used to measure the temporal changes in oxy-Hb, deoxy-Hb, and total hemoglobin during the perspective taking task. Near-infrared light at three wavelengths (775, 850, and 910 nm) was used as the light source. The distance between the emitter and the detector was set to 4 or 5 cm. The sampling rate was 1 Hz.

The hemoglobin concentrations were calculated by subtraction from the baseline concentrations. Two probe holders were placed on the left and right sides of the forehead corresponding to the ventral area of the prefrontal cortex. These positions were localized between Fp1 and F7 (left) and between Fp2 and F8 (right), according to the international 10–20 system.

2.3 Results and discussion

First, the orienting task confirmed that the operation of the social relationship between the participants and the opponents succeeded. The rating scores of "cooperativeness" showed that cooperative others were rated as more cooperative than uncooperative others and neutral others, while uncooperative others were rated as more uncooperative than cooperative others and neutral others. In the rating scores of "likeness," it was confirmed that the cooperative others were liked, whereas the uncooperative others were disliked.

2.3.1 Behavioral data

Figure 1 shows behavioral data of the pleasantness points in the perspective taking task. For the pleasantness points, a 2 × 3 × 3 (perspective taking, social relationship, and facial expression) analysis of variance (ANOVA) showed main effects of the three factors. The analysis also showed a significant 3-way interaction. The results showed that taking the other's perspective yielded no differences between high and low abilities of perspective taking. This indicated that the ability of perspective taking was not reflected in the behavioral data.

Further analyses of the interaction indicated that for the cooperative others in both the self- and other-perspective taking, the mean score in the happy condition was higher than that in the neutral and anger conditions, and the mean score in the neutral condition was higher than that in the anger condition (all $p < .05$). However, for the uncooperative others, these differences between facial expressions were only significant in the other-perspective taking. Note that in the self-perspective taking condition to uncooperative others, there was no difference among the rating scores of the three facial expressions.

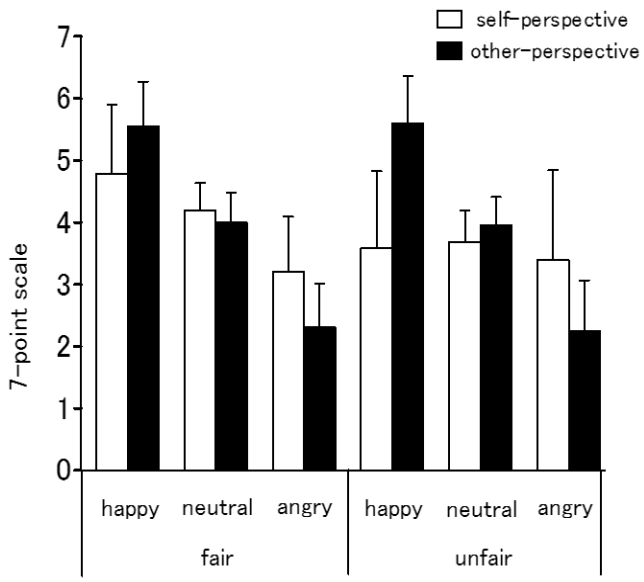

Fig. 1. Behavioral evaluation of the validity of the mean value of each condition on a 7-point scale ranging from "pleasantness" to "unpleasantness." Adapted from Nomura et al. (2010).

2.3.2 NIRS data

Figure 2 shows the mean concentration change of the oxy-Hb in the right VLPFC. For the NIRS data, a 2 × 2 × 3 × 2 (perspective taking ability, perspective taking, social relationship, and hemisphere) ANOVA showed a significant 4-way interaction. No main effect was found in any of the factors. In the unfair condition, the oxy-Hb concentrations significantly increased in the right VLPFC while taking the other's perspective as compared to the self-perspective (Figure 3). Accordingly, taking the other's perspective while perceiving the facial expressions of an unfair opponent significantly activated the right VLPFC only when the participants have high perspective-taking ability.

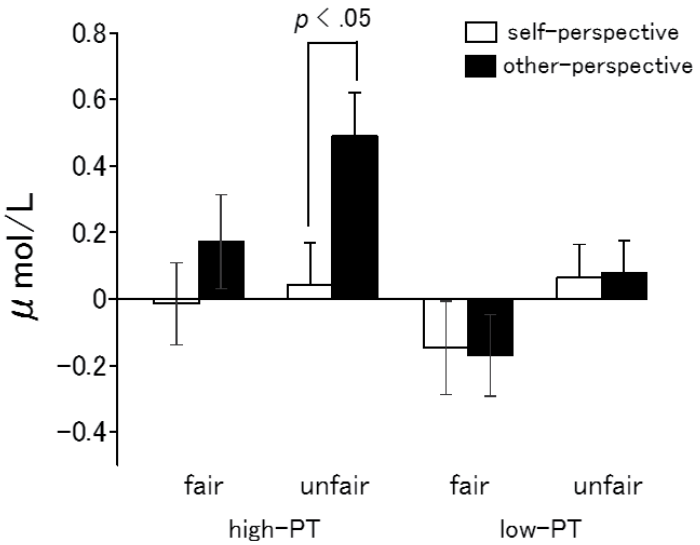

Fig. 2. Mean concentration changes in oxy-Hb during hemodynamic response in the right VLPFC. Adapted from Nomura et al. (2010).

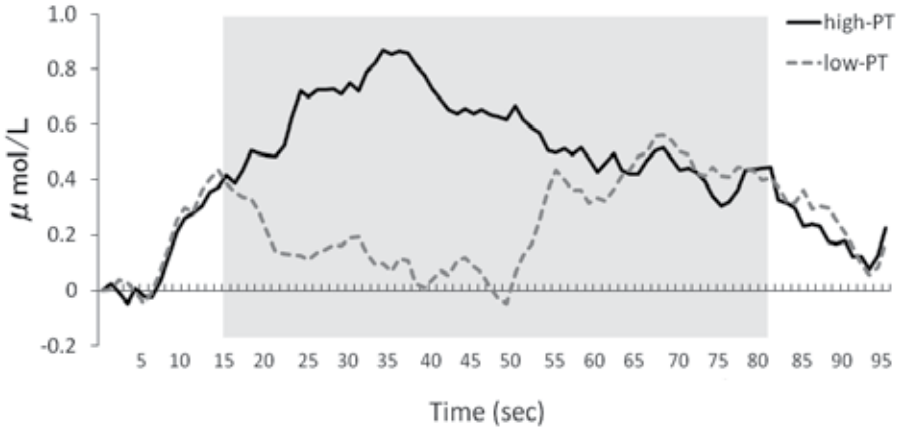

Fig. 3. Averaged oxy-Hb concentration time changes in the right VLPFC hemodynamic response. Gray zone indicates task interval times and white zone indicates rest interval times in the unfair and other's perspective condition. Adapted from Nomura et al. (2010).

3. Conclusions and future directions

3.1 Neural mechanisms of empathic process and social relationships

As described above, in line with individual differences in the ability of empathic processing, Nomura et al. (2010) revealed that for a person who has a high ability of perspective taking, the right VLPFC activates to take the other-perspective of the unfair other. Previous studies have presented evidence that the right VLPFC can modulate the activity of the amygdala even when emotional responses in the amygdala are implicitly evoked by emotional signals independent of the current conscious cognitive processing (Hariri, Bookheimer, & Mazziotta, 2000; Nomura, Ohira, Haneda, Iidaka, Sadato, Okada, & Yonekura, 2004).

According to these findings, the results reported by Nomura et al. (2010) suggest that the amygdala activation in the participants with high perspective-taking ability is suppressed while taking the perspective of an unfair person, and this leads to a decrease in their subjective negative emotions. The suppression of negative emotion is formed by the cognitive appraisal of the social behaviors of others by top-down processing. It was found that because participants with a higher perspective-taking ability evaluate the valence of emotions from the others' perspective when observing a happy facial expression by disliked others, they possibly use top-down intentional processing to effectively suppress the negative emotion evoked automatically by bottom-up processing. In contrast, participants with a lower perspective-taking ability could not suppress the negative emotion when they took the perspective of the disliked other. This reflects the decreased activation in the right VLPFC. In this way, the sensitivity to stimuli to evoke emotions varies according to the individual difference of the empathic ability, and this would produce different brain activities associated with the suppression of negative emotions. Further studies using fMRI and PET are needed to assess the neural basis related to the empathic process, including the activity of the amygdala.

3.2 Application and prospects of NIRS

We finally describe the advantages and disadvantages of brain imaging techniques using NIRS. Although fMRI and PET also measure the local bloodstream of the brain, each of these NIRS devices has its own advantages and disadvantages and is chosen depending on the purpose of research.

The disadvantage of NIRS in comparison with other imaging techniques is that the spatial resolution is lower. In addition, NIRS cannot measure deep parts of the brain such as the amygdala, brainstem, and cerebellum because brain tissues can only be measured approximately 3 cm from the surface of the head. Furthermore, it is difficult to identify the detailed anatomical position associated with brain function. The brain regions cannot be identified precisely from the scalp, and it becomes necessary to measure three-dimensional MR images in order to confirm the positions between the probes and brain regions. However, the positions of the probes can be determined according to the international 10-20 system for electroencephalogram recording, and at present, a number of studies using NIRS adopt this system.

On the other hand, NIRS has some strong advantages. First, it is highly non-invasive and thus safe. The burden on participants is relatively low, since they are not injected with

radioisotopes into the blood-stream and do not need to be restricted in a noisy device like fMRI and PET. Accordingly, it is possible to examine brain activity during performance tasks with natural body movement (cf. Morioka, in this book), as well as the brain activity of infants and children (cf. Ozawa; Kaneko, Yoshikawa, Ito, Nomura, & Okada, in this book). The second advantage is that the temporal resolution of NIRS is higher than those of fMRI and PET. The third is that a NIRS device has high portability with its relatively compact size and does not need special laboratory equipment. In addition, it offers easy operation. As a result of these advantages, NIRS techniques are contributing to the progress of evaluations such as the embodiment and development of infants and children, which were difficult to examine by fMRI or PET in the early cognitive neuroscience.

In this chapter, we discussed the neural basis underlying the empathic process based on the approach of social cognitive neuroscience. As explained above, given the limitations of NIRS, i.e., the lower spatial resolution and the inability to measure the deeper parts of the brain, it is difficult for this technology to contribute to brain function imaging studies on its own. In the future, we will need to construct a model of neural mechanisms underlying social cognition, adopting the evidence obtained from imaging techniques using fMRI or PET in a complementary manner. Furthermore, psychological and brain neuroimaging studies with concurrent biochemical and pharmacological measurement of both neurotransmitter functions, in particular those investigating the effect of gene polymorphisms, appear to be useful for clarifying the relationship between social brain functions and personality traits.

NIRS can also be used with devices measuring eye movement and skin electricity activity at the same time. The use of these combinations with NIRS will enable us to investigate issues such as detection of intentionality and eye-direction, as well as emotion. Furthermore, it will be relatively easy to measure the brain activity of two persons cooperatively performing a task at the same time. Consequently, we can anticipate the application of NIRS to interpersonal relationships and cooperative behavior. Further research on social cognitive neuroscience will be expected to provide new evidence for the neural mechanisms underlying cognitive functions, including emotions, empathy and joint attention under a bidirectional situation.

4. References

Adolphs, R., Tranel, D., Damasio, H., & Damasio, A. (1994). Impaired recognition of emotion in facial expressions following bilateral damage to the human amygdala. *Nature*, Vol.372, No.6507, (December 1994), pp. 669–672, ISSN 1476-4687

Adolphs, R., Tranel, D., Damasio, H., & Damasio, A. (1995). Fear and the human amygdala. *The Journal of Neuroscience,* Vol.15, No.9, (December 1995), pp. 5879–5891, ISSN 0270-6474

Batson, C. D., Early, S., & Salvarini, G. (1997). Perspective taking: Imagining how another feels versus imagining how you would feel. *Personality & Social Personality Bulletin,* Vol.23, No.7, (July 1997), pp. 751-758, ISSN 0146-1672

Brothers, L. (1990). The social brain: A project for integrating primate behavior and neurophysiology in a new domain. *Concepts in Neuroscience,* Vol.1, No.1, pp. 27–51, ISSN 01290568

Cacioppo, J. T., & Berntson, G. G. (1992). Social psychological contributions to the decade of the brain: Doctrine of multilevel analysis. *American Psychologist,* Vol.47, No.8, (August 1992), pp. 1019–1028, ISSN 0003-066X

Davis, M. H. (1983). Measuring individual differences in empathy: Evidence for a multidimensional approach. *Journal of Personality and Social Psychology,* Vol.44, No.1, (January 1983), pp. 113–126, ISSN 0022-3514

Decety, J. (2006). Human empathy. *Japanese Journal of Neuropsychology,* Vo.22, No.1, (March 2006), pp. 11–33, ISSN 0911-1085

Decety, J., & Cacioppo, J. T. (Eds.). (2011). *The Oxford Handbook of Social Neuroscience*. Oxford University Press, ISBN 978-0-19-534216-1, New York, USA

Decety, J., & Grèzes, J. (2006). The power of simulation: Imagining one's own and other's behavior. *Brain Research,* Vol.1079, No.1, (March 2006), pp. 4–14, ISSN 0006-8993

Decety, J., & Ickes, W. (2009). *The Social Neuroscience of Empathy*. MIT Press, ISBN 978-0-262-01297-3, Cambridge, MA

Hariri, A. R., Bookheimer, S. Y., & Mazziotta, J. C. (2000). Modulating emotional responses: Effects of a neocortical network on the limbic system. *NeuroReport,* Vol.11, No.1, (January 2000), pp. 43–48, ISSN 0959-4965

Hatfield, E., Rapson, L., & Le, Y. C. L., (2009). Emotional contagion and empathy. In: *The Social Neuroscience of Empathy*, J. Decety & W. Ickes, (Eds.), pp. 19-30, MIT Press, ISBN 978-0-262-01297-3, Cambridge, MA

Herrmann, M. J., Ehlis, A. C., & Fallgatter, A. J. (2003). Frontal activation during a verbal-fluency task as measured by near-infrared spectroscopy, *Brain Research Bulletin,* Vol.61, No.1, (June 30), pp. 51–56, ISSN 0361-9230

Herrmann, M. J., Plichta, M. M., Ehlis, A. C., & Fallgatter, A. J. (2005). Optical topography during a Go–NoGo task assessed with multi-channel near-infrared spectroscopy. *Behavioural Brain Research,* Vol.160, No.1, (May 2005), pp. 135–140, ISSN 0166-4328

Hoshi, Y., & Tamura, M. (1993). Dynamic multichannel near-infrared optical imaging of human brain activity. *Journal of Applied Physiology,* Vol.75, No.4, (October 1993), pp. 1842–1846, ISSN 8750-7587

Jackson, P. L., Brunet, E., Meltzoff, A. N., & Decety, J. (2006). Empathy examined through the neural mechanisms involved in imagining how I feel versus how you feel pain, *Neuropsychologia,* Vol.44, No.5, (April 2006), pp. 752–761, ISSN 0028-3932

Lieberman, M. D., Eisenberger, N. I., Crockett, M. J., Tom, S. M., Pfeifer, J. H., & Way, B. M. (2007). Putting feelings into words: Affect labeling disrupts amygdala activity to affective stimuli. *Psychological Science,* Vol.18, No.5, (May 2007), pp. 421–428, ISSN 0956-7976

Noguchi, Y., Takeuchi, K., & Sakai, K. (2002). Lateralized activation in the inferior frontal cortex during syntactic processing: Event-related optical topography study, *Human Brain Mapping,* Vol.17, No.2, (October 2002), pp. 89–99, ISSN 1065-9471

Nomura, Y., Ogawa, T., & Nomura, M. (2010). Perspective taking associated with social relationships: A NIRS study. *NeuroReport,* Vol.21, No.17, (December 2010), pp. 1100–1105, ISSN 0959-4965

Nomura, M., Ohira, H., Haneda, K., Iidaka, T., Sadato, N., Okada, T., & Yonekura, Y. (2004). Functional association of the amygdala and ventral prefrontal cortex during cognitive evaluation of facial expressions primed by masked angry faces: An event-

related fMRI study. *NeuroImage,* Vol.21, No.1, (January 2004), pp. 352–363, ISSN 1053-8119

Ochsner, K. N., & Lieberman, M. D. (2001). The emergence of social cognitive neuroscience, *American Psychologist,* Vol.56, No.9, (September 2001), pp. 717–734, ISSN 0003-066X

Preston, S. D., & de Waal, F. B. M. (2002). Empathy: Its ultimate and proximate bases. *Behavioral and Brain Sciences,* Vol.25, No.1, (February 2002), pp. 1–20, ISSN 0140-525X

Schroeter, M. L., Zysset, S., Kruggel, F., & Yves von Cramon, D. (2003). Age dependency of the hemodynamic response as measured by functional near-infrared spectroscopy, *NeuroImage,* Vol.19, No.3, (July 2003), pp. 555–564, ISSN 1053-8119

Shimada, S., Hiraki, K., Matsuda, G., &, Oda, I. (2004). Decrease in prefrontal hemoglobin oxygenation during reaching tasks with delayed visual feedback: A near-infrared spectroscopy study. *Cognitive Brain Research,* Vol. 20, No.3, (August 2004), pp. 480–490, ISSN 0926-6410

Singer, T., Seymour, B., O'Doherty, J. P., Kaube, H., Dolan, R. J., & Frith, C. D. (2004). Empathy for pain involves the affective but not sensory components of pain. *Science,* Vol. 303, No.5661, (February 2004), pp. 1157-1162, ISSN 0036-8075

Singer, T., Seymour, B., O'Doherty, J. P., Stephan, K. E., Dolan, R. J., & Frith, C. D. (2006). Empathic neural responses are modulated by the perceived fairness of others. *Nature,* Vol. 439, No.7075, (January 2006), pp. 466–469, ISSN 0028-0836

Suzuki, M., Gyoba, J., & Sakuta, Y. (2005). Multichannel NIRS analysis of brain activity during semantic differential rating of drawing stimuli containing different affective polarities, *Neuroscience Letters,* Vol.375, No.1, (February 2005), pp. 53–58, ISSN 0304-3940

Villinger, A., & Chance, B. (1997). Non-invasive optical spectroscopy and imaging of human brain function. *Trends in Neuroscience,* Vol.20, No.10, (October 1997), pp. 435-442, ISSN 0166-2236

Wager, T. D., Davidson, M. L., Hughes, B. L., Lindquist, M. A., & Ochsner, K. N. (2008). Prefrontal-subcortical pathways mediating successful emotion regulation. *Neuron,* Vol.59, No.6, (September 2008), pp. 1037–1050, ISSN 1097-4199

Wicker, B., Michel, F., Henaff, M., & Decety, J. (1998). Brain regions involved in the perception of gaze: A PET study. *NeuroImage,* Vol.8, No.2, (August 1998), pp. 221–227, ISSN 1053-8119

6

Introduction of Non-Invasive Measurement Method by Infrared Application

Shouhei Koyama, Hiroaki Ishizawa,
Yuki Miyauchi and Tomomi Dozono
Shinshu University
Japan

1. Introduction

The infrared light analysis has become an indispensable part of life for humankind. The infrared measurement has been studied in the worldwide, because can be qualitative and quantitative analysis for trace samples. Today, infrared spectrophotometer has been installed in many laboratories and universities, and being used over a very wide field. So, the number of papers on infrared spectroscopy is so many. We also are one of a research group of infrared measurement. Our research policy is "non-destructive measurement using infrared light". In general, blood glucose measurements of the human body to extract blood, and to determine the composition of textile products will break down to samples. If we can measure these value in non-destructive, we can contribute to society. So I described our past "non-destructive measurement using infrared light" research in this document.

2. Measurement system

2.1 FT-IR (Fourier Transform Infrared Spectrophotometer)

In this study, measuring systems are used a FT-IR (IR-Prestige-21 : SHIMADZU, Travel-IR : SensIR Technologies) as in Fig.1. The block diagram of measurement system is shown in Fig.2. The broadband infrared light is interfering by Michelson interferometer, and sent to the sample place. In the sample place, we selected the best method (ATR method, diffuse reflection method, IR fiber probe method) by each sample. We are only using the MCT (mercury cadmium tellurium) detector in IR fiber probe method, using the DLATGS (Deuterated L-Alanine Triglycine Sulphate) detector in other method. Absorption infrared interference light is detected by the optical detector, appear on the PC as an interferogram signal. This signal transformed by Fourier transformation, we get the IR absorption spectrum. The horizontal axis of spectrum is wavenumber, and the vertical axis is absorbance.

2.2 Attenuated Total Reflectance method (ATR method)

ATR method is performed as follows. We place to the sample on the prism. At this time, if there is a gap, the S/N ratio is lower. Infrared light goes into the prism, and goes forward by repeating the total reflection. When IR light repeats total reflection in the prism, evanescent

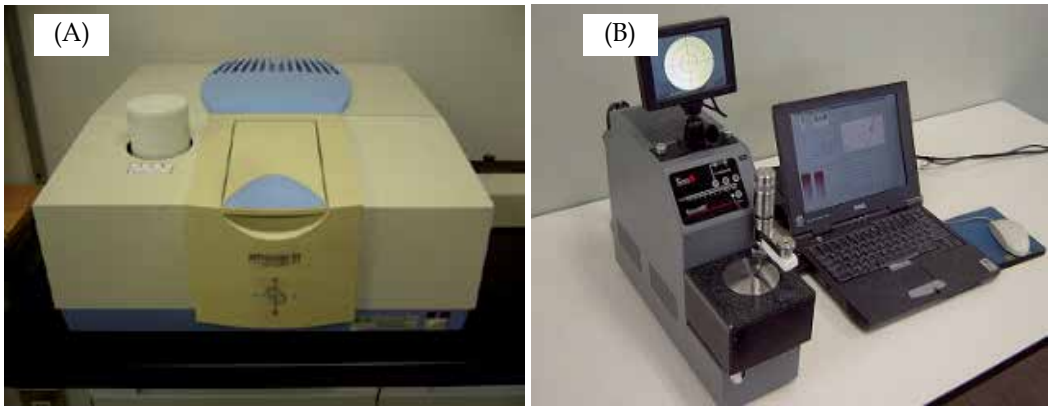

Fig. 1. FT-IR (IR-Prestige-21 (A), Travel-IR(B))

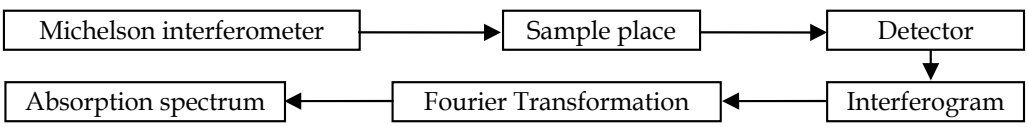

Fig. 2. The block diagram of measurement system

lights goes into the sample. Evanescent light attenuates by absorbance in sample surface set on the prism. The absorbed infrared light from the sample is detected.

In the ATR prism, we use the ZnSe prism of plate type and the prism of diamond mounted on ZnSe. Optical path length of the evanescent light to go into the sample is shown in equation 1.

$$dp=\lambda/2\pi n_1[\sin^2\theta-(n_2/n_1)^2]^{1/2} \quad (1)$$

dp: depth of penetration of evanescent light, θ: angle of incidence
λ: Wavelength, n_1: refractive index of ATR prism, n_2: refractive index of sample

By the equation 1, optical path length of evanescent light in the sample will get longer as the long wavelength side. Therefore, the absorption by the sample is strong in the long wavelength side. Accordingly, coefficient of divide "Absorbance of standard wavenumber" by "Absorbance of each wavenumber" is multiplied by the absorbance at each wavelength. In this calculation, optical path length of the evanescent light is standardize, and to correct the absorbance of spectrum. This calculation method is "ATR correction".

2.3 Diffuse reflection method

If the infrared light irradiated to powder or fibers, we can be measured the diffused reflection light from sample inside and the regular reflection light from sample surface. Infrared light penetrate inside the sample, then repeated the transmission and reflection, and come out of sample. In diffuse reflection method, this light is measured. We used to the UP-IR (Pike Tech) in this method. 30mm diameter hole is in the top of the UP-IR, the sample is placed to cover the hole.

2.4 IR fiber probe method

The infrared light passes through the light source side fiber probe, and irradiated to the sample. The infrared light reflected from the sample goes into the detector side fiber probe, and detected by MCT detector. This method can be irradiated with infrared light directly on the sample for the movement of the measuring place. The fiber probe (REMSPEC IMM-07S) composed of 19 fibers (the light source side 7 and the detector side 12) made by the chalcogenide glass. A fiber diameter is 500 μm, and a fiber probe diameter is 5 mm.

3. The spectrum analysis method

The absorption spectrum has various information of sample by each wavelength. In other words, the absorption spectrum has multidimensional vector information. Therefore, it is to analyze the spectra by multivariate analysis. In multivariate analysis for the use of multiple explanatory variables, it is increasing the amount of information. Thereby to reduce noise to a relative, it is possible to build a greater precision calibration curve. We performed correction to the absorption spectrum, and used to the PLSR in quantitative analysis, and used to the SIMCA method and the KNN method in the pattern analysis.

3.1 Spectral correction

We can extract the maximum information from the spectrum by performed correction to the absorption spectrum. We used to the spectral correction to the normalization and the differential. In the normalization correction, the absorbance of the designated peak is "1", and the coefficient "1/(absorbance of the specified peak)" is multiplied to the absorbance of each wavenumber. For example, there are the measured spectra of sample including material A and B. When you want to get the results of material A, the information of material B in the spectrum is the noise. In here, normalized to all spectra by the absorption peak of material B, and appears only information of material A. In this correction, that can be minimized by measurement error.

On the other hand, the differential correction is a correction of the slope of the spectrum, it is possible to eliminate the effects of baseline. Also, if the wavenumber of several absorption peaks is very close, is able to separate these peaks. The first differential correction is calculated at the slope of each wavenumber in spectrum, the intensity of absorption peaks wavenumber is "0". Derivative spectrum half-width of the higher orders is narrowed, and the noise increases for in lower S/N ratio. For these reasons, we used first differential correction in this study.

3.2 Partial Least Squares Regression (PLSR)

We are using PLSR for a quantitative analysis. PLSR has not the Multilinear regression (MLR) exists multicollinearity, Measurement accuracy of PLSR is better than Principal Components Regression (PCR) in a small number of factors. In the PLSR, the explanatory variables are the infrared spectra, the objective variables are the reference values. The explanatory variables and the objective variables are assumed to each have an error margin, extracted to PLS factors, calculate a regression, and new objective variables are calculated. Next, a similar calculation using the new objective variables and explanatory variables, add a PLS factor, re-calculate the objective variables. A number of PLS factors increase, and the Standard Error of Calibration (SEC) is smaller.

But, increasing the number of factors too, applies Standard Error of Prediction (SEP) increases (Over Fitting). Therefore, we validate the optimal number of PLS factors by Leave-one-out method. The Prediction Residual Error Sum of Squares$_1$ (PRESS$_1$) values calculated from the objective variables by the following equation 2

$$PRESS_n = \Sigma (y_{obs}-y_{ref})^2 \quad (2)$$

y_{obs}: new objective variables, y_{ref}: reference values

After, the new objective variables are calculated by calibration curve adding a new PLS factor. PRESS$_2$ value is calculated from the objective variables obtained again. If the residual is significant before and after (The difference between the PRESS$_1$ and PRESS$_2$), adding the PLS factor. If the residual is not significant before and after, select the model that was built before. After, we measured to the spectrum of sample of unknown amount, and calculated by using calibration curve and this spectrum. By the above process, it is possible to be measured quantitatively of unknown sample.

3.3 Soft Independent Modeling of Class Analogy (SIMCA)

We used SIMCA for the qualitative analysis. A class is made by infrared spectra of known sample and builds a classification model. Each class is analysed by analysis of principal component and the distinction space is set. This space is called SIMCA box. It is classified into the class suited most by applying infrared spectra of unknown sample to SIMCA box. Moreover, the rest error is calculated by applying each spectrum that composes the class to other classes. And, Discrimination Power that can specify the factor in which it distinguishes between classes is obtained. We confirmed the validity of the classification model constructed by using Discrimination Power.

3.4 K-Nearest Neighbor method (KNN)

KNN method is one of pattern analysis to determine the class by comparing the similarity between the patterns not based on specific statistical distributions. To determine the class of an unknown sample is made on "voting". First, calculate the Euclidean distance between samples for the known and unknown class samples. Next, select a known class samples for the number of "K" close to the distance from an unknown class sample. "K" is odd number. The class of an unknown sample is determined to a most numerous class in the "K".

For example, if the "K=5", analyse the closest class of 5 samples from an unknown sample class. Five classes (1,2,3,3,3), (1,3,3,2,1) are classified at Class "3", (1,1,2,1,2), (2,1,3,1,1) are classified at Class "1". For such analysis, impact on the accuracy of the analysis is a combination of variables used to calculate the distance and the number of "K".

4. Development of non-invasive measurement of blood glucose of diabetic

4.1 Background

Recently, increasing of diabetic has been brought to public attention. According to WHO, the number of diabetics is 170 million. To treat diabetes, diabetics should always check blood glucose monitoring. Therefore, they need to self-monitor blood glucose (SMBG).

SMBG is measured by blood sampling method, but this method the patient suffering and stress, including issues such as the risk of infection. And, the economic burden on patients is very large, because medical needles and measurement kit are disposable. Medical expenses of diabetes and its complications are estimated at about 3,000 billion dollars worldwide, and are expected to continue to increase in the future. Those various studies have been conducted around the world, because the medical expenses have become large economic markets. But, the effective blood glucose measurement method to overcome these problems, have not yet been developed. Therefore, it is desired to develop a method to measure non-invasive blood glucose measurement. Over the past few years, several studies have been made on non-invasive blood glucose measurement based on ATR infrared spectroscopy. The purpose of this study is to examine the accuracy of blood glucose in clinical trial.

4.2 Measurement system for non-invasive measurement of blood glucose

This study used FT-IR (Travel-IR) and ATR method. The block diagram of measurement system is shown in Fig.3. In the ATR prism, used to the prism of diamond mounted on ZnSe (3 times reflection).

The measurement part is the tip of the left hand middle finger of subject. The middle finger was washed with ethanol. The 5μl squalene oil was applied on the prism by micropipette in each measurement. Squalene oil is used as an internal standard method described below. The measurement part of subject put on the prism, pressed from above with a constant pressure. We measured in this state, and got the absorption spectrum including the blood glucose value information.

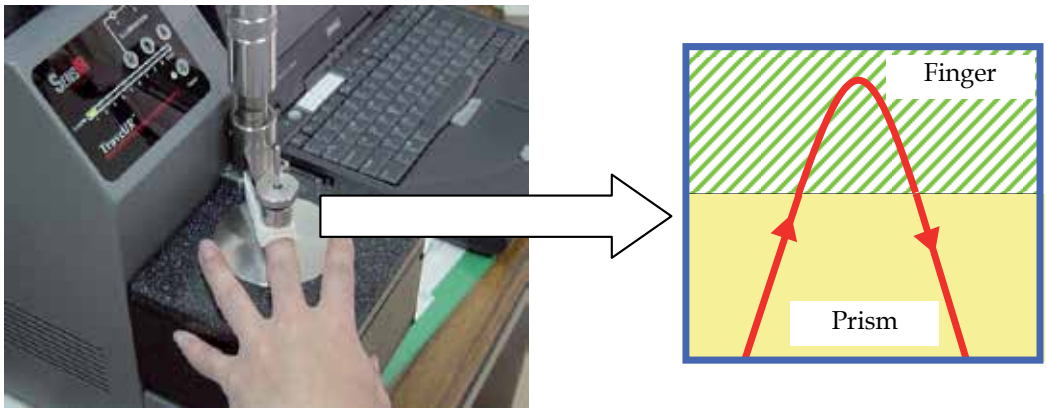

Fig. 3. Non-invasive measurement system for blood glucose

The absorption spectrum was applied to the ATR correction. We used 1800 cm^{-1} wavenumber in standard wavenumber of ATR correction, because absorption peak and noise are not in this wavenumber. After, all measured spectra were applied data correction between 2700 cm^{-1} and 1750 cm^{-1} to remove the absorption noise of diamond prism, and, were applied normalization correction in the absorption peak of squalene oil. We used these corrected absorption spectra in analysis. In the measurement condition, measurement wavenumber range is 4000~700 cm^{-1}, resolution is 4 cm^{-1}, and accumulation is 30 times.

4.2.1 Internal standard method by squalene oil

In measuring the subject's blood glucose value, the good accuracy calibration curve is essential. To improve the accuracy of the calibration curve must be accurately extract glucose information on the infrared absorption spectrum.

In the ATR method, it is important to stick a sample to the prism. Many people of diabetes are elderly, person with dry skin on the fingertips are also often elderly. Squalene oil is used as internal standard method for the different dry skin of the subject's finger surface. To eliminate the effects of dry skin by applying the squalene oil, we can measure the subjects under the same conditions. And, there is no effect of squalene oil to apply normalization correction in the absorption peak of squalene oil. Furthermore, the S/N ratio of the spectrum is better, because to block the air from between the finger and prism by the oil.

4.2.2 How to calculate the blood glucose value from the spectrum

We calculated the blood glucose value by using absorption spectra and PLSR. The invasion type blood glucose sensor (Antsense-2, DAIKIN) by enzyme electrode method is used for the measuring the reference blood glucose value.

First, we developed the calibration curve by PLSR, the measuring absorption spectra were used as the explanatory variable, measuring the blood glucose values by Antsense-2 were used as the objective variable. In calibration curve, the horizontal axis is the Antsense blood glucose value, and the vertical axis is the estimated blood glucose value by PLSR. Next, we measured to the new absorption spectra to measure the blood glucose value. Then, the blood glucose was calculated by using the measured absorption spectrum and calibration curve. And, we calculated the SEC and the SEP. Their values were used as the evaluated the accuracy of the calibration curve.

4.2.3 Error Grid Analysis (EGA)

EGA was developed by William L. Clarke in the University of Virginia. EGA is an indicator of clinical efficacy of blood glucose sensor. In fact, an error grid has been assembled to stay in the ideal range of 70 ~ 180 mg/dl blood glucose value.

The Clarke grid of EGA is shown in Fig.4. The horizontal axis is the actual blood glucose, and the vertical axis is the blood glucose value obtained from the developed blood glucose sensors. In this study, when measuring the blood glucose must be clinically effective. We judged the efficacy as a blood glucose sensor using the EGA.

4.3 Absorption spectra of glucose, squalene oil, and finger

In measuring the blood glucose value, must know the absorption peak of glucose spectrum.

In addition, we need to know the absorption wavelengths of squalene oil to be used as an internal standard method. Each sample was measured by ATR method (plate type prism). The absorption spectra of glucose powder and squalene oil are shown in Fig.5. The absorption spectrum of glucose has some absorption peaks in 1030 cm^{-1} (Fig.5-A, C-OH stretching vibration), 1130cm^{-1} (Fig.5-B, C-O-C antisymmetric stretching vibration), and 1450 cm^{-1} (Fig.5-C, CH_2 scissoring vibration). The absorption spectrum of squalene oil has some

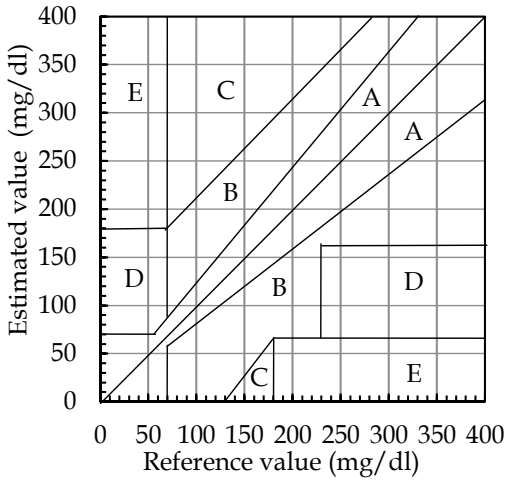

Zone	Judge
A	Safety
B	
C	Little danger
D	Danger
E	

Fig. 4. Clarke grid

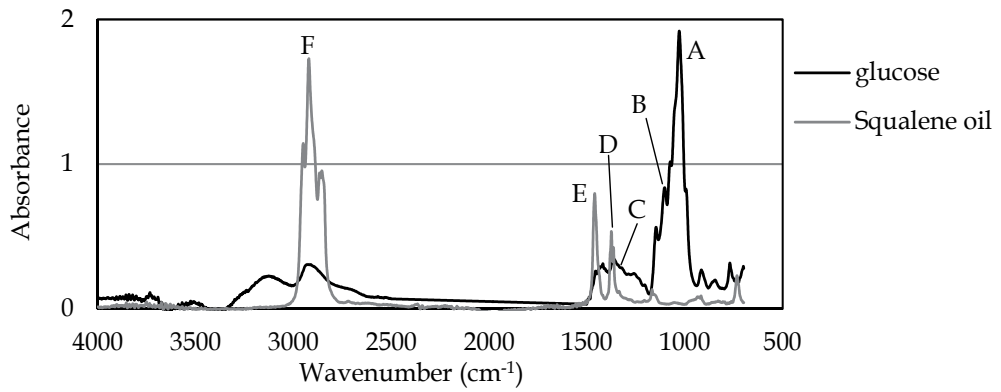

Fig. 5. The absorption spectra of glucose powder and squalene oil

absorption peaks in 1377 cm^{-1} (Fig.5-D), 1462cm^{-1} (Fig.5-E), and 2922 cm^{-1} (Fig.5-F). The absorption peak of glucose and oil were not overlap.

The absorption spectra of the finger in before and after coating to squalene oil are shown in Fig.6. In absorption spectrum of finger, absorption peaks in 1377 cm^{-1} and 1462 cm^{-1} did not appear. But, absorption spectrum of finger coated with squalene oil has absorption peaks in 1377 cm^{-1} (Fig.6-D) and 1462 cm^{-1} (Fig.6-E). Therefore, it is possible to reduce individual differences in skin surface conditions due to the absorption spectra normalized at the absorption peak of squalene oil. We confirmed that the squalene oil is suitable as an internal standard method, and can measure the blood glucose value by absorption peaks of glucose.

4.4 Non-invasive blood glucose measurement in subjects

4.4.1 Development of calibration curve

The subjects were healthy eight men in their 20s. When developing a calibration curve, glucose tolerance test were performed on each subjects. In glucose tolerance test, first, the

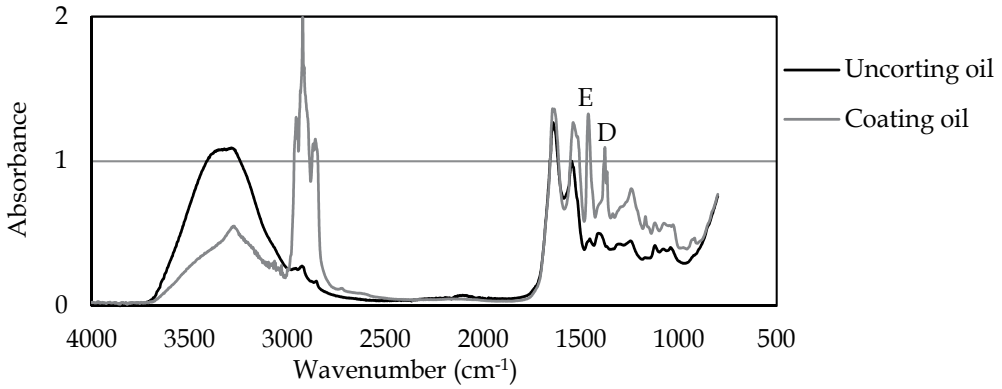

Fig. 6. The absorption spectra of the finger in before and after coating to squalene oil

subjects fasted for 12 hours. Then, subjects are ingested 75 g glucose, temporary increases in blood glucose value of subject. After the glucose tolerance test, we measured to the infrared absorption spectra and the invasive blood glucose measurement in every three minutes 20 times. Furthermore, after breakfast, before and after lunch, before and after dinner, we measured for four days (five times measurement in a day). We measured the total 40 times in one subject. The calibration curve is developed using these infrared absorption spectra.

Fig.7 shows the calibration curve developed in 320 infrared absorption spectra by all 8 subjects. In these results, the average blood glucose of the subjects was 120 mg/dl, correlation coefficient (CC) was 0.79, and measurement accuracy (SEC) was ± 21 mg / dl. This result in this sample scale has been obtained a significant correlation, but, this result was not satisfactory as a blood glucose measurement system. As the cause of this, it is considered to the individual differences by moisture content of each subject. Therefore, we developed each individual calibration curve using the infrared absorption spectrum of each subjects. The results of individual calibration curves are shown in Table 1. Comparing the individual calibration curves and all subjects calibration curve has improved the

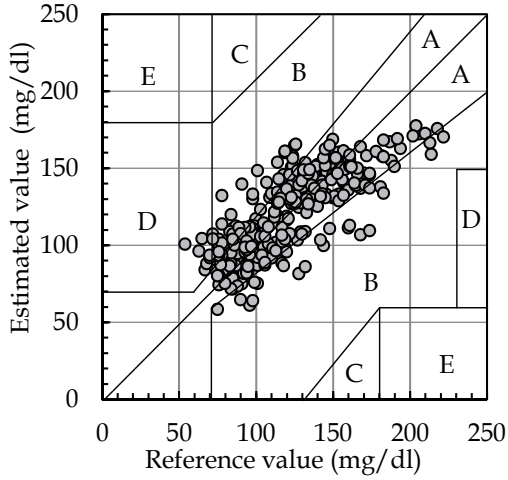

Fig. 7. The calibration curve developed by all subjects

	CC	SEC	A zone	B zone	C zone	D zone	E zone
All	0.79	21	77%	22%	0%	1%	0%
#1	0.90	13	90%	7%	0%	3%	0%
#2	0.95	16	90%	10%	0%	0%	0%
#3	0.71	22	68%	32%	0%	0%	0%
#4	0.71	14	83%	17%	0%	0%	0%
#5	0.90	7	100%	0%	0%	0%	0%
#6	0.84	16	90%	10%	0%	0%	0%
#7	0.67	28	60%	35%	0%	5%	0%
#8	0.96	9	95%	5%	0%	0%	0%

(CC : Correlation coeficience, SEC : mg/dl)

Table 1. The results of all subjects and individual calibration curves by PLSR

measurement accuracy of 6 among 8 subjects. In addition, the EGA results have improved in the same 6 subjects. The individual differences are eliminated by the individual calibration curve, and may be considered to be developed the most suitable calibration curve of each subject. Therefore, we measure blood glucose value of subjects by using the all subject calibration curve and individual calibration curve.

4.4.2 Non-invasive blood glucose measurement by calibration curve

Each subject was measured again 20 times the infrared absorption spectra. We measured the blood glucose value by these absorption spectra and developing calibration curve in section 4.4.1. The result by calibration curve in all subjects and individual calibration curve are shown in Fig.8. The average blood glucose value was 100 mg/dl.

In the result of blood glucose value calculated by all subjects calibration curve in Fig.8-(A), the SEP was ±32 mg/dl. This result was not good. On the other hand, in the result of blood glucose value calculated by individual calibration curve in Fig.8-(B) the SEP was ±13 mg/dl,

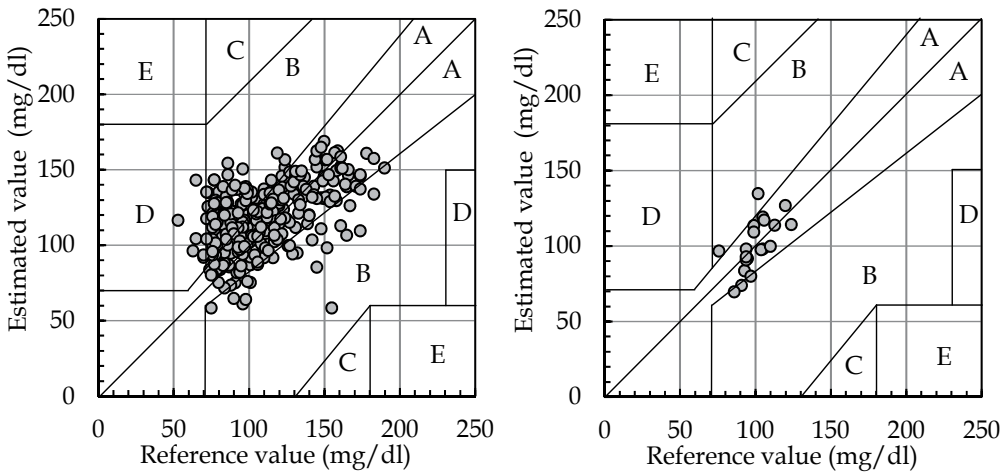

(A) The result by all subjects calibration curve (B) The result by #8 calibration curve

Fig. 8. The result by developed calibration curve in all subjects and individual

this result was dramatically improved. And, by the EGA result, A-zone is 90%, and B-zone is 10%, this result was shown to be clinically effective. It is also considered to the impact of individual differences as this reason. Evanescent light is measured to invasion into the finger of about 0.3~2 μm in the ATR method, and, it is considered the infrared light not get to the blood vessel inside finger. Therefore, we are considered measured the interstitial tissue fluid. When the glucose comes out in tissue fluid from blood vessel, there is the time difference in between individual. So, if the subject measure the blood glucose by the calibration curve including other subjects information, the result have come to greatly affect these individual differences. For the above reasons, we measure the blood glucose value by using individual calibration curve of each subject.

4.4.3 Verification of the calibration curve by loading vector

In order to verify the validity of the calibration curve, we focused on the weighting of the loading vector obtained from the developed calibration curve. The loading vector is the calibration curve of data (infrared absorption spectra). In other words, the loading vector shows the wavenumber band to the impact to the calibration curve. The weighting of the loading vector by individual calibration curve in section 4.4.1 is shown in Fig.9-(A). The horizontal axis is the wavenumber, and the vertical axis is the weight of the loading vector.

There are absorption spectra three weighting curves because the number of PLS factors (principal components) obtained are three factors. In Fig.9-(A), in this loading vector, the wavenumber in 1220 cm^{-1} (Fig.9-(A)-A), 1150 cm^{-1} (Fig.9-(A)-B), 1020 cm^{-1} (Fig.9-(A)-C) were found to significant impact on the calibration curve.

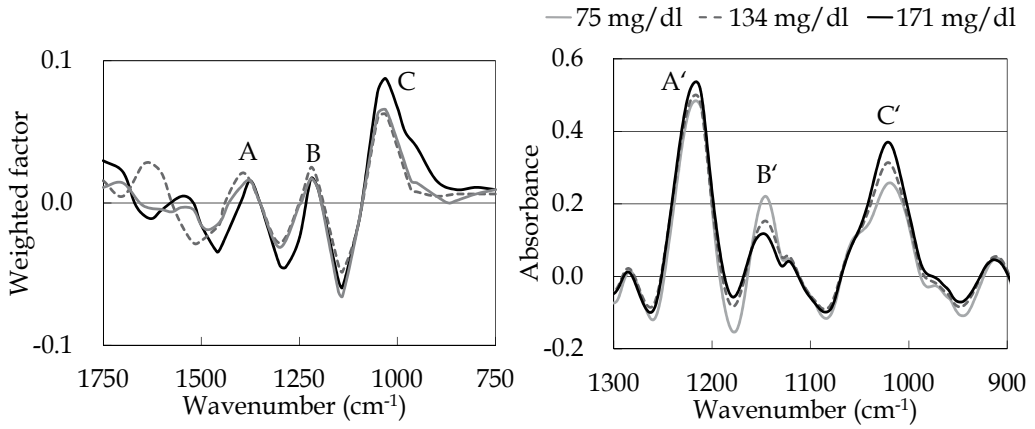

(A) The weighting of the loading vector (B) Absorption spectra

Fig. 9. The weighting of the loading vector and each blood glucose value

Fig.9-(B) shows the infrared absorption spectra in large discrepancy between the subjects blood glucose value. In Fig.9-(B), characteristic absorption peaks can be found in 1220 cm^{-1} (Fig.9-(B)-A′), 1150 cm^{-1} (Fig.9-(B)-B′), 1020 cm^{-1} (Fig.9-(B)-C′). It is proportional to the blood glucose value and the absorbance in 1220 cm^{-1} and 1020 cm^{-1}, and found a negative proportional relationship in 1150 cm^{-1}. The weighting of the loading vector is almost

matched by changes in infrared absorption spectra of blood glucose variability. From the above, it has been shown to accurately measure the blood glucose value from the glucose information in this method. Therefore, we can be proposed as a non-invasive blood glucose measurement by the infrared spectral measurements.

4.5 Clinical application of measurement system

We have measured the diabetics that have been actually measured blood glucose. Subject is four diabetics. We were measured before and after meals for 4 to 5 days in each subject. First, we developed the individual calibration curve of each subjects by using the PLSR analysis and infrared absorption spectra obtained in the three-day measurement. Then, the measured infrared absorption spectra in the 1-2 day were substituted in the developed calibration curve, and the blood glucose value was estimated.

Table 2 shows the blood glucose data for each subject obtained by the conventional method for three days from the first day, and the results of the developed calibration curve for each subject by using the measured infrared absorption spectra. And Fig.10 shows the calibration curve of subject #1. From these results, this measurement system can be constructed to calibration curve for measuring blood glucose of diabetics, because, significant correlation has been obtained in this sample scale. The result of subject #4 show very good results than the other subjects. As this cause, the number of samples is very few for construct calibration

Subject #	Number	Ave.	Max.	Min.	S.D.	C.C	SEC
1	15	226	339	156	56	0.758	± 35
2	16	216	330	150	44	0.519	± 37
3	10	157	221	108	41	0.645	± 29
4	9	113	203	58	44	0.997	± 3

Table 2. The blood glucose data and the results of the calibration curve for each subject

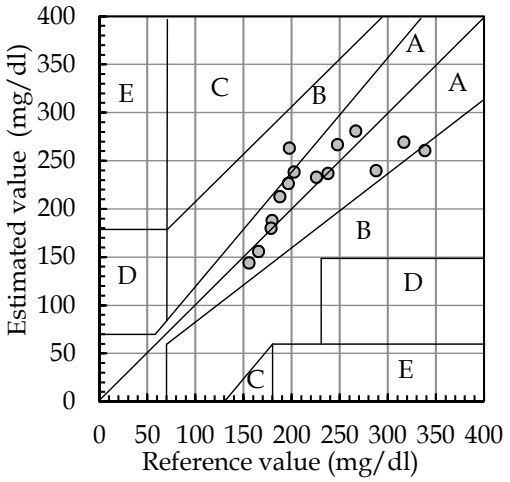

Fig. 10. The calibration curve of subject #1

curves, and the average blood glucose value is small. In addition, it is considered to over-fitting, because the PLS factor number is 5.

The spectra of diabetics as measured by the fourth day and fifth day were substituted in the individual calibration curve of each subject. Table 3 shows the accuracy of predicted blood glucose value and the EGA result. In addition, the scatter diagram of the Clark grid result of each subject is shown in Fig.11. From the EGA result, all data with one exception of subject #4 data are plotted in A and B zone of clinically safety ranges. Improvement of measurement accuracy is better, but, the important in clinical practice is give first aid when the blood glucose value showed abnormal. Therefore, from a good EGA results, this system can be treated as a reasonable measurement method of blood glucose value in diabetics in clinical practice.

Subject #	SEP	EGA-Zone				
		A	B	C	D	E
1	± 70	50%	50%	0%	0%	0%
2	± 60	67%	33%	0%	0%	0%
3	± 49	20%	80%	0%	0%	0%
4	± 59	45%	45%	0%	10%	0%

Table 3. The accuracy of predicted blood glucose value and the EGA result

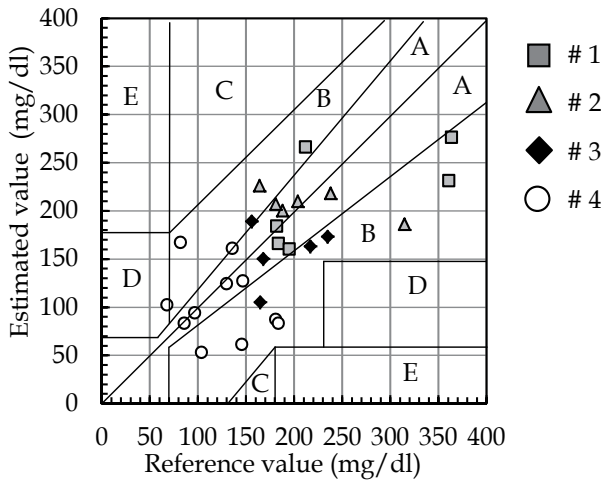

Fig. 11. The Clark grid result of each subject

To measure simply place a finger on the prism, this system has the advantage of measuring blood glucose value very easily for diabetics in many elderly. In addition, the burden on nurses is reduced, because the patient can measure in their own. Since the measurement time is about 1 minute, it is possible to measure the many patients in a short time. This is a worthwhile part in the clinical practice. When this system is used as a self-monitor blood glucose sensor of diabetic patients, the measurement error is a large. In particular, SEC of the subject #4 was ± 3 mg/dl, but SEP has become extremely large forecast error in ± 59 mg/dl. This cause is considered to the over-fitting, when building a calibration curve as previously described. In PLSR, if the increasing the number of the PLS factor, SEC is a smaller, SEP becomes large. Therefore, it is necessary to construct a standard curve with the optimal

number of the PLS factors. From the comparison of the SEP and SEC, the optimal number of PLS factors for this measurement system is considered to be 2 or 3. Thus, with less data in after the start of measurement, we shall construct the calibration curve careful in the number of PLS factors. To improve measurement accuracy, we need to consider improving the system. If increased in the amount of information obtained from absorption spectra, we can be measured blood glucose value more accurately. That is, if increased the amount of infrared light obtained from the subjects' finger, the measurement accuracy is improved.

4.6 Conclusion of non-invasive measurement for blood glucose by IR spectroscopy

We can confirm non-invasive blood glucose measurement system developed in this study is effective tools in clinical practice. In this measurement system, there is no pain which was felt by many diabetics so far. Because measurement time is 1 minute, it can be measured very easily and quickly. There is no stress to the patient, can measure to blood glucose value several times a day because the measurement time is very short.

Future challenges of this study are shown below. The number of subjects and the number of measurement times must be increasing. We must show in this measurement reproducibility. And, we must show that this system can be applied to any subject. If the blood glucose measurement sensor has been developed in this measurement method, future, this research will contribute significantly in community of increasing diabetics.

5. Non-destructive analysis of the composition and mixture ratio for textile products based on infrared spectroscopy

5.1 Background

This section describes a Non-destructive analysis of the composition and mixture ratio for textile products. In Japan, the composition display of textile goods is obligated by the "Household Goods Labeling law". Therefore, analysis of the composition and mixture ratio for textile products in accordance with JIS method (L 1030-1,-2) are executed. But, existing methods is the destructive inspection, and a lot of time (six hours or more) and proficiency is necessary for the analysis. Also has concern about the safety and the environmental impact of such tests to use chemicals such as organic solvents. In addition, if the amount of remaining dirt on the sample is very small, if the remaining dirt color is same color of sample, the dirt cannot be verified visually.

In here, it proposes the application of the infrared spectroscopy for improve those problems. The method that we propose is non-destructive measurement, quickly and easy. We measured an infrared absorption spectrum of a textile by using a FT-IR. And we examined the possibility of a composition classification and a mixture ratio calculation by chemometrics. These experiments showed that the measurement system was effective.

5.2 Analysis of the composition and mixture ratio for yarn products by ATR

5.2.1 Measurement system for yarn products

Measuring system in this study, FT-IR (IRPrestige-21) and ATR method (DuraSampler-IR) was used. Measuring system is shown in Fig.12. The measuring yarn is folded, and set to cover on the prism. After, the measurement part of the prism and yarns were contacted by

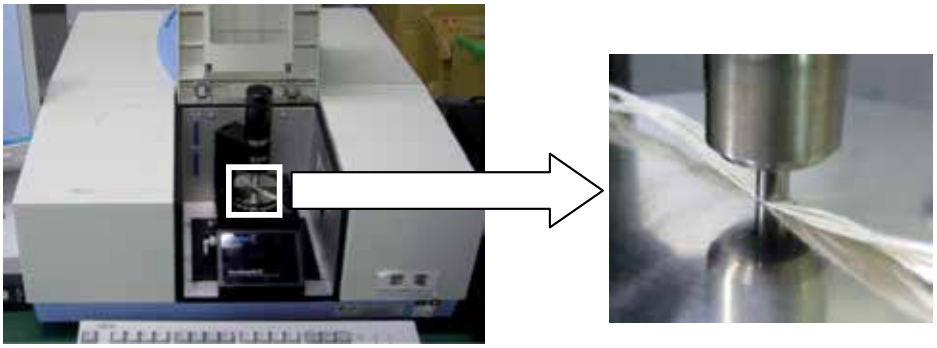

Fig. 12. Measurement system for yarn products

pressing parts from above. IR spectrum is measured with this device. It is quickly because the measurement time is about two minute. The resolution, the accumulation, the measuring wavenumber range set at 4 cm^{-1}, 50 times, 4000~500cm^{-1} (wavelength 2.5~20 μm) measurement condition.

5.2.2 Analysis of the composition of yarn products

We used 7 samples, Cotton, Silk, Hemp, Wool, Polyester, Rayon, and PET. We used the KNN method to determine the composition of textile products. Building a KNN space was divided into seven classes by type for each spectrum. KNN space was built by a total 140 spectra by 20 spectra for each sample. 10 spectra of each sample as an unknown sample are put into space. We tried each spectrum to be divided into classes. KNN space was constructed in wavenumber range in 1800-650 cm^{-1}. Because, there were characteristic peaks of each samples in this wavenumber range.

The result of qualitative analysis for each sample is shown in Table 4. Results showed that all samples are classified correctly from Table 4. Therefore, it is possible to the qualitative evaluation in a single composition yarn by this measurement method. We were able to determine the cellulose yarns of cotton and hemp, is very good results.

Infrared absorption spectra of cotton and hemp are shown in Fig.13. These spectra in Fig.13 are very similar, because the main component of cotton and hemp is cellulose. Very different point is the absorbance intensity of 1180 cm^{-1} (Arrow in Fig.13). This absorbance

	Cotton	Silk	Wool	Hemp	Polyester	Rayon	PET
Cotton	10/10	0/10	0/10	0/10	0/10	0/10	0/10
Silk	0/10	10/10	0/10	0/10	0/10	0/10	0/10
Wool	0/10	0/10	10/10	0/10	0/10	0/10	0/10
Hemp	0/10	0/10	0/10	10/10	0/10	0/10	0/10
Polyester	0/10	0/10	0/10	0/10	10/10	0/10	0/10
Rayon	0/10	0/10	0/10	0/10	0/10	10/10	0/10
PET	0/10	0/10	0/10	0/10	0/10	0/10	10/10

Table 4. The result of qualitative analysis for each sample by KNN

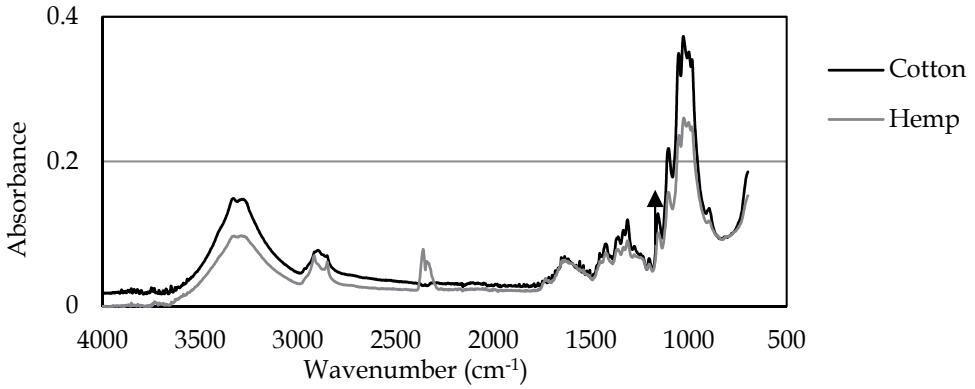

Fig. 13. Infrared absorption spectra of cotton and hemp

intensity difference is the difference between the percentage of cellulose in cotton and hemp. And, the cotton and hemp has slightly different components (such as pectin) present, but those absorption peaks are very small. In this method to accurately measure this subtle difference, qualitative analysis for each yarn was possible.

5.2.3 Measurement of mixture ratio of mixed yarn

In textile products, the mixed yarn including multiple compositions is present. In the mixed yarn should seek the composition and percentage of each composition. Measurement of composition percentage of mixed yarn, we used cotton and polyester mixed yarn samples 45 kinds. These yarns were measured 5 times each spectrum, the average of the measured spectra. Developing a calibration curve by PLSR, focusing on the absorbance wavenumber specific absorption peaks in the components of the cotton and polyester in average spectra. Substituting the spectrum of the unknown sample to the calibration curve, calculated the composition percentage of cotton.

The absorption spectra of the yarn are shown in Fig.14. In the Fig.14, "C" shows for the percentage of cotton, and "P" shows for the percentage of polyester (C100P0 : 100% cotton yarn, C90P10 : 90% cotton and 10% polyester mixed yarn,... , C0P100 : 100% polyester yarn). These absorption spectra are changing the percentage of mixed of the cotton and polyester in increments of 10 %. There are several wavenumber ranges of absorbance changing just like the mixture ratio. The absorbance of 3392 cm^{-1}, 1624 cm^{-1}, 1226~1039 cm^{-1} peaks are proportional to the percentage of cotton. And, the absorbance of1738 cm^{-1}, 1409 cm^{-1}, 1298 cm^{-1} peaks are proportional to the percentage of polyester. Therefore, by analysis in the wavenumber range including these characteristic absorption peaks, we can determine the mixture ratio. Using the spectra of cotton and polyester mixed yarn, the results of PLSR in wavenumber range in 3000~700 cm^{-1} is shown in Fig.15-A. The absorption spectrum was subjected to spectral correction and differential for the measurement S/N ratio in order to standardize. The horizontal axis represents the composition percentage of cotton, and the vertical axis is the estimated value of cotton from the PLSR. The results of the correlation coefficient and the measurement accuracy (SEC) were 0.988 and ±3.4%. This result indicates a highly significant correlation. This calibration curve is considered to be reasonable. Thus, this calibration curve is good result, we used this calibration curve of cotton and polyester mixed yarn.

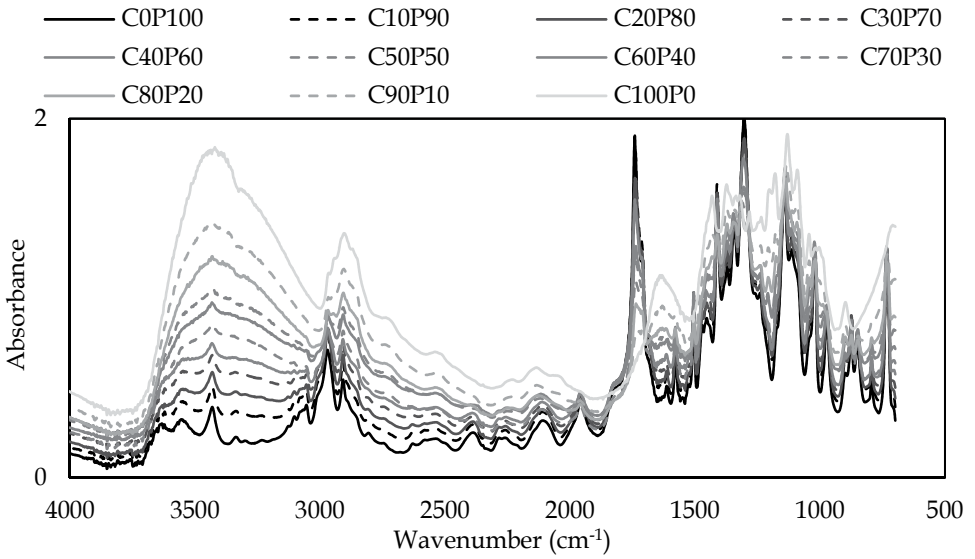

Fig. 14. The infrared absorption spectra of the mixed yarns

And for the validated on calibration curve, the 10 samples were measured. The validation result of the calibration curve is shown in Fig.15-B. The result of SEP is ±6.2%. To view the percentage of mixed yarn in increments of 5 %, measurement error is preferably less than ± 2.5%. This result cannot accurately display the percentage of mixed yarn. As a cause, it is a small number of spectrum using in the calibration curve. Therefore, the next a problem to be solved, increased the number of spectra without lowering the accuracy of the SEC, and to create a more reliable calibration. If we have overcome the challenges, it is possible to reduce the SEP of the percentage of mixed yarn, and possible to measure accurately the percentage of mixed yarn.

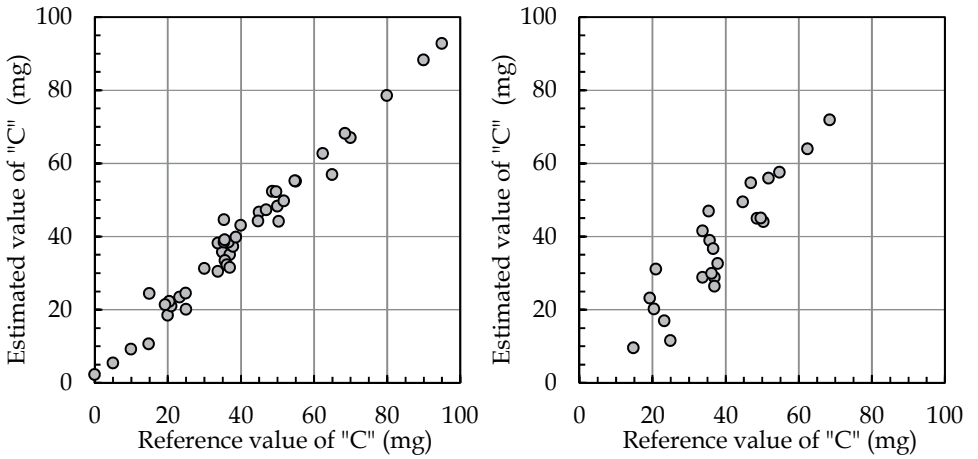

(A)The calibration curve (B) The validation result

Fig. 15. The calibration curve and validation result for mixed yarn

5.3 Analysis of the composition and mixture ratio for fabric products by diffuse reflection method

5.3.1 Measurement system for fabric products

There are yarn products as well as a lot of fabrics products. We have to measure analysis of the composition and mixture ratio for fabric products. Measuring system for fabric products, FT-IR (IRPrestige-21) and diffuse reflection method (UP-IR) was used. Measuring system is shown in Fig.16. The sample fabric is placed to cover the hole of the top of the UP-IR, and a mirror mounted on the sample fabric.

Fig. 16. Measurement system for fabric products

As test samples, we used 38 fabrics of cotton 100%, 42 fabrics of polyester 100%, 71 mixed fabrics of cotton - polyester (CP sample). In the sample, there are woven fabric and knitted fabric, colour and thickness is different respectively. The ratio of polyester and cotton in P/C sample is also various. In measurement of spectrum, measuring range, resolution, and accumulation were 4000~700 cm^{-1}, 4 cm^{-1}, and 20 times. In addition,we were measured in five points on each sample to measure the entire fabric.

5.3.2 Analysis of the composition of cotton and polyester fabric products

The composition of the fabric products were analysed using these absorption spectra and SIMCA. The fabric samples are classified into 100% cotton class (Class C), cotton and polyester mixed fabric class (Class CP), 100% polyester class (Class P). For the development to classification model, the absorption spectra of the 100% cotton and the 100% polyester were used each 20 samples (100 spectra), the absorption spectra of mixed fabric were used 35 sample (175 spectra). The remaining sample spectra were used to validate the classification model. We constructed four times classification models by SIMCA, and tried the classification of the spectrum. Those models changed random the combination of spectrum for class making and spectrum for verification and were constructed.

The result of constructed classification model is shown in Table 5. A high distinction rate was obtained in each model. From these results, the information on each sample was able to be extracted accurately by SIMCA. Especially, the percentage of correct answers in Class C

	1st	2nd	3rd	4th
Class C	97%	93%	93%	97%
Class CP	95%	94%	96%	97%
Class P	81%	81%	91%	88%

Table 5. The result of constructed classification model

and Class CP is all over 90 %. Meanwhile, the percentage of correct answers in Class P is lower than other classes. As this cause, it is considered the polyester included different components as the polyethylene terephthalate (PET) and poly trimethylene terephthalate (PTT). The first differential spectra of cotton and polyester and discrimination power are shown in Fig.17. Discrimination power indicates the magnitude of the effect of each wavelength, when the samples are classified into each class. By Fig.17, it was confirmed that it had been classified by composition information because main peak of discrimination power was corresponding to peak of spectra. Therefore, the validity of classification model was shown.

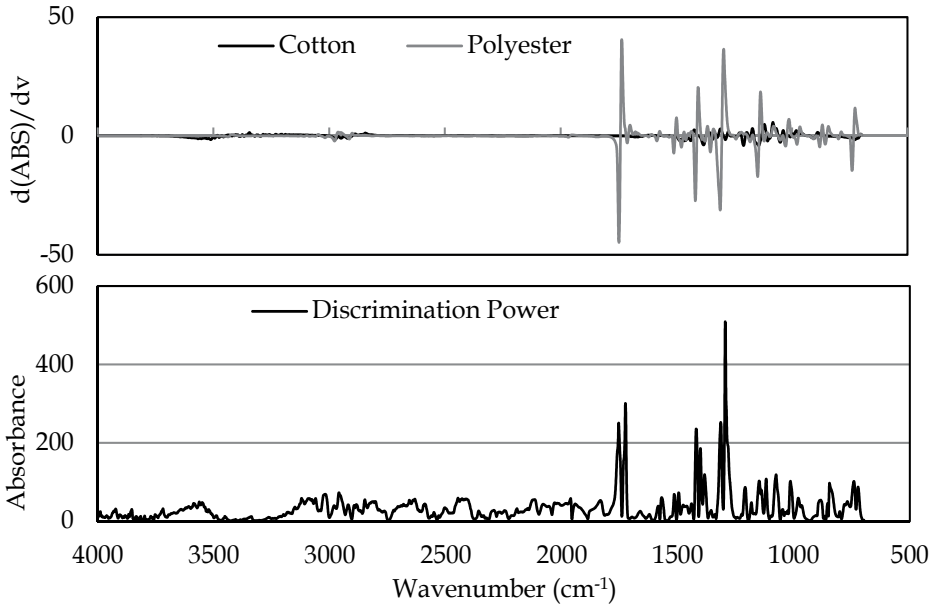

Fig. 17. The first differential spectra of cotton and polyester, and discrimination power

5.3.3 Measurement of mixture ratio of fabric products

We must seek a mixture ratio of the sample, when the sample is classified as mixed fabric by SIMCA method. Therefore, mixed ratio determined using the PLSR. The samples and measurement method are same to section 5-3-1. However, the average spectrum of five spectra obtained from one sample was used as a measured absorption spectrum of this sample. We developed the calibration curve by using absorption spectra and known mixture ratio. In this time, the known mixture ratio is used the mixture ratio of the polyester.

The measurement result is shown in Fig.18-(A). In this Fig.18-(A), this result has a highly significant correlation. And, SEC is 2.9 %. To display in increments of 5 % to the product mixture ratio, SEC needs to be less than 2.5 %. If you check the Fig.18-(A), the sample near the reference mixture ratio 40~50 % is distant from Y = X. The absorption spectra of this sample (Sample-A) and sample of close to the Y = X (Sample-B) are shown in Fig.19. In Fig.19, the mixture ratio of two samples is very similar, but, the shape of the absorption spectra is different. This was the impact of textile design different of each sample. Ratio of the kind of strings that appear on the surface is different by two sides when the composition is different because of warp yarn and weft yarn. It influences the spectrum shape.

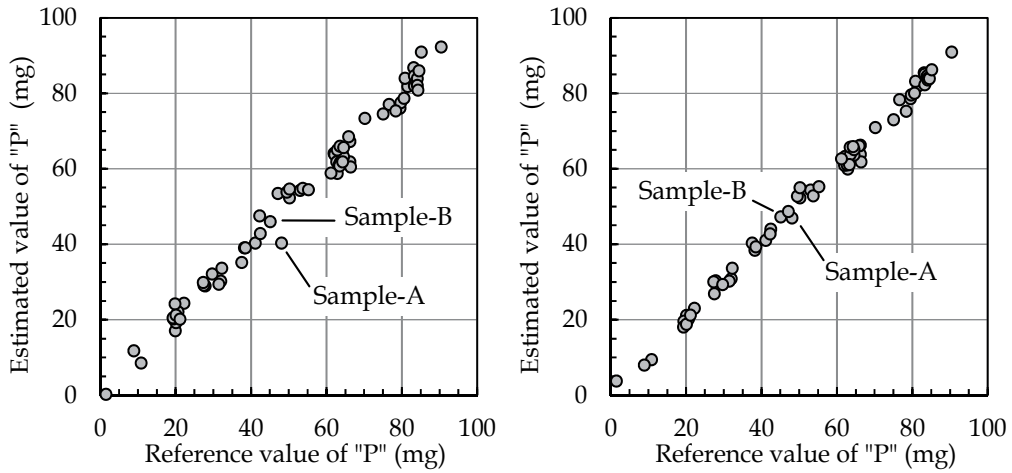

(A) Calibration curve by normal spectra (B) Calibration curve by AVE spectra

Fig. 18. Prediction result of mixture ratio of polyester in normal spectra and average spectra

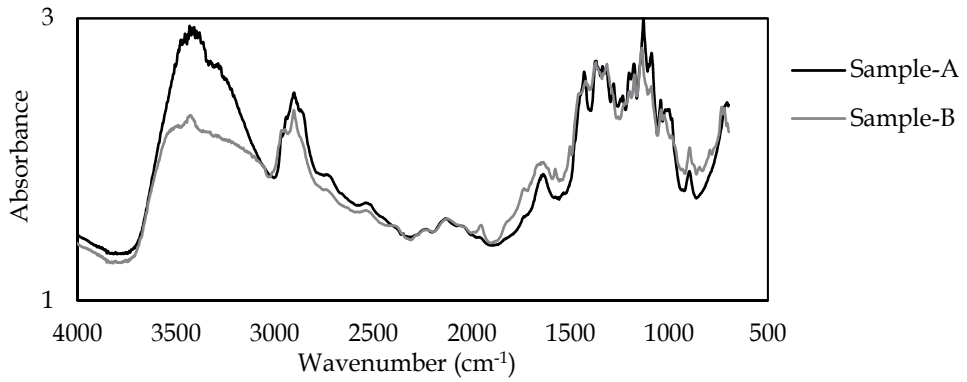

Fig. 19. The absorption spectra of sample A and B

Consequently, the diffuse reflectance spectrum was acquired on both sides of these samples.

The top surface and bottom surface in each sample was measured five times, averaged of obtained 10 spectra. Result of calibration curve developed by using average spectra and PLSR is shown in Fig.18-(B). The sample near the reference mixture ratio 40~50 % is close

in Y = X, and SEC has also improved. Furthermore, this system can be measured mixture ratio of mixed fabric products, because we could be obtained the good result which SEC is 1.8%.

5.4 Conclusion of non-destructive analysis of the composition and mixture ratio for textile product

In this paper, qualitative analysis of a single composition yarn could determine the exact composition of all. And, the measurement of percentage of mixed yarn can build a good calibration curve, which can be mixed with non-destructive measurement. IR spectrum with each feature of polyester and cotton and CP fabric sample quickly was able to be acquired by using the diffused reflection method of FT-IR. It turned out that our method was able to be applied from this outcome of an experiment to textile goods.

In the future, we need to build calibration curves for mixed yarn of other materials. If measurement method will be developed, could be proposed as a new method having better characteristics for measuring of textile products. The measurement time is about 10 minutes in this system. Since this system has the characteristics of these, bring significant benefits to such the samples of indestructible material determine the historical artefact and cultural heritage. From these results, we propose a new evaluation method of textile products not previously exist.

6. Measurement system of remaining dirt on inner surface of a narrow tubule based on infrared spectroscopy

6.1 Background

There is surely remaining dirt on the used products. In order to use the product for long periods, you need to wash the dirt. Therefore, many studies have been done for the dirty washing techniques and cleaning agents, analysis of remaining dirt. It has been researched in so many fields as the industrial, medical, food, yarn sector. The study of wash technology is so many, but washed cleanliness assessment has been neglected. As one of the reasons, we are under the impression that convinced that the product which satisfactory results were obtained by visual evaluation has not remaining dirt.

Especially, in the medical institutions, must be careful to hospital acquired infections. To prevent hospital acquired infections, cleanness is essential for all medical equipment. In particular, the instruments used in the human body must be aware of the cleanness. If you cannot detect small amounts of remaining dirt by visual evaluation, might be robbed a life. Therefore, the nurse must evaluate the cleanliness of the equipment used after cleaning and sterilizing. So far, the cleanness of medical equipment has been evaluated by visual inspection, test soil method or ATP method. But, these measurement methods have several disadvantages (individual differences, re-cleaning, numerical evaluation is difficult et al). This paper examines the application of qualitative and quantitative evaluation to residual contamination on the medical devices by infrared spectroscopy, and discussed the possibility of a new cleanness evaluation method. It is also difficult to evaluate the cleanness of a narrow tubule which is used by endoscope or drip tube. In this study, we developed a measurement system of the remaining dirt on the inner surface of narrow tubule.

6.2 Measurement system by IR fiber probe method

By the measurement method of remaining dirt on inner surface of narrow tubule, devised a system that combines the cone-shaped mirror and IR fiber probe, as shown in Fig.20. This system is inserted into the narrow tubule. Infrared light passing through the fiber probe is reflected by the cone-shaped mirror, and to irradiate the inner surface of the narrow tubule. If the dirt remains on inner surface of tubule, the infrared light is absorbed by the amount of dirt. Absorbed infrared light is reflected by the cone-shaped mirror, and is detected after passing through the fiber probe. We measured four times for one measured value. The cone-shaped mirror (Bottom diameter and Height: 4mm) placed inside the aluminium pipe. The fiber probe was arranged on 1 mm distance from the top of the aluminium pipe. We measured in this arrangement (1st time), and aluminium pipe was rotated 180 degrees (2nd times), and turn aluminium pipe upside down (3rd times), and aluminium pipe was rotated 180 degrees again (4th times). We averaged the four IR spectra detected in the measurements. The resolution, the accumulation, the measuring wavenumber range set at 4 cm^{-1}, 100 times, 4000~900 cm^{-1} measurement condition.

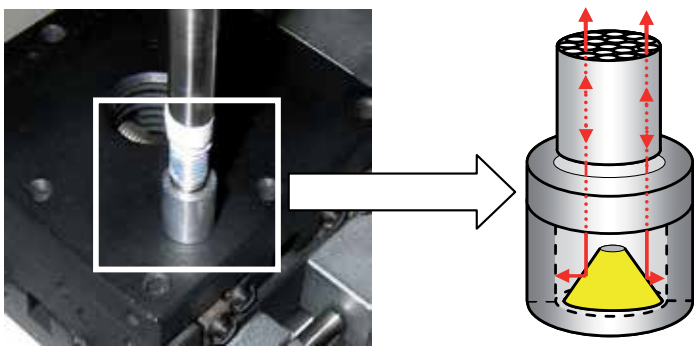

Fig. 20. Measurement system of remaining dirt on inner surface of narrow tubule

6.3 Qualitative analysis of lard

The remaining dirt of endoscope is excreted from the human body. For example, blood, protein and lipid dirt. We used the lard as a model of triolein contained in the lipid dirt. The absorption spectra of lard and triolein are shown in Fig.21. Many peaks by lard can be seen in spectra (2920 cm^{-1}, 2850 cm^{-1} : stretching vibrations by CH_2 groups, 1470 cm^{-1} : scissoring vibration by CH_2 group, 750 cm^{-1} : bending vibration by CH, 1740 cm^{-1} : stretching vibrations by C=O, 1160 cm^{-1} : antisymmetric stretching vibrations by CO). From this absorption spectrum, lard is the ideal remaining dirt model because is very similar to triolein present in the human body.

In the sample preparation, lard and aluminum pipe (ID: 5 mm, OD: 10mm, height: 8 mm) were used as the model substance of the human soil and narrow tubule. Model sample were prepared by the following process. Lard is dissolved in the hexane solution. The aluminum pipe has been kept in the solution for 1 minute. The sample pipe is left in the laboratory for five minutes until the residual hexane is fully evaporated. The dirt on the outer surface of aluminum pipe is wiped off. The weight of aluminum pipe before and after these processes was measured by using the electronic balance. The weight difference of aluminum pipe was used as the remaining amount of the lard (measured value).

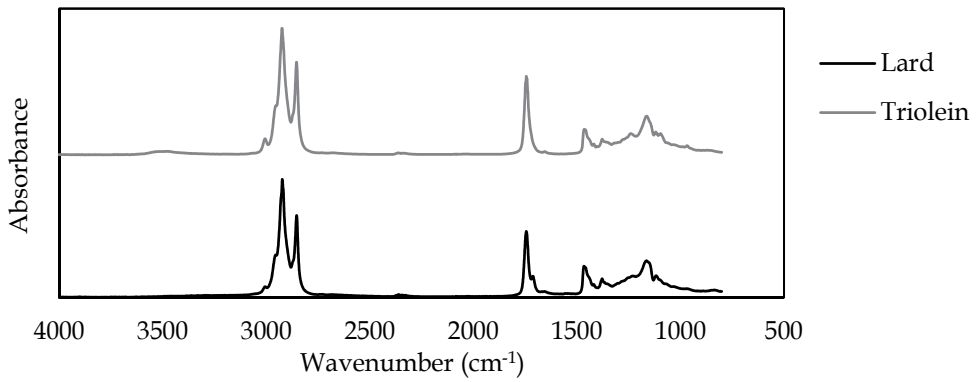

Fig. 21. The absorption spectra of lard and triolein

6.4 Cleanness evaluation of inner surface of the narrow tubule by PLSR

This study uses the PLSR analysis to obtain more accurate information contained in the infrared absorption spectrum of contaminants. To measure the amount of remaining dirt on the inner surface of the narrow tubules, first, we measured the infrared absorption spectrum of a known amount of remaining dirt, and the calibration curve was made using the measured infrared spectra by PLSR. Then, measuring the infrared absorption spectrum of an unknown amount of remaining dirt samples, we calculated the amount of deposited from the calibration curve was constructed. The number of sample are 50 kinds, the average amount of remaining lard is 0.65mg. As a cleanness evaluation of inner surface of the tubule, calibration curves were constructed with the PLSR. The analysis wavenumber range is 1800~1000 cm^{-1}.

The correlation scatter diagram of the calibration curve is shown in Fig.22-(A). The absorption spectrum was subjected to spectral correction and differential for the measurement S/N ratio in order to standardize. The horizontal axis represents the amount of lard, the vertical axis is the estimated weight obtained from the PLSR. The results of the correlation coefficient and the SEC were 0.843 and ± 0.19 mg/cm^2. This result indicates a highly significant correlation. This calibration curve is considered to be reasonable. The main causes of this, many lard information was considered obtained more than a single absorption peak because we analyzed a wide wavenumber band including a plurality of absorption peaks on the infrared spectra.

And for the validated on calibration curve, the 10 samples were measured. The estimated remaining dirt value is calculated from assign the measured spectra to a calibration curve. And, we weighed the samples, obtained this weight as the reference value. The validation result of the calibration curve is shown in Fig.22-(B). The results of the correlation coefficient is 0.957, and the SEP is ± 0.10 mg. EI (Evaluation index) method was applied for validation of the calibration curve, the EI value was shown to 21.5%. This value is classified into highly practical rank B. Thus, the amount of remaining dirt on the inner surface of narrow tubule could be measured quantitatively. And shown in Fig.22-(B), substituting the infrared absorption spectrum of minimum coating weight was calculated 0.08 mg by the calibration curve, the detection limit of this method is considered to be less than 0.08mg, as well as other measurement method. These results lead us to the conclusion that the cleanness on the inner surface of narrow tubule can be measured by this measurement system.

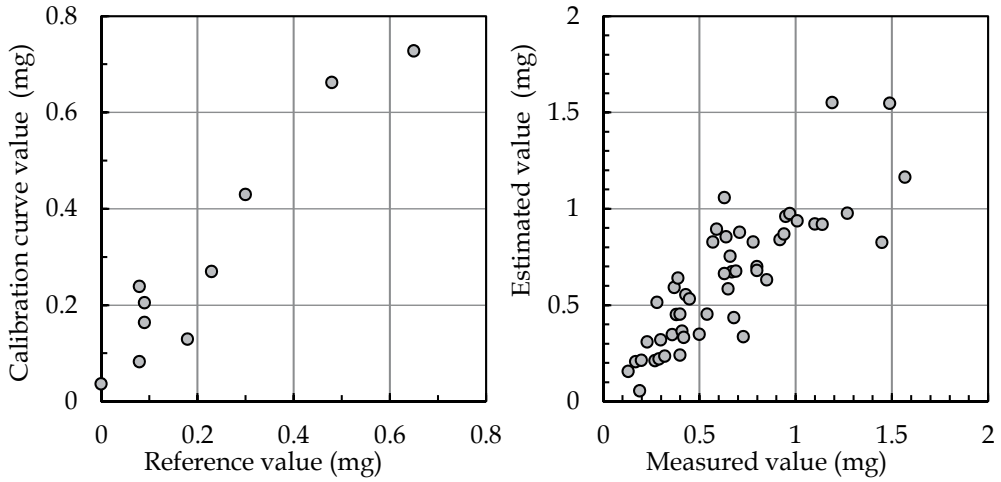

(A) The calibration curve for cleanness (B) The validation result of calibration curve

Fig. 22. The calibration curve and the validation result

6.5 Conclusion of cleanness evaluation by IR spectroscopy

The results obtained in this study, this measurement system was only possible to evaluate the cleanness of the inner surface of a narrow tubule.

The measurement time is about 2 minutes, which is shorter than the other measurement methods. In addition, this system is possible to measure in non-contact and non-destructive, because only the infrared light irradiation. And, we can detect the multiple dirt by using FT-IR. Therefore, even if protein and blood are remained together with lipid contamination, respectively dirt can be detected by this measurement method.

The next challenge is to integrate the fiber and the cone-shaped mirror. When we overcome the next challenges, this measurement system also can be used to long narrow tubules. If there is no dirt, the absorption peak is not detected, only if the dirt is remaining, to detect infrared spectra. From the position of the fiber probe when dirt is detected, the remaining dirt position can be identified. The type of remaining dirt can be identified from the shape of infrared absorption spectrum, and the amount of remaining dirt is detected by using a calibration curve.

By the characteristics of more than, this measurement system has so many advantages, we report as a new method of measuring remaining dirt. Thus, this system is possible to evaluate the cleanliness of the inner surface in narrow tubules. And can be reduce the risk of nosocomial infections in clinical practice.

7. Conclusion

As has been mentioned above, a non-destructive measurement can perform in many areas by using FT-IR. And, Infrared spectroscopy can be measured in quickly, non-contact, non-destructive. Therefore, various sensors will be able to develop by devise of measurement method and analysis method. Infrared spectroscopy can measure liquids and gases. In

addition, infrared spectroscopy can also detect very small concentrations and small quantities such as invisible. So, you will be able to be developed a better measurement systems and sensors that measure did not previously exist.

Challenges of Infrared Spectroscopy, is miniaturization or lighter or less expensive. In the now, these challenges are resolved in the near infrared wavelength range. However, in the mid-infrared wavelength range has not yet been resolved. This is a challenge must be overcome if you want to commercialization. However, if you will be successfully to size down, would be used as more advanced sensors. By using infrared spectroscopy, it will be developed a sensor that can measure accurately than current sensors. We want to propose, the Infrared spectroscopy is not just equipment but can be applied to a variety of measurements. We are wishing, in the future, infrared spectroscopy research will be expanded, and, FT-IR become more familiar measuring device. If that era will be arrival, the people would be receiving significant benefits from the infrared spectroscopy.

8. References

Aishima, T. (1992). *Chemometrics*, Maruzen, ISBN 4-621-03721-8, Tokyo, Japan

Dozono, T. et al. (2011). Identification and Quantitative Analysis of Fiber Mixtures by Infrared Spectroscopy, *Journal of the Illuminating Engineering Institute of Japan,* Vol.95, No.8A, (Aug 2011), pp. 450-453, ISSN 0019-2341

Koyama, S. et al. (2011). SICE Annual Conference 2011, *Proceedings of SICE Annual Conference 2011*, pp. 82-86, ISBN 978-4-907764-38-8, Tokyo, Japan, Sep 13-18, 2011

Koyama, S.; Miyauchi,. Y. & Ishizawa, H. (2010). Clinical Application of Non-invasive Blood Glucose Monitoring System by Infrared Spectroscopy, *Journal of the Illuminating Engineering Institute of Japan,* Vol.95, No.5, (May 2011), pp. 251-254, ISSN 0019-2341

Koyama, S.; Miyauchi,. Y. & Ishizawa, H. (2010). SICE Annual Conference 2010, *Proceedings of SICE Annual Conference 2010*, pp. 3425-3426, ISBN 978-4-907764-35-7, Taipei, Taiwan, Aug 18-21, 2010

7

Brain Activity and Movement Cognition – Vibratory Stimulation-Induced Illusions of Movements

Shu Morioka
Kio University
Japan

1. Introduction

Feedback information on movement from the musculoskeletal system plays an important role in appropriate control of movement as well as acquisition of new movements. Especially, information on limb movement and location of the movement conveyed from the musculoskeletal system to the brain is assumed to play an essential role in the creation of a body image in the brain. When human limbs actually move, multiple pieces of sensory information are input into the brain by the skin, muscles, joints, etc. Information from muscle spindles has been demonstrated to be most important for cognition of limb movement.[1,2)]

A sense of movement can be intentionally aroused by imposing vibratory stimulus to the tendon, regardless of whether actual movement takes place. Such stimulation makes muscle spindles discharge signals as afferent impulses toward the brain. A human recipient of these impulses feels movement of the body in an illusion through perception of muscle extension. (Fig. 1)[1)] This illusion is elicited mainly by activation of Ia fibers from the muscle spindle. In usual movements, muscle spindles are activated as the muscle is extended. Therefore, if vibratory stimulus activates muscle spindles, information on movement is conveyed to the brain as if the muscle were extended. Hence, a subject can experience limb movement during vibratory stimulation of the tendon despite the absence of actual limb movement. Specifically, tendon stimulation by vibration can induce a sense of movement in the absence of real movement. If brain activity at that moment can be detected, it is possible to study brain activity at the time movement is perceived.

In fact, it was demonstrated that the motor area contralateral to the stimulated limb was activated when illusory hand joint extension was produced by vibratory stimulation of the hand extensor tendon.[3)] It was, however, reported that the brain was predominantly active in the right hemisphere irrespective of which hand was stimulated as far as premotor and parietal areas were concerned.[4)] Such vibratory stimulation-based illusory movement-induced activity of the brain is nearly identical to that occurring during real movement; this is especially true of premotor and supplementary motor areas, the cerebellum, and the parietal lobe.[5)] On the other hand, when the hand extensor tendon is stimulated with vibration while an object is being held by the hand, an illusory sense of both hand flexion

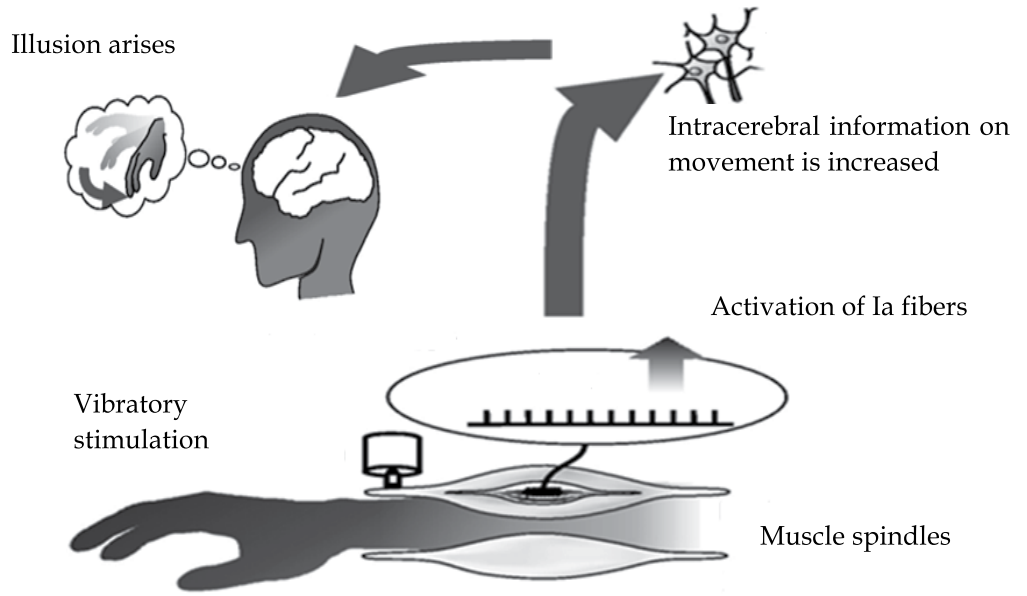

Fig. 1. Schema of tendon stimulation-induced illusory movement

and of the object moving in the same direction is felt. When an object is felt to move in an illusion, the left hemisphere is predominantly activated and regions of interest are the lobule of the inferior parietal lobe and Brodmann's area 44/45.[6-8)]

However, when an object is placed within the angle of a self-experienced illusion without the object being grasped, it remains to be clarified how much such visual information influences the degree of illusory movement and how the brain is activated. This chapter reports such influences as well as brain activity **as** explored by functional near-infrared spectroscopy (fNIRS).

2. Methods

2.1 Subjects

Eight healthy adults in their 20s were initially examined for the intensity of the sensation of illusory movement after vibratory stimulation of the hand extensor tendon using the vibratory stimulation apparatus described below. Intensity was graded on a 5-stage scale. The 7 individuals who were assessed as having scale 4 (strong illusory sensation) or greater were studied. These 7 subjects were observed for brain activity when they experienced illusory sensations and were found to have increased blood flow in the area that responded to illusory movement sensation.[6)] They were therefore considered eligible for this study. According to the Helsinki Declaration, they were given an explanation about the purpose of this study before providing written informed consent.

2.2 Vibratory stimulation apparatus

We used the SL-0105 LP (Asahifactory Corp., Tokyo) (Fig. 2) for vibratory stimulation under conditions of frequency of 80 Hz and intensity of 0.2 – 0.3, which was reported to most

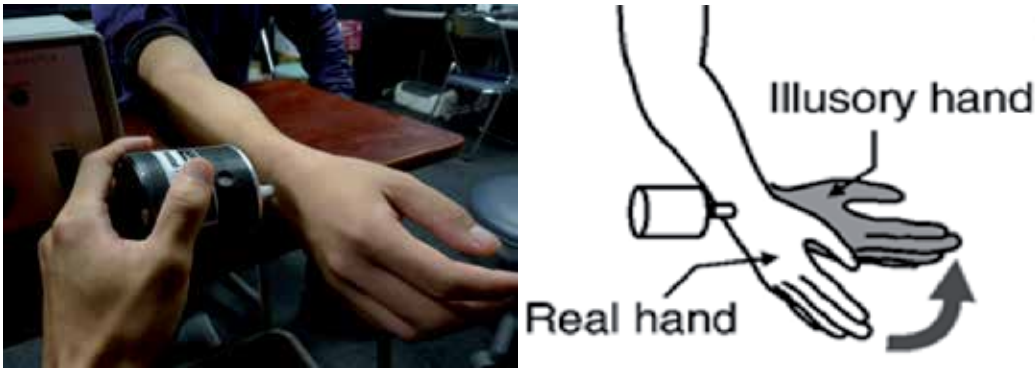

a) b)

a) Apparatus is in contact with the hand extensor tendon to elicit an illusion of hand joint flexion. (Situation 1)
b) Illustration of illusory movement.

Fig. 2. Application of vibratory stimulus

efficiently excite illusions by an earlier study.[4)] There were two experimental situations. In situation 1, vibratory stimulation was imposed to the hand extensor tendon without placing an object near the subject; In situation 2, stimulation was similarly imposed with an object (umbrella) standing upright within range of illusory flexion. (Fig. 3) In either situation, the skin near the tendon was stimulated, which served as a control. The purpose of this stimulation was to acquire data on brain activity that was elicited when skin irritation receptors (Meissner corpuscles, Pacinian corpuscles, etc.) were excited that could be subtracted from data acquired by tendon stimulation so that pure illusory brain activity could be calculated.

Fig. 3. An object (umbrella) is placed within range of illusory movement. Situa (tion 2)

2.3 Protocol of tasks

A task to create an illusion for a period of more than 20 seconds was imposed between two 10-second resting times. This session was uninterruptedly repeated under each situation. The illusory flexion angle was estimated as follows. After accomplishment of a task, a

subject was requested to reenact with an actual motion the illusory limb movement and the flexion angle was measured with an electric geniometer (SG150, Biometrics, Phoenix).

2.4 Measurement by fNIRS

Cerebral blood flow was measured using fNIRS FOIRE-3000 (Shimazu Co., Kyoto). (Fig. 4) Probes were fixed using a flexible holder to cover the entire head, which was placed on the surface of the scalp covering the bilateral frontal and parietal lobes. (Fig. 4) The distance between the pair of emission and detector probes was 3.0 cm and the pair was set as a channel (ch). The Cz of the International 10-20 method for EEG was set at the point where a line drawn between the bilateral external auditory pores and a perpendicular line from the nose intersect. Emission probe #7 was placed at the Cz to allow measurement sites be shared equally by all the subjects. Fifteen emission probes (E) and detection probes (D), respectively, were placed in a 5X6 arrangement in order starting from the left forehead. It total, 49 channels were provided. (Fig. 5) To prevent the hair from protruding, fibers (multi-component glass band fibers) were set **through the hair to a fiber holder to ensure that their tips contacted the scalp.**

Emission and detector probes are placed at a distance of 3 cm from each other and each pair of probes works as a channel.

Fig. 4. Subject wearing flexible probe holder covering the entire scalp.

2.5 Data analysis

Brain active sites were identified using 3 SPACE FASTRAK (POLHEMU Co., Vermont) and were superimposed on images obtained by magnetic resonance imaging (MRI) using FUSION imaging software (Shimazu, Co., Kyoto).

Oxidized hemoglobin (oxy-Hb) levels at tendon stimulation acquired from 3 continuous task sessions were averaged to get an arithmetic mean from which another arithmetic mean, that which was similarly acquired as the skin was stimulated, was subtracted. Final values were statistically analyzed. Since it is known that there is a time lag of several seconds between the onset of neural activity and change in cerebral blood flow as detected by fNIRS,

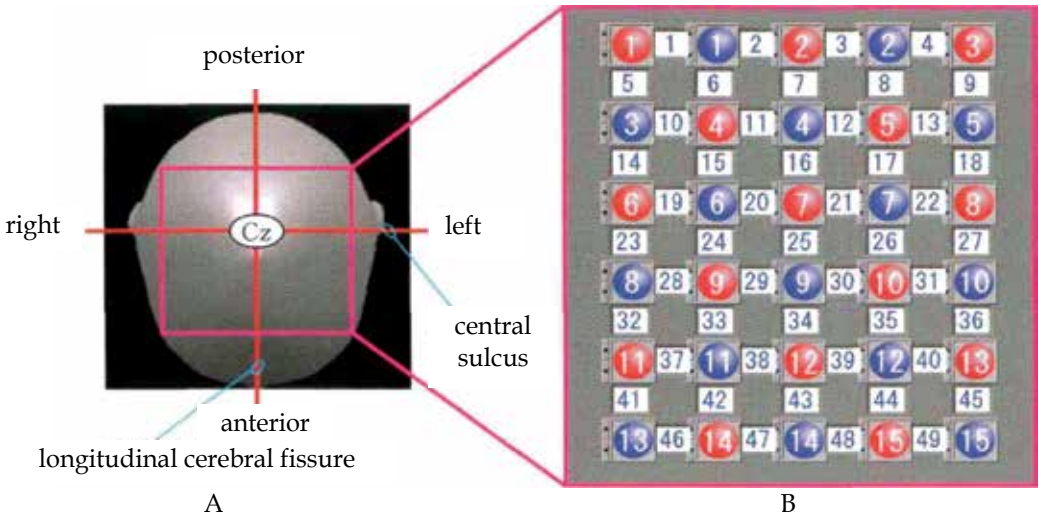

Emission probe #7 was placed at the Cz (panel A) as defined by the International 10-20 method so that measurement sites were the same in all subjects (panel B).

Fig. 5. Schematic arrangement of emission and detection probes.

levels of oxy-Hb acquired over the first 5 seconds were discarded and levels obtained over another 5 seconds were subjected to analysis during both tasks and resting times. Furthermore, the issue of optical path length was solved by calculation of effect sizes (=[(an arithmetic mean value of oxy-Hb levels at a task) – (that at a resting time)]/standard deviation at a resting time).[9] In addition, effect sizes were separately averaged for each region of interest. Specifically they were analyzed as follows: ch 1, 2, 5, 6, 10, and 11 representing the right parietal lobe; ch 3, 4, 8, 9, 12, and 13, the left parietal lobe; ch 14 -27, bilateral sensorimotor areas; ch 28, 29, 32, 33, 37, 38, 41, 46, and 47, the right premotor area; and ch 30, 31, 35, 36, 44, 45, 48, and 49, the left premotor area. (Fig. 6)

Differences in brain activity between situations 1 and 2 were tested with Wilcoxon matched-pairs signed-ranks test. Angles of illusions were analyzed by the t-test. Pearson's correlation coefficients were calculated to examine relations between differences in the angles of illusions between situations 1 and 2 and similar differences in the brain activity. Level of significance was set as $p < 0.05$.

3. Results

Angles of the illusion were significantly decreased in situation 2 compared to situation 1 (Fig. 7, $p < 0.05$), while brain activity in the premotor area as assessed by effect size was reduced in situation 2. To confirm this finding, cerebral areas related to these channels were superimposed on MRI images and were identified as the right premotor area. (Fig. 8) On the other hand, there was a positive relationship, although not significant ($p = 0.17$), between a decrease in illusion angles and a reduction in activity in the right premotor area ($r = 0.58$).

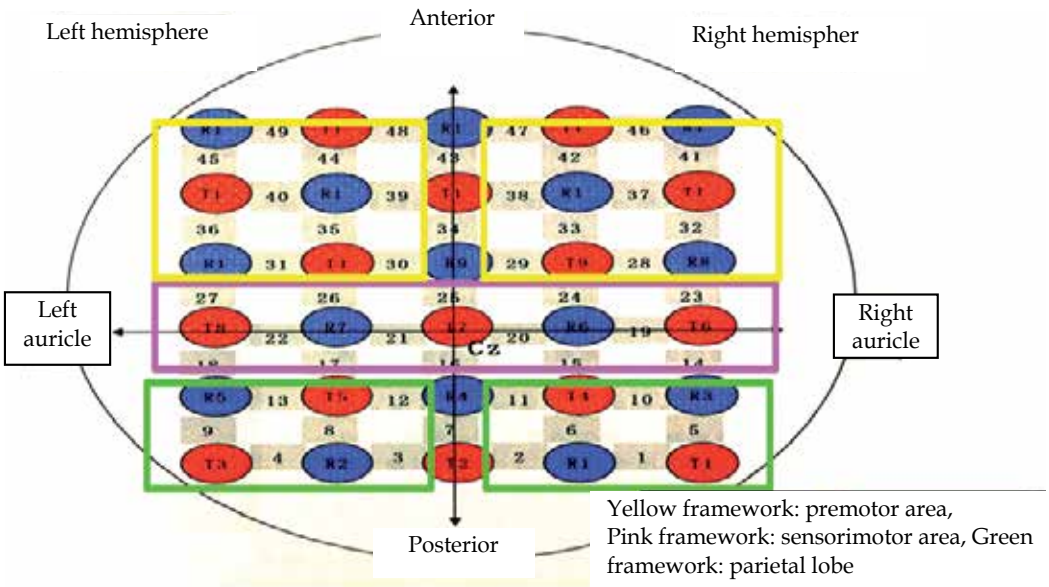

Channels were grouped into 5 regions and effect sizes from each region were averaged.

Fig. 6. Schema of regions of interest analysis

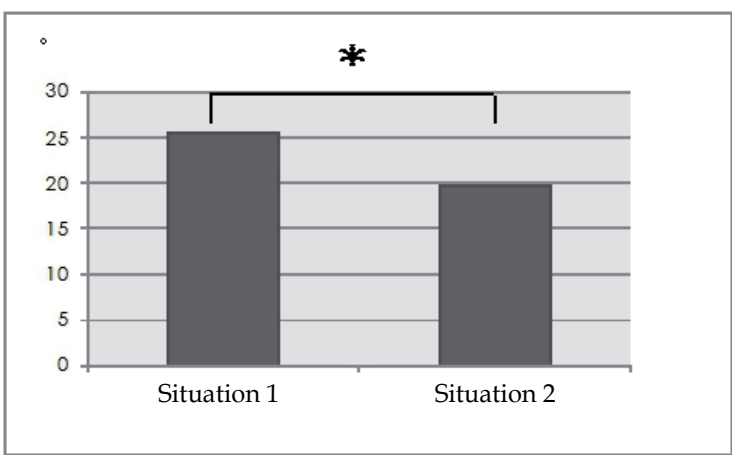

* P<0.05

Situation 1: No object is presented, Situation 2: An object is presented.
There is a significant reduction of flexion angles in situation 2 compared to situation 1. In other words, object presentation reduces the degree of illusory hand joint flexion.

Fig. 7. Differences in angles of hand joint flexion between Situations 1 and 2

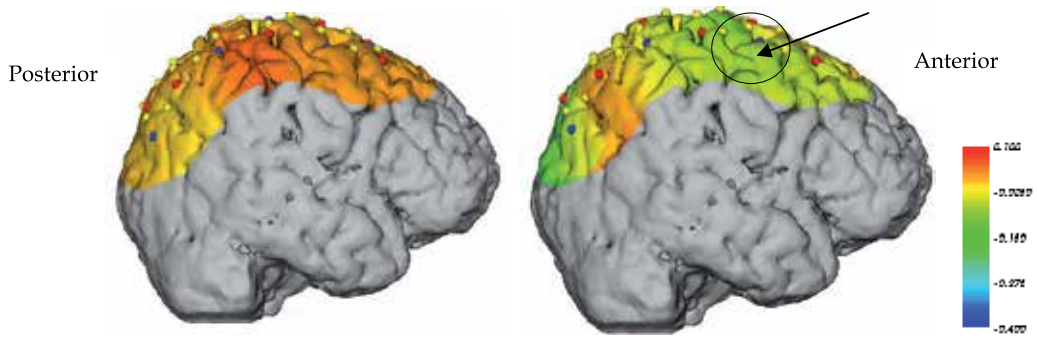

Warm colors denote a relative increase in blood flow, while cold colors denote a relative decrease in blood flow.
In situation 2, in the right premotor area there is a reduction in activity compared to situation 1. (Arrow within circle)

Fig. 8. Comparison of cerebral cortical activities between situations 1 and 2.

4. Discussion

The present results clarified that the angle of illusion was decreased by placing a visible object within the range of illusory movement of the subject's own hand. It is therefore evident that visual sensation can modify illusory movement, indicating that the environment largely influences movement cognition. The effect size of the channels corresponding to the right premotor area were significantly reduced when vibratory stimulation was given in the presence of a visible object in comparison with absence of an object. In summary, the reduction in activity of the right premotor area was assumed to have diminished illusory movement as suggested by a positive correlation between intensities of the area activity and those of the illusion. That this correlation was not significant may have been because of the small subject population. It was thus clear that the activity of the premotor area of the right hemisphere influenced perception of movement and that the degree of activation of the right premotor area was involved in formation or suppression of movement perception.

The right premotor area is the region responsible for bodily self-attribution as evidenced by Ehrsson et al.[10] Evidence of the predominance of the right hemisphere in illusory perception of limb movement elicited by tendon vibration was also reported.[8] Our present study added new information that a decline in activity in the premotor area suppressed illusory movements. Pinocchio's illusion[11] helps explain this observation. When an illusory movement of elbow extension is provoked by vibratory stimulation with your nose being pinched, you feel as if your nose got longer. This phenomenon occurs to clear up a contradiction between illusory limb movements and constant input of tactile sensation from the nose. In this study, the subject should have touched an object due to illusory movements if it had existed within the illusory angle of the subject's own hand. Our results suggested that the degree of illusory movements was lowered due to lack of tactile sensation and that the right premotor area might be involved in variability of illusory movements.

From these results it was clarified that movement perception based on activity of muscle spindles was easily modified by a change in visual information even though the intensity of

vibratory stimulus was fixed. Namely, bottom-up processing of sensory information from afferent fibers is influenced by its top-down processing. On the other hand, it remains unclear what directly reduced the activity of the right premotor area. To answer this question, it is necessary to examine if an object presented outside the angle of illusion changes the degree of illusory movements. In addition, it will be necessary to study the status of activities of visual cortical areas as well as of prefrontal areas rather than study premotor areas.

5. References

[1] Roll JP, et al: Kinaesthetic role of muscle afferents in man, studied by tendon vibration and microneurography. Exp Brain Res 47: 177-190, 1982

[2] Roll JP, et al: Alteration of proprioceptive messages induced by tendon vibration in man: a microneurographic study. Exp Brain Res 76: 213-222, 1989

[3] Naito E et al: Illusory arm movements activate cortical motor areas: a positron emission tomography study. J Neurosci 19(14):6134-6144, 1999

[4] Naito E et al: Kinesthetic illusion of wrist movement activates motor-related areas. Neuroreport 12: 3805-3809, 2011

[5] Naito E, et al: Internally simulated movement sensations during motor imagery activate cortical motor areas and the cerebellum. J Neurosci 22: 3683-3691, 2002

[6] Naito E, et al: Somatic sensation of hand-object interactive movement is associated with activity in the left inferior parietal cortex. J Neurosci 26: 3783-3790, 2006

[7] Naito E, et al: Human superior parietal lobule is involved in somatic perception of bimanual interaction with an external object. J Neurophysiol 99: 695-703,2008

[8] Naito E, et al: Dominance of the right hemisphere and role of area 2 in human kinesthesia.J Neurophysiol 93 :1020-1034,2005

[9] Schroeter L, et al：Age dependency of the hemodynamic response as measured by functional near-infrared spectroscopy.Neuroimage19: 555-564,2003

[10] Ehrsson HH, et al: That's my hand! Activity in premotor cortex reflects feeling of ownership of a limb. Science 305: 875-877,2004

[11] Lankner JR: Some proprioceptive influences on the perceptual representation of body shape and orientation. Brain 111:281-297,1988

8

Probing Brain Oxygenation Waveforms with Near Infrared Spectroscopy (NIRS)

Alexander Gersten[1], Jacqueline Perle[2],
Dov Heimer[3], Amir Raz[4] and Robert Fried[5]
[1]*Department of Physics, Ben-Gurion University, Beer-Sheva*
[2]*Department of Psychology,*
Hunter College of the City University of New York, NY
[3]*Pulmonary Unit, Soroka University Hospital, Beer-Sheva*
[4]*McConnell Brain Imaging Centre, Montreal Neurological Institute,*
McGill University, Montreal
[5]*City University of New York, NY*
[1,3]*Israel*
[2,5]*USA*
[4]*Canada*

1. Introduction

Breathing may have dramatic effects on the human cerebral blood flow (CBF) and cognition. This was already known long time ago to Chinese (Li Xiuling, 2003), Hindus (Kuvalayananda, 1983) and Tibetans (Mullin, 1996). The main parameter influencing the CBF is the arterial partial pressure of carbon dioxide ($PaCO_2$). About 70% increase in $PaCO_2$ may double the blood flow (Sokoloff, 1989, Guyton, 1991). The increase of blood flow to the brain results in an increase of nutrients and oxygen, which may influence to great extent brain's physiology.

On the other hand lowering the $PaCO_2$ through hyperventilation found an application in neurosurgery (Feihl and Perret, 1994).

An evaluation of the CBF dependence on $PaCO_2$ was given by Gersten (Gersten, 2011). The human normal value of $PaCO_2$ is about 40 mmHg. Fig. 1 depicts our estimation of the changes of CBF as a result of changing $PaCO_2$ from normal. The estimate is based on the data of Refs. (Reivich 1964, Ketty and Schmidt 1948, Raichle et all 1970). An increase of only 12.5% from normal in $PaCO_2$ leads to the state of hypercapnia ($PaCO_2$ above 45 mm Hg).

With aging both CBF and $PaCO_2$ tends to fall down, therefore breathing exercises (or procedures) with the aim to increase $PaCO_2$ and CBF might be important in preventing and alleviating neurodegenerative diseases. They may be also important in improving intellectual abilities. The amount of $PaCO_2$ in our arteries is proportional to the CO_2 which was metabolized by the organism and inversely proportional to the lung ventilation (i.e. to the amount of air exchanged between the lungs and the environment in one minute).

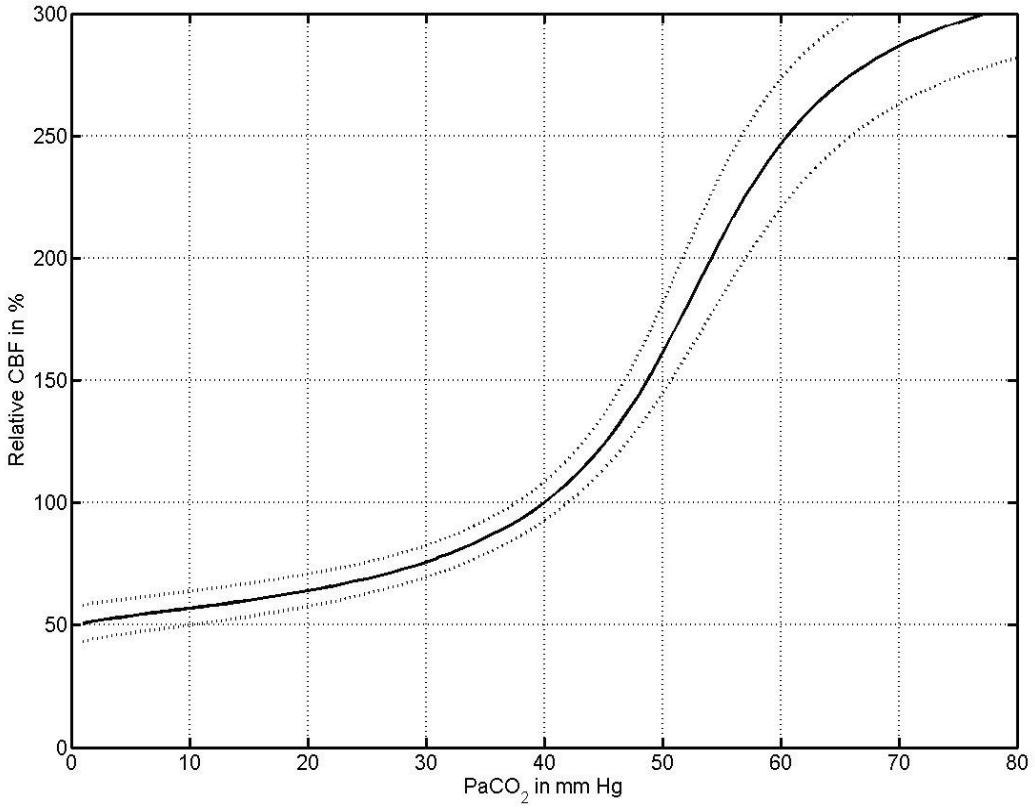

Fig. 1. Estimated changes of human CBF from normal (100%) against $PaCO_2$. Normal $PaCO_2$ =40 mm Hg is assumed, it corresponds to ordinate value of 100%. From (Gersten, 2011).

An instantaneous way to change $PaCO_2$ can be accomplished by influencing the ventilation. Respiratory periodicities were observed in fMRI, but they were treated as artifacts (Windischberger et al., 2002) or as a noise (Raj et al., 2001). The main research effort was directed towards the elimination of the effect of the respiratory periodicities. Our aim is to study the effect of respiration on brain's oxygenation and performance.

Near infrared spectroscopy (NIRS) is an efficient way to probe brain's oxygenation (Rolfe, 2000; Thavasothy et al., 2002; Elwell et al., 1996). Brain oxygenation increases with an increase of $PaCO_2$ (Imray et al.,2000, Thavasothy et al., 2002). In this chapter we examine the dependence of brain's oxygenation on $PaCO_2$.

The technique of near infrared spectroscopy (NIRS) allows to measure the oxygenation of the brain tissue. The particular problems involved in detecting regional brain oxygenation (rSO2) are discussed. The dominant chromophore (light absorber) in tissue is water. Only in the NIR light region of 650-1000 nm, the overall absorption is sufficiently low, and the NIR light can be detected across a thick layer of tissues, among them the skin, the scull and the brain. In this region, there are many absorbing light chromophores, but only three are important as far as the oxygenation is concerned. They are the hemoglobin (HbO2), the

deoxy-hemoglobin (Hb) and cytochrome oxidase (CtOx). In the last 20 years there was an enormous growth in the instrumentation and applications of NIRS.

The devices that were used in our experiments were : Somanetics's INVOS Brain Oximeter (IBO) and Toomim's HEG spectrophotometer. The performances of both devices were compared including their merits and drawbacks. The IBO is based on extensive efforts of an R&D group to develop a reliable device, which measures well the rSO2. It is now used efficiently in operating rooms, saving human lives and expenses. Its use for research however has two drawbacks: the sampling rate is too small and the readings are limited to only two significant digits. The HEG device does not have these drawbacks, but is not developed sufficiently at this time to measure rSO2. We have measured the HEG readings and compared them with the rSO2 readings of the IBO. Our findings show that the HEG can be used to measure relative changes of rSO2.

Results of an experiment are presented whose aim is to explore the relationship between respiration and cerebral oxygenation. Measurements of end tidal CO_2 ($EtCO_2$) were taken simultaneously with cerebral oxygen saturation (rSO_2) using the INVOS Cerebral Oximeter of Somanetics. Due to the device limitations we could explore only subjects who could perform with a breathing rate of around 2/min or less. Six subjects were used who were experienced in yoga breathing techniques. They performed an identical periodic breathing exercise including periodicity of about 2/min. The results of all six subjects clearly show a periodic change of cerebral oxygenation with the same period as the breathing exercises. Similar periodic changes in blood volume index were observed as well.

We tested the hypothesis that simple breathing exercises may significantly increase cerebral blood flow (CBF) and/or cerebral oxygenation. Eighteen subjects ranging in age from nineteen to thirty nine participated in a four-stage study during which measurements of end tidal CO_2 (EtCO2 - by capnometer) and local brain oxygenation (by near-infrared spectroscopy (NIRS) sensor) were taken. The four stages were 1) baseline, 2) breathing exercises, 3) solving an arithmetic problem, and 4) biofeedback. During the breathing exercises there was a significant increase in $EtCO_2$ indicating a significant increase in global CBF. The increase in global CBF was estimated on the basis of a theoretical model. During the arithmetic and biofeedback tasks there was a significant increase in the local (Fp1) oxygenation, but it varied between the different participants. The results may lead to new clinical applications of CBF and brain oxygenation monitoring and behavioral control.

2. Fundamentals of NIRS

The study of the human brain made a big step forward with the introduction of noninvasive techniques, among them the near-infrared spectroscopy (NIRS). This technique allows to measure the oxygenation of the brain tissue (Alfano et al., 1997, 1998; Chance 1998, 1998a; Delpy and Cope, 1997; Hoshi, 2003; Obrig, 2003; Rolfe, 2000; Strangman et al., 2002).

The light, with wavelengths 650-1000 nm, penetrates superficial layers of the human body, among them the skin, the scull and the brain. It is either scattered within the tissue or absorbed by absorbers present in the tissue (chromophores).

The visible light has wavelengths 400-700 nm, some individuals can see up to 760 nm. Formally, the red light extends within the wavelengths of 630-760 nm, and the near infrared

light within 760-1400 nm. However, these terms are not precise, and are used differently in various studies. Here we will refer to the near infrared light as having the spectrum of 650-1000 nm, i.e. the light that penetrates superficial layers of the human body.

The dominant chromophore in tissue is water. It absorbs strongly below 300 nm and above 1000 nm. The visible part of the light spectrum, between 400 and 650 nm, is almost non-transparent due to strong absorption of hemoglobin and melanin. Only in the NIR light region of 650-1000 nm, the overall absorption is sufficiently low, and the NIR light can be detected across a thick layer of tissue.

In the following pages, we will be concerned with utilizing the NIR light to determine the oxygenation of the brain tissue. In the rather transparent NIR region, there are many absorbing light chromophores, but only three are important as far as the oxygenation is concerned. They are the hemoglobin (HbO_2), the deoxyhemoglobin (Hb) and cytochrome oxidase (CtOx), Hb and HbO_2 (which carries the oxygen) are found inside the red blood cells. CtOx is the enzyme which ends the cellular respiratory chain, and is located in the mitochondrial membrane. Quantitatively important is the difference between the absorption spectra of the oxidised and reduced forms of CtOx. The concentration of cytochrome oxidase in living tissue is usually at least an order of magnitude below that of hemoglobin (Sato et al., 1976); therefore, its contribution is often neglected.

In the last 20 years there was an enormous growth in the instrumentation and applications of NIRS. A separate section will be devoted to the instrumentation. We will compare two NIRS devices: the INVOS Brain Oximeter (IBO) of Somanetics and the HEG device of H. Toomim.

3. Oxygen utilization

The amount of oxygen in the arterial blood depends upon the inspired oxygen and the pulmonary gas exchange. It depends on the arterial blood gas partial pressures of oxygen (PaO_2) and carbon dioxide ($PaCO_2$). The units of partial pressures may cause some confusion. Three types of units are in use. One unit is kiloPascal (kPa) equivalent to 7.5006 mmHg (or Torr). It can be measured also in %, when 100% corresponds to atmospheric pressure of 760 mmHg (Torr), i.e 1% corresponds to 7.6 Torr (mmHg). The arterial hemoglobin saturation (SaO2) is measured in %. The normal value is about 95%. A typical oxygen carrying capacity of the blood is 19.4 ml of O_2 per dl of blood with 19.1 ml O_2/dl carried by hemoglobin and only 0.3 ml O_2/dl dissolved in plasma (Cope, 1991). It should be noted that the oxygen delivery to the tissues is by diffusion and the hemoglobin acts as a buffer to maintain plasma's oxygen which is extracted by the tissue.

A typical averaged value for adult cerebral blood flow (CBF) is 47.7 ml/100 ml/min (Frackowiak et al., 1980) corresponding to total oxygen delivery 9.25 ml O2/100 ml/min. (Cope, 1991). Typical oxygen consumption of the adult brain is 4.2 ml O2/100 ml/min (Frackowiak et al., 1980). CBF, cerebral blood volume (CBV) and cerebral oxygen extraction (COE) are significantly greater in grey matter compared to white matter in normal human adults (Lammertsma et al., 1983; cope, 1991). The CBF and the cerebral blood volume (CBV) of grey matter in normal human adults is approximately 2.5 times that of white matter, while the cerebral oxygen extractions (COE) are 0.37 and 0.41 for grey and white matter respectively (Lammertsma et al., 1983; cope, 1991). Only part of the arterial oxygen which

arrives in the brain is absorbed and utilized. The fraction which is utilized, known as the oxygen extraction fraction (OEF), is defined as

$$OEF=(SaO_2 - SvO_2)/SaO_2 ,$$

where SaO_2 and SvO_2 are the arterial and venous oxygen saturations respectively.

According to Derdeyn et al (Derdeyn et al, 2002) the EOF, measured in their normal control subjects, was 0.41±0.03. Assuming SaO_2 equal to 0.95 the SvO_2 will be, using Eq. (6), equal to 0.56±0.03. In the brain tissue the absorption of the oxygenated and deoxygenated hemoglobin is mostly venous. Assuming a 75% venous contribution, the brain tissue regional oxygen saturation (rSO_2) in the frontal region will be about 66±3%, a mean value which is observed in experiments. With a decrease of CBF there is a bigger demand for oxygen and EOF will increase (Kissack et al, 2005). Accordingly, with an increase of CBF the OEF will decrease.

4. NIRS Instrumentation

Several types of NIRS equipment, based on different methods, are commercially available. They measure the concentrations of Hb, HbO_2 and the total hemoglobin tHb. If the redox state of CytOx is also taken into account, then measurements with 3 wavelengths has to be done. Instruments with 2 wavelengths do not evaluate the CytOx contribution.

Three types of instruments are in use according to the used method : continuous intensity, time resolved and intensity modulated. For details, see (Delpy and Cope, 1997). Most of the commercial instruments utilize continuous wave (CW) light. In combination with the modified Lambert-Beer law it allows to measure changes in Hb and HbO_2. In a biological tissue, quantification of the NIRS signal is difficult. Different methods have been proposed to improve the resolution. One of them is the spatially resolved spectroscopy (SRS), which uses CW light and a multi-distance approach. With this method the rSO_2 (the absolute ratio of HbO_2 to the total Hb content-tHb), can be evaluated (Suzuki et al., 1999).

A further distinction among the instruments can be made. The simplest are the photometers, which use single-distance and CW, light, usually with one sensor (channel).

The oximeters are more sophisticated. They use multi-distance (SRS) techniques with CW and usually two sensors (channels). For details, see (Ferrari et al., 2004; Delpy and Cope, 1997; Rolfe, 2000). Recently several groups have begun to use multi-channel CW imaging systems generating images of a larger area of the subject's head with high temporal resolution up to 10 Hz (Ferrari et al., 2004; Miura et al., 2001; Obrig and Villringer, 2003; Quaresima el al., 2001a. 2002a).

In the following we will compare two instruments: the INVOS Cerebral Oximeter of Somanetics (www.somanetics.com; Thavasothy et al., 2002), and the hemoencelograph (HEG) (Toomim and Marsh, 1999; Toomim et al., 2004).

4.1 The INVOS oximeter

The Somanetics INVOS Cerebral Oximeter (ICO) system measures regional hemoglobin oxygen saturation (rSO_2) of the brain in the area underlying the sensor and uses two

wavelengths, 730 and 810 nm. The sensor, ("SomaSensor"), is applied to the forehead with an integrated medical-grade adhesive. Two sensors can be placed in the forehead near Fp1 and Fp2. The spatially resolved spectroscopy (SRS) method is applied by using in the sensor two source-detector distances: a "near" (shallow), 3 cm from the source and a "far" (deep), 4 cm from the source. Both sample almost equally the shallow layers in the tissue volumes directly under the light sources and detectors in the sensor, but the distant "far" penetrates deeper into the brain. Using the SRS method, subtraction of the near signal from the far should leave a signal originating predominantly in the brain cortex. The measurement takes place in real time, providing an immediate indication of a change in the critical balance of oxygen delivery and oxygen consumption.

According to the producers: "Using the model at a 4 cm source-detector spacing and no signal subtraction, the overlying tissue and skull contribute, on average, about 45 percent of the signal while 55% is cerebral in origin. Subtracting the data from the 3 cm spacing (as the Oximeter does) reduces this extracerebral contribution to less than 15 percent. While the potential exists to develop an instrument that will reduce the extracerebral contribution to zero, subject-dependent variations in anatomy and physiology will likely cause variations of ±10%. While the extracerebral contribution is not zero, the noninvasive Somanetics INVOS Cerebral Oximeter provides a "predominately cerebral" measurement where over 85 percent of the signal, on average, is exclusively from the brain" (www.somanetics.com).

The INVOS Cerebral Oximeter is an important tool in surgery rooms, saving lives and expenses. The producers explain: " Declining cerebral oximeter values occur frequently in cardiac surgery and reflect the changing haemodynamic profile of the balance between brain oxygen delivery and consumption. Since low rSO2 values correlate with adverse neurological and other outcomes, continuous assessment is a valuable patient management tool. Declining or low cerebral oximeter values are corrected with simple interventions".

4.2 The HEG

The hemoencephalograph (HEG) is a single-distance CW spectrophotometer, which uses NIR light with two wavelengths, 660 and 850 nm. The light source consist of closely spaced emitting diodes (LED optodes). The source and an optode light receiver are mounted on a headband. The distance between the source and receiver is 3 cm.

The HEG measures the ratio of the intensity of the 660 nm light to the intensity of the 850 nm light.

The HEG is not intended to measure rSO_2. Nevertheless it is an important tool in the biofeedback research.

Hershel Toomim, the inventor of HEG has noticed that he can influence the outcome by looking at the results. Since then many people were able to increase the HEG readings via such a biofeedback.

The HEG became an important tool for training local brain oxygenation. The HEG is a very sensitive device. The distance between the source and receiver is the same as the distance of the shallow detector of the Somanetics INVOS Cerebral Oximeter. Therefore the INVOS Oximeter covers larger brain tissue and is more stable and less influenced by biofeedback.

What is the HEG measuring? According to the producers: "The HEG ratio is the basis of blood flow training. A normalized basis for HEG was established using measurements at Fp1 of 154 adult attendees at professional society meetings. A normalized reference value of 100 (SD=20) was thus established and served to calibrate all further spectrophotometers". The calibration was achieved by multiplying the intensities ratio by 200. We have shown (Gersten et. al. 2006) that one can relate the readings of the HEG to rSO_2 and even calibrate it separately for each individual.

5. Experimental detection of oxygen waveforms

We started this research in Israel in the Pulmonary Unit of the Soroka University Hospital in Beer-Sheva. The study protocol was approved by the Helsinki (Ethics) Committee of the Soroka University Hospital. The investigation conforms with the principles outlined in the Declaration of Helsinki. The nature of the study was explained, and all subjects gave written consent to participate.

At the beginning our research was based on capnometer measurements of end tidal CO_2 ($EtCO_2$). The capnometer measures the CO_2 concentration of the expired air. During the inspiration or breath holding the capnometer indications are zero. The capnometer enable us to follow the breathing periodicity.

We continued the research in the USA using the INVOS Cerebral Oximeter model 5100B of Somanetics Corporation and a capnometer of Better Physiology, Ltd. Both devices are noninvasive. The INVOS Cerebral Oximeter is based on most recent technological developments of near infrared spectroscopy (NIRS). With this device data are collected of regional oxygen saturation (rSO_2) near the forehead with two optical sensors (for more details see www.somanetics.com). In addition to rSO_2 one can determine the Blood Volume Index (BVI), which is an indicator of blood changes in the brain. This is a relative quantity, which could not be normalized with our oximeter.

The fastest recording rate of the 5100B oximeter is every 12 seconds from both left and right sensors. This time is much longer then the average period of about 4 seconds of normal respiration. In order to detect oxygenation periodicity we had to study respiration periods of about 36 seconds or larger (i.e. 3 data points or more for each breathing period). This is still a rather small amount of data points per respiration period. We have compensated for this small number by using a cubic spline interpolation of the data points, adding new interpolation points through this method. The cubic spline interpolation is a very effective method of smooth interpolation.

We found six people well acquainted with yoga pranayama, who could easily perform breathing exercises with periods around 36 seconds. All of them performed the following routine which lasted for 15 minutes.

They were asked to breathe in the following way: to inhale for 4 units of time (UOT), to hold the breath for 16 UOT and to exhale for 8 UOT, this we denote as the 4:16:8 (pranayama) routine.

The unit of time (UOT) is about 1 second. The yoga practitioners develop an internal feeling of UOT which they employ in their practices. They learn to feel their pulse or they learn to count in a constant pace. Often they practice with eyes closed. In order not to distract or

induce additional stress we preferred not to supply an external uniform UOT. The primary concern for this research was to have a constant periodicity and in this case the practitioners have succeeded to maintain it. The data were analyzed with spectral analysis which took into account non-stationary developments, which were subtracted from rSO_2 and BVI data. Sharp picks corresponding to the breathing periodicity were found in the spectral analysis of $EtCO_2$ (the amount of CO_2 during expiration).

The motivation for this exercise was to see the relation of rSO_2 (oxygenation) to the increasing amount of $PaCO_2$. Actually instead of $PaCO_2$ the end tidal CO2 (EtCO2) was measured (the maximal CO_2 at exhalation), a quantity which approximate well the $PaCO_2$**.** The periodicity of rSO2 was studied during the 4:16:8 respiration period (of approximately 32 UOT).

The rSO_2 was measured with the aid of two sensors placed on the forehead, detecting oxygenation from the left hemisphere (frontal part in about 3 cm depth) and the right hemisphere (frontal part in about 3 cm depth)**.** At the same time data for evaluation of BVI were collected. In Fig. 2 the results of simultaneous measurements of $EtCO_2$, rSO_2 and differences in BVI are presented for the 6 subjects.

In order to check more precisely the periodic behavior, spectral analysis was performed on the $EtCO_2$ data and the interpolated rSO_2 and BVI data. The rSO_2 and BVI data have a non-stationary component. The spectral analysis was performed on the raw $EtCO_2$ data and on rSO_2 and BVI interpolated data from which the non-stationary components were subtracted. The results are shown in Fig. 2a., Fig. 2b, Fig. 2c, Fig. 2d, Fig. 2e, Fig. 2f and Table 1. There is a clear overlapping between the periodicity of $EtCO_2$ and the periodicities of rSO_2 and BVI.

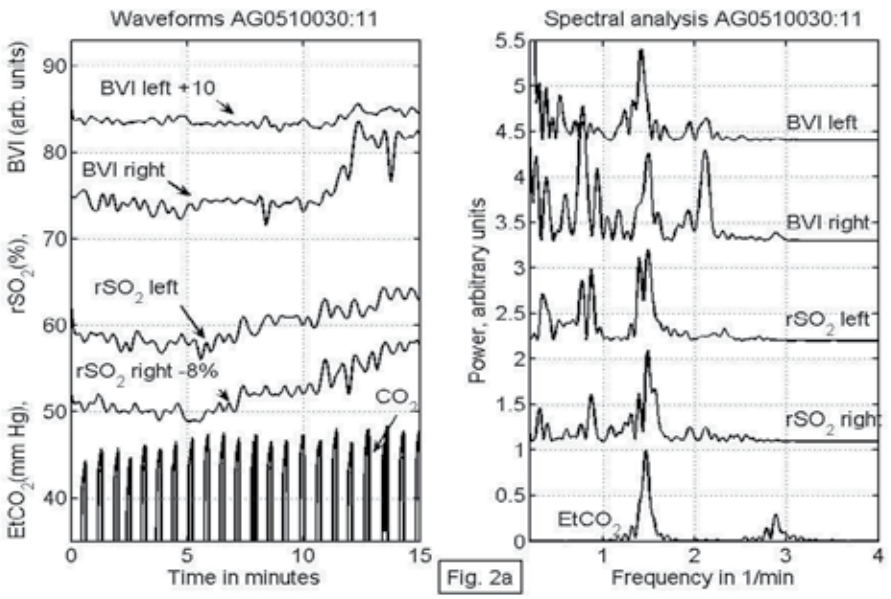

Fig. 2a. On the left hand side are given from the bottom to top: the readings of the capnometer in mm Hg, rSO_2 from the right sensor (subtracted with 8%), rSO_2 from the left sensor, the difference of BVI from the right sensor, and the difference of BVI from the left sensor (increased by 10). On the right hand side the corresponding spectral analyses of the waveforms are given.

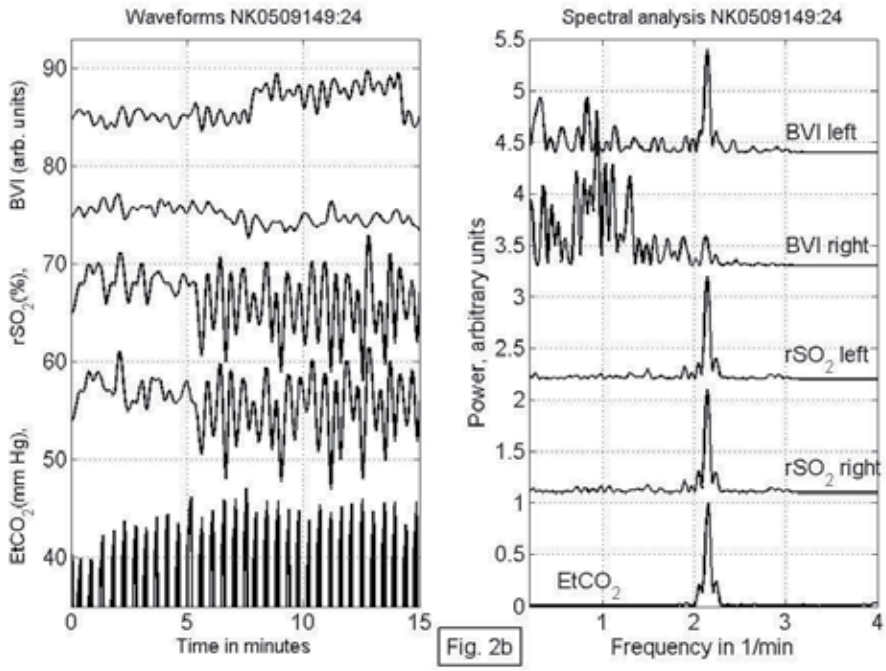

Fig. 2b. As Fig.2a.

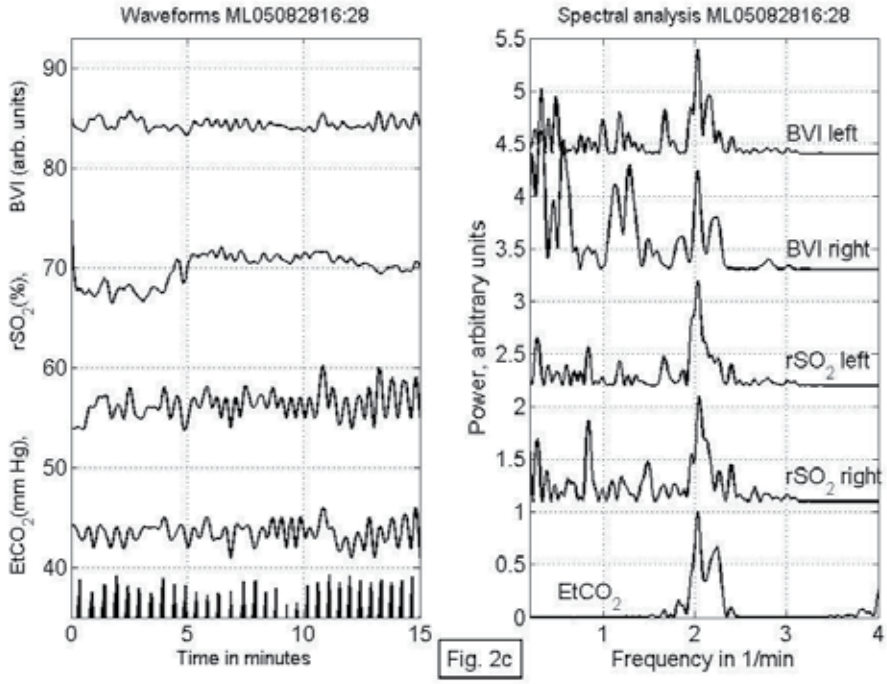

Fig. 2c. As Fig.2a.

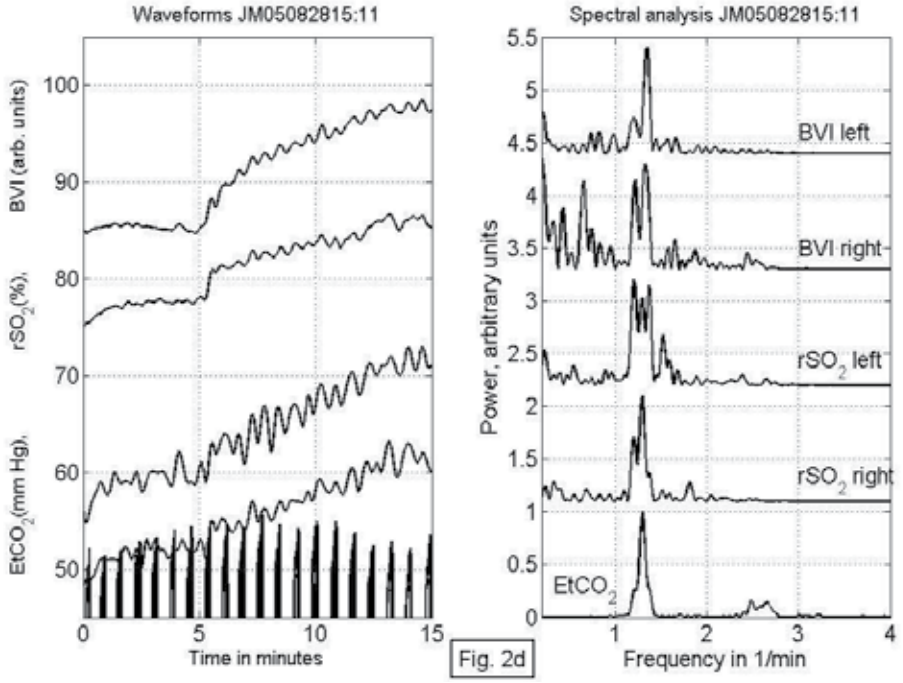

Fig. 2d. As Fig.2a.

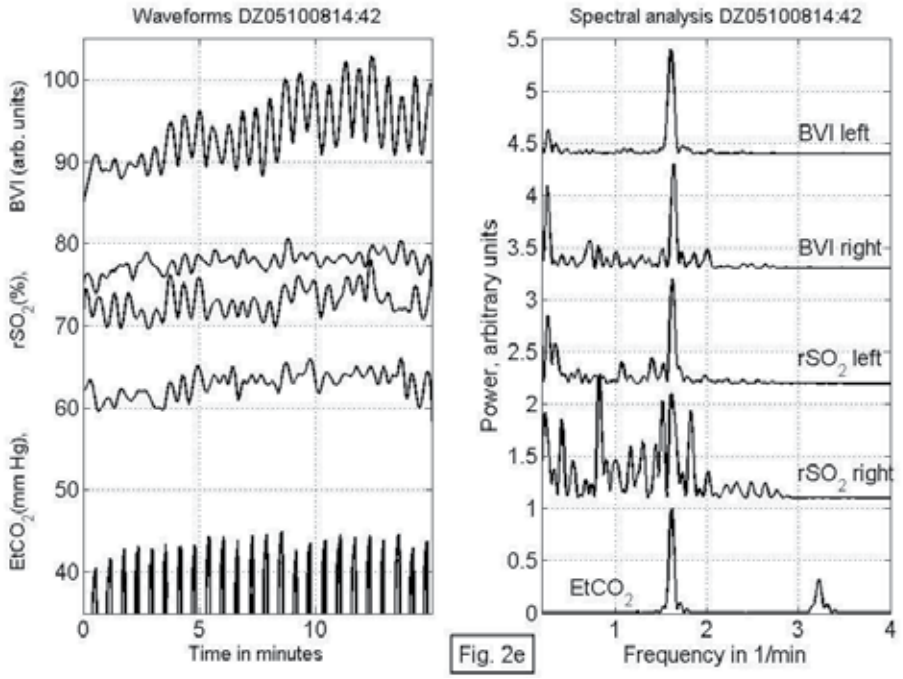

Fig. 2e. As Fig.2a.

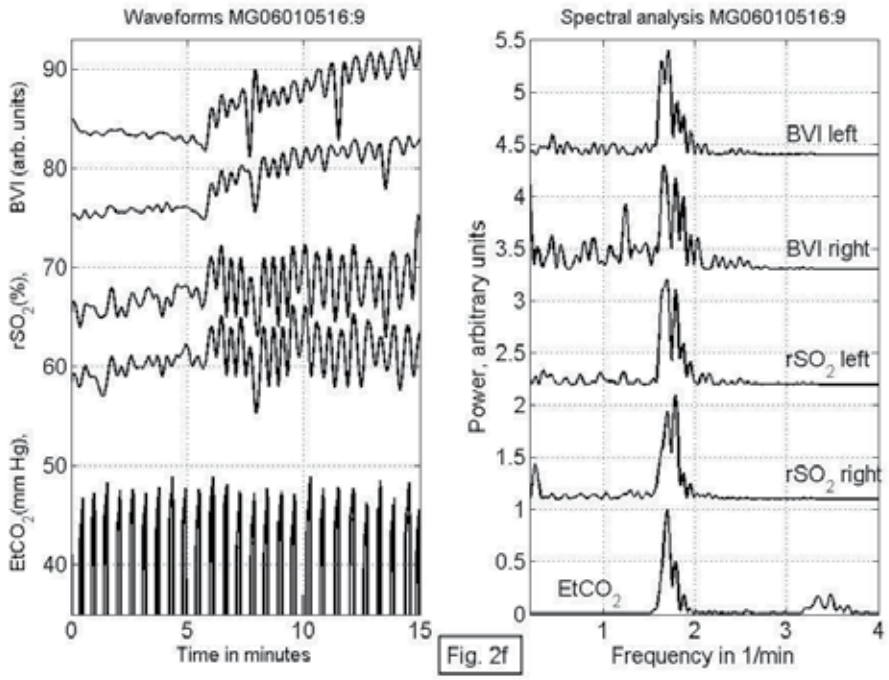

Fig. 2f. As Fig.2a.

	$PaCO_2$	rSO_2 right	rSO_2 left	BVI right	BVI left
AG	1.47 (1.42-1.51)	1.49 (1.45-1.53)	1.48 (1.45-1.54)	1.49 (1.42-1.53)	1.42 (1.38-1.47)
NK	2.15 (2.12-2.18)	2.14 (2.12-2.17)	2.14 (2.12-2.17)	----------	2.14 (2.11-2.17)
ML	2.03 (1.98-2.07)	2.05 (2.01-2.15)	2.03 (1.95-2.08)	2.03 (1.99-2.07)	2.03 (2.00-2.06)
JM	1.30 (1.26-1.34)	1.30 (1.26-1.33)	1.30 (1.17-1.40)	1.33 (1.29-1.37)	1.35 (1.31-1.38)
DZ	1.62 (1.59-1.65)	1.62 (1.59-1.67)	1.62 (1.60-1.65)	1.63 (1.61-1.67)	1.61 (1.57-1.65)
DG	1.70 (1.65-1.73)	1.79 (1.65-1.82)	1.70 (1.62-1.82)	1.66 (1.62-1.89)	1.71 (1.61-1.74)

Table 1. The position of the dominant frequencies (in units of 1/minute) of Fig. 2 in the spectral analysis, in parenthesis the extension of the half width is given.

6. Simple exercises

Can simple exercises be devised to increase cerebral blood flow (CBF) and/or cerebral oxygenation? We investigated exactly that question by using three different techniques, namely: a simple breathing procedure, solving an arithmetic problem and biofeedback.

Elsewhere (Gersten , 2011) we have analyzed the influence of arterial partial pressure of CO_2 ($PaCO_2$) on CBF and found that it may dramatically change the CBF. The changes involve the blood flow of the whole brain. It is a global effect. These results were used in another investigation (Gersten et al., 2011) in which yoga practitioners were increasing their $PaCO_2$ through periodic yoga (pranayama) breathing techniques.

We will demonstrate that significant increase of $PaCO_2$ (and of total CBF) can be achieved with untrained people using very simple breathing procedures. The reason for that is the dependence of $PaCO_2$ on ventilation (West, 1992)

$$PaCO_2 = K\frac{\dot{V}_{CO2}}{\dot{V}_A},\ K = 863\,mm\,Hg \tag{1}$$

where $\dot{V}_{CO2}$ is the CO_2 production (dependent on the metabolism) and $\dot{V}_A$ is the alveolar ventilation. This means that the $PaCO_2$ is inversely proportional to ventilation. Therefore it is possible to control the $PaCO_2$ by either breathing slowly (and not increasing the tidal volume substantially) or by holding the breath. Untrained people increase their tidal volume while breathing more slowly, but the overall effect is usually a slight increase in $PaCO_2$. People trained in breathing exercises may increase their $PaCO_2$ considerably by learning to control their tidal volume. For very small ventilation a correction is needed to the $PaCO_2$ formula (Riggs, 1970),

$$PaCO_2 = K\frac{\dot{V}_{CO2}}{\dot{V}_A - \dot{V}_D},\ \dot{V}_D = 2.07\ l/\min\ , \tag{2}$$

where $\dot{V}_D$ is the contribution of the dead space.

It is well known that concentrating on a mental problem changes brain's oxygenation locally (Chance et al, 1993). This finding was also applied further to solving a simple arithmetic problem on local brain oxygenation near the Fp1 area.

Hershel Toomim (Toomim et al., 2004) developed the device called hemoencephalograph (HEG), whose readings is related to regional cerebral oxygenation (Gersten et. al, 2007c). The device has many advantageous features which allowed us to use it in our experiment. Toomim has observed that he can influence the results by looking at the HEG display, which is essentially a biofeedback technique used by us as well. As a result of Toomim findings many biofeedback experiments were conducted with the HEG, confirming the effect. The readings of the HEG are very sensitive to changes in the range of normal oxygenation of the brain. This is not the case with INVOS brain oximeters used in operation rooms whose main aim is to detect abnormally low oxygenation states. For that reason we preferred to use the HEG to detect biofeedback effects even though it is much simpler and less sophisticated compared with INVOS cerebral oximeters (Gersten et al., 2009).

The readings of the HEG are normalized to 100 (SD=20), the average on 154 adult attendants at professional meetings (Toomim et al, 2004). We have compared (Gersten et al., 2009) the readings of HEG with the regional saturation of oxygen (rSO_2) readings of the INVOS cerebral oximeter of Somanetics. This allowed us to make estimates of the ratios of rSO_2 using the HEG. We found,

$$x_1/x_2 = \ln(y1/32.08)/\ln(y2/32.08),\ x \equiv rSO_2,\ y \equiv \text{HEG readings}, \tag{3}$$

where ln is the natural logarithm, but the ratio of logarithms does not depend on logarithm's basis.

Measurements were taken using HEG and a capnometer (a device measuring end tidal CO_2) simultaneously. End tidal CO_2 is closely related to $PaCO_2$. Eighteen subjects

participated in the experiment in which HEG and CO_2 data were recorded for 5 intervals of baseline, simple breathing exercises, simple arithmetic tasks and biofeedback. The results show that almost all participants could increase their brain oxygenation or CBF, but in each case it was strongly dependent on one of the three methods used. We can conclude that it is possible to substantially increase local oxygenation or global CBF using one of the three methods described above, but the preferred method is highly individual. The protocol of this research was approved by the IRB of Hunter College of the City University of New York.

6.1 Methods and materials

It is well known that breathing patterns affect the CO_2 levels in the arteries (Fried and Grimaldi, 1993), which in turn can affect cerebral (brain's) blood circulation and oxygenation. Mental work and biofeedback may affect both local as well as global oxygen levels in the brain.

The influence of breathing exercises, problem solving and biofeedback on brain oxygen and CO2 arterial levels were considered in an experiment outlined below. The experiment dealt with 3 topics

1. The physiological effects of mild breathing exercises on increasing CO_2 and oxygen levels in the brain.
2. The physiological effects of problem solving (a particular case of mental performance) on the CO_2 and oxygen levels in the brain.
3. The physiological effects of biofeedback on the CO_2 and oxygen levels in the brain.

An experiment dealing with the second and third topic gives qualitative information about how much the oxygen levels will rise during problem solving and biofeedback, while an experiment dealing with the first topic will give the same information, but this time, from breathing exercises. It is important to note that in the first topic global CBF is concerned, while in the second and third topic the local brain oxygenation at the Fp1 area.

The participants were connected to the two devices needed for the experiment: the capnometer that measured end tidal CO_2 and the Cerebral Oximeter. The connection used was made via a sensor placed on the forehead at Fp1. The CO_2 levels were estimated using a capnometer produced by Better Physiology LTD, which measures end tidal CO_2 ($EtCO_2$) of the exhaled air ($EtCO_2$ is highly correlated with the $PaCO_2$ levels of the arteries). All participants received their own new nasal insert which were sterilized before each use and connected to the capnometer. The data were detected via USB output cable connected to the computer and stored for subsequent review.

The oxygen levels were estimated using two devices: the HEG which was calibrated to the INVOS Cerebral Oximeter produced by Somanetics Corp. (see www.somanetics.com) and based on advanced near infrared spectroscopy (NIRS) technology. A sensor was attached to the forehead measuring the oxygenation in a depth of about one inch inside the brain. The devices that were used were non-invasive and FDA approved, fully automated and did not require special precautions. The data were stored on a computer.

The data of the capnometer and oximeters were combined together and analyzed using Matlab subprograms. The participants were asked to do paced breathing exercises as

instructed by the experimenters. Before the 3 experiments baseline data were taken for 5 minutes using the INVOS oximeter, and another 5 minutes using the HEG and capnometer. The participants were prevented from seeing the screens of the devices in order to avoid biofeedback.

In the first experiment (lasting 5 minutes) participants were asked to walk slowly, breathe in for 3 steps, hold their breath during the next 3 steps, exhale during the next 3 steps, and hold their breath for the next 3 steps after exhaling. We made sure that the participants understood these instructions. The participants also did not see the screens of the devices in order to avoid biofeedback.

In the second experiment (lasting 5 minutes) participants were given an arithmetical problem to solve while being attached to the HEG and capnometer. The theoretical basis for this experiment is that more oxygen is needed while solving problems. A simple arithmetical problem of subtracting the number 7 continuously, starting from 1200 (1193,1186,...) was used. The participants were again prevented to see the screens of the devices in order to avoid biofeedback.

In the third experiment (lasting 5 minutes) participants were asked to look at the HEG display trying to raise the curve by mental feedback. This time they were allowed to look at the display.

6.2 Participants

The participants were 18 participants from the introductory course to psychology (PSY 100) in Hunter College of the City University of New York. All participants had to sign an informed consent. At least two experimenters were present during each experiment. The confidentiality of the participants was protected.

6.3 Results

All experimental results of all participants can be found in (Gersten et al., 2011a).

To better illustrate the results a few examples of HEG and CO_2 data will be included. In Fig. 3, subplot $HC3_1$, the baseline data of participant No. 3 are displayed. The HEG baseline was not constant during the 5 minutes of data taking.

In the subplot $HC3_2$ the result of the breathing exercise are displayed. Even though this was a first trial, the CO_2 pattern seems to be quite periodic. The CO_2 pattern has a periodicity of about 15 secs per period, while normal breathing has a periodicity of about 4 secs per period. The prolongation of the respiratory period should lead to an accumulation of arterial CO_2 and an increase of global CBF, provided there is no greater increase in the tidal volume. In this case there was only small increase in arterial CO_2 but a significant increase in oxygenation (HEG). The increase of arterial CO_2 depends on the control over the tidal volume. Individuals trained in this breathing exercise, can easily increase their arterial CO_2 by about 20-30%.

Solving the arithmetic problem (see Fig. 3, subplot $HC3_3$) led to an increase of the HEG readings (oxygenation), but we notice that the respiration was speeded up probably due to increased tension. After all, to subtract 7 and calculate and evaluate the result in the mind is not a very pleasant enterprise.

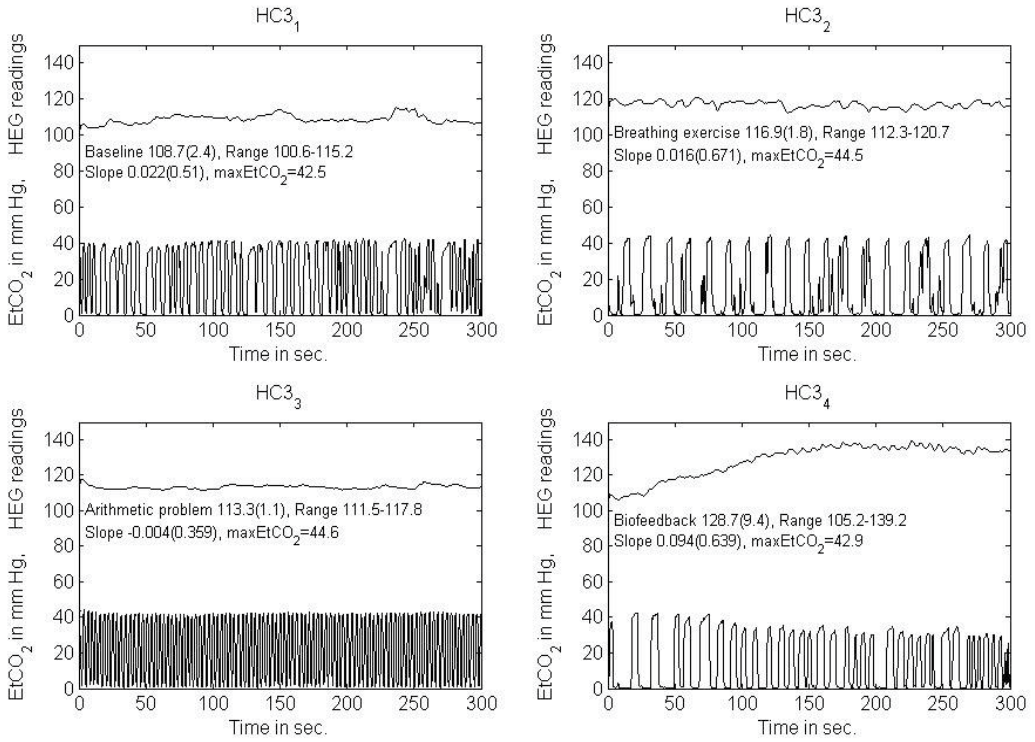

Fig. 3. The HEG readings and the capnometer displays ($EtCO_2$) of participant No. 3are shown for the 4 cases: baseline (subplot $HC3_1$), breathing exercise (subplot $HC3_2$), arithmetic problem (subplot $HC3_3$) and biofeedback (subplot $HC3_4$). The upper curves are the HEG readings, the lower curves the CO_2 values (at exhale). The numbers with numbers in parenthesis are the mean values and standard deviations respectively.

Subplot $HC3_4$ of Fig. 3 is very interesting. In this case the subject was looking at the display of the HEG line trying mentally to raise it up. The performance (without previous training) is very impressive. Starting from baseline values the HEG readings were climbing up for about 2.5 minutes to values about 30% higher (a local increase of oxygenation at the Fp1 area). This case teaches us that in the evaluation of the results we must not only consider average values but also the maximal values which are an indicative of the possible potential. The respiration pattern indicates a slow but a very deep breathing (hyperventilation). The arterial CO_2 decreased for more than 20% which should lead to a significant decrease of global CBF. The biofeedback was very successful in spite of the hyperventilation.

While analyzing the data we must take into account that the participants were performing their tasks for the first time. Most of the tasks were performed relatively well. Most participants were able to increase their mean HEG readings in at least one task. When averaging all participant's data there were no significant changes were found, indicating that no one method was preferable.

More informative, are the ratios of the maxima to the mean of the baseline. The maxima indicate the potential of the exercises. These maximal values should be easily reached with

practice. There was a maximal increase of 30% during breathing exercises, 32% during solving the arithmetic problem and 28% during the biofeedback.

Results with rSO_2 ratios determined according to Eq. (3) are quite similar to the HEG ratios, indicating that the HEG ratios are quite reliable in estimating the rSO_2 changes.

Of the 18 participants 14 were able to increase the HEG readings by at least 10% during one of the exercises (5 during the breathing exercise, 9 while solving the arithmetic problem, 8 during the biofeedback). Of the 18 participants 7 were able to increase the HEG readings by at least 18% during one of the exercises (3 during the breathing exercise, 6 while solving the arithmetic problem, 5 during the biofeedback).

The breathing exercise was the most difficult for the participants. It took them an average of 6 minutes to fully understand the instructions. The exercise required some discipline and experience. Most of the participants performed it relatively well.

Fig. 4 shows that participant No. 9 has performed the breathing exercises relatively well (subplot $HC9_2$). His CO_2 pattern was periodic and amplitude stable. The pattern was not completely smooth. This is understandable, since it was his first attempt to perform the exercise. In the same subplot, the corresponding HEG curve is very interesting. The HEG waveform has the same period as the CO_2 pattern.

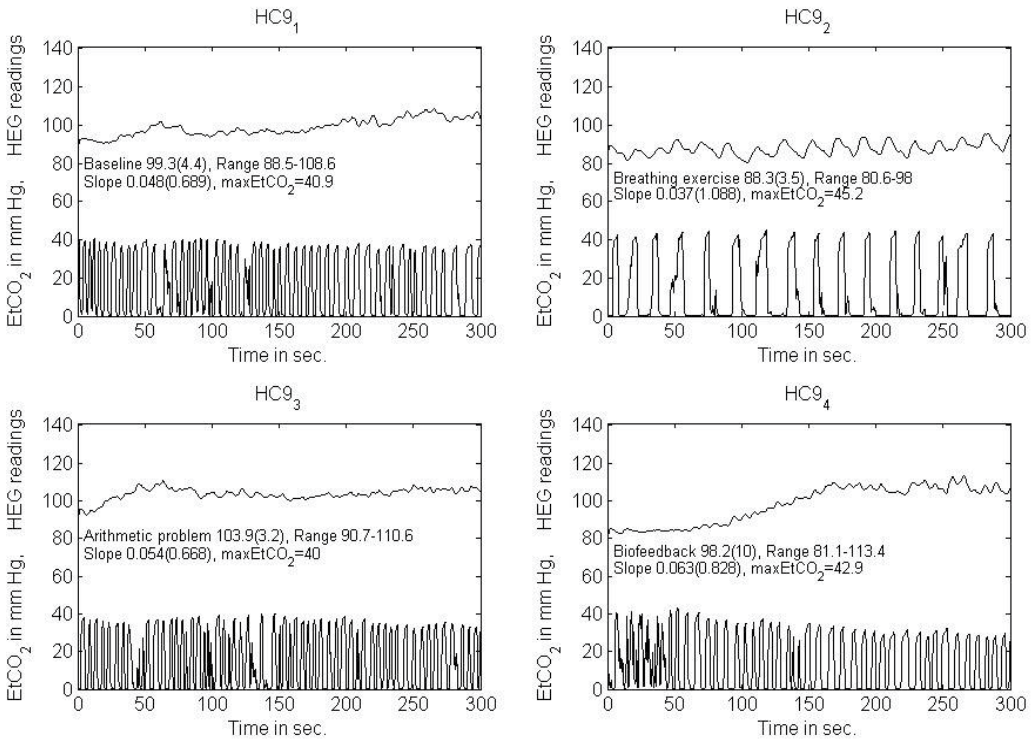

Fig. 4. The HEG readings and the capnometer displays ($EtCO_2$) are shown for the 4 cases: baseline (subplot $HC9_1$), breathing exercise (subplot $HC9_2$), arithmetic problem (subplot $HC9_3$) and biofeedback (subplot $HC9_4$). The upper curves are the HEG readings, the lower curves the CO_2 values (at exhale).

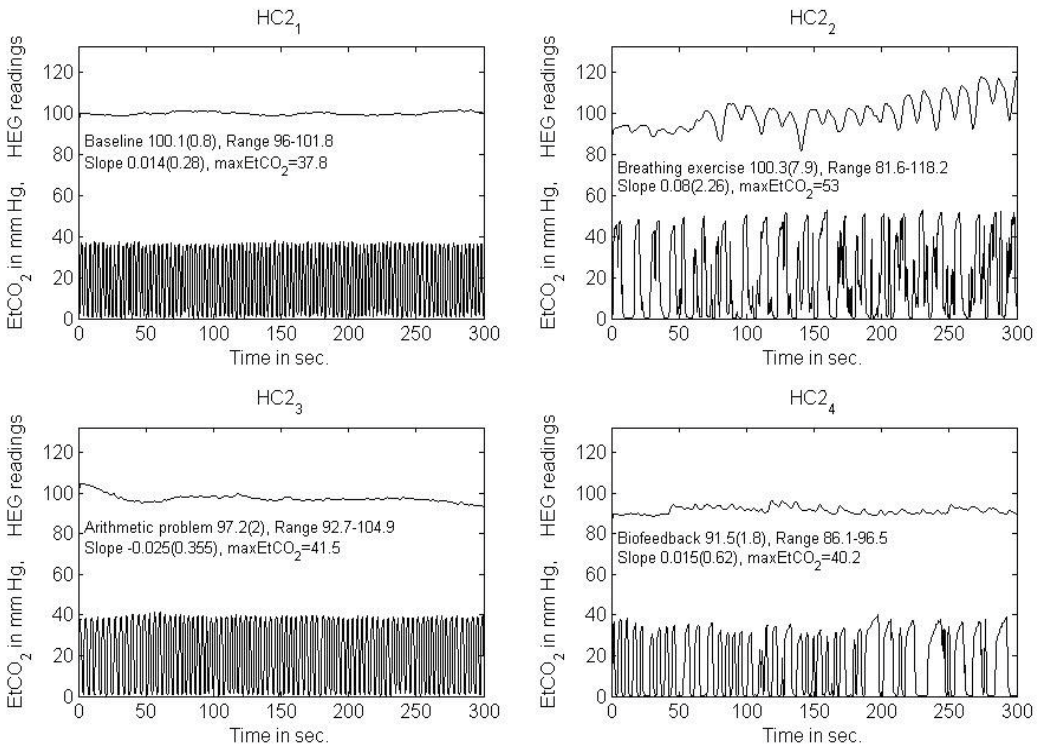

Fig. 5. The HEG readings and the capnometer displays ($EtCO_2$) are shown for the 4 cases: baseline (subplot $HC2_1$), breathing exercise (subplot $HC2_2$), arithmetic problem (subplot $HC2_3$) and biofeedback (subplot $HC2_4$). The upper curves are the HEG readings, the lower curves the CO_2 values (at exhale).

In Fig. 5 participant No. 2 had difficulty performing the breathing exercise (the CO_2 pattern in subplot $HC2_2$). Although the 3 step pattern was kept correctly, the participant was inhaling during some of the breath holding periods. When done correctly the 3 step breathing cycle should last for about 15 seconds. As the participant was breathing in between, the average breath length was only 7.2 seconds. Interestingly the HEG waveform of subplot $HC2_2$ has a period of about 15 seconds irrespective of the breathing in between the 3 step pattern.

The performance of the breathing exercises, when well performed, the period should be longer than 10 seconds. Twelve of 18 participants have performed the breathing exercise well.

Interestingly the HEG waveform has the same periodicity as the CO_2 pattern. This coincidence is well presented in Fig. 6, where the correlation between the power spectra of

the $EtCO_2$ periodic pattern and the corresponding HEG periodic pattern is depicted by their multiplication. The power spectra are normalized to unity. Maximal correlation is achieved when the multiplication is equal to one.

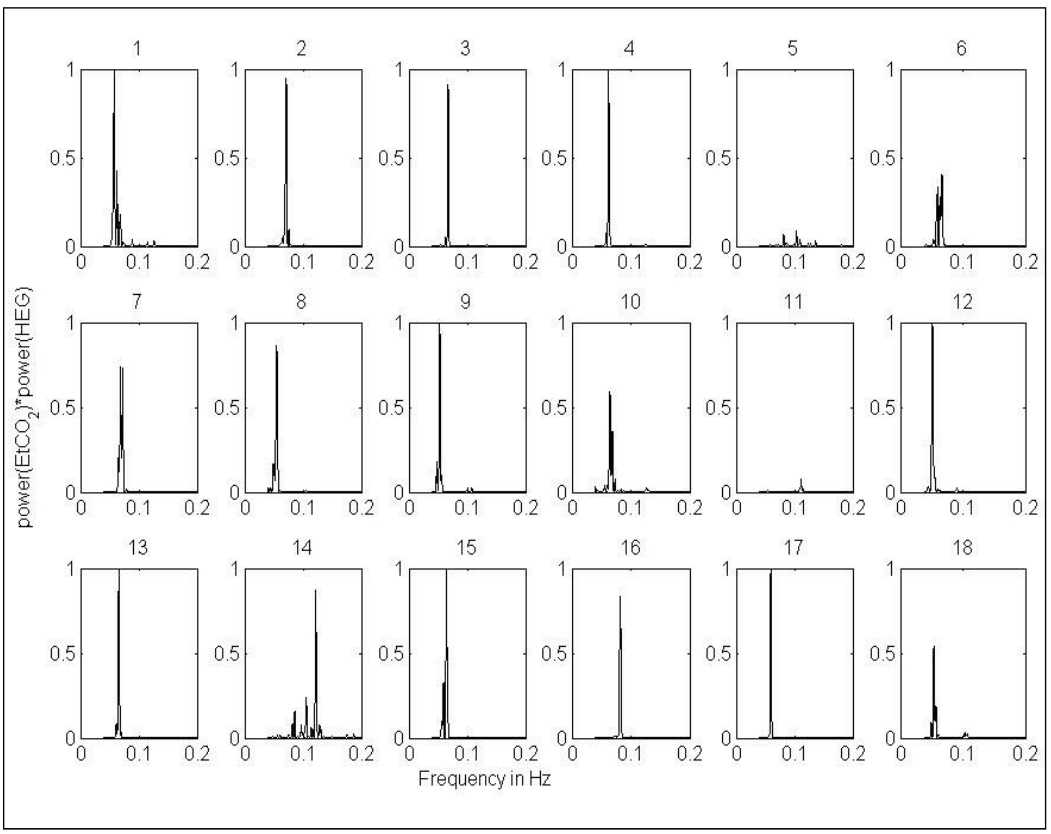

Fig. 6. The correlation between the power spectra of the $EtCO_2$ periodic pattern and the corresponding HEG periodic pattern is depicted by their multiplication. The power spectra are normalized to unity. Maximal correlation is achieved when the multiplication is equal to one.

7. Conclusions

The near infrared spectroscopy (NIRS) is a powerful non-invasive method that probes brain oxygenation. The subject is of great interest to researchers and the medical profession, resulting in many clinical, neuroscience and physiology of exercise studies and publications. NIRS is a noninvasive and easy to handle method, and will provide a new direction for functional mapping.

We have verified that breathing may affect to great extent the brain physiology. With breathing exercises the arterial CO_2 can be increased, which in turn increases CBF and brain oxygenation.

The most important finding of our experiments is the periodic correlation between respiration, oxygenation and blood volume changes. The results clearly show a periodic change of cerebral oxygenation with the same period as the breathing exercises, indicating that with each breath the brain oxygenation was periodically changing. Similar periodic changes in blood volume indicate that the brain pulsates with a frequency of respiration.

Present results were achieved by using very slow breathing patterns with the INVOS Cerebral Oximeter (ICO). If the present ICO devices will be modified to allow sampling of rSO_2 at frequencies higher than the frequency of normal respiration and higher than the heart rate, it will be possible to observe new types of brain waveforms. These waveforms may have new information about brain oxygenation, cognitive function, brain pulsation and brain motion. Under these circumstances it will be possible to understand much better the correlations between respiration and brain physiology. The sampling of rSO_2 should go up to, or preferably above 4 Hz. The accuracy of the reading device also should be changed from 2 significant digits to 3 digits. We believe that these changes will enable new explorations and new insights on the influence of respiration on brain's physiology. The HEG, which does not measure directly the rSO_2 can serve this purpose by using Eq. (3), which determines the ratios of rSO_2. The difference between the ICO and the HEG is that the ICO penetrates dipper into the brain, while the HEG penetrates only the surface near the probe. The ICO results are more stable and are related to larger volumes in the brain.

Neurodegenerative diseases are characterized by low CBF, in our research we have found effective ways to increase CBF. We will continue our research in order to explore the possibilities of increased CBF and its influences on intellectual abilities and on fighting degenerative diseases. Devices displaying the oxygenation periodic waveforms should be developed for new diagnostic and research purposes.

Our method to obtain the above results is through the use of human subjects. This is a new avenue in approaching the study of CBF, brain oxygenation, improving the cognitive function and especially in view of the growing elderly population.

Our three methods used in simple execises can be used on the general population, are non-invasive, without the use of pharmaceuticals and have no side effects. They differ from each other in that the breathing affects mostly the global blood flow, arithmetic problem solving and biofeedback affects the regional blood flow (in our case the Fp1 region).

Both our theoretical and experimental work differs from other studies due the specific instrumentation and our experimental procedure. Most of the results came close to our expectation.

We concluded that breathing can be used effectively to control CBF by the ventilatory control of end tidal CO_2. This research may have implications for complementary diagnosis and treatment of conditions involving regional cerebral metabolism such as cerebral vascular ischemia, seizures disorders, stroke, Alzheimer's disease, and more. Following that thought could lead us to improved cognitive function through a higher supply of oxygen to specific regions of the brain.

We foresee future more detailed investigations to be made in the area of the effect of CO_2 on specific regions of the brain. This would be of great interest because a higher CO_2 supply

results in a higher blood flow and thus to more oxygen and better overall brain function, specifically cognitive function.

8. References

Alfano RR, Demos SG, Gayen SK.(1997). Advances in optical imaging of biomedical media. *Ann N Y Acad Sci.* vol. 820, pp. 248-70

Angerson WJ, Sheldon CD, Barbenel JC, Fisher AC and Gaylor JDS (Eds.) (1989). *Blood Flow in the Brain*, Clarendon Press, Oxford.

Chance B., Zhuang Z., UnAh Chu, Alter C., and Lipton L. (1993), "Cognition activated low frequency modulation of light absorption in human brain," *Proc. Natl. Acad. Sci. USA*, Vol.90, pp.3770-3774. B. (1998). Near-infrared images using continuous, phase-modulated, and pulsed light with quantitation of blood and blood oxygenation. *Ann N Y Acad Sci*; 838: 29-45

Cope M. (1991). The application of near infrared spectroscopy to non invasive monitoring of cerebral oxygenation in the newborn infant. *Ph.D. thesis,* University College, London

Delpy DT, Cope M. (1997). Quantification in tissue near-infrared spectroscopy. *Philosophical Transactions of the Royal Society of London, Series B- Biological Sciences*. 352(1354): 649-659

Derdeyn C.P. et al. (2002). Variability of cerebral blood volume and oxygen extraction: stages of haemodynamic impairment revisited. *Brain*, Vol. 125, pp. 595-607

Elwell C.E. et al. (1996),"Influence of Respiration and Changes in Expiratory Pressure on Cerebral Haemoglobin Concentration Measured by Near Infrared Spectroscopy. *J. Cereb. Blood Flow Metab.* Vol. 16, pp. 353-357

Feihl F. and Perret C. (1994). Permissive Hypercapnia, How Permissive Should We Be?, *American Journal of Respiratory and Critical Care Medicine Vol.* 150, pp. 1722-1737.

Ferrari M, Mottola L, Quaresima V. (2004) . Principles, Techniques, and Limitations of Near Infrared Spectroscopy. *Can J Appl Physiol*; Vol. 29(4), pp. 463-487

Frackowiak RSJ, Lenzi GL, Jones T, Heather JD. (1980). Quantitative measurement of regional cerebral blood flow and oxygen metabolism in man using 15O and positron emission tomography: theory, procedure, and normal values. *J Comput Assist Tomogr*,Vol. 4, pp. 727-736

Fried, R. and Grimaldi, J. (1993) *The Psychology and Physiology of Breathing,* Plenum, New York,

Gersten A et al. (2009), Probing brain oxygenation with near infrared spectroscopy, *NeuroQuantology,* Vol 7, Issue 2, pp. 258-266.

Gersten A (2011), Peculiarities of Brain's Blood Flow : Role of Carbon Dioxide http://arxiv.org/ftp/arxiv/papers/1103/1103.5491.pdf

Gersten A et al. (2011) Oxygenation and Blood Volume Periodic Waveforms in the Brain, http://arxiv.org/ftp/arxiv/papers/1103/1103.5493.pdf

Gersten A et al. (2011a), Simple exercises that significantly increase cerebral blood flow and cerebral Oxygenation. http://arxiv.org/ftp/arxiv/papers/1103/1103.5494.pdf

Guyton AC (1991) *Textbook of Medical Physiology,* W.B. Saunders, New York 1991

Harper A.M. (1989). Measurement of Cerebral Blood Flow – Basic Physiological Principles. In (Angerson et al., 1988) pp. 1-10.

Hoshi Y. (2003). Functional near-infrared optical imaging: utility and limitations in human brain mapping. *Psychophysiology*, Vol. 40, pp. 511-520

Imray C.H.E .et al. (2000), "Cerebral Oxygenation at high altitude and the response to carbon dioxide, hyperventilation and oxygen", *Clinical Science* 98, 159-164

Kety S.S., & Schmidt C.F. (1948). Effects of arterial tensions of carbon dioxide and oxygen on cerebral blood flow and cerebral oxygen consumption of normal young men. *Journal of Clinical Investigation, Vol. 27,* pp. 484-492.

Kissack, C.M., Garr1, R.R., Wardle, S.P., Weindling, A.M. (2005). Cerebral fractional oxygen extraction is inversely correlated with oxygen delivery in the sick, newborn, preterm infant. *J Cereb Blood Flow & Metab*, Vol. 25. pp. 545–553

Kuvalayannda, Swami (1983) *Pranayama,* Kaivalyadama, Lonavla, India.

Lammertsma, A.A. et al. (1990). Cerebral Blood flow, blood volume and oxygen utilization: Normal values and the effect of age. *Brain*, Vol. 113. pp. 27-47

Li Xiuling (2003), *Healing with Ki-Kou: The Secrets of Ancient Chinese Breathing Techniques*, Agora Health Books; 2nd ed.

Mullin G.H. (1996). *Tsongkhapa's Six Yogas of Naropa*, Snow Lion, Ithaca NY

Obrig H., Villringer A. (2003). Beyond the visible - imaging the human brain with light. *J. Cereb. Blood Flow & Metab.*, Vol. 23, pp. 1-18

Raichle, M.E., Posner, J.B. and Plum F. (1970), Cerebral Blood Flow During and After Hyperventilation, *Arch. Neurol.* Vol. 23, pp. 394-403.

Raj D, Anderson AW and Gore JC, (2001), "Respiratory effects in human functional magnetic resonance imaging due to bulk susceptibility changes', *Physics in Medicine and Biology*, Vol. 46, pp. 3331-3340.

Reivich, M. (1964). Arterial $PC0_2$ and cerebral hemodynamics. *American Journal of Physiology, 206,* 25-35.

Riggs, D.S. (1970) *Control Theory and Physiological Feedback Mechanisms*, Williams & Wilkins, Baltimore.

Rolfe, P. (2000). In Vivo Near-Infrared Spectroscopy. *Annu. Rev. Biomed. Eng.* Vol. 02, pp. 715-54

Sato, N., Hagihara, B., Kamada, T., Abe, H. (1976) *Anal Biochem*, Vol. 74. Pp. 105-117

Sokoloff, L. (1989). Circulation and Energy Metabolism of the Brain., In: Siegel GJ (ed.), *Basic Neurochemistry*, 4th ed., Raven Press, New York NY

Strangman G., Boas D.A., Smton J.P. (2002). Non-invasive neuroimaging using near-infrared light. *Biol Psychiatry*. Vol. 52. pp. 679-693

Suzuki S., Takasaki S., Ozaki T., Kobayashi Y. (1999). A tissue oxygenation monitor using NIR spatially resolved spectroscopy. *Proc SPIE*; Vol. 3597. Pp. 582-592

Thavasothy et al. (2002), "A comparison of cerebral oxygenation as measured by the NIRO 300 and the INVOS 5100 Near-Infrared Spectrophotometers". *Anesthesia*, 57, 999-1006

Toomim H. et al. (2004), "Intentional Increase of Cerebral Blood Oxygenation Using Hemoencelography (HEG): An Efficient Brain Exercise Therapy", *Journal of*

Neurotherapy 8(3), pp 5-21 and In: Tinius T. (Ed.) *New Developments in Blood Flow Hemoencephalography*, Haworth Medical Press, pp 5-21.

West, J.B. (1992) *Pulmonary Pathophysiology – the essentials*, 4th Ed., Williams & Wilkins, Baltimore.

Windischberger C, et al. (2002), "On the origin of respiratory artifacts in BOLD-EPI of the human brain". *Magnetic Resonance Imaging*, Vol. 20, pp. 575-582.

9

Comparison of Cortical Activation During Real Walking and Mental Imagery of Walking – The Possibility of Quickening Walking Rehabilitation by Mental Imaginary of Walking

Jiang Yinlai[1], Shuoyu Wang[1], Renpeng Tan[1],
Kenji Ishida[2], Takeshi Ando[3] and Masakatsu G. Fujie[3]
[1]*Kochi University of Technology*
[2]*Kochi University*
[3]*Waseda University*
Japan

1. Introduction

Non-invasive brain imaging technologies have become an increasingly important part of research in neurosciences. The thirst for information about brain function is universal, and imaging of the human brain has been used by many as a medium for the discussion. So far, Functional brain imaging with positron emission tomography (PET), functional magnetic resonance imaging (fMRI), electroencephalographic (EEG), and Magnetoencephalography (MEG) have greatly increased scientists' ability to study localized brain activity in humans and carry out studies for better understanding of the neural basis of mental states. They have been used extensively to map regional changes in brain activity, not only in neuroscience researches, as well as in social sciences to objectively and quantitatively evaluate psychological problems. PET and fMRI are based on changes in local circulation and metabolism (Raichle & Mintun, 2006). PET produces detailed three-dimensional images of certain processes in the brain by detecting gamma rays emitted indirectly by radioactive material which has been injected into the person's blood stream prior to scanning. fMRI produces high quality pictures of the brain's delicate soft tissue structures using strong magnets and pulses of radio waves to manipulate the natural magnetic properties of hydrogen, creating useful images of organs and soft tissues. MEG and EEG image electrical activity in the brain. MEG measures magnetic fields generated by small electrical currents in neurons of the brain using arrays of SQUIDs (superconducting quantum interference devices). EEG uses multiple electrodes fixed to the person's scalp to measure the dynamic pattern of electrical fields in the brain. In cognitive neuroscience, researchers use EEG technology to study event-related potentials (ERPs)—brain measurements that are associated with a response to a stimulus.

These methods provide information about changes in electrical, hemodynamic and metabolic activities. Each of these techniques has its advantages and disadvantages, but

helps to elucidate certain aspects of the capacity of neural networks to process information. MEG and EEG provide unique insights into the dynamic behaviour of the human brain as they are able to follow changes in neural activity on a millisecond time-scale. In comparison, PET and fMRI are limited in temporal resolution to time scales on the order of one second by physiological and signal-to-noise considerations. On the other hand, MEG, PET and fMRI provide high resolution brain images. The resolution of fMRI is about 2-3 mm at present, limited by the spatial spread of the hemodynamic response to neural activity. However, MEG, PET and fMRI techniques are very expensive, highly sensitive to motion artifact, confine participants to restricted positions, which severely limits their application in daily use outside hospitals and research centers. Although EEG is much cheaper, it is highly sensitive to artifacts whose amplitude can be quite large relative to the size of amplitude of the cortical signals of interest. The artifacts include both biological artifacts such as eye-induced artifacts, cardiac artifacts and muscle activation induced artifacts, and environmental artifacts such as body movement, settling of the electrodes, and electrical appliances. Therefore, EEG, MEG, PET and fMRI are difficult to measure brain activity in natural environment. A brain imaging technology, which is non-invasive, less constrictive, low-cost, with a relatively higher temporal and spatial resolution, is desirable.

Functional near-infrared spectroscopy (fNIRS) is an emerging brain imaging technology monitoring concentration changes of oxygenated hemoglobin (oxy-Hb) and deoxygenated hemoglobin (deoxy-Hb) at the cortex by measuring the absorption of near infrared light between 650nm and 950nm through the intact skull (Chance et al., 1993; Villringer et al, 1993). Specifically, the transmission and absorption spectra of oxy-Hb and deoxy-Hb are distinct in this wavelength region. The fundamentals of the optical topography system utilize the phenomenon, using the better penetrating near infrared light, rather than visible light, to measure changes in blood hemoglobin concentrations in the brain. As shown in Fig.1, a laser optode is illuminated onto head from optical fibers attached to the scalp. The near infrared light passes through the skull and reaches the cerebral cortex. It is scattered by hemoglobin in the blood. The light is partially reflected back through the scalp. The reflected light back on the scalp contains the information about the cerebral cortex. When a specific area of the brain is activated, the localized blood volume in that area changes quickly. It can thus be detected, where and how active the specific regions of the brain are, by continuously monitoring the blood hemoglobin levels according to the absorption level of near infrared light, while having the examinee do some specific action or task paradigm.

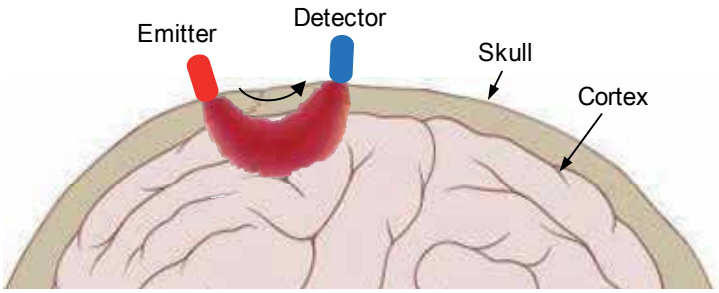

Fig. 1. Cortical activation measurement with near infrared light.

fNIRS has several unique advantages over current measurement methods. It is non-invasive, and can be used under a variety of conditions with minimal restriction on the examinee. Measurements can be made under more natural conditions, giving more freedom in task design. It also enables simultaneous measurements with other testing modalities such as EEG, fMRI and MEG because near infrared light is not interfered by EEG, fMRI and MEG, and does not interfere them. fNIRS facilitates longitudinal studies and monitoring over extended time periods. Therefore, fNIRS technology allows the design of portable, safe, affordable and accessible monitoring systems. These qualities pose fNIRS as an ideal candidate for monitoring cognitive activity-related hemodynamic changes not only in laboratory settings but also under natural conditions. The reliability of fNIRS signals has in most cases been proven to be sufficient at a group level for observation of brain activity (Plichta et al., 2006; Sato et al., 2005; Sato et al., 2006).

The authors and their colleagues have been developing machines for walking rehabilitation and walking support. In an aging society with a low birth rate in countries like Japan, people suffering from walking impairments due to illness or accident are increasing and the number of physical therapist cannot meet with the demand for walking rehabilitation. Therefore, rehabilitation machines, which can help with early recovery and relieve burden of physical therapists, have drawn great attentions (Okada et al., 2001; Horst, 2009). In previous studies, we have developed omnidirectional walkers for standing exercise (Tan et al., 2011) and seated exercise, shown in Fig. 2(a) and Fig. 2(b) respectively. The walker for standing exercise is designed for those able to keep standing posture by themselves, and the walker for sitting exercise is designed for the severe patients unable to stand. Omnidirectional walking exercise has been proved effective for early recovery of walking disabilities (Ishida et al., 2008).

(a) For standing exercise

(b) For seated exercise

Fig. 2. Omnidirectional walkers.

The causes for walking disabilities include not only muscle weakness but also neural dysfunctions due to stroke or Alzheimer's disease. 58% of walking disabilities are caused by problems in the neural system. However, up to now, most of the developed walking rehabilitation machines aim at enhancing muscle strength, neglecting the recovery of the neural system. Thus it is necessary to consider the brain activities besides muscle strength in walking rehabilitation, in order to improve the efficiency of walking rehabilitation. Furthermore, for the severe patients who are completely bed-ridden, it is important to activating their neural system related to walking movement. A hybrid walking

rehabilitation system is proposed which includes both muscle strength enhancement by walking rehabilitation machines and neurological rehabilitation by imaginary of walking. This system has the following most prominent advantages compared with traditional rehabilitation methods considering only physical rehabilitation.

- Early rehabilitation of cognitive functions related to walking. After falling ill (stroke et al.), surgery or injure, physical rehabilitation might not be able to performed in a certain period of time according to the patient's condition. During this period, neurological rehabilitation by imaginary of walking is considered to be an effective method to keep the brain areas related to walking active and maintain the cognitive functions related to walking.
- Quickening walking rehabilitation. Walking is a complex cognitive task that is associated with higher-level cognitive function (Fukuyama, 1997; Riecker et al., 2003). Even routine walking is suggested to be considered as a relatively complex task that involves higher-level cognitive input (Hausdorff et al., 2005). In hospitals or rehabilitation facilities, physical rehabilitation time is limited due to the schedule of the physical therapist or the condition of the patients. However, there is no such limit in neurological rehabilitation. Therefore, the combination of physical rehabilitation and neurological rehabilitation may lead to earlier recovery of walking ability.

However, the neural mechanism of neurological rehabilitation is yet to be elucidated and there is no standard method to carry out neurological rehabilitation.

Recently, motor imagery, as a method of neurological rehabilitation, is drawing more and more attention.Motor imagery is widely used in sport to improve performance, which raises the possibility of applying it as a rehabilitation method. The effectiveness of motor imagery training at restoring motor function after stroke has been indicated by several studies (Sharma et al., 2006; Dickstein et al., 2004). However, the underlying mechanism of motor imagery training-induced improved performance remains unexplained. Understanding the effect of rehabilitative techniques on brain plasticity is potentially important in providing a neural substrate to underpin rehabilitation and hence in developing novel rehabilitation strategies. An fMRI study has shown that premotor cortex (PM) and supplementary motor area (SMA), as shown in Fig. 3, are involved in the observation of gait and related conditions in combination with motor imagery of gait (Iseki et al., 2008; Wagner et al., 2008). However, since the MRI environment excluded real gait movement, the comparison between brain activities involved in walking and imaginary walking was still insufficient. In this chapter, we compared the activation in motor area of the brain during real walking and imaginary walking by means of fNIRS. Two experiments were conducted.

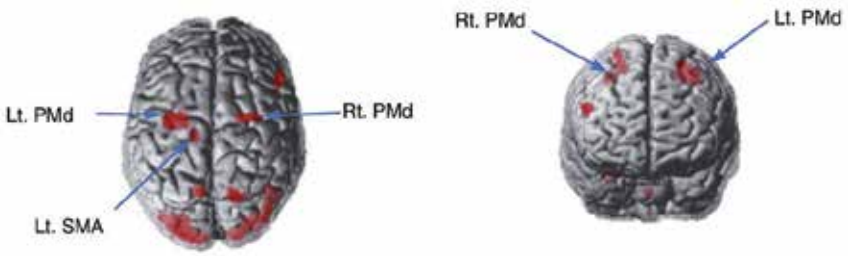

Fig. 3. Activated brain regions by mental imagery of walking (Iseki et al., 2008;).

In the first experiment, we compared the activation in motor area of the brain during real walking (RW) and walking observation (WO) (Jiang et al., 2010). Two subjects participated in the experiment. During WO, the subjects were instructed to imagine that they were walking with the same pace to a person in the video being shown to the subjects. As a result, the concentration of oxygenated hemoglobin in motor area during WO was higher than that during RW in both of the subjects. This was because that it was not necessary to pay attention to the movements of the legs and feet during normal walking on the plain road without any obstacles, while movement planning was required when the subjects imagined their walking in the same way to another person. The experiment result indicated that it is possible to quicken walking rehabilitation by mental imagery of walking.

In the second experiment, we compared the activation in motor area during RW, virtual walking (VW), and WO. Subjects stood on a treadmill throughout the experiment (Jiang et al., 2011). In the VW, subjects were shown moving scenes of a virtual visual environment in which subjects easily imagined as if they were actually walking from the first-person perspective. In the WO, subjects were instructed to imagine that they were walking with the same pace to a person in the video being shown to the subjects (third-person perspective). Four subjects participated in the experiment. As a result, the oxy-Hb in motor area during both VW and WO were higher than that during RW on the average. This was because that it was not necessary to pay attention to the movements of the legs and feet during normal walking, while movement planning was required when the subjects imagined their walking according to the videos. There was no significant difference between the oxy-Hb during VW and that during WO. The importance of stimulus diversity in mental imagery of walking was suggested.

2. fNIRS measurement

Regional hemodynamic changes in brain tissue were monitored using fNIRS system ETG-7100 (Hitachi Medical Corporation) (Fig. 4). This system uses two wavelengths of near-infrared light (695 nm and 830 nm) to separate the two types of hemoglobin concentration

Fig. 4. ETG-7100 system and its shell to hold 4×4 optodes.

changes independently. The distance between the detector optode and emitter optode was 30 mm, which enabled cerebral blood volume measurement at a 2 to 3 cm depth from the surface of cerebral cortex (Toronov et al., 2001). The midpoints of pairs of emitter-detector optodes were regarded as the points of measurement (channels). Data were measured with a sampling rate of 10 Hz. Light emitters and detectors were alternated at an equal distance of 3 cm to give one 4×4 optode probe sets (Fig. 4). All of the transmitted intensities of the two wavelengths that left the tissue were continuously recorded over 24 channels to estimate changes in the concentrations of oxy-Hb and deoxy-Hb.

Data collection by this system is comfortable for subjects, since it requires less constrictive circumstances of measurements and fewer movement restrictions, yielding more ecologically valid conditions. The whole system is fixed on a platform installed with casters so that the system can move with the subject in moving tasks. In our study, the subjects walked in the experiment. Therefore fNIRS is more suitable for this study (Suzuki et al., 2004; Miyai et al., 2001).

3. Cortical activation during real walking and mental imagery of walking

This section introduces two experiments in which we compared the cortical activation during real walking and that during mental imagery of walking.

3.1 Experiment 1

We compared the activation in the primary motor area and the primary somatosensory area of the brain during RW and WO by means of fNIRS. The possibility to quickening walking rehabilitation by mental imagery of walking is discussed based on the experiment results.

3.1.1 Subjects

Two male graduate students (SL and ZJ) of Kochi University of Technology participated in the experiment. Their ages were 27 to 28 years. All were right-handed and had no medical history of neurological or psychiatric disorders.

3.1.2 fNIRS measurement

As shown in Fig. 5, the optodes were fixed with a plastic shell and placed on the subject's left frontal areas according to the international 10-20 system, which is widely used in EEG measurement (Homan et al., 1987; Steinmetz et al., 1989; Okamoto et al., 2004). The numbers between the emitters and detectors were channel numbers. Channels were labelled from front to back as CH1-CH24. Data were measured with a sampling rate of 10 Hz. CH16 was placed on Cz · The areas measured by CH11, 12, 15, 18, 19 and CH13, 14, 17, 20, 21 covered the primary somatosensory cortex which processes the sensory information and the primary motor cortex which plans and executes movements related to walking.

3.1.3 Stimuli

The experiment scene is shown in Fig. 6. During the RW task, the subjects walked along a straight line at 0.3 m/s. The ETG-7100 system was pushed to follow the subject

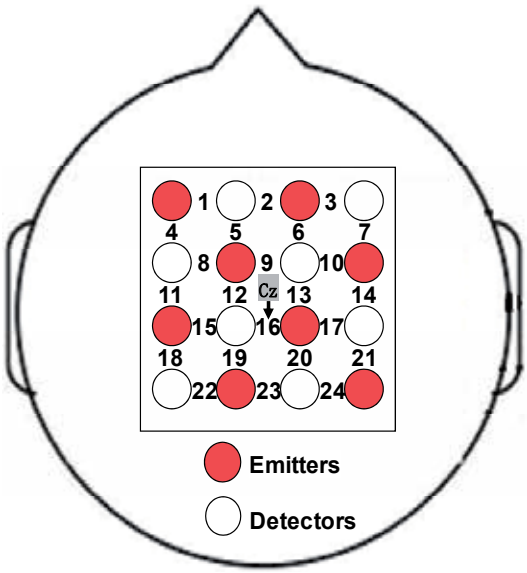

Fig. 5. Schematic placement of the emitter and detector optodes on the subject's head

(a) Real walking (b) Walking observation

Fig. 6. Experiment scene

in the task. During the WO task, the subjects were shown a video (Fig. 7) in which a person walks along a line at the same speed (0.3 m/s). The subjects were instructed to imagine that they were walking the same as the person in the video, especially to match their gaits to the video, while keep standing on the ground. The video was shot in a corridor against the wall.

3.1.4 Task paradigm

The experiment procedure is shown in Fig. 8. During the experiment, a 20 s real walking task and a 20 s imaginary walking task were performed, with a 60 s rest period before and after each task. In order to avoid the influence by the order of the tasks, two procedures were conducted. In procedure 1, the real walking task was before the imaginary walking task while in procedure 2 the order was reversed.

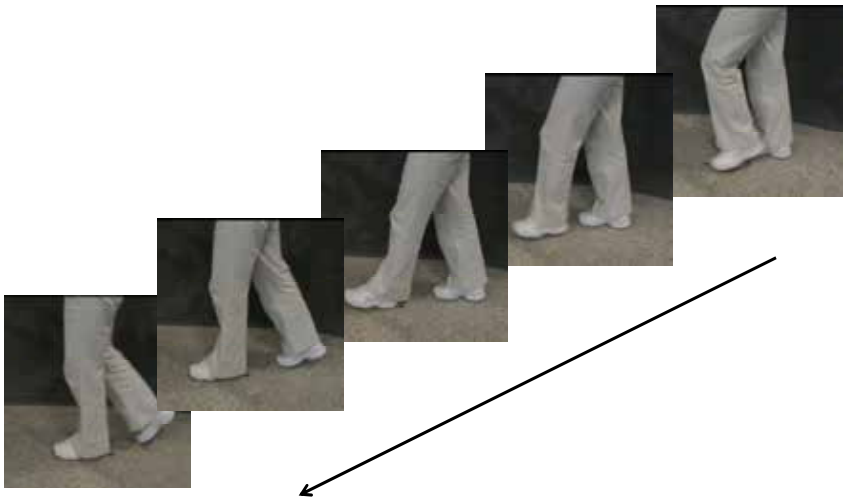

Fig. 7. Walking video shown to the subjects during WO task

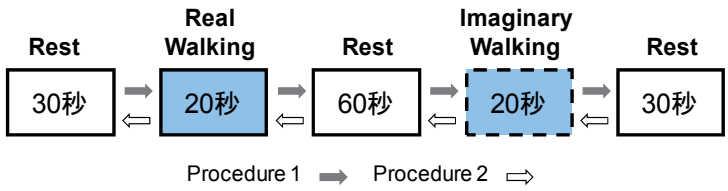

Fig. 8. Walking video shown to the subjects during WO task

3.1.5 Data analysis

According to previous studies, oxy-Hb is more useful for analysis of cortical activation than deoxy-Hb because of its higher reproducibility (Plichta 2006; Sato 2005), lower inter-subject variability (Sato 2006), and higher correlation with fMRI signals. Therefore, in the present study, oxy-Hb was measured as an indicator of changes in blood volume. The measurements of the subjects were checked visually for artifacts due to body movements. Obtained data were analyzed using the "integral mode" in the ETG-7100 software. We defined a 48 s measurement block made up of a 9 s pretask baseline period before task period (20 s), a 12s recovery period and a 7 s posttask baseline period (Fig. 9). Linear fitting

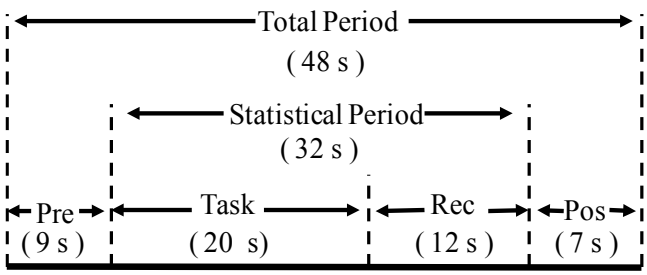

Fig. 9. Parameters of the integral mode in the ETG-7100 analysis software

was applied to the data between these two baselines. The data in the statistical period, which was made up of task and recovery periods, were considered as the activation signals which were used to analyze the cerebral blood volume difference between real walking and imaginary walking. In the analysis we compared the average oxy-Hb of CH11, 12, 15, 18, 19 and CH13, 14, 17, 20, 21 between the RW task and the WO task.

3.1.6 Results and discussions

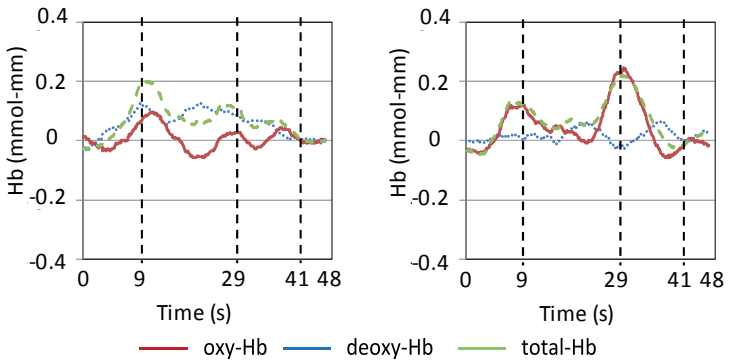

(a) Real walking (b) Imaginary walking

Fig. 10. Results of procedure 1

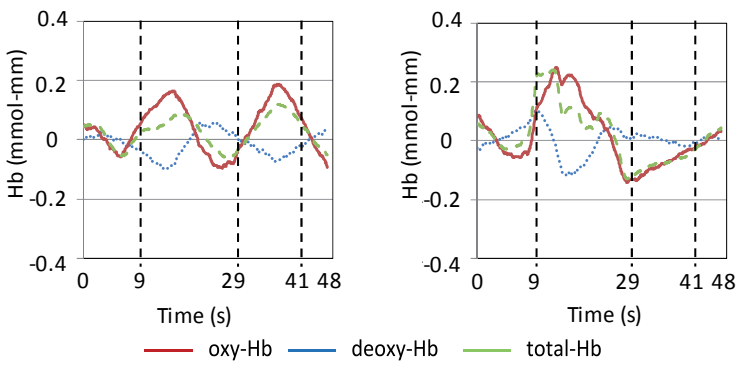

(a) Imaginary walking (b) Real walking

Fig. 11. Results of procedure 2

The average oxy-Hb of subject SL and ZJ during the statistical period of procedure 1 and 2 are shown in Fig. 10 and Fig. 11, respectively. In Fig. 10 and Fig. 11, the horizontal axis is the time shown in Fig. 9. Both oxy-Hb and deoxy-Hb, and their sum total-Hb are shown. It can be seen from the experiment results that both in procedure 1 and procedure 2, oxy-Hb increased significantly no matter the subject really walked or just imagined walking. The experiment results suggest that the cortical areas related to walking is activated by both RW and WO. The possibility of brain exercise for walking rehabilitation by mental imagery of walking was implied.

The average oxy-Hb of subject SL and ZJ during the statistical period are listed in Table 1 · We can conclude from Table 1 that although individual difference was significant, the oxy-Hb during the imaginary walking task was higher than that during the real walking task, regardless of the order of the tasks.

	Procedure 1		Procedure 2	
	RW	WO	RW	WO
Subject SL	0.027	0.147	0.056	0.114
Subject ZJ	0.043	0.135	-0.087	-0.062

**oxy-Hbs are given in mM·mm

Table 1. Average oxy-Hb during RW and WO tasks

fNIRS measures cerebral blood volume. When we walk along a straight line on a level road without any obstacles, the primary somatosensory cortex and the primary motor cortex do not involve much, with the cerebellum controlling the movement of the legs. On the other hand, during the imaginary walking task of the experiment, the subjects have to conceive their movement to match their gaits with those in the video. Although the subjects did not move, they have to plan their walking in their brain. This might be the reason why the oxy-Hb during the WO task was higher than that during the RW task. However, at present since fNIRS can only measure cerebral blood flow in cortex, not in deeper structures, how the other neural systems, such as cerebellum, the spinal cord and the peripheral nervous system, involve in mental imagery of walking is still not clear.

3.2 Experiment 2

In the second experiment, we compared the activation in the primary motor area and the primary somatosensory area of the brain during RW, VW and WO by means of fNIRS, in order to find an effective way to activate the motor area in mental imagery. The difference between VW and WO is that VW is first-person perspective, imaging oneself is walking following the visual scene in the video, while WO is third-person perspective, imaging oneself is following the gait of the person in the video. We quantitatively compared their brain activation effect based on the experiment results.

3.2.1 Subjects

Four students (YJ, RL, QQ and LS) of Kochi University of Technology participated in the experiment. Their ages were 28 to 31 years. All were right-handed and had no medical history of neurological or psychiatric disorders.

3.2.2 fNIRS measurement

As shown in Fig. 12, the concentrations of oxy-Hb and deoxy-Hb were measured by ETG-7100 system. The subject stood on a treadmill throughout the experiment. Data were measured with a sampling rate of 10 Hz.

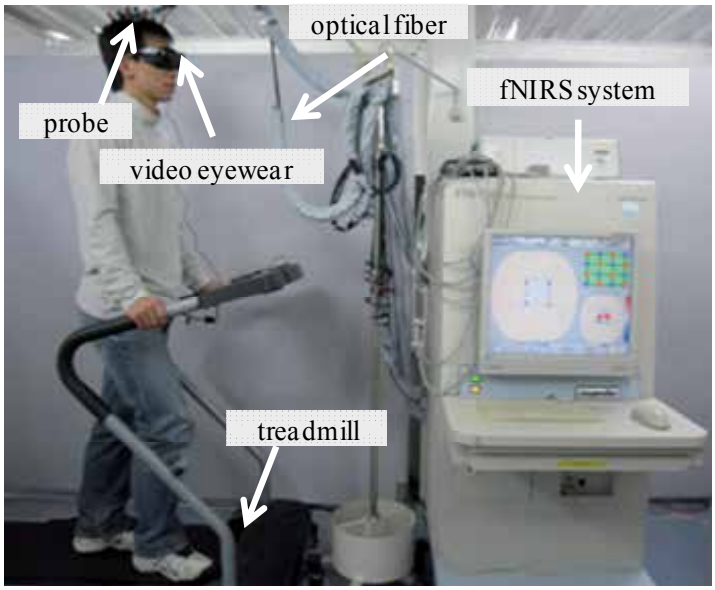

Fig. 12. Experiment scene

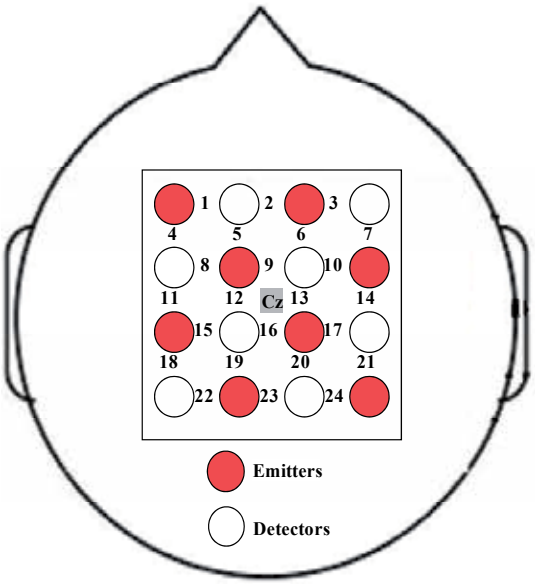

Fig. 13. Schematic placement of the emitter and detector optodes on the subject's head

Fig. 13 shows the positions of optodes on the head of the subjects. The optodes were fixed with a plastic shell and placed on the subject's head according to the international 10-20 system. The numbers between the emitters and detectors were channel numbers. Channels were labelled from front to back as CH1-CH24. The midpoint between CH12 and CH13 was placed on Cz of the International 10-20 system. According to the correlation between the international 10–20 system and cortical region, the areas measured by CH4, 5, 8, 11, 12 and

CH6, 7, 10, 13, 14 covered PM, SMA and the primary motor cortex (M1) which plans and executes movements related to walking.

3.2.3 Stimuli

There were three tasks, real walking (RW), virtual walking (VW), and walking observation (WO) in the experiment. During the RW task, the subjects walked on a treadmill at 1.0 km/h. For the VW task, a video clip was taken by a cameraman who was naturally walking down a corridor at 1.0km/h (Fig.14). Subjects were instructed to imagine as if they were actually walking from the first-person perspective. For the WO task, a video clip in which a person walks down the same corridor at 1.0 km/h was taken (Fig.14). Subjects were instructed to imagine that they were walking the same as the person in the video, especially to match their gaits to the video.

(a) Shooting location of the video

(b) Scene for walking observation. (c) Scene for virtual walking.

Fig. 14. Walking videos shown to the subjects during imaginary walking

The subjects wore a video eyewear (Wrap920, Vuzix Corporation, NY, USA) with lightshield to block distracting outside light (Fig. 12), to display the video stimuli. This eyewear displays the video on a virtual 67-inch screen as seen from 10 feet. During the rest period between the tasks, a video clip in which there is a cross mark on a white board was displayed.

3.2.4 Task paradigm

RW, VW and WO tasks were performed 40 s every time, with a 30 s of rest before and after each task. In order to avoid the influence by the order of the tasks, two procedures were carried. Procedure 1 was performed in the following order.

Rest (30s) →VW (40s) →Rest (30s) →RW (40s) → Rest (30s) →WO (40s) →Rest (30s) →RW (40s) →Rest (30s)

Procedure 2 was performed in the following order.

Rest (30s) →RW (40s) →Rest (30s) →VW (40s)→ Rest (30s) →RW (40s)→Rest (30s) →WO (40s) →Rest (30s)

3.2.5 Data analysis

Oxy-Hb was considered as an indicator of changes in blood volume. The measurements of the subjects were checked visually for artifacts due to body movements. Obtained data were analyzed by calculating the average oxy-Hb level during RW, VW and WO. In the analysis we compared the average oxy-Hb of CH4, 5, 6, 7, 8, 10, 11, 12, 13, 14 which covered PM, SMA and M1 involved in planning and execution of movements related to walking.

3.2.6 Results and discussions

In Fig.15 and Fig.16, the color maps of typical activation pattern of oxy-Hb were extracted. These maps were created by interpolation to the measurement data of 24 measure points. It

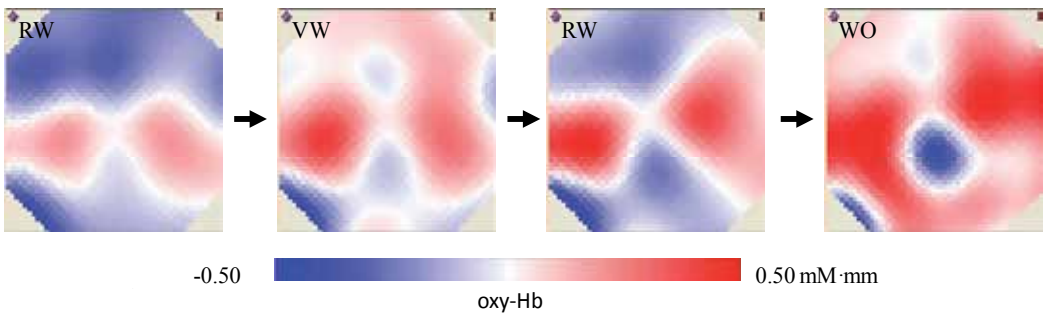

Fig. 15. Color maps of typical activation pattern in procedure 1

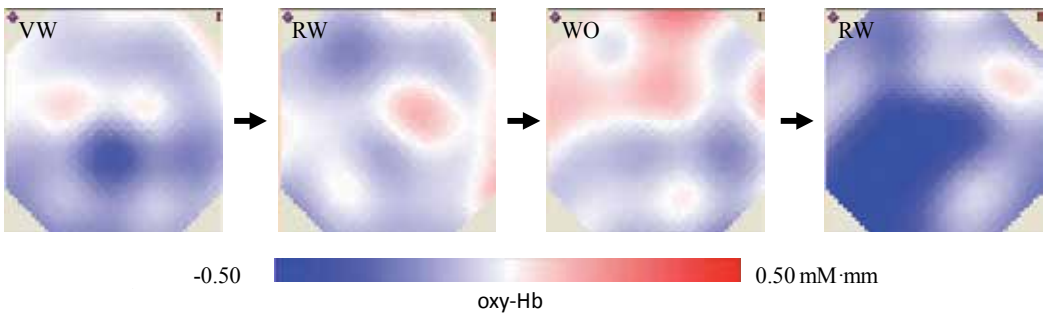

Fig. 16. Color maps of typical activation pattern in procedure 2

can be observed from the experiment results that both in procedure 1 and procedure 2, oxy-Hb increased significantly no matter the subject really walked or just imagined walking in first-person perspective and third-person perspective. The experiment results suggest that the cortical areas related to walking was activated by both real walking and imaginary walking. The oxy-Hb in procedure 2 was generally lower that in procedure 1. The same video clips were used in procedures 1 and 2. The adaptation of the subject to the tasks might be the reason for the decrease in oxy-Hb.

The average oxy-Hb of the 4 subjects during the tasks in procedures 1 and 2 are listed in Table 2. In procedure 1, for all the subjects, oxy-Hb during VW and RW were higher that that during the RW before them. In procedure 2, although the oxy-Hb was generally lower than procedure 1, the same pattern (oxy-Hb were higher during VW and RW than the RW after them.) was observed except one subject QQ with oxy-Hb during WO of -0.054 and oxy-Hb during RW of -0.031. We can conclude from Table 2 that although individual difference was significant, on the average, the oxy-Hb levels during VW and WO were higher than the RW, regardless of the order of the tasks. There was no significant difference observed in the oxy-Hb during VW and WO. Whether the subjects imagined from first-person perspective or from third-person perspective did not lead to significant difference in cortical activation of the brain regions we measured.

	Procedure 1				Procedure 2			
	RW	VW	RW	WO	VW	RW	WO	RW
YJ	-0.062	0.124	0.109	0.310	-0.050	-0.130	0.015	-0.038
RL	0.043	0.179	0.101	0.105	0.030	-0.092	-0.005	-0.090
QQ	0.182	0.286	0.387	0.443	-0.047	-0.090	-0.054	-0.031
LS	-0.047	0.002	0.002	0.056	-0.180	-0.300	-0.284	-0.311
Avg	0.029	0.148	0.150	0.228	-0.062	-0.153	-0.082	-0.117

**oxy-Hbs are given in mM·mm

Table 2. Average oxy-Hb during RW, VW and WO tasks

4. Conclusion

In our study, in order to verify the possibility of conducting neurological rehabilitation by mental imagery of walking and to find an effective way to activate the motor area in mental imagery, we compared the activation in motor areas during RW, VW, and WO, making use of the advantages of fNIRS. fNIRS measures cerebral hemodynamics non-invasively by monitoring the attenuation of near infrared light passing through tissue.

fNIRS measurement is comfortable for subjects, since it requires less constrictive circumstances of measurements and fewer movement restrictions. These advantages allow us to measure the cortical activation during real walking. The experiment results showed that the oxy-Hb during the mental imagery of walking task (VW and WO) was higher than that during the RW task. No significant difference was observed in the oxy-Hb during VW and WO, showing that they have the similar effect on the brain regions we measured. The importance of stimulus diversity was suggested in continuous stimulation of mental imagery of walking because the oxy-Hb level decreased with the adaptation of the brain to the stimuli.

On the other hand, the disadvantage of fNIRS is that it can only monitor limited brain areas and the spatial resolution is relatively low. fNIRS can only measure cerebral blood flow in the cortices, not in deeper structures. We need another method to find out how the other neural systems, such as cerebellum, the spinal cord and the peripheral nervous system, involve in mental imaginary of walking. Recently, a lot of studies which combined fNIRS with EEG (Wallois et al., 2011; Fazli et al., 2011) or fMRI with EEG (Horovitz et al, 2008; Mantini et al., 2010) have been reported. These combinations enable to make the best use of the advantages of each technology. The advantage of simultaneous EEG-fNIRS measurement is to provide a better temporal resolution and quantitative information about oxy-Hb and deoxy-Hb. The combination of EEG and fMRI is to make use of the high temporal resolution of EEG and the high spatial resolution of fMRI. A multimodal approach is necessary for better understanding the similarity and difference between RW, VW and WO.

5. Acknowledgment

This study was supported by Grants-in-Aid for Scientific Research No. 20240058 and No. 21300212 from the Japan Society for the Promotion of Science. It was also supported by a Grant-in-Aid for Young Scientists (B) from Japan Society for the Promotion of Science (No. 23700316).

6. References

Chance, B., Zhuang, Z., UnAh, C., Alter, C., & Lipton, L. (1993). Cognition-Activated Lowfrequency Modulation of Light Absorption in Human Brain. *Proceedings of the National Academy of Sciences of the United States of America*, Vol.90, No.8, (April 1993), pp.3770-3774, ISSN 0027-8424.

Dickstein, R., Dunsky, A., & Marcovitz, E. (2004). Motor Imagery for Gait Rehabilitation in Post-Stroke Hemiparesis, *Physical Therapy*, Vol.84, No.12, (December 2004), pp.1167-1177, ISSN 0031-9023.

Fukuyama, H., Ouchi, Y., Matsuzaki, S. Nagahama, Y., Yamauchi, H., Ogawa, M., Kimura, J., & Shibasaki, H. (1997) Brain Functional Activity during Gait in Normal Subjects: a SPECT study. *Neuroscience Letters*, Vol.228, No.3, (June 1997), pp.183–186, ISSN 0304-3940.

Fazli, S., Mehnert, J., Steinbrink, J., Curio, G., Villringer, A., Müller, K. R., & Blankertz B. (2011). Enhanced Performance by a Hybrid NIRS–EEG Brain Computer Interface, *NeuroImage*, (August 2011), doi:10.1016, ISSN 1053-8119.

Hausdorff, J. M., Yogev, G., Springer, S., Simon, E. S., & Giladi, N. (2005). Walking is More Like Catching than Tapping: Gait in the Elderly as a Complex Cognitive Task. *Experimental Brain Research*. Vol.164, No.4, (April 2005), pp.541-548, ISSN 1432-1106.

Hitachi Medical Corporation, *Optical Topography System*, Available from http://www.hitachi-medical.co.jp/product/opt/etg/index.html

Homan, R.W., Herman, J., & Purdy, P. (1987). Cerebral Location of International 10-20 System Electrode Placement. *Electroencephalography and Clinical Neurophysiology*, Vol.66, No.4, (April, 1987), pp.376-382, ISSN 0013-4694.

Horovitz, S. G., Fukunaga, M., de Zwart, J. A., van Gelderen, P., Fulton, S. C., Balkin, T. J., Duyn, J. H. (2008). Low Frequency BOLD Fluctuations during Resting Wakefulness and Light Sleep: a Simultaneous EEG-fMRI Study. *Human Brain Mapping*, Vol.29, No.6 (June 2008), pp.671‐682, ISSN 1097-0193.

Horst, R.W. (2009). A Bio-Robotic Leg Orthosis for Rehabilitation and Mobility Enhancement, *Proceedings of the 31st Annual International Conference of the IEEE EMBS*, ISBN 978-1-4244-3296-7, pp. 5030-5033, Moffett Field, USA, September 2009.

Iseki, K., Hanakawa, T., Shinozaki, J., Nankaku, M., & Fukuyama H. (2008). Neural Mechanisms Involved in Mental Imagery and Observation of Gait, *Neuroimage*, Vol.41, No.3, (July 2008), pp.1021-1031, ISSN 1053-8119.

Ishida, K., Wang, S. Y., Nagano, T., & Kishi, K. (2008). Development of All-way Mobile Walker, *The Journal of Physical Medicine*, Vol.19, No.4, (December 2008), pp.246-250, ISSN 1342-7776.

Jiang, Y.L., Wang, S.Y., Tan, R.P., Ishida, K., Ando, T., & Fujie, M. G. (2010). The Possibility of Quickening Walking Rehabilitation by Imaginary Walking, *ICIC Express Letters, Part B: Applications*, Vol.1, No.2, (December 2010), pp.189-194, ISSN 2185-2766.

Jiang, Y.L., Wang, S.Y., Tan, R.P., Ishida, K., Ando, T., & Fujie, M. G. (2011). Study of Activation in Motor Cortex during Mental Imagery of Walking Using fNIRS, *Proceedings of the 2011 IEEE International Conference on Complex Medical Engineering*, ISBN 987-1-4244-9322-7, pp.637-640, Harbin, China, May 2011.

Mantini, D., Marzetti L., Corbetta M., Romani G. L., & Del Gratta C. (2010). Multimodal Integration of fMRI and EEG Data for High Spatial and Temporal Resolution Analysis of Brain Networks, *Brain Topography*, Vol.23, No. 2, (June 2010), pp.150-158, ISSN 0896-0267.

Miyai, I., Tanabe, C. H., Sase, I., Eda, H., Oda, I., Konishi, I., Tsunezawa, Y., Suzuki, T., Yanagida, T., & Kubota, K., Cortical Mapping of Gait in Human: a Near-Infrared Spectroscopic Topography Study, *NeuroImage*, Vol.14, No.5, (November 2001), 1186-1192, ISSN 1053-8119.

Okada, S., Sakaki, T., Hirata, R., Okajima, Y., Uchida, S., & Tomita, Y. (2001). TEM: a Therapeutic Exercise Machine for the Lower Extremities of Spastic Patients, *Advanced Robotics*, Vol.14, No.7, (January 2011), pp.597-606, ISSN 0169-1864.

Okamoto, M., Dan, H., Sakamoto, K., Takeo, K., Shimizu, K., Kohno, S., Oda, I., Isobe, S., Suzuki, T., Kohyama, K., & Dan, I. (2004). Three-Dimensional Probabilistic

Anatomical Cranio-Cerebral Correlation via the International 10-20 System Oriented for Transcranial Functional Brain Mapping, *Neuroimage*, Vol.21, No.1, (January 2004), 99-111, ISSN 1053-8119.

Plichta, M. M., Herrmann, M. J., Baehne, C. G., Ehlis, A-C., Richter, M. M., Pauli, P., & Fallgatter, A. J. (2006). Event-Related Functional Near-Infrared Spectroscopy (fNIRS): Are the Measurements Reliable?, *Neuroimage*, Vol.31, No.1, (January 2006), pp.116-124, ISSN 1053-8119.

Raichle, M. E. & Mintun, M. A. (2006). Brain Work and Brain Imaging, Annual Review of Neuroscience, Vol. 29, (July 2006), pp.449-476, ISSN 1545-4126.

Riecker, A., Wildgruber, D., Mathiak, K., Grodd, W., & Ackermann, H. (2003). Parametric Analysis of Rate-dependent Hemodynamic Response Functions of Cortical and Subcortical Brain Structures during Auditorily Cued Finger Tapping: a fMRI Study. *Neuroimage*, Vol.18, No.3, (March 2003), pp.731–739, ISSN 1053-8119.

Sato, H., Fuchino, Y., Kiguchi, M., Katura, T., Maki, A., Yoro, T., & Koizumi, H. (2005). Intersubject Variability of Near-Infrared Spectroscopy Signals during Sensorimotor Cortex Activation, *Journal of Biomedical Optics*, Vol.10, No.4, (August 2005), 044001, ISSN 1083-3668.

Sato, H., Kiguchi, M., Maki, A., Fuchino, Y., Obata, A., Yoro, T., & Koizumi H. (2006). Within-Subject Reproducibility of Near-Infrared Spectroscopy Signals in Sensorimotor Activation after 6 Months, *Journal of Biomedical Optics*, Vol.11, No.1, (Feburary 2006), 014021, ISSN 1083-3668.

Sharma, N., Pomeroy, V. M., & J. C. Baron. (2006). Motor Imagery: a Backdoor to the Motor System after Stroke?, *Stroke*, Vol.37, No.7, (June 2006), pp.1941-1952, ISSN 0039-2499.

Steinmetz, H., Fürst, G., & Meyer, B. U. (1989). Craniocerebral Topography within the International 10-20 System. *Electroencephalography and Clinical Neurophysiology*, Vol.72, No.6, (June 1989), pp.499-506, ISSN 0013-4694.

Suzuki, M., Miyai, I., Ono, T., Oda, I., Konishi, I., Kochiyama, T., & Kubota, K. (2004). Prefrontal and Premotor Cortices are Involved in Adapting Walking and Running Speed on the Treadmill: an Optical Imaging Study, *Neuroimage*, Vol.23, No.3, (November 2004), pp.1020-1026. ISSN 1053-8119.

Tan, R.P., Wang, S.Y., Jiang, Y.L, Ishida, K., Fujie, M. G., & and M. Nagano(2011). Adaptive Control Method for Path Tracking Control of an Omni-Directional Walker Considering Center of Gravity Shift and Load Change, *International Journal of Innovative Computing, Information and Control*, Vol.7, No.7, (July 2011), pp.4423-4434, ISSN 1349-418X.

Villringer, A., Planck, J., Hock, C., Schleinkofer, L., & Dirnagl, U. (1993). Near Infrared Spectroscopy (NIRS): a New Tool to Study Hemodynamic Changes during Activation of Brain Function in Human Adults. *Neuroscience Letters*, Vol.154, No.1-2, (May, 1993), pp.101-104, ISSN 0304-3940.

Wallois, F., Mahmoudzadeh, M., Patil, A., & Grebe, R. (2011). Usefulness of Simultaneous EEG–NIRS Recording in Language Studies, *Brain and Language*, (May 2011), ISSN 0093-934X, 10.1016.

Wagner, J., Stephan, T., Kalla, R., Brückmann, H., Strupp, M., Brandt, T., & Jahn K. (2008). Mind the Bend: Cerebral Activations Associated with Mental Imagery of Walking along a Curved Path, *Experimental Brain Research*, Vol.191, No.2, (November 2008), pp.247-255, ISSN 1432-1106.

10

Near-Infrared Spectroscopic Assessment of Haemodynamic Activation in the Cerebral Cortex – A Review in Developmental Psychology and Child Psychiatry

Hitoshi Kaneko[1], Toru Yoshikawa[2], Hiroyuki Ito[3], Kenji Nomura[1], Takashi Okada[2] and Shuji Honjo[1]
[1]*Center for Developmental Clinical Psychology and Psychiatry, Nagoya University*
[2]*Department of Psychiatry for Parents and Children, Nagoya University Hospital*
[3]*Osaka-Hamamatsu Joint Center for Child Development, Hamamatsu University School of Medicine*
Japan

1. Introduction

This chapter aims to shed light on developmental cognitive neuroscience studies that use near-infrared spectroscopy (NIRS) to examine the cortical response in developmental psychology and child psychiatry. NIRS was first applied to the human brain in 1977 (Jöbsis, 1977) for the noninvasive measurement of the haemodynamic activation in the cerebral cortex. NIRS is advantageous over other neuroimaging methods in terms of its ease of measurement and low cost. Therefore, extensive studies have investigated neural correlates using the NIRS technique in healthy people and in neurological or psychiatric patients. Furthermore, NIRS has been applied to multiple age groups from neonates to adults. It is beyond the scope of this chapter to provide an exhaustive list of the neuroscience research based on NIRS. Here, we focus mainly on the studies that examine cognitive function from the viewpoint of developmental cognitive neuroscience.

We believe that studies on brain function in children from birth to adolescence who are healthy or have psychiatric disorders provides knowledge about the trajectory of cognitive and neural development. The advantages of NIRS over magnetoencephalography (MEG) or functional magnetic imaging (fMRI) include easy measurement and less susceptibility to signal distortion by motion artefacts (Gervain et al., 2011; Lloyd-Fox et al., 2010). Furthermore, NIRS enables the measurement of human cerebral activity in less restricted and less noisy conditions. This advantage is particularly important in studies that investigate children from infancy to adolescence. NIRS enables researchers to easily present auditory stimuli (Kaneko et al., 2011) and to conduct experiments in relatively natural social settings (Ito et al., 2011). NIRS can be performed on infants even while they sit upright on

the lap of a parent. Therefore, NIRS is especially suited for research on children from birth to the toddler years (Lloyd-Fox et al., 2010).

2. Techniques for assessment of brain function

Compared to other clinical neurological methods such as electroencephalography (EEG), positron emission tomography (PET), fMRI, and MEG, NIRS was recently developed. EEG is a noninvasive method that directly measures the electrical activity of the brain via electrodes placed on the scalp. EEG has a high temporal resolution but poor spatial resolution. PET is an invasive method that uses radioactive tracers to measure the metabolism of the brain. PET provides high specific spatial resolution but poor temporal resolution. fMRI is a noninvasive method that measures the changes in blood oxygenation, and provides good spatial resolution but limited temporal resolution. MEG is a noninvasive method that measures the magnetic fields induced by electrical activity in the brain. MEG has good spatial and temporal resolution; however, MEG also requires the participants to remain very still during measurement.

NIRS is completely noninvasive, more patient-friendly, and can be performed very easily compared to other neurological techniques. It is relatively inexpensive compared to fMRI, making it possible to measure haemodynamic changes at a low cost. Furthermore, the NIRS instrument is portable; measurements can be obtained *in situ*, for example, at the bedside. In addition, the NIRS probe for assessing brain activity is very flexible, and does not require the patient to be still or maintain the head in any particular position (Minagawa-Kawai et al., 2008). These attributes are especially useful when the patients are children, as it enables them to feel relaxed even in an experimental setting. fMRI and MEG studies are difficult to perform in children, because these techniques require the patients to be still. Most fMRI studies in infants have been performed while they are asleep or are sedated inside the imaging tunnel (Lloyd-Fox et al., 2010; Minagawa-Kawai et al., 2008).

NIRS has a higher temporal resolution than fMRI. Haemodynamic changes at 10 Hz can be measured with commercially available products, whereas a typical fMRI instrument provides a temporal resolution of a few seconds. NIRS provides the concentration changes in both oxy-haemoglobin and deoxy-haemoglobin, whereas fMRI measures only deoxy-haemoglobin. NIRS is not as noisy as fMRI, and the NIRS signal is less affected by motion artefacts compared to signals of fMRI or MEG. Additionally, NIRS permits continuous and repeated measurement.

However, one limitation of NIRS is that it assesses brain function indirectly by measuring the haemodynamic changes in haemoglobin via an optical fibre probe attached to the scalp. The working principle of NIRS is that neural activation requires oxygen consumption; therefore, the haemoglobin concentration in the blood vessels depends on the neural activity. EEG, in contrast, assesses brain function directly by measuring the electrical potential of neurons via electrodes attached to the scalp. Additionally, although NIRS assesses brain activity via haemodynamic changes in the cerebral cortex, it is unable to examine deep brain activation. Specifically, NIRS allows the assessment of haemoglobin concentrations up to only 2 or 3 cm below the skull; therefore, the activation in the deep brain regions cannot be measured. Furthermore, NIRS has a low spatial resolution compared to fMRI or MEG; the spatial resolution of NIRS is 20–30 mm, whereas that of fMRI is 1–2 mm.

3. NIRS: Principles and methods in the assessment of the human cerebral cortex

Biological tissue is relatively transparent to light in the near-infrared range. In NIRS, light at wavelengths of 700–900 nm is illuminated onto the scalp. Oxy-haemoglobin and deoxy-haemoglobin chromophores have different absorption spectra that are used to assess the attenuated light levels via changes in the chromophore concentration; these concentration changes can be used to determine the haemodynamic response.

Because oxygen consumption increases in the region of the brain with the greatest activity, changes in the oxygen content of the blood can be used to measure the relative levels of brain activity. The specific parameters of the response monitored with NIRS represent changes in the levels of oxygenated and deoxygenated haemoglobin at specific regions across the cerebral cortex during stimulation. The detailed principles of NIRS have been described previously (e.g. Gervain et al., 2011; Hoshi, 2007; Minagawa-Kawai et al., 2008; Strangman et al., 2002).

4. Applications in developmental psychology

4.1 Functional brain activity in infants

After Jöbsis first applied NIRS to the human brain (Jöbsis, 1977), there has been an increasing interest in measuring the haemodynamic response in the cerebral cortex of humans, especially in neonatal patients in the neonatal intensive care unit (NICU). NIRS is especially suitable for studies in neonates and is increasingly used in high-risk neonates, including low-birth-weight infants, neonates with congenital heart defects, and neonates with other pathological states (Goff et al., 2010; Wyatt et al., 1986). The neonatal skull is thinner than that of adults; therefore, near-infrared light can penetrate deeper into the neonatal cortex than into the adult cortex. The first study to use NIRS to evaluate cerebral oxygenation saturation in pre-term infants was published in 1985 (Brazy et al., 1985). Subsequently, extensive research has revealed that NIRS is highly effective for monitoring cerebral oxygenation saturation in the NICU (Brazy et al., 1985).

Although numerous studies have demonstrated that NIRS is valuable for the assessment of neonates in the NICU, the use of NIRS in measuring cognitive function in infants has not been fully investigated. Early NIRS studies examined infants who were presented with stimuli while they were asleep (Aoyama et al., 2010; Homae et al., 2007; Saito et al., 2007a, 2007b, 2009).

Over the last decade, NIRS has been successfully applied to awake infants in experimental settings (Homae et al., 2010; Hyde et al., 2010; Nakano et al., 2009; Taga et al., 2003; Taga & Asakawa, 2007; Watanabe et al., 2010; Wilcox et al., 2008, 2009, 2010). Figure 1 shows an experimental setting where infants can sit upright on the lap of a parent wearing NIRS probes and headgear designed for infants.

In the next section, we address the neural activation during face recognition in infants. Face recognition is important for infants and adults, because the face represents not only the personal identity but also the emotional expressions of an individual. In social communication, it is essential to understand the thoughts of a person via their facial expressions. Although many event rerated potential (ERP) studies in infants have examined

Fig. 1. Experimental setting using NIRS for awake infants

the neural substrates of facial recognition (de Haan et al., 2003), relatively few NIRS studies have been documented. However, NIRS has been applied to other research areas such as cerebral lateralization and speech acquisition (Minagawa-Kawai et al., 2008).

4.2 Haemodynamic responses in infants during face recognition

Haemodynamic changes during the face recognition process as assessed by NIRS have been documented in several studies (Blasi et al., 2007; Csibra et al., 2004; Grossmann et al., 2008; Honda et al., 2010; Ichikawa et al., 2010; Nakato et al., 2009, 2011a, 2011b; Otsuka et al., 2007). Newborns showed a spontaneous preference for face-like stimuli over non-face-like patterns (Fantz, 1961). It is crucial for infants to discriminate the face of their caregiver face from the faces of other persons to elicit care. The ability to recognise emotion in facial expressions is also important for infants to communicate effectively to caregivers, and this represents the emergence of social communication. Numerous behavioural and electrophysiological studies have demonstrated that 5–7-month-old infants can visibly discriminate different facial expressions and exhibit an attention bias towards salient facial expressions (Leppanen & Nelson, 2009). Recent NIRS studies have demonstrated that infants show different haemodynamic responses to different facial stimuli (Nakato et al., 2009, 2011a, 2011b).

Infants respond to happy faces and angry faces with distinct haemodynamic changes in their cortical regions (Nakato et al., 2011b). Nakato et al. found that the left temporal region, particularly the left superior temporal sulcus, was significantly activated in response to happy faces, whereas the right temporal region was activated in response to angry faces. Furthermore, happy faces increased the haemodynamic response gradually, and the response was maintained even after the happy face stimuli disappeared. In contrast, when angry face stimuli were presented, the haemodynamic response peaked quickly and decreased more rapidly after the angry faces disappeared.

The infants' response to their mother's face and to the faces of unfamiliar women was also accompanied by haemodynamic changes in the cortical regions (Nakato et al., 2011a). In response to the mother's face, the oxy-Hb and total-Hb concentrations increased in the right and left temporal cortices. In contrast, in response to the faces of unfamiliar women, no activation was observed in the left temporal cortex, although the total-haemoglobin concentration in the right temporal cortex was increased.

Moreover, infants have shown developmental changes in haemodynamic activity during the recognition of faces in frontal view and profile view (Nakato et al., 2009). The oxy-haemoglobin and total-haemoglobin concentrations in 5-month-old infants only increased for the frontal view in the right temporal regions. However, the oxy-haemoglobin and total-haemoglobin concentrations in 8-month-old infants increased for both frontal and profile views. These studies suggest that the right temporal hemisphere is specialised for face recognition in infants (Carlsson et al., 2008; Nakato et al., 2011; Nakato et al., 2009; Otsuka et al., 2007). Previous neuroimaging studies in adults also indicated that the right temporal cortex is involved in face recognition. Thus, it is suggested that the components of the facial recognition system that adults possess emerge as precursors in the early infant periods.

Although accumulating evidence indicates that infants respond to face stimuli differently in terms of the haemodynamic changes in the temporal cortex, other brain areas, e.g. the fusiform face area and lateral occipital cortex, have not been fully investigated. The fusiform face area is considered to play a crucial role in face perception, especially in face identification (Johnson, 2005; Kanwisher & Yovel, 2006; Tsao & Livingstone, 2008). However, the fusiform face area is deeply located, and hence, its activity cannot be measured by NIRS. The orbitofrontal cortex and amygdala areas of that have been implicated in the recognition of the emotions of facial expressions (Leppanen & Nelson, 2009).

4.3 Neural basis of infant-mother attachment

Infant-mother attachment is essential for the development of infants. Infants use attachment behaviours to deepen the intimacy with their caregiver, thereby eliciting ample care from their caregiver and increasing their prospect for surviving. Many researchers have investigated the attachment behaviour of infants in developmental psychology; however, few studies have investigated the neural substrates of infant-mother attachment. fMRI studies have indicated that the brains of mothers are more activated by their own infants than by other infants stimuli (Kim et al., 2011; Lenzi et al., 2009; Noriuchi et al., 2008). Noriuchi et al. found that the right orbitofrontal cortex, periaqueductal gray, anterior insula,

and dorsal and ventrolateral putamen of mothers responded more positively to video clips of their own infants than to clips of unfamiliar infants (Noriuchi et al., 2008).

In contrast, surprisingly, little research is available about the neural correlates of infant brain activity associated with infant-mother attachment. Recently, using NIRS for awake infants, Minagawa-kawai et al. found that infants showed greater activation in the orbitofrontal cortex when they were presented with movie clips in which their own mothers smiled (Minagawa-Kawai et al., 2009).

Additionally, an fMRI study on adults revealed that the orbitofrontal cortex is activated by attractive faces (O'Doherty et al., 2003; Tsukiura & Cabeza, 2011). Similarly, the orbitofrontal cortex has been shown to have various functions, such as social cognition, motivational evaluation, emotional processing, and decision-making (Adolphs, 2003; Kringelbach, 2005).

Infant-mother attachment underpins the basis for life-long interpersonal relationships. Infants begin their life with affectionate social interactions with their mothers immediately after delivery. Many studies have shown that social interaction with caregivers is essential for healthy development in children (e.g. Smyke et al, 2007). However, little is known about how the brains of children develop continually until adulthood through social interaction with caregivers.

Face-to-face communication between mothers and infants is highly complicated, and is affected by many confounding variables, such as face expression, pitch of speech, and contingency of turn-taking. Therefore, it is technically difficult in experimental paradigms to examine the effects of face-to-face communication of mothers and infants. Further research is required to improve experimental paradigms that better approximate real life (Grossmann & Johnson, 2007) and to examine effects of face-to-face communication with the mother on the development of the brain of the infant.

4.4 Cognitive development in preschool children

In contrast to infant studies, studies on cognitive development in preschool children have largely not used neuroimaging methods. However, several studies have examined haemodynamic changes of the cerebral cortex using NIRS during cognitive shifting (Moriguchi & Hiraki, 2009, 2011) or working memory tasks (Tsujii et al., 2009, 2010; Tsujimoto et al., 2004).

Moriguchi & Hiraki (2009) found that 3-year-old children who committed perseverative errors lacked activation in their inferior prefrontal regions during cognitive shifting tasks, whereas those who performed the tasks correctly displayed activation of the right inferior prefrontal regions. Furthermore, a longitudinal study of prefrontal function in 3–4-year-old children showed that children who performed better tasks at 3 years of age showed significant activation of the right inferior prefrontal regions at 3 years of age, and significant activation of the both inferior prefrontal regions at 4 years of age (Moriguchi & Hiraki, 2011). Children who showed poorer performance at 3 years of age exhibited no significant inferior prefrontal activation at 3 years of age, but significant left inferior prefrontal activation at 4 years of age. It was therefore suggested that inferior prefrontal activation on either the right or left side may be more important for successful cognitive shifting than

sustained right inferior prefrontal activation. Moreover, multiple patterns of prefrontal activation were observed during the cognitive shifting tasks.

Tsujimoto et al. (2004) examined the cortical response of preschool children aged 5–6 years during spatial working memory tasks and found that the oxy-haemoglobin concentration was increased in the lateral prefrontal cortex, which is associated with working memory processes in adults. In another research group, Tusjii et al. found that the frontal activation was greater in 5-year-old children than in 7-year-old children during a spatial working memory task (Tsujii et al., 2009). Furthermore, right hemisphere dominance was observed in older children, but no significant hemispheric differences were observed in younger children. Children with strong lateralization showed improved performance from 5 to 7 years of age. These findings suggest that right lateralization for spatial working memory may start between 5 and 7 years of age.

Although NIRS is better suited for use in preschool children compared to other neuroimaging methods, brain function in preschool children measured by NIRS has not been well-documented. Numerous investigations have examined various aspects of brain function in human adults using fMRI or MEG. However, to date, no studies have addressed how the human brain develops and organises diverse cognitive ability from birth to adulthood. Further research needs to elucidate the development of brain function in preschool children.

5. Applications in child psychiatry

5.1 Brain dysfunction in children with autism spectrum disorders

Autism spectrum disorders (ASDs), including autistic disorder and Asperger disorder, are diagnosed by cataloguing behavioural features including the impairment of reciprocal social interaction and communication, as well as the presence of repetitive ritualistic behaviour or interests. Methodological differences make it difficult to compare epidemiological studies; therefore, there are discrepancies in the reported prevalence of ASDs. However, the prevalence of ASDs has been conservatively estimated at 36.4/10,000 (Fombonne, 2005). The severity of impairment varies greatly among patients, and they occasionally show mental retardation. The impairment is evident at least prior to the age of 3 years, and its effects persist life-long.

ASDs are characterised by pervasive impairments in social behaviour. Accumulating evidence suggests that adults with ASDs have altered brain activity in regions related to social interactions (Neuhaus et al., 2010), such as the superior temporal gyrus (Meresse et al., 2005), fusiform gyrus (Koshino et al., 2008), amygdala (Pinkham et al., 2008), and prefrontal cortex (Gilbert et al., 2009). Although previous studies have elucidated that adults with ASDs show reduced or altered activation in the aforementioned regions compared with healthy adults, surprisingly, little neuroimaging data are available for autistic children.

Kawakubo et al. examined prefrontal haemodynamic activation during a verbal fluency task in children and adults with ASDs (Kawakubo et al., 2009). In children, there were no significant differences in the haemodynamic changes between patients with ASDs and healthy controls. However, the concentration of oxy-haemoglobin in adults with ASDs was

significantly lower than that in healthy controls. These findings suggest that developmental changes in prefrontal activity of individuals with ASDs emerge before adulthood, i.e. they appear during adolescence.

5.2 Brain dysfunction in children with attention-deficit hyperactivity disorder

Attention-deficit hyperactivity disorder (ADHD) is a neurodevelopmental disorder whose prevalence has been estimated to be 3% to 7% of school-age children (American Psychiatric Association [APA], 2000). The essential clinical symptoms include inattention and/or hyperactivity-impulsivity. Some hyperactive-impulsive or inattentive symptoms must be present before the age of 7 years, although some symptoms that cause impairment tend to persist life-long. Some impairment from the symptoms is typically evident at school and at home, with behaviour that is clearly inappropriate for the developmental age in social, academic, or occupational settings.

In particular, ADHD is characterised by impairments in executive function, i.e. the failure of inhibitory control and the dysregulation of brain systems mediating reward and response (Sonuga-Barke, 2003). The Go/NoGo task, stop-signal task, and Stroop colour-word task have been used to investigate the inhibition process in these patients. Some studies have examined brain function in ADHD children during the Stroop colour-word task using NIRS. Moser et al. examined the brain activation in the dorsolateral prefrontal cortex (Moser et al., 2009), and showed that the oxy-haemoglobin concentration peaked later in ADHD children than in healthy children. Additionally, the concentration of deoxy-haemoglobin increased just after the onset of stimulation in ADHD children but decreased in healthy children. Negoro et al. examined the activation of frontal regions in the brain using 24-channel NIRS during the Stroop colour-word task (Negoro et al., 2010), and showed that the concentration of oxy-haemoglobin in the inferior prefrontal cortex in ADHD children decreased compared with that in healthy children, especially in the both the inferior lateral prefrontal cortex.

The trail-making test, which assesses executive function, has been used for the measurement of brain activation in ADHD children. Weber et al. showed that the concentration of oxy-haemoglobin increased in ADHD children during the short attention phase, whereas no significant change was observed in healthy children (Weber et al., 2005). A significant increase in oxy-haemoglobin was also reported for both groups during the extended attention phase, although an additional increase was observed in deoxy-haemoglobin level only in the healthy children.

These findings suggest that during tasks involving executive function, the haemodynamic responses in ADHD children are different from those in healthy children.

6. Conclusions

NIRS can greatly aid in extending our existing experimental paradigms. With NIRS, we can measure haemodynamic changes in the cerebral cortex of children, and accumulate more information on brain activity from infancy to adolescence. Such information is of great importance in studying brain function from a developmental perspective. However, surprisingly, the available research, even on topics like the typical trajectory of functional brain development, is less.

Furthermore, research on atypical brain function in ASDs or ADHD is needed to clarify the differences between typical and atypical functional brain development. The understanding of brain function in children with psychiatric disorders is key to developing effective intervention methods. For early intervention, we need to elucidate the process of cognitive neurodevelopment in the early stages of development. Thus, NIRS is a valuable modality for monitoring and investigating brain activity in children with psychiatric disorders.

7. References

Adolphs, R. (2003). Cognitive neuroscience of human social behaviour. *Nature Reviews Neuroscience,* Vol.4, pp.165-178, ISSN 1471-0048

Aoyama, S., Toshima, T., Saito, Y., Konishi, N., Motoshige, K., Ishikawa, N., Nakamura, K., & Kobayashi, M. (2010). Maternal breast milk odour induces frontal lobe activation in neonates: A NIRS study. *Early Human Development,* Vol.86, pp.541-545, ISSN 0378-3782

American Psychiatric Association. (2000). *Diagnostic and Statistical Manual of Mental Disorders, Fourth Edition, Text Revision (DSM-IV-TR).* American Psychiatric Association, ISBN 0-89042-025-4 Arlington, VA

Blasi, A., Fox, S., Everdell, N., Volein, A., Tucker, L., Csibra, G., Gibson, A. P., Hebden, J. C., Johnson, M. H., & Elwell, C. E. (2007). Investigation of depth dependent changes in cerebral haemodynamics during face perception in infants. *Physics in Medicine and Biology,* Vol.52, pp.6849-6864, ISSN 0031-9155

Brazy, J. E., Lewis, D. V., Mitnick, M. H., & Vandervliet, F. F. J. (1985). Noninvasive Monitoring of cerebral oxygenation in preterm infants: Preliminary observations. *Pediatrics,* Vol.75, pp.217-225, ISSN 0031-4005

Carlsson, J., Lagercrantz, H., Olson, L., Printz, G., & Bartocci, M. (2008). Activation of the right fronto-temporal cortex during maternal facial recognition in young infants. *Acta Paediatrica,* Vol.97, pp.1221-1225, ISSN 0803-5253

Csibra., G., Henty., J., Volein., Á., Elwell., C., Tucker., L., Meek., J., & Johnson., M. H. (2004). Near infrared spectroscopy reveals neural activation during face perception in infants and adults. *Journal of pediatric neurology,* Vol.2, pp.85-89, ISSN 1304-2580

de Haan, M., Johnson, M. H., & Halit, H. (2003). Development of face-sensitive event-related potentials during infancy: a review. *International Journal of Psychophysiology,* Vol.51, pp.45-58, ISSN 0167-8760

Fantz, R. L. (1961). The origin of form perception. *Scientific American,* Vol.204, pp.66-72, ISSN 0036-8733

Fombonne, E. (2005). Epidemiological surveys of pervasive developmental disorders, In: *Autism and pervasive developmental disorders.* Volkmar, F. R., Paul, R., Klin A., & Cohen D. pp.42–69, Cambridge University Press. ISBN 0-471-71696-0, New York. USA

Gervain, J., Mehler, J., Werker, J. F., Nelson, C. A., Csibra, G., Lloyd-Fox, S., Shukla, M., & Aslin, R. N. (2011). Near-infrared spectroscopy: A report from the McDonnell infant methodology consortium. *Developmental Cognitive Neuroscience,* Vol.1, pp.22-46, ISSN 1878-9293

Gilbert, S. J., Meuwese, J. D. I., Towgood, K. J., Frith, C. D., & Burgess, P. W. (2009). Abnormal functional specialization within medial prefrontal cortex in high-functioning autism: a multi-voxel similarity analysis. *Brain,* Vol.132, pp.869-878, ISSN 0006-8950

Goff, D. A., Buckley, E. M., Durduran, T., Wang, J., & Licht, D. J. (2010). Noninvasive cerebral perfusion imaging in high-risk neonates. *Seminars in Perinatology,* Vol.34, pp.46-56, ISSN 0146-0005

Grossmann, T., & Johnson, M. H. (2007). The development of the social brain in human infancy. *European Journal of Neuroscience,* Vol.25, pp.909-919, ISSN 0953-816X

Grossmann, T., Johnson, M. H., Lloyd-Fox, S., Blasi, A., Deligianni, F., Elwell, C., & Csibra, G. (2008). Early cortical specialization for face-to-face communication in human infants. *Proceedings of the Royal Society B-Biological Sciences,* Vol.275, pp.2803-2811, ISSN 0962-8452

Homae, F., Watanabe, H., Nakano, T., & Taga, G. (2007). Prosodic processing in the developing brain. *Neuroscience Research,* Vol.59, pp.29-39, ISSN 0168-0102

Homae, F., Watanabe, H., Otobe, T., Nakano, T., Go, T., Konishi, Y., & Taga, G. (2010). Development of global cortical networks in early infancy. *Journal of Neuroscience,* Vol.30, pp.4877-4882, ISSN 1529-2401

Honda, Y., Nakato, E., Otsuka, Y., Kanazawa, S., Kojima, S., Yamaguchi, M. K., & Kakigi, R. (2010). How do infants perceive scrambled face?: A near-infrared spectroscopic study. *Brain Research,* Vol.1308, pp.137-146, ISSN 0006-8993

Hoshi, Y. (2007). Functional near-infrared spectroscopy: Current status and future prospects. Journal of Biomedical Optics, Vol.12, pp.062106-1–062106-9, ISSN 1083-3668

Hyde, D. C., Boas, D. A., Blair, C., & Carey, S. (2010). Near-infrared spectroscopy shows right parietal specialization for number in pre-verbal infants. *Neuroimage,* Vol.53, pp.647-652, ISSN 1053-8119

Ichikawa, H., Kanazawa, S., Yamaguchi, M. K., & Kakigi, R. (2010). Infant brain activity while viewing facial movement of point-light displays as measured by near-infrared spectroscopy (NIRS). *Neuroscience Letters,* Vol.482, pp.90-94, ISSN 0304-3940

Ito, H., Yamauchi, H., Kaneko, H., Yoshikawa, T., Nomura, K., & Honjo, S. (2011). Prefrontal overactivation, autonomic arousal, and task performance under evaluative pressure: A near-infrared spectroscopy (NIRS) study. *Psychophysiology*, pp.1563-1571, ISSN 1469-8986

Jöbsis, F. F. (1977). Noninvasive, infrared monitoring of cerebral and myocardial oxygen sufficiency and circulatory parameters. *Science,* Vol.198, pp.1264-1267, ISSN 0036-8075

Johnson, M. H. (2005). Subcortical face processing. *Nature Reviews Neuroscience,* Vol.6, pp.766-774, ISSN 1471-0048

Kaneko, H., Yoshikawa, T., Nomura, K., Ito, H., Yamauchi, H., Ogura, M., & Honjo, S. (2011). Hemodynamic changes in the prefrontal cortex during digit span task: A near-infrared spectroscopy study. *Neuropsychobiology,* Vol.63, pp.59-65, ISSN 0302-282X

Kanwisher, N., & Yovel, G. (2006). The fusiform face area: a cortical region specialized for the perception of faces. *Philosophical Transactions of the Royal Society B-Biological Sciences,* Vol.361, pp.2109-2128, ISSN 0962-8436

Kawakubo, Y., Kuwabara, H., Watanabe, K., Minowa, M., Someya, T., Minowa, I., Kono, T., Nishida, H., Sugiyama, T., Kato, N., & Kasai, K. (2009). Impaired prefrontal hemodynamic maturation in autism and unaffected siblings. *PLoS One,* Vol.4, ISSN 1932-6203

Kim, P., Feldman, R., Mayes, L. C., Eicher, V., Thompson, N., Leckman, J. F., & Swain, J. E. (2011). Breastfeeding, brain activation to own infant cry, and maternal sensitivity. *Journal of Child Psychology and Psychiatry,* Vol.52, pp.907-915, ISSN 0021-9630

Koshino, H., Kana, R. K., Keller, T. A., Cherkassky, V. L., Minshew, N. J., & Just, M. A. (2008). fMRI investigation of working memory for faces in autism: Visual coding and underconnectivity with frontal areas. *Cerebral Cortex,* Vol.18, pp.289-300, ISSN 1047-3211

Kringelbach, M. L. (2005). The human orbitofrontal cortex: Linking reward to hedonic experience. *Nature Reviews Neuroscience,* Vol.6, pp.691-702, ISSN 1471-0048

Lenzi, D., Trentini, C., Pantano, P., Macaluso, E., Iacoboni, M., Lenzi, G. L., & Ammaniti, M. (2009). Neural basis of maternal communication and emotional expression processing during infant preverbal stage. *Cerebral Cortex,* Vol.19, pp.1124-1133, ISSN 1047-3211

Leppanen, J. M., & Nelson, C. A. (2009). Tuning the developing brain to social signals of emotions. *Nature Reviews Neuroscience,* Vol.10, pp.37-47, ISSN 1471-0048

Lloyd-Fox, S., Blasi, A., & Elwell, C. E. (2010). Illuminating the developing brain: The past, present and future of functional near infrared spectroscopy. *Neuroscience and Biobehavioral Reviews,* Vol.34, pp.269-284, ISSN 0149-7634

Meresse, I. G., Zilbovicius, M., Boddaert, N., Robel, L., Philippe, A., Sfaello, I., Laurier, L., Brunelle, F., Samson, Y., Mouren, M. C., & Chabane, N. (2005). Autism severity and temporal lobe functional abnormalities. *Annals of Neurology,* Vol.58, pp.466-469, ISSN 0364-5134

Minagawa-Kawai, Y., Matsuoka, S., Dan, I., Naoi, N., Nakamura, K., & Kojima, S. (2009). prefrontal activation associated with social attachment: Facial-emotion recognition in mothers and infants. *Cerebral Cortex,* Vol.19, pp.284-292, ISSN 1047-3211

Minagawa-Kawai, Y., Mori, K., Hebden, J. C., & Dupoux, E. (2008). Optical Imaging of infants' neurocognitive development: Recent advances and perspectives. *Developmental Neurobiology,* Vol.68, pp.712-728, ISSN 1932-8451

Moriguchi, Y., & Hiraki, K. (2009). Neural origin of cognitive shifting in young children. *Proceedings of the National Academy of Sciences of the United States of America,* Vol.106, pp.6017-6021, ISSN 0027-8424

Moriguchi, Y., & Hiraki, K. (2011). Longitudinal development of prefrontal function during early childhood. *Developmental Cognitive Neuroscience,* Vol.1, pp.153-162, ISSN 1878-9293

Moser, S. J., Schroeter, M. L., Cutini, S., & Weber, P. (2009). Right prefrontal brain activation due to Stroop interference is altered in attention-deficit hyperactivity disorder — A functional near-infrared spectroscopy study. *Psychiatry Research-Neuroimaging,* Vol.173, pp.190-195, ISSN 0925-4927

Nakano, T., Watanabe, H., Homae, F., & Taga, G. (2009). Prefrontal cortical involvement in young infants' analysis of novelty. *Cerebral Cortex,* Vol.19, pp.455-463, ISSN 1047-3211

Nakato, E., Otsuka, Y., Kanazawa, S., Yamaguchi, M. K., Honda, Y., & Kakigi, R. (2011a). I know this face: Neural activity during mother' face perception in 7- to 8-month-old infants as investigated by near-infrared spectroscopy. *Early Human Development,* Vol.87, pp.1-7, ISSN 0378-3782

Nakato, E., Otsuka, Y., Kanazawa, S., Yamaguchi, M. K., & Kakigi, R. (2011b). Distinct differences in the pattern of hemodynamic response to happy and angry facial expressions in infants - A near-infrared spectroscopic study. *Neuroimage,* Vol.54, pp.1600-1606, ISSN 1053-8119

Nakato, E., Otsuka, Y., Kanazawa, S., Yamaguchi, M. K., Watanabe, S., & Kakigi, R. (2009). When do infants differentiate profile face from frontal face? A near-infrared spectroscopic study. *Human Brain Mapping,* Vol.30, pp.462-472, ISSN 1065-9471

Negoro, H., Sawada, M., Iida, J., Ota, T., Tanaka, S., & Kishimoto, T. (2010). Prefrontal dysfunction in attention-deficit/hyperactivity disorder as measured by near-infrared spectroscopy. *Child Psychiatry and Human Development,* Vol.41, pp.193-203, ISSN 0009-398X

Neuhaus, E., Beauchaine, T. P., & Bernier, R. (2010). Neurobiological correlates of social functioning in autism. *Clinical Psychology Review,* Vol.30, pp.733-748, ISSN 0272-7358

Noriuchi, M., Kikuchi, Y., & Senoo, A. (2008). The functional neuroanatomy of maternal love: Mother's response to infant's attachment behaviors. *Biological Psychiatry,* Vol.63, pp.415-423, ISSN 0006-3223

O'Doherty, J., Winston, J., Critchley, H., Perrett, D., Burt, D. M., & Dolan, R. J. (2003). Beauty in a smile: the role of medial orbitofrontal cortex in facial attractiveness. *Neuropsychologia,* Vol.41, pp.147-155, ISSN 0028-3932

Otsuka, Y., Nakato, E., Kanazawa, S., Yamaguchi, M. K., Watanabe, S., & Kakigi, R. (2007). Neural activation to upright and inverted faces in infants measured by near infrared spectroscopy. *Neuroimage,* Vol.34, pp.399-406, ISSN 1053-8119

Pinkham, A. E., Hopfinger, J. B., Pelphrey, K. A., Piven, J., & Penn, D. L. (2008). Neural bases for impaired social cognition in schizophrenia and autism spectrum disorders. *Schizophrenia Research,* Vol.99, pp.164-175, ISSN 0920-9964

Saito, Y., Aoyama, S., Kondo, T., Fukumoto, R., Konishi, N., Nakamura, K., Kobayashi, M., & Toshima, T. (2007). Frontal cerebral blood flow change associated with infant-directed speech. *Archives of Disease in Childhood-Fetal and Neonatal Edition,* Vol.92, pp.F113-F116, ISSN 1359-2998

Saito, Y., Fukuhara, R., Aoyama, S., & Toshima, T. (2009). Frontal brain activation in premature infants' response to auditory stimuli in neonatal intensive care unit. *Early Human Development,* Vol.85, pp.471-474, ISSN 0378-3782

Saito, Y., Kondo, T., Aoyama, S., Fukumoto, R., Konishi, N., Nakamura, K., Kobayashi, M., & Toshima, T. (2007). The function of the frontal lobe in neonates for response to a prosodic voice. *Early Human Development,* Vol.83, pp.225-230, ISSN 0378-3782

Smyke, A. T., Koga, S. F., Johnson, D. E., Fox, N. A., Marshall, P. J., Nelson, C. A., Zeanah, C. H., & Grp, B. C. (2007). The caregiving context in institution-reared and family-reared infants and toddlers in Romania. *Journal of Child Psychology and Psychiatry,* Vol.48, pp.210-218, ISSN 0021-9630

Sonuga-Barke, E. J. (2003). The dual pathway model of AD/HD: an elaboration of neuro-developmental characteristics. *Neuroscience & Biobehavioral Reviews,* Vol.27, pp.593-604, ISSN 0149-7634

Strangman, G., Boas, D. A., & Sutton, J. P. (2002). Non-invasive neuroimaging using near-infrared light. Biological Psychiatry, Vol.52, pp.679-693, ISSN 0006-3223

Taga, G., & Asakawa, K. (2007). Selectivity and localization of cortical response to auditory and visual stimulation in awake infants aged 2 to 4 months. *Neuroimage,* Vol.36, pp.1246-1252, ISSN 1053-8119

Taga, G., Asakawa, K., Maki, A., Konishi, Y., & Koizumi, H. (2003). Brain imaging in awake infants by near-infrared optical topography. *Proceedings of the National Academy of Sciences of the United States of America,* Vol.100, pp.10722-10727, ISSN 0027-8424

Tsao, D. Y., & Livingstone, M. S. (2008). Mechanisms of face perception *Annual Review of Neuroscience* Vol. 31, pp. 411-437, ISSN 0147-006X

Tsujii, T., Yamamoto, E., Masuda, S., & Watanabe, S. (2009). Longitudinal study of spatial working memory development in young children. *Neuroreport,* Vol.20, pp.759-763, ISSN 0959-4965

Tsujii, T., Yamamoto, E., Ohira, T., Takahashi, T., & Watanabe, S. (2010). Antihistamine effects on prefrontal cortex activity during working memory process in preschool children: A near-infrared spectroscopy (NIRS) study. *Neuroscience Research,* Vol.67, pp.80-85, ISSN 0168-0102

Tsujimoto, S., Yamamoto, T., Kawaguchi, H., Koizumi, H., & Sawaguchi, T. (2004). Prefrontal cortical activation associated with working memory in adults and preschool children: An event-related optical topography study. *Cerebral Cortex,* Vol.14, pp.703-712, ISSN 1047-3211

Tsukiura, T., & Cabeza, R. (2011). Remembering beauty: Roles of orbitofrontal and hippocampal regions in successful memory encoding of attractive faces. *Neuroimage,* Vol.54, pp.653-660, ISSN 1053-8119

Watanabe, H., Homae, F., & Taga, G. (2010). General to specific development of functional activation in the cerebral cortexes of 2- to 3-month-old infants. *Neuroimage,* Vol.50, pp.1536-1544, ISSN 1053-8119

Weber, P., Lutschg, J., & Fahnenstich, H. (2005). Cerebral hemodynamic changes in response to an executive function task in children with attention-deficit hyperactivity disorder measured by near-infrared spectroscopy. *Journal of Developmental and Behavioral Pediatrics,* Vol.26, pp.105-111, ISSN 0196-206X

Wilcox, T., Bortfeld, H., Woods, R., Wruck, E., Armstrong, J., & Boas, D. (2009). Hemodynamic changes in the infant cortex during the processing of featural and spatiotemporal information. *Neuropsychologia,* Vol.47, pp.657-662, ISSN 0028-3932

Wilcox, T., Bortfeld, H., Woods, R., Wruck, E., & Boas, D. A. (2008). Hemodynamic response to featural changes in the occipital and inferior temporal cortex in infants: a preliminary methodological exploration. *Developmental Science,* Vol.11, pp.361-370, ISSN 1363-755X

Wilcox, T., Haslup, J. A., & Boas, D. A. (2010). Dissociation of processing of featural and spatiotemporal information in the infant cortex. *Neuroimage,* Vol.53, pp.1256-1263, ISSN 1053-8119

Wyatt, J. S., Delpy, D. T., Cope, M., Wray, S., & Reynolds, E. O. R. (1986). Quantification of Cerebral oxygenation and hemodynamics in sick newborn-infants infrared spectrophotometry. *Lancet,* Vol.2, pp.1063-1066, ISSN 0140-6736

Section 2

Cereals, Fruits and Plants

11

The Application of Near Infrared Spectroscopy in Wheat Quality Control

Milica Pojić[1], Jasna Mastilović[1] and Nineta Majcen[2]
[1]*University of Novi Sad, Institute of Food Technology*
[2]*Metrology Institute of the Republic of Slovenia, Celje*
[1]*Serbia*
[2]*Slovenia*

1. Introduction

The application of near infrared spectroscopic technique for the quantitative analysis of food products and commodities is nowadays widely accepted. However, 160 years passed from the discover of near infrared part of the spectrum to its first analytical application which is related to the work of Karl Norris who firstly demonstrated the potential of the NIRS in quantitative analysis particularly for prediction of moisture and protein content in wheat. The intense development of this technique during the last 50 years has been challenged by the development of powerful computers, softwares and chemometric tools, since the NIRS data processing is quite demanding task. The near infrared spectroscopy is an instrumental technique based on measuring the intensity of reflectance or intensity of transmission of radiation from the near infrared region of the electromagnetic spectrum (800-2500 nm) by the test sample. The intensity of the reflection and transmission depends on the rate of absorption of radiation by the sample, which leads to excitation of hydrogen bonds (CH, NH, OH). As the tested samples are very complex in composition, it happens that on the same wavelength, several organic bonds involving hydrogen vibrate producing overlapped spectral bands. Therefore, the resulting NIR spectrum looks like a slightly wavy line with no clearly defined features, with very broad and overlapped molecular overtone and combination bands, which complicate to assign them to specific chemical constituent and make impossible to determine the direct relationship between the concentration of ingredients of interest and the absorbed radiation energy (Fig. 1).

Due to the significant overlapping of NIR bands, the prerequisite for the NIRS application is the development of the calibration model which relates the concentration of certain analyte found in a sample to the spectral data collected from that sample. Calibration model development process implies the extraction of useful information from the NIR spectra by applying chemometrics methods. Multivariate calibration techniques (e.g. principal components analysis, partial least squares, or artificial neural networks) are often employed to extract the desired chemical information from the spectral data. Calibration model allows relating the NIR optical data with the compound (or property) of interest that is used to define the quality of the sample:

$$[C] = [A][\beta] + [\varepsilon] \quad (1)$$

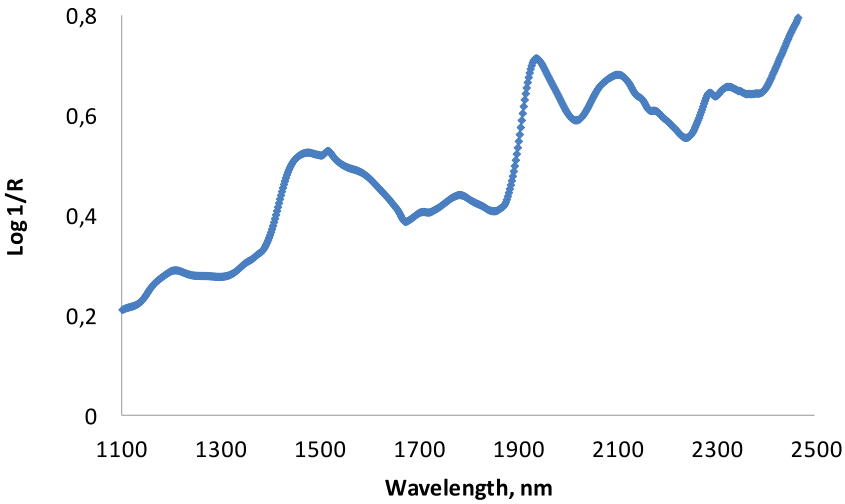

Fig. 1. NIR reflectance spectrum of wheat flour (1100-2500 nm) recorded by FOSS's NIRSystem 6500

Also, the application of NIRS technique has been extended to determination of certain functional properties of tested samples which do not represent the unique chemical entities which manifest absorption in NIRS spectral region, but manifest relationship with certain constituents that can be used as a basis for calibration model development. So far, a number of applications of the NIRS technique have been demonstrated having commercial and/or scientific significance that was developed on the basis on different NIR spectral ranges, different ways of recording and processing of spectra, different sample presentations, various chemometrics techniques used for calibration development and different use of validation statistics.

2. Near infrared spectroscopy: A rapid analytical tool in cereal quality control

In the 60s, the initial application of the NIRS technique in routine analysis was demonstrated and it was related to the determination of moisture and protein in cereals. The first stage of commercial application of the NIRS technique, during the 1970s, was predominantly related to the prediction of protein, moisture and oil content in cereals. In the second stage, during the 1980s, the NIRS prediction of more complex constituents such as complex carbohydrates was enabled. The third stage of NIRS application in cereal technology has been related to the prediction of functional properties of grains. The success of this technique lays in numerous advantages it offers over wet chemical analysis such as:

- Significant reduction of testing time,
- No requirement for the use of chemicals and their preparation,
- No requirement for the sample preparation
- No requirement for additional technical expertise to carry out examination

However, the application of NIR spectroscopy is characterized by the relevant restrictions, which are primarily related to the nature of NIRS as an indirect method (Dowell et al., 2006; Jirsa et al., 2008; Miralbés, 2008; Pierce et al., 1996; Pojić et al. 2002; Pojić et al., 2003). To

facilitate the application of this method, it is necessary to develop the calibration model by which the obtained spectral data are translated into the required result – the content of the selected compound of interest, and it is often necessary to check and update the calibration models due to changes in the sample matrix. However, this restriction has been significantly overcome by development and application of calibration models based on artificial neural networks that handle very large data set and proved to be very accurate, stable, transferable and therefore globally applicable (Büchman et al, 2001).

The potential of wheat to be processed in wide range of different final products gives it the significance of upmost grain of commerce (Williams, 2002). Application of the NIRS technique in wheat quality control has been characterized by rapid development from prediction of major constituents in wheat grains (moisture, protein, oil starch, cellulose) to prediction of functional properties of wheat that define its capability to meet the requirements of the intended purposes (production of bread, pastry, cookies, pasta). Since the functionality of the commodity is strongly affected by its physico-chemical properties which do not manifest characteristics absorption in NIR spectral region, the use of NIRS to predict functionality is based on the relationship between physico-chemical properties and certain constituent having absorptions in NIR region (protein, oil, starch etc) (Williams, 2007). The value of wheat grain is dependent on its composition, functionality and safety, that all have an equal importance in wheat breeding, trade and processing (Fig. 2) (Williams, 2002).

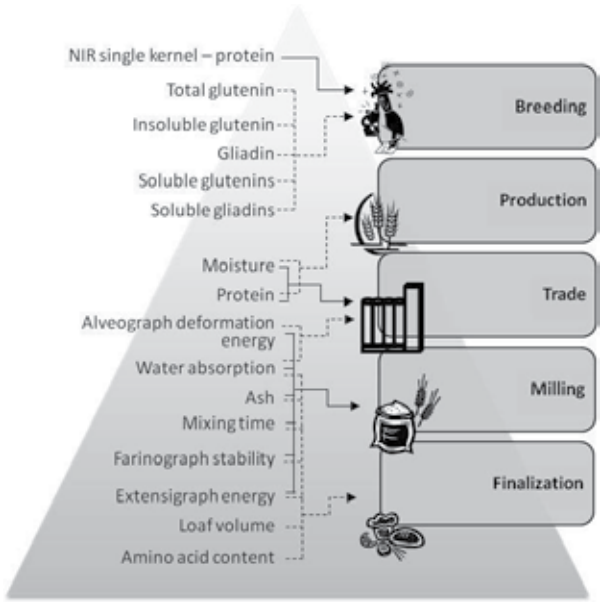

Fig. 2. The relationship between different NIRS applications in wheat quality control

2.1 The role of NIRS in cereal breeding

The breeding purposes require the knowledge on both composition and functional properties of grain, whilst the functionality of wheat grain has always been an issue of a great concern for wheat breeders. Functionality in wheat includes prediction of milling yield, kernel texture, rheological parameters of dough, loaf volume, product appearance,

etc. Most of these parameters are dependent on the protein-proteinase complex of wheat grain and the condition of carbohydrate complex as well (Williams, 2007).

First attempt to determine the functional properties of wheat was made by Rubenthaler and Pomeranz (1987) by development of NIRS model for prediction of water absorption, mixing time and loaf volume. The following work presented by Williams et al. (1988) showed the potential of NIRS to predict Farinograph stability, Extensigraph energy and Alveograph deformation energy. Further research reported by Pawlinsky and Williams (1998), Hrušková et al. (2001), Hrušková and Šmejda (2003), Miralbés (2003, 2004), Dowell et al. (2006) and Vázquez et al. (2007) were carried out by using analyzers of higher generation – scanning monochromators. The efficiency of the models developed were affected by the form of the samples used (whole grain, ground grain or flour), by the composition of the sample sets which were insufficiently variable and by the inherent variability of the reference rheological methods.

One of the first attempts to develop NIRS calibration model for prediction of protein composition was made by Delwiche et al. (1998). It was possible due to the fact that the main fractions of gluten - glutenin and gliadin, exhibit some differences in their NIR spectra which enable them to be determined in mixtures with starch (Wesley et al., 1999) Total glutenin, insoluble glutenin and gliadin contents can also be measured in whole wheat kernel by NIRS against HPLC as a reference method (Delwiche et al., 1998; Dowel et al., 2006; Wesley et al., 1999; Seabourn et al., 1998; Wesley, 2001) with sufficient accuracy for screening purposes in breeding programs. Although some authors has recommended the use of instrument with a monochromator in reflectance mode over the range of 2000 to 2300 nm for these application (Wesley, 2001),it has been proved that use of instruments in transmittance mode with narrower spectral range below 2000 nm could also be applicable (Dowell et al., 2006; Scholz et al., 2007). Concerning the carbohydrate complex of grain, the NIR spectra of amylose and amylopectin are very similar since they consist of the same glucose unit. Therefore, very little progress has been made in estimating the quality of carbohydrate components in wheat. Scanning visible–NIR spectrophotometers are often applicable for research and development purposes, since this application requires wider spectral ranges such as 400-2500 nm, 400-1700 nm, 1100-2500 or 1000-2600 nm. Also, since breeders commonly face with insufficient quantity of samples, the development of NIRS single kernel characterization systems has been initiated.

2.2 The role of NIRS in cereal trade

Methods based on near infrared spectroscopy are accepted worldwide for cereal quality control in trade, especially according to the fact that it is capable of generating results for several quality parameters rapidly and in a non-destructive way. Although different countries established their own systems for classifying wheat on the basis of different quality parameters, wheat grading systems is commonly based on the wheat protein content (Williams, 2007; Hulasare et al., 2003; Váradi et al., 1999). The price of wheat is dependent on the protein content, often with substantial price increments between grades. Measuring protein content in wheat and wheat flour has been demonstrated as successful NIRS application due to its strong and broad absorption bands in the NIR region which affect easy calibration model development. Therefore, the segregation or blending grain prior to delivery is inconceivable without the use of NIR technology. When using NIR analysis for

above mentioned purposes, special attention must be paid to demonstrate that it generates technically valid results satisfying the regulatory requirements for analytical procedures. Stand-alone bench type instruments, designed for testing whole grains by measuring the intensity of transmission of NIR radiation from the spectral range 850-1050 nm are the most suitable for cereal trade purposes. Moreover, the measurement infrastructure comprised of the network of NIRS instrument significantly improved the cereal testing in trade.

2.2.1 The role of NIRS networks

A significant advance in the application of the NIRS technique in cereal trade has been achieved by the development of global ANN calibration models, and by the establishment of measurement infrastructure composed of multiple NIRS devices interconnected in the network. Operation of the NIRS instruments through the network significantly improved the routine application of NIRS method, eliminated specified shortcomings and significantly facilitated the application of the NIRS method for the end-users. Hence, the independent measurements of protein content that are internationally equivalent have triggered off the establishment the NIRS networks in many countries around the world (Büchman, 1996; Pojić & Mastilović, 2006).

NIRS networks are formed in order to:

- ensure metrological traceability of results of measurement of grain quality
- define the common interests of entities involved in the network system
- distribute costs and improve network operation domain

Establishing a network of NIRS devices allows achieving of the same level of accuracy of determining the protein content regardless of location of devices. In addition, the NIRS networks ensure reliability and uniformity of quality control of grain crops as well as simplification of procedures for calibration model monitoring and their improvement.

NIRS network consists of two to several hundred or even thousands of NIRS devices that are controlled and configured from the central so-called master device. The initial idea of operation of NIRS instruments through the network came from FOSS Analytical AB, and currently the most impressive networks worldwide consist of FOSS's instruments - scanning monochromator Infratec 1241 Grain Analyzer. The success of such measurement infrastructure is highly dependent on the network organization and procedures and tasks proposed and divided between:

- reference laboratory that analyze samples using the reference (wet chemical) tests and monitor performance of the used calibrations
- administrative center, which manages databases, communication between devices in the network and performs the standardization of network devices
- calibration center that develops new calibration models
- network management body for the decision-making on the organization of network and calibrations updates.

Procedures that enable undisturbed functioning of the NIRS network and confirm compliance of results obtained by wet chemical tests on the one hand and consistency of results of individual devices with the central (master) device on the other hand is achieved through the following activities:

- monitoring of the accuracy of measurements of the central (master) device,
- standardization of individual NIRS devices and
- monitoring of the stability of measurements of individual NIRS device.

2.3 The role of NIRS in cereal processing

Analytical methods based on near infrared spectroscopy have the potential to significantly improve the quality of final cereal products by testing the products through the entire production process in processing industry (raw materials, intermediate and final products). For these purposes, on-line instruments as well as stand-alone bench type instruments designed for testing whole grains by measuring the intensity of transmission of NIR radiation from the spectral range 850-1050 nm or the intensity of diffuse reflection of NIR radiation from the spectral range 1000-1400 nm are the most suitable. For example, the determination of ash by NIRS is particularly useful for process control in the wheat milling industry to monitor the consistency of milling and the compliance with flour specifications. Although inorganic substances do not absorb energy in the NIR spectral region, some authors demonstrated that the NIRS method can be used for reliable prediction of the ash content (Dowell et al, 2006; Deaville & Flinn, 2000; Osborne, 2007; Pérez-Marín et al., 2004; Armstrong et al., 2006; Mentink et al., 2006; Pojić et al., 2010). Since ash content cannot be directly measured by NIRS, it is assumed that it is predicted by correlation with the total amount of organic compounds and water present, because of the large number of wavelengths used in the process of calibration development that give significant information (Osborne, 2007; Clark et al., 1987; Garnsworthy et al., 2000; Frankhuizen, 2008).

3. Validation protocol for the NIRS method

Demonstration that the NIRS method is fit for intended purpose has the great importance for the compliance with regulations, process control, making regulatory decisions, support national and international trade, support research etc.

When we talk about the validation of the NIRS as an analytical method we must be aware of the duality of the term „validation'' used within the analytical chemists utilizing NIRS. The most common use of the term „validation" implies using an independent sample set to test the accuracy of the calibration model developed (Mark & Workman, 2007). That process results in certain statistical indicator explained later in the text. This process must be distinguished from the process of validation of NIR spectroscopic method aimed at confirmation, through the provision of objective evidence, that the requirements for a specific intended use of application are fulfilled (Lauwaars & Anklam, 2004; Dybkaer, 2011). Hence, the objective of the validation of the NIRS method is to demonstrate that its characteristics are suitable for its intended purpose. When we talk about the application of the NIRS method in wheat quality control, the validation experiment should include the testing of characteristics of NIRS method and demonstration its fitness for purpose.

The validation protocol that was performed in our laboratory in order to provide the evidence that the NIRS method as being applied in wheat quality control for protein content prediction fitted for purpose included: accuracy, repeatability, reproducibility, intermediate precision, linearity, robustness and transferability (Fig. 3). The NIRS instrument used was a

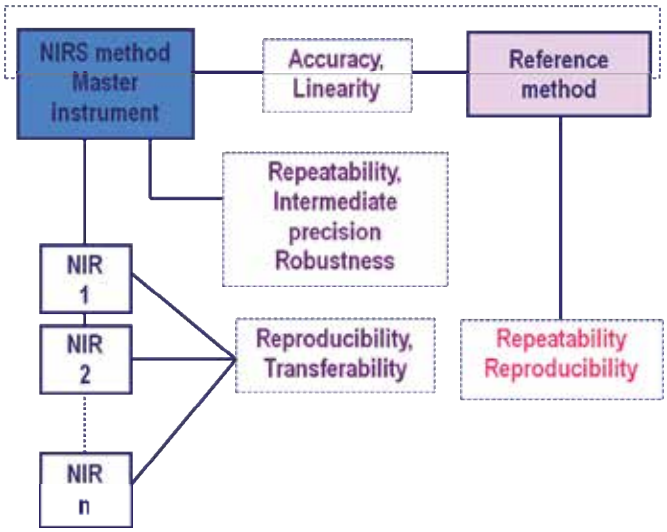

Fig. 3. The validation protocol of the NIRS method as being applied in wheat quality control

scanning monochromator Infratec 1241 Grain Analyzer with the ANN calibration model for protein content used in the transmittance mode (FOSS Analytical, Denmark).

3.1 Accuracy

Accuracy, defined as the closeness of agreement between a measured value and a true value of a measurand, in the case of the NIRS method expresses a measure of how well NIRS predicted value match a given reference value obtained by a reference (wet chemistry) method. The accuracy of the NIRS method is commonly described by statistical terms such as SEC (standard error of calibration), SECV (standard error of cross validation), R^2 (coefficient of determination), explained variance (1-VR), residual predictive deviation (RPD), standard error of prediction (SEP) etc. (Konieczka & Namieśnik, 2009). These values describe the agreement between the predicted NIRS values and the reference method values from the same sample (Ritchie et al., 2002; Moffat, 2004). SEC, SECV, R2 and 1-VR values are calculated on the basis of samples used to develop the calibration model itself, whilst the SEP value is calculated on the basis of independent sample set not included in the calibration model development procedure:

$$SEP = \sqrt{\frac{\sum_{i=1}^{N}(y_r - y_p)^2}{N-1}} \tag{2}$$

where y_r is the reference value of *i* samples, y_p is the NIRS predicted value of i sample, N the number of samples.

The selection of suitable statistical term to express the accuracy of the NIRS method depends on the availability of the samples covering the whole range of component concentration with its even distribution. The accuracy of the NIRS method to a large extent is influenced by nonhomogeneity of sample, laboratory error, physical and chemical variation in sample

with time, population sampling error, different nature of spectroscopic and wet chemical measurements, instrument noise, sample presentation, calibration modeling, calibration transfer etc. (Workman, Jr., 2008). Statistical term used to express a systematic difference between the two sets of results obtained by the reference method and the NIRS method is bias (Workman, Jr., 2008; Shenk et al., 2008):

$$\text{Bias} = \frac{\sum_{i=1}^{N}(y_r - y_p)}{N} \tag{3}$$

where y_r is the reference value of *i* samples, y_p is the NIRS predicted value of i sample, N the number of samples.

The accuracy can be improved by a bias and slope adjustment, but it requires precaution due to the fact that the bias only fixes the problem on a temporary basis.

Subsamples	1. validation set			2. validation set		
	BIAS, %	RMSEP, %	SEP, %	BIAS, %	RMSEP, %	SEP, %
5	-0.32[a]	0.4887[a]	0.3851[a]	0.03[a]	0.2461[a]	0.2494[a]
7	-0.30[a]	0.4926[a]	0.4028[a]	0.02[a]	0.2385[a]	0.2444[a]
10	-0.32[a]	0.5096[a]	0.4088[a]	0.04[a]	0.2474[a]	0.2517[a]

Values in the same column marked with the same letters are no significantly different (P <0.05, LSD test)

Table 1. The predictive ability of the NIRS model for protein content prediction depending on the number of subsamples in a single measurement

The accuracy of the NIRS method was evaluated by calculating bias, RMSEP and SEP in three different cases, using five, seven and ten subsamples in a single NIRS measurement. To determine the accuracy of protein content prediction, two independent validation sample sets were used where the first validation set was used before, and the second one after the bias correction. The parameters of predictive ability of protein content (RMSEP and SEP) were not influenced by variable number of subsamples. Bias adjustment affected better predictive ability for protein content expressed by lower RMSEP and SEP values for the second validation set (Table 1). By the assessment of comparable views of protein content obtained by the reference and NIRS method from measurements of 5, 7 and 10 subsamples, before and after bias adjustment, the negligible difference between the reference and NIRS method could be noticed after the bias adjustment regardless the number of subsamples in a single measurement (Fig. 4).

3.2 Precision (repeatability, reproducibility)

Precision is more important NIRS method characteristics than accuracy since it cannot be changed by a simple adjustment. It is affected by the instrument, the calibration and the operator. Precision can be defined as the closeness of agreement between measured values obtained by replicate measurements on the same or similar objects under specified conditions. It is commonly associated with random errors and represents a measure of

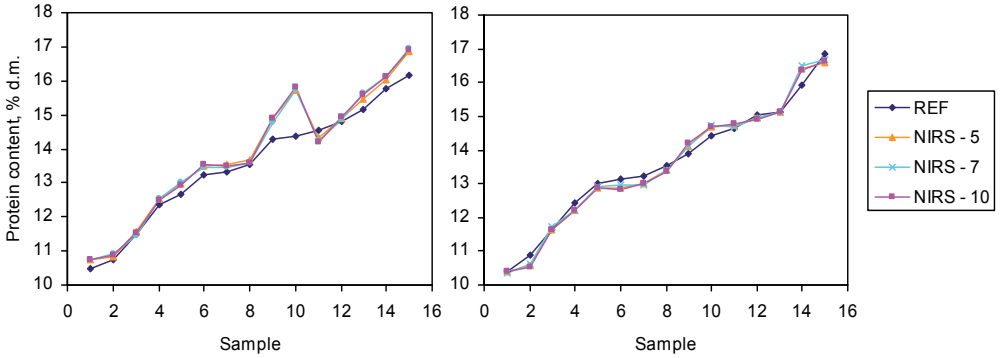

Fig. 4. Comparable view of protein content obtained by the NIRS and reference method, derived from 5, 7 and 10 subsamples, before and after bias adjustment

dispersion of results around the mean value. The precision can be considered by monitoring of repeatability, intermediate precision and reproducibility. All of them can be quantified on the basis of standard deviation, relative standard deviation, or the coefficient of variation (Konieczka & Namieśnik, 2009).

3.2.1 Repeatability

Repeatability is a method characteristic that indicates the measure of dispersion of results obtained under the same measurement conditions (a given laboratory, analyst, measuring instrument, reagents, etc.). Since the recommendation for repeatability determination implies measurements on samples characterized with different analyte concentrations and different matrix composition, repeatability of the NIRS methods for protein content prediction included eight consecutive measurements under the repeatability condition using a set of 15 samples.

To assess the acceptability of the repeatability, a modified Horwitz's equation can be used:

$$RSD_r = 2^{(1-0,5\log C)} * 0,67 \quad (4)$$

where the acceptable repeatability is determined on the basis of comparison of actual relative standard deviation ($RSD_{r,i}$) calculated from measured values and predicted relative standard deviation (RSD_r) calculated from the Horwitz's equation:

$$RSD_{r,i} < RSD_r \quad (5)$$

The results showed in Table 2 indicates that the repeatability of the NIRS method is better than that of the reference methods expressed by lower $SD_{r,i}$, $RSD_{r,i}$ and r_i.

The results shown in Fig. 5 show that repeatability relative standard deviation calculated from actual NIRS results for protein content ($RSD_{r,i}$) are lower than Horwitz's relative standard deviation (RSD_r). Thereby, the criterion of repeatability of NIRS method for protein content prediction is fulfilled.

	REF method			NIRS method		
	$SD_{r,i}$, %	$RSD_{r,i}$, %	r_i	$SD_{r,i}$, %	$RSD_{r,i}$, %	r_i
Mean	0,0858	0,6301	0,2401	0,0755	0,5736	0,2113
Min	0,0503	0,3540	0,1408	0,0041	0,0280	0,0115
Max	0,2484	1,7407	0,6955	0,1173	1,0867	0,3284

Table 2. Results that define the repeatability of the reference and NIRS methods for protein content determination

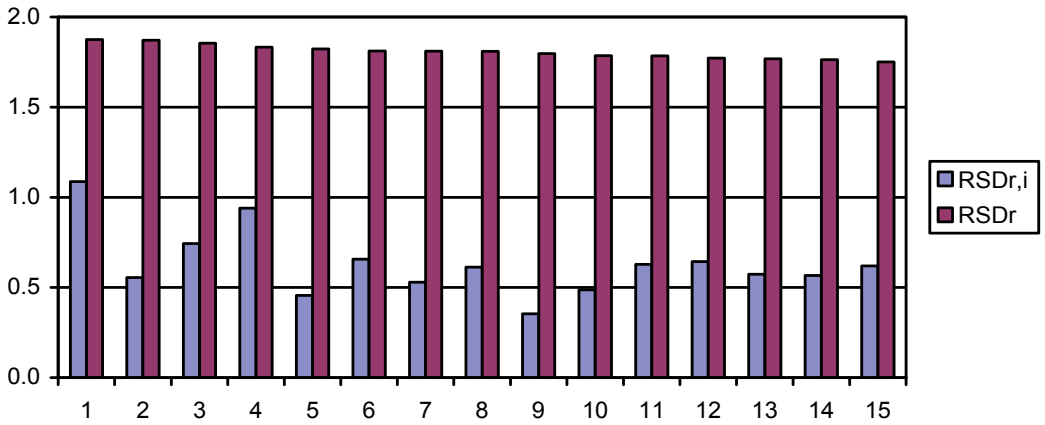

Fig. 5. Comparable view of actual $RSD_{r,i}$ and Horwitz's RSD_r values for determining protein content by the NIRS method

3.2.2 Reproducibility

Reproducibility is a method characteristic that indicates the measure of dispersion of results obtained in different laboratories using a given measurement method. To assess the reproducibility of NIRS determination of protein in wheat with the Infratec 1241, set of 15 samples was measured with the 5 available NIRS anaylzers Infratec 1241. As a criterion for the acceptability of the reproducibility the HORRAT value was used, which was calculated by dividing the actual value of $RSD_{R,i}$ and RSD_R calculated from the Horwitz equation:

$$HORRAT_R = RSD_{R,i} / RSD_R \quad (6)$$

Values lower than 2.0 are considered acceptable for among-laboratory precision, expressed as a $HORRAT_R$ value (Fig. 6).

The results showed in Table 3 indicates that the reproducibility of the NIRS method is better than that of the reference methods expressed by lower $SD_{R,i}$, $RSD_{R,i}$ and R_i.

The results shown in Fig. 6 indicates excellent reproducibility of the NIRS method as being applied for protein content prediction by the chosen NIRS instrument (Infratec 1241, FOSS Analytical AB) since all HORRAT values were less than 2.

	REF method			NIRS method		
	$SD_{R,i}$, %	$RSD_{R,i}$, %	R_i	$SD_{R,i}$, %	$RSD_{R,i}$, %	R_i
Mean	0,1743	1,400	0,4872	0,0712	0,5449	0,1993
Min	0,1231	0,9613	0,3443	0,0350	0,2178	0,0980
Max	0,2622	1,9544	0,7320	0,1825	1,6357	0,5110

Table 3. Results that define the reproducibility of the reference and NIRS methods for protein content determination

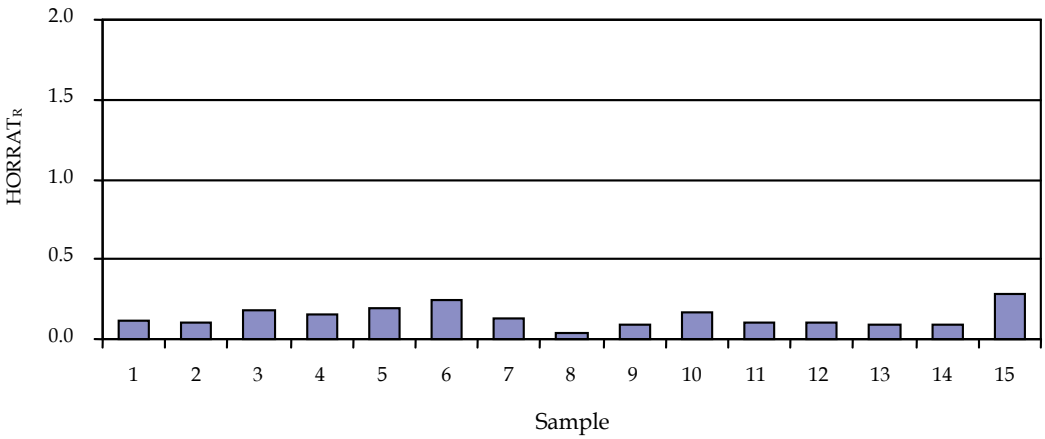

Fig. 6. HORRAT values for assessing the reproducibility of NIRS method for determining protein content

3.2.3 Intermediate precision

Intermediate precision is a method characteristic that indicates the measure of dispersion of results obtained in a given laboratory over a long-term process of measuring defining the long-term stability or variability of a measurement process. In this way, the influence of various random effects in the measurement process (e.g. personal effects, instrumental effects, environmental effects etc.) can be monitored and quantified. Due to that, this characteristic has a wider scope than repeatability. The intermediate precision for protein content prediction was monitored over 62 days by using control (Shewart) chart (Fig. 7), having a key significance for raising wheat quality control system to the highest level. Even in cases where the measurement process is under control, control chart is a valuable tool for detection the disturbances in the measuring process. Also, this type of control represents a contribution to the accreditation of the NIRS method based on the requirements of ISO/IEC 17025.

The results shown in Fig. 7 indicats excellent stability of the NIRS method as being applied for protein content prediction by the chosen NIRS instrument (Infratec 1241, FOSS Analytical AB) since all measured values are within control limits.

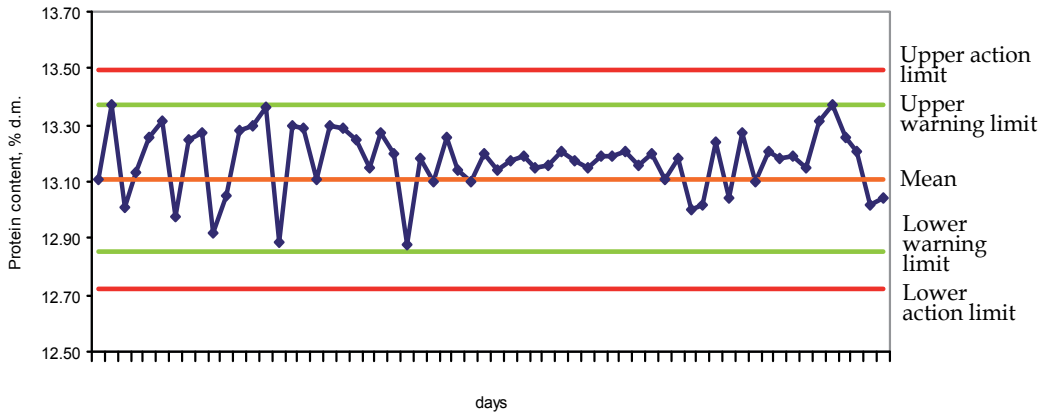

Fig. 7. Shewart (control) chart for determing protein content by the NIRS method

3.3 Robustness

The robustness can be defined as the resistance of a method to small deliberate changes in the experimental conditions that provides an indication of its reliability during routine use (Vander Heyden et al., 2001; Goupy, 2005; Dejaegher & Vander Heyden, 2007). The robustness test of the NIRS method for its application in analysing wheat samples examines the potential sources of variability in responses (analytical and spectral). The factors that can cause variability in the NIRS responses refer to the operational and environmental conditions. The robustness of a method is commonly examined in an experimental design, in the intervals that slightly exceed the variation that can be expected in a routine use of the method (Vander Heyden et al., 2001). Experimental design used to determine the robustness of an applied analytical method can be based on unvariate (one-variable-at-a-time, OVAT) or multivariate approaches (multi-variate-at-a-time, MVAT) (Dejaegher et al., 2007; Pojić et al., 2012).

To check the robustness of the NIRS method, the OVAT experimental design included deliberate changes of number of subsamples to be measured in single NIRS measurement, environmental and sample temperature, environmental air humidity, instrument voltage and lamp aging in order to determine how tightly controlled the experimental factors should be (Table 4). The obtained results indicated that the NIRS method for determination of protein content appeared to be robust for its application in wheat quality control regardless the deliberate changes in operational conditions (Table 4) (Pojić et al., 2012).

Fig. 8 shows the average SNV second derivative spectra of wheat samples in spectral range 850-1050 nm obtained within the OVAT experimental design. It could be noticeable that the spectral differences were very small. The largest spectral variations were observed in the spectral region around 950 nm associated with OH band for water and around 968 nm, 982 nm and 1014 nm associated with overtone bands (Infrasoft International, 2000; Pojić et al., 2012).

Experimental factors		Protein, % d.m.
Number of subsamples (NS)	5	13.79[a]
	10	13.79[a]
	15	13.83[a]
Sample temperature (ST)	5°C	13.90[a]
	20°C	13.83[a]
	35°C	13.84[a]
Ambient temperature (AT)	10°C	13.83[a]
	20°C	13.83[a]
	30°C	13.81[a]
Environmental humidity (EH)	40%	13.81[a]
	60%	13.83[a]
	80%	13.86[a]
Instrument voltage (IV)	200V	13.80[a]
	220V	13.83[a]
	240V	13.84[a]
Lamp aging (L)	Old	13.83[a]
	New	13.85[a]

Table 4. Values in the same column marked with the same letters are no significantly different (P <0.05, LSD test) (Pojić et al., 2012).

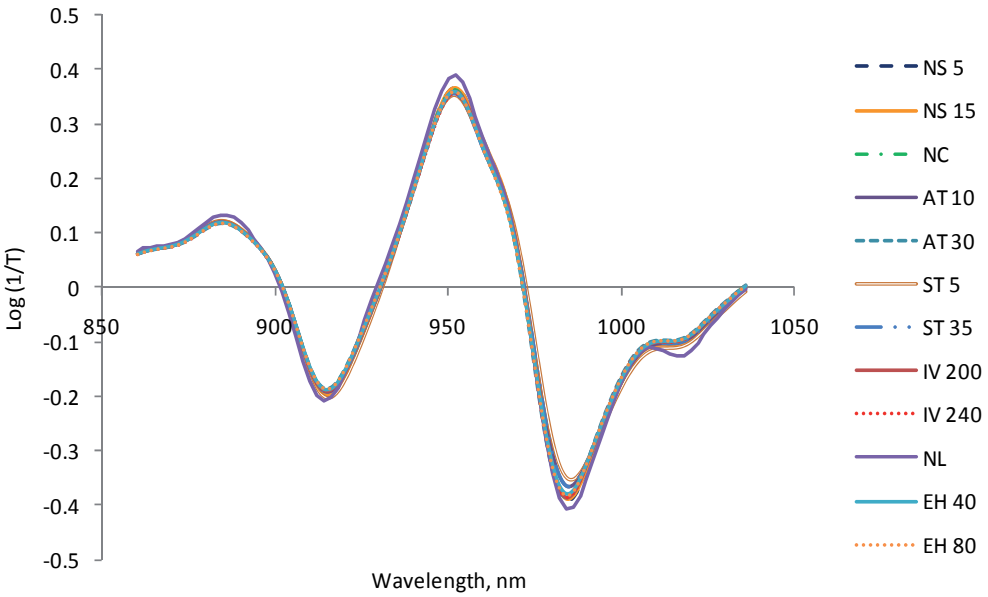

Fig. 8. The average second derivative spectra of wheat samples obtained at different experimental conditions within OVAT experimental design (NS 5, NS 15 – Five and fifteen subsamples in NIRS measurement; NC – Nominal conditions; AT 10, AT 30 – Ambient temperature of 10° and 30°C; ST 5, ST 35 – Sample temperature of 5° and 35°C; IV 200, IV 240 – Instrument voltage of 200 and 240V; NL – New lamp; EH 40, EH 80 – Environmental humidity of 40% and 80 %) (Pojić et al., 2012).

4. Conclusion

Characteristics of the NIRS method as being applied for protein content determination tested within the validation experiment expressed superior quality over the wet chemical method for protein content determinaton. Due to that, it is not surprising that the NIRS method has been accepted as the standard method by the ISO, AACC, AOAC and ICC, which confirms its applicability for routine use. Before its adoption as an official analytical method, special attention had to be paid to the regulatory requirements for analytical procedures especially due to the fact that the NIRS technique heavily relies on the use of chemometrics calibration and statistical analysis of data. For this reason, it is of upmost importance to verify the characteristics of the NIRS method to demonstrate its fitness for intended purpose. The validation protocol for the NIRS method presented represents an important contribution to the accreditation of the NIRS method based on the requirements of ISO/IEC 17025.

5. Acknowledgment

The financial support of FOSS Analytical AB (Hillerød, Denmark) towards this study is hereby gratefully acknowledged. The results expressed and conclusions arrived at are the part of the project (project number III46001) funded by Ministry of Education and Science, Republic of Serbia.

6. References

Armstrong, P. R.; Maghirang, E. B., Xie, F. & Dowell, F. E. (2006). Comparison of dispersive and fourier-transform NIR instruments for measuring grain and flour attributes. *Applied Engineering in Agriculture,* 22, 3, pp. (453-457). ISSN: 0883-8542.

Broad, N.; Graham, P., Hailey, P., Hardy, A., Holland, S., Hughes, S., Lee, D., Prebble, K., Salton, N. & Warren, P. (2002). Guidelines for the development and validation of near-infrared spectroscopic methods in the pharmaceutical industry. In: *Handbook of Vibrational Spectroscopy, vol. 5*, J. Chalmers & P. Griffiths (Eds.), (pp. 3590-3610), John Wiley, ISBN: 0471988472, Chichester.

Büchman, N. B. (1996). Near infrared networking – the ultimate control. *Near Infrared Spectroscopy: The Future Waves - Proceedings of 7th International Conference on Near Infrared Spectroscopy*, ISBN: 0952866609, Montreal, Canada, August 1995.

Büchman, N. B.; Josefsson, H. & Cowe, I. A. (2001). Performance of European artificial neural network (ANN) calibrations for moisture and protein in cereals using Danish near-infrared transmission (NIT) network. *Cereal Chemistry*, 78, 5, (September-October 2001), pp. (572-577), ISSN: 0009-0352.

Büning-Pfaue, H. (2003). Analysis of water in food by near infrared spectroscopy. *Food Chemistry*, 82, 1, (July 2003), pp. (107-115). ISSN: 0308-8146.

Deaville, E. R. & Flinn, P. C. (2000). Near-infrared (NIR) spectroscopy: an alternative approach for the estimation of forage quality and voluntary intake, In: Forage Evaluation in Ruminant Nutrition, D. I. Givens, E. Owen, R. F. E. Axford, H. M. Omed (Eds.), pp. (201-220), CAB International, Wallingford, ISBN: 0851993443.

Dejaegher, B. & Vander Heyden Y. (2007). Ruggedness and robustness testing. *Journal of chromatography A*, 1158, 1-2, (July 2007), pp. (138-157). ISSN: 0021-9673.

Dejaegher, B.; Dumarey, M., Capron, X., Bloomfield, M. S. & Vander Heyden, Y. (2007). Comparison of Plackett–Burman and supersaturated designs in robustness testing. *Analytica Chimica Acta*, 595, 1-2, (July 2007), pp. (59-71). ISSN: 0003-2670.

Delwiche, S. R. & Massie, D. R. (1996). Classification of wheat by visible and near-infrared reflectance from single kernels. *Cereal Chemistry*, 73, 3, (May/June 1996), pp. (399-405). ISSN: 0009-0352.

Delwiche, S. R. (1995). Single wheat kernel analysis by near-infrared transmittance: protein content. *Cereal Chemistry*, 72, 1, (January/February 1995), pp. (11-16), ISSN: 0009-0352.

Delwiche, S. R.; Bean, M. M., Miller, R. E., Webb, B. D. & Williams, P. C. (1995). Apparent amylose content of milled rice by near-infrared reflectance spectrophotometry. *Cereal Chemistry,* 72, 2, (March-April 1995), pp. (182-187). ISSN: 0009-0352.

Delwiche, S. R.; Graybosch, R. A. & Peterson, J. (1998). Predicting protein composition, biochemical properties, and dough-handling properties of hard red winter wheat flour by near-infrared reflectance. *Cereal Chemistry*, 75, 4, (July/August 1998), pp. (412-416), ISSN: 0009-0352.

Dowell, F. E.; Maghirang, E. B., Xie, F., Lookhart, G. L., Pierce, R. O., Seabourn, B. W., Bean, S. R., Wilson, J. D. & Chung, O. K. (2006). Predicting wheat quality characteristics and functionality using near-infrared spectroscopy. *Cereal Chemistry,* 83, 5, (September-October 2006), pp. (529-536). ISSN: 0009-0352.

Dybkaer, R. (2011). ''Verification'' versus ''validation'': a terminological comparison. *Accreditation and Quality Assurance*, 16, 2, (February 2011), pp. (105–108), ISSN: 1432-0517.

Goupy, J. (2005). What kind of experimental design for finding and checking robustness of analytical methods?. *Analytica Chimica Acta*, 544, 1-2, (July 2005), pp. (184-190). ISSN: 0003-2670.

Hrušková, M. & Šmejda, P. (2003). Wheat flour dough alveograph characteristics predicted by NIRsystems 6500. *Czech Journal of Food Sciences,* 21, 1, pp. (28–33). ISSN: 1212-1800.

Hrušková, M.; Bednářová, M. & Novotný, F. (2001). Wheat flour dough rheological characteristics predicted by NIRSystems 6500. *Czech Journal of Food Sciences*, 19, 6, pp. (213-218). ISSN: 1212-1800.

Hulasare, R. B.; Jayas, D. S. & Dronzek, B. L. (2003). Grain-grading systems, In: *Handbook of Postharvest Technology - Cereals, Fruits, Vegetables, Tea, and Spices*, A. Chakraverty, A. S. Majumdar, G.S.V. Raghavan, H. S. Ramaswamy (Eds), pp. (41-55), Marcel Dekker, Inc., New York, ISBN: 0-8247-0514-9.

ISO 5725-1:2003 (2003): Accuracy (trueness and precision) of measurement methods and results—part 1: general principles and definitions

Jirsa, O.; Hrušková, M. & Švec, I. (2008). Near-infrared prediction of milling and baking parameters of wheat varieties. *Journal of Food Engineering*, 87, 1, (July 2008), pp. (21-25), ISSN: 0260-8774.

Konieczka, P. & Namieśnik, J. (2009). *Quality Assurance and Quality Control in the Analytical Chemical Laboratory – A Practical Approach*, Taylor & Francis Group, ISBN: 978-1-4200-8270-8, Boca Raton.

Lauwaars, M. & Anklam, E. (2004). Method validation and reference materials. *Accreditation and Quality Assurance*, 9, 4-5, (March 2004), pp. (253-258), ISSN: 1432-0517.

Maghirang, E. B. & Dowell, F. E. (2003). Hardness measurement of bulk wheat by single-kernel visible and near-infrared reflectance spectroscopy. *Cereal Chemistry*, 80, 3, (May/June 2003), pp. (316-322), ISSN: 0009-0352.

Mark, H. & Workman, J. (2007). *Chemometrics in Spectroscopy* (First edition), Elsevier, ISBN: 978-0-12-374024-3, Oxford.

Mark, H.; Ritchie, G. E., Roller, R. W., Ciurczak, E. W., Tso, C. & MacDonald, S. A. (2002). Validation of a near-infrared transmission spectroscopic procedure, part A: validation protocols. *Journal of Pharmaceutical and Biomedical Analysis*, 28, 2, (April 2002), pp. (251-260), ISSN: 0731-7085.

Mastilović, J.; Janić Hajnal, E., Torbica, A., Pojić, M., Živančev, D., Kevrešan, Ž., Novaković, A. & Radusin, T. (2011). Contemporary approach to grain warehouse management, Institute of Food Technology, Headmade, Novi Sad.

Mastilović, J.; Torbica, A., Živancev, D. & Pojić, M. (2010). Development of novel approaches for micro- and macro methods based evaluation of wheat varieties, *Proceedings of the 5th International Congress Flour–Bread '09 and 7th Croatian Congress of Cereal Technologists*, ISBN: 978-953-7005-21-4, Opatija, Croatia, October 2009.

Mentink, R. L.; Hoffman, P. C. & Bauman, L. M. (2006). Utility of near-infrared reflectance spectroscopy to predict nutrient composition and *in vitro* digestibility of total mixed rations. *Journal of Dairy Science,* 89, 6, (June 2006), pp. (2320–2326). ISSN: 0022-0302.

Miralbés, C. (2003). Prediction chemical composition and alveograph parameters on wheat by near-infrared transmittance spectroscopy. *Journal of Agricultural and Food Chemistry,* 51, (September 2003), pp. (6335-6339). ISSN: 0021-8561.

Miralbés, C. (2004). Quality control in the milling industry using near infrared transmittance spectroscopy. *Food Chemistry*, 88, 4, (December 2004), pp. (621-628). ISSN: 0308-8146.

Miralbés, C. (2008). Discrimination of European wheat varieties using near infrared reflectance spectroscopy, *Food Chemistry*, 106, 1, (January 2008), pp. (386–389), ISSN: 0308-8146.

Moffat, A. C. (2004). Validation of NIR methods for pharmaceutical analyses, *Near Infrared Spectroscopy: Proceedings of the 11th International Conference*, ISBN: 0952866641, Córdoba, Spain, April 2003.

Osborne, B. G. (2007). Flours and breads, In: Near-infrared Spectroscopy in Food Science and Technology, Y. Ozaki, W. F. McClure, A. A. Christy (Eds.), pp. (281-296), John Wiley & Sons, Hoboken, ISBN: 978-0-471-67201-2.

Pawlinsky, T. & Williams P. (1998). Prediction of wheat bread-baking functionality in whole kernels, using near infrared reflectance spectroscopy. *Journal of Near Infrared Spectroscopy*, 6, 1, pp. (121-127). ISSN: 09670335

Pérez-Marín, D. C.; Garrido-Varo, A., Guerrero-Ginel, J. E. & Gómez-Cabrera, A. (2004). Near-infrared reflectance spectroscopy (NIRS) for the mandatory labelling of compound feedingstuffs: chemical composition and open-declaration. *Animal Feed Science and Technology,* 116, 3-4, (October 2004), pp. (333-349). ISSN: 0377-8401.

Pierce, R. O.; Funk, D. B., & Brenner, C. A. (1996). Applying near infrared spectroscopy to the needs of US grain inspection, *Near Infrared Spectroscopy: The Future Waves - Proceedings of 7th International Conference on Near Infrared Spectroscopy*, ISBN: 0952866609, Montreal, Canada, August 1995.

Pojić M.; Mastilović, J. & Pestorić, M. (2002) Bliska infracrvena spektroskopija u kontroli kvaliteta žita i proizvoda na bazi žita – I deo. *Žito-hleb*, 29, 5-6, pp. (193-204), ISSN: 0351-0999.

Pojić M.; Mastilović, J. & Pestorić, M. (2003) Bliska infracrvena spektroskopija u kontroli kvaliteta žita i proizvoda na bazi žita – II deo. *Žito-hleb*, 30, 1, pp. (1-8), ISSN: 0351-0999.

Pojić, M. & Mastilović, J. (2006). The standardization of NIRT Infratec 1241 instruments in Serbian network. *Proceedings of 3rd International Congress Flour-bread 2005 and 5th Croatian Congress of Cereal Technologists*, Opatija, Croatia, October 2005.

Pojić, M.; Mastilović, J., Palić, D. & Pestorić, M. (2010). The development of near-infrared spectroscopy (NIRS) calibration for prediction of ash content in legumes on the basis of two different reference methods. *Food Chemistry*, 123, 3, (December 2010), pp. (800-805). ISSN: 0308-8146.

Pojić, M.; Mastilović, J., Pestorić, M., Daković, S. (2009). A comparative study of two analytical methods for fat content determination in brewer's grits. *Journal of the American Society of Brewing Chemists*, 67, 3, pp. (167-169), ISSN: 0361-0470.

Pojić, M.; Mastilović, J., Majcen, N. (2012). Robustness of the near infrared spectroscopy method determined using univariate and multivariate approach. *Food Chemistry*, DOI: 10.1016/j.foodchem.2012.03.104, ISSN: 0308-8146.

Ritchie, G. E.; Roller, R. W., Ciurczak, E. W., Mark, H., Tso, C. & MacDonald, S. A. (2002). Validation of near-infrared spectroscopic procedure, part B: Application to alternate content uniformity and release assay methods for pharmaceutical solid dosage forms. *Journal of Pharmaceutical and Biomedical Analysis*, 29, 1-2, (June 2002), pp. (159-171), ISSN: 0731-7085

Rubenthaler, G. L. & Pomeranz, Y. (1987). Near-infrared reflectance spectra of hard red winter wheats varying widely in protein content and breadmaking potential. *Cereal Chemistry*, 64, 6, (November-December 1987), pp. (407-411), ISSN: 0009-0352.

Shenk, J. S.; Workman, J. J. & Westerhaus, M. O. (2008). Application of NIR spectroscopy to agricultural products, In: *Handbook of Near-Infrared Analysis*, D. A. Burns, E. W. Ciurczak (Eds.), pp. (347-386), Taylor & Francis Group, ISBN: 978-0-8493-7393-0, Boca Raton.

Uhlig, S.; Niewöhner, L. & Gowik, P. Can the usual validation standard series for quantitative methods, ISO 5725, be also applied for qualitative methods?. *Accreditation and Quality Assurance*, DOI: 10.1007/s00769-011-0811-0, ISSN: 1432-0517.

Vander Heyden, Y.; Nijhuis, A., Smeyers-Verbeke, J., Vandeginste, B. G. M., & Massart, D. L. (2001). Guidance for robustness/ruggedness test in method validation. *Journal of Pharmaceutical and Biomedical Analysis*, 24, 5-6, (March 2001), pp. (723-753). ISSN: 0731-7085.

Váradi, M.; Boros, I., Turza, S. & Budai, J. (2000). A new approach to the method approval system in Codex Alimentarius: Perspectives of near infrared spectroscopy for official methods, *Proceedings of 9th International Conference on Near Infrared Spectroscopy*, ISBN: 9780952866619, Verona, Italy, June 1999.

Vázquez, D.; Williams, P. C. & Watts, B. (2007). NIR spectroscopy as a tool for quality screening, Wheat Production in Stressed Environments: Proceedings of the 7th

International Wheat Conference, ISBN: 978-1-4020-5496-9, Mar del Plata, Argentina, November- December 2005.

Villareal, C. P.; de la Cruz, N. M. & Juliano, B. O. (1994). Rice amylose analysis by near-infrared transmittance spectroscopy. *Cereal Chemistry,* 71, 3, (May-June 1994), pp. (292-296). ISSN: 0009-0352.

Wesley, J.; Uthayakumaran, S., Anderssen, R. S., Cornish, G. B., Bekes, F., Osborne, B. G. & Skerritt, H. (1999). A curve-fitting approach to the near infrared reflectance measurement of wheat flour proteins which influence dough quality. *Journal of Near Infrared Spectroscopy,* 7, 4, pp. (229–240). ISSN: 09670335.

Williams, P. (2007). Grains and seeds, In: *Near-Infrared Spectroscopy in Food Science and Technology*, Y. Ozaki, W. F. McClure, A. A. Christy (Eds.), pp. (165-217), John Wiley & Sons, Inc., ISBN: 978-0-471-67201-2, Hoboken.

Williams, P. C.; El-Haramein, F. J., Ortiz-Fereira, G. & Srivastava, J. P. (1988). Preliminary observations on the determination of wheat strength by near-infrared reflectance. *Cereal Chemistry*, 62, 2, (March-April), pp. (109-114). ISSN: 0009-0352.

Workman Jr., J. J. (2008). NIR spectroscopy calibration basics, In: *Handbook of Near-Infrared Analysis*, D. A. Burns, E. W. Ciurczak (Eds.), pp. (123-150), Taylor & Francis Group, ISBN: 978-0-8493-7393-0, Boca Raton.

12

Vis/Near- and Mid- Infrared Spectroscopy for Predicting Soil N and C at a Farm Scale

Haiqing Yang[1] and Abdul M. Mouazen[2]
[1]*College of Information Engineering, Zhejiang University of Technology, Hangzhou*
[2]*School of Applied Sciences, Cranfield University, Bedfordshire*
[1]*P.R. China*
[2]*United Kingdom*

1. Introduction

a. In spectroscopic analysis, visible (Vis), near infrared (NIR) and mid infrared (MIR) ranges are often used as they include plenty of information on physical, chemical and biological properties of objects. Commonly, wavelengths ranges are from 350 to 760 nm for Vis, 760-2500 nm for NIR, and 2500 to 25000 nm for MIR (often used in its wavenumber form 4000 to 400 cm^{-1}). Frequencies in the Vis are due to electronic transition while those in the NIR are generally overtones and combination bands from the fundamental vibrations occur in the MIR, mainly O-H, N-H, and C-H bonds (Viscarra Rossel*, et al.*, 2006). When NIR and MIR radiations are focused onto a sample, the molecules in the sample will increase their vibration energy by absorbing energy at specific frequencies depending on the molecular geometry, bond strengths and atomic masses. The resulting Vis, NIR and MIR lights are thus modified, creating a spectrum or 'signatures' of the targeted object with peaks at the absorbing frequencies.
b. The combined contributions from the various soil components can result in a very complex spectrum, difficult to analyze visually, but multivariate calibration models can be built to derive useful qualitative and quantitative relationships or models between the spectral signatures and many soil properties. Spectrometry is the combination of spectroscopy and chemometric (multivariate statistical) methods. It should be noted that the Vis-NIR-MIR spectrometry technique can predict multiple soil properties simultaneously.
c. Recently, there is an increasing interest in the development of time- and cost-effective methods for the measurement of soil nitrogen (N) and carbon (C), due to the growing concerns about the effect of excessive use of N fertilizer in the environment and the increase of atmospheric C content, which could be limited through soil C sequestration. In order to manage N and C in soils in an efficient manner detailed information about these properties is needed. Previous reports confirm the presence of within-field variability of soil properties including N and C, which requires analysis of large number of soil samples (Mouazen*, et al.*, 2007). Due to the fact that standard procedures for the measurement of soil N and C are time-consuming and expensive (Sinfield*, et al.*,

2010), attention is being given to possible alternatives such as Vis-NIR and/or MIR spectroscopy. Numerous analyses of soil N and C have been conducted during the past decades using this technique, for examples, to predict the soil C and N mineralization rates (Fystro, 2002; Mutuo, *et al*., 2006), to derive spectral characteristics for classifying conventional and conservation agricultural practices (Haché, *et al*., 2007), to assess soil changes due to site disturbance during forest harvesting (Ludwig, *et al*., 2002), to evaluate the recovery of microbial functions during soil restoration (Schimann, *et al*., 2007), to determine carbon inventories (Reeves III, *et al*., 2002), to determine (*in situ*) organic matter composition of coatings at crack surfaces and linings of earthworm burrow walls (Reeves III, *et al*., 2002) and others (Chang, *et al*., 2001; Chang & Laird, 2002; Yang, *et al*., 2011a).

d. Applying Vis-NIR spectroscopy to predict soil properties needs no special sample preparation. However, MIR spectra are traditionally obtained by a FT-IR spectrometer with samples pressed in KBr pellets, which requires labour and specific skills. Fortunately, newly-developed ATR (attenuated total reflection) and DRIFT (diffuse reflectance infrared Fourier Transform) accessories are becoming the predominant FT-IR sample analysis tool. This is because sample handling is greatly simplified and sample preparation is eliminated. Hence, Vis-NIR-MIR spectrometry without sample preparation will bring about new wave of soil research.
e. This study investigated the potential of calibrating Vis-NIR, ATR-FTIR and DRIFT spectra to soil N and C concentrations with an aim of comparing the performance of two spectrometers, namely, a Vis-NIR spectrometer vs. a FT-IR spectrometer with ATR and DRIFT accessories. The models developed for N and C were then compared to those developed with the combination of Vis-NIR and ATR-FTIR spectra (Vis-NIR-ATR) and the combination of Vis-NIR and DRIFT spectra (Vis-NIR-DRIFT) for investigating whether the combination of Vis-NIR spectrometer and FT-IR spectrometer could improve the prediction accuracy of soil N and C. For each spectrometer, spectral data were subjected to various spectral transformation approaches before model calibration, aiming at model optimization.

2. Material and methods

2.1 Samples

Samples archived in the Soil Labs at Cranfield University were originally collected from the top 0-20 cm of the soil layer from five fields in Silsoe experimental farm at Bedfordshire, United Kingdom. Figure 1 illustrates the location of these fields, namely, Avenue Field (#A), Orchard (#B), Ivy Ground (#C), Showground (#D) and Copse Field (#E). According to the soil descriptions presented on www.landis.org.uk, managed by the National Soil Resources Institute (MSRI), Cranfield University, these fields belong to two major soil World Reference Base (WRB) classifications, namely, Cambisol and Luvisol. Of them, Ivy Ground (Sample codes: C15, C21-C39), Orhcard (B01-B25) and Copse Field (E01- E23) are Cambisols and Showground (D01-D35) is Luvisol, while Avenue Filed (A01-A12, A14-A20) comprises of both soils. The parent material underlying these fields is mainly siliceous stones.

A total of 122 bulk soil samples used in this study are with various proportions of sand, slit and clay (Table 1) and hence belong to three soil textures, e.g. sandy loam, clay loam and clay, according to the United States Department of Agriculture (USDA) triangular diagram

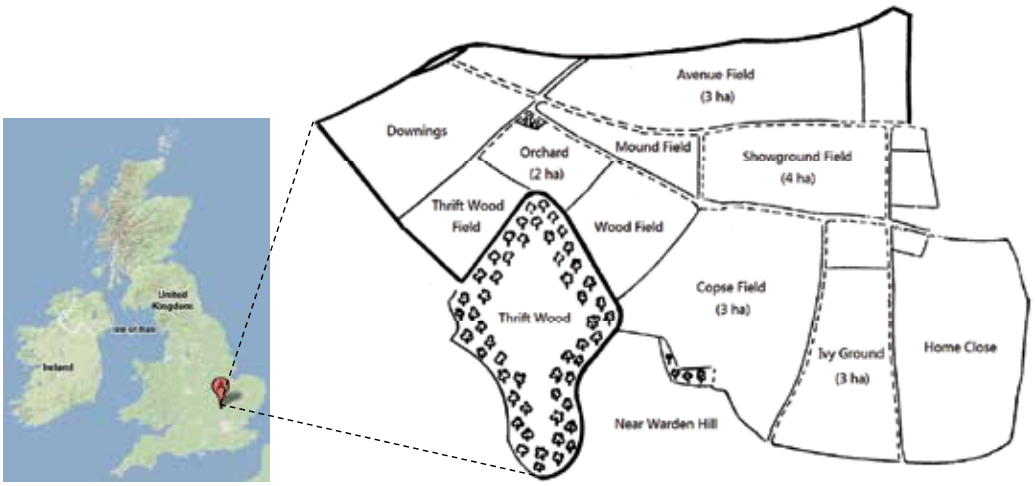

Fig. 1. Location of the five fields targeted in the study (www.landis.org.uk)

Code	Field Name	Vegetation	Soil type	Sand (%)	Silt (%)	Clay (%)	Soil texture[a]
A	Avenue Ground	wheat	C+L[b]	61.9	20.1	18.1	Sandy loam
B	Orchard	wheat	Cambisol	40.1	27.4	32.5	Clay loam
C	Ivy Ground	Soybean	Cambisol	21.1	27.2	51.7	Clay
D	Showground	wheat	Luvisol	65.0	20.9	14.1	Sandy loam
E	Copse Field	wheat	Cambisol	14.6	27.8	57.6	Clay

[a] according to USDA triangular diagram relating particle size distribution to soil texture.
[b] mixture of Cambisol and Luvisol types.

Table 1. Description of the five targeted farm fields

of soil texture classification. Soil samples were air-dried and crushed at first. Plant residues and stones were then removed. After that, the samples were sieved to pass a 2 mm mesh and air-dried again at 40℃ for 48h. A small amount of soil was used for chemical analysis, whereas the majorities were left for spectrophotometer measurement.

2.2 Reference methods

Particle size distribution was determined by a combination of wet sieving and hydrometer tests using the USDA soil texture classification system. Reference values of N and C were analyzed through a sequence of processes. First, a 50 mg sample was used for the measurement of TN and TC by a TrusSpecCNS spectrometer (LECO Corporation, St. Joseph, MI, USA) using the Dumas combustion method. Next, another 50 mg from each soil sample was mixed with 5% HCl and then oven-dried at 90℃ for 4 h in order to remove IC. Then, OC in IC-free samples were measured by the same Dumas combustion method. Finally, IC was calculated by the difference between TC and OC.

2.3 Vis-NIR spectra acquisition

The soil samples were equilibrated to room temperature (20-25℃) and carefully mixed before spectral measurement. A sub-sample of ~5g was loaded into a static ring cup and measured using a LabSpec 2500 spectrophotometer (Analytical Spectral Devices Inc. Boulder, CO, USA) equipped with a fibre-optic probe. The light source was a quartz-halogen bulb of 3000K°. The light source and reflectance fibre were gathered with a certain angle of 35°. One Si photodiode array in the range of 350-1000 nm and two Peltier cooled InGaAs detectors in the ranges of 1000-1800 nm and 1800-2500 nm were used. All spectra were recorded in diffuse reflection mode over the wavelength range of 400-2500 nm at 1 nm data spacing interval, which resulted in 2101 wavelengths per spectrum. The reflectance spectra were transformed into absorbance spectra using Log(1/R), as absorbance is directly proportional to the concentration of an absorber according to Beer-Lambert Law. The actual spectra resolution was 3 nm at 700 nm and 10 nm at 1400 and 2100 nm. Before sample spectral acquisition, twenty five reference scans were taken on a ceramic standard supplied with the spectrophotometer. Ten photometric scans were conducted for each sample, followed by another ten scans of the refilled sample cup. The twenty scans were then averaged in one spectrum for each sample.

2.4 MIR spectra acquisition

MIR spectra were collected by an ALPHA Fourier transform infrared (FT-IR) spectrometer (Bruker Optics, Billerica, MA, USA) with wavelength range of 7500–375 cm^{-1}, equipped with two exchangeable QuickSnap™ sampling modules. This instrument acquired spectra with two sampling accessories, namely, ATR and DRIFT. ATR is an easy-to-use FT-IR sampling method that is ideal for both solids and liquids and does not require any sample preparation. The Eco ATR is a single reflection ATR sampling module equipped with a versatile high throughput ZnSe ATR crystal for the analysis of powders, solids, pastes and liquids. The DRIFT module is an economical analysis option for a broad variety of solid samples: powders, inorganic material, gem stones, papers, textiles and others. The DRIFT module is designed for easy sampling and high light-throughput.

2.4.1 Principles of ATR-FTIR

An attenuated total reflectance accessory operates by measuring the changes that occur in a totally internally reflected infrared beam when the beam comes into contact with a sample (Fig.2). An infrared beam is directed onto an optically dense crystal with a high refractive index at a certain angle. This internal reflectance creates an evanescent wave that extends beyond the surface of the crystal into the sample held in contact with the crystal. It can be easier to think of this evanescent wave as a bubble of infrared that sits on the surface of the crystal. This evanescent wave protrudes only a few microns ($0.5\mu - 5\mu$) beyond the crystal surface and into the sample. Consequently, there must be good contact between the sample and the crystal surface. In regions of the infrared spectrum where the sample absorbs energy, the evanescent wave will be attenuated or altered. The attenuated energy from each evanescent wave is passed back to the IR beam, which then exists at the opposite end of the crystal and is passed to the detector in the IR spectrometer. The system then generates an infrared spectrum (www.perkinelmer.com).

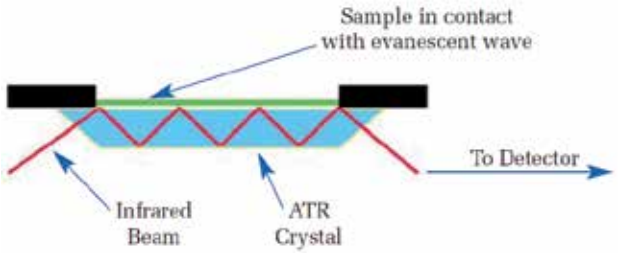

Fig. 2. A multiple reflection ATR system (www.perkinelmer.com)

When measuring solids by ATR, it is essential to ensure good optical contact between the sample and the crystal. The accessories have devices that clamp the sample to the crystal surface and apply pressure. This works well with elastomers and other deformable materials, but many solids give very weak spectra because the contact is confined to small areas. The effects of poor contact are the greatest at shorter wavelengths where the depth of penetration is the lowest. The issue of solid sample/crystal contact has been overcome to a great extent by the introduction of ATR accessories with very small crystals, typically about 2 mm across. The most frequently-used small crystal ATR material is diamond because it has the best durability and chemical inertness. These small area ATR crystal top-plates generally provide only a single reflection but this is sufficient, given the low noise levels of PerkinElmer's modern FT-IR spectrometers. Much higher pressure with limited force can now be generated onto these small areas. As a result, spectra can be obtained from a wide variety of solid materials including minerals.

After the crystal area has been cleaned and the background collected, the soil material is placed onto the small crystal area. Then the pressure arm should be positioned over the crystal/sample area. Force is applied to the sample, pushing it onto the diamond surface. It is good practice to apply pressure until the strongest spectral bands have an intensity which extends beyond 70%T, namely, from a baseline at 100%T down to 70%T. Then, the data are collected in the normal manner. Unlike transmission measurements, ATR sampling does not produce totally absorbing spectral bands because the effective path-length is controlled by the crystal properties thereby minimizing sample re-preparation time. After the spectrum has been collected, the crystal area must be cleaned before placing the next sample on the crystal. A 100%T line with no spectral features should be seen if the crystal is clean, if spectral features are seen, the crystal should be cleaned again using a solvent soaked tissue.

In the case of a solid sample, it is pressed into direct contact with the crystal. Because the evanescent wave into the solid sample is improved with a more intimate contact, solid samples are usually firmly clamped against the ATR crystal, so that trapped air is not the medium through which the evanescent wave travels, as that would distort the results.

2.4.2 Principles of DRIFT

Diffuse reflectance occurs when light impinges on the surface of a material and is partially reflected and transmitted. Light that passes into the material may be absorbed or reflected out again. Hence, the radiation that reflects from an absorbing material is composed of surface-reflected and bulk re-emitted components, which summed are the diffuse

reflectance of the sample (www.uksaf.org). DRIFT analysis of powders is conducted by focusing infrared light onto the powder (sometimes diluted in a non absorbing matrix, e.g. KBr) and the scattered light is collected and relayed to the IR detector.

In practice, DRIFT is most conveniently and rapidly used for soil analysis in diffuse reflection mode, where the incoming radiation is focused onto the soil sample surface, often in the form of a dry powder or <2 mm micro-aggregates, and the reflected radiation is passed back into the spectrophotometer (Fig.3, www.clw.csiro.au). In this study, infrared spectra were recorded in diffuse reflection mode with an Alpha spectrometer with DRIFT accessory. Bulk soil samples were scanned 20 times in the range from 4000 to 400 cm^{-1}. DRIFT spectra were corrected against atmospheric CO_2 and water vapour. Finally, the infrared reflectance spectra were transformed into absorbance spectra using Log(1/R).

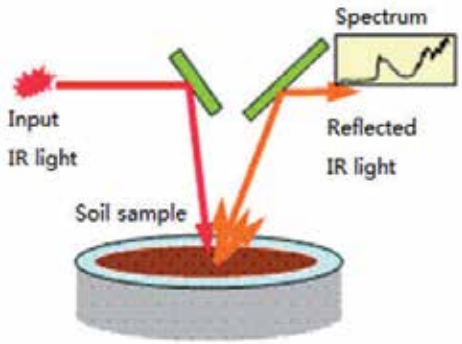

Fig. 3. A description of the method of acquiring a DRIFT spectrum (www.clw.csiro.au)

2.5 Spectral processing and development of calibration models for soil N and C

2.5.1 Principal components analysis (PCA)

PCA is a data compression process (i.e. a bilinear modelling process), which can be used to reduce a complex multidimensional data (e.g. spectra) into a smaller number of principal components (PCs) which reflect the underling structure of the original dataset. The first principal component typically explains most of the variation in the dataset with further principal components being orthogonal to the preceding PC and explaining less variation in the dataset. By plotting the PCs in two or three dimensional data space, interrelationships between the samples and variables can be examined (www.clw.csiro.au).

2.5.2 Partial least-squares regression (PLSR) analysis

For PLSR, spectral information is arranged as N × M matrix which consists of N spectra with absorbance values for M wavelengths, and the calibration data is expressed as a single vector with measured values for these spectra. The PLSR algorithm decomposes the M-dimensional spectra space into few factors termed latent variables (LVs), which represent the best projections of the calibration vector onto the N × M matrix. One of the advantages of PLSR compared to other chemometric methods like PCA is the possibility to interpret the first few LVs, because they show the correlations between the property values and the

spectral features. Furthermore, PLSR takes as well variations of the absorbance as variations of the calibration data into account. PLSR is a rapid analysis, can handle co-linear data, and can provide useful qualitative information.

2.5.3 Procedure of spectral processing and model calibration

Before the absorbance spectra were calibrated to predict soil properties, PCA was conducted to detect sample outliers in raw data set of Vis-NIR spectra, ATR spectra and DRIFT spectra. The identified sample outlier/s was/were excluded from further investigation. The remaining spectra were then subjected to various spectral pre-processing algorithms to reduce or eliminate noise, offset and bias in raw spectra. The investigated spectral pre-processing techniques included Savitzky-Golay smoothing, standard normal variate (SNV), multiplicative scatter correction (MSC), baseline offset correction (BOC), centre & scale, 1st- and 2nd- detrendings, and 1st- and 2nd- derivatives. Several spectral normalizations were also included. They were conducted according to maximum, range, mean and quantile values. Details of these algorithms are available in www.camo.com. PLSR algorithm was used to decompose both raw and transformed spectra matrix into 10 LVs. All PLSR models were validated with full cross-validation approach in which each spectrum was in turn excluded from the calibration sample set and was predicted by the PLSR model calibrated for the remaining spectra. By decomposing the spectra into 10 LVs, it was assumed that the PLSR model would be over-fitted because signal noise of the spectral measurements could also be correlated with the property vector. The optimal number of LVs was determined by minimizing the predicted residual error sum of squares (PRESS). For better understanding the importance of different wavelength ranges in the prediction of soil N and C, PLSR models were also developed for the combinational Vis-NIR-ATR and Vis-NIR-DRIFT spectra. Spectral transformation and model calibration were conducted using the UnscramblerX10.1® (CAMO, Oslo, Norway).

2.6 Model assessment criteria

The validation accuracy of PLSR models is given by the root mean squared error (RMSE):

$$\mathrm{RMSE} = \sqrt{\frac{1}{\mathrm{N}}\sum\nolimits_{\mathrm{N}}(\mathrm{X_i} - \mathrm{Y_i})^2}$$

where X_i is the predicted value, Y_i the measured (reference) value and N the number of soil samples. To compare model performance, we recorded the residual predictive deviation (RPD), which is the ratio of standard deviation of reference values to RMSE of the calibration set during cross-validation. The criteria adopted for RPD classification (Mouazen, *et al.*, 2006) was that an RPD value below 1.5 indicates very poor model/predictions and that such as value could not be useful; an RPD value between 1.5 and 2.0 indicates a possibility to distinguish between high and low values, while a value between 2.0 and 2.5 makes approximate quantitative predictions possible. For RPD values between 2.5 and 3.0 and above 3.0, the prediction is classified as good and excellent, respectively. Meanwhile, we compared the coefficient of determination (R^2) in cross-validation of calibration models. Generally, a good model would have high values of R^2 and RPD for cross-validation.

3. Results and discussion

3.1 Laboratory analyses

Means and distributions of the reference values of total nitrogen (TN), total carbon (TC), organic carbon (OC), inorganic carbon (IC), the ratio of TC to TN, and the ratio of OC to TN in samples are summarized in Table 2. The averaged content (±s.d.) for TN, TC and OC are 0.2(±0.06)%, 2.11(±0.57)% and 1.98(±0.54)%, respectively. The IC concentration for the studied samples is very low with an average value of 0.12%, although its coefficient of variance (c.v.) is 1.08. This leads to large skewness of IC content distribution in samples. The ratio of OC to TN is as nearly constant as 10 with very low c.v. value of ~0.05. The inter-correlation coefficients among these properties are summarized in Table 3. TN, TC and OC were strongly correlated to each other (r=0.97~0.99), while they have weak correlation with IC (r=0.13~0.35). The TC/TN or OC/TN was poorly correlated to TN, TC and OC, however, they had good correlation with IC (r=0.53 or -0.49).

Soil property	Reference value[a]				
	Mean	Median	Range	s.d.[b]	c.v.[c]
TN(%)	0.20	0.19	0.09-0.31	0.06	0.30
TC(%)	2.11	2.00	0.95-3.41	0.57	0.27
OC(%)	1.98	1.84	0.85-3.02	0.54	0.27
IC(%)	0.12	0.09	0.00-0.64	0.13	1.08
TC/TN	10.57	10.47	9.56-13.12	0.59	0.06
OC/TN	9.95	9.92	8.88-12.47	0.52	0.05

[a] one sample outlier (A02) detected by PCA was not included.
[b] standard deviation
[c] coefficient of variance(=s.d./Mean)

Table 2. Laboratory reference statistics for soil total nitrogen (TN), total carbon (TC), organic carbon (OC), inorganic carbon (IC), TC/TN and OC/TN

All	TN(%)	TC(%)	OC(%)	IC(%)	TC/TN	OC/TN
TN(%)	1	0.97	0.99	0.23	-0.25	-0.24
TC(%)	0.97	1	0.97	0.35	-0.07	-0.18
OC(%)	0.99	0.97	1	0.13	-0.19	-0.07
IC(%)	0.23	0.35	0.13	1	0.53	-0.49
TC/TN	-0.25	-0.07	-0.19	0.53	1	0.41
OC/TN	-0.24	-0.18	-0.07	-0.49	0.41	1
PC-1(Vis-NIR)	0.77	0.74	0.76	0.13	-0.22	-0.16
PC-2(Vis-NIR)	-0.48	-0.48	-0.46	-0.23	0.08	0.22
PC-1(ATR-FTIR)	0.90	0.87	0.88	0.19	-0.29	-0.28
PC-2(ATR-FTIR)	0.15	0.16	0.21	-0.17	0.05	0.30
PC-1(DRIFT)	0.56	0.55	0.52	0.26	-0.12	-0.24
PC-2(DRIFT)	-0.71	-0.68	-0.71	-0.05	0.24	0.16

Table 3. Correlation matrix between soil properties and the first two principal component scores of the Vis-NIR spectra, ATR-FTIR spectra and DRIFT spectra of 121 samples

3.2 Vis-NIR spectral analysis and model calibrations

Different wavelength bands respond to different chemical compositions or molecular groups in soil. However, this response is strongly influenced by soil texture classes. Figure 4 shows the representative Vis-NIR absorption spectra of samples from each soil texture class, e.g. sandy loam (field #D), clay loam (field #B) and clay (fields #C and #E), with high and low TC content. The shift in overall baseline in the Vis-NIR spectra is likely caused by the overall difference in the particle size distribution (Madari, *et al.*, 2006). The clay soil has a finer texture compared to the others, which results in a higher baseline. In general, smaller particle size results in higher reflectance or lower absorbance, but for our case, the higher absorption coefficients for the clay fraction apparently dominate the particle size effect resulting in higher absorbance. Within the clay texture class, the samples with higher TC content tend to exhibit stronger absorption in Vis-NIR spectra than those with lower TC contents (Fig.4). This observation seems true for sandy loam soils but not for clay loam soils, which might be attributed to the effect of soil colour. In Fig.4, the sample from clay loam class with low TC content of 1.59% shows higher absorbance than that with high TC content of 2.44%. This is probably due to particle size effect. The Vis-NIR spectra are characteristic of absorption bands associated with colour (400-760 nm), the bending (1413 nm) and stretching (1916 nm) of the O-H bonds of free water and lattice minerals at around 2210 nm (Madari, *et al.*, 2006).

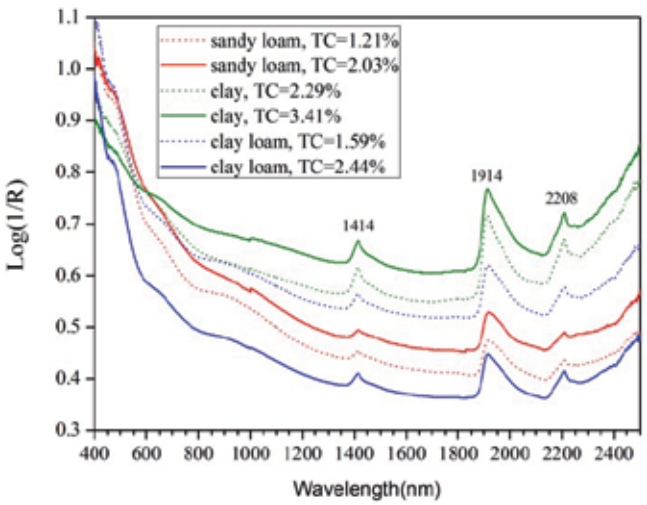

Fig. 4. Vis-NIR absorption spectra of samples from each soil texture class with high and low TC content.

3.2.1 PCA analysis for Vis-NIR spectra

Figure 5 shows all raw Vis-NIR spectra, PCA scores plot for the spectra, and residual X-variance for PC-1 and PC-2. PC-1 and PC-2 explains 96% and 3% of total variance, respectively. The PC-1 may explain variation related to SOM of the samples, as the PC-1 was better correlated to TN, TC and OC (r=0.74~0.76) than to PC-2 (r =-0.46~-0.48) (Table 3). Samples originated from different fields can be divided into two clusters: one for Luvisol soils (Showground Field, #D) and another for Cambisol soils (Orchard, #B; Ivy Ground, #C;

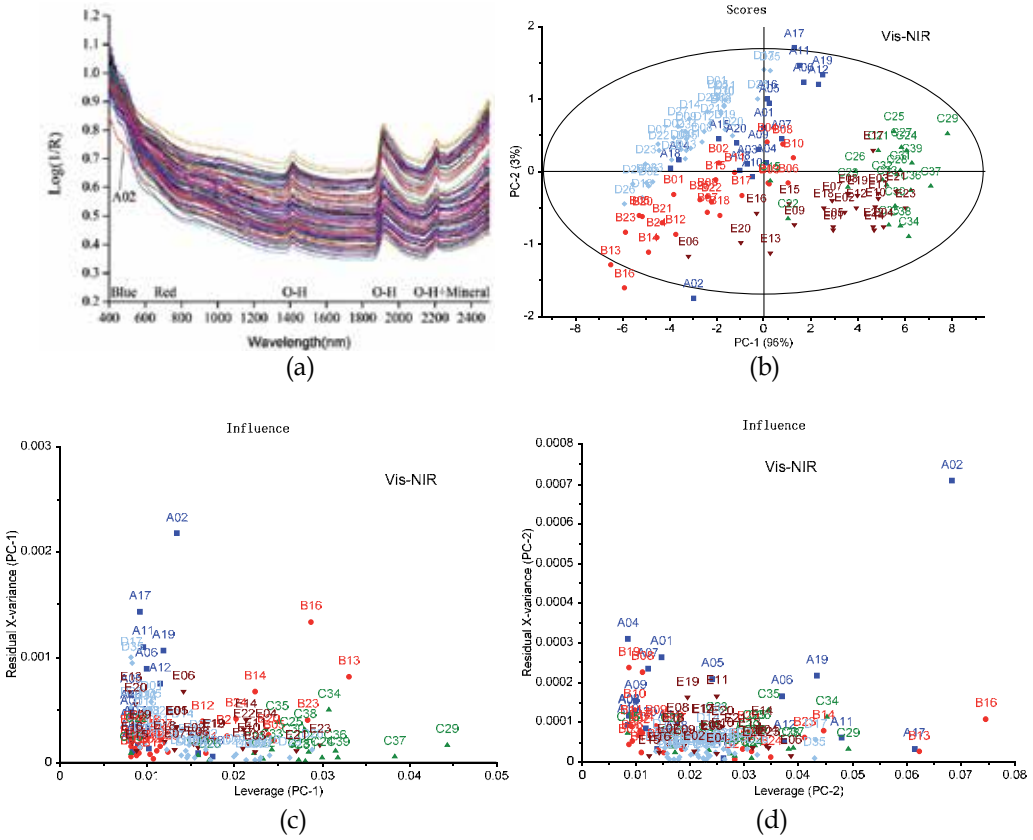

Fig. 5. Vis-NIR absorption spectra of all samples (a), principal components analysis scores plot for the Vis-NIR spectra (b), and residual X-variance for PC-1 (c) and PC-2 (d).

Copse Field, #E). Samples from Avenue Field (#A) exhibit partially mixing with the two clusters (Fig.5b). This might be attributed to the nature of this field as it is a mixture of Cambisol and Luvisol types. Although being of the same soil type of Cambisol, samples from field #B are clearly separated from those from fields #C and #E (Fig.5b). This is mainly due to different soil textures, namely, clay loam vs. clay (Table 1). Several samples located outside of the Hotelling T^2 ellipse become the candidates of samples outliers (Fig.5b). However, apart from sample A02, other outliers locate close to their member samples. In addition, sample A02 exhibits large residual X-variance for PC-1 (Fig.5c) and PC-2 (Fig.5d). The raw spectrum of sample A02 also shows distinct color features (lowest absorbance in visible range) from other samples (Fig.5a). Thus, sample A02 was considered as an outlier and excluded from further investigation.

3.2.2 Vis-NIR calibration models

Table 4 summarizes the cross-validation results of the PLSR models developed with raw and various transformed Vis-NIR spectra against each soil property. For raw spectra, PLSR models produced good or excellent prediction accuracy with R^2 of 0.86~0.90 and RPD of 2.73~3.33 for soil TN, TC and OC. Coupled with appropriate spectral pre-processing

Spectral pretreatment method	PLSR models calibrated for Vis-NIR spectra											
	Total N			Total C			Organic C			Inorganic C		
	LVs	R^2	RPD	LVs	R^2	RPD	LVs	R^2	RPD	LVs	R^2	RPD
None	5	0.90	3.33	5	0.86	2.73	5	0.90	3.16	**5**	**0.42**	**1.34**
SNV	**3**	**0.91**	**3.75**	3	0.87	2.74	**4**	**0.91**	**3.44**	3	0.37	1.29
MSC	4	0.90	3.33	4	0.87	2.74	4	0.90	3.20	3	0.39	1.31
BOC	4	0.90	3.33	4	0.86	2.70	5	0.91	3.27	5	0.37	1.29
Center & Scale	5	0.91	3.53	**5**	**0.87**	**2.78**	5	0.90	3.21	6	0.42	1.34
Normalization												
Maximum-	4	0.89	3.33	4	0.86	2.69	4	0.89	3.05	5	0.38	1.29
Range-	5	0.90	3.33	5	0.87	2.74	5	0.90	3.23	4	0.34	1.26
Mean-	4	0.89	3.16	4	0.85	2.61	4	0.89	3.00	4	0.39	1.31
Quantile-	5	0.91	3.53	5	0.87	2.78	5	0.91	3.25	6	0.42	1.34
De-trending												
1st-	4	0.90	3.53	4	0.87	2.75	4	0.90	3.20	4	0.38	1.30
2nd-	3	0.89	3.16	3	0.85	2.57	4	0.89	3.05	3	0.39	1.31
Derivative												
1st-	1	0.85	2.73	1	0.80	2.26	1	0.85	2.63	3	0.17	1.12
2nd-	4	0.61	1.71	1	0.56	1.51	4	0.63	1.65	1	0.14	1.11

Table 4. Cross validation result of PLSR models calibrated for raw and various transformed Vis-NIR spectra with 121 samples

algorithms, model performance was improved for a certain degree. For examples, PLSR model developed for TN after SNV-transformed spectra resulted in R^2 of 0.91 and RPD of 3.75. By the same pre-processing technique, prediction of soil OC was improved with R^2 of 0.91 and RPD of 3.44. The best calibration model for TC was obtained when the spectra were transformed by Center-&-Scale technique. It is worth noting that these optimized PLSR models need less latent variables (3-5) than those for raw spectra. In general, the fewer the latent variables used, the better is the model developed, as the calibration is more apt to be applicable to new samples (Madari, *et al.*, 2006). For IC, PLSR calibration with raw and various transformed spectra failed to produce useful models with $R^2 \leq 0.42$ and RPD≤1.34. Figure 6 shows the correlation between the measured and PLSR-predicted values of each soil property. The linear fitting slopes for TN, TC and OC are close to 1, which suggests that PLSR models developed with Vis-NIR absorption spectra for predicting soil TN, TC and OC are successful.

3.2.3 B-coefficients analysis of PLSR models for Vis-NIR spectra

B-coefficients curves of the PLSR models calibrated for the best transformed Vis-NIR spectra against each soil property are shown in Fig.7. The B-coefficients for TN, TC and OC exhibit strong similarity among them. This is mainly due to their high correlation obtained for

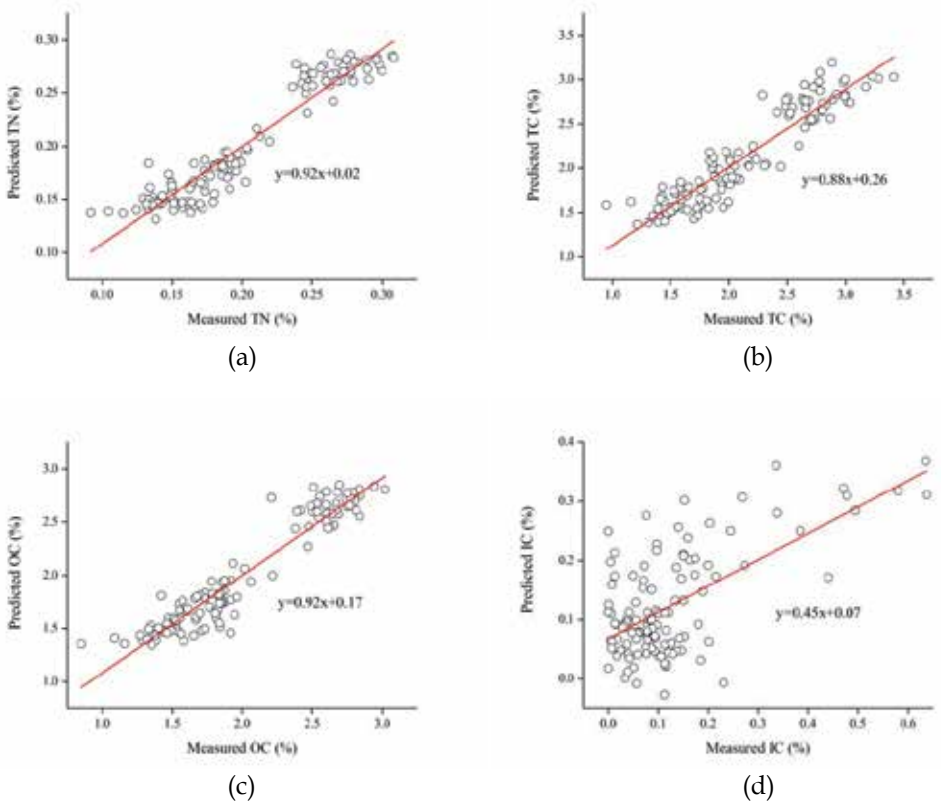

Fig. 6. Measured vs. predicted values of soil TN (a), TC (b), OC (c) and IC (d) based on Vis-NIR absorption spectra.

reference values (r=0.97-0.99, Table 3). It is worth noting that the visible range (400-760 nm) associated with soil colour shows huge influence on model accuracy, which is in line with other reports (Stenberg, *et al.*, 2010; Viscarra Rossel, *et al.*, 2006). The absorption feature in the visible and short-wave NIR (400-1000 nm) might be due to the Fe oxides in soil, mainly haematite and goethite (Viscarra Rossel & Behrens, 2010). The influential wavelengths located between 1000 and 2500 nm can be attributed to water, clay minerals and organic matter (Viscarra Rossel & Behrens, 2010). Using samples collected from Belgium and Northern France, Mouazen *et al*. (2006) compared the performance of two commercially available spectrophotometers with different wavelength ranges for the measurement of selected soil attributes including TC and TN. They found that the best accuracy was obtained when using a full wavelength range of 451-2459 nm, as compared to a short wavelength range of 401-1770 nm. Using samples collected from two depths along 11 km section of floodplain, Vohland and Emmerling (2011) reported that genetic algorithm (GA) allocated significant wavelengths most frequently to the range of 1970-2490 nm for soil OC, which is not particularly in line with those bands shown in Fig.7. One reason might be the use of farm-scale local set in our case in which the visible range associated with soil colours has the most influence on model calibration, whereas the NIR range has a smaller influence. This contradictory results against those published by others might be explained by the same

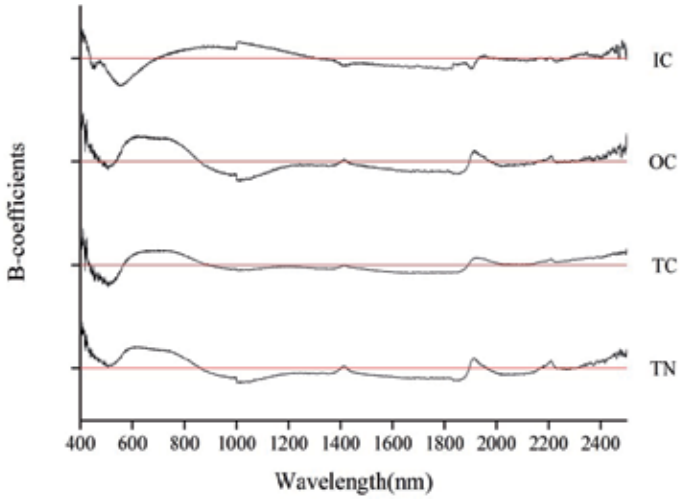

Fig. 7. B-coefficients curves obtained from PLSR analysis with the SNV-transformed Vis-NIR spectra for TN and OC, Center-&-Scale-transformed Vis-NIR spectra for TC, and raw Vis-NIR spectra for IC.

mineralogy of the data set originated from the same parent material in the current study, as compared to those using larger scale data sets (e.g. Mouazen, *et al.*, 2006; Vohland & Emmerling, 2011). Although the prediction accuracy of IC did not satisfy with lowest quantification standard (RPD>2.0), the characteristic bands of carbonate in 2300 and 2500 nm (Gaffey, 1986; Reeves III, *et al.*, 2002; Viscarra Rossel & Behrens, 2010) can be clearly identified in its B-coefficients curve.

3.3 DRIFT spectral analysis and model calibrations

The procedure of analyzing DRIFT spectra was the same as that presented for Vis-NIR spectral analysis.

3.3.1 DRIFT spectral response

Figure 8 shows the representative DRIFT absorption spectra of samples from each soil texture class, e.g. sandy loam (field #D), clay loam (field #B) and clay (fields #C and #E), with high and low TC content. Obviously, the absolute magnitude and range of the DRIFT absorptions are much greater than those found for corresponding Vis-NIR spectrum (Fig.4). The DRIFT spectrum generally shows more distinctive spectral features than the Vis-NIR spectrum. The peaks between 3698 and 3620 cm^{-1} and various peaks below 1100 cm^{-1} are characteristic for kaolinite (Madari, *et al.*, 2006). Soil organic matter also has characteristic absorption bands in the Mid-IR range (Table 5), however, due to its low concentration in the soil samples, and their overlapping with mineral peaks, most of these could not readily be identified by simple visual analysis of spectra. For example, the small bands around 2940-2935 cm^{-1} and 2886-2877 cm^{-1} indicate the presence of organic aliphatic C-H stretching (Table 5). This band is more evident in the spectra of soil samples having higher concentrations of organic carbon (Madari, *et al.*, 2006). Other organic peaks overlap with the mineral peaks. Viscarra Rossel *et al.* (2006) has compared the usefulness of visible, NIR and Mid-IR diffuse

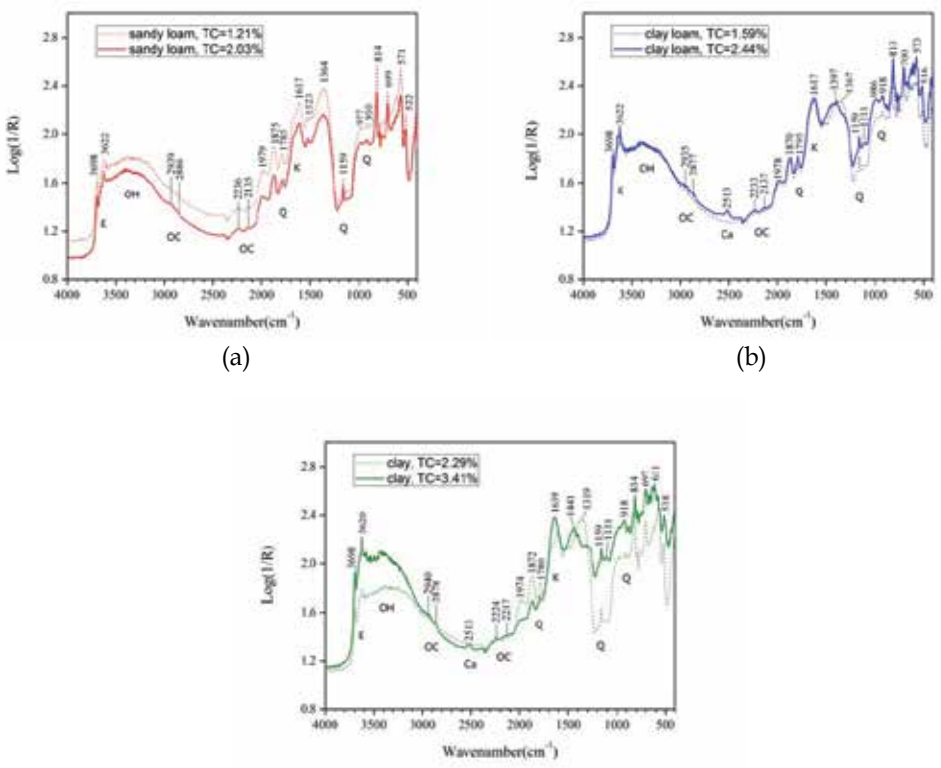

Fig. 8. DRIFT absorption spectra of samples from each soil texture class with high and low TC content. Some dominant soil components and absorption peaks are shown for quartz (Q), organic compounds (OC), calcite (Ca), kaolinite (K), and the (OH) features of free water and lattice minerals (Viscarra Rossel*, et al.*, 2006).

reflectance spectroscopy by examining PLSR factor loadings weights. They showed that frequencies in the Mid-IR range corresponding to the absorption of organic compounds, like organic acids, or acidic functional groups, like alkyl, amide and aromatic groups, were indicators of correlation between organic carbon concentrations in the bulk soil samples and the Mid-IR spectra.

3.3.2 PCA analysis for DRIFT spectra

Figure.9a shows all Mid-IR spectra obtained by FT-IR spectrometer with DRIFT accessory. Figure 9 also shows the PCA scores plot for the DRIFT spectra, and residual X-variance for PC-1 and PC-2. PC-1 and PC-2 explains 83% and 14% of total variance contained in the spectra, respectively. The PC-1 axis may explain differences attributed to SOM content of the samples as the PC-1 was better correlated to TN, TC and OC (r=0.87~0.90) than to PC-2 (r=0.15~0.21) (Table 3). Samples originated from different fields can be separated into two clusters according to soil types: one for Luvisol soils from Showground Field (#D) and another for Cambisol soils from Orchard (#B), Ivy Ground (#C) and Copse Field (#E),

Mid-IR band (cm^{-1})	Assignments	Vis-NIR wavelength (nm)
3380	O-H stretching of phenolic OH	
3400-3300	O-H stretching (H bonded OH groups),	
3300	N-H stretching	1500,1000,751
3030	Aromatic C-H strecthing	1650,1100,825
2940-2900	Aliphatic C-H stretching	
2930,2850	Alkyl asymmetric-symmetric C-H stretching	1706,1754,1138, 1170,853,877
2600	O-H stretching of H-bonded -COOH	
1725-1720	C=O stretching of –COOH and ketones	1930,1449
1660-1630	C=O stretching of amide groups (amide I band), quinine C=O and/or C=O of H-bonded conjugated ketones	2033,1524
1620-1600	Aromatic C=C stretching and/or asymmetric –COO stretching	
1610	N-H stretching of Amine	2060
1590-1517	COO- symmetric stretching, N-H deformation+C=N stretching (amide II band)	
1525	Aromatic C=C strecthing	
1460-1450	Aliphatic C-H	2275,1706
1400-1390	OH deformation and C-O stretching of phenolic OH, C-H deformation of CH2 and CH3 groups, COO- asymmetric stretching	
1350	Symmetric COO- stretching and/or –CH bending of aliphatics	
1270	C-OH stretching of phenolic OH	1961
1280-1200	C-O stretching and OH deformation of COOH, C-O stretching of aryl ethers	
1225	C-O stretching and OH deformation of COOH	
1170-950	C-O stretching of polysaccharides or polysaccharide-like substances	2137
1170	C-OH stretching of aliphatic OH, C-C stretching of aliphatic groups	
1050	C-O stretching of carbohydrates	2381
830	Aromatic CH out of plane bending	
775	Aromatic CH out of plane bending	

Table 5. Absorption bands of C and N in organic bonds in the Mid-IR range (Madari, *et al.*, 2006) and corresponding wavelengths in the Vis-NIR range (Stenberg, *et al.*, 2010)

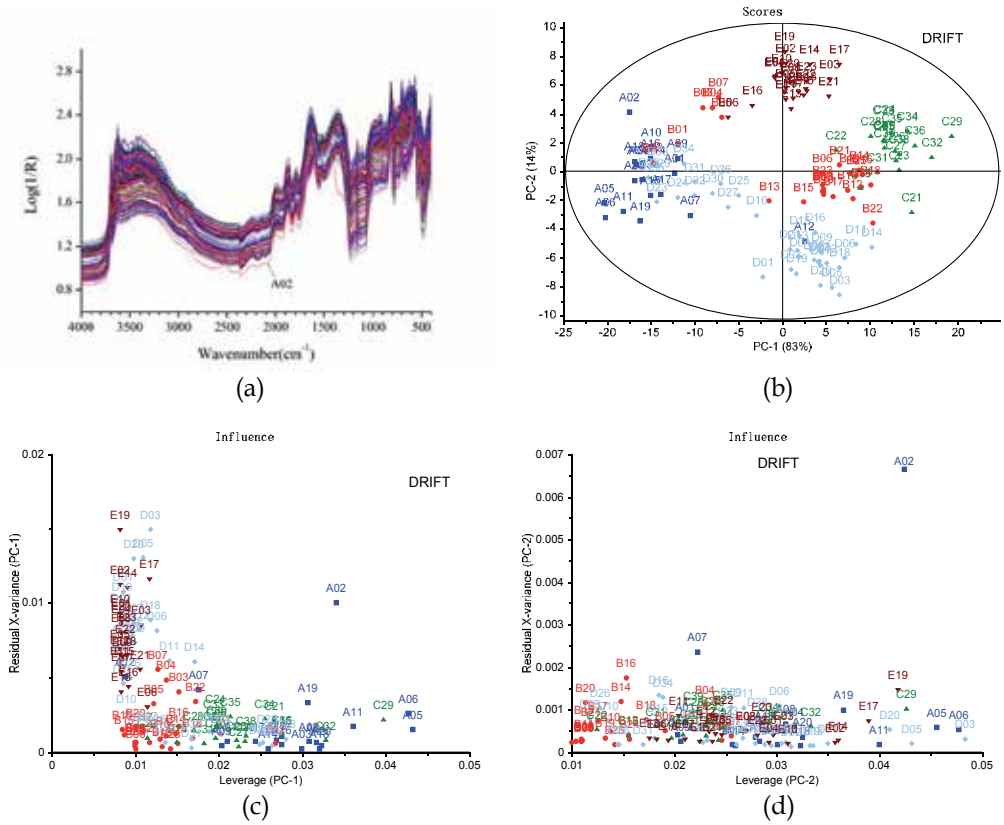

Fig. 9. DRIFT absorption spectra of all samples (a), principal components analysis scores plot for the DRIFT spectra (b), residual X-variance for PC-1 (c) and PC-2 (d).

although several samples from the field #B were mixed with former cluster. Samples from the field #A completely mixed together with the former cluster, although some of them belong to latter cluster. It seems that the soil type has no effect on samples separation into different classes but the texture diversity within the sample population used for calibration has clear effect (Madari, *et al.*, 2006). Samples from the fields #C and #E are totally separated although they are of same clay texture. This is mainly due to their distinct SOM-related soil properties concentrations as different vegetations have been growing in both fields (soybean in the field #C with TN of 0.28±0.02%, TC of 2.94±0.23% and OC of 2.73±0.15%; wheat in the field #E with TN of 0.25±0.02%, TC of 2.62±0.15% and OC of 2.56±0.16%). No sample locates outside of the Hotelling T^2 ellipse. Although sample A02 exhibits low residual X-variance for PC-1 (Fig.9c) which accounts for the most amount of variance in the DRIFT spectra, it displays large residual X-variance for PC-2 (Fig.9d). Also, in the raw spectrum, sample A02 shows quite different from the others (Fig.9a). Thus, sample A02 was considered as a sample outlier and excluded from further investigation.

3.3.3 DRIFT calibration models

Table 6 summarizes the cross-validation results of the PLSR models developed with raw and various transformed DRIFT spectra against each soil property, e.g. TN, TC, OC and IC.

Spectral pretreatment method	PLSR models calibrated for DRIFT spectra											
	Total N			Total C			Organic C			Inorganic C		
	LVs	R^2	RPD	LVs	R^2	RPD	LVs	R^2	RPD	LVs	R^2	RPD
None	5	0.95	4.62	5	0.93	3.93	5	0.94	4.19	5	0.70	1.86
SNV	4	0.94	4.29	5	0.94	3.93	4	0.94	4.06	3	0.68	1.82
MSC	4	0.94	4.29	4	0.92	3.63	4	0.94	4.15	3	0.68	1.81
BOC	5	0.95	4.62	**6**	**0.94**	**4.10**	5	0.95	4.25	4	0.71	1.88
Center & Scale	5	0.95	4.62	5	0.93	3.88	5	0.94	4.25	**4**	**0.71**	**1.89**
Normalization												
Maximum-	6	0.94	4.29	6	0.93	3.80	6	0.94	4.15	5	0.68	1.80
Range-	6	0.94	4.62	6	0.93	3.85	6	0.94	4.22	5	0.69	1.84
Mean-	5	0.94	4.29	6	0.93	3.85	5	0.94	4.12	5	0.67	1.78
Quantile-	**5**	**0.95**	**5.00**	5	0.94	4.01	**5**	**0.95**	**4.43**	4	0.70	1.88
De-trending												
1st-	4	0.94	4.62	4	0.94	4.04	4	0.95	4.35	4	0.70	1.86
2nd-	5	0.94	4.62	5	0.93	3.83	5	0.95	4.32	3	0.67	1.79
Derivative												
1st-	2	0.83	2.61	2	0.79	2.18	2	0.79	2.21	5	0.30	1.22
2nd-	2	0.69	1.94	2	0.66	1.70	2	0.65	1.71	1	0.10	1.01

Table 6. Cross validation result of PLSR models calibrated for raw and various transformed DRIFT spectra with 121 samples

For raw spectra, PLSR models produced excellent prediction accuracy with R^2 of 0.93~0.95 and RPD of 3.93~4.62 for TN, TC and OC. These models were calibrated with 5 latent variables. Coupled with proper spectral pre-processing techniques, model prediction was improved. For examples, the best model for soil TN produced prediction accuracy with R^2 of 0.95 and RPD of 5.00 using spectral pre-processing of quantile normalization. It was also effective for OC model improvement with R^2 of 0.95 and RPD of 4.43. For TC, the best model was built using spectral transformation of BOC, although this model needed 6 latent variables. Figure 10 shows the correlation between the measured and PLSR-predicted values of each soil property. The linear fitting lines for TN, TC and OC are closer to 1:1 as compared to the corresponding plots for Vis-NIR spectra (Fig.6). DFIRT spectra outperformed Vis-NIR spectroscopy for the prediction of these three properties (Table 4 & 6). Even for IC, almost all PLSR models developed with raw and various transformed DRIFT spectra outperformed their counterparts for Vis-NIR spectra. Accuracy obtained for IC can be used to distinguish high and low content with RPD>1.5 (Table 6). These results suggest that PLSR models developed with DRIFT absorption spectra for predicting these soil properties are more accurate.

3.3.4 B-coefficients analysis of PLSR models for DRIFT spectra

B-coefficients curves obtained after PLSR analyses with the best transformed DRIFT spectra for each soil property are combined in Fig.11. The B-coefficients for TN, TC and OC exhibit

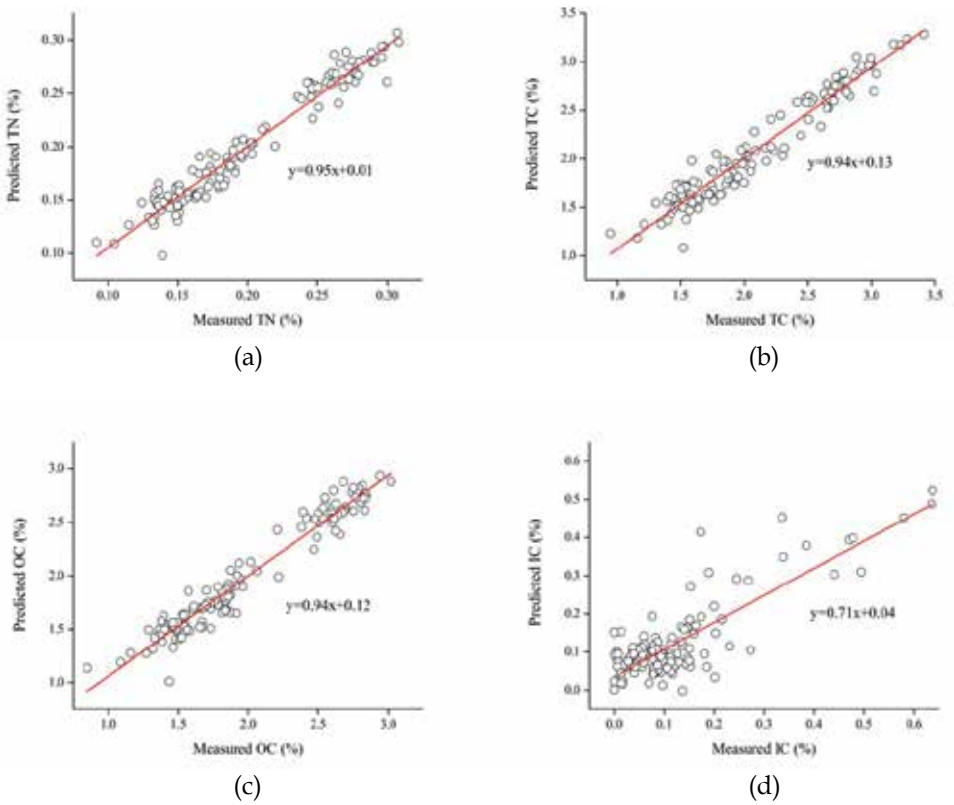

Fig. 10. Measured vs. predicted values of soil TN (a), TC (b), OC (c) and IC (d) based on DRIFT absorption spectra.

strong similarity among them. This is mainly due to their high correlation obtained with reference values (r=0.97-0.99, Table 3). Overall, the most influential frequencies for predicting these soil properties locate in the wavenumber range from 2100 to 1200 cm^{-1}. As indicated in Table 5, the peaks at around 1620-1558 cm^{-1} are for aromatic C=C stretching and/or asymmetric –COO stretching; the peaks at 1460 cm^{-1} and 1229 cm^{-1} are corresponding to Aliphatic C-H stretching and C-O stretching/OH deformation of COOH. Other significant wavebands can be found at round 2930 cm^{-1}, corresponding to Aliphatic C-H stretching. Interestingly, although the DRIFT-calibrated models are not accurate enough for IC quantification, the corresponding B-coefficients curve exhibits several distinctive frequencies for model calibration. The most influential frequency locates at around 1474 cm^{-1} with two subordinate ones at 1795 cm^{-1} and 2513 cm^{-1}, which are characteristic of existence of calcium carbonate (Reeves III, *et al.*, 2002). Viscarra Rossel and Behrens (2010) found the carbonate of clay minerals in the NIR band of 2336 nm to be associated with the third overtones of CO_3^{-2} in MIR of 1415 cm^{-1}.

3.4 ATR-FTIR spectral analysis and model calibrations

The procedure of analyzing ATR-FTIR spectra was the same as that presented for Vis-NIR and DRIFT spectral analysis.

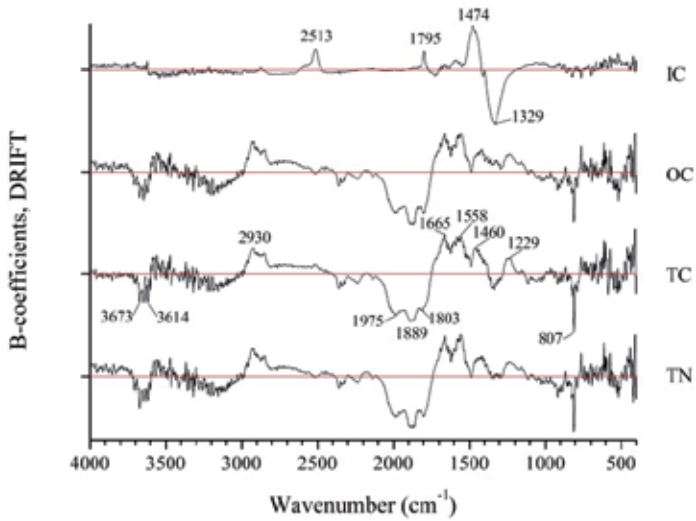

Fig. 11. B-coefficients curves obtained from PLSR analyses with the transformed DRIFT spectra by quantile normalization for TN and OC, baseline offset correction for TC, and Center & Scale for IC.

3.4.1 ATR-FTIR spectral response

Figure12 shows the representative ATR-FTIR spectra of samples from each soil texture class with high and low TC content. Obviously, the absolute magnitude and range of the ATR-FTIR light intensity are much lower than those for corresponding DRIFT spectra. Besides, the ATR-FTIR spectra of the samples present quite different shape together with absence of many characteristic peaks between 3000 and 1700 cm^{-1}, compared to the corresponding DRIFT spectra of these samples. The peaks between 3696 and 3620 cm^{-1} and various peaks

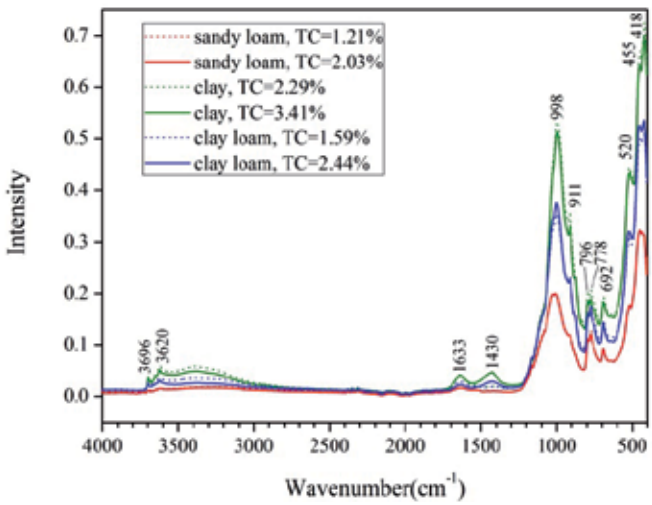

Fig. 12. ATR-FTIR spectra of samples from each soil texture class with high and low TC content.

below 1100 cm^{-1} might be characteristic for kaolinite (Madari, *et al.*, 2006). However, most characteristic wavebands of soil organic matter presented in Table 5, due to their low concentrations in the soil samples and their overlapping with mineral peaks, could not readily be identified by simple visual observation. For example, the bands around 2940-2935 cm^{-1} and 2886-2877 cm^{-1}, indicating the presence of organic aliphatic C-H stretching (shown in DRIFT spectra, Fig.8), are nearly vanished. Although the ATR-FTIR spectra present severe deviations from corresponding DRIFT spectra, the light intensity in ATR-FTIR spectra exhibits strong correlation with particle size distribution. For example, samples of clay texture with fine particles present strongest light intensity, whereas samples with sandy loam texture with coarse particle size have lowest light intensity. The clay loam texture samples with middle size particles correspond to intermediate light absorption. For each soil texture class, the spectral difference due to high and low TC content is not apparent. All these spectra appear to be free from baseline offset.

3.4.2 PCA analysis for ATR-FTIR spectra

Figure 13 shows all Mid-IR spectra obtained by FI-IR spectrometer with ATR accessory together with the PCA scores plot for the spectra and residual X-variance for PC-1 and PC-2. PC-1 and PC-2 explained 98% and 1% of total variance of the spectra, respectively. The PC-2

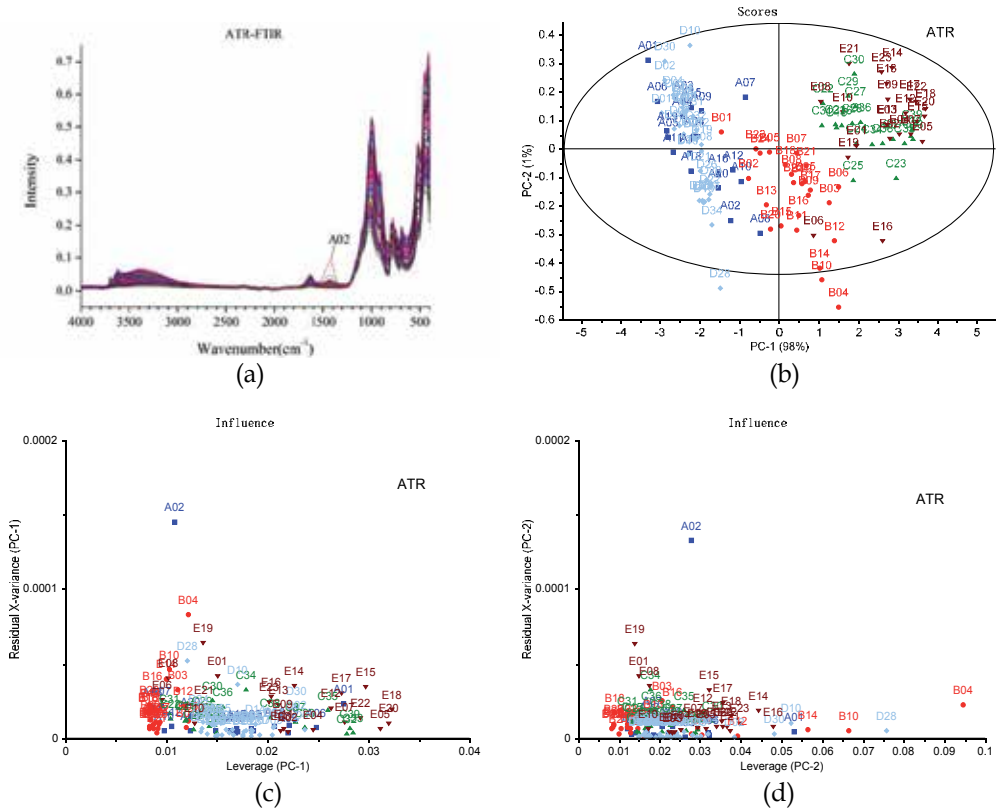

Fig. 13. All ATR-FTIR spectra (a), principal components analysis scores plot for the ATR-FTIR spectra (b), and residual X-variance for PC-1 (c) and PC-2 (d).

shows variation related to SOM of the samples as the PC-2 was better correlated to TN, TC and OC (r=-0.68~0.71) than to PC-1 (r=0.52~0.56) (Table 3). Samples originated from different fields can be divided into one cluster for Luvisol type soils (field #D) and another for Cambisol type soils (fields #B, #C, and #E). Although samples from the field #A are the mixture of Cambisol and Luvisol types, most of them locate within the former cluster. Samples from the fields #C and #E are hardly separated, although they are of the same soil texture of clay (Table 1). Compared to the samples D28, B04 and B10 located outside of the Hotelling T^2 ellipse (Fig.13b), sample A02 exhibits large residual X-variance for PC-1 (Fig.13c) and PC-2 (Fig.13d). Thus, sample A02 was considered as a sample outlier and excluded from further investigation.

3.4.3 ATR-FTIR calibration models

Table 7 summarizes the cross-validation results of PLSR models developed with the raw and various transformed ATR-FTIR spectra against each soil property. For raw spectra, PLSR models produced excellent prediction accuracy for TN, TC and OC with R^2 of 0.89~0.92 and RPD of 3.02~3.75. These models were developed with 6 latent variables. None of spectral pre-processing techniques adopted can effectively improve the prediction accuracy of these models. This might be due to absence of the baseline offset of spectra (Fig.12). For IC, all models can be used to distinguish high and low concentration with RPD

Spectral pretreatment method	PLSR models calibrated for ATR-FTIR spectra											
	Total N			Total C			Organic C			Inorganic C		
	LVs	R^2	RPD	LVs	R^2	RPD	LVs	R^2	RPD	LVs	R^2	RPD
None	**6**	**0.92**	**3.75**	**6**	**0.89**	**3.02**	**6**	**0.89**	**3.10**	6	0.71	1.91
SNV	5	0.90	3.33	5	0.88	2.89	3	0.87	2.74	4	0.69	1.82
MSC	5	0.90	3.33	4	0.87	2.75	3	0.87	2.74	4	0.69	1.82
BOC	7	0.91	3.53	7	0.88	2.95	7	0.89	3.07	4	0.70	1.87
Center & Scale	6	0.91	3.53	6	0.89	2.97	6	0.89	2.97	4	0.70	1.88
Normalization												
Maximum-	5	0.90	3.33	5	0.87	2.79	5	0.87	2.78	5	0.70	1.85
Range-	5	0.90	3.53	4	0.86	2.71	6	0.88	2.93	5	0.70	1.85
Mean-	6	0.91	3.53	4	0.86	2.69	5	0.88	2.87	5	0.70	1.87
Quantile-	7	0.91	3.75	6	0.88	2.89	6	0.89	3.00	4	0.70	1.87
De-trending												
1st-	6	0.90	3.53	6	0.87	2.79	7	0.89	3.09	**5**	**0.72**	**1.93**
2nd-	6	0.91	3.53	6	0.87	2.79	5	0.88	2.92	5	0.72	1.91
Derivative												
1st-	4	0.88	3.16	4	0.85	2.60	4	0.86	2.69	5	0.71	1.91
2nd-	3	0.78	2.31	3	0.75	1.99	2	0.74	1.98	7	0.60	1.61

Table 7. Cross validation result of PLSR models developed with raw and various transformed ATR-FTIR spectra with 121 samples

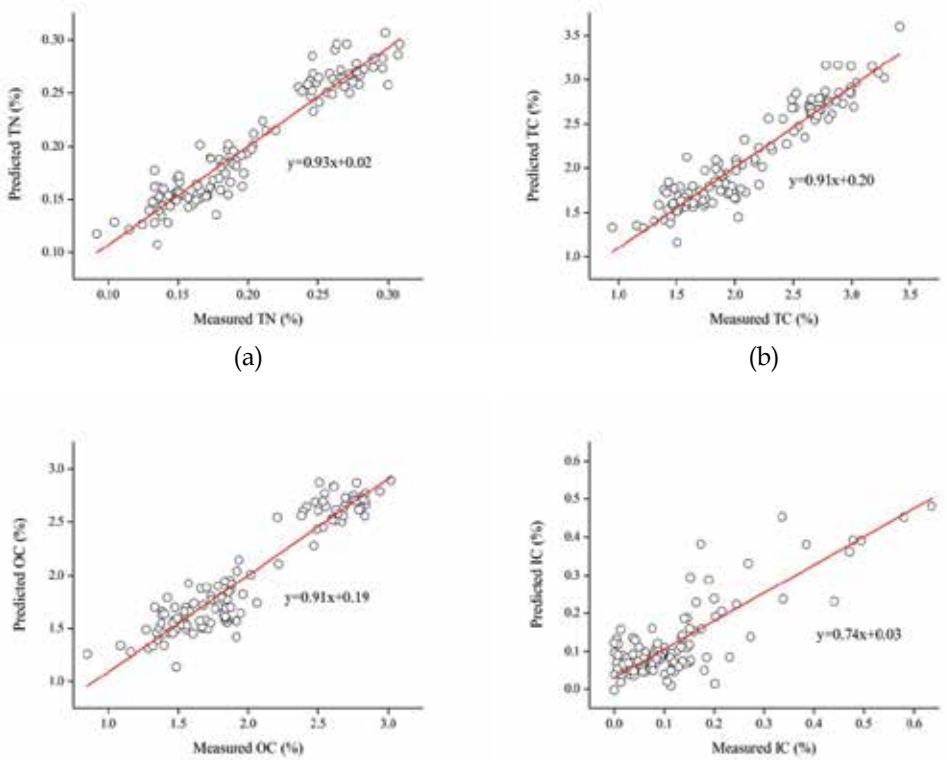

Fig. 14. Measured vs. predicted values of soil TN (a), TC (b), OC (c) and IC (d) based on the ATR-FTIR spectra.

of 1.61~1.93. Figure 14 shows the correlation between the measured and predicted values of each soil property. The linear fitting lines for TN, TC and OC are closer to the 1:1 lines as compared to the corresponding plots for Vis-NIR spectra (Fig.6a-c), but not so well as those for DRIFT spectra (Fig.10a-c). However, the linear fitting for IC is better than that for Vis-NIR spectra (Fig.6d) and that for DRIFT spectra (Fig.10d).

3.4.4 B-coefficients analysis of PLSR models for ATR-FTIR spectra

B-coefficients curves of the PLSR models developed with the best transformed ATR-FTIR spectra for each soil property are compared in Fig.15. The B-coefficients for TN, TC and OC exhibit strong similarity among them. This is mainly due to the high correlation obtained with the reference values (r=0.97-0.99, Table 3). Overall, the most significant wavebands for predicting these soil properties locate in the wavenumber range between 1700 and 400 cm^{-1}. As indicated in Table 5, the peaks at 1612-1551 cm^{-1} are for aromatic C=C stretching and/or asymmetric –COO stretching and the peaks at around 1050 cm^{-1} correspond to Polysaccharides. Other significant wavebands can be found at round 2925 cm^{-1}, which correspond to Aliphatic C-H stretching. Interestingly, although the ATR-calibrated models are not accurate enough for IC quantification, its B-coefficients curve for IC exhibits several

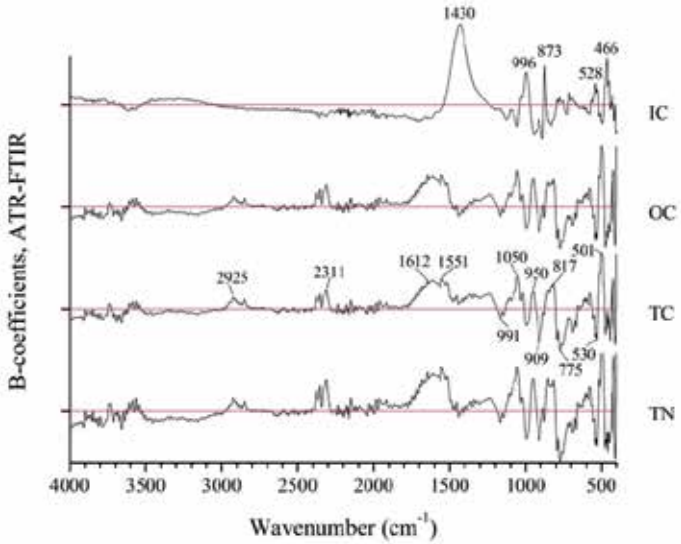

Fig. 15. B-coefficients curves obtained from PLSR analysis with the raw spectra for TN, TC and OC, and the 1st-detrending-transformed spectra for IC.

distinctive bands, similar to those obtained with DRIFT spectroscopy. The most significant band locates at around 1430 cm^{-1}, which corresponds to calcium carbonate ($CaCO_3$). However, compared to the B-coefficients curve for IC based on DRIFT spectra (Fig.11), two characteristic bands of $CaCO_3$ at 1795 cm^{-1} and 2513 cm^{-1} disappear completely, which is mainly due to the weaker light response of ATR-FTIR spectra compared to DRIFT spectra.

3.5 Model calibrations for combinational Vis-NIR-MIR spectra

The raw Vis-NIR and Mid-IR spectra were combined to develop PLSR calibration models of soil TN, TC, OC and IC concentrations. Table 8 shows the cross-validation results of the PLSR models. For the Vis-NIR-ATR spectra, PLSR models produced excellent prediction accuracy with R^2 of 0.89~0.91 and RPD of 3.00~3.75 for TN, TC and OC. By comparison, PLSR models calibrated for the Vis-NIR-DRIFT spectra achieved higher prediction accuracy than those with Vis-NIR-ATR spectra, with R^2 of 0.93~0.95 and RPD of 3.83~4.62 for TN, TC and OC. For IC, PLSR model for Vis-NIR-ATR spectra was developed with 10 latent variables and validated

Combinational spectra	PLSR models calibrated for raw combinational Vis-NIR-MIR spectra											
	Total N			Total C			Organic C			Inorganic C		
	LVs	R^2	RPD	LVs	R^2	RPD	LVs	R^2	RPD	LVs	R^2	RPD
Vis-NIR-ATR	5	0.91	3.75	5	0.89	3.00	6	0.91	3.42	10	0.69	1.83
Vis-NIR-DRIFT	6	0.95	4.62	6	0.93	3.83	6	0.95	4.32	5	0.70	1.88

Table 8. Cross validation result of PLSR models developed with raw Vis-NIR-MIR spectra with 121 samples

with R^2 of 0.69 and RPD of 1.83, whereas PLSR model for Vis-NIR-DRIFT spectra calibrated with 5 latent variables performed better than Vis-NIR– ATR with higher prediction accuracy (R^2 of 0.70 and RPD of 1.94). These models for combinational spectra performed slightly better than those for Vis-NIR spectra (Table 4). However, these models did not produce better performance than those for DRIFT spectra (Table 6) and ATR spectra (Table 7) with only exception of Vis-NIR-ATR models for OC with R^2 of 0.91 and RPD of 3.42.

3.6 Comparison of PLSR model performance among Vis-NIR, ATR-FTIR, DRIFT and combinational spectra

As shown in Tables 4, 6 and 7, model performance is not only a function of wavelength ranges used during PLS regression analysis, but also a function of spectral pre-processing techniques. Overall, for TN, TC and OC, PLSR models calibrated for DRIFT spectra outperformed those for Vis-NIR spectra and ATR-FTIR spectra. For IC, both ATR-FTIR and DRIFT models outperformed Vis-NIR models no matter what spectral pre-processing techniques were applied. However, if coupled with appropriate spectral pre-processing techniques, Vis-NIR models for TN and OC can produce competitive prediction performance (R2>0.90 and RPD>3.0) with less number of latent variables (3 or 4) as compared to best ATR-PLSR models calibrated with 6 latent variables. For TC, ATR-FTIR models performed slightly better than Vis-NIR models. The lower accuracy for the calibration of IC compared to TN, TC and OC may be attributed to errors in the reference method for IC determination, since IC is calculated by difference between TC and OC.

Researchers have reported that the particle size distribution within the soil sample population and also within each sample of the calibration set affects the accuracy of calibration for TC and OC both in Mid-IR and Vis-NIR (Madari, *et al.*, 2006; Mouazen, *et al.*, 2005, Yang, *et al.*, 2011b). However, Vis-NIR proved to be more sensitive to particle size effects than the Mid-IR range (Madari, *et al.*, 2006). Vis-NIR spectroscopy performed very well for a very homogenous sample population, even slightly better than Mid-IR, but with increasing heterogeneity among and within the soil samples the accuracy decreased drastically. By contrast, the particle size distribution had less effect in the Mid-IR range. For the very homogeneous sample population, the accuracy was slightly lower than Vis-NIR, but with the increase in the heterogeneity of the sample population the accuracy did not diminish drastically and was higher than using with Vis-NIR (Madari, *et al.*, 2006). Thus Mid-IR spectroscopy coupled with appropriate chemometrics can be considered to be more robust than Vis-NIR.

3.7 Fundamentals of predicting N in soil

Soil N content is often highly correlated with C (Martin, *et al.*, 2002). For example, Chang, *et al.* (2001) reported r of 0.95 between TC and TN. In this study, the mean (±s.d.) values of TC/TN and OC/TN are 10.6(±0.59) and 9.95(±0.52), respectively (Table 2). It is an interesting point to explore whether there is an independent spectral basis for the determination of N in soil by infrared (IR) spectroscopy or whether N is predicted through high correlation with C. In the work by Chang and Laird (2002), in which C and N were added to a soil resulting in a wide range of C-to-N ratios, N was proved to be predicted in soil independently of C. Although the N absorbers are present in the soil spectra, their absorbance is not as strong as that of C bonds, as the mass of C in soil is generally an order of magnitude higher than that of N (about 10 times in our case). Thus, Martin *et al.* (2002) explained that N is predicted best

on its correlation with C if a high C-to-N correlation exists. In the current study, the excellent prediction of TN might be due to its high correlation with TC or OC (r=0.97-0.99) (Table 3), which can be proved by the similar distribution of their B-coefficients curves for Vis-NIR spectra (Fig.7), DRIFT spectra (Fig.11), and ATR-FTIR spectra (Fig.15).

4. Conclusions

The Mid-IR spectroscopy, including ATR and DRIFT, and Vis-NIR spectroscopy were implemented for the prediction of soil TN, TC, OC and IC. Results proved that both Vis-NIR and Mid-IR when combined with chemometric methods have great potential to quantify soil N and C at the field scale. It was also shown that DRIFT is more robust than Vis-NIR or ATR in terms of prediction accuracy. Although the Mid-IR spectra holds more information and usually easier to interpret as compared to Vis-NIR spectra with overtones and combinations features, until recently the MIR instruments are less portable and born to easier damage of optical materials. In contrast, the Vis-NIR has some advantages related to portability, mobile (on-line) measurement, remote sensing and others. This study suggests that Vis-NIR spectroscopy, if coupled with proper spectral pre-processing techniques, has the potential for successful prediction of soil N and C, although the combination and overtone peaks in the Vis-NIR spectral range are usually weak.

5. Acknowledgment

We gratefully thank the Soil Labs in Cranfield University for the provision of spectrophotometer. Sincere thanks are given to Dr. Boyan Kuang for assisting soil sampling and laboratory reference measurement, and Dr. Robert J. A. Jones for assisting soil description. Financially supported by Natural Science Foundation of Zhejiang Province, P.R.China (Project No.Y1090885) and by the State Scholarship Fund of China (Grant No.[2009]3004).

6. References

Chang, C.-W. & Laird, D. A. (2002). Near-Infrared Reflectance Spectroscopic Analysis of Soil C and N. *Soil Science*, Vol.167, No.2, pp.110-116, ISSN 0038-075X

Chang, C.-W.; Laird, D. A.; Mausbach, M. J. & Hurburgh, C. R. (2001). Near-Infrared Reflectance Spectroscopy–Principal Components Regression Analyses of Soil Properties. *Soil Sci. Soc. Am. J.*, Vol.65, No.2, (2001/3), pp.480-490, ISSN 0361-5995

Fystro, G. (2002). The prediction of C and N content and their potential mineralisation in heterogeneous soil samples using Vis-NIR spectroscopy and comparative methods. *Plant and Soil*, Vol.246, pp.139-149, ISSN 0032-079X

Gaffey, S. J. (1986). Spectral reflectance of carbonate minerals in the visible and near infrared (0.35-2.55 microns):calcite, aragonite, and dolomite. *American Mineralogist*, Vol.71, pp.151-162, ISSN 0003-004X

Haché, C.; Shibusawa, S.; Sasao, A.; Suhama, T. & Sah, B. P. (2007). Field-derived spectral characteristics to classify conventional and conservation agricultural practices. *Computers and Electronics in Agriculture*, Vol.57, No.1, pp.47-61, ISSN 0168-1699

Ludwig, B.; Khanna, P. K.; Bauhus, J. & Hopmans, P. (2002). Near infrared spectroscopy of forest soils to determine chemical and biological properties related to soil

sustainability. *Forest Ecology and Management*, Vol.171, No.1-2, pp.121-132, ISSN 0378-1127

Madari, B. E.; Reeves Iii, J. B.; Machado, P. L. O. A.; Guimarães, C. M.; Torres, E. & McCarty, G. W. (2006). Mid- and near-infrared spectroscopic assessment of soil compositional parameters and structural indices in two Ferralsols. *Geoderma*, Vol.136, No.1-2, pp.245-259, ISSN 0016-7061

Martin, P. D.; Malley, D. F.; Manning, G. & Fuller, L. (2002). Determination of soil organic carbon and nitrogen at the field level using near-infrared spectroscopy. *Canadian Journal of Soil Science*, Vol.82, No.4, pp.413-422, ISSN 0008-4271

Mouazen, A. M.; Baerdemaeker, J. D. & Ramon, H. (2006). Effect of wavelength range on the measurement accuracy of some selected soil constituents using visual-near infrared spectroscopy. *Journal of Near Infrared Spectroscopy*, Vol.14, No.3, pp.189-199, ISSN 0967-0335

Mouazen, A. M.; Karoui, R.; De Baerdemaeker, J. & Ramon, H. (2005). Classification of soil texture classes by using soil visual near infrared spectroscopy and factorial discriminant analysis techniques. *Journal of Near Infrared Spectroscopy*, Vol.13, No.4, pp.231-240, ISSN 0967-0335

Mouazen, A. M.; Maleki, M. R.; De Baerdemaeker, J. & Ramon, H. (2007). On-line measurement of some selected soil properties using a VIS-NIR sensor. *Soil and Tillage Research*, Vol.93, No.1, pp.13-27, ISSN 0167-1987

Mutuo, P. K.; Shepherd, K. D.; Albrecht, A. & Cadisch, G. (2006). Prediction of carbon mineralization rates from different soil physical fractions using diffuse reflectance spectroscopy. *Soil Biology and Biochemistry*, Vol.38, No.7, pp.1658-1664, ISSN 0038-0717

Reeves III, J.; McCarty, G. & Mimmo, T. (2002). The potential of diffuse reflectance spectroscopy for the determination of carbon inventories in soils. *Environmental Pollution*, Vol.116, No.Supplement 1, pp.S277-S284, ISSN 0269-7491

Schimann, H.; Joffre, R.; Roggy, J.-C.; Lensi, R. & Domenach, A.-M. (2007). Evaluation of the recovery of microbial functions during soil restoration using near-infrared spectroscopy. *Applied Soil Ecology*, Vol.37, No.3, pp.223-232, ISSN 0929-1393

Sinfield, J. V.; Fagerman, D. & Colic, O. (2010). Evaluation of sensing technologies for on-the-go detection of macro-nutrients in cultivated soils. *Computers and Electronics in Agriculture*, Vol.70, No.1, pp.1-18, ISSN 0168-1699

Viscarra Rossel, R. A. & Behrens, T. (2010). Using data mining to model and interpret soil diffuse reflectance spectra. *Geoderma*, Vol.158, No.1-2, pp.46-54, ISSN 0016-7061

Viscarra Rossel, R. A.; Walvoort, D. J. J.; McBratney, A. B.; Janik, L. J. & Skjemstad, J. O. (2006). Visible, near infrared, mid infrared or combined diffuse reflectance spectroscopy for simultaneous assessment of various soil properties. *Geoderma*, Vol.131, No.1-2, pp.59-75, ISSN 0016-7061

Vohland, M. & Emmerling, C. (2011). Determination of total soil organic C and hot water-extractable C from VIS-NIR soil reflectance with partial least squares regression and spectral feature selection techniques. *European Journal of Soil Science*, Vol.62, pp.598-606, ISSN 1351-0754

Yang, H.; Kuang, B. & Mouazen, A. M. (2011a). Prediction of soil TN and TC at a farm-scale using VIS-NIR spectroscopy. *Advanced Materials Research Journal*, Vol.225-226, pp.1258-1261, ISSN 1022-6680

Yang, H.; Kuang, B. & Mouazen, A. M. (2011b). Selection of Preprocessing Parameters for PCA of Soil Classification Affected by Particle Sizes Based on Vis-NIR Spectroscopy. *Key Engineering Materials Journal*, Vol.467-469, pp.725-730, ISSN 1013-9826

13

The Application of Near Infrared Spectroscopy for the Assessment of Avocado Quality Attributes

Brett B. Wedding[1,2], Carole Wright[1], Steve Grauf[1] and Ron D. White[2]
[1]*Rapid Assessment Unit, Department of Employment, Economic Development and Innovation, Queensland*
[2]*Rapid Assessment Unit, James Cook University, Queensland*
Australia

1. Introduction

Quality and safety evaluation of agricultural products has become an increasingly important consideration in market/commercial viability and systems for such evaluations are now demanded by customers, including distributors and retailers. Unfortunately, most horticultural products struggle with delivering adequate and consistent quality to the consumer. Removing inconsistencies and providing what the consumer expects is a key factor for retaining and expanding both domestic and international markets. Most commercial quality classification systems for fruit and vegetables are based on external features of the product, for example: shape, colour, size, weight and blemishes. However, the external appearance of most fruit is generally not an accurate guide to the internal or eating quality of the fruit. Internal quality of fruit is currently subjectively judged on attributes such as volatiles, firmness, and appearance. Destructive subjective measures such as internal flesh colour, or objective measures such as extraction of juice to measure sweetness (^{o}Brix) or assessment of dry matter (DM) content are also used, although obviously not for every fruit – just a sample to represent the whole consignment.

For avocado fruit, external colour is not a maturity characteristic, and its smell is too weak and appears later in its maturity stage (Gaete-Garreton et al., 2005). Since maturity is a major component of avocado quality and palatability, it is important to harvest mature fruit, so as to ensure that fruit will ripen properly and have acceptable eating quality. Currently, commercial avocado maturity estimation is based on destructive assessment of the %DM, and sometimes percent oil, both of which are highly correlated with maturity (Clark et al., 2003; Mizrach & Flitsanov, 1999). Avocados Australia Limited (AAL (2008)) recommend a minimum maturity standard for its growers of 23 %DM (greater than 10% oil content) for the 'Hass' cultivar, although consumer studies indicate a preference for at least 25 %DM (Harker et al., 2007).

The inability to consistently guarantee internal fruit quality is an important commercial consideration of the Australian avocado industry (HAL & AAL, 2005). Retail and consumer surveys over the last 15+ years have shown that consumers are not always satisfied with avocado quality, mainly because of poor flesh quality that can not be determined until the fruit is cut (Embry, 2009; Gamble et al., 2008; Harker et al., 2007; Hofman & Ledger, 1999). The surveys show that only 30% of the Australian population eat avocados and they expect to discard one in every four pieces of fruit they purchase because of poor internal quality (Avocados Australia Limited & Primary Business Solutions, 2005). Other reasons contributing to reduced consumption include concerns over spoilage, convenience, price and limited availability (Harker, 2009). The surveys revealed that consumers select bruising as the major defect, followed by body and stem end rots (Harker, 2009). Bruising was found to be a more important barrier to purchasing than price (Harker, 2009).

Fruit quality reliability is a key factor impacting on supply chain efficiency and related profitability since repeat purchasing by consumers is significantly affected by a bad eating experience. For example, avocados with internal defects of 10% or more have a dramatic negative impact on the consumer repurchasing (Embry, 2009; Petty & Embry, 2011). Research has shown that if a consumer is dissatisfied with the quality of fruit purchased, then that consumer will not purchase that commodity for another 6 weeks (Embry, 2009). Australian avocado quality surveys have shown that increased levels of purchase can be achieved by improving overall quality. For example, there is potential to increase consumer purchasing by 9% by reducing the average level of damage or defects by 15% (Embry, 2009).

Australian avocado production is expanding rapidly and there are strong financial incentives to increase sales domestically and to export product to increase returns directly. Reliable export of avocados from Australia by sea freight requires long storage times, typically 2 - 3 weeks to Asia and 5 - 6 weeks to the European Union (Hofman & Marques, 2009). The biggest risk during transport is the development of rots and flesh disorders resulting in a poor quality product. The additional time and distance associated with most export markets results in longer times from harvest to consumption which increases the risks of quality loss before the consumer receives the fruit. The key factor for retaining and expanding both domestic and international markets is removing inconsistency and providing what the consumer expects, i.e., a consistent quality product with suitable DM content and fruit free of bruises and flesh disorders. A rapid and non-destructive system that can accurately and rapidly monitor internal quality attributes would allow the avocado industry to provide better, more consistent fruit eating quality to the consumer, and thus improve industry competitiveness and profitability.

The development of automated technologies has enabled commercially feasible non-invasive methods for estimating internal quality attributes of agricultural products. These methods are generally based on one of the following properties: nuclear magnetic resonance (NMR) and magnetic resonance imaging (MRI), ultrasonics for vibrational characteristics, X-ray and gamma ray transmission, electrical properties, firmness, density, optical reflectance and transmission. Today, emphasis is put on the development of non-destructive methods for real-time in-line applications. Although several non-invasive techniques exist for this (Abbott, 1999; Butz et al., 2005; Chen & Sun, 1991; Gaete-Garreton et al., 2005; Mizrach, 2000; Mizrach & Flitsanov, 1999), NMR and near infra-red spectroscopy (NIRS) are the leading candidates for the application to fruit and vegetables. NMR has been demonstrated to have

the potential to measure the DM percentage in avocados (Chen et al., 1993; Kim et al., 1999), but the cost and challenges for in-line use in the sorting line means that it is not currently a commercially viable application for high volume, low value items such as fruit and vegetables (Clark et al., 1997; Clark et al., 2003).

NIRS has been demonstrated to be an accurate, precise, rapid and non-invasive alternative to wet chemistry procedures for providing information about relative proportions of C-H, O-H and N-H bonds. Analysis of NIRS absorption spectra aids in the qualitative and quantitative determination of many constituents and properties of horticultural produce, including oil, water, protein, pH, acidity, firmness, and particularly soluble solids content or total soluble solids of fresh fruits (Abbott, 1999; Butz et al., 2005; Scotter, 1990). Of particular importance for the current study, NIRS has been used to estimate %DM in various horticultural products (Birth et al., 1985; Hartmann & Bijning-Pfaue, 1998; McGlone & Kawano, 1998; Sivakumar et al., 2006; Xiaobo et al., 2006) including avocados (Clark et al., 2003; Schmilovitch et al., 2001; Walsh et al., 2004). The technique requires minimal or no sample preparation, and avoids wastage and the need for reagents. Furthermore, it is multi-analytical, allowing estimates of several characteristics simultaneously and has the potential to test every piece of product in an in-line setting.

NIRS is a secondary method of determination and therefore must be calibrated against a primary reference method to develop a calibration model. However, to develop these predictive models requires many samples, many hours of work and many computer calculations to develop a statistical model which can be used to predict future samples (Davies, 2005). The validity of the calibration models for future predictions depends on how well the calibration set represents the composition of new samples. With horticultural products, the major challenge is to ensure that the calibration model is robust, that is, that the calibration model holds across growing seasons and potentially across growing districts.

NIR as a tool to assess internal quality attributes of intact horticultural produce is well established in literature. In general however, the robustness of calibration models with respect to biological variability from different seasons has been neglected and therefore these calibration models may be optimistic with respect to prediction accuracies on future samples in practical applications, such as grading lines (Nicolaï et al., 2007). Nicolai et al. (2007) report that model prediction error in general may easily double when a calibration model is applied to a spectral data set of a different season or orchard. This lack of robustness often translates into bias (Golic & Walsh, 2006; Nicolaï et al., 2007). Robustness of calibration is consequently a critical issue (Nicolaï et al., 2007; Sánchez et al., 2003) and there has been recent work on fruit that considers the effect of different seasons (Peiris et al., 1998; Peirs et al., 2003; Miyanoto and Yoshinobu, 1995; Liu et al., 2005; Guthrie et al., 2005). These studies generally found that incorporating data from multiple growing seasons in the calibration model improved the predictive performance, compared with those calibration models developed using an individual season. Peiris et al. (1998) studied model robustness for the determination of soluble solids (SS) content of peaches and reported that a calibration developed on a population from three consecutive growing seasons had an improvement in prediction performance on a combined season validation set (standard error of prediction (SEP) of 0.94 - 1.26 %SS, and bias 0.17 - 0.38 %SS) over that developed from an individual season population (SEP of 0.90 - 1.36 %SS and bias 0.17

- 2.08 %SS). Peirs et al. (2003) studied the robustness of calibration models for SS content (°Brix) of 'Golden Delicious' apples, with respect to the effects of orchard, season and cultivar. It was found that the largest source of spectral variation between measurements on different fruit was due to seasonal effects. When more seasonal variability was included in the calibration set, for example the model based on the data of all three seasons, the predictive error reduced by approximately 10 to 60%. Similar studies on the seasonal effects for various fruit report similar outcomes (Guthrie, 2005; Liu et al., 2005; Miyanoto & Yoshinobu, 1995).

There have been limited investigations of avocado maturity based on %DM using NIRS. Schmilovitch et al. (2001) used a dispersive NIR spectrophotometer in reflectance mode to assess the 'Ettinger' and 'Fuerte' cultivars (both relatively thin-skinned) in the range 1200 - 2400 nm. Preliminary results identified standard errors of prediction for both 'Ettinger' and 'Fuerte' as 0.9 and 1.3%, respectively, over a 14 – 24 %DM range. Clark et al. (2003) investigated the use of a fixed polychromatic/diode array (PDA) spectrophotometer for estimating %DM in whole New Zealand 'Hass' avocado fruit using both reflectance and interactance modes. They concluded that interactance mode was a better predictor of %DM compared with reflectance. Reflectance models required high numbers (12 to 20) of latent variables (LV), indicating the models struggled against spectral noise and so required incorporation of many small spectral features to improve accuracy. Clark et al. (2003) reported interactance validation statistics of R^2 (coefficient of determination) prediction >0.83, and root mean square error of prediction (RMSEP) <1.8 %DM, over a range of 20 – 45 %DM, while the corresponding reflectance results were <0.75 and >1.9 %DM, respectively. Walsh et al. (2004), using a fixed PDA spectrophotometer (Ziess MMS1/NIR-enhanced spectrometer, Germany) in the 300 - 1100 nm range, reported calibration results of r (correlation coefficient) = 0.89, root mean square error of cross-validation (RMSECV) = 1.14, with a standard deviation ratio (SDR = standard deviation of the data set divided by the RMSECV or RMSEP) = 2.2, for %DM of avocado fruit of unspecified cultivar. The SDR statistic is the measurement of the ability of an NIRS model to predict a constituent and enables comparison of model performance across populations with different standard deviations (Baillères et al., 2002; Golic & Walsh, 2006). The higher the SDR statistic the greater the power of the model to predict the chemical composition accurately (Cozzolino et al., 2004). SDR values between 2.0 and 2.4 for 'difficult' applications, such as high moisture materials including fruit and vegetables are regarded as adequate for rough screening; a value between 2.5 and 2.9 are regarded as adequate for screening; a value between 3.0 and 3.4 is regarded as satisfactory for quality control; a value between 3.4 and 4.0 is regarded as very good for process control; values above 4.1 are excellent for any application (Nicolaï et al., 2007; Schimleck et al., 2003; Williams, 2008).

This study assessed the potential of FT-NIR diffuse reflectance spectroscopy as an objective non-invasive method for determining internal quality attributes of whole 'Hass' avocado fruit. These include: (a) to predict maturity and thereby eating quality based on %DM; (b) to predict the risk of developing internal rot disorders (i.e., rot susceptibility) as an indication of shelf-life; (c) to detect bruises. The study also demonstrates the importance of the calibration model development process to incorporate seasonal and geographical variability to ensure model robustness.

2. Materials and methods

2.1 Avocado fruit samples

2.1.1 Fruit for dry matter model development

'Hass' avocado fruit were obtained over the 2006, 2007 and 2008 growing seasons (Harvest months: May to November) from two commercial farms in the major production districts of Bundaberg, South East Queensland (Latitude: 24° 52' South, Longitude: 152° 21' East) and Childers, South East Queensland (Latitude: 25° 14' South, Longitude: 152° 16' East). Avocado fruit were harvested at three maturity stages through each season, corresponding to early, mid and late season harvests over the three growing seasons. This allowed for sufficient variability in the %DM range and other seasonal factors to be included in the calibration procedure. A minimum of 100 fruit were collected at each harvest giving a total of a minimum of 900 individual fruit for each growing region. All fruit were harvested at the hard green stage of ripeness.

2.1.2 Fruit for impact and rot model development

'Hass' avocado fruit were obtained over the 2008 growing season from two farms in Queensland, Australia. The first farm is located near Ravenshoe on the Atherton Tablelands in North Queensland (Latitude: 17° 38' South, Longitude: 145° 29' East) and the second farm is located in the major production district of Toowoomba, South East Queensland (Latitude: 27° 33' South, Longitude: 151° 58' East). Fruit from Ravenshoe were used for the impact assessment trials (n = 102), while Toowoomba fruit (n = 125) were used for rot susceptibility (shelf life) trials. All fruit were harvested at the hard green stage of ripeness.

2.2 NIR data collection

2.2.1 Dry matter NIR data

The spectra of whole, intact avocado fruit were collected using a commercially available Matrix-F, FT-NIR spectrophotometer (Bruker Optics, Ettlingen, Germany; operating software: OPUS™ version 5.1 - 6.5) in the 830 – 2500 nm range. Spectra were obtained in diffuse reflectance mode, using a standard 4 x 20 watt tungsten light source fibre-coupled emission head fitted to the spectrometer. The external emission head was placed directly above the avocado fruit (0^{o} configuration). A light reducing box with a 60 mm diameter cut out window was used to hold the fruit, so that the fruit skin was directly exposed to the focal point of the emission head. A path-length of approximately 170 mm from the external emission head light source to the surface of the fruit provided a spectral scan diameter on the avocado of approximately 50 mm. In obtaining each sample spectrum, 32 scans at a resolution of 8 cm^{-1} were collected and averaged. Due to the large variability in the %DM within a fruit (Schroeder, 1985; Wedding et al., 2010; Woolf et al., 2003) two NIR spectra were collected from each fruit, one spectra from each opposing side midway from the peduncle and base (i.e., equatorial region). A white spectralon standard was used as the optical reference standard for the system prior to the collection of each set of sample spectra. Fruit spectra were acquired after sample temperature equilibration in an air-conditioned laboratory at approximately 22 - 24 °C, and within two days of harvest.

2.2.2 Impact and rot assessment NIR data

For both impact (bruise) and rot assessment trials, diffuse reflectance spectra of whole, intact 'Hass' avocado fruit were collected in the 830 – 2500 nm range using a Bruker Matrix-F, FT-NIR spectrophotometer as discussed in section 2.2.1. Spectra for rot susceptibility prediction were collected from each opposing half of the hard green fruit prior to fruit being placed into 20 °C storage at 85 - 95% relative humidity. At eating ripe fruit were then assessed for rots based on a weight percentage of the flesh volume affected.

For impact assessment, hard green fruit were stored at 20 °C and 85 - 95% relative humidity until fruit reached the sprung stage of ripeness. The sprung stage of ripeness is where the flesh deforms by 2 - 3 mm under extreme thumb pressure (White et al., 2001). Individual spectra were collected from a single side of the fruit on reaching the sprung stage of ripeness. Following initial spectra collection, fruit were dropped from a height of 100 cm against a slate paver (height: 400 mm, length: 400 mm, width: 40 mm) placed upright and supported by concrete blocks to simulate impact damage. Individual fruit were placed into a cotton mesh bag which was firmly suspended by two strings attached to the laboratory ceiling. Each fruit was positioned so that the scanned area would impact against the paver. The fruit in the mesh bag was pulled backwards away from the slate paver and released to swing in a pendulum motion to impact against the slate paver. Fruit were only allowed to impact the paver once. The height from the ground to the middle of the fruit was measured with the fruit sitting freely against the slate paver. The drop height was measured as the difference between the height at the top of the arch, and the height at the bottom of the arch where the fruit hit the paver.

The impacted area was re-scanned after 1 - 2 hours (maximum of 4) and again after 24 hours. Fruit were then placed back into 20 °C storage at 85 - 95% relative humidity and assessed for bruises at eating ripe (approximately 5 days following impact). Bruise assessment was based on visual estimate of percentage bruise development of the flesh within the scanned area.

2.3 Chemical analysis

The %DM reference measurement was obtained from the same area of the fruit that was used to obtain the NIR spectra. To determine the %DM, a 50 mm diameter core equal to the NIR scan area was taken perpendicular to the surface of the fruit, at a depth of approximately 10 - 15 mm. The skin (2 - 4 mm) was removed from the avocado flesh, and the flesh was diced to facilitate drying in a fan-forced oven at 60 - 65 °C to constant weight (approximately 72 hours). The %DM is defined by the percentage ratio of the weight of the dried flesh sample to the original moist flesh sample. It should be emphasized that fruit spectra and %DM were acquired after sample temperature equilibration in an air-conditioned laboratory at approximately 22 - 24 °C and within two days of harvest.

2.4 Data analysis

2.4.1 Dry matter data analysis

Data analysis was carried out using the commercially available chemometric software package 'The Unscrambler™' version 9.8 (CAMO, Oslo, Norway). The sample spectra for

each data set were separated into a calibration set and prediction set to develop the calibration and prediction models respectively. Fruit were assigned to the calibration set from the principal component analysis (PCA) results to provide a global representation of the attributes of the entire fruit population while eliminating repetition. All remaining fruit where used in the validation sets. Partial least squares (PLS) regression was used to build the prediction models of the diffuse reflectance spectral data, using segmented cross validation (20 segments in this case). Before calibration model development, the variation of the spectral data was analysed by PCA, and obvious spurious spectra eliminated. Data pretreatment and smoothing for the individual %DM models for each growing location in this study were based on a combination of: a 25 point Savitsky-Golay (SG) spectral smoothing (2nd order polynomial) and a second derivative transformation (25 point SG smoothing and 2nd order polynomial) for the Bundaberg models; and a 25 point SG spectral smoothing (2nd order polynomial) and a multiplicative scatter correction (MSC) transformation for the Childers models. For the combined Bundaberg and Childers model, data pretreatment and smoothing was based on a combination of a 25 point SG spectral smoothing (2nd order polynomial) and a first derivative transformation (25 point SG smoothing and 2nd order polynomial). Among all spectra collected, significant noise was found at the extremities of the spectral range (830 – 843 and 2414 - 2503 nm). Therefore all raw spectra used for analysis were truncated to a range of 843 - 2414 nm before model development. Typical absorbance spectra for 'Hass' avocado fruit are shown in Figure 1. Model performance was based on the R^2 of the calibration (R_c^2) and validation/prediction (R_v^2) data sets; RMSECV; RMSEP in relation to the bias (average difference between predicted and actual values) (Buning-Pfaue, 2003), and the SDR.

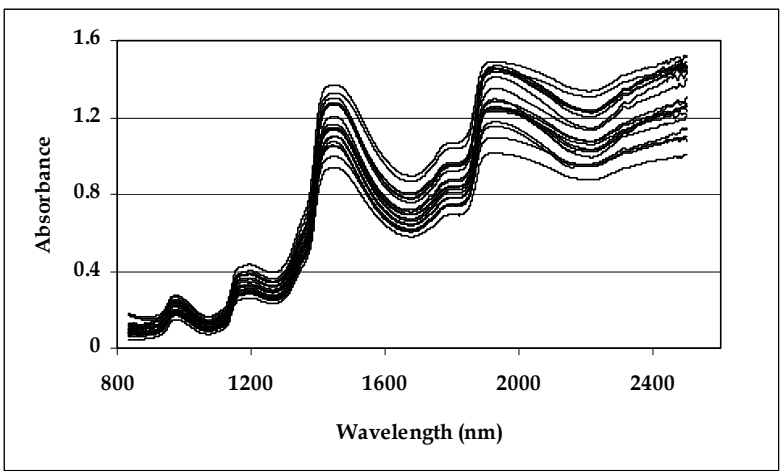

Fig. 1. Typical absorbance spectra for whole 'Hass' avocado fruit.

2.4.2 Impact and rot data analysis

'The Unscrambler™' version 10.1, (CAMO, Oslo, Norway) was used for discriminative analysis to separate the avocados into categories based on percentage rot and percentage bruise development of the scanned area. The 1 – 2 hours impact wavelengths were subjected to weighting by the standard deviation prior to analysis.

3. Results and discussion

3.1 Dry matter prediction

The calibration and prediction model (Figure 2) statistics for each individual year (Table 1) for both harvest locations indicate that FT-NIRS in diffuse reflectance has potential as a screening tool to predict %DM on whole 'Hass' avocado fruit. The 2006 and 2007 harvest seasons had lower standard deviations (SD) than the 2008 season for both the Bundaberg and Childers locations. For the two harvest locations the 2008 harvest season calibration and prediction statistics were the best in terms of regression (R^2) and SDR. The RMSEP for each harvest season varied between 1.29 to 1.49 %DM and 1.41 to 1.94 %DM for Childers and Bundaberg respectively. This suggests that the fruit obtained from the 2006 and 2007 harvest seasons possibly did not include a sufficiently broad variability in physiological attributes to develop a more suitable calibration model as seen with the 2008 harvest season, although other biological or environment effects may have contributed. The number of latent variables are within an acceptable range for the number of samples for all models (Hruschka, 1987; Lammertyn et al., 2000).

Location - Year	Spectra n (OR)	%DM range	Mean	SD	LV	R^2	RM SECV	RM SEP	Bias	Slope	SDR
Bu-2006	629	18.2-35.0	27.5	3.2							
CAL	222(2)	18.2-35.0	27.2	3.5	7	0.75	1.76		-0.159	0.759	2.0
PRE	407	20.334.2	27.6	3.0	7	0.75		1.50	-0.582	0.818	2.0
Bu-2007	609	19.0-34.4	25.7	2.7							
CAL	211(0)	19.0-34.4	25.7	2.8	8	0.76	1.39		-0.0024	0.779	2.0
PRE	398(0)	19.7-32.5	25.7	2.6	8	0.70		1.41	0.112	0.754	1.8
Bu-2008	606	15.2-35.5	25.7	5.7							
CAL	209(1)	15.2-35.5	25.6	5.7	6	0.90	1.76		-0.0036	0.910	3.2
PRE	397(0)	15.6-35.1	25.8	5.7	6	0.88		1.94	0.1526	0.865	2.9
Ch-2006	632	21.4-39.7	29.8	3.4							
CAL	207 (2)	21.4-39.7	30.2	3.7	9	0.82	1.57		0.006	0.829	2.4
PRE	425 (0)	21.7-37.9	29.5	3.3	9	0.80		1.47	0.0761	0.850	2.2
Ch-2007	609	21.9-36.8	29.2	3.1							
CAL	209 (0)	21.9-36.8	29.1	3.3	8	0.83	1.36		-0.0098	0.842	2.4
PRE	400 (1)	22.2-36.2	29.2	3.0	8	0.81		1.29	-0.2867	0.835	2.3
Ch-2008	608	16.1-36.2	25.8	5.3							
CAL	209 (2)	16.1-36.2	25.6	5.2	7	0.93	1.39		0.0098	0.934	3.8
PRE	399 (0)	16.5-36.1	26.0	5.4	7	0.92		1.49	-0.1594	0.858	3.6

Table 1. PLS calibration (CAL) and prediction (PRE) statistics for %DM for whole 'Hass' avocado fruit harvested from Bundaberg (Bu) and Childers (Ch) over the 2006, 2007 and 2008 seasons. *Note: OR = outliers removed; LV = latent variables; n = number of samples.*

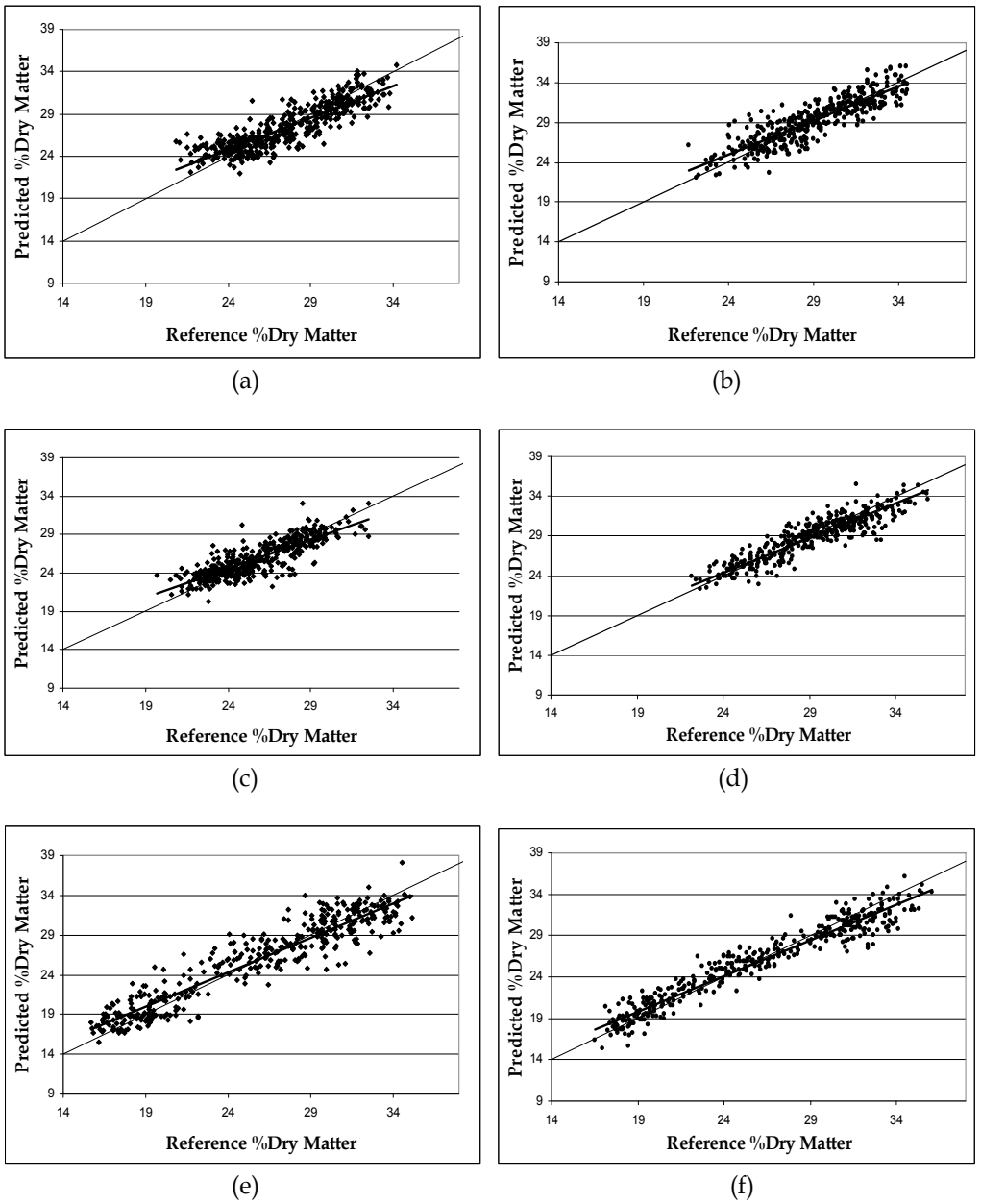

Fig. 2. Model predictions plotted against actual constituent values for %DM for (a) Bundaberg 2006 season, (b) Childers 2006 season, (c) Bundaberg 2007 season, (d) Childers 2007 season, (e) Bundaberg 2008 season, and (f) Childers 2008 season.

Large seasonal effects have a major consequence for calibration models for horticultural produce, since the spectral deviations due to biological variability of future samples cannot be predicted (Peirs et al., 2003). The influence of seasonal variability was investigated for the Bundaberg and Childers growing locations over three years. For both growing locations, the

2006 calibration model was used to predict on the 2007 season population. A combined calibration set using spectra from 2006 and 2007 seasons was used to develop a calibration model that was then subsequently used to predict the 2008 season population. A combined calibration set of 2006, 2007 and 2008 seasons was used to predict over all 3 years. Table 2 displays the summary statistics of the PLS calibration and prediction models for these combinations.

Location - Year		Spectra n (OR)	%DM range	SD	LV	R^2	RM SECV	RM SEP	Bias	SDR
CAL	PRE									
Bu-2006		222(2)	18.2-35.0	3.5	7	0.75	1.76		-0.159	2.0
	Bu-2007	609	14.1-34.4	2.7		0.09		5.07	4.358	0.5
Bu-2006-07		426	14.1-35.0	3.1	9	0.75	1.60		0.112	1.9
	Bu-2008	606	15.2-35.5	5.7		0.45		4.3	0.161	1.4
Bu-2006-08		600(4)	15.8-35.4	4.2	6	0.86	1.55		-0.009	2.7
	Bu-2006-08	1244(1)	14.1-35.6	4.1	6	0.87		1.48	0.0104	2.8
Ch-2006		207(2)	21.4–39.7	3.7	9	0.82	1.57		0.006	2.4
	Ch-2007	609(0)	21.9-36.9	3.1	9	0.14		2.84	1.601	1.1
Ch-2006-07		415(1)	21.4-39.7	3.5	12	0.82	1.49		0.003	2.4
	Ch-2008	608(0)	16.1-36.2	5.3	12	0.79		2.45	-0.547	2.2
Ch-2006-08		624(1)	16.1-39.7	4.6	10	0.88	1.62		-0.001	2.8
	Ch-2006-08	1224(0)	16.5-37.9	4.3	10	0.89		1.43	-0.021	3.0

Table 2. PLS calibration (CAL) and prediction (PRE) statistics for %DM for whole 'Hass' avocado fruit from both Bundaberg (Bu) and Childers (Ch) for 2006, 2006-07 and 2006-08 seasons predicting on 2007, 2008 and 2006-08 seasons respectively. *Note: OR = outliers removed; LV = latent variables; n = number of samples.*

As expected, the application of single seasonal calibrations to populations from other growing seasons was not very successful due to seasonal biological variation. For example, the 2006 calibration models for both Bundaberg and Childers could not be used to predict the 2007 season population for the corresponding harvest location. Model predictive performance improved as more biological variability was included in the models, as seen when the combined 2006 and 2007 models was used to predict on the 2008 season. The combined 2006, 2007 and 2008 calibration models (Figure 3) was sufficiently robust to predict %DM of whole Hass avocado to within 1.48% with an R_v^2 = 0.87 and SDR of 2.8 for Bundaberg; andto within 1.43 %DM with and an R_v^2 = 0.89 and SDR of 3.0 for the Childers harvest location. This indicated an ability to sort the fruit into three categories with approximately 80% accuracy (Guthrie et al., 1998).

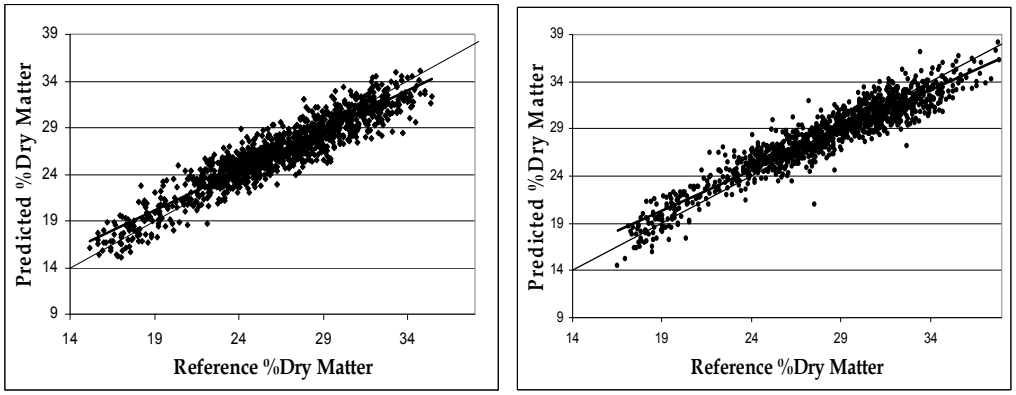

Fig. 3. Model prediction for the combined 2006-08 calibration model for both (a) Bundaberg and (b) Childers locations predicting on the combined 2006-08 prediction set plotted against actual constituent values for %dry matter.

This study demonstrated that including data from multiple growing seasons in the calibration model will improve the predictive performance, in comparison to calibration models developed using an individual season. This is in agreement with the previous studies on this topic (Peiris et al., 1998; Peirs et al., 2003; Miyanoto and Yoshinobu, 1995; Liu et al., 2005; Guthrie et al., 2005). As more biological variability is built into the model, the prediction accuracy becomes less sensitive to unknown changes of external factors (Bobelyn et al., 2010). However, in some cases, including more biological variability (at the risk of including atypical data) in the calibration set can significantly reduce the models prediction accuracy (Bobelyn et al., 2010).

Geographic location (growing regions) effects may also have a major consequence on model robustness as fruit composition is subject to within tree variability (i.e., tree age, crop load, position within the tree, light effects); within orchard variability (i.e., location of tree, light effects); and intra-orchard variability (i.e., soil characteristics, nutrition, weather conditions, fruit age and season variability) (Marques et al., 2006; Peirs et al., 2003). The influence of geographic location variability on %DM for whole avocado fruit was subsequently investigated by assessing calibration model performance using avocado fruit obtained from Bundaberg and Childers locations collected over 3 years.

The PLS calibration and prediction model statistics for both the Bundaberg and Childers harvest locations and combination of both regions are presented in Table 3. The Bundaberg data set of 1844 spectra was separated into a calibration set (n = 600) and a prediction set (n = 1244). The validation statistics of the calibration model were quite good and delivered an R_v^2 = 0.87 with an RMSEP = 1.48 and SDR of 2.8 for %DM. An SDR value between 2.5 and 2.9 is regarded as adequate for screening (Nicolaï et al., 2007; Schimleck et al., 2003; Williams, 2008). The Bundaberg PLS model was used to predict on the entire Childers population. As expected the application of the Bundaberg model to a population from another growing region was not as successful, providing a substantially reduced predictive performance with an R_v^2 = 0.59, RMSEP = 2.84 and SDR of 1.55. Similarly, the Childers data set of 1848 spectra were separated into a calibration set (n = 624) and prediction set (n = 1224).

Harvest Location		Spectra n (OR)	%DM Range	SD	LV	R^2	RM SECV	RM SEP	SDR
Calibration	Prediction								
Bundaberg		600(4)	15.8-35.4	4.2	6	0.86	1.55		2.7
	Bundaberg	1244(1)	14.1-35.6	4.1	6	0.87		1.48	2.8
	Childers	1847	16.1-39.7	4.4	6	0.59		2.84	1.55
Childers		624(1)	16.1-39.7	4.6	10	0.88	1.62		2.8
	Childers	1224(0)	16.5-37.9	4.3	10	0.89		1.43	3.0
	Bundaberg	1844(1)	14.1-35.5	4.2	10	0.74		2.14	1.96
Bundaberg & Childers		1224(4)	15.8-39.7	4.5	9	0.88	1.55		2.9
	Bundaberg & Childers	2468(1)	14.1-37.9	4.3	9	0.89		1.42	3.1

Table 3. PLS calibration and prediction statistics for %DM for whole 'Hass' avocado fruit harvested over three seasons for Bundaberg and Childers growing locations and combination of both regions. *Note: OR = outliers removed; LV = latent variables; n = number of samples.*

The Childers PLS model also produced reasonable validation statistics (R_v^2 = 0.89 with an RMSEP = 1.43 and SDR of 3.0) when predicting fruit from within the Childers region. As with the Bundaberg model, the Childers model did not perform as well when it was used to predict %DM of fruit from a different geographic location such as the combined 2006-08 Bundaberg population (R_v^2 = 0.74 with an RMSEP = 2.14 and SDR of 1.96).

A calibration model was developed by combining both Bundaberg and Childers populations, incorporating biological variability from both regions over three growing seasons. Model predictive performance of the combined population was comparable to the individual regional models of Bundaberg and Childers, with an R_v^2 = 0.89, RMSEP = 1.42, and SDR of 3.1 (Figure 4). These results demonstrate that there are spectral differences between growing districts and that each individual regional model does not incorporate the relevant spectral information enabling the model to successfully predict samples containing biological variability from a different growing district without reduced predictive performance. It is therefore important that calibrations be developed on populations representative in which sorting is to be attempted.

Interpreting NIR models in terms of the various fruit components is often difficult due to spectral co-linearity where information in a model may not necessarily be carried by just a few independent wavelengths, but is possibly a combined effect of many wavelengths with each contributing only relatively little information (McGlone & Kawano, 1998). For oil, strong electromagnetic absorption is reported around 2200 – 2400 nm (CH_2 stretch bend and combinations), with weaker absorption around 1750, 1200 and 900 – 920 nm ranges, and

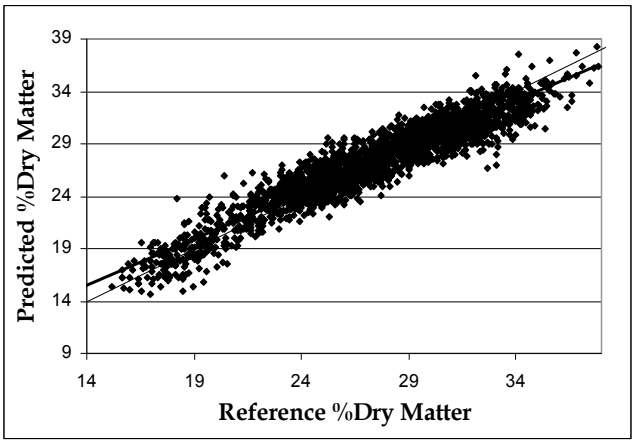

Fig. 4. Model prediction for the Bundaberg and Childers combined 2006-08 calibration model predicting on the Bundaberg and Childers combined 2006-08 prediction set plotted against actual constituent values for %DM.

930 nm (overtones of CH_2 stretching) (Clark et al., 2003; Guthrie et al., 2004; Osborne et al., 1993). Williams and Norris (1987) report that the 1300 - 1750 nm range is very fruitful for absorbers for use in the determination of protein and oil. The 900 - 920 nm absorbance band is often cited as the most important band for %DM and/or sugar determination, as it is removed from the troublesome interferences from the water absorbance peaks that typically dominate spectra of fruit (Clark et al., 2003). However, light penetration depth is wavelength dependent (Lammertyn et al., 2000). The 700 - 1100 nm short-wavelength NIR region allows better penetration into biological material, while wavelengths above 1100 nm (long-wavelength region) have limited penetration providing information only relatively close to the surface (Guthrie et al., 2004; Saranwong & Kawano, 2007). In some instances, there may be secondary correlations between skin properties and those of the bulk flesh and in these circumstances the long-wavelength region can provide relevant information.

The regression coefficient vectors β for the dry matter calibration models across all years in this avocado study had many similar peak positions over the 850 – 2250 nm range. However as expected, there were slight differences in wavelength selection from one year to another which can be attributed to seasonal variability. Relevant spectral information for the calibration models was obtained primarily from oil, carbohydrate and water absorbance bands clustered in the 900 - 980 nm region (second and third overtone), with further contribution from absorbance bands for oil in the vicinity of 1360, 1703, 1722 and 1760 nm. However, these assignments can only be tentative because of other peaks and troughs present here-abouts in the β vectors.

The results of this study are very encouraging and compare favourably to the results obtained by Clark et al. (2003) (RMSEP of 2.6 %DM over a 20 - 45 %DM range and an R_v^2 of 0.75) and Walsh et al. (2004) (R_c^2 = 0.79, RMSECV = 1.14, SDR = 2.2, for %DM of an unspecified cultivar) using a fixed PDA spectrometer in reflectance mode. The current FT-NIRS reflectance combined models for both Bundaberg and Childers compare well with the model accuracy obtained by Clark et al. (2003) (R_v^2 of 0.88 and an RMSEP of 1.8 %DM) using a PDA spectrometer in interactance mode, indicating reflectance FT-NIRS may be a suitable

alternative for in-line and at-line environments. Another comparative study was conducted by Schmilovitch et al. (2001) for two relatively thin skin cultivars, 'Ettinger' and 'Fuerte', during a single season. They used a dispersive NIR spectrophotometer in reflectance mode in the 1200 - 2400 nm range, reporting errors of prediction for 'Ettinger' and 'Fuerte' of 0.9% and 1.3% respectively, for fruit having a 14 – 24 %DM range. It is likely that the relatively smooth to medium textured, thin-skin cultivars would not suffer to the same extent from the physiological limitations experienced in the thick rough skin of 'Hass', and prediction errors would certainly be expected to be lower. We must emphasize however, it is difficult to make a meaningful comparison of the various techniques as there is insufficient detail presented in these papers to establish if the differences are associated with the spectroscopic technique or with the geometry of the configurations used.

3.2 Impact and rot assessment

Classification statistics for the prediction of percentage rot development are presented in Table 4. The preliminary study found that by applying discriminative analysis techniques, 92.8% of the test population could be correctly classified into 2 categories, above and below 30% rot development for the area scanned. The percentage correctly classified decreased slightly to 86.8% when the classification was reduced to above and below 10% rot development for the scanned area.

Item assessed	Spectra (n)	Defined classification (%)	LV	Spectra misclassified (%)	Spectra correctly classified (%)
%Rots of scanned area	250	(i) 0-30; (ii) 31-100	8	7.2 (n=18)	92.8 (n=232)
	250	(i) 0 -10; (ii) 11 – 100	9	13.6 (n=33)	86.8 (n=217)

Table 4. Classification statistics for prediction of percentage rot development (shelf life) of whole 'Hass' avocado fruit. *Note: LV = latent variables; n = number of samples.*

Table 5 depicts the classification statistics for the prediction of percentage bruise development. The results indicate that 90% of the population could be correctly classified into 2 categories based on percentage bruise development in the scanned area (≤10%, ≥11%) using scans conducted 1 - 2 hours following impact. Of the 10 (9.8%) samples misclassified, 6 (5.9%) samples visually rated with bruising greater than 11% were placed into the <10% bruise category and 4 (3.9%) samples with bruising visually rated below 10% were placed into the ≥11% bruise category. The 4 samples misclassified with bruising below 10% were all on the ambiguous change over point of the two defined classification categories at 10% bruising.

These results improved to >95% correctly classified when the fruit were rescanned after 24 hours following impact. It appears the 24 hour time delay allowed more time for the bruising to develop assisting with classification. This would indicate that in a commercial situation it would be an advantage to hold the fruit for 24 hours prior to scanning. The 5 (4.9%) samples misclassified were all samples with bruising visually rated below 10% and placed into the ≥11% bruise category. Of these samples 4 (3.9%) were at the ambiguous change over point of the two defined classification categories at 10% bruising.

Item assessed	Time after impact (hours)	Spectra (n)	Defined classification (%)	LV	Spectra misclassified (n)	Spectra correctly classified (%)
%Bruising of scanned area	1-2	102	(i) 0 - 10; (ii) 11 - 100	10	9.8 (n=10)	90.2 (n=92)
	24	102		8	4.9 (n=5)	95.1 (n=97)

Table 5. Classification statistics for prediction of percentage bruise development in whole 'Hass' avocado fruit. *Note: LV = latent variables; n = number of samples.*

4. Conclusion

NIRS has come to be extensively used in many applications for the non-invasive rapid assessment of a wide variety of products. These both include quantitative compositional determinations and qualitative determinations. The present study indicates the potential of FT-NIRS in diffuse reflectance mode to be used as a non-invasive method to predict the %DM of whole 'Hass' avocado fruit and the importance of incorporating seasonal and geographical variation in the calibration model. The results showed that the calibration model robustness increased when data from more than one season, incorporating a greater range of seasonal variation, was included in the calibration set. Also, that there are spectral differences between geographical regions and that, specific regional models may have significantly reduced predictive performance when applied to samples containing biological variability from a different growing region. It is therefore important that calibrations be developed on populations representative in which sorting is to be attempted.

As shown, there is also great potential to use FT-NIRS as a tool to predict impact damage of whole avocados based on percentage bruise development, and to predict shelf-life based on rot development (susceptibility). It should be considered that the preliminary work presented here is a first step towards shelf-life prediction and bruise detection for avocado fruit. However, this was only a preliminary study and the classification models require many more samples, incorporating seasonal and geographical biological variations, to enable the development of a robust model suitable for commercial use.

Overall, FT-NIR reflectance spectroscopy shows promise for the application in a commercial, in-line setting for the non-destructive evaluation of %DM, bruises and rot susceptibility of whole avocado fruit, although optimisation of the technology is required to address speed of throughput and environmental issues. Incorporating fruit physiological variability over future seasons and growing regions will be essential to further increase model robustness and ensure the predictive performance suitable for commercial use.

Unfortunately, the process of calibration development is a major impediment to the rapid adoption of NIRS in industry. The collection and precise analysis of the reference samples remains a time-consuming and a potentially costly exercise depending on the type of analysis. With this said, NIRS has an obvious place in agriculture and environmental applications with its core strength in the analysis of biological materials, plus low cost of

analysis, simplicity in sample preparation, no chemical reagent requirements, simultaneous analysis of multiple constituents, good repeatability and high throughput capability.

5. Acknowledgments

The authors would like to acknowledge the financial support of the Australian Research Council (LP0562294); BRET-TECH; Department of Employment, Economic Development and Innovation (DEEDI); and James Cook University (JCU) for this project.

The authors also wish to thank Lachlan Donovan, Warren Jonsson, Brian Lubach and Aldo Piagno for the supply of fruit; staff from the Horticulture and Forestry Sciences group within the DEEDI for the organising and collection of fruit; Peter Hofman, Jeff Herse, Bonnie Tilse and Jamie Fitzsimmons for technical assistance during the project.

6. References

Abbott, J. A. (1999). "Quality measurements of fruit and vegetables." *Postharvest Biology and Technology* 15: 207-225.

Avocados Australia Limited (2008). "Avocados Australia New Maturity Standard." *Talking avocados* 19(4): 24.

Avocados Australia Limited & Primary Business Solutions (2005). The current and emerging business environment of the industry: overview of the current situation of industry. *2005-2010 strategic plan for the Australian Avocado Industry*. Sydney, Australian Avocado Ltd and Horticultural Australia Ltd: 11-12.

Baillères, H., Davieux, F. & Ham-Pichavant, F. (2002). "Near infrared analysis as a tool for rapid screening of some major wood characteristics in eucalyptus breeding program." *Annals of Forrest Science* 59: 479-490.

Birth, G. S., Dull, G. G., Renfore, W. T. & Kays, S. J. (1985). "Non-destructive spectraphotometric determination of dry matter in onions." *Journal of American Society of Horticultural Science* 110: 297-303.

Bobelyn, E., Serban, A.-S., Nicu, M., Lammertyn, J., Nicolai, B. M. & Saeys, W. (2010). "Postharvest quality of apple predicted by NIR-spectroscopy: Study of the effect of biological variability on spectra and model performance." *Postharvest Biology and Technology* 55(3): 133-143.

Buning-Pfaue, H. (2003). "Analysis of water in food by near infrared spectroscopy." *Food Chemistry* 82: 107–115.

Butz, P., Hofmann, C. & Tauscher, B. (2005). "Recent developments in noninvasive techniques for fresh fruit and vegetable internal quality analysis." *Journal of Food Science* 70(9): 131-141.

Chen, P., McCarthy, M. J., Kauten, R., Sarig, Y. & Han, S. (1993). "Maturity Evaluation of Avocados by NMR Methods." *Journal of Agricultural Engineering Research* 55(3): 177-187.

Chen, P. & Sun, Z. (1991). "A review of non-destructive methods for quality evaluation and sorting of agricultural products." *Journal of Agricultural Engineering Research* 49: 85-98.

Clark, C. J., Hockings, P. D., Joyce, D. C. & Mazucco, R. A. (1997). "Application of magnetic resonance imaging to pre- and post-harvest studies of fruits and vegetables." *Postharvest Biology and Technology* 11: 1-21.

Clark, C. J., McGlone, V. A., Requejo, C., White, A. & Woolf, A. B. (2003). "Dry matter determination in `Hass' avocado by NIR spectroscopy." *Postharvest Biology and Technology* 29(3): 300-307.

Cozzolino, D., Esler, M. B., Dambergs, R. G., Cynkar, W. U., Boehm, D. R., Francis, I. L. & Gishen, M. (2004). "Prediction of colour and pH in grapes using a diode array spectrophotometer (400-1100nm)." *Journal of Near Infrared Spectroscopy* 12: 105-111.

Davies, T. (2005). "NIR spectroscopy. An introduction to near infrared spectroscopy. Karl H. Norris." *NIR news* 16(7): 9-11.

Embry, J. (2009). Avocado retail quality surveys. *4th Australian and New Zealand Avocado Growers Conference 21-24 July 2009.* Cairns, Queensland Australia: 48.

Gaete-Garreton, L., Varfas-Hern-Ndez, Y., Leon-vidal, C. & Pettorino-Besnier, A. (2005). "A novel non-invasive ultrasonic method to assess avocado ripening." *Journal of Food Science* 70(3): 187-191.

Gamble, J., Wohlers, M. & Jaeger, S. R. (2008). A survey of Australian avocado consumers: Products experiences, health benefit awareness, and impact of defect on purchase intentions. *Report to HAL and Avocado Australia, Project AV07019*. Auckland, New Zealand, The Horticulture and Food Research Institute of New Zealand Ltd.

Golic, M. & Walsh, K. B. (2006). "Robustness of calibration models based on near infrared spectroscopy for the in-line grading of stonefruit for total soluble solids content." *Analytica Chemica Acta* 555(2): 286-291.

Guthrie, J., Greensill, C., Bowden, R. & Walsh, K. (2004). "Assessment of quality defects in Macadamia kernels using NIR spectroscopy." *Australian Journal of Agricultural Research* 55(4): 471-476.

Guthrie, J., Wedding, B. & Walsh, K. (1998). "Robustness of NIR calibrations for soluble solids in intact melon and pineapple." *Journal of Near Infrared Spectroscopy* 6: 259-265.

Guthrie, J. A. (2005). Robustness of NIR calibrations for assessing fruit quality. *Faculty of Arts, Health and Sciences*. Rockhampton, Central Queensland University. Doctor of Philosophy.

Guthrie, J. A., Reid, D. J. & Walsh, K. B. (2005). "Assessment of internal quality attributes of mandarin fruit. 2. NIR calibration model robustness." *Australian Journal of Agricultural Research* 56: 417-426.

HAL & AAL (2005). The current and emerging business environment of the industry: overview of the current situation of industry. *2005-2010 Strategic Plan for the Australian Avocado Industry*. Sydney, Australian Avocado Ltd and Horticultural Australia Ltd: 11-12.

Harker, F. R., Jaeger, S. R., Hofman, P., Bava, C., Thompson, M., Stubbings, B., White, A., Wohlers, M., Heffer, M., Lund, C. & Woolf, A. (2007). Australian consumers' perceptions and preferences for 'Hass' avocado. Sydney, Horticulture Australia Ltd.

Harker, R. (2009). Consumer preferences and choice of fruit: the role of avocado quality. *4th Australian and New Zealand Avocado Growers Conference 21-24 July 2009.* Cairns, Queensland, Australia: 48.

Hartmann, R. & Bijning-Pfaue, H. (1998). "NIR determination of potato constituents." *Potato Research* 41: 327- 334.

Hofman, P. & Ledger, S. N. (1999). "Retail surveys showed little quality improvement." *Talking avocados* 10: 22-23.

Hofman, P. & Marques, J. (2009). Exporting Australian avocado fruit: technical challenges, options and research. *4th Australian and New Zealand Avocado Growers Conference 21-24 July 2009.* Cairns, Queensland, Austrlia.: 46.

Hruschka, W. R. (1987). *Data analysis: wavelength selection methods*, The American Association of Cereal Chemist, Inc, Minnesota USA.

Kim, S., Chen, P., McCarthy, M. & Zion, B. (1999). "Fruit internal quality evaluation using online nuclear magnetic resonance sensors." *Journal of Agriculture Engineering Research* 74: 293-301.

Lammertyn, J., Peirs, A., De Baerdemaeker, J. & Nicolai, B. (2000). "Light penetration properties of NIR radiation in fruit with respect to non-destructive quality assessment." *Postharvest Biology and Technology* 18(2): 121-132.

Liu, Y., Wang, J., Fu, X., Ye, Z. & Lu, H. (2005). *Effect of biological variability on the robustness of FT-NIR models for sugar content of pears*. ASAE Annual International Meeting, Tampa Convention Center, Tampa, Florida.

Marques, J. R., Hofman, P. J. & Wearing, A. H. (2006). "Between-tree variation in fruit quality and fruit mineral concentrations of Hass avocados." *Australian Journal of Experimental Agriculture* 46: 1195-1201.

McGlone, V. A. & Kawano, S. (1998). "Firmness, dry-matter, and soluble-solids assessment of postharvest kiwi fruit by NIR spectroscopy." *Postharvest Biology and Technology* 13(2): 131-141.

Miyanoto, K. & Yoshinobu, K. (1995). "Non-destructive determination of sugar content in satsuma mandarin fruit by near infrared transmittance spectroscopy." *Journal of Near Infrared Spectroscopy* 3: 227-237.

Mizrach, A. (2000). "Determination of avocado and mango fruit properties." *Ultrasonics* 38: 717-722.

Mizrach, A. & Flitsanov, U. (1999). "Nondestructive ultrasonic determination of avocado softening process." *Journal of Food Engineering* 40(3): 139-144.

Nicolaï, B. M., Beullens, K., Bobelyn, E., Peirs, A., Saeys, W., Theron, K. I. & Lammertyn, J. (2007). "Nondestructive measurement of fruit and vegetable quality by means of NIR spectroscopy: A review." *Postharvest Biology and Technology* 46(2): 99-118.

Osborne, B. G., Fearn, T. & Hindle, P. H. (1993). *Practical NIR spectroscopy with applications in food and beverage analysis, second edition.*, Longman Scientific and Technical, Longman Group UK Ltd, Harlow, England.

Peiris, K. H. S., Dull, G. G., Leffler, R. G. & Kays, S. J. (1998). "Near-infrared Spectrometric Method for Nondestructive Determination of Soluble Solids Content of Peaches." *Journal of the American Society for Horticultural Science* 123(5): 898-905.

Peirs, A., Tirry, J., Verlinden, B., Darius, P. & Nicolaï, B. M. (2003). "Effect of biological variability on the robustness of NIR models for soluble solids content of apples." *Postharvest Biology and Technology.* 28(2): 269-280.

Peirs, A., Tirry, J., Verlinden, B., Darius, P. & Nicolaï, B. M. (2003). "Effect of biological variability on the robustness of NIR models for soluble solids content of apples." *Postharvest Biology and Technology* 28: 269-280.

Petty, J. & Embry, J. (2011). *Avocado testing helps lead to improved eating quallity for consumers*. VII World Avocado Congress 2011, Cairns Convention Centre, Cairns - Australia.

Sánchez, N. H., Lurol, S., Roger, J. M. & Bellon-Maurel, V. (2003). "Robustness of models based on NIR spectra for sugar content prediction in apples." *Journal of Near Infrared Spectroscopy.* 11(2): 97-107.

Saranwong, S. & Kawano, S. (2007). Fruit and vegetables. In: Near-infrared spectroscopy in food science and technology. Y. Ozaki, W. F. McClure & A. A. Christy, John Wiley & Sons, Inc., New Jersey, United States of America.: 219-245.

Schimleck, L. R., Mora, C. & Daniels, R. F. (2003). "Estimation of the physical wood properties of green Pinus taeda radial samples by near infrared spectroscopy." *Can. J. For. Res.* 33: 2297-2305.

Schmilovitch, Z., Hoffman, A., Egozi, H., El-Batzi, R., Degani, C. & 175-179., p. (2001). "Determination of avocado maturity by near infrared spectrometry." *Proceedings: Sensors in Horticulture III, Acta Horti. 562 ISHS* 175-179.

Schroeder, C. A. (1985). "Physiological gradient in avocado fruit." *California Avocado Society 1985 Yearbook* 69: 137-144.

Scotter, C. (1990). "Use of near infrared spectroscopy in the food industry with particular reference to its applications to on/in-line food processes." *Food Control*: 142-149.

Sivakumar, S. S., Qiao, J., Wang, N., Gariépy, Y. & Raghavan, G. S. V. (2006). *Detecting Maturity Parameters of Mango Using Hyperspectral Imaging Technique*. ASABE Annual International Meeting, Oregon Convention Center, Portland, Oregon.

Walsh, K. B., Golic, M. & Greensill, C. V. (2004). "Sorting of fruit using near infrared spectroscopy: application to a range of fruit and vegetables for soluble solids and dry matter content." *Journal of Near Infrared Spectroscopy* 12: 141-148.

Wedding, B. B., White, R. D., Grauf, S., Wright, C., Tilse, B., Hofman, P. & Gadek, P. A. (2010). "Non-destructive prediction of 'Hass' avocado dry matter via FT-NIR spectroscopy." *Journal of the Science of Food and Agriculture* 91(2): 233-238.

White, A., Woolf, A. & Hofman, P. (2001). *AvoCare Assessment Manual*. New Zealand, The Horticulture and Food Research Institue of New Zealand Ltd.

Williams, P. (2008). *Near-Infrared Technology - Getting the best out of light* Nanaimo, Canada, PDK projects, Inc.

Williams, P. C. & Norris, K. H. (1987). *Qualitative application of near-infrared reflectance spectroscopy*. St Paul, Minnesota, USA., The American Association of Cereal Chemist, Inc.

Woolf, A., Clark, C., Terander, E., Phetsomphou, V., Hofshi, R., Arpaia, M. L., Boreham, D., Wong, M. & White, A. (2003). "Measuring avocado maturity; ongoing developments." *The Orchidardist*: 40-45.

Xiaobo, Z., Jiewen, Z. & Yanxiao, L. (2006). "Selection of the efficient wavelength regions in FT-NIR spectroscopy for determination of SSC of 'Fuji' apple based on BiPLS and FiPLS models." *Vibrational Spectroscopy*: 1-8.

14

Time-Resolved FTIR Difference Spectroscopy Reveals the Structure and Dynamics of Carotenoid and Chlorophyll Triplets in Photosynthetic Light-Harvesting Complexes

Alexandre Maxime and Rienk van Grondelle
VU University of Amsterdam
Netherlands

1. Introduction

Infrared spectroscopy is a very powerful tool to determine the chemical nature of molecules.

Differential infrared spectroscopy allows to select only those chemical vibrations involved in a light induced reaction. The structure and environment of unstable and short lived excited states can be probed by using step scan FTIR time resolved spectroscopy. In this chapter we present an application of time resolved FTIR step scan spectroscopy to the light harvesting complexes involved in the collection of solar energy in photosynthesis. The time resolved data are analysed using a global and target analysis procedure which allows identification of the dynamic and the spectral properties of short lived intermediates such as triplet states. Triplet state of chlorophyll a (Chl a) can react with oxygen and lead to the formation of singlet oxygen. Carotenoids avoid this reaction via triplet excitation energy transfer (TEET) and quench the triplet of Chl a. The peridinin chlorophyll protein (PCP), an algal light harvesting complex, which binds Per and Chl a is a good system to study photoprotection mechanism by infrared spectroscopy. Indeed Per and Chl a have both conjugated carbonyl groups that are efficient probes of the molecular state in the infrared. We first investigated by step scan spectroscopy the TEET reaction of Per and Chl a in solvent to get their respective spectral signature. Such a study leads to the identification of several mechanisms associated with the formation of triplet states in solution. Secondly the triplet formation is observed in two different PCP complexes leading to the unexpected conclusion that the Per triplet state is delocalised over the Chl a. In a third part we reveal that the same process of triplet sharing between Chl and carotenoid is also present in higher plants, in sharp contrast with purple bacteria for which the triplet is fully localised on the carotenoid. Our finding strongly suggests that in higher plants and algae a much stronger interaction between carotenoids and chlorophylls is at the basis of photoprotection, and represents an example of molecular adaptation in oxygenic photosynthesis.

2. Differential FTIR spectroscopy and data analysis

2.1 Time-resolved infrared spectroscopy

To gain information about the dynamics of the system time-resolved infrared spectroscopy has to be used. Characterization of unstable and short-lived reaction intermediates is required to understand the photo-chemical reactions of light harvesting systems. To investigate the dynamics of such systems time-resolved pump-probe spectroscopy is required. Two different time-resolved infrared (trIR) techniques are commonly used namely ultrafast midIR and step scan FTIR spectroscopy.

In these cases the light-induced difference of infrared absorption (ΔOD) of a sample is measured as a function of time. Then, the ΔOD signal at a given wavenumber and at a given delay time between the pump and the probe, ΔOD(υ,t), is given by:

$$\Delta OD(\upsilon,t) = OD(\upsilon,t)_{Light} - OD(\upsilon)_{Dark} = -\log\frac{I(\upsilon,t)_{Light}}{I(\upsilon)_{Dark}} \quad (1)$$

TrIR can provide many molecular details of the reaction mechanism of protein, associated with their specific lifetimes, which are complementary to X-ray and NMR structure analysis, such as:

- the electronic, redox, protonation and conformational state of the chromophore.
- the H-bonding, the protonation, the charge distribution of side chains of protein residues.
- the H-bonding state of the C=O and C-N-H involved in the peptide bond of the protein backbone which give informations about secondary structure dynamics and the propagation of structural changes.
- the H-bonding state of water molecules which are as essential as the side chain of the residues in achieving protein function in photoreceptors (Garczarek and Gerwert 2006).

Ultrafast midIR and step scan FTIR spectroscopy are complementary. On the sub-nanosecond time scale most of the reaction is confined to the chromophore and the neighboring amino acid residues in the binding pocket and can be monitored using ultrafast IR spectroscopy. Long lived excited states such as triplet state, side chain (de)protonation and large scale protein motion involving changes in secondary-tertiary structure of the protein generally take place on the nanosecond to millisecond time scale and can be monitored using step scan FTIR spectroscopy. In this chapter step scan spectroscopy will be described in detail.

2.2 Step scan-Time resolved FTIR spectroscopy

Step scan-Time resolved FTIR spectroscopy allows monitoring molecular reaction mechanism of proteins at longer time-scales than ultrafast IR spectroscopy. The absorbance changes can be monitored with time resolutions down to nanoseconds and followed for time periods ranging over nine orders of magnitude. The technique has already been successfully applied to the light-driven proton pump bacteriorhodopsin (Kotting and Gerwert 2005), the photosynthetic reaction center and the GTPase Ras (Kotting 2005), PYP (Brudler, Rammelsberg et al. 2001) and Appa (Majerus, Kottke et al. 2007). In contrast to

ultrafast mid-IR which uses a spectrograph containing a grating to disperse the probe beam on a 32-element MCT detector, Fourier-Transform Infrared (FTIR) spectroscopy is an interferometric method. The FTIR spectrometer consists of an infrared source, an interferometer, the sample, and the infrared detector. The interferometer is the heart of the spectrometer and consists in its simplest form of a beam splitter, a fixed mirror, and a moving mirror scanning back and forth. Therefore, the spectrum is not directly measured but its interferogram, i.e. the IR intensity reaching the detector as a function of the mirror position. The spectrum is subsequently obtained by Fourier transformation of the interferogram. The major advantages of FTIR spectroscopy, as compared to conventional dispersive IR spectroscopy, are the so-called multiplexing advantage (Felgett advantage) and the high energy flux reaching the detector (Jacquinot advantage), allowing rapid spectrum acquisition at a high signal to noise ratio. In the step-scan mode, the interferometer moving mirror may be visualized as being held stationary at the interferogram mirror position x_n. The protein activity is initiated, by a laser flash, and the time dependence of the intensity change at this interferogram position x_n is measured. Then the interferometer "steps" to the next interferogram data position x_{n+1}, and the reaction is repeated and measured again. This process is continued at each sampling position of the interferogram.

2.3 Data analysis for time-resolved infrared spectra. Global and target analysis

TrIR experiments result in a 3-dimensional dataset as the changes in intensity ($\Delta OD(\upsilon,t)$) are measured as a function of time and wavelength. A typical dataset results in ~20 000 data points. To analyze such large amounts of data a Global analysis procedure is required (van Stokkum, Larsen et al. 2004). Global analysis implies a simultaneous analysis of the entire 3-dimensional dataset which gives a correlation between different wavelength-regions and time scales. The total dataset is a superposition of contributions from different species (components) having their own time constants (lifetime). Description of such a total dataset should be obtained with a minimum amount (i) of time constants (k_i) that result in a good quality fit. Each component starts with a given concentration (c_i) that decays in time and possesses its own specific time-independent spectrum (ε_i). Mathematically, the observed signal S at any given time (t) or wavenumber (υ) can be described with:

$$S(\upsilon,t) = \sum_{i=1}^{n} c_i(t) * \varepsilon_i(\upsilon) \tag{2}$$

with $c_i = e^{(-k_i t)}$

The resulting spectra ε_i may represent mixture of known physico-chemical species and then do not contain directly physically relevant information. In such case decisions have to be made about a model that not only describes the raw data, but also generates relevant and meaningful spectra. Data previously obtained using different experimental techniques can be helpful in such context. The simplest model describing the measured data has to be chosen. The simplest model templates are the sequential and parallel models (Figures 1A and 1B) where one compartment flows directly into the next compartment with increasing lifetimes or to the ground state, respectively. A compartment represents a spectroscopic distinct state or physico-chemical species and symbolizes a component of the reaction with

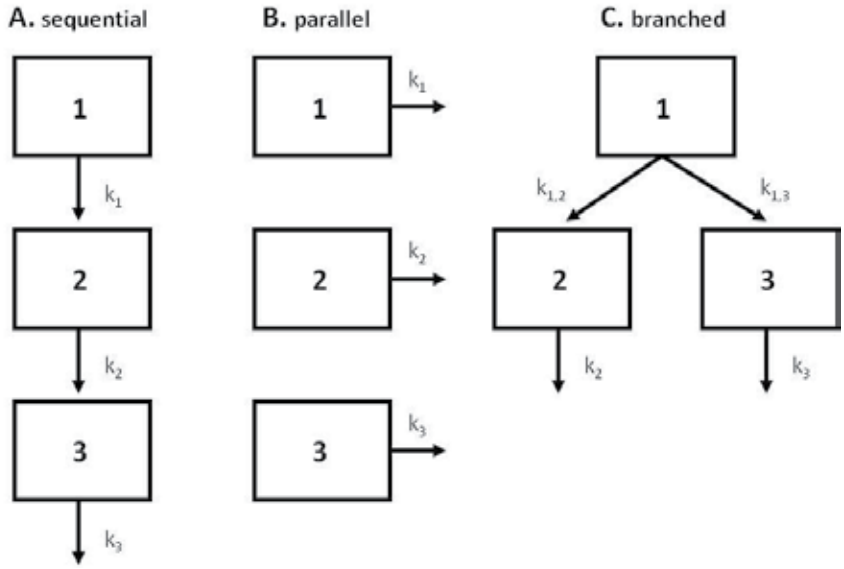

Fig. 1. Schematic view of a sequential model (A), a parallel model (B) and a branched scheme (C).

its spectrum (ε_i) and associated lifetime (k_i). Spectra that result from the application of a sequential and parallel model are called evolution associated difference spectra (EADS) and decay associated difference spectra (DADS), respectively. EADS estimated by a sequential model may represent mixtures of coexisting molecular states, since the possibility of branched or parallel dynamics are not taken into account. In order to disentangle the contributions a more complicated model must be used such as a branched model (Figure 1C), where one compartment can populate two other compartments. If one data set is analyzed with the three described models, then the resulting spectra for each compartment are different, except for compartment 1. Using a model different from the sequential or the parallel model is called a target analysis and can only be done if the data allows for it and/or if additional information is available from other techniques. In this latter case the spectra are no longer called DADS or EADS but species associated difference spectra (SADS).

3. Carotenoid and chlorophyll triplet state dynamic

3.1 Photoprotection mechanisms in Peridinin chlorophyll proteins. The chlorophyll triplet quenching by peridinin

Photosynthesis is the process by which some terrestrial and marine organisms acquire energy from sunlight and transform it into chemical energy (organic compounds) (Gest 2002). Life on earth began roughly ~3.8 billion years ago (Schopf 1992), with some cyanobacterial species being the first photosynthetic organisms to appear. Accumulation of oxygen in our atmosphere has thus been possible due to the presence of these organisms, capable of performing oxygenic photosynthesis. Later the appearance of higher plants led to the production of organic compounds which constitute the basic source of energy for most living organisms. The photosynthetic process and, therefore the abundance and diversity of

life on Earth, ultimately depends on the energy provided by the Sun. Photosynthetic organisms use antenna pigment-proteins to harvest light. Absorbed solar energy is transferred to the reaction center (RC) where it is converted into an electrochemical gradient, which is used to synthesize ATP, powering the cell (van Grondelle, Dekker et al. 1994). Together with (Bacterio)Chlorophyll ((B)Chl) carotenoids are the main pigments of photosynthesis. In addition to their structural involvement in the antenna architecture, carotenoids have a dual function namely light harvesting and photoprotection (Frank and Cogdell 1996). They harvest light in the blue –green spectral region where (B)Chl absorbs weakly thus increasing the absorption cross-section of the light harvesting system where sunlight is optimal. Carotenoid excitation is followed by ultrafast energy transfer to (B)Chl with a high efficiency (Shreve, Trautman et al. 1991; Ritz, Damjanovic et al. 2000; Walla, Linden et al. 2000; Zhang, Fujii et al. 2000; Papagiannakis, Kennis et al. 2002; Holt, Kennis et al. 2003; Zigmantas, Hiller et al. 2004). (B)Chl intersystem crossing (ISC) may lead to triplet formation, the efficiency of which depends on the singlet excited state lifetime. The long-lived (ms timescale) (B)Chl triplet reacts with ground state oxygen (which is a triplet state) to produce the highly reactive oxygen singlet ($^1O_2$) (Krieger-Liszkay 2005). In light harvesting complexes (LHC), this process competes with fast (ns timescale) (B)Chl triplet excitation energy transfer to the carotenoid thereby (Krieger-Liszkay 2005) avoiding formation of $^1O_2$ and ultimately the destruction of the light harvesting apparatus. In addition, carotenoids are also able to scavenge singlet oxygen.

Singlet oxygen can be formed by the quenching of chlorophyll triplet states:

^{3}Chl-*a** + $^3O_2 \rightarrow$ Chl-*a* + $^1O_2^*$ (singlet oxygen formation)

To prevent this reaction, carotenoids with their low-lying triplet states quench long-lived chlorophyll triplets (Nagae, Kakitani et al. 1993; Frank and Cogdell 1996; Krueger, Scholes et al. 1998; Krueger, Scholes et al. 1998; Damjanovic, Ritz et al. 1999; Damjanovic, Ritz et al. 2000) and scavenge singlet oxygen (Cogdell, Howard et al. 2000):

^{3}Chl-*a** + Car $\rightarrow$ Chl-*a* + ^{3}Car* (chlorophyll triplet quenching)

$^1O_2^*$ + Car $\rightarrow$ $^3O_2$ + ^{3}Car (singlet oxygen scavenging)

In PCP, the triplet states of Chl-*a* are formed *via* intersystem crossing (ISC) from Chl-*a* singlet states. The latter are formed after direct Chl-*a* excitation or after excitation energy transfer (EET) which follows direct excitation of Per (Bautista, Hiller et al. 1999; Krueger, Lampoura et al. 2001; Zigmantas, Hiller et al. 2002). The Per triplet states are populated by triplet excitation energy transfer (TEET), which is governed by an electron-exchange interaction (Dexter mechanism) (Dexter 1953; Cogdell and Frank 1987). The PCP visible T-S spectra (Carbonera, Giacometti et al. 1996; Kleima, Wendling et al. 2000) exhibit a Q_y Chl-*a* differential signal assigned to Chl-*a*-carotenoid interaction and is similar to carotenoid T-S spectra found in bacterial and higher plant antennae (Van der Vos, Carbonera et al. 1991; Angerhofer, Bornhauser et al. 1995; Peterman, Dukker et al. 1995). This interaction signal shows concerted dynamics with the carotenoid triplet (Peterman, Dukker et al. 1995; Kleima, Wendling et al. 2000) and has been discussed in terms of a Stark effect, but its exact nature remains unclear. It is then of interest to investigate such triplet dynamic using microsecond time-resolved FTIR spectroscopy to measure triplet formation in PCP by monitoring excitation-induced variations in the vibrational modes of the chromophores. For

infrared spectroscopy a good model to study this photoprotection mechanism is the water soluble LHC from the dinoflagellate *Amphidinium carterae*, A-PCP. Indeed it binds only one type of carotenoid and chlorophyll, Per and Chl a, respectively. In addition, Per and Chl-*a* possess conjugated carbonyl groups which are sensitive to the protein environment and the electronic state of the pigment. In other words, the carbonyl modes are the molecular probes for the pigments: the 9-keto mode of the Chl-*a* and the carbonyl group of the lactone ring of Per. The keto modes are generally expected at lower energies (≤ 1700 cm^{-1}) compared to lactone modes (> 1700 cm^{-1}) which makes them easily distinguishable.

The 2.0 Å crystal structure of A-PCP reveals a trimeric arrangement. The protein is mainly composed of α-helices structure and surrounds a hydrophobic cavity in which besides the pigments also two lipids are bound. The A-PCP monomer contains 2 Chlorophyll-*a* and 8 Peridinins. The molecular structures of Chlorophyll-*a* (Chl-*a*) and peridinin (Per) are shown Figure 2A and 2B. In each half of the PCP monomer one Chl-*a* is closely surrounded by 4 Per (Figure 2C) (Hofmann, Wrench et al. 1996; Hofmann 1999) leading to high efficiency for both light harvesting and photoprotection (Kleima 2000; Alexandre, Luhrs et al. 2007). The N- and C-terminal halves of the polypeptide to which the two clusters of pigments are bound form almost identical domains related by a pseudo two-fold symmetry axis. PCP most likely functions as a LHC that transfers its energy mainly to the PSII RC complex (Knoetzel and Rensing 1990; Mimuro, Tamai et al. 1990). Since the latter complex is located in the photosynthetic membrane, transfer has to occur from a water-soluble complex to a membrane bound complex. As no specific binding site has been identified so far, PCP could in principle either transfer its energy directly to the PSII RC or indirectly *via* the membrane bound Chl-a/c complex, which is an analog of LHCII of green plants. Per has a unique

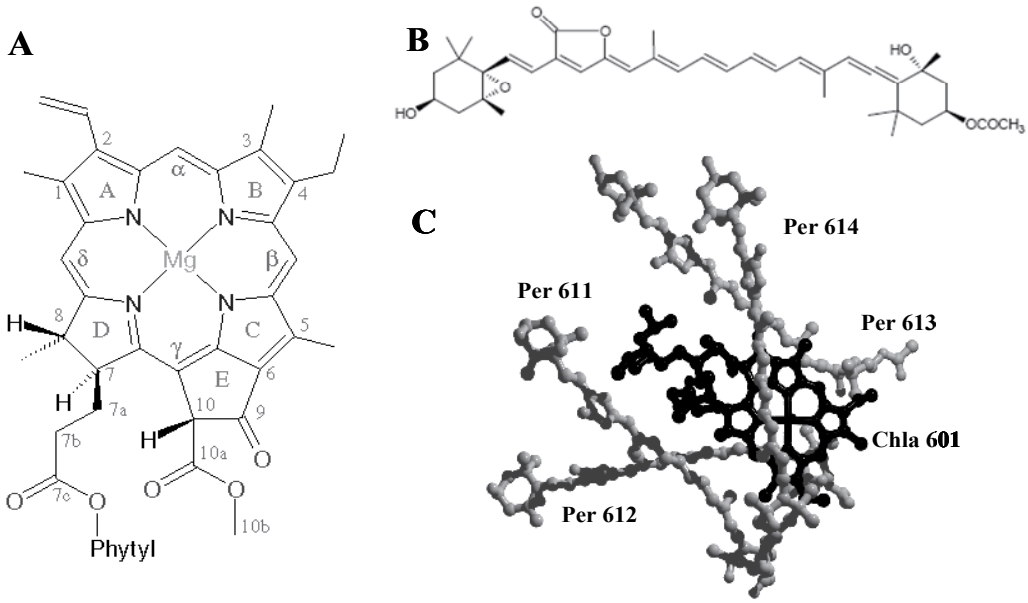

Fig. 2. Molecular structure of Chl-*a* (A) and Per (B). Pigments organization, one Chl-*a* (black) surrounded by 4 Per (grey) (C).

molecular structure constituted of an allene moiety and a lactone ring in conjugation with the π-electron system of the carotenoid backbone, an epoxy group with a secondary alcohol group on one beta-ring and an ester group located on the opposite beta-ring with a tertiary alcohol group (Figure 2B). The structural differences between Per and other carotenoids are most likely related to its specific function in PCP. In contrast to most photosynthetic LHCs, the carotenoid (Per), and not Chl-*a*, is the main light-absorbing pigment in PCP. Per's unusual structure and especially its conjugated lactone carbonyl confers a high plasticity of absorptivity and reactivity to this carotenoid, for instance by mixing CT states with the lower excited states (Bautista, Connors et al. 1999; Zigmantas, Hiller et al. 2002; Vaswani, Hsu et al. 2003; Ilagan, Shima et al. 2004; Zigmantas, Hiller et al. 2004; Premvardhan, Papagiannakis et al. 2005).

A different dinoflagellate species *Heterocapsa pygmaea* uses a LHC closely related to A-PCP, H-PCP. H-PCP has the same pigment stoichiometry as A-PCP but its peptide unit is about half the size of that of A-PCP and contains only half the number of pigments (Song, Koka et al. 1976; Norris and Miller 1994; Hiller, Crossley et al. 2001). The overall identity of the H-PCP monomer with that of the N and C terminal domains of A-PCP is about 70% (Hiller, Crossley et al. 2001). 3-D Modeling of the H-PCP sequence on the high-resolution x-ray structure of A-PCP has shown only major differences in the trimer interface (Hiller, Crossley et al. 2001). In nature, H-PCP is found as a dimer. Thus, the A-PCP monomer can be considered as the covalent equivalent of the H-PCP dimer and the pigment conformation in both systems should be very similar. This view is supported by the high similarity of the spectroscopic properties (Abs, CD, T-S spectra) of the two complexes (Carbonera, Giacometti et al. 1996).

3.2 Peridinin and chlorophyll triplet state in solvent

It is important to firmly establish our spectral assignment of Per and Chl-*a* modes in the ^{3}Per and ^{3}Chl-*a* states using an artificial system where Per and Chl-*a* are not strongly coupled. To this end, we performed step-scan time resolved FTIR measurements on Per mixed with Chl-*a* in organic solvent to observe TEET on the μs timescale and extract their individual spectra using global and target analysis. The two chromophores were mixed in THF with a stoichiometric ratio Per: Chl-*a* of 1:8 with a Chl-*a* OD (670 nm) of about 100 cm^{-1}. Time-resolved FTIR data has been obtained by direct excitation of Chl-*a* at 625 nm and the ensuing spectral evolution was analyzed using global and target analysis. Global analysis in terms of a sequential kinetic scheme shows that three components are required to fit the data. In order to determine the origin of the third component, we used target analysis. The best fit was obtained with a three level scheme, in which the first component decays in 3.5 μs in parallel to the second and the third component, which decay to the ground state in 7 μs and 3 ms, respectively. The kinetic model is displayed in Fig.3. The first component decays into the second and third components with an estimated yield of 60% and 12% respectively. About 28% of the first component amplitude is lost *via* triplet-triplet annihilation and decays to the ground state. Experiments with Chl-*a* only in THF confirmed that the first component decays into a component having similar lifetime and spectral features as compared to the third component observed in the mixed Chl-*a*/Per sample. We note that Per is unable to quench the third component which suggests that it can be assigned to a radical state of Chl-*a*. The three SADS that result from the target analysis of the mixed Chl-*a*/Per data are shown

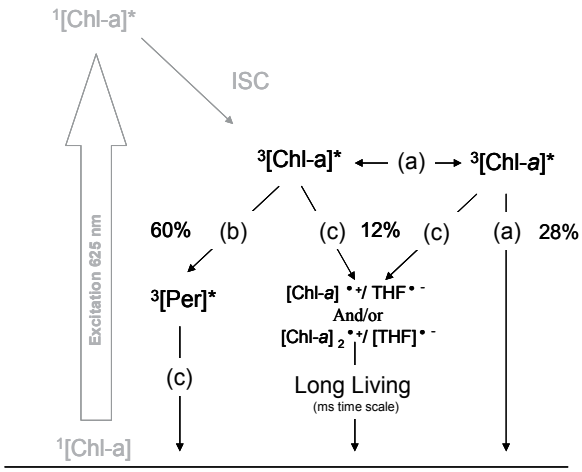

(a) Triplet-triplet annihilation proceeds with a yield of 28% (^{3}[Chl-*a*]* + ^{3}[Chl-*a*]* = ^{1}[Chl-*a*]* + ^{1}[Chl-*a*]). (b) Triplet excitation energy transfer from Chl-*a* to Per takes place in 3.5 µs with a yield of 60%. (c) Chl-*a* radical formation have a yield of 12%.

Fig. 3. Target analysis kinetic model applied to the time-resolved data of Per mixed with Chl-*a* in THF (excitation at 625 nm).

in Figure 4. The first component (SADS1), shown in black in Fig. 4, is assigned to ^{3}Chl-*a* and has a lifetime of 3.5 µs. Its short lifetime indicates that the ^{3}Chl-*a* is strongly quenched in the presence of Per. This SADS matches the FTIR triplet minus singlet (T-S) spectrum of Chl-*a* in THF at 90K (Breton, Nabedryk et al. 1999). Bands at 1747(-)/1733(+) and 1698(-)/1671(+) cm^{-1} are assigned to the Chl-*a* *10a*-ester and *9*-keto carbonyl, respectively. The *9*-keto carbonyl stretch of Chl-*a* in THF at 1698 cm^{-1} is non H-bonded and in a moderately polar environment.

In SADS1 (Fig. 4), the band at 1599 (-) cm^{-1} is typical of a 6-coordinated Chl-*a* Mg-atom (Fujiwara 1986; Fujiwara and Tasumi 1986; Groot 2004). If Chl-*a* is monomeric, then Chl-*a* will be 6-coordinated with two THF molecules ligated to the central Mg atom forming the complex [Chl-*a*]-[THF]$_2$. However the presence of a dip in the ESA at 1657 cm^{-1}, which is not present in the FTIR T-S spectra in ref.(Breton, Nabedryk et al. 1999), may indicate that the observed triplet state actually resides on aggregated Chl-*a*. Chl-*a* at high concentration in an apolar solvent, in the absence of water, is known to aggregate with a typical IR band near 1657 cm^{-1} for Chl-*a* dimers (Katz, Ballschmiter et al. 1968). The aggregation most likely follows from the high concentration used for the FTIR experiments of about 1 mM (OD at 670 nm of about 100 cm^{-1}) in THF. Assuming that Chl-*a* is dimeric in our sample, the 1657 cm^{-1} band most likely indicates a second Chl-*a* (Chl-*a*2) with its 9-keto bound to the Mg atom of the first Chl-*a* (Chl-*a*1) (Katz, Ballschmiter et al. 1968; Fujiwara 1986). As SADS1 is dominated by modes of Chl-*a*1, this suggest that the triplet state is mainly localized on this Chl-*a* for which the ester and keto are free of (H-) bonding.

The second SADS rises in 3.5 µs and decays in 7 µs. It is assigned to ^{3}Per (dash-dot gray SADS in Fig. 3) according to its characteristic decay time. ^{3}Per is formed *via* TEET from ^{3}Chl-*a*, note that this component is not observed in Chl-*a* only samples in THF. The ^{3}Per SADS is dominated by a band-shift at 1761(-)/1733(+) cm^{-1}, assigned to the C=O lactone stretch of

Per. Thus, C=O lactone conformers in THF, which is moderately polar and aprotic, are relatively homogenous and non H-bonded with a main frequency at 1761 cm^{-1}.

In SADS2, the small amplitude bandshift observed around 1697(-)/1666(+) cm^{-1} arises from a contribution by SADS1 (i.e. ^{3}Chl-*a*) that the target analysis fails to fully remove due to our limited time resolution, S/N ratio and baseline fluctuations. A Chl-*a* – Per sample at a 1:1 stoichiometric ratio (OD_{670} = 150 cm^{-1}) exhibits a shorter ^{3}Chl-*a* lifetime of about 1 µs. Target analysis resulted in a ^{3}Per SADS (SADS-Per) almost free of ^{3}Chl-*a* contributions. By comparing this latter SADS-Per with SADS2 (Figure 4, light gray line) we can confirm that in SADS2 (Figure 4) the small amplitude bandshift observed around 1697(-)/1666(+) cm^{-1} follows from a spurious contribution from SADS1 (^{3}Chl-*a*).

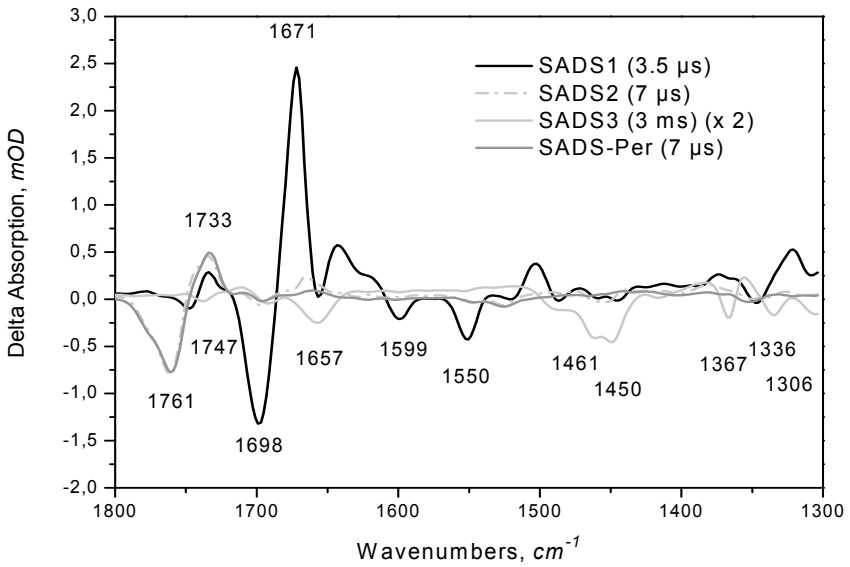

Fig. 4. SADS resulting from target analysis applied to data obtained upon direct Chl-*a* excitation at 625 nm of Per and Chl-*a* mixed in THF with a stoichiometric ratio Per: Chl-*a* of 1:8 with a Chl-*a* OD at 670 nm of about 100 cm^{-1}. The black spectrum is assigned to ^{3}[Chl-*a*]*, it decays in 3.5 µs into the dash-dot gray and light gray SADS. The dash-dot gray SADS is assigned to ^{3}[Per]* and decays to the ground state in 7 µs. The light gray SADS contains signature of Chl-*a* cation and THF radical anion; it decays in 3 ms. The gray spectrum (SADS-Per) is obtained upon direct Chl-*a* excitation at 625 nm of Per and Chl-*a* mixed in THF with a stoichiometric ratio Per: Chl-*a* of 1:1 with a Chl-*a* OD at 670 nm of about 150 cm^{-1}.

The third SADS has an overall low amplitude. It is assigned to the Chl-a^+/THF^- radical pair which is formed with a relatively low yield from the ^{3}Chl-*a* and decays with an estimated lifetime of 3 ms. In the carbonyl region, the third SADS exhibits up-shifted ester and keto C=O stretch frequencies at 1738(-)/1751(+) and 1692(-)/1712(+), 1657(-)/1680(+) cm^{-1}, characteristic for radical cation formation (Breton, Nabedryk et al. 1999). The presence of

two different 9-keto stretches confirms our earlier hypothesis that a Chl-*a* dimer (Chl-*a*1/Chl-*a*2) is present under these conditions. In contrast to the triplet state, which seemed to be mainly localized on Chl-*a*1 (SADS1), the radical appears to be delocalized over the two Chl-*a* molecules of the dimer, as its infrared signature is in fact similar to $P700^+$ in the Photosystem I RC (Breton, Nabedryk et al. 1999). Below 1500 cm^{-1} new bands have appeared in SADS3. A strong negative band with a double peak character is observed centered at 1450 and 1461 cm^{-1} in addition to bands at 1367, 1336 and 1306 cm^{-1}. These bands are typical for THF (data not shown) and up-shifted after Chl-*a* excitation to 1630-1515, 1382, 1354 and 1321 cm^{-1}, respectively. Such up-shifts indicate radical formation of THF, probably the radical anionic ([THF]•-) state, forming the [Chl-*a*]•+/[THF]•- radical pair.

3.3 A PCP triplet state dynamic

In this section we use microsecond time-resolved FTIR spectroscopy to measure triplet formation in PCP by monitoring excitation-induced variations in the vibrational modes of the PCP chromophores. In the following paragraphs, we present the estimated lifetimes, the decay associated difference spectra (DADS) and the vibrational mode assignment of three sets of time-resolved IR data resulting from excitation of Chl-*a* at 670 nm (Q_y), and Per at 480 nm (maximum of Per absorption) and 530 nm (red edge of Per absorption, Fig.5). Excitation at 550 nm gave essentially the same result as 530 nm (data not shown).

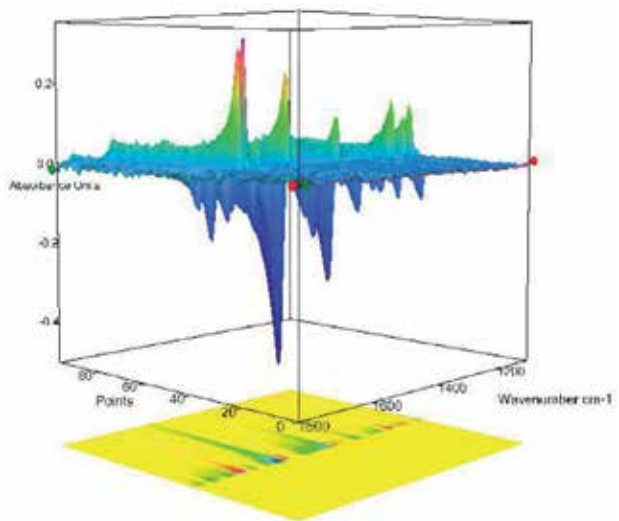

Fig. 5. Differential absorbance signals of PCP obtained by step-scan Fourier-transform infrared spectroscopy. Raw data with 5 μs time resolution for 530 nm excitation; intensity 2 mJ/cm^2.

Time-resolved mid-IR spectra were collected (Fig. 6A) and globally analyzed at frequencies between 1100 and 1800 cm^{-1}, and the resulting decay associated difference spectra (DADS) are shown in Fig. 6B. To describe the time resolved data, we used a parallel model, which required three components: two fast lifetimes, of the order of tens of microseconds and a longer one that we do not consider further We find the triplet state dynamics of PCP at RT to be described by lifetimes of 13 and 42 μs which are typical of carotenoid triplets. Previous

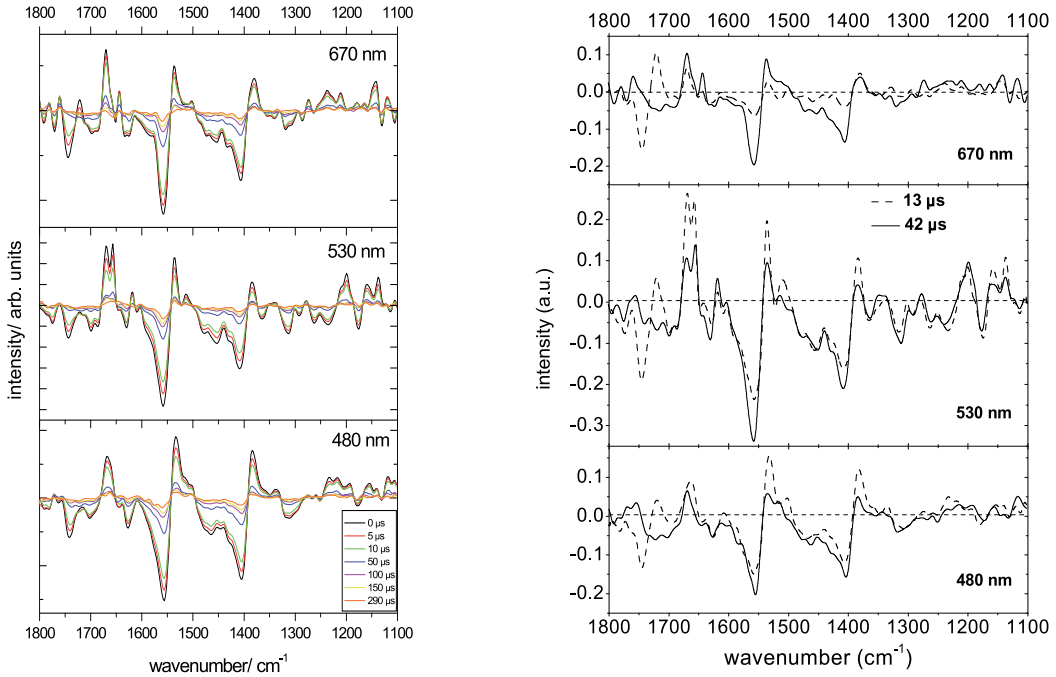

Fig. 6. (A) Time slices of raw data at different excitations. (B) DADS of PCP obtained using a parallel model after different excitations. DADS1 (dotted line) and DADS2 (black line) are associated with a 13 and 42 µs lifetime, respectively.

experiments on PCP in the visible spectral region reported one Per triplet lifetime of 10 µs at RT (Bautista, Hiller et al. 1999; Kleima, Wendling et al. 2000) and two lifetimes of 13 and 40 µs at 77 K (Kleima, Wendling et al. 2000) and 13 and 58 µs up to 200 K (Carbonera, Giacometti et al. 1999), respectively. In Fig. 6 the positive DADS signals originate from excited state absorption (ESA) of the triplet states, and negative DADS signals from the bleach of the ground state.

3.3.1 Spectral analysis

In our spectral analysis, we distinguish four regions of interest: The carbonyl region (1800-1630 cm^{-1}); the C=C stretch region, characteristic of the polyene backbone of carotenoids and chlorophylls giving rise to bands between 1610 and 1525 cm^{-1}; the CH-deformations and possible lactone-ring modes in the region of 1450-1380 cm^{-1} and the fingerprint region below 1380 cm^{-1} with e.g. CH-out-of-plane, C-C and C-O stretches and their combinations.

As we can see in Fig. 6B, the two DADS show many spectral similarities. The weak bands at 1623,1633 cm^{-1} (bleach) and strong bands at around 1555/1530 cm^{-1} (bleach/ESA) are Per C=C stretching modes. Typically, carotenoid C=C stretching modes are around 1520 cm^{-1} – e.g. spheroidene, ß-carotene (Noguchi, Hayashi et al. 1990; Hashimoto, Koyama et al. 1991) – and down-shifted by 20 cm^{-1} to around 1500 cm^{-1} in the T_1 state (Hashimoto, Koyama et al. 1991). In Per we observe slightly higher frequencies, indicating a decrease in bond-order, as observed normally for peripheral C=C stretches (Nagae, Kuki et al. 2000). Moreover, the broad band extending from ~1480 cm^{-1} to lower frequencies (bleach) due to CH-deformation

modes is characteristic of carotenoids (Bernhard and Grosjean 1995). The reported modes of Chl-*a* in PCP (Kleima, Wendling et al. 2000) at 1610, 1553 and 1526 cm^{-1} might also contribute to these bands to a minor extent. Additional recognizable modes are at ~1450 cm^{-1} the methylene C-H deformation and the methyl asymmetric bending modes, as well as the symmetric methyl bending mode of the Per backbone peaks at 1408/1380 cm^{-1} (bleach/ESA) (Bernhard and Grosjean 1995).

Carbonyl region – molecular probes

The carbonyl region contains contributions from Per and Chl-*a* since both have carbonyl groups in conjugation with their electronic system. These carbonyl modes are very sensitive to electronic changes and can be used as molecular probes for the individual chromophores. The carbonyl modes that can be expected in this region are the lactone mode of Per, and the 10a-ester and 9-keto modes of Chl-*a* (Fig. 7).

After global analysis, the DADS in the carbonyl region show five major frequencies in the ground state bleach (best resolved with 530 nm excitation): 1745 cm^{-1} (DADS1), 1741, 1720 cm^{-1} (DADS2), 1699 and 1686 cm^{-1} (both DADS) as seen Figure 7.

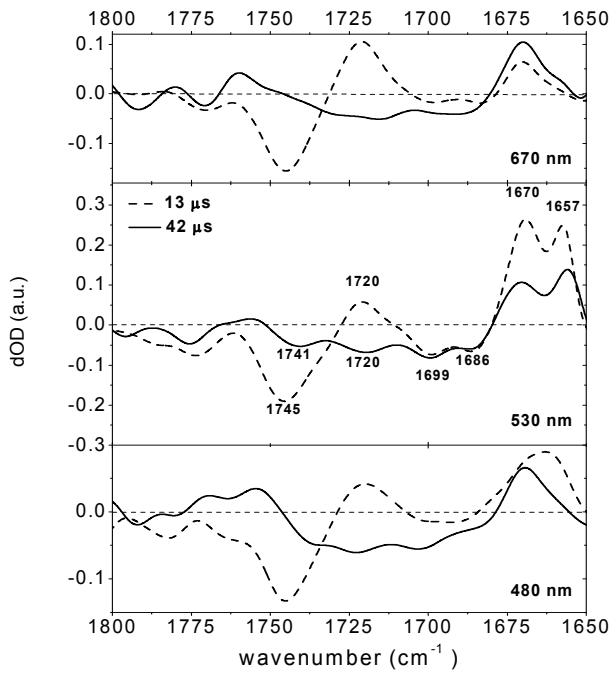

Fig. 7. Comparison of the carbonyl modes of the PCP DADS at 670, 530 and 480 nm excitations.

Carbonyl modes of Chl-a

The bands at ~1699, 1686 cm^{-1} (bleach), shown in Fig. 6 and 7, match the 1697 and 1681 cm^{-1} ones reported from fluorescence line narrowing (FLN) spectra at 4 K (Kleima, Wendling et al. 2000). The ESA of the two bands has shifted down to 1670 and 1657 cm^{-1}, respectively. Such a down-shift is typical for the 9-keto vibration of Chl-*a* in T-S FTIR spectra and can be

perfectly overlapped with the T-S FTIR spectrum of Chl-*a* in THF (Breton, Nabedryk et al. 1999). Chl-*a* triplets are known to exhibit a down-shift in the ESA, while Chl-*a* cations are up-shifted (Breton, Nabedryk et al. 1999; Breton 2001; Noguchi 2002). A hypothetical charge transfer state leading to Per (+)/Chl-*a*(-),would be expected to downshift the 9-keto vibration of Chl-*a* anion by about 55 to 92 cm^{-1} as observed for BPheo/$BPheo^-$ in THF (Mantele, Wollenweber et al. 1988), Pheo/$Pheo^-$ in PSII (Okubo and Noguchi) and BChl-a/$BChl\text{-}a^-$ (Hartwich, Geskes et al. 1995). In our data the 9-keto vibration of Chl-*a* down shifts by 30 cm^{-1} and strongly suggests that only Chl-*a* triplets exist on typical triplet carotenoid lifetimes and we can exclude the presence of Chl-*a* cations and anions. From the 9-keto-mode-amplitudes at 1699, 1686 cm^{-1}, we conclude that both Chl-*a* molecules of the quasi-symmetric PCP monomer are involved in the triplet state dynamics at RT, however, to a different extent depending on the excitation wavelength. The 9-keto mode is the strongest mode in T-S Chl-*a* FTIR difference spectra, about three times more intense than the 10a-ester mode (Breton, Nabedryk et al. 1999; Breton 2001), so we assign the other strong carbonyl modes to the lactone vibration of Per.

Carbonyl modes of Per

The remaining three ground state bleach modes – again best resolved after 530 nm excitation– at 1745 cm^{-1} (DADS1), 1741 (DADS2) and 1720 cm^{-1} (DADS2) represent the lactone carbonyl modes of three distinguishable Per conformers; however the 1741 cm^{-1} (DADS2) conformer is absent under 670 nm excitation. (Fig. 7) The Per ester group, which could be a possible candidate for these frequencies is located at one of the cyclo-hexane end-groups, and isolated from the conjugated backbone. For this reason, we do not expect contributions of the ester group after electronic excitation. The carbonyl-stretch of a five-membered lactone has a typical frequency of 1765±5 cm^{-1} (Kristallovich, Shamyanov et al. 1987), which can downshift by 20 cm^{-1} in conjugation with a π-system, as in Per, and even further in a polar environment or with hydrogen bonding of the carbonyl to the protein pocket. Moreover, the 25 cm^{-1} down-shift of the ESA corresponding to the 1745/1720 cm^{-1} bands would be large compared to 5 cm^{-1} for ester groups (as reported e.g. for chlorophyll) (Breton 2001). The observed ground state bleach modes are in agreement with Per resonant (530 nm) Raman data for PCP (unpublished data, Papagiannakis, E. and Robert B.) which display only two broad bands at 1745 and 1720 cm^{-1} in the carbonyl region. In addition, the resonant Raman spectrum of Per in methanol shows only one broad carbonyl frequency peaking around 1740 cm^{-1}.

The spectral assignments leads to the conclusions that:

- several conformers are involved in the triplet decay dynamics with bands at 1745, 1741, 1725 cm^{-1} and bands at 1695 and 1681 cm^{-1} assigned to various Pers and Chl-*a* conformers, respectively, experiencing different protein environment.
- Differential signals of Per and Chl-*a* are characteristic for their respective triplet states, which disappear with typical carotenoid triplet decay time constants. This implies that in PCP, while the triplet is on the Per, the triplet wavefunction is delocalised over the Chl-*a*, and both triplet signals decay with typical carotenoid tripet lifetimes.
- In addition, both Per and Chl-*a* infrared differential signals show an excitation wavelength dependence. The low frequency keto carbonyl Chl-*a* is more populated and the 1741 cm^{-1} Per conformer appears in DADS2 upon direct red Per excitation (530 and/or 550 nm) in comparison to direct Chl-*a* excitation (670 nm). The 1720 cm^{-1}

dynamics shows a strong wavelength dependence suggesting increased population of this Per conformer upon direct Per excitation. These spectral changes are accompanied by an overall increase of signal amplitude observed from 670 to 480 and to 530 nm. This wavelength dependence indicates that Per triplet formation proceeds via different pathways.

3.4 Triplet quenching in HPCP

It is of interest to investigate whether the same "triplet sharing" occurs in H-PCP as observed in A-PCP. In A-PCP, we previously observed the coexistence of Per and Chl-*a* carbonyl modes during the Per triplet lifetimes of 13 and 42 μs (Alexandre, Luhrs et al. 2007), which led us to conclude that in this triplet state, ^{3}Chl-*a* and ^{3}Per are mixed. Here, we investigated the H-PCP complex by step scan time-resolved FTIR spectroscopy to assess the nature of its triplet state. Upon excitation of peridinin at 530 nm, the H-PCP triplet decay is satisfactorily fitted with a single time constant of 10 μs. Excitation of H-PCP at 670 nm gave essentially the same result (data not shown). Figure 8 shows the DADS with a 10 μs lifetime in H-PCP (black line), plotted along with the 13 μs DADS observed in A-PCP (gray line), reproduced from ref. (Alexandre, Luhrs et al. 2007). Note that in A-PCP, also a 42 μs decay component with a distinctly different infrared signature was observed in the step-scan FTIR experiment (Alexandre, Luhrs et al. 2007). The H-PCP triplet state is spectrally very similar to the triplet state of A-PCP that decays in 13 μs. In both complexes, specific Per C=O lactone conformers are involved in the triplet state, of which the 1745(-)/~1720(+) cm^{-1} is the principal signature. In H-PCP, the bands at 1745(-)/1724(+) are assigned to the Per C=O lactone, while the 1700(-)/1667(+) cm^{-1} shift is attributed to the Chl-*a* C=O 9-keto (Breton, Nabedryk et al. 1999), showing that in the H-PCP triplet IR spectrum, explicit ^{3}Chl-*a* modes are present. This result indicates that some Chl-*a*/Per specific conformations and interactions are conserved in both A-PCP and H-PCP to achieve the efficient photo-protective TEET. This is consistent with the similar T-S ODMR spectra obtained for both complexes (Carbonera, Giacometti et al. 1996). Thus we conclude that both in A-PCP and in H-PCP the triplet state is shared by Per and Chl-*a* in a similar fashion.

In the 10 μs DADS of H-PCP (Figure 8), at least two C=O lactone conformers (1745 and 1710 cm^{-1} in a relative stoichiometry of about 80 and 20%) can be identified for H-PCP, independent of the excitation wavelength. For A-PCP one or two conformers at 1745 and 1745-1725 cm^{-1} depending on the excitation wavelength have been observed, i.e. 670 and 480-530 nm for the 13 μs component (Alexandre, Luhrs et al. 2007). In the two components of A-PCP, three Per conformers have been identified with lactone carbonyl vibrations at 1745, 1741 and 1725 cm^{-1}. This is consistent with the observation that the Per bound to the protein in H-PCP and A-PCP adopts multiple conformations (Hofmann, Wrench et al. 1996). Excitation of A-PCP yielded two triplet decay components of 13 and 42 μs (Alexandre, Luhrs et al. 2007). The differences between A-PCP and H-PCP may be related to the different protein structure, i.e., H-PCP is a 15.5 kDa homo-dimer and A-PCP is a 32 kDa trimer. The 32 kDa unit of A-PCP is asymmetric, composed of two different N-terminal and C-terminal units that share 56% of identity (Hofmann, Wrench et al. 1996). In contrast, H-PCP is a symmetric homo-dimer. The asymmetry within the A-PCP monomer is responsible for the Chl-*a* singlet equilibration on a ps timescale (Kleima, Hofmann et al. 2000; Salverda 2003). Possibly, the asymmetry in A-PCP leads to the observed triplet populations with different lifetimes.

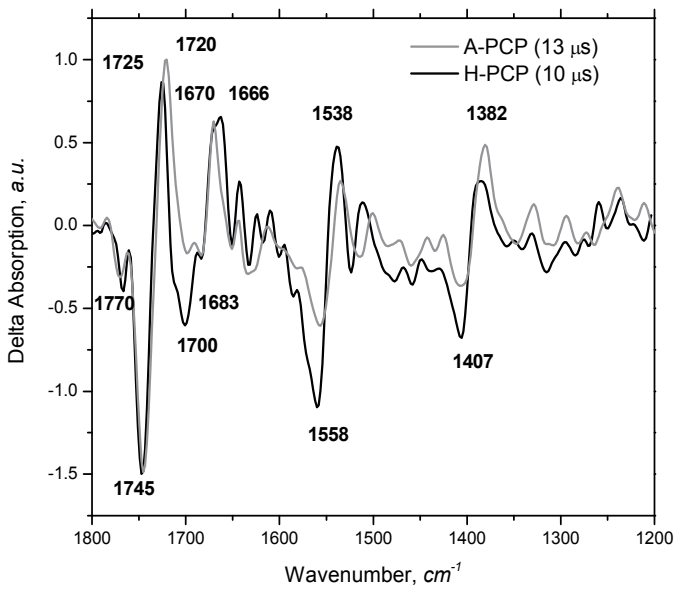

Fig. 8. Decay-Associated Difference Spectra (DADS) that result from a global analysis of step-scan FTIR data of H-PCP and A-PCP. The black line represents the 10 μs component in H-PCP. The gray line represents the 13 μs DADS in A-PCP.

The second component in A-PCP has been observed below 200 K by Carbonera *et al*. (Carbonera, Giacometti et al. 1999) and at 77K by Kleima *et al*., while only a 10 μs component was present at room temperature in the latter work (Kleima, Wendling et al. 2000). We reproduced Kleima's result at room temperature under aerobic and anaerobic conditions, by measuring the triplet decay in the visible using a diluted A-PCP solution. We found only the 10 μs component under aerobic and anaerobic conditions, which excludes an effect related to oxygen (data not shown). Thus, it seems that the appearance of the ~40 μs component is likely related to a protein conformational change induced by cooling and/or high concentrations used for FTIR, rather than a temperature effect on the equilibration among the triplet sublevels (Carbonera, Giacometti et al. 1999).

We previously proposed that the Per conformers involved in the photoprotective mechanism were likely Per 612/622 and Per 614/624. In a recent TR-EPR study (Di Valentin, Ceola et al. 2008), participation of the Per 612/622 pair in the ^{3}Chl-*a* quenching was considered unlikely on the basis of the similarity of the ^{3}Per triplet spectra in Main Form A-PCP (MFPCP) and High Salt A-PCP (HSPCP), since the latter does not bind the Per 612/622 pair. Comparison between experimental and calculated EPR spectra led the authors to conclude that the triplet was mainly (~80%) localized on the Per 614/624 pair, which has the shortest center-to-center distance to the Chl-*a*. This conclusion is consistent with the result of MD calculations showing that in the triplet state, the highest spin density is localized in the center of the Per backbone (Di Valentin, Ceola et al. 2008). Thus, it seems likely that in the step-scan FTIR experiments, the main Per conformer at 1745(-)/~1720(+) cm^{-1} corresponds to Per 614, Per 624, or both. Hence, we conclude that in A-PCP and H-PCP, Per 614 and/or 624 likely constitute the principal ^{3}Chl-*a* quenchers, and that their specific interaction with Chl-*a* promotes the mixing of the ^{3}Chl-*a* and ^{3}Per states during the lifetime of ^{3}Per.

3.5 Triplet state in higher plants

It has been recently reported that the TEET in LHCII takes place in less than 4 ns and is characterised by the lack of accumumaltion of Chl a triplet state. In order to understand the mechanisms underlying the very efficient triplet-triplet transfer, we investigated LHCII by step-scan time-resolved FTIR spectroscopy. Upon excitation of LHCII carotenoids at 475 nm, the triplet decay was satisfactorily fitted with two components only using global analysis. The first component decays with a time constant of 20 µs, while the second component, which does not account for more than 10% of the signal, does not decay within the time window of the measurement (about 320 µs). Figure 9A displays the first decay-associated

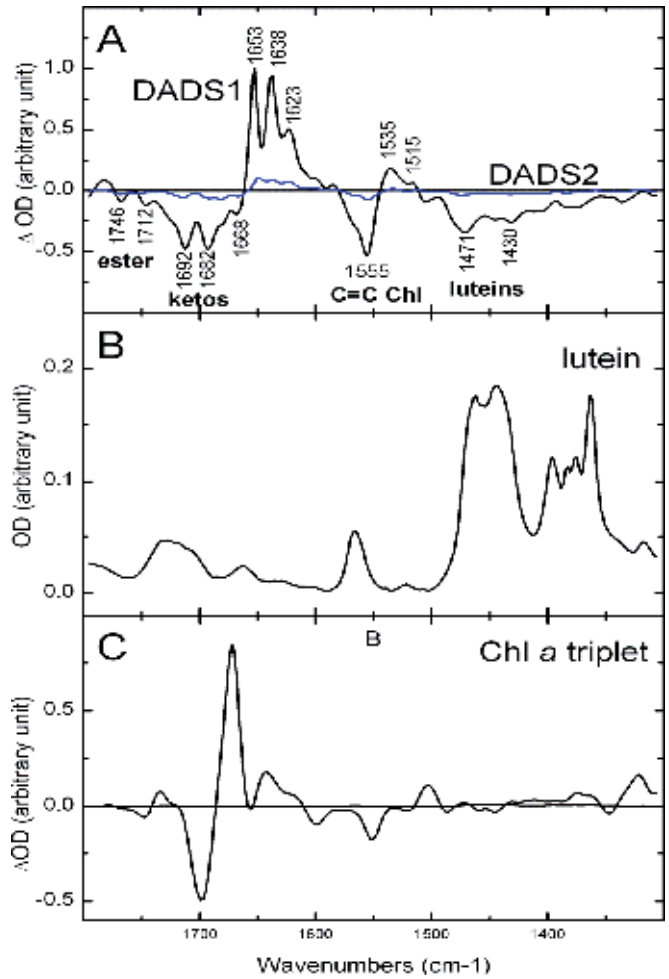

(A) The Decay-Associated Difference Spectra (DADS) have a 20 µs component (black trace, termed DADS1), with an amplitude of 90% (Lutein-Chls shared triplet) and a non-decaying component (blue trace termed DADS2) which has an amplitude of 10% (unquenched Chls). For clarity, the spectra have been normalized to the keto modes. For comparison, the FTIR of lutein (B) and Chl *a* (C) triplet (redrawn from (Bonetti, Alexandre et al. 2009)) in THF are also plotted

Fig. 9. Global analysis of step-scan FTIR data of LHCII excited at 475 nm showing the Lutein-Chls shared triplet state.

difference spectrum (DADS) normalized to the contribution of the keto group at 1653 cm^{-1}. Taking into account the time-resolved absorption data displayed above, the first decay-associated spectrum must be assigned to the carotenoid triplet (Fig. 9A, black spectrum and termed DADS1). In view of its long time the second one is attributed to unquenched Chl, *i.e.* a small proportion of triplet chlorophyll states which have not been transferred to the carotenoid molecules (Fig. 9A, blue spectrum and termed DADS2). It has already been observed that a small fraction of chlorophyll triplet may not be quenched by the carotenoid molecules (Mozzo, Dall'Osto et al. 2008). Considering the results of time-resolved absorption, DADS1 should contain positive contributions of the carotenoid triplet state and negative contributions of its ground state. Although such contributions clearly appear in the difference spectrum (region termed luteins), additional bands are obviously present in this spectrum. Indeed, no intense contribution in the higher frequency region is expected from lutein molecules (see Fig. 9B). On the contrary, in this region, DADS1 is typical of the spectrum of a chlorophyll triplet in solvent which is plotted in Fig. 9C for comparison (Breton, Nabedryk et al. 1999; Bonetti, Alexandre et al. 2009). The negative contributions around 1700 cm^{-1} represent bleaching of bands arising from the stretching modes of conjugated keto carbonyl groups. These groups, when conjugated with the Chl macrocycle, experience large downshifts upon triplet formation, which results in positive contributions at lower frequencies. Nevertheless, DADS1 has a lifetime characteristic of carotenoid triplets, and so we conclude that in LHCII these chlorophyll infrared modes decay with the same lifetimes as carotenoid modes. Then "sharing" of the triplet wavefunction is also observed for higher plants.

4. Comparison of higher plant and purple bacteria triplet state

Resonance Raman is a very sensitive and selective technique which allows access to the vibrational modes of molecules via inelastic scattering. In this section we describe the use of Resonance Raman to confirm the triplet delocalisation observed by step scan spectroscopy.

In solution, upon triplet state formation, the frequency of stretching modes of the conjugated C=C's of the molecule dramatically downshifts from 1522 to 1494 cm^{-1} for ß-carotene in tetrahydrofuran (THF; (Hashimoto, Koyama et al. 1991), (Fujiwara, Yamauchi et al. 2008)), or from 1529 to 1500 cm^{-1} for *all-trans* spheroidene in hexane (Mukai-Kuroda, Fujii et al. 2002). This reflects the localization of the triplet throughout the conjugated system (triplet high spin density "hot spot" is mainly in the centre of the conjugated system; ((Mukai-Kuroda, Fujii et al. 2002), (Di Valentin, Ceola et al. 2008)), which causes a reduction in the C=C bond order. The frequencies of the ν_1 resonance Raman bands observed in protein-bound carotenoid triplet spectra are reported in Table 2 and compared to those observed for triplet states of other carotenoids, including ß-carotene in solution and spheroidene bound to the bacterial reaction center. The downshift depends on the carotenoid configuration, and it is always larger in *cis* configurations ((Hashimoto, Koyama et al. 1991; Mukai-Kuroda, Fujii et al. 2002)). For rhodopin glucoside in LH2, this downshift of the band from 1517 to 1493 cm^{-1} is very similar to that observed for all-trans ß-carotene and spheroidene in solution (24 cm^{-1} *vs.* 23-25 cm^{-1}). In contrast, the observed downshifts for this band for both luteins in LHCII trimers, LHCII monomers, CP29 and CP43 are much smaller and in all cases close to 18 cm^{-1}, *i.e.* approximately 75% of the 23-25 cm^{-1}shift that is observed for all-*trans* carotenoid triplets in solution (see Table 2). Such a reduction of the ν_1

band's downshift reflects a dramatic alteration of the nature of the triplet state, which correlates very well with a reduction in the energy gap between the S_0/S_2 and T_1/T_n transitions observed for these carotenoids in LHCII (see Table 1; it is harder to determine this gap with precision for CP43 due to the larger number of carotenoid molecules in this complex).

Carotenoid (complex)	Number of C=C	$S_0 \rightarrow S_2$ (nm)	$T_1 \rightarrow T_n$ (nm)	ΔE (cm^{-1})
Neurosporene (LH2)	9	495	516	822
Spheroidene (LH2)	10	514	537	833
Rhodopin(LH2)	11	529	556	918
Lutein 1 (LHCII trimers)	10	494	506	480
Lutein 2 (LHCII trimers)	10	510	525	560
Lutein 1 and 2 (LHCII monomers, CP29)	10	494,494	508,505	558,441

Table 1. Electronic transitions of triplet carotenoid states in some LH2 complexes from purple bacteria (values obtained from (Angerhofer, Bornhaeuser et al. 1995)) and in higher plant LHCs prepared as trimers (lines 4 and 5, ((Peterman, Dukker et al. 1995), (Lampoura, Barzda et al. 2002), (Croce, Mozzo et al. 2007)) and monomers (line 6, ((Croce, Mozzo et al. 2007), (Peterman, Gradinaru et al. 1997)), and in CP29* (Croce, Mozzo et al. 2007).

Carotenoid	v_1 (cm^{-1})	Δv_1 (cm^{-1})
LH2 rhodopin glucoside ground state	1517	24
LH2 rhodopin glucoside triplet	1493	
LHCII trimer Lutein1 ground state	1530	18
LHCII trimer Lutein 1 triplet	1512	
LHCII trimer Lutein 2 ground state	1526	18
LHCII trimer Lutein 2 triplet	1508	
LHCII monomer lutein ground state	1526	18
LHCII monomer lutein triplet	1508	
CP29 lutein ground state	1526	18
CP29 lutein triplet	1508	
CP43 lutein ground state	1522	18
CP43 lutein triplet	1504	
all-*trans* β-carotene singlet state in THF	1522	25
all-*trans* β-carotene triplet in THF	1497	
all-*trans*-spheroidene singlet state in *n*-hexane	1523	23
all-*trans*-spheroidene triplet in *n*-hexane	1500	

Table 2. Comparison of the position of v_1 vibrational band in resonance Raman spectra of rhodopin glucoside in LH2, of lutein 1 (ground state of the latter from ref (Ruban, Berera et al. 2007)) and 2 in LHCII trimers and other carotenoid-containing complexes with all-*trans*-ß-carotene, and other carotenoids, in solution (taken from (Hashimoto, Koyama et al. 1991; Mukai-Kuroda, Fujii et al. 2002; Rondonuwu, Taguchi et al. 2004)).

5. Triplet state dynamic in purple bacteria, higher plant and algae, a molecular adaptation of the photoprotection mechanism

Recent time-resolved absorption spectra show that no chlorophyll *a* triplet is accumulated in LHCII and PCP while, on the other hand, the FTIR difference spectra strongly suggest the presence of Chl *a* contributions long after the initial excitation. In order to explain this apparent contradiction, the simplest hypothesis is that the triplet could be shared between carotenoid and chlorophyll molecules. This question has already been addressed in the literature. In order to explain the influence of the carotenoid triplet state on the absorption bands of the BChl molecules in LH complexes from purple bacteria, Angerhofer *et al.* proposed 'a small delocalization of the carotenoid triplet over an adjacent BChl molecule' (10). They also noted that the apparent rate of Bchl to carotenoid triplet-triplet transfer seems to correlate with how much the carotenoid triplet state is able to influence the BChl transition. However, it should be pointed out that in LH complexes from purple bacteria, the carotenoid and BChl molecules are very closely located (an essential condition for triplet/triplet transfer), and therefore they each constitute a sizeable part of the environment (or solvation) of the other. It would thus be expected that the dielectric changes following the appearance of the carotenoid triplet state would have a measurable influence on the BChl absorption transitions. Hence, these previous results do not formally demonstrate a sharing of the triplet. In contrast, the resonance Raman spectra reported in this chapter provides a direct and unambiguous measurement of the sharing of the triplet of the carotenoid molecule. Indeed, upon sharing, the carotenoid triplet should progressively loose its pure triplet character, and the Raman signature of this state should become intermediate between ground- and triplet-state. In the case of rhodopin glucoside in LH2 from *Rbl. acidophilus*, the downshift of the ν_1 band is quite similar to that of ß-carotene or spheroidene in solution. We may thus safely conclude that there is very little, if any, wavefunction sharing between carotenoid and BChl triplet states in the LH2 complex from *Rbl. acidophilus*.

In LHCs from higher plants, the presence of the triplet state of the lutein molecules is known to induce a net bleaching of the electronic absorption transition of the neighboring chlorophyll molecules (Peterman, Gradinaru et al. 1997). However, delocalization of the triplet was for a long time considered unlikely, due to the large energy gap between the triplet states of carotenoid and chlorophyll molecules (Peterman, Gradinaru et al. 1997). This position is challenged by time-resolved FTIR studies on PCP and LHCII, which demonstrate a co-existence of chlorophyll and carotenoid triplets throughout the entire triplet lifetime (Alexandre, Luhrs et al. 2007). In addition, resonance Raman spectroscopy provides additional information on the nature of the carotenoid triplet in these complexes. The sensitivity of the v_1 bands of the ground and triplet states is expected to exhibit similar responses to the environment. However, in LHCII we observe a reduction of the energy gap between the v_1 bands of the ground- and triplet states by more than 30%. This unambiguously indicates that the electronic state gained by the carotenoid has lost a fraction of its carotenoid triplet character, and consequently part of the triplet must be localized on another molecule. From the results of the step-scan time-resolved FTIR measurements (Fig. 9A), we may safely conclude that a neighbouring chlorophyll molecule is the acceptor of the carotenoid triplet. The fact that the same effect was found for both luteins to the same extent strongly substantiates this conclusion. Each lutein experiences a different protein environment (which induces the red-shift of the electronic transitions of lutein 2; (Liu, Yan et

al. 2004)), but is surrounded by a number of similarly-positioned chlorophylls. The fact that both luteins exhibit the same 75/25 sharing of the triplet is thus most easily explained as a result of the pseudo-symmetry of the position of these chlorophyll molecules (Liu, Yan et al. 2004). The same conclusion can be drawn for monomeric LHCII, CP29 and CP43.

A closer analysis of the recently-obtained time-resolved FTIR data obtained for the PCP peridinin triplet supports this analysis. In FTIR, the intensity and frequency of the bands arising from the vibrational modes of the triplet state should reflect the triplet sharing. Since most of the bands are distorted by the differential method and by overlapping contributions, an accurate determination of their precise intensity and frequency is difficult except in the case of well-isolated bands. In the case of LHCII (Fig. 9), no carotenoid band can safely be used for that purpose. In the PCP spectra, the band arising from the stretching mode of the lactone carbonyl of peridinin is well isolated and contributes at *ca.* 1745 cm^{-1}. From FTIR steady-state measurements of peridinin mixed with Chl *a* in THF (data not shown) the peridinin C=O lactone extinction coefficient was estimated to be similar to that of the Chl *a* C=O keto group. This allows us to estimate the extent of the 'triplet sharing' between peridinin and Chl *a*. From Fig. 8 the negative band area assigned to 9-keto C=O corresponds to about 25 and 40 % of the negative band area assigned to lactone C=O for A-PCP and H-PCP, respectively. Taking into account the similar C=O extinction coefficient of peridinin lactone C=O and Chl *a* 9-keto C=O, about 25 and 40 % of the ^{3}peridinin is shared with Chl *a* in A-PCP and H-PCP, respectively. This conclusion is in good agreement with the relative amplitude of the Q_y bleach as compared to the peridinin bleach of about 20 % in the

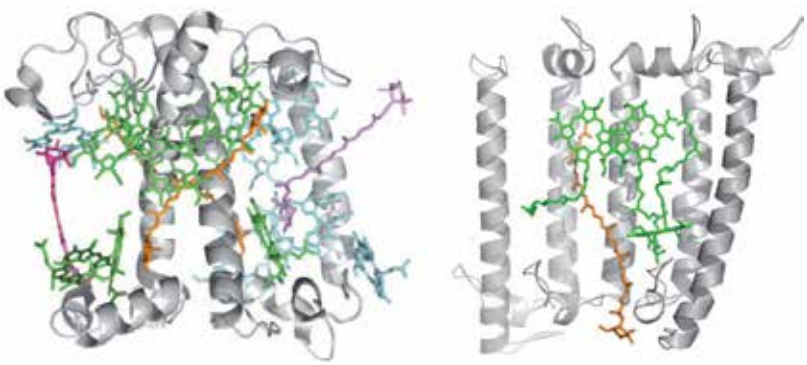

(A) A slice of the nonameric structure of the LH2 complex from *Rhodoblastus acidophilus* viewed in parallel with the membrane plane and from the outside of the protein. For clarity the central outer-helice, from three α/β-apoprotein dimers has been removed allowing the interaction of the Car (orange) with its nearest-neighbour Bchl *a* (green) molecules to be visualised. The contacts between Car and Bchl molecules essentially occur at the very end of the C=C conjugated chain of the carotenoid. Protein Data Bank accession number 1KZU. (B) View of a monomer of LHCII from *Spinacia oleracea* viewed in parallel with the membrane plane. The colours of the luteins (L1 and L2), neoxanthin (neo) and xanthophyll (xan) cycle carotenoids are orange, purple and magenta, respectively. The Chl *a* and Chl *b* molecules are coloured green and blue, respectively. The closest contacts between Chl *a* and luteins in LHCII occur at the middle of the C=C polyenic chain. Although the Chl molecules have a pseudo-symmetry within the monomer lutein 1 (L1) and lutein 2 (L2) experience a different protein environment. Protein Data Bank accession number 1RWT.

Fig. 10. The organisation of the (bacterio)chlorophyll and carotenoid molecules in LH2 and LHCII.

T-S spectra of A-PCP (Kleima, Hofmann et al. 2000). This estimate of a 25 and 40 % triplet sharing in A-PCP and H-PCP is also in line with the smaller observed bandshift of the carbonyl lactone for H-PCP (*i.e.* 20 cm^{-1} as compared to 25 cm^{-1} for A-PCP and 28 cm^{-1} for Per in THF).

Thus, in contrast to photosynthetic bacteria, our results provide compelling evidence of triplet sharing between carotenoid and chlorophyll molecules in plant and algal light-harvesting complexes. It is obviously tempting to try to unravel which molecular mechanisms may be at the origin of this difference. In LH2, contacts between carotenoid and bacteriochlorophyll molecules essentially occur at the very end of the C=C conjugated chain of the carotenoid (Fig. 10A and Ref. (McDermott, Prince et al. 1995)), and the minimum distance between these molecules is 3.42 Å (Prince, Papiz et al. 1997). In strong contrast, the closest contacts between Chl *a* and luteins in LHCII occur at the middle of the C=C polyenic chain (Fig. 10B), and the pigments are slightly more closely packed in these complexes. Taking into account the expected molecular structure of the carotenoid triplet state, the relative positioning of carotenoid and chlorophyll molecules in LHCII appears definitely more favourable for triplet sharing between these molecules

6. Conclusion

To summarize, our results clearly show that the nature of the triplet excited state of carotenoid molecules is fundamentally different in the LH2 from *Rbl. acidophilus* and the antenna isolated from spinach. In the former case, the triplet state is mainly (if not totally) localized on the rhodopin glucoside molecule. According to the work of Angerhofer *et al.*, (Angerhofer, Bornhaeuser et al. 1995), this is the case for the vast majority of light-harvesting proteins from purple photosynthetic bacteria. This localization of the triplet state is associated with a relatively slow triplet-triplet transfer between the BChl and carotenoid molecules, in the 20-200 ns time scale. In LHCII complexes from higher plants, there is a sharing of the triplet between luteins and their neighbouring chlorophylls. As this is also the case in CP43 and CP29, as well as in PCP, it is likely that this triplet sharing exists in all light-harvesting proteins from plants and algae. This delocalization is associated with an ultrafast transfer/equilibration of the triplet between the chlorophyll and carotenoid molecules, which results in the absence of any measurable accumulation of pure triplet chlorophyll in these complexes. However, the price to pay to avoid the accumulation of this species is that the triplet state is shared between the chlorophyll and the carotenoid lasts for several microseconds. Apparently such mechanism drags the energy of the shared triplet below that of singlet oxygen. The resultant decrease in the probability of production of singlet oxygen thereby optimizes photoprotection of these complexes. It is striking that this tuning of photoprotection was found only in those organisms which perform photosynthesis in the presence of large amounts of molecular oxygen. We propose that triplet sharing represents an adaptation of the molecular mechanisms of protection against photo-oxidative stress, associated with the evolution of oxygenic photosynthesis.

7. References

Alexandre, M. T., D. C. Luhrs, et al. (2007). "Triplet state dynamics in peridinin-chlorophyll-a-protein: a new pathway of photoprotection in LHCs?" Biophys J 93(6): 2118-28.

Angerhofer, A., F. Bornhaeuser, et al. (1995). "Optical and optically detected magnetic resonance investigation on purple photosynthetic bacterial antenna complexes." Chem. Phys. 194(2,3): 259-74.

Bautista, J. A., R. E. Connors, et al. (1999). "Excited state properties of peridinin: Observation of a solvent dependence of the lowest excited singlet state lifetime and spectral behavior unique among carotenoids." Journal of Physical Chemistry B 103(41): 8751-8758.

Bautista, J. A., R. G. Hiller, et al. (1999). "Singlet and triplet energy transfer in the peridinin-chlorophyll a protein from Amphidinium carterae." Journal of Physical Chemistry A 103(14): 2267-2273.

Bernhard, K. and M. Grosjean (1995). Infrared Spectroscopy. Carotenoids. G. Britton, S. Liaaen-Jensen and H. Pfander. Basel, Boston, Berlin, Birkhäuser Verlag. 1B.

Bonetti, C., M. T. A. Alexandre, et al. (2009). "Chl-a triplet quenching by peridinin in H-PCP and organic solvent revealed by step-scan FTIR time-resolved spectroscopy." Chemical Physics Excited State Dynamics in Light Harvesting Materials 357(1-3): 63-69.

Breton, J. (2001). "Fourier transform infrared spectroscopy of primary electron donors in type I photosynthetic reaction centers." Biochimica et Biophysica Acta (BBA) - Bioenergetics 1507(1-3): 180-193.

Breton, J., E. Nabedryk, et al. (1999). "FTIR study of the primary electron donor of photosystem I (P700) revealing delocalization of the charge in P700(+) and localization of the triplet character in (3)P700." Biochemistry 38(36): 11585-11592.

Brudler, R., R. Rammelsberg, et al. (2001). "Structure of the I1 early intermediate of photoactive yellow protein by FTIR spectroscopy." Nat Struct Biol 8(3): 265-70.

Carbonera, D., G. Giacometti, et al. (1996). "Carotenoid interactions in peridinin chlorophyll a proteins from dinoflagellates - Evidence for optical excitons and triplet migration." Journal of the Chemical Society-Faraday Transactions 92(6): 989-993.

Carbonera, D., G. Giacometti, et al. (1999). "Model for triplet-triplet energy transfer in natural clusters of peridinin molecules contained in Dinoflagellate's outer antenna proteins." Journal of Physical Chemistry B 103(30): 6357-6362.

Cogdell, R. J. and H. A. Frank (1987). "How Carotenoids Function in Photosynthetic Bacteria." Biochimica Et Biophysica Acta 895(2): 63-79.

Cogdell, R. J., T. D. Howard, et al. (2000). "How carotenoids protect bacterial photosynthesis." Phil. Trans. Royal Soc. London Ser B 355: 1345-1349.

Croce, R., M. Mozzo, et al. (2007). "Singlet and triplet state transitions of carotenoids in the antenna complexes of higher-plant Photosystem I." Biochemistry 46(12): 3846-3855.

Damjanovic, A., T. Ritz, et al. (1999). "Energy transfer between carotenoids and bacteriochlorophylls in a light harvesting protein." Physical Review E 59: 3293-3311.

Damjanovic, A., T. Ritz, et al. (2000). "Excitation transfer in the peridinin-chlorophyll-protein of *Amphidinium carterae*." Biophysical Journal 79(4): 1695-1705.

Dexter, D. L. (1953). "A theory of sensitized luminescence in solids." Journal of Chemical Physics 21: 834-850.

Di Valentin, M., S. Ceola, et al. (2008). "Pulse ENDOR and density functional theory on the peridinin triplet state involved in the photo-protective mechanism in the peridinin-chlorophyll a-protein from Amphidinium carterae." Biochim Biophys Acta 1777(3): 295-307.

Di Valentin, M., S. Ceola, et al. (2008). "Identification by time-resolved EPR of the peridinins directly involved in chlorophyll triplet quenching in the peridinin-chlorophyll a-protein from Amphidinium carterae." Biochim Biophys Acta 1777(2): 186-95.

Frank, H. A. and R. J. Cogdell (1996). "Carotenoids in photosynthesis." Photochemistry and Photobiology 63(3): 257-264.

Fujiwara, M. and M. Tasumi (1986). "Metal-sensitive bands in the Raman and infrared spectra of intact and metal-substituted chlorophyll a." Journal of Physical Chemistry 90(22): 5646-5650.

Fujiwara, M., Tasumi, M. (1986). "Resonance Raman and Infrared Studies on Axial Coordination to Chlorophylls-a and Chlorophylls-B Invitro." Journal of Physical Chemistry 90(2): 250-255.

Fujiwara, M., K. Yamauchi, et al. (2008). "Energy dissipation in the ground-state vibrational manifolds of ß-carotene homologues: a sub-20-fs time-resolved transient grating spectroscopic study." Phys Rev B 77: 205118-1-10.

Garczarek, F. and K. Gerwert (2006). "Functional waters in intraprotein proton transfer monitored by FTIR difference spectroscopy." Nature 439(7072): 109-12.

Gest, H. (2002). "History of the word photosynthesis and evolution of its definition." Photosynthesis Research 73(1-3): 7-10.

Groot, M. L., Breton, J., van Wilderen, L.J.G.W., Dekker, J.P., van Grondelle, R. (2004). "Femtosecond visible/visible and visible/mid-IR pump-probe study of the photosystem II core antenna complex CP47." Journal of Physical Chemistry B 108(23): 8001-8006.

Hartwich, G., C. Geskes, et al. (1995). "Fourier-Transform Infrared-Spectroscopy of Electrogenerated Anions and Cations of Metal-Substituted Bacteriochlorophyll-Alpha." Journal of the American Chemical Society 117(29): 7784-7790.

Hashimoto, H., Y. Koyama, et al. (1991). "S1 and T1 species of .beta.-carotene generated by direct photoexcitation from the all-trans, 9-cis, 13-cis, and 15-cis isomers as revealed by picosecond transient absorption and transient Raman spectroscopies." Journal of Physical Chemistry 95: 3072-3076.

Hashimoto, H., Y. Koyama, et al. (1991). "S1 and T1 Species of Beta-Carotene Generated by Direct Photoexcitation from the All-Trans, 9-Cis, 13-Cis, and 15-Cis Isomers as Revealed by Picosecond Transient Absorption and Transient Raman Spectroscopies." Journal of Physical Chemistry 95(8): 3072-3076.

Hiller, R. G., L. G. Crossley, et al. (2001). "The 15-kDa forms of the apo-peridinin-chlorophyll a protein (PCP) in dinoflagellates show high identity with the apo-32 kDa PCP forms, and have similar N-terminal leaders and gene arrangements." Mol Genet Genomics 266(2): 254-9.

Hofmann, E. (1999). Strukturanalyse der Lichtsammler Peridinin-Chlorophyll a-Proteine (PCPs) von Amphidinium carterae und Heterocapsa pygmaea. Dr. rer. nat. der Fakult¨at f¨ur Biologie Universit¨at Konstanz.

Hofmann, E., P. M. Wrench, et al. (1996). "Structural basis of light harvesting by carotenoids: Peridinin- chlorophyll-protein from Amphidinium carterae." Science 272(5269): 1788-1791.

Holt, N. E., J. T. M. Kennis, et al. (2003). "Carotenoid to chlorophyll energy transfer in light harvesting complex II from Arabidopsis thaliana probed by femtosecond fluorescence upconversion." Chemical Physics Letters 379: 305-313.

Ilagan, R. P., S. Shima, et al. (2004). "Spectroscopic properties of the main-form and high-salt peridinin-chlorophyll a proteins from Amphidinium carterae." Biochemistry 43(6): 1478-1487.

Katz, J. J., K. Ballschmiter, et al. (1968). "Electron paramagnetic resonance of chlorophyll-water aggregates." Proc Natl Acad Sci U S A 60(1): 100-7.

Kleima, F. J., E. Hofmann, et al. (2000). "Förster excitation energy transfer in peridinin-chlorophyll-a-protein." Biophys J 78(1): 344-53.

Kleima, F. J., Hofmann, E., Gobets, B., van Stokkum, I. H. M., van Grondelle, R., Diederichs, K., van Amerongen, H. (2000). "Forster excitation energy transfer in peridinin-chlorophyll-a-protein." Biophysical Journal 78(1): 344-353.

Kleima, F. J., M. Wendling, et al. (2000). "Peridinin chlorophyll a protein: Relating structure and steady-state spectroscopy." Biochemistry 39(17): 5184-5195.

Knoetzel, J. and L. Rensing (1990). "Characterization of the Photosynthetic Apparatus from the Marine Dinoflagellate Gonyaulax-Polyedra .1. Pigment and Polypeptide Composition of the Pigment-Protein Complexes." Journal of Plant Physiology 136(3): 271-279.

Kotting, C. and K. Gerwert (2005). "Proteins in action monitored by time-resolved FTIR spectroscopy." Chemphyschem 6(5): 881-8.

Krieger-Liszkay, A. (2005). "Singlet oxygen production in photosynthesis." J Exp Bot 56(411): 337-46.

Kristallovich, E. L., I. D. Shamyanov, et al. (1987). "Frequencies and Integral Intensities of Lactone and Ester Carbonyls of Natural Guaianolides." Khimiya Prirodnykh Soedinenii(6): 805-811.

Krueger, B. P., S. S. Lampoura, et al. (2001). "Energy transfer in the peridinin chlorophyll-a protein of Amphidinium carterae studied by polarized transient absorption and target analysis." Biophysical Journal 80(6): 2843-2855.

Krueger, B. P., G. D. Scholes, et al. (1998). "Calculation of couplings and energy-transfer pathways between the pigments of LH2 by the *ab initio* transition density cube method." Journal of Physical Chemistry B 102: 5378-5386.

Krueger, B. P., G. D. Scholes, et al. (1998). "Electronic excitation transfer from carotenoid to bacteriochlorophyll in the purple bacterium *Rhodopseudomonas acidophila*." Journal of Physical Chemistry B 102: 2284-2292.

Lampoura, S. S., V. Barzda, et al. (2002). "Aggregation of LHCII leads to a redistribution of the triplets over the central xanthophylls in LHCII." Biochemistry 41(29): 9139-9144.

Liu, Z., H. Yan, et al. (2004). "Crystal structure of spinach major light-harvesting complex at 2.72Å resolution." Nature 428(6980): 287-292.

Majerus, T., T. Kottke, et al. (2007). "Time-resolved FT-IR spectroscopy traces signal relay within the blue-light receptor AppA." Chemphyschem 8(12): 1787-9.

Mantele, W. G., A. M. Wollenweber, et al. (1988). "Infrared Spectroelectrochemistry of Bacteriochlorophylls and Bacteriopheophytins - Implications for the Binding of the Pigments in the Reaction Center from Photosynthetic Bacteria." Proceedings of the National Academy of Sciences of the United States of America 85(22): 8468-8472.

McDermott, G., S. M. Prince, et al. (1995). "Crystal structure of an integral membrane light-harvesting complex from photosynthetic bacteria." Nature 374(6522): 517-521.

Mimuro, M., N. Tamai, et al. (1990). "Characteristic Fluorescence Components in Photosynthetic Pigment System of a Marine Dinoflagellate, Protogonyaulax-

Tamarensis, and Excitation-Energy Flow among Them - Studies by Means of Steady-State and Time-Resolved Fluorescence Spectroscopy." Biochimica Et Biophysica Acta 1016(2): 280-287.

Mozzo, M., L. Dall'Osto, et al. (2008). "Photoprotection in the antenna complexes of photosystem II: role of individual xanthophylls in chlorophyll triplet quenching." J Biol Chem 283(10): 6184-92.

Mukai-Kuroda, Y., R. Fujii, et al. (2002). "Changes in molecular structure upon triplet excitation of all-trans-spheroidene in n-hexane solution and 15-cis-spheroidene bound to the photo-reaction center from Rhodobacter sphaeroides as revealed by resonance-Raman spectroscopy and normal-coordinate analysis." Journal of Physical Chemistry A 106(14): 3566-3579.

Nagae, H., T. Kakitani, et al. (1993). "Calculation of the Excitation Transfer-Matrix Elements between the S(2) or S(1) State of Carotenoid and the S(2) or S(1) State of Bacteriochlorophyll." Journal of Chemical Physics 98(10): 8012-8023.

Nagae, H., M. Kuki, et al. (2000). "Vibronic Coupling through the In-Phase, C=C Stretching Mode Plays a Major Role in the 2Ag- to 1Ag- Internal Conversion of all-trans--Carotene. pp 4155 - 4166;." Journal of Physical Chemistry A 104(18): 4155-4166.

Noguchi, T. (2002). "Dual Role of Triplet Localization on the Accessory Chlorophyll in the Photosystem II Reaction Center: Photoprotection and Photodamage of the D1 Protein." Plant and Cell Physiology 43(10): 1112-1116.

Noguchi, T., H. Hayashi, et al. (1990). "Frequencies of the Franck-Condon active a_g C=C stretching mode in the 2 $1A^-_g$ excited state of carotenoids." Chemical Physics Letters 175(3): 163-169.

Norris, B. J. and D. J. Miller (1994). "Nucleotide sequence of a cDNA clone encoding the precursor of the peridinin-chlorophyll a-binding protein from the dinoflagellate Symbiodinium sp." Plant Mol Biol 24(4): 673-7.

Okubo, T. and T. Noguchi "Selective detection of the structural changes upon photoreactions of several redox cofactors in photosystem II by means of light-induced ATR-FTIR difference spectroscopy." Spectrochimica Acta Part A: Molecular and Biomolecular Spectroscopy In Press, Corrected Proof.

Papagiannakis, E., J. T. M. Kennis, et al. (2002). "An Alternative carotenoid-to-bacteriochlorophyll energy transfer pathway in photosynthetic light harvesting." Proceedings of the National Academy of Sciences (USA) 99(9): 6017-6022.

Peterman, E. J., C. C. Gradinaru, et al. (1997). "Xanthophylls in light-harvesting complex II of higher plants: light harvesting and triplet quenching." Biochemistry 36(40): 12208-15.

Peterman, E. J. G., F. M. Dukker, et al. (1995). "Chlorophyll a and carotenoid triplet states in light-harvesting complex II of higher plants." Biophysical Journal 69(6): 2670-2678.

Premvardhan, L., E. Papagiannakis, et al. (2005). "The Charge-Transfer Character of the S0->S2 Transition in the Carotenoid Peridinin is revealed by Stark Spectroscopy." Journal of Physical Chemistry B 109: 15589-15597.

Prince, S. M., M. Papiz, . Z., et al. (1997). "Apoprotein structure in the LH2 complex from Rhodopseudomonas acidophila strain 10050: modular assembly and protein pigment interactions." J. Mol. Biol. 268(2): 412-423.

Ritz, T., A. Damjanovic, et al. (2000). "Efficient light harvesting through carotenoids." Photosynthesis Research 66(1-2): 125-144.

Rondonuwu, F. S., T. Taguchi, et al. (2004). "The energies and kinetics of triplet carotenoids in the LH2 antenna complexes as determined by phosphorescence spectroscopy." Chemical Physics Letters 384(4-6): 364-371.

Ruban, A. V., R. Berera, et al. (2007). "Identification of a mechanism of photoprotective energy dissipation in higher plants." Nature 450(7169): 575-8.

Salverda, J. M. (2003). Interacting pigments in light-harvesting complexes studied with nonlinear spectroscopy. Amsterdam, Vrije Universiteit.

Schopf, J. W. (1992). The oldest fossils and what they mean. Major events in the history of life. J. W. Schopf, Jones and Bartlett: 29-63.

Shreve, A. P., J. K. Trautman, et al. (1991). "Femtosecond Energy-Transfer Processes in the B800-850 Light- Harvesting Complex of Rhodobacter-Sphaeroides-2.4.1." Biochimica Et Biophysica Acta 1058(2): 280-288.

Song, P. S., P. Koka, et al. (1976). "Molecular Topology of Photosynthetic Light-Harvesting Pigment Complex, Peridinin-Chlorophyll-a-Protein, from Marine Dinoflagellates." Biochemistry 15(20): 4422-4427.

Van der Vos, R., D. Carbonera, et al. (1991). "Microwave and optical spectroscopy of carotenoid triplets in light-harvesting complex LHC II of spinach by absorbance-detected magnetic resonance." Appl. Magn. Res. 2: 179.

van Grondelle, R., J. P. Dekker, et al. (1994). "Energy-Transfer and Trapping in Photosynthesis." Biochimica Et Biophysica Acta-Bioenergetics 1187(1): 1-65.

van Stokkum, I. H., D. S. Larsen, et al. (2004). "Global and target analysis of time-resolved spectra." Biochim Biophys Acta 1657(2-3): 82-104.

Vaswani, H. M., C. P. Hsu, et al. (2003). "Quantum chemical evidence for an intramolecular charge-transfer state in the carotenoid peridinin of peridinin-chlorophyll- protein." Journal of Physical Chemistry B 107(31): 7940-7946.

Walla, P. J., P. A. Linden, et al. (2000). "Femtosecond dynamics of the forbidden carotenoid S-1 state in light-harvesting complexes of purple bacteria observed after two-photon excitation." Proceedings of the National Academy of Sciences (USA) 97: 10808-10813.

Zhang, J. P., R. Fujii, et al. (2000). "Mechanism of the carotenoid-to-bacteriochlorophyll energy transfer via the S_1 state in the LH2 complexes from purple bacteria." Journal of Physical Chemistry B 104(15): 3683-3691.

Zigmantas, D., R. G. Hiller, et al. (2004). "Effect of a conjugated carbonyl group on the photophysical properties of carotenoids." Physical Chemistry Chemical Physics 6(11): 3009-3016.

Zigmantas, D., R. G. Hiller, et al. (2002). "Carotenoid to chlorophyll energy transfer in the peridinin- chlorophyll-*a*-protein complex involves an intramolecular charge transfer state." Proceedings of the National Academy of Sciences of the United States of America 99(26): 16760-16765.

Section 3

Biomedical Applications

15

The Role of β-Antagonists on the Structure of Human Bone – A Spectroscopic Study

J. Anastassopoulou[1], P. Kolovou[1],
P. Papagelopoulos[2] and T. Theophanides[1]
[1]*National Technical University of Athens, Chemical Engineering Department, Radiation Chemistry and Biospectroscopy, Zografou Campus, Zografou, Athens*
[2]*National and Kapodistrian University of Athens, School of Medicine, Department of Orthopaedic Surgery and Traumatology, Athens*
Greece

1. Introduction

Human bones are inherently complex materials consisting of minerals, collagen, water, non-collagenous proteins, lipids, vascular elements and cells. The bone is a physiologically active and reactive tissue (Petra et al., 2005). Through hormonal or mechanical signals the osteoblasts and osteoclasts are forming the bones. It is known that the role of osteoblasts is to create a collagen-rich extracellular matrix, which will become mineralized (bone formation) with calcium. On the other hand, the main role of osteoclasts is to degrade calcified bone tissue (resorption) (Shier et al., 1996). In the bone microenvironment, there is a dynamic balance between resorption and formation that maintains skeletal homeostasis. This process between bone formation and bone resorption is called remodelling. Bone remodelling and bone loss, is in function of age, external mechanical loads originating from physical activity and diseases.

The inorganic component of bone accounts approximately to 65% of the wet weight of bone and it is not pure hydroxyapatite, $Ca_{10}(PO_4)_6(OH)_2$, but a poorly crystalline calcium hydroxide in a deficient biological apatite, containing numerous trace anions, the most abundant of which is carbonate (CO_3^{2-}) and acid phosphate (HPO_4^{2-}), fluoride (F^-) and citrate ($C_6H_5O_7^{3-}$) anions, as well as, magnesium (Mg^{2+}), potassium (K^+) cations. These anions and cations are common substitutes of calcium and hydroxide (OH) in hydroxyapatite (Petra et al., 2005; Maguire and Cowan, 2002). The major organic component of bone is collagen, predominantly type I, which provides the bone with elasticity and flexibility and directs the organisation of matrix. Water accounts for 5-10% and collagen with proteins are about 25-30% of the weight of bone tissue. Hydrogen bonds between water and collagen contribute to the stabilisation of a triple helix, and there have been suggestions that dehydration of the collagen may take place during demineralization of bone (Petra et al., 2005; Buckwalter et al., 2000).

In the last decade, there is an increasing interest in using infrared spectroscopy to evaluate and study biological systems (Petra et al., 2005; Mantsch et al., 1986; Anastassopoulou et al., 2008, 2009, 2011; Conti et al., 2008; Kolovou and Anastassopoulou, 2007;Pissaridi etal., 2011;

Mamarelis et al., 2010, Theophanides, 1979; Theophanides et al., 1993). FT-IR spectroscopy is a powerful non destructive technique and easy to investigate complex systems as bones with this technique. The absorption of infrared radiation excites the vibrations of the chemical bonds to higher energy levels, by changing the dipole moment of the molecule with which it interacts. This change and interaction gives the absorption spectrum with the characteristic absorption bands based on the total vibrational modes of biological molecules within the sample, such as hydroxyapatite. This powerful technique permits the study of homogenous and inhomogeneous systems, such as, bone, providing information from all tissue components, both organic and inorganic.

Adrenergic receptors are well known to be present in osteoblastic cells, and it is known that the α- and β-receptors could activate pharmacologically the proliferation of these cells (Suzuki et al., 1998). It is also known that adrenergic agonists efficiently activate β-adrenoreceptors on osteoblasts and can stimulate bone resorption in intact mouse calvaria (Moore et al., 1993). Furthermore, it has been reported that propranolol inhibited cAMP formation induced by β–adrenergic agonists in bone organ cultures (Takeuchi et al., 2000) increased bone strength and the rates of endochondral bone formation in rats (Dietrich et al., 1979; Minkowitz et al., 2005).

The purpose of this *in vitro* work is to study the role of the non-selective beta-adrenergic receptor and beta1-selective adrenoreceptor blocking agents on demineralization of human bones, which was induced by EDTA.

2. Materials and methods

The chemical compounds:

Timolol, (S)-1-[(1,1-dimethylethyl)amino]-3-[(4-4(morpholinyl)-1,2,5-thiadiazol-3-yl] oxy] -2-propanol (Z) –butenedioate, with the empirical formula $C_{13}H_{24}N_4O_3S$ and chemical structure, A:

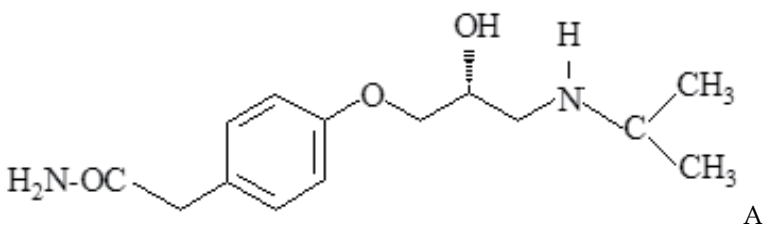

A

And Atenolol, 4-[2′-hydroxy-3′-[(1-methyl-ethyl) amino] propoxyl, $C_{14}H_{22}N_2O_2$ with chemical structure, B:

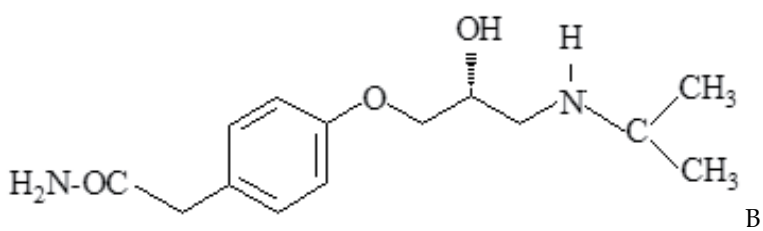

B

Ethylene Diamino Tetracetic Acid (EDTA), $(C_{10}H_{14}O_8N_2Na_2).2H_2O$ $[CH_2N(CH_2COOH)$ $CH_2COO].2H_2O$ and benzeneacetamide [4-[2′-hydroxy-3′-[(1-methyl-ethyl)amino] propoxyl] were products of Sigma.

The bones were obtained intra-operatively from heads of femur of 65-75 year patients undergoing osteotomy. The samples were prepared in slices in order to preserve better the natural characteristics of the bones. The bone was cut into slices of 2 mm perpendicular to the longitudinal axis of the head (Fig. 1). The histological evaluation of representative sections of the biopsies showed no evidence of any metabolic disease, osteopenia, or bone cancer.

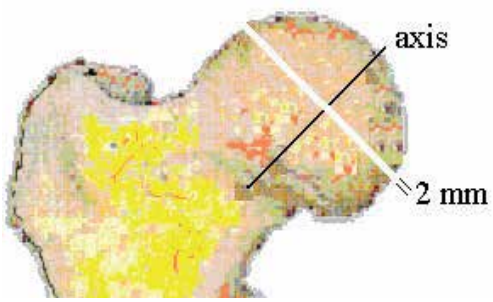

Fig. 1. The anatomic location and the size of the bone sections.

The bone sections were immersed successively in hydrogen peroxide solution (H_2O_2) and in acetone, according to a modification of the method described (Petra et al., 2005). Another bone section was reacted with aqueous EDTA solution and was left for a week in 4 ^oC (Veis and Schlueter, 1964). Twenty mg of bone were mixed with 200 mg of KBr powder in a pestle and was grownded in a mortar and compressed into a pellet. Two more sections were reacted with 2ml aqueous solutions of Na_2EDTA 0,5 M in the presence of timolol 0,5 M and 0,5 M atenolol. The mixture was left for a week at 4^0 C.

2.1 Preparation of bone samples

Fresh cancellous bone was immersed successively in hydrogen peroxide solution (H_2O_2) and in acetone, according to a modification method (Petra et al., 2005). Hydrogen peroxide and acetone processing is known to reduce blood chromophores of fresh bones and the fat tissues of the bone (Petra et al., 2005), but it does not remove the organic components completely. The processed bone sample was cut with microtome in multiple slices of 2 mm thickness each.

One dry slice was demineralized. The demineralization of the bone was carried out by extraction of calcium ions with 0.5 M EDTA at 4^oC, where the pH was adjusted to pH 7.4 with potassium hydroxide (Veis and Schlueter, 1964). Then the bone slice was washed thoroughly with repeated changes of distilled water and acetone.

Two bone slices were left to become demineralized in the same way by extraction at 4^oC with 0.5 M EDTA adjusted to pH 7.4 with potassium hydroxide in the presence of 0.25 M timolol or atenolol, for one week. Twenty milligrams of the cancellous section of the slices were mixed with 200 mg KCl powder in a pestle and mortar and compressed into a pellet to

be studied by FT-IR. A small section of the bone slices was also studied with SEM. It must be noticed that both compounds A and B did not interact with EDTA.

2.2 FT-IR spectroscopy

Fourier Transform Infrared (FT-IR) spectra were recorded in a frequency range of 4000-400 cm-1 using an FTS 3000 MX BioRad, Excalibur Series spectrophotometer and were processed with the Bio-Rad Win-IR Pro 3.0 Software. Twenty mg of fresh bone were mixed with 200 mg of KBr powder in a pestle and mortar and compressed into a pellet. Typically, 32 scans were collected at 4 cm^{-1} resolution over the wavenumber range of 400-4000 cm^{-1}.

2.3 Scanning Electron Microscopy (SEM)

The morphologic and chemical composition of the compounds was obtained by Scanning Electron Microscopy (SEM) with a Quanta 200, (FEI, Hillsboro, Or, Usa) apparatus equipped with an X-ray detector EDS, Saphire CDU, (Edax Int, Mawhaw, NJ, USA). The spectra were obtained with acceleration of 10 kV and beam light 100 μÅ was applied. The samples were covered with graphite with an SCD 004 Sputter-Coater and OCD 30 attachment (Bal-Tec, Vaduz, Liechtenstein). The SEM spectral maps were processed with the Gemin (3.5 version, Edax Int) Software.

3. Results and discussion

3.1 FT-IR spectra

The FT-IR spectra of homogenized bone samples before and after interaction with EDTA solution is shown in Figs. 2a and 2b, respectively.

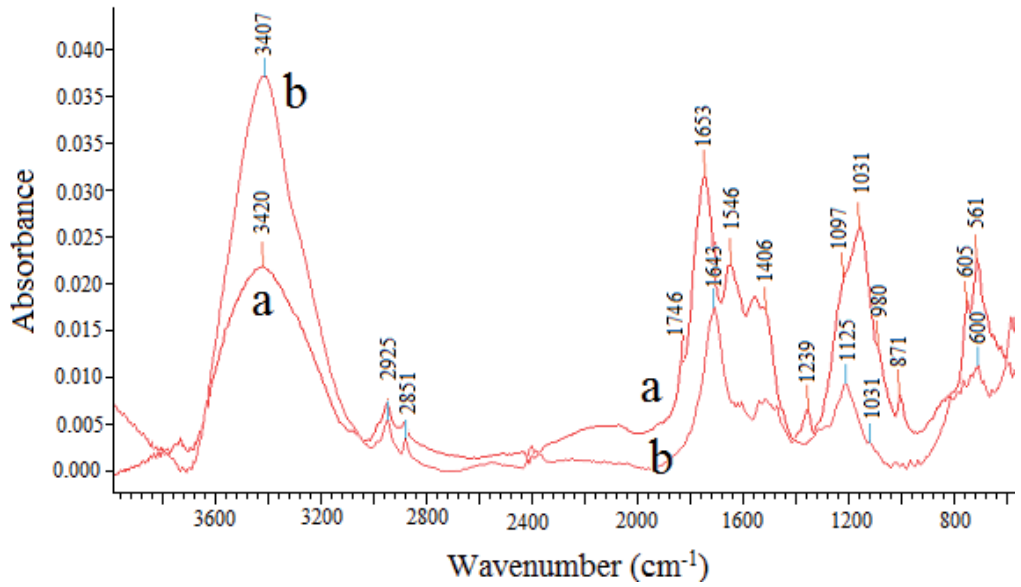

Fig. 2. FT-IR spectra of a) bone and b) bone after the first week of demineralization with EDTA

The infrared absorption bands (cm^{-1}) and their assignments are given in Table 1.

Unprocessed cm^{-1}	**After the 1st week of demineralization with EDTA cm^{-1}**	**Assignment**
3420	3407	υOH, υN-H
3067		υCH=
2925	2924	$\upsilon_{as}CH_2$
2852	2851	$\upsilon_s CH_2$
1746		υC=O non-ionised -COOH
1653	1643	νC=O + δN-H Amide I
1546		δN-H in-plane + νC-N, Amide II
1452		$\delta_{as}CH_3$ + $\nu_3CO_3^{2-}$, AB carbonate
1406		νCOO^- & $\nu_3CO_3^{2-}$, AB carbonate
1337		ρ_w-CH_2 wagging
1239		νCN + δNH in-plane, Amide III
1097 sh		ν_3-PO_4^{3-},non stoich. HA
1031	1031	ν_3-PO_4^{3-}, stoich. HA
960 sh		ν_1-PO_4^{3-}, stoich. HA
871		$\nu_2CO_3^{2-}$, B carbonate$^-$
605	609	ν_4-PO_4^{3-}, HA
561		ν_4-PO_4^{3-}, HA

Table 1. Peak assignments of the FT-IR spectra of homogenized bone before and after a week of demineralization with EDTA.

Significant differences are shown in the spectra of the bone (Fig. 1b) after interaction with EDTA. The broad band which appears at 3420 cm^{-1}in the bone spectrum shifts to 3407 cm^{-1} after decalcification of the bone. This band is dominated by absorptions from stretching vibration of υOH and υNH functional groups of hydroxyapatite and proteins, respectively and is particularly sensitive by decalcification of the bone. This band shows that the OH groups of HA are reduced, while there are other free NH groups, which do not give neither inter- nor intra-molecular hydrogen bonds, leading to the result that the decalcification changes the secondary structure of proteins. The band at 3067 cm^{-1} is attributed to υ=CH stretching vibration of oxidized lipids (Petra et al., 2005; Mamarelis et al., 2010).

The bands in the spectra between 3000 and 2800 are characteristic of the antisymmetric and symmetric stretching vibrations of methyl (CH_3) and methylene (CH_2) groups. The bands near 2925 cm^{-1} and near 2852 cm^{-1} correspond to antisymmetric and symmetric stretching vibrations of υCH_2, respectively. These bands do not shift after demineralization, but increase in intensity. These changes show that the secondary structure of proteins changed and their environment became less lipophilic (Mamarelis et al., 2010; Anastassopoulou and Theophanides, 1990). The characteristic peak at 1746 cm^{-1} due to the stretching vibration of

νC=O of the non-ionized carboxyl group –COOH (Petra et al., 2005; Kolovou and Anastassopoulou, 2007; Anastassopoulou et al., 2008; Mythili et al., 2000) is absent in the spectrum of the demineralized bone. In the spectrum of the unprocessed cancellous bone, an intense band is seen near 1031 cm-1, which is characteristic of stoichiometric biological apatites, with two shoulders, one at 1097 cm^{-1}, which is assigned to non-stoichiometric hydroxyapatite (HA), containing HPO_4^{2-} and/or CO_3^{2-} groups[3] and one at 960 cm^{-1}, which is assigned to the symmetric stretching vibration of the PO_4^{3-} groups (Petra et al., 2005; Graham et al., 2008). The bands near 1452, 1406 and 871 cm^{-1}, are v_3 and v_2 carbonate groups and the bands near 605 and 561 cm^{-1}, are due to the $\nu_4PO_4^{3-}$ vibrational modes. These are clearly seen in the spectrum of the unprocessed cancellous bone and are absent in the spectrum of the decalcified or demineralized bone, since decalcification eliminates the calcium phosphates, $Ca_3(PO_4)_2$.

Significant changes were observed in the region of 1670 - 1540 cm^{-1}, where the Amide I and Amide II absorb. In many biological samples the Amide I band arises from the C=O stretching vibration with contribution of bending δNH of peptide bond of proteins. These Amide bands shifted to lower frequencies and are found at 1653 cm^{-1} and 1546 cm^{-1}, respectively in demineralized bones. This observation leads to the conclusion that the decalcification changes the secondary structure of collagen matrix from α-helix to β-sheet formation (Anastassopoulou et al., 2008, 2011; Kolovou and Anastassopoulou, 2007; Pissaridi et al., 2011; Mamarelis et al., 2010). This observation shows also that the hydrogen bonds between proteins and hydroxyl apatite have been broken and that the proteins have much more freedom in vibrational movements. This is also in agreement with the increase of the bands, which were observed in the region of 3000-2850 cm^{-1}, where as we noticed, the antisymmetric and symmetric stretching vibrations of methyl vCH3 and methlylen vCH$_2$ groups absorb. The above results were expected, since EDTA subtracts the Ca^{2+} cations from the bone to form complexes (Fig. 3) leading to its demineralization.

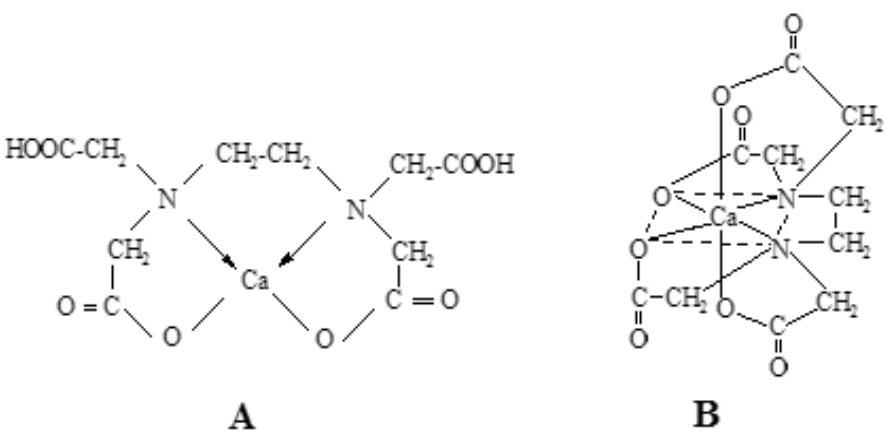

Fig. 3. EDTA-Ca complexes A. Tetrahedral coordination and B. Octahedral coordination

The non-intense band at 1239 cm^{-1} is assigned to Amide III, which arises from the in-phase δN-H in plane bending and vC-N stretching vibrations, which almost disappeared after demineralization. This band is also sensitive to protein structural changes.

In order to study the role of demineralization on the bone structure and to extrapolate the results to possible various bone diseases, we used calcium antagonists during demineralization with EDTA. The FT-IR spectra of bone, which were recorded after demineralization with EDTA in the presence of β- (timolol) and α- (atenolol) blockers after one week of reaction, are shown in Figs. 4b and 4c, respectively, in comparison with the spectra of untreated bone (Fig. 4a). The band assignments are given in Table 2.

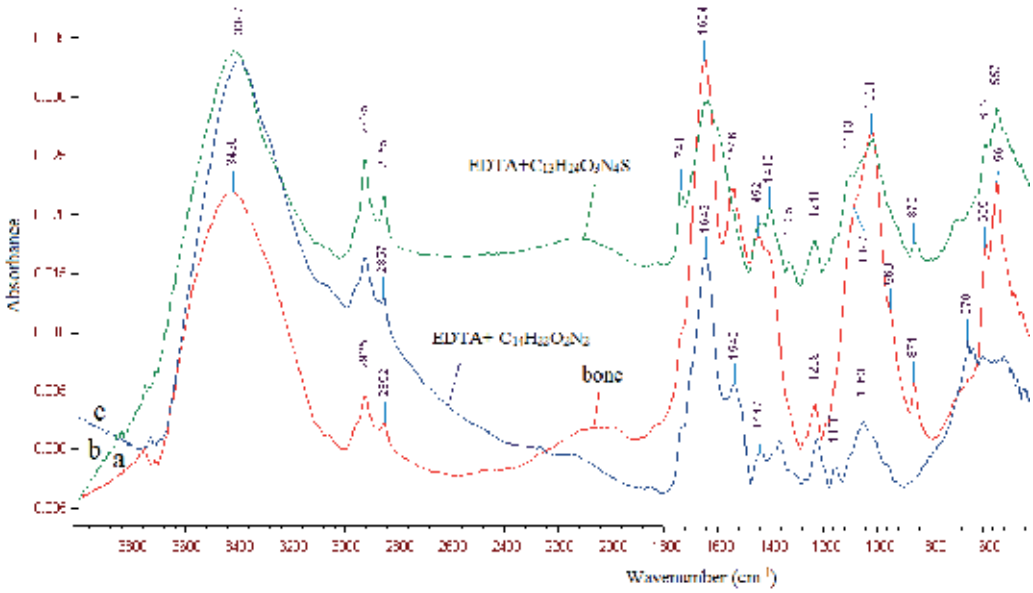

Fig. 4. FT-IR spectra of a) homogenized cancellous bone, b) homogenized and demineralized, cancellous bone with EDTA in the presence of timolol, $C_{13}H_{24}N_4O_3S$, and c) homogenized and demineralized cancellous bone with EDTA in the presence of atenolol, $C_{14}H_{22}O_2N_2$, for 1 week, in the region 4000-400 cm^{-1}.

By comparison of the spectra it was observed that the presence of β-blocker differentiates the reaction between EDTA and the bone. Especially, in the region 1700-1500 cm^{-1}, where the bands of Amide I and Amide II are located, the spectra show that the collagen loses partly the α-helix structure. On the other hand, in demineralized samples and in the presence of α-blocker the secondary structure of collagen changed from α-helix to β-pleated sheet. Interesting are also the results of the spectra in the region of the phosphate groups between 1110 cm^{-1} and 870 cm^{-1} are characteristic. Furthermore, from the spectral data (Fig.3) and Table 2 it results again that there is a competition reaction between EDTA and β-blocker for calcium cations (Ca^{2+}). Taking into account the chemical structure of the two calcium antagonists it was suggested that they should bind to hydroxyapatite of the bones with hydrogen bonds and thus inhibit the demineralization. These results are in accordance with the data of other investigators who reported that β-adrenoblockers prevented bone loss in animals (Mano et al., 2010).

Unprocessed cm^{-1}	Decalcified bone $C_{13}H_{24}N_4O_3S$	Decalcified bone $C_{14}H_{22}O_2N_2$	Assignments
3420	3414	3397	υN-H, υOH
3067	3067	3067	υ=CH
2925	2924	2924	$\upsilon_{as}CH_2$
2852	2855	2857	υ_sCH_2
1746	1741	1741	υC=O non-ionised -COOH
1653	1653		νC=O + δN-H Amide I
	1648	1649	νC=O + δN-H Amide I
1546	1550	1540	δN-H in-plane + νC-N, Amide II
1452	1450	1447	$\delta_{as}CH_3$ + $\nu_3CO_3^{2-}$, AB carbonate
1406	1410	1394	νCOO^- & $\nu_3CO_3^{2-}$, AB carbonate
1337	1335	1335	ρ_w-CH_2
1239	1241	1233	νCN + δNH in-plane, Amide III
1097 sh	1113		ν_3-PO_4^{3-},non stoich. HA
1031	1028		ν_3-PO_4^{3-}, stoich. HA
960 sh	960		ν_1-PO_4^{3-}, stoich. HA
871	870		$\nu_2CO_3^{2-}$, B carbonate
605	602		ν_4-PO_4^{3-}, HA
561	557		ν_4-PO_4^{3-}, HA

Table 2. Band assignments of the FT-IR spectra of homogenized decalcified bones with EDTA in the absence and presence of 0.5 M antagonists $C_{13}H_{24}N_4O_3S$ and $C_{14}H_{22}O_2N_2$ for 1 week.

In the case of the presence of atenolol during demineralization, the pattern of the spectrum in the region 1097-960 cm^{-1} has changed to that of the characteristic amorphous structure of hydroxyapatite (Kolovou and Anastassopoulou, 2007;Anastassopoulou et al., 2008) as shown in Fig. 4.

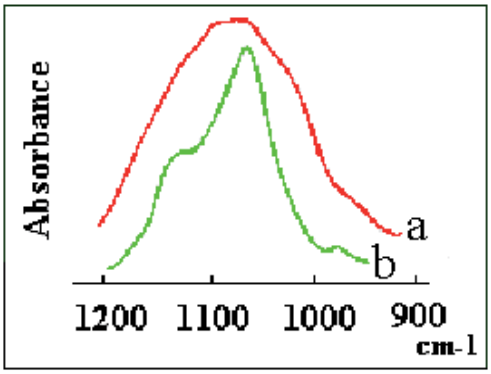

Fig. 5. FT-IR spectra of a) amorphous and b) biological hydroxyapatite.

This pattern of the infrared spectra, which correspond to amorphous structure of hydroxyapatite was also observed upon irradiation of bones (Anastassopoulou et al., 2008; Pissaridi et al., 2011) as well as in cancerous bones (Anastassopoulou et al., 2011), which suggest that under oxidative stress the bone loses its native molecular structure, in the same way as under artificial demineralization.

3.2 SEM spectroscopy

The spectra of the quantitative analysis of all the bone samples, obtained from the scanning electron microscope are shown in Fig. 6 and the results are shown in Table 3.

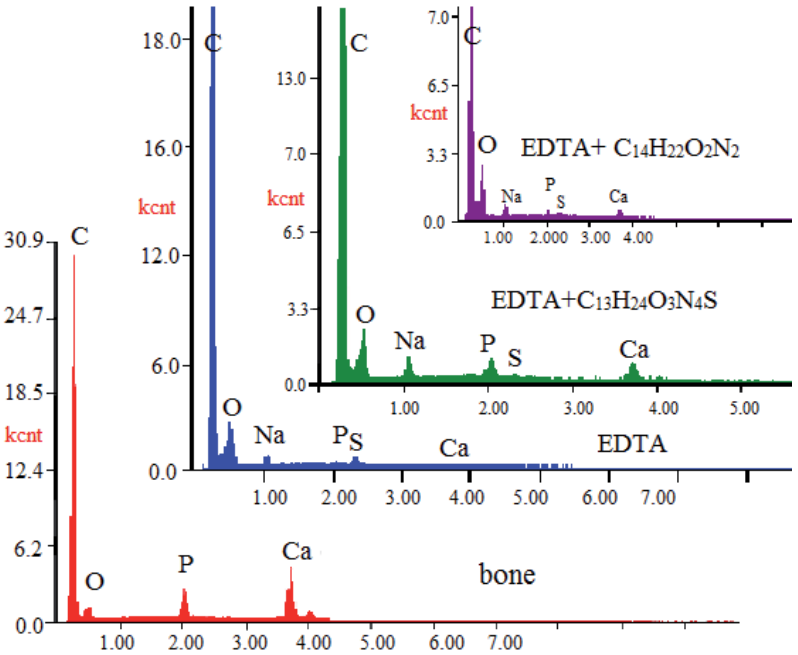

Fig. 6. Spectra of quantitative analysis of the bone samples.

Element	bone	Decalcified bone with EDTA	Decalcified bone EDTA+$C_{13}H_{24}N_4O_3S$	Decalcified bone EDTA+$C_{14}H_{22}O_2N_2$
O	59.01	69.71	64.24	76.90
Na	-	21.33	19.20	15.16
P	11.70	02.54	07.56	01.70
S	-	05.31	01.38	02.31
Ca	29.29	01.11	07.62	03.94

Table 3. Quantitative analysis data of the bone samples (% wt composition)

From the percentage data it is clear that the concentration of calcium has the highest value in the non-demineralized bone. The reaction of the bone tissue with EDTA leads to the disappearance of calcium of the bone. The presence of timolol during the reaction of the bone with EDTA seems to inhibit partially the decalcification of the bone tissues, since the

concentration of calcium increases up to 07.62. A similar result was obtained in the presence of atenolol, $C_{14}H_{22}O_2N_2$, but in both cases the calcium concentration was less than normal concentration.

In Fig. 7 are given the SEM images of cancellous bone sections with enlargement of X80. From the architecture and morphology of the images it is shown that after the reaction of bone with EDTA the sample does not show any bright regions, since the density of the bone is minimized (Fig. 7b) after the elimination of minerals of bone tissue.

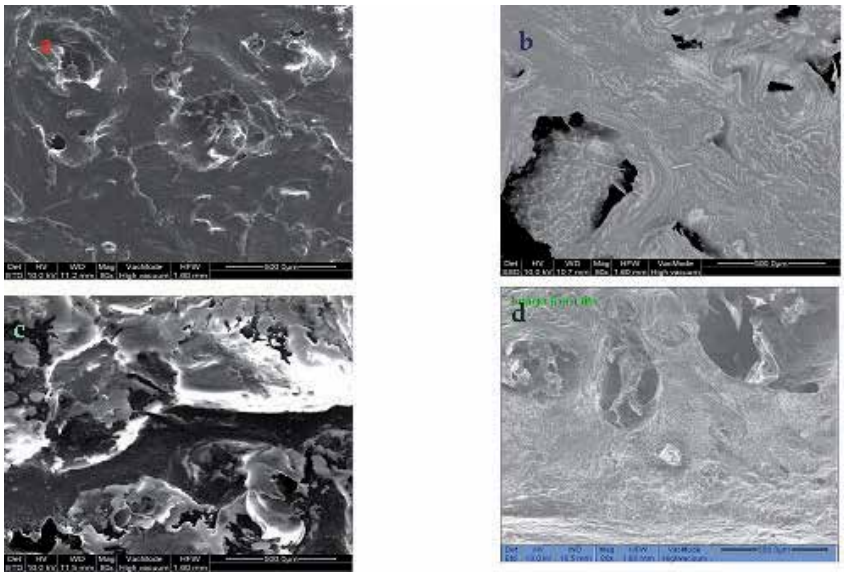

Fig. 7. SEM images of bone a) without any penetration, b) after demineralization with EDTA, c) after demineralization in the presence of $C_{13}H_{24}N_4O_3S$ and d) after demineralization in the presence of $C_{14}H_{22}O_2N_2$.

Significant changes in the brightness of the image are observed, when the demineralization takes place in the presence of $C_{13}H_{24}N_4O_3S$. It is observed an increase in bone density and the deposition of calcium on bone tissue is obvious (Fig. 7c). The image in Figure 6d corresponds to the result, which was obtained after the reaction of bone with EDTA in the presence of $C_{14}H_{22}O_2N_2$. The picture shows that the bone gets a more amorphous structure. These results are in agreement with the FT-IR data, which led to the suggestion that the biological hydroxyapatite changed from low crystallinity to amorphous state.

4. Conclusions

From FT-IR spectra in the region 1700-1500 cm^{-1}, which characterises the secondary structure of proteins, is found that demineralization changes the secondary structure of collagen from α-helix to β-pleated and random coil. Considerable intensity decrease was observed also in the region 1200-900 cm^{-1}, where the absorptions bands of phosphates from hydroxyapatite appear, which are due to bone demineralization and bone damage. The presence of calcium antagonists inhibits partly the demineralization of bones, which is induced from EDTA. These results could lead to the conclusion that the bone diseases

maybe change their secondary structure. These experimental data indicate that β-blockers may prevent bone loss in humans and new drugs to cure osteoporosis could be synthesized on this base.

5. References

Anastassopoulou, J. & Theophanides, T. (1990). Raman studies of model vesicle systems. *J. Appl. Spectrosc.,* Vol.44, pp.523.

Anastassopoulou, J., Kolovou, P. (2007). Synchrotron FT-IR spectroscopy of human bones. The effect of aging, in: *Brilliant Light in Life and Material Science*, Springer, pp. 267-272.

Anastassopoulou, J., Kolovou, P. & Mavrogenis, A. (2008). Bone and Cancer. A synchrotron micro- infrared study. *Metal Ions Biol. Medic.* Vol. 10, pp. 210-213.

Anastassopoulou, J., Boukaki, E., Conti, C., Ferraris, P., Giorgini, E., Rubini, C., Sabbatini, S., Theophanides, T. & Tosi, G. (2009). Microimaging FT-IR spectroscopy on pathological breast tissues. *Vibrational Spectroscopy*, Vol. 51, pp.270-275

Anastassopoulou, J., Kyriakidou, M., Maurogenis, A.E., Papagelopoulos, P.J. & Theophanides, T. (2011). Demineralization of bones due to breast cancer metastasis: an Infrared study. *Met. Ions Biol. Med.* Vol. 11, pp.123.

Buckwalter, J.A., Einhorn, T.A. & Simon, S.R. (2000). *Orthopaedic Basic Science*. American Academy of Orthopaedic Surgeons, pp. 320–332.

Conti, C., Ferraris, P., Giorgini, E., Rubini, C., Sabbatini, S., Tosi, G., Anastassopoulou, J., Arapantoni, P., Boukaki, E., Theophanides, T. & Valavanis, C. (2008). FT-IR Microimaging Spectroscopy:Discrimination between healthy and neoplastic human colon tissues. *Journal of Molecular Structure*, Vol. 881, pp. 46-51

Dietrich, J.W., Mundy, G.R. & Raisz, LG. (1979). Inhibition of bone resorption in tissue culture by membrane-stabilizing drugs. *Endocrinology*, Vol. 104, pp. 1644–1648.

Graham, S., Hammond-Jones, D., Gamie, Z., Polyzois, I., Tsiridis, E. & Tsiridis, E.(2008). The effect of beta-blockers on bone metabolism as potential drugs under investigation for osteoporosis and fracture healing. *Expert Opin Investig Drugs*,Vol.17, pp. 1281-1299.

Kolovou, P. & Anastassopoulou, J. (2007). Synchrotron FT-IR spectroscopy of human bones. The effect of agin. In: *Brilliant Light in Life and Material Sciences*, V. Tsakanov and H. Wiedemann (Eds.), pp. 267-272, Springer

Maguire, M. E. & Cowan, J.A. (2002). Magnesium chemistry and biochemistry. *BioMetals* Vol.15, pp. 203–210.

Mamarelis, I., Pissaridi, K., Dritsa, V., Kotileas, P., Tsiligiris, V., Tzilalis, V. & Anastassopoulou, J. (2010). Oxidative stress and atherogenesis. An FT-IR spectroscopic study. *In Vivo*, Vol. 24, pp.883-888

Mano, T., Nishimura, N. & Iwase, S. (2010). Sympathetic neural influence on bone metabolism in microgravity. *Acta Physiol Hung.,* Vol.4, pp.354-361.

Mantsch, H.H., Casal, H.L. & Jones, R. N. (1986). Resolution Enhancement of Infrared Spectra of Biological Systems. In: *Spectroscopy of Biological Systems*, pp: 1-46, Wiley, New York.

Minkowitz, B., Boskey, A.L, Lane, J.M., Pearlman, H.S. & Vigorita, V.J. (2005). Effects of propranolol on bone metabolism in the rat. *J. Orthop. Res.*, Vol. 9, pp.869 –875

Moore, R.E., Smith, C.K., Bailey, C.S., Voelkel , E.F. & Tashijian, A.H.(1993). Characterization of beta-adrenergic receptors on rat and human osteoblastlike cells and demonstration that beta-receptor agonists can stimulate bone resorption in organ culture. *Bone Miner* , Vol.23, pp.301–315.

Mythili, J., Sastry, T.P. & Subramarian, M. (2000). Preparation and characterization of a new bioinorganic composite: collagen and hydroxyapatite. *Biotechnol Appl Biochem,* Vol. 32, pp. 155-159.

Petra, M., Anastassopoulou, J., Theologis, T. & Theophanides T. (2005). Synchrotron micro-FT-IR spectroscopic evaluation of normal paediatric human bone. *Journal of Molecular Structure*, Vol. 78, pp. 101-116

Pissaridi, K., Dritsa, V., Mamarelis., I, Koutoulakis, E., Kotulas, Ch. & Anastassopoulou, J. (2011). The role of Molybdenum on atheromatic plaque formation. *Metal Ions Biol.Med*, Vol.11 , pp. 219-224.

Shier, D., Butler, J. & Lewis, R. (1996). *Hole's Human Anatomy*. McGraw-Hill, pp. 184-197.

Suzuki, A., Palmer, G., Bonjour, J.P. & Caverzasio, J. (1998). Catecholamines stimulate the proliferation and alkaline phosphatase activity of MC3T3–E1 osteoblast-like cells. *Bone*, Vol. 23, pp.197–203.

Takeuchi, T., Tsuboi, T., Arai, M. & Togani, A. (2000). Adrenergic stimulation of osteoclastogenesis mediated by expression of osteoclasts differentiation factor in MC3T3-E1 osteoblast-like cells, Biochem. Pharmacology, Vol. 61, pp. 579-586Theophanides, T. (1978). *Infrared and Raman spectroscopy of biological molecules.* NATO Advanced Study Institute, D Reidel Publishing Co, Dodrecht.

Theophanides, T., Anastassopoulou J. & Fotopoulos N. (1993). Vibrational Circular Dichroism of Proteins in H_2O Solution, *Fifth International Conference on the Spectroscopy of Biological Molecules,* Kluwer Academic Publishers, The Netherlands.

Veis, A. & Schlueter, R.J. The macromolecular Organization of Dentine matrix Collagen I. Characterization of Dentine Collagen. Biochemistry, Vol. 3, pp:1650-1657.

16

FT-IR Spectroscopy in Medicine

Vasiliki Dritsa
National Technical University of Athens, NTUA
Greece

1. Introduction

Infrared spectroscopy has been widely applied for the characterisation of various substances. Due to its sensitivity to the chemical information and architecture of the molecule, infrared spectroscopy can play an important role in new applications such as in the life-science field and not only in the traditional fields of physics and chemistry. Spectroscopic techniques are simple, reproducible, non-destructive without particular sample preparation. As a result, they provide information for the functional groups, bonds and molecular structure.

Herschel discovered the existence of infrared radiation when he tried to measure the heat produced by separate colors of a rainbow spectrum in 1800. He noted that the highest temperature fell beyond the red end of the spectrum, implying the existence of invisible light beyond the red. Herschel termed this light *calorific rays*. Infrared spectra originate on the vibrational motions of atoms in chemical bonds within molecules. When a beam of light containing the IR radiation band is passed through a sample, light energy from the photons is absorbed by the chemical bonds and excites the vibrational motions. As a molecule absorbs radiation at a specific frequency, it produces a band in the infrared spectrum at the corresponding wavenumber. The approximate position of an infrared absorption band is determined by the vibrating masses and the chemical bonds (single, double, triple). The exact position of the band depends also on electron withdrawing or donating effects of the intra- and intermolecular environment and coupling with other vibrations. The strength of absorption increases with increasing polarity of the vibrating atoms. The modes of vibration in a molecule that can absorb infrared radiation are many and increase with increasing complexity of the molecule. The vibrations that contribute to the spectrum are bending and stretching vibrations between atoms and rocking, twisting and wagging of a functional group (Theophanides, 1984; Goormaghtigh et al., 1999).

Fourier transform infrared spectroscopy is preferred over dispersive or filter methods of infrared spectroscopy due to the sensitivity and the rapid data collection. The FT-IR spectrometer uses an interferometer to modulate the wavelength from a broadband infrared source. Light emitted from the infrared source is split by a beam splitter. Half of the light is reflected towards a fixed mirror and from there reflected back towards the beamsplitter where about 50% passes to reach the detector. The other half of the initial light intensity passes the beam splitter on its first encounter, is reflected by the moving mirror back to the beamsplitter where 50% of it is reflected towards the detector (Figure 1).When the two

beams recombine, they interfere and there will be constructive or destructive interference depending on the optical path difference. A detector measures the intensity of transmitted or reflected light as a function of its wavelength. The signal obtained from the detector is an interferogram, which is analyzed by a computer using Fourier transforms to obtain a single-beam infrared spectrum (Barth, 2007).

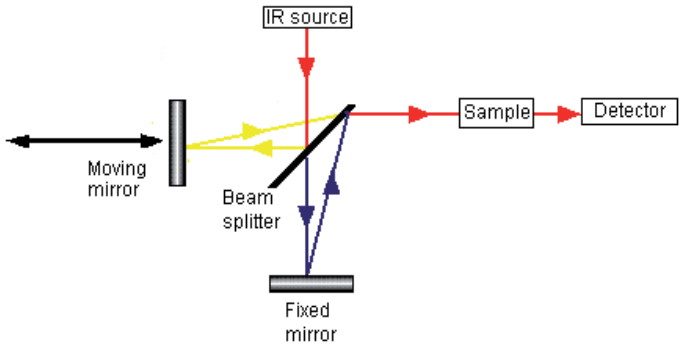

Fig. 1. Schematic function of an FT-IR set-up.

Fourier transform infrared (FT-IR) spectroscopy has proven to be a fundamental and valuable technique in biology and medicine due to its high sensitivity to detecting changes in the functional groups belonging to tissue components such as lipids, proteins and nucleic acids. Each of these tissue components can be detected and characterized by their characteristic absorption bands at specific wavelengths within a single spectrum. For biological spectroscopy, the important vibrations occur in the mid-infrared region (4000 to 400 cm^{-1}) where most organic molecules show characteristic spectral features (Theophanides, 1978). The domain of biological applications of infrared spectroscopy encompasses a wide range of very different molecular structures. Biological molecules are categorized into proteins, nucleic acids, lipids, membranes, blood tissues. Different biomolecules interact among themselves, comprising electrostatic interactions, hydrogen bondings and van der Waals interactions, which can be readily studied by infrared spectroscopy.

For complex samples that transmit infrared radiation poorly or no changes must take place in their specimen, attenuated total reflection (ATR) is applied. The technique was developed by Harrick (1960) and Fahrenfort (1961). ATR is a specialised sampling technique, where the sample is placed on ATR crystal. An infrared beam is passed through the ATR crystal, reflects of the interface of the crystal and the sample, and is passed through to the detector. During the reflection, an evanescent wave extends beyond the crystal into the sample, which enables the absorption of energies corresponding to infrared frequencies by the sample. The penetration depth of the evanescent wave is a function of wavelength with deeper penetration at longer wavelengths. This may lead to distortions in the relative intensities of infrared peaks if sample thickness is insufficient for complete coverage of the evanescent wave (Goormaghtigh et al., 1999). Figure 2 shows the diagram of a basic ATR set up.

Attenuated total reflection (ATR) coupled with FT-IR, can obtain the infrared spectrum of solid or liquid samples in their native state. The resultant FT-IR spectra provide molecular information of samples. Samples with minimal size can be non-destructively analyzed,

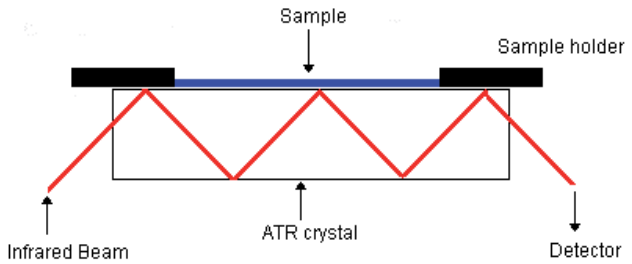

Fig. 2. Diagram of the ATR setup.

particularly in the biomedical sciences. High quality spectra can be obtained from cell suspensions containing l0-50.000 cells, depending upon the size of the cells. In the case of tissues, such measurements generally require a sample size of 1 mm^3 (Legal, 1991). Additionally, ATR has been established as a method of choice of analyzing samples that are either too thick or too strongly absorbing to analyse by other transmitting techniques. The use of these techniques have become a great potential over other diagnostic methods for the determination of the chemical components of tissues at various diseases states, due to the rapid and reagent free procedure. An advantage of ATR-FTIR to study the structure of biomembranes is that the membrane can be deposited on the surface of the internal reflection element (IRE) as a thin film of highly oriented membranes by evaporation of the water. Variations in spectral signatures arising from nucleic acids, proteins and lipids can provide important information in a number of disease states.

1.1 Medical applications of FT-IR spectroscopy

In 1949 Blout, Mellors and Woernley in 1952 reported that infrared spectra of human and animal tissues could provide information on the molecular structure of tissues. These studies met with limited success due to non-developed instrumentation available and little knowledge of spectroscopic properties of biological molecules and the complexity of the samples. At the same time, Elliot and Ambrose (1950) proposed empirical correlations between peptide structure and the Amide I and Amide II bands. The development of sensitive and high throughput spectrometers led to a wide field of medical applications of FT-IR spectroscopy. The rapid experimental and theoretical development took place in 1970s, where Fourier Transform interferometers interfaced to digital computers.

FT-IR has been extensively applied for the determination of a biochemical metabolite in biological fluids. The improved sensitivity and data processing capability of new instruments, the presence of water is no longer a serious obstacle in the analysis of fluids. Current enzymatic methods require frequent calibration controls and reagents, and this is very costly. FT –IR spectroscopy has been used for the determination of glucose, total protein, urea, triglyceride, cholesterol, chylomicron and very low density lipoproteins in plasma and serum, in order to replace commonly used ultracentrifugation techniques (Deleris and Petibois, 2003; D. Krilov et al., 2009).The differences in the size, lipid composition and apolipoprotein structure in particular classes of lipoproteins are reflected in the characteristic spectral bands of lipid and protein moiety.

FTIR has received much attention as a promising tool for non-destructive characterisation of the molecular features of atherosclerosis due to the fact that vibrational spectra are sensitive

to structures of biological molecules and their changes with the diseased state. Additionally, FTIR-spectroscopy on biological samples was pioneered in the medical sciences where it is used as a clinical tool to distinguish between malignant and healthy human cells. Acquired spectra of cells/ tissues give a detailed biochemical fingerprint that varies dependent on the clinical status. It has been successfully applied in the study of various human tissues such as mineralized tissue (Kolovou and Anastasopoulou, 2007), skin (McIntosh, 1999), colon (Conti et al., 2008), breast (Anastassopoulou et al., 2009), arteries (Mamarelis et al., 2010), cartilage(Petra et al., 2005), the urinary tract (prostate, bladder) (Gazi etal., 2003), lung(Yano et al., 2000), liver(Li et al., 2004), heart and spleen (Chua-anusorn and Webb, 2000; Gough et al., 2003).

According to a wide range of studies, it has been proved that FT-IR spectroscopy has been a significant clinical technique, which provides detailed information of the chemical components of the tissues (proteins, lipids, carbohydrates, DNA). By analysing chemical and biochemical changes, specific spectral features are to be considered for a diagnostic evaluation. In this chapter, it is discussed FT-IR spectroscopy in the field of atherosclerosis in carotid and coronary arteries. Experimental studies are summarized demonstrating the possibilities and prospects of these methods to detect and characterize the disease.

1.2 Atherosclerosis

Atherosclerosis, the most common form of cardiovascular diseases, is a leading cause of death affecting almost one third of humans in developed countries. Atherosclerosis is the usual cause of heart attacks, strokes, and peripheral vascular disease. Ross and Glomset (1973) were the first who introduced that atherosclerosis forms as a result of damage of endothelium. Multiple factors contribute to atherosclerosis, such as hypertension, smoking, diabetes mellitus, obesity, hypercholesterolemia and genetic predisposition. The major characteristics of human atherosclerosis are based on studies of coronary and carotid artery lesions. Atherosclerosis is a chronic inflammatory disease characterised by a stenotic lesion of arterial walls. Atherosclerotic lesions can cause stenosis with potentially lethal distal ischemia or can trigger thrombotic occlusion of major conduit arteries to the heart, brain, legs and other organs. The extracellular and intracellular accumulation of lipids from the circulating blood results in the thickening of the inner layer of the arterial wall. Analyses of human lesions by modern computer methods and biomechanical testing have established the probable link between this characteristic morphology and the actual rupture event (Lee and Libby, 1997).

During atherogenesis, the structure of the arterial wall changes in the intimal layer. The disease process consists of the intimal smooth muscle cell proliferation, the formation of large amounts of connective tissue matrix by the proliferated smooth muscle and the deposition of lipids within the cells and in the connective tissues surrounding them.

In the early stages of atherogenesis, fatty deposition occurs.

Atherogenic lipoproteins such as low-density lipoproteins (LDLs) enter the intima, where they are modified by oxidation or enzymatic activity and aggregate within the extracellular intima. Monocytes are transformed into macrophages, take up lipoproteins and become foam cells. The accumulation of foam cells leads to the formation of fatty streaks, which are often present in the aorta of children, the coronary arteries of adolescents, and other

peripheral vessels of young adults (Steinberg and Witztum, 1999). Fatty streaks are widely considered to be the initial lesion leading to the development of complex atherosclerotic lesions (Figure 3). The progression requires an additional stimulus, i.e. risk factor for the development of atherosclerosis. Smooth muscle cells secrete extracellular-matrix components (proteoglycans), increasing the retention and aggregation of lipids to monocytes (Stary, 1994).

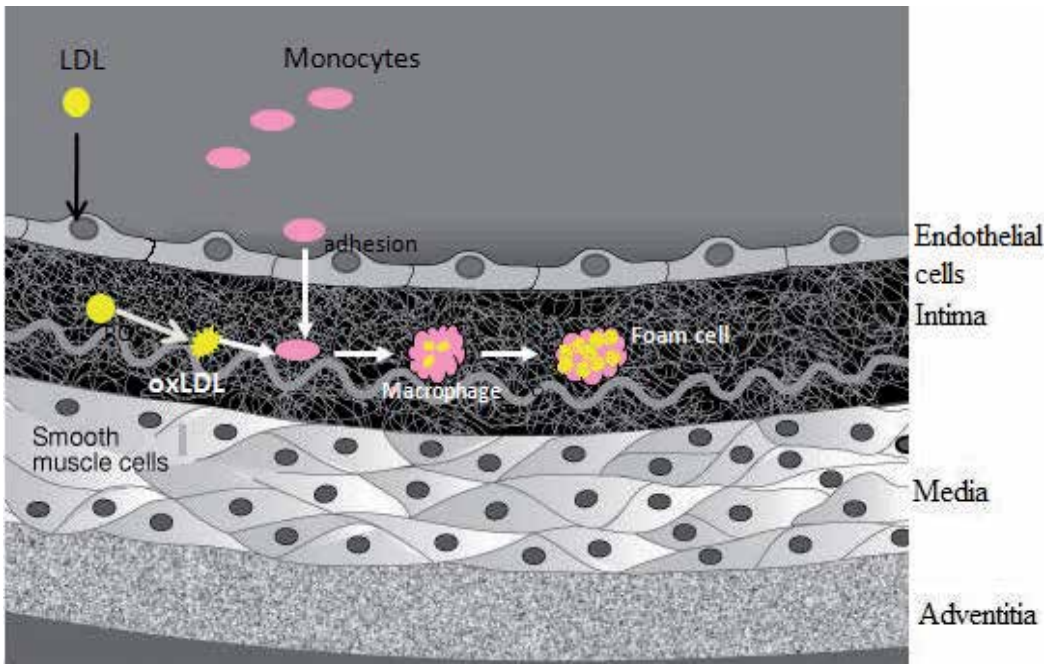

Fig. 3. Formation of atherosclerotic plaque.

1.3 Study of atheromatous plaques by FT-IR

Atherosclerosis is a complex process and the behaviour of vulnerable atherosclerotic plaques is believed to be closely related to plaque composition. Knowledge of the composition and physical chemistry of atherosclerotic plaques is essential for understanding how these plaques originate and mature and how reversal of the pathological process may be achieved (Insull, 2009). It is therefore important to develop an effective technique for examining plaque constituent properties. FT-IR provides information on the molecular and structural composition directly in the untreated, unfixed, and unstained whole tissue, thus preserving the integrity of the original cells. In this work, Fourier transform infrared spectroscopy using attenuated total reflectance (FTIR-ATR) has been used to assess and analyze the biochemical properties of human atherosclerotic plaques. Additionally, Scanning electron microscopy (SEM) has been used to provide valuable information on the general characteristics of the morphology and structure of carotid and coronary arteries. SEM allows the scanning of large area in the atheromatous plaque and the use of large magnification provides a detailed view. Human tissues were viewed directly without any conductive coatings.

2. Materials and methods

20 samples from carotid and coronary arteries from patients (60-85 years old) who underwent endarterectomy were used for the study (Figure 4). Representative sections of the Carotid atheromatic plaques and coronary arteries were restored in formalin. The FT-IR spectra were obtained with a Nicolet 6700 thermoscientific spectrometer, connected to an attenuated total reflection, ATR, accessory. For each region a series of spectra were recorded and every spectrum consisted of 120 co-added spectra at a resolution of 4 cm−1 and the OMNIC 7.1 software was used for data analysis. All the spectra for each patient and region were obtained in the same way. The analysis of bacterial morphology was performed by Scanning Electron Microcopy –SEM using a Fei Co at an accelerating potential 25 kV. Uncoated freeze dried cells were examined with LFD and BSED detectors. Qualitive elemental data analysis of the samples was determined by EDX (Energy-dispersive X-ray spectroscopy).

Fig. 4. Sample from carotid arteryA: atheromatous plaque, B: adventitia , C: intima

3. Analysis and discussion of FT-IR spectra

Two representative FT-IR absorption spectra of a carotid and coronary artery in the region 4000 -400 cm^{-1} are shown in Figure 5. The spectra provide distinct features for the determination of the chemical composition and the diagnostic classification of arterial wall.

The spectra in high frequency region, 4000–2500 cm^{-1}, mainly consist of vOH, vNH, asymmetric and symmetric methyl (CH_3) and methylene (CH_2) stretching vibrations. Significant differences are observed among carotid and coronary artery. In the case of coronary artery, the shoulder observed at 3524 cm^{-1} is assigned to vOH vibration of hydroxyl groups produced by the hyperoxidation of lipids and proteins and by addition of hydroxyl ($HO^{\bullet}$) free radicals to the double bonds of the fatty acids. The band at 3282 cm^{-1} is assigned to vNH stretching of the peptide bond (–NHCO-) of proteins (Theophanides et al., 1988). According to the intensity of vNH band, it is estimated that the coronary artery has a higher damage in proteins compared to the carotid artery.

The olefinic band v=C-H at 3077 cm^{-1} arises from the unsaturated lipids. In coronary artery, the high intensity of the band indicates that the foam cells are rich in low density lipoproteins (LDL). It is known that unsaturated lipids are more prone to lipid peroxidation (Mamarelis et al., 2010). The integrated area of the olefinic CH band can be used as an index of relative concentration of double bonds in the lipid structure from unsaturated fatty acyl

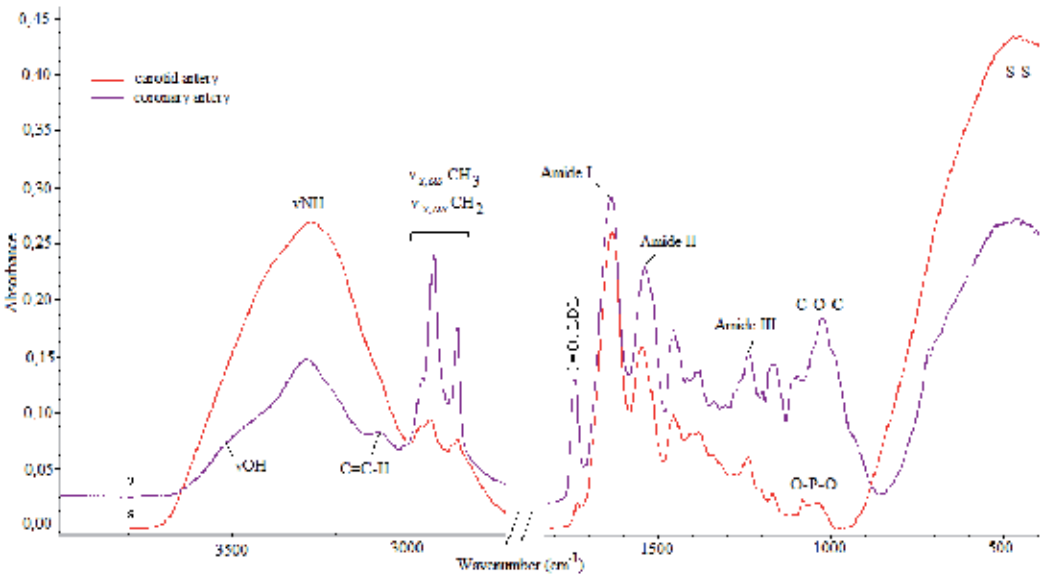

Fig. 5. FT-IR adsorption spectra obtained from human tissues (a) carotid artery, (b) coronary artery in the region of 4000-400 cm^{-1}.

chains (e.g. linolenic, arachidonic, etc.), and/or due to lipid peroxidation. For this reason, the intensity of this band can be used as a diagnostic band of LDL.

The CH_2 asymmetric (2929 cm^{-1}) and symmetric (2851 cm^{-1}) stretching vibrations give intense bands, while asymmetric CH_3 stretching at 2955 cm^{-1} and symmetric stretching at 2865 cm^{-1} bands are seen as shoulders. The bands arise from lipids, phospholipids and membranes. The intensity of symmetric and asymmetric stretching vibrations of CH_2 and CH_3 reflect lipid hyperoxidation (Liu et al., 2002). The increase in the intensity of the bands in coronary artery shows that the environment is less lipophilic due to fragmentation of the lipoproteins and accumulation of free cholesterol and cholesterol esters in the atheromatous core, as a result membrane fluidity changes significantly (Anastassopoulou and Theophanides, 1990).

Significant changes are also observed in the infrared absorption bands in the region 1800-1500cm^{-1}, as it is shown in the spectra. The presence of cholesterol esters and other ester-containing compounds is also identified from the carboxyl ion (-O-C=O) stretching absorption at 1735 cm^{-1} apart from the C=C-H stretching band (3077 cm^{-1}). This band confirms lipid hyperoxidation and the increased intensity of the band indicates increased LDL concentrations according to the blood analyses of the patient. All the patients who underwent coronary endarterectomy showed higher intensity in the specific band. The bands at 1735 and 3077 cm^{-1} can be used as indicators for LDL cholesterol of patients.

The Amide I absorption band, arises mainly from the C=O stretching vibration with minor contributions from the out-of-phase CN stretching vibration, the CCN deformation and the NH in-plane bend. The Amide I band is down-shifted near 1635 cm^{-1}, approximately 20 cm^{-1} difference compared to the absorption of a normal tissue (1656 cm^{-1}), suggesting a

conformational change in a –helixes (Anastassopoulou et al., 2009). The shifting of the Amide I band suggests that proteins lose their structure from a-helix to random coil due to fragmentation induced from free radical reactions. The exposure of proteins to free radicals induces secondary structural changes, since secondary structure is stabilized by hydrogen bonding of peptide backbone. Proteins are organized into a-helixes, but the hydrogen bond is damaged, so the chains opens and are more prone to free radicals, leading to the change of a-helix to random coil.

The change of dipole moment of peptide bond, as it is shown in equation [1] at resonance structures, leads to a change in the orientation of amino groups (NH) to the carbonyl group C=O, resulting in the destruction of alpha –helix and the secondary structure of proteins.

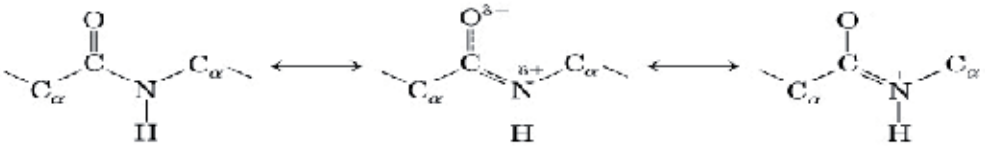

(1)

The band at 1537 cm^{-1} is attributed to the vibrations of Amide II. The amide II mode is the out-of-phase combination of the NH in plane bend and the CN stretching vibration with smaller contributions from the CO in plane bend and the NC stretching vibrations. The bands of Amide I and Amide II are representative of –NH-CO- vibrations of proteins (Theophanides et al., 1988). The analysis of the spectra by Fourier self-deconvolution was used to enhance resolution in the region 1800-1500 cm^{-1} (figure 6 and 7).

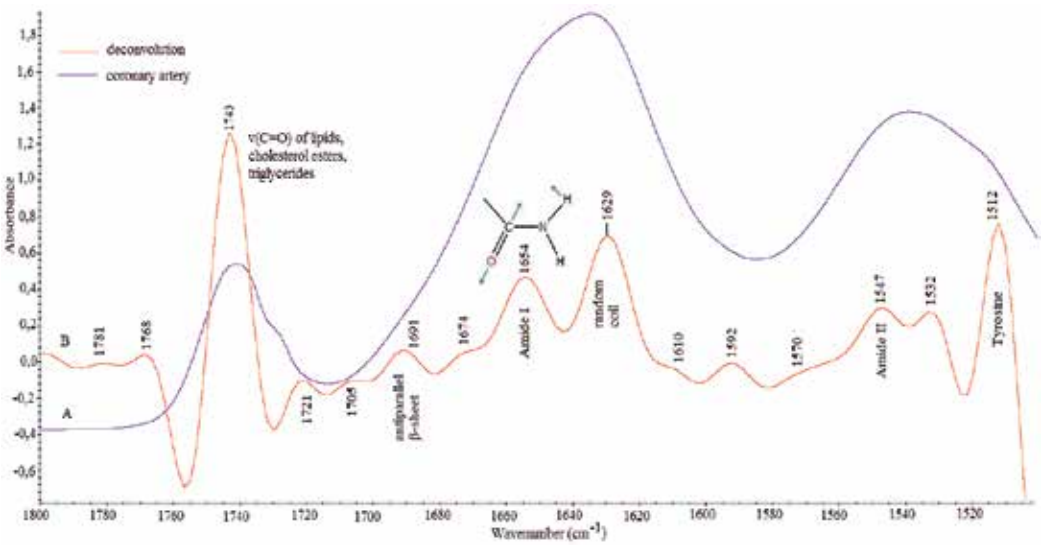

Fig. 6. A: FT-IR spectra of coronary artery in the region 1800-1500 cm^{-1}, B: Deconvolution of the spectra in the same region.

As it is determined from the deconvolution in the spectra of the coronary artery of a patient, the band at 1781 and 1768 cm^{-1} is attributed to the carboxyl anions –COO- of the

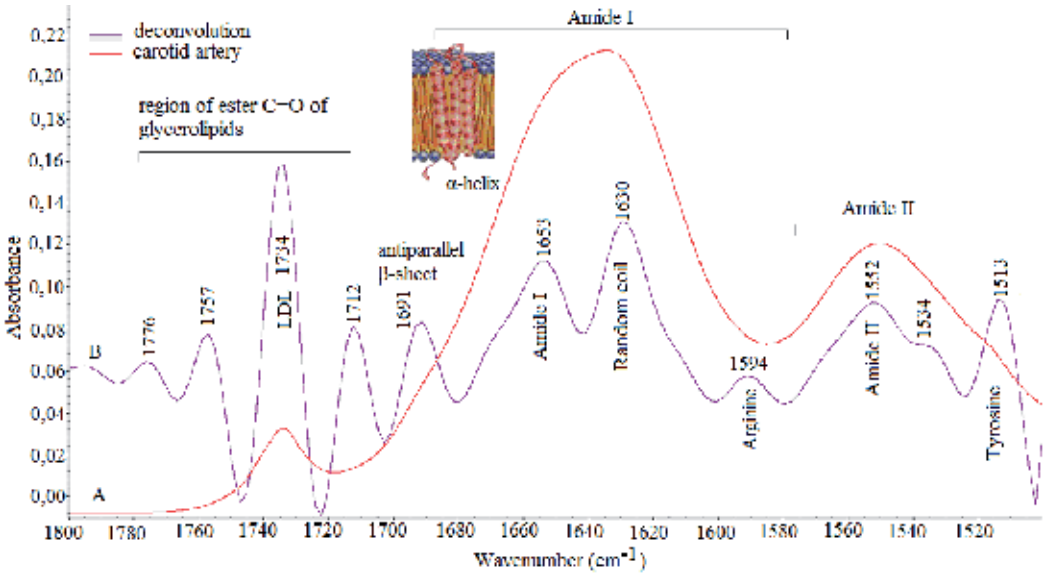

Fig. 7. A: FT-IR spectra of carotid in the region 1800-1500 cm^{-1}, B: Deconvolution of the spectra in the same region.

atheromatous plaque, which are probably connected to metal with high molecular weight. The broad band in the region 1750—1720 cm^{-1} appears to be the summation of two underlying components by deconvolution, giving one band at 1743cm^{-1} and a second one at 1721 cm^{-1}. These bands are assigned to LDL cholesterol and are due to stretching vibrations of the carbonyl group involved in ester bonds. These bands arise from the interfacial region of the glycerolipid moiety and are responsive to changes in their environment, such as hydrogen bonding or polarity (Arrondo and Goni, 1998).

The broad band at 1700–1600 cm^{-1} is Amide I band, constituted from the bands at 1691, 1674, 1654, 1629, and 1610 cm^{-1}. The main amide I band at 1654 cm^{-1} is indicative of a high content of a-helical structure, although part of the absorption at this frequency also corresponds to random coil structure at 1630cm^{-1} and antiparallel β-sheet at 1691 cm^{-1} (Barth, 2007). Particularly, the band at 1691 cm^{-1} arises from the peptide bond of proteins and mainly from the vibration of C=O compared to NH group. The band at 1674 cm^{-1} is attributed to apolipoprotein ApoC-III, which resides in HDL and inhibits the lipolysis of triglyceride-rich lipoproteins. The decrease of a-helix absorbance band compared to random coil confirms the fragmentation due to free radical interactions.

The bands at the wavelengths 1592, 1570, 1547 and 1512, which are assigned to the groups of arginine, aspartic acid, glutaminic acid and tyrosine of apolipoproteins Apo A-I. The specific bands were revealed after the deconvolution treatment of spectra. The wide band at 1537 cm^{-1} is split into two bands, one in 1550cm^{-1}, which is characteristic of Amide II absorption due to the stretching vibrations C-N and bending vibration N-H because of the influence of lipids. The apolipoproteins of Apo A-I and A-II, are components of HDL (High density Lipoproteins) and control HDL metabolism (Nara et al., 2002). The distinctive structures and properties of apoA-I and apoA-II, the two major HDL proteins, determine in different ways the thermodynamic stability of HDL - the former through its greater plasticity and the latter by its higher lipophilicity. Apo A-I protects phospholipids from oxidation due to a

conformational constraint governed by adjacent amphiphatic a-helices located in C-terminal lipid-binding domain. Apo A-I is a potent inhibitor of lipid peroxidation, protecting the phospholipids from water-soluble and lipophilic free radical initiators (Bolanos-Garcia and Miguel, 2003). The reduction of Apo A-I and A-II and the increase of the characteristic band of LDL at 1735 cm^{-1} are connected to the blood analyses of the patients.

Relatively, the deconvolution in the carotid artery spectra of a patient as it is shown in figure 7, revealed the bands at 1776 and 1757 cm^{-1}, which are attributed to the carboxyl anions –COO- of the atheromatous plaque. The lipid content is indicated by the lipid ester band at 1734 cm^{-1}. The wide band of amide I is split to the bands at 1691, 1653, 1630 cm^{-1}, which reveals the destruction of a-helical structure of proteins due to the free radicals reactions. The peptide bond appears another characteristic band at the region of amide II absorption, which is constituted from the bands at 1592, 1552, 1534 and 1513, which are attributed to arginine, a-helix of collagen, random coil and tyrosine.

In carotid and coronary artery, the deconvolution confirmed the peroxidation of lipids and lipoproteins. The intensity of the aldehydes due to peroxidation of LDL (1735 and 1742 cm^{-1}) is higher in the case of coronary artery. Various small molecular weight aldehydes such as acrolein, malondialdehyde (MDA), and 4-hydroxy-2-nonenal (HNE) are formed during lipid peroxidation as secondary or decomposition products. The main product of aldehydes in this region is malonaldehyde (MDA), which is an end product of lipid peroxidation that starts with abstracting a hydrogen atom from an unsaturated fatty acid chain, and this peroxidation spreads to the adjacent fatty acids continually. It has been proved that MDA inhibits the metabolism of high density lipoproteins (HDL), which are protecting factors of human organism. Thus, the increase of LDL, which is relative to the clinical condition of the patients, is associated with a higher risk of cardiovascular disease.

In figure 8, the wide band at 1454 cm^{-1} is constituted of two bands at at 1461 $cm^{-1}$and 1443 cm^{-1} in the coronary artery, which arise from the carbon chain of lipids, combination of bending vibrations of δCH_2 of carbon chains of lipids and δCOOH of non-ionic groups, respectively. The deconvolution of the band in the carotid artery revealed three bands, at 1467, 1454, 1443 cm^{-1}, which are assigned to the bending vibrations of $\delta_{as}CH_3$ of lipids, stretching vibration of νCO_3^{2-} and δCOOH of non-ionic groups, respectively. In the coronary artery, the intense increase of the band results in the decrease of lipophilic environment of membrane. This observation is in agreement with the increase of the stretching vibration bands in the region 3000-2870 cm^{-1}.

The absorptions at 1238, 1173 and 1024 cm^{-1} matched the spectral patterns that arise from amide III (in plane N –H bending and C-N stretching vibrations) and the asymmetric and symmetric stretching modes of PO_2^- in DNA or the phosphodiester groups of the phospholipids, cholesterol ester and –C-O-C- vibrations of fatty acids and ketals (Mamarelis et al., 2010), respectively, which are product of atheromatous plaque of coronary and carotid artery due to hyperoxidation of membranes (Figure 9).. The comparison of coronary and a carotid artery reveals that intense hyperoxidation has taken place in the coronary artery, as it is determined from the C-O-C vibrations of aldehyde groups. To the contrary, the vibrations of phosphate groups PO_2 of phospholipids and DNA band together with the bending vibration $v_4CO_3^{2-}$ at 874 cm^{-1} suggests that the atheromatic plaque is consisted from calcium carbonate ($CaCO_3$) and that the foam cells are rich in calcium minerals(Petra et

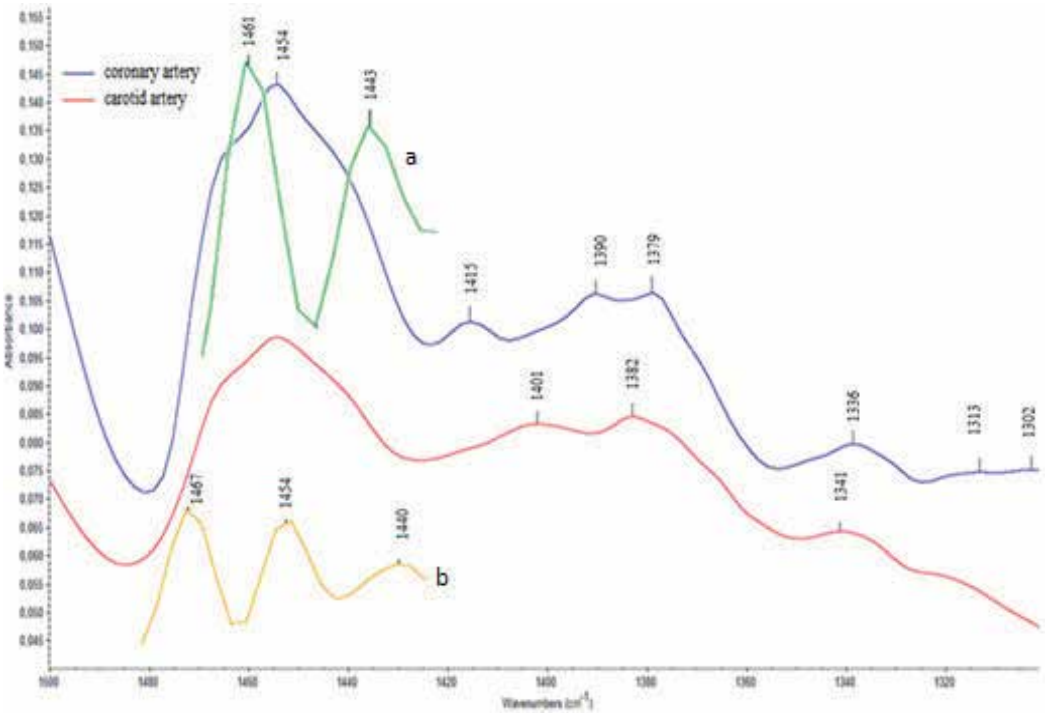

Fig. 8. FT-IR spectra of carotid and coronary artery in the region 1500-1300 cm^{-1} and the deconvolution of the band at 1454 cm^{-1} of coronary (a) and carotid (b) artery.

al., 2005). The calcified atherosclerotic plaque spectra are dominated by bands from calcified minerals such as hydroxyapatite and carbonated apatite.

4. Scanning electron microscopy

Scanning electron microscopy (SEM) was used for imaging biological specimens, thus enabling rapid and high-resolution imaging of atherosclerotic lesions (Kamar et al., 2008). High resolution images can be obtained without gold coating, thereby enabling imaging of atherosclerotic lesions close to its original state. Significant structural alterations and mineral salts were observed in carotid and coronary arteries. The membrane morphology of carotid artery is shown in figure 10.

The architecture of foam cells is heterogenous as well as the size of white stones. It was found that this region is rich in phosphorous. It has been found that initiation of atheromats takes place in this region and thus, it is expected to be a region, which corresponds to atheromatic plaque rich in phospholipipases (Lp-PLA2). The enzyme Lp-PLA2 hydrolyses the oxidized phospholipids to lysophosphatydil choline and causes to atherogenesis (Gorelick, 2008; Parthasarathy et al., 2008). The ratio of [Ca]/[P] according to elemental analysis (EDAX)demonstrates that the stones of carotid are hydroxyapatite.

On the contrary, the coronary artery is rich in calcium but no phosphorus was detected (Figure 11). As a result, carbonated apatite is mainly formed in coronary arteries. This observation is in agreement with the results from FT-IR spectra. Many of the mineral salts

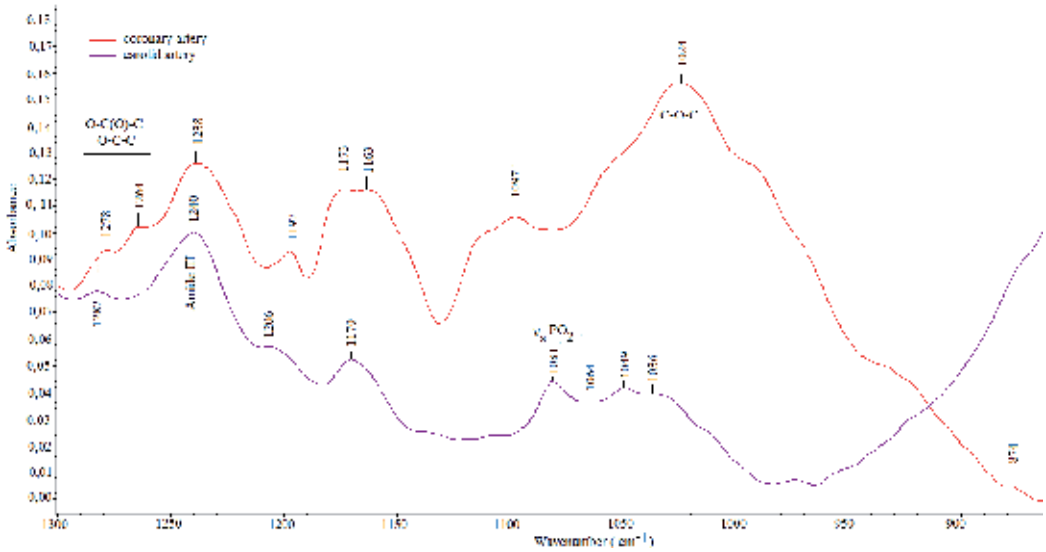

Fig. 9. FT-IR spectra of carotid and coronary artery in the region 1300-800 cm^{-1}.

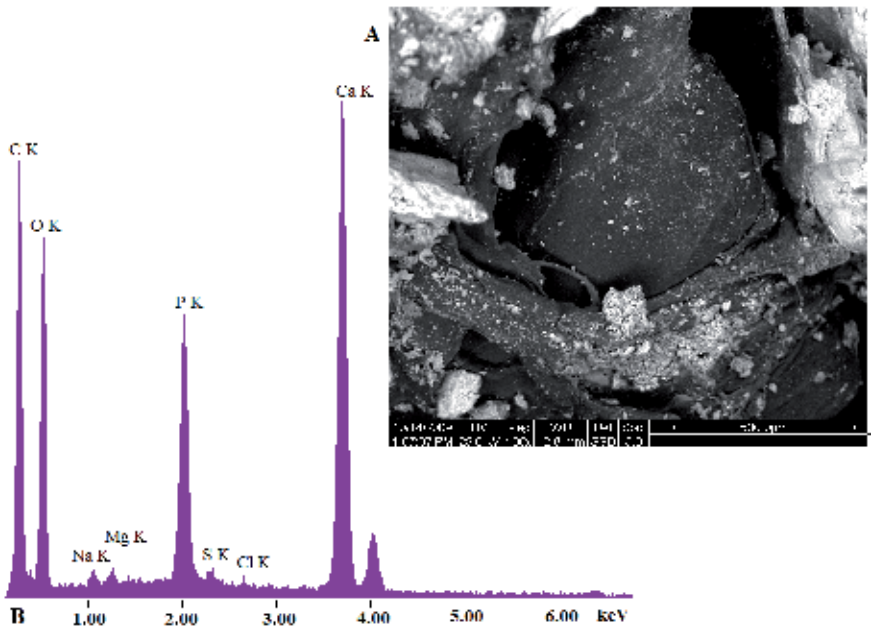

Fig. 10. A:SEM imaging of carotid membrane, region rich in mineral deposits (scale 500 μm), B: EDAX analysis of a white spot.

are not connected to the tissues while other are bound by chemical bonds. Additionally, an increased number of fibrils are presented that confirm the fact that free radicals play an important role in the development of atheromas. The architecture of surface is rich in spheres of LDL, as it was demonstrated from FT-IR spectra. The molecules of LDL obtain the shape of sphere that corresponds to the minimum energy.

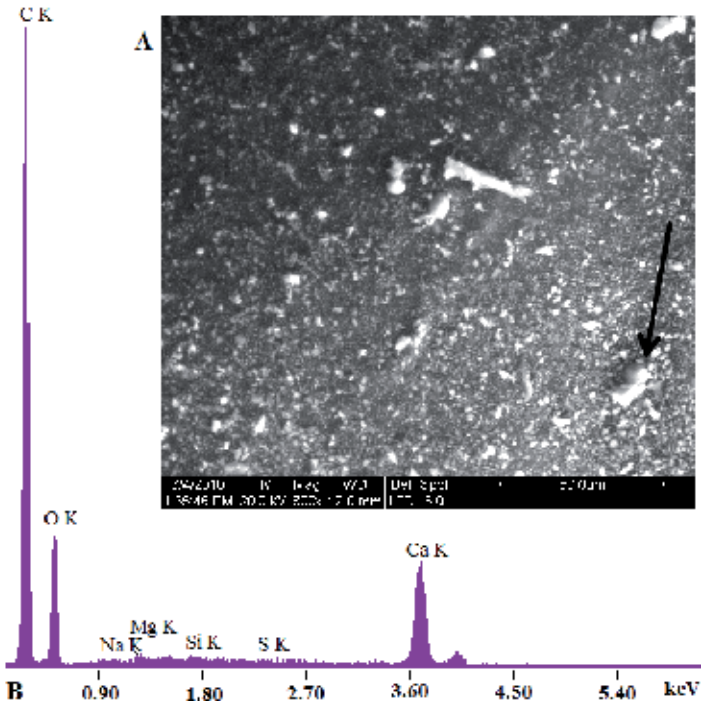

Fig. 11. A: SEM imaging of coronary membrane, region rich in mineral deposits (scale 50 μm), B: EDAX analysis of a white spot.

5. Oxygen-centered free radicals

The ubiquitous presence of oxygen in higher species and diatomic oxygen's ability to readily accept electrons has made oxygen-centered free radicals the most frequently encountered radical species, which are involved in the pathogenesis of atherosclerosis. The hydrogen peroxide molecules are intermediate products in the catalytic cycle of oxidation of P_{450} cytochrome according to the reaction [2]:

$$O_2 \xrightarrow{e} O_2^{\cdot -} \xrightarrow{2H^+} H_2O_2 \tag{2}$$

The main factors for the production of free radicals are the iron cations (Fe2+) of the hemoproteins and bivalent copper cations (Cu^{2+}) from copper proteins(Halliwell & Gutteridge, 2000; Anastassopoulou & Dovas, 2007). The irons cations react with hydrogen peroxide and produce hydroxyl free radicals (·OH), according to Fenton or Haber-Weiss like reactions:

$$Fe^{2+} + H_2O_2 \longrightarrow Fe^{3+} + HO^{\cdot} + OH^- \tag{3}$$

Lipids, usually polyunsaturated fatty acids react with the produced hydroxyl radicals by hydrogen abstraction leading to the formation of lipid free radicals, according to the reaction [4]:

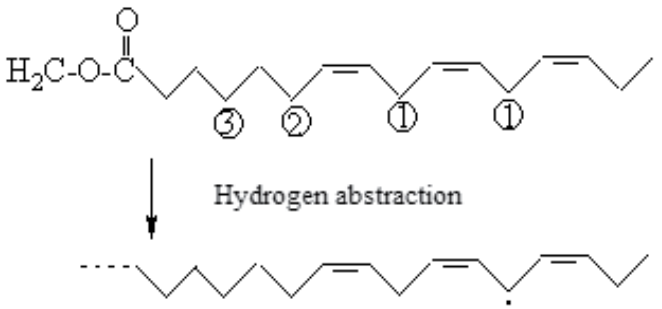

(4)

The produced lipid free radical is reproduced rapidly, leading to stable dimer products as it is shown in equation 5:

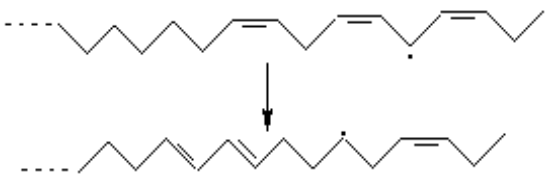

(5)

Lipid radicals react with each other, leading to the generation of one terminal double bond [6].

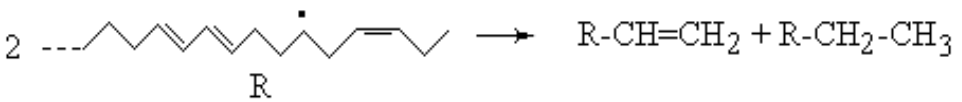

(6)

The former reaction explains the increasing of the intensity of the olefinic band at 3077 cm^{-1}.

Taking into account that human lives under aerobic conditions, the oxygen in the form of double free radical (•O=O•) reacts rapidly with the lipid free radicals or other biomolecules such as collagen, elastin, resulting in the formation of lipid hydroperoxyl radical [7]. This step is the initiation of peroxidation.

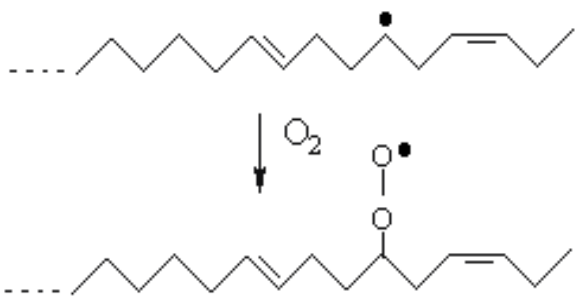

(7)

The abstraction of hydrogen (adjacent lipids, thiols) from lipid hydroperoxyl radical leads to the generation of hydroperoxyl groups (–C-O-OH), which are non-ionic and lead to fixation of lipid damage.

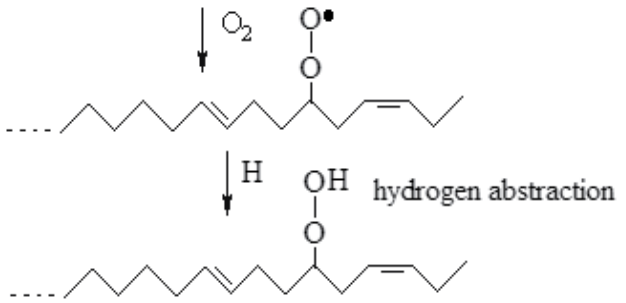

(8)

Peroxidized lipids decompose easily, generating both free and core aldehydes and ketones according to the reaction [9] (Mamarelis et.al. 2010).

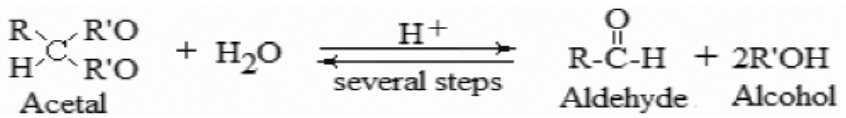

(9)

These reactions explain the FT-IR spectra of coronary and carotid artery. In the region of 1800-1600 cm^{-1}, the band at 1735 cm^{-1} which was assigned to the carbonyl group of lipid esters and the presence of malonaldehyde is confirmed by the former reactions. Malondialdehyde (MDA) is frequently measured as indicator of lipid peroxidation and oxidative stress (Dotan et al., 2004). It is produced from lipid hydroperoxyl radical due to the following reactions:

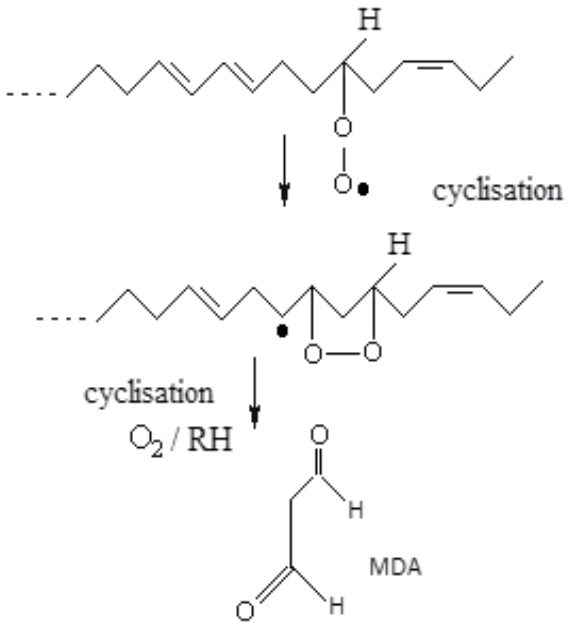

The non-destructive nature of FT-IR spectroscopy and the ability to directly probe biochemical changes lead to an understanding of the biochemical and structural changes associated with arteriosclerosis. The decrease in the intensity of the band at 1651 cm^{-1} and

the shifting to lower wavenumber (approximately 1630cm^{-1}) justify the way of disappearance of the Amide I band and the change in the structure of proteins from alpha – helix to random coil due to free radicals reactions.

The bands at the region 1280 - 1170 cm^{-1} are attributed to the presence of O-C-C, O-C(O)-C groups due to the peroxidation of membranes. Thus, the presence of characteristic bands in the region 4000 -400 cm^{-1} confirms the peroxidation of membranes.

6. Conclusions

FT-IR spectra showed that hyperoxidation of lipids, phospholipids and membranes take place during atherogenesis. The plaque formation and the increase of LDL lead to change of tertiary structure of proteins from α-helix to random one. FT-IR spectra clearly revealed prominent spectral features corresponding to plaque constituents such as the presence of lipids, lipid esters, fibrous tissues and phosphate group (calcification). Spectral data were correlated well with patients' analyses. The present work demonstrates that infrared spectroscopy can be used to accurately estimate the chemical composition of coronary and carotid arteries. In vivo information about the chemical composition of atherosclerotic lesions may provide a powerful method to detect and characterize sites of atherosclerosis.

7. References

Anastassopoulou, J., Boukaki, E., Conti, C., Ferraris, P., Giorgini, E., Rubini, C., Sabbatini, S., Theophanides, T. & Tosi, G. (2009). Microimaging FT-IR spectroscopy on pathological breast tissues. *Vibrational Spectroscopy*, Vol. 51, pp.270-275

Anastassopoulou, J. & Dovas, A. (2007). *Metal ions and cancer*. In S Missailidis(Ed.), The cancer Clock. John Wiley, pp. 27-49

Anastassopoulou, J. & TheophanidesT.(1990). Raman studies of model vesicle systems. J Appl Spectrosc. Vol. 44, pp. 523-525

Arrondo, J.L.R. & Goni, F.M. (1998). Infrared studies of protein-induced perturbation of lipids in lipoproteins and membranes. *Chemistry and Physics of Lipids*, Vol. 96, pp. 53–68

Blout, E. R., & Mellors, R. C. (1949). Infrared Spectra of Tissues. *Science*, Vol. 110, pp.137–138

Barth, A. (2007).Infrared spectroscopy of proteins. *Biochimica et Biophysica Acta*,Vol. 1767, No.9, pp. 1073-101

Bolanos-Garcia, V.C. & Miguel, R.N. (2003). On the structure and function of apolipoproteins: more than a family of lipid binding proteins. *Progress in Biophysics and Molecular Biology*, Vol. 83, pp. 47-68

Chua-anusorn, W. & Webb, J. (2000). Infrared spectroscopic studies of nanoscale iron oxide deposits isolated from human thalassemic tissues. *Journal of Inorganic Biochemistry*, Vol. 79, pp.303–309

Conti, C., Ferraris, P., Giorgini, E., Rubini, C., Sabbatini, S., Tosi, G., Anastassopoulou, J., Arapantoni, P., Boukaki, E., Theophanides, T. & Valavanis, C. (2008). FT-IR Microimaging Spectroscopy:Discrimination between healthy and neoplastic human colon tissues. *Journal of Molecular Structure*, Vol. 881, pp. 46-51

Deleris, G. & Petibois, C. (2003). Applications of FT-IR spectrometry to plasma contents analysis and monitoring. *Vibrational Spectroscopy*, Vol. 32, pp.129–136

Dotan, Y., Lichtenberg , D.& Pinchuk, I. (2004). Lipid peroxidation cannot be used as a universal criterion of oxidative stress. *Progress in Lipid Resea*rch, Vol. 43, No. 3, pp. 200-227

Elliot, A. & Ambrose, E. (1950). Structure of Synthetic Polypeptides. *Nature*, Vol.165, pp.921

Fahrenfort, J. (1961). Attenuated total reflection: A new principle for the production of useful infra-red reflection spectra of organic compound. *Spectrochimica Acta*, Vol. 17, pp. 698-709

Gazi, E., Dwyer, J., Gardner, P., Ghanbari-Siakhani, A., Wde, A.P., Lockyer, N.P.,Vickerman, J.C., Clarke, N.W., Shanks, J.H., Scott, L.J., Hart, C.A. & Brown, M. (2003). Applications of Fourier transform infrared microspectroscopy in studies of benign prostate and prostate cancer. A pilot study. *Journal of Pathology*, Vol. 201, pp. 99–108

Gorelick, P.B.(2008). Lipoprotein-Associated Phospholipase A2 and Risk of Stroke. *American Journal of Cardiology*, Vol. 101, pp. 34-40

Goormaghtigh, E., Raussens, V. & Ruysschaert, J.-M. (1999). Attenuated total re£lection infrared spectroscopy of proteins and lipids in biological membranes. *Biochimica et Biophysica Acta*, Vol. 1422, pp.105-185

Gough, K. M., Zelinski, D., Wiens, R., Rakand, M. & Dixon, M.C. (2003). Fourier transform infrared evaluation of microscopic scarring in the cardiomyopathic heart: Effect of chronic AT1 suppression. *Analytical Biochemistry*, Vol. 316, pp.232–242

Halliwell, B. & Gutteridge, J.M.C. (2000). Free radicals in biology and medicine, 3rd ed. London: Oxford University Press, Oxford, UK

Harrick, N.J. (1960). Study of Physics and Chemistry of Surfaces from Frustrated Total Internal Reflections. *Physical Reviews Letters*, Vol. 4, pp. 224–226

Insull, W. (2009). The Pathology of Atherosclerosis: Plaque Development and Plaque Responses to Medical Treatment. *The American Journal of Medicine*, Vol. 122, No 1A, pp. S3–S14

Kamari, Y., Cohen, H., Shaish, A., Bitzur, R., Afek, A., Shen, S., Vainshtein, A. & Harats, D. (2008). Characterisation of atherosclerotic lesions with scanning electron microscopy (SEM) of wet tissue. *Diabetes and Vascular Disease Research,* Vol. 5, 44-47

Kolovou, P. & Anastassopoulou, J. (2007). Synchrotron FT-IR spectroscopy of human bones. The effect of agin. In: *Brilliant Light in Life and Material Sciences*, V. Tsakanov and H. Wiedemann (Eds.), pp. 267-272., Springer

Krilov, D., Balarin, M., Kosovic, M., Gamulin, O. & Brnjas-Kraljevic, J. (2009). FT-IR spectroscopy of lipoproteins—A comparative study. *Spectrochimica Acta Part A*, Vol. 73, pp. 701–706.

Lee, R. T. & Libby, P.(1997). The Unstable Atheroma. *Arteriosclerosis, Thrombosis, and Vascular Biology*, Vol. 17, pp.1859-1867.

Legal, J.M., Manfait, M. & Theohanides, T. (1991). Applications of FTIR spectroscopy in structural studies of cells and bacteria. *Journal of Molecular structure*, Vol. 242, pp.397-407

Li, X., Lin, J., Ding, J., Wang, S., Liu, Q. & Qing, S. (2004). Raman spectroscopy and fluorescence for the detection of liver cancer and abnormal liver tissue, *Annual Inter Conf IEEE EMBS*, San Francisco, September 1–5, 2004

Liu, K.Z., Bose, R. & Mantsch, H.H. (2002). Infrared spectroscopic study of diabetic platelets. *Vibrational Spectroscopy,* Vol. 28, pp. 131-136

Mamarelis, I., Pissaridi, K., Dritsa, V., Kotileas, P., Tsiligiris, V., Tzilalis, V. & Anastassopoulou, J. (2010). Oxidative stress and atherogenesis. An FT-IR spectroscopic study. *In Vivo*, Vol. 24, pp.883-888

McIntosh, L.M., Jackson, M., Mantsch, H., Stranc, M.F. , Pilavdzic, D. &.Crowson, A.N.(1999) Infrared Spectra of Basal Cell Carcinomas are Distinct from Non-Tumor-Bearing Skin Components. *Journal of Investigative Dermatology,* Vol. 112, pp. 951–956.

Nara, M., Okazaki, M., & Kagi, H. (2002). Infrared study of human serum very-low-density and low-density lipoproteins. Implication of esterified lipid C-O stretching bands for characterizing lipoproteins. *Chemistry and Physics of Lipids,* Vol. 117, pp. 1–6.

Petra, M., Anastassopoulou, J., Theologis, T. & Theophanides T. (2005). Synchrotron micro-FT-IR spectroscopic evaluation of normal paediatric human bone. *Journal of Molecular Structure*, Vol. 78, pp. 101-116

Parthasarathy, S., Litvinov, D., Selvarajan, K. & Garelnabi M. (2008).Lipid peroxidation and decomposition — Conflicting roles in plaque vulnerability and stability. *Biochimica et Biophysica Acta*, Vol. 1781, pp. 221–231

Ross, R. & Glomset, J. A. (1973). Atherosclerosis and the arterial smooth muscle cell. *Science* Vol. 180, pp. 1332–1339

Stary, H.C. (2000). Natural history and histological classification of atherosclerotic lesions: an update. *Arteriosclerosis, Thrombosis, and Vascular Biology*, Vol. 20, pp. 1177-1178

Steinberg, D. & Witztum, J.L. (1990). Lipoproteins and atherogenesis. *Journal of American Medical association* . Vol. 264, pp. 3047–3052

Theophanides, T., Angibust, J.P. & Manfait M. (1988). *Protein and Nucleic Acid Changes*. In Twardowski (Ed.), Spectroscopic and Structural Studies of Biomaterials, I. Proteins, Sigma Press, Wilmslow, UK, pp. 3-14

Theophanides, T. (1984). *Fourier Transform Infrared Spectroscopy*. D. Reidel Publishing Co., Dodrecht.

Theophanides, T. (1978). *Infrared and Raman spectroscopy of biological molecules*. NATO Advanced Study Institute, D Reidel Publishing Co, Dodrecht

Woernley, D. L. (1952). Infrared Absorption Curves for Normal and Neoplastic Tissues and Related Biological Substances. *Cancer Research*, Vol. 12, pp. 516

Yano, K., Ohoshima, S., Gotou, Y., Kumaido, K., Moriguchi, T. & Katayama H. (2000). Direct Measurement of Human Lung Cancerous and Noncancerous Tissues by Fourier Transform Infrared Microscopy: Can an Infrared Microscope Be Used as a Clinical Tool? *Analytical Biochemistry*, Vol. 287, pp. 218-225

17

Chemometrics of Cells and Tissues Using IR Spectroscopy – Relevance in Biomedical Research

Ranjit Kumar Sahu and Shaul Mordechai*
Department of Physics, Ben-Gurion University of the Negev, Beer-Sheva
Cancer Research Center, Ben-Gurion University of the Negev, Beer-Sheva
Israel

1. Introduction

Biochemical analyses of substances rely upon the ability of techniques to identify qualitatively and quantitatively the components present and are based on physicochemical characteristics as well as chemical nature of substances being detected. While chemical analyses usually depend on reactions of a given substance and can be destructive, spectral studies are usually non-destructive and deal with describing a substance based on properties like absorption or transmission of light (e.g. UV, Visible, Infrared (IR)), light scattering ability, fluorescence /phosphorescence using various optical techniques. Thus, the technique (Fourier transform infrared) spectroscopy has gained prominence in both research and applications in different fields of science. Among the various techniques, IR spectroscopy owing to its lower potency of causing damage compared to X-rays, gamma rays and UV rays (as it is based on weak vibrational energies) has become the technique of choice during chemical analysis of substances. IR spectroscopy can not only provide information about the various components in a complex material but is also unique in its ability to be modified into different kinds of instrumentations based on requirement. The various IR spectroscopy based instruments from a simple IR based spectroscope that helps to obtain the absorbance spectra of a chemical compound to the complex imaging systems that employ computational methods in addition to the technical sophistication are based on a simple principle that every compound or a particular combination of compounds can be described by means of a FTIR (Fourier transform infra red) spectra qualitatively and quantitatively.

The guiding principle of all such analyses lies in the fact that when IR radiation of different wave numbers are simultaneously passed through a sample, specific wave numbers are absorbed based on the vibrations of molecules, creating a unique fingerprint of each sample, from a simple molecule like a protein molecule to a more complex structure like eukaryotic tissues. In spite of the fact that the cells and tissues can be discriminated based on their spectral fingerprints in the mid IR/NIR region, their signatures are the result of contribution from several biological components that at times absorb at similar or overlapping wave

* Corresponding Author

numbers. In order to explain the contribution of different metabolites like carbohydrates, nucleic acids, proteins and lipids in a sample, spectra of pure components are collected and analyzed for specific patterns. Comparison of compound that vary in one or more functional groups aids in the determination and assignment of particular groups and defines the specificity of signature for each along the entire spectral region. Assignment of the exact contribution of each component to the entire spectra therefore makes the method quantitative as well as qualitative.

Figure 1A shows representative spectra of blood fractions obtained by FTIR-MSP (Fourier Transform Infrared Microscopy), mounted on ZnSe slides in transmission mode. It is observed that in spite of the diversity of the source and type of the samples, absorbance of IR occurs at similar wave numbers, implicating that the samples are composed of similar basic substances as mentioned above. Simultaneously it also shows how the variation occurs among these substances and what are the likely principal components of each, contributing to its unique spectra. For example, plasma has less sugar compared to the bacterial cell which has a capsule and thus has more prominent peaks in the region 900-1185. Similarly, the RBCs that lack nucleic acids show diminished peaks while WBCs show clear absorbance peaks between 1185 cm^{-1} and 1300 cm^{-1}.

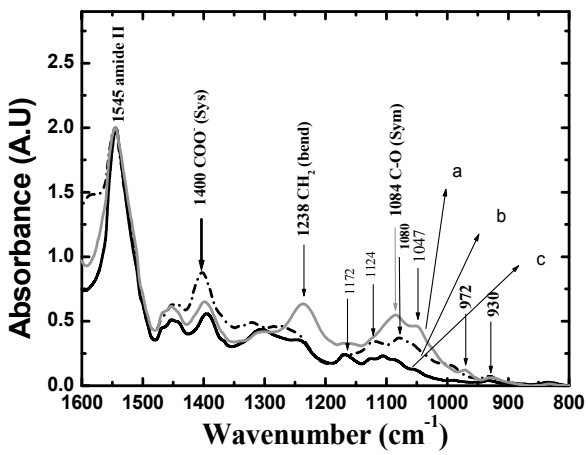

Fig. 1A. Amide II normalized average spectra in the region 800-1800 cm^{-1} of different ZnSe mounted blood components (a-WBC, b-Plasma and c-RBC) analyzed by FTIR-MSP in transmission mode showing few peaks absorbance and the functional groups associated with it.

Thus a qualitative assessment can be made regarding the composition of a sample by looking at its spectra and also defining what type of functional groups could be contributing to absorbance at specific wave numbers.

Several tissues and organisms can show common peaks due to similarity in composition. As shown in Figure 1b, there is absorbance at wave numbers corresponding to components (like carbohydrates, proteins) that are present across a wide range of samples. Owing to large number of data due to the availability of several characteristic wave numbers for individual compounds, mathematical and computational methods are developed that can analyze spectra as per the requirement, providing users the convenience of obtaining the

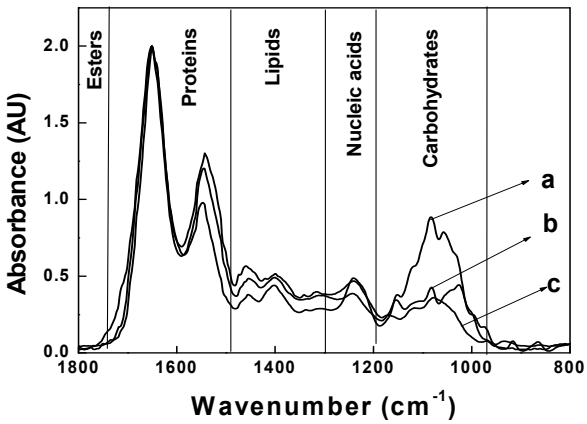

Fig. 1B. Amide I normalized, averaged spectra of (a) bacteria (*Streptococcus pneumoniae*), (b) Cervical epithelium intermediate layer and (c) colonic crypt in transverse section to show absorbance of different biological components at different regions of mid IR. Note that though the carbohydrates absorbance occurs principally in the region between 1200-900 cm^{-1}, the pattern differs across samples, giving a preliminary information of their different origins.

data in usable and interpretable forms. Advancements in computational techniques have added to the utility of the FTIR based instruments by making spectral calculations rapid and automatic, leading to their application in diverse fields of chemistry and biology for both applied and basic research. The potential of FTIR spectroscopy thus serves not only for routine applications but also as a diagnostic tool where other optical methods become difficult to apply. In view of these developments an ever expanding field of biomedical research based on FTIR based technologies has arisen over the last few decades. With its unique abilities, the technique has been applied mostly in cancer diagnosis and monitoring, microbial identification and drug efficacy evaluations to name a few. The present chapter describes in brief the different aspects of applications of FTIR in biomedicine and their suitability and relevance to biomedical research.

2. Brief historical perspective of FTIR spectroscopy in biomedical research

IR spectroscopy has been in use for chemical analysis for several decades. The recognition of its ability to distinguish between normal and abnormal based on fingerprints of the cells and tissues has been utilized to describe changes at molecular and cellular levels (Yang et al 1995, Malik et al 1996, Schultz et al 1996, Malins et al 1997) opened up a new area in the field of biodiagnostics. Other studies paved way for the examination of the technique as a diagnostic tool for identification of disease especially malignancy (Cohenford et al 1997, Rigas et al 1990, Wang et al 1997). This was followed by expanding the methods to study tissues from several different organs such as skin, cervix, liver among others with an emphasis on cancer identification which would be at par with conventional diagnostic techniques without the negative factors like toxicity to live tissues. Early works focused on defining the tissue variability in terms of IR spectra (Chiriboga et al 1998a,b,c, Wood et al 2004). This led to a large number of studies with different tissues and cell lines with an objective to make the technique relevant to oncology (Fukuyama et al 1999, Diem et al 2000, Gao et al 1999, Yano et al 2000, Malins et al 2003). The potential application in other

biomedical fields was expanded by studying the classification of microorganisms using the technique and using it for identifying pathogens (Kirschner et al 2001, Choosmith et al 2001, Sandt et al 2003, Essendoubi et al 2005). These studies led to the development of the concept of "biomarkers" which are parameters or statistics derived from the spectral data that help to identify or differentiate among samples. The most promising biomarkers have been repeatedly used though developments have led to utilization of more complex spectral information rather than simple ratios. For example the region between 900-1300 cm^{-1}. There were also studies undertaken to identify universally suitable biomarkers which could be used in different cells or tissue types to identify malignancies (Sahu et al 2004b, 2005, Mordechai et al 2004). Thus, there was a parallel development of mathematical and computational methodologies to utilize the spectral data and improve the sensitivity and specificity of the diagnosis and helping clearly defining ambiguous samples or accounting for outliers. These methods include linear discriminant analysis (LDA) (Krafft et al 2006), probabilistic neural networks (PNN) (Mark et al 2004), Principal component analysis(PCA) (Muralikrishna et al 2005) artificial neural networks (ANN) (Zhang et al 2003, Lasch et al 2007) and Discriminant classification functions (DCF) (Sahu et al 2010, Bogomolny et al 2007). The methods like clustering of spectra based on either Wards algorithm using Euclidean distances or Mahalanobis distances have been used to classify tissues and used as a means of developing pseudocolor images during FPA mapping of tissues (Lasch and Naumann, 1998). Similarly while the diagnosis of tissues using FTIR was continuing, the detection of changes in single cells using more sophisticated techniques like synchrotron or SERS were undertaken (Chekun et al 2002). Studies were undertaken to elucidate the contribution of individual components like the nucleic acids which held a great promise as biomarkers (Malins et al 2005, Sahu et al 2008). The works were also supported by inducing transformation in cells using various biological and chemical reagents and studying the spectral manifestations (Ramesh et al 2001, Salman et al 2003, Bogomolny et al 2008). The other significant technical development undertaken was the fiber optic systems that could be used for surface scanning or as probes and these are based on the ATR systems. Parallel research was also carried out to help identify and exclude contaminants in samples (Wood et al 1998, Romeo et al 2003, Sahu et al 2005) or use samples from paraffin embedded systems (Ly et al 2008). The effect of physical phenomenon like Mie scattering and its contribution to the FTIR data was also studied (Kohler et al 2008, Lee et al 2007) with an aim to understand how it can interfere with and influence the basic spectral data. Thus in the last two decades progress has been made in several directions to help realize the full potential of the technique in various biomedical fields making the data both qualitatively and quantitatively relevant. Table I lists a few studies where detection of cancers was carried out using FTIR based instrumentation.

3. Different types of FTIR spectroscopy and their suitability to different fields of biomedical research

Currently the simplest and most familiar IR spectrometers existing consist of a source of IR beam, a sample holder and a detection system to monitor the absorbance. Utilizing several different matrices that are IR transparent (KBr, BaF2, CaF_2, ZnSe), it is possible to obtain the spectra from samples as diverse as pure compounds such as proteins, lipids, drugs and metabolites to homogeneous preparations such as body fluids, microorganisms, cell lines that can be mounted without destroying their chemical nature. While it is imperative that

Authors	Tissue/Organs	Analysis	Region/Wave number
Yang et al 1995	Fibrosacrcoma	Intensity	1085
Fujioka et al 2004	Gastric cancer	Discriminant Analysis	925-1660
Podshyvavlov et al 2005	Cervical cancer	PNN	900-1800
Krishna et al 2007	Ovarian tissue	Cluster analysis	1540-60 & 1720-1780
Ali et al 2008	Brain tumor	Cluster analysis	Higher region, 1735.
Maziak et al 2007	Oesophagus	Ratios	Several
Harvey et al 2007	Prostate	FTIR-acoustics	
Argov et al 2002	Colon	ANN	900-1800
Yano et al 2000	Lung	Ratios	1045,1467
Wu et al 2001	Oral tissues	Intensity	1745
Lasch and Naumann 1998	Melanoma	ANN/cluster analysis	
Andrus and Strickland 1998	Lymphoma	Ratio	1020,1121

Table 1. Malignancy in different types of tissue studied by FTIR spectroscopy.

each sample would require a different approach before being mounted for analysis, the common requirement is removal of water (that interferes with the spectra) through processes like lyophilization or even heating thermo stable samples in an oven. The samples are at times dissolved in D_2O to over come the effect of water especially where they are aqueous soluble. Such systems are used to study interactions between biological molecules such as proteins and nucleic acids with ligands like toxins and antibiotics (Pratibha and Malathi, 2008, Bourassa et al 2011).

A slightly different approach is required for cells and microbes where a homogeneous material is available (e.g cell lines, bacteria). Such samples require removal of extraneous materials that can confound the spectra and are usually subjected to washes by normal saline before being dried for spectral acquisition. For example, bacterial cells from cultures in log phase are harvested after treatment with chloroform and the media removed by centrifugation. Subsequently they are washed several times in normal saline (without phosphates) and mounted on discs or any IR transparent support for spectra collection (Sahu et al 2006b).

When dealing with eukaryotic cells like cell lines, the cells are harvested and washed in a buffered solution several times to get rid of the media components and finally washed in normal saline before removing the excess water by a process of air drying. Similarly, different components of blood can be separated and fractions of plasma directly dried on the support. For the cellular components of blood or fluid biopsies like fine needle extracts by different biophysical techniques can be used for obtaining a given population of cells such as RBC, WBCs, monocytes or T cells and B cells which after purification are treated similar to cell lines for spectroscopic measurements. Most of these samples can be measured with routine spectrometers.

The approach becomes more complex when dealing with spectroscopy of tissues. In case of a relatively homogeneous tissue like liver, spectra can more or less be obtained from any region of the biopsy while tissues like cervical tissues that have clearly differentiated zones would need measurements at precise locations to alleviate spectral variation due to location

effects (Chiriboga et al 1998a). However these samples necessitate a microscopic evaluation before measurement. Colonic biopsies that display a more or less uniform pattern in the cross section are measured on the circles of crypts for diagnosis of malignancies. However the longitudinal sections of the crypt require a more defined location for measurement and invariably depend on the utilization of microscope. More complicated measurements of tissues where several different kind of cells are required to be measured depend on focal plane array detectors where each pixel of the measured area can be represented by a spectra. The requirement of methodologies for reconstruction of a pseudo image based on spectral characteristics become the norm and essential feature of such measurements.

4. FTIR instrumentation and their applications in biomedicine

The simplest FTIR spectrometers have been most widely used to study cells and plasma samples. When a sample's spectra are obtained, they are normalized, averaged and baseline corrected. The usual practice is to undertake a baseline correction in the spectral region of interest using the rubber band form and locating the two extreme points of the region of interest. The cut spectra are then normalized again to the highest peak or the area. The different methods of baseline correction in specified regions would greatly alter the results. Hence application of similar data processing on all spectra being considered in a study becomes essential. The intensities at selected wave numbers are then used to define ratios or biomarkers that can define the criterion being sought for the diagnosis. Extracting intensity ratios is preferred than band intensity, since it yields a dimensionless quantity which is mostly independent on the exact normalization procedure used (such as Min-Max or vector normalization). Other than the intensities, many studies report shifts in peak wave numbers which can provide additional valuable information. However instruments that can measure only a few wave numbers can also be used when more sophisticated instrumentations are not available. For example measuring the band intensities of the CH_2 and CH_3 vibrations between 2800-3200 cm^{-1} can provide information about the status of the tissue (Sahu et al 2006a,2005). Similarly various other parameters have been routinely used in diagnosis of diseases and cancer. The ratio of Amide I /Amide II quantified using the integrated absorption of Amide I and Amide II (1750-1590 cm^{-1}, 1590-1480 cm^{-1}) was one of the first ratios found suitable for diagnosis and is an indicator for the DNA absorbance variation (Liquier and Talliander,1996, Benedetti et al., 1997; Gasparri & Muzio, 2003). RBCs (red blood cells) from humans that lack nuclei posses a ratio of unity for this parameter and maybe used as a reference when understanding nuclear changes using these wave number regions.

Similarly quantification of phosphate metabolites calculated by measuring the integrated area of phosphate symmetric (990-1145 cm^{-1}) and antisymmetric (1190-1275 cm^{-1}) bands have been used to understand the stages of the cell (Yang at al. 1995). The most promising phosphate absorbance that has been used in many studies is the RNA/DNA ratio dependent on the phosphate absorbance arising from the symmetric vibrations of DNA and RNA namely at 1020 and 1121 cm^{-1} respectively. Several other band intensities have been used individually or in combination as listed in table 1 for evaluating cells, tissues and biopsies. The band at 1045 cm^{-1} is attributed to the vibrational frequency of -CH_2OH groups and the C-O stretching frequencies coupled with C-O bending frequencies of the C-OH groups of carbohydrates (including glucose, glycogen, etc.) as well as the capsular

carbohydrates of bacteria. The ratio of the integrated absorbance at 1045 cm^{-1} to that at 1545 cm^{-1} provides an estimate of the carbohydrate absorption (Parker, 1971). When a normalization is made to the amide II band the intensities at this wavenumber can be assumed to directly correlate with the amount of carbohydrates and is similar to normalizing the amount to protein in cells and tissues using chemical analyses.

5. Protocols for sample preparation

As the sources of samples for FTIR spectroscopy can be different, they need special preparations adopting different kinds of procedures depending on the samples.

5.1 FTIR spectroscopy of homogeneous materials

5.1.1 Drug macromolecules interactions

Studies of drug interactions by FTIR spectroscopy are easily carried out in systems using D_2O. Various approaches are possible. The drug and protein/nucleic acid interaction is carried out under solution conditions at predetermined stoichiometry and the mixture is then added to a film from which spectral data are obtained. The individual components are also used as references or controls. The difference spectra between the control and with the ligands is sued to quantify the amount of bound ligands or study the changes in the protein secondary structure by monitoring the shifts in peak intensities or variation in peak intensities of different functional groups (Bourasssa et al 2011). FTIR-ATR system can also be used for studying the interactions using a dialysis system.(Krasteva et al 2006, Kumar & Barth (2011).

5.1.2 Microbial cultures

Bacterial cultures growing in the log phase are fixed with formaldehyde (final concentration 0.25%) and washed three times with saline containing 0.25% formaldehyde and once with saline only. The pellet is resuspended with saline to an OD_{450} = 0.3 (about 20 ml). One microliter of the suspension is spotted on Zinc-Selenium slides and air dried for 6 hours to remove any water in the sample under a laminar air flow chamber. Microscopic FTIR measurements are made in transmission mode using the FTIR microscope IRscope II with a mercury-cadmium-telluride (MCT) detector, coupled to the FTIR spectrometer (Bruker Equinox model 55/S, OPUS software). Absorbance is measured from an area of 100 nm diameter by setting the slit to 100 microns. Regions of thickness of about 10 microns (as seen from the ADC values) are selected and 128 scans co added for each spectrum. For each sample at least five spots are measured and the average spectra calculated. Similar procedure can be adopted for yeast cells. In case of fungi which have a tendency to grow as filaments (hyphae), the filaments are harvested and briefly tweezed or torn to get uniform untangled mass as observed under the microscope. These are then washed in water or saline before mounting on the slides. These can also be measured using ATR systems as they are highly adherent and a spread sample is likely to have non uniformity in thickness owing to the clumping tendency of the filaments (Salman et al 2011).

5.1.3 Cell lines and transformed cultures

Cell lines are cultured under suitable conditions (e.g. 37°C in RPMI medium supplemented with 10% of newborn calf serum (NBCS) and the antibiotics penicillin, streptomycin) and

passed to obtain confluent cells . Adherent cells are harvested using a cell lifter while cells in suspension are taken directly. The cell suspensions is centrifuged for 5 minutes at 3000 rpm and the pellet washed in phosphate buffered saline several times (3-5 times). After the washing, the cells are washed at least two times in normal saline and resuspended in saline such that the cells density is about $1x10^6$/ml. One microlitre of this suspension is spotted on a ZnSe window and allowed to air dry in a laminar air flow chamber for several hours. A microlitre of the last supernatant before suspension may also be spotted to be used as a reference for any unwanted materials. Spectra from this sample should ideally be similar to the background spectra. Cells and microbes like fungus may also be grown on IR transparent matrices when they are analyzed by ATR or in reflectance mode. Precautions are however required to avoid artifacts due to very thin layers of drying of cells (Mourant et al 2003a).

5.1.4 Samples from body fluids such as blood or urine

Body fluids usually contain cells and non cellular components, tissue debris and a fluid or matrix. When the cells are the material of interest, they are isolated into pure or homogeneous forms using various separation techniques that utilize the different sedimentation coefficient of the cells and including Fluorescence activated cell sorter (FACS) when required to isolate a pure population based on their cell surface markers. In case of blood samples, the collection is made in heparin or EDTA to prevent the clotting. Then they are separated by a histopaque or Ficoll gradient. The cells are then washed in PBS followed by normal saline as for cultured cells. For spectra of other components such as plasma from blood, the plasma or sera obtained from blood is directly spotted on the ZnSe windows without further processing. However, if the liquid is very viscous, it can lead to super saturated spectra. To avoid this, the fluid is spread by dragging the drop in several directions with the tip and spreading it. Study of other body fluids like urine may require filtration of the liquid to remove debris and its concentration to reduce the amount of water before it is loaded on matrices. In case of study of the cellular components, a prior separation of different cell components maybe required.

5.2 FTIR spectroscopy of tissue samples

Most of the diagnostic potential of FTIR spectroscopy has been evaluated in tissues that relate to carcinogenesis with an objective to diagnose malignancy or premalignancy. Thus, conventionally the material available was formalin fixed, paraffin embedded tissues. In most of these cases, the tissue is sliced to a suitable thickness(usually 10 microns), processed to remove the embedding material and mounted on a slide (usually a ZnSe slide) before it is used for measurements. Such slides are stored in histology frames dipped in 70% ethanol to prevent contamination. A consecutive section that is congruent to the section being measured is usually used for H&E staining. Thus, both the optical as well as the FTIR measuring capabilties of the microscope are used to pin point the exact location of measurement. For example, in tissues like cervical epithelium, where there is a decrease in glycogen level from the superficial layer to the basal layer (Chiriboga et al 1998a), and also the reduction of glycogen is an important marker for CIN or cervical cancer, it becomes important to measure at defined regions, namely the intermediate layers of the tissue to accurately be able to classify the stage of CIN (Figure 3a)(Mark et al 2004). In case of colonic epithelium, the tissue can

contain regions where the crypts are seen in a transverse or longitudinal section. The measurements can be made on either type of section. However, the transverse sections are usually measured for conventional diagnosis and grading for cancer or premalignancy (Argov et al 2002, Argov et al 2004). Measurements along the crypt height have been employed to understand metabolic activity in terms of spectral changes (Salman et al 2004) or to define abnormal proliferation in the epithelium (Sahu et al 2004a, Sahu et al 2010). In these cases, a region of the slide free from contaminants is used for the background. The histology of the tissue is evaluated on the complementary slide which is stained with H&E. Regions are selected that indicate the required stage of disease and then measured by locating the identical spots on the ZnSe slide. At least five measurements on each sample are carried out. The morphology of the colonic epithelium is well defined and it is easy to locate the crypts even while viewing under the optical microscope. Thus, it is easier to locate the crypts and measure them. Usually in these tissues, measurements are made by adjusting the slit to 120 microns that results in an area of 100 micron diameter. As most formalin fixed tissues are paraffin embedded and processed, the spectroscopy in the higher region can also be used to monitor contaminants like blood and paraffin or any residual cleansing reagent like xylol (Sahu et al 2005). Both the transverse sections of the crypt, where the entire crypt would fit into the area of measurement or several locations along the crypt in the longitudinal section can be measured based on the requirement of the studies (Argov et al 2002, Argov et al 2004, Sahu et al 2004a, Salman et al 2004). In case of measurement along the length of the crypt the replication is carried out by measuring several crypts at similar distance form the base or apex unlike the cross section where several crypt circles are measured. For more complex tissues such as skin, where different kinds of abnormalities occur (both benign and malignant) the exact location of the sample measurement area requires the involvement of an expert dermatologist/pathologist to pin point and mark the areas on the complementary slides (Hammody et al 2007). Advancement in technologies have made it possible to automatically measure entire regions of the biopsy using the FPA detector systems and the spectra corresponding to every pixel of the measured area can be obtained. This type of measurement is slow though automated and helps to map entire regions. However the study on a complementary slide to demarcate the exact location of histological entities is still essential to precisely correlate the spectra. The processing is similar to microscopy but owing to a large amount of acquired data, automated computational methods become necessary.

5.3 Cellular transformations

Cellular transformations are used to understand spectral changes happening due to biological changes in cells and tissues, often inducing controlled changes in cell lines using genes or viruses. Cells grown in tissue culture plates are treated with polybrene (a cationic polymer required for neutralizing the negative charge of the cell membrane) for 24 h before infection with the virus. Free polybrene is removed and incubated with the high titer infecting virus stock at 37°C for 2 h. The unabsorbed virus particles are removed by washing the cells in fresh warm medium and fresh medium is added. Several wells are used in a study including a control group passed through similar conditions without the infecting virus. After various stages of progression the cells are examined for the appearance of malignant transformation and cells from sets of wells harvested at different time intervals used for spectra acquisition. Cells can also be grown on soft agar or stained to confirm their malignant transformation.

6. Spectra acquisition and data processing

Spectra can be obtained either in transmission or reflective mode or both from a FTIR microscope (Argov et al 2002, Chang et al 2003). Samples loaded on a mounting material such as a ZnSe slide are observed under the microscope for their uniformity and thickness and representative regions are selected. Prior to measuring the samples a background measurement is made in a region free of any samples or reference material. This spectrum is saved as a background (Figure 2a). The data processor automatically subtracts these

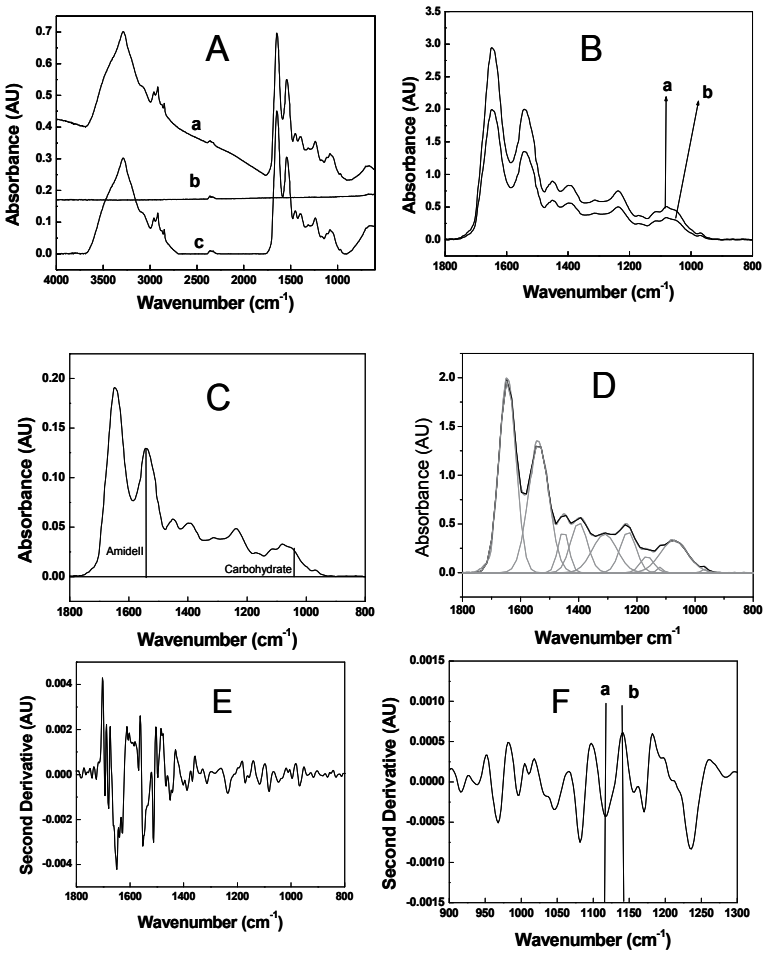

A. Initial absorbance spectrum collected in transmission mode (a), background (b) and background subtracted and rubber band baseline corrected spectrum (c). B. Spectra in the region 800-1800 cm^{-1} after cutting from the entire spectrum, baseline correction and normalization to amide I peak (a) or amide II peak (b). C. Area normalization of the spectrum after cutting the region between 800-1800 cm^{-1} preceded by baseline correction and followed by offset correction. The vertical lines denote intensities at 1545 and 1045 cm^{-1} which can be used for quantification of carbohydrates. D. Deconvolution of the spectra to obtain intensity at various peaks using Gaussian fit of the spectra. (E.) Second derivative of the spectra. (F) Selected region in the second derivative spectra where the intensity at a selected wavenumber is calculated by taking the intesities at the minimum (a) and the adjacent maximum (b).

Fig. 2. Spectral acquisition and processing.

background spectra when further measurements are made. The reference samples if any are then measured. The thickness of the sample is usually reflected in the ADC rates. A ADC value of less than 3000 usually denotes a thickness of less than 10 microns and often leads to noisy spectra. On the other hand regions with a very high ADC value of (>6000) can give rise to supersaturated spectra. Once a set of reference spectra are obtained and they display required characteristics, the samples are measured. Ideally 3-5 spots are measured on each spotted sample.

The background corrected spectra is then baseline corrected for the entire region using a rubber band baseline function (Figure 2A). Selected spectral regions of interest are then separately cut from the entire spectrum and a second baseline correction is made (e.g region between 800-1800 cm^{-1}). This is followed by a normalization of the spectra (Fig.2B,C). The different spectra are then averaged and the average spectra used to represent a sample. Intensities at different wavenumbers obtained form this processed spectra are the inputs for various mathematical analyses. For example, the ratio of intensities at 1545 and 1045 cm^{-1} (Figure 2C) or peak areas after deconvolution (Figure 2D).

Usually a region with normal morphology is taken as a reference or control while identifying the malignancy in a tissue to avoid any heterogeneity due to individual variations while comparing normal and abnormal tissues (Argov et al 2002). With recognition of the fact that normal tissues may still display abnormal FTIR spectra it becomes important to precisely define a normal tissue or biological entity which in itself could lead to better understand dynamics of spectral variation during disease progression (Sahu et al 2010).

Second derivatives and higher order derivatives of spectra are used to avoid the errors creeping in due to bias originating from baseline selection methods (Figure 2E). In this case when the intensities are measured, the minima correspond to the maxima (peak intensity) in the original spectra. Sum of the value at the minima with the value at the nearest maxima is taken to indicate the intensity at the particular wavenumber (Fig 2F).

6.1 Spectral acquisition using ATR/FEWS systems

ATR measurements can be done using Bruker FT-IR Tensor 27 Spectrometer equipped with a liquid nitrogen cooled mercury-cadmium-telluride (MCT) detector and coupled with Horizontal Attenuated Total Reflectance Accessory (HATR (Horizontal Attenuated Total Reflectance), PIKE technologies Inc,) systems (Bogomonly et al 2009). The accessory is connected with a nitrogen reservoir, which enables to preserve dryness of the sample and maintaining an inert atmosphere. The design employs a pair of transfer optics to direct the infrared beam to one end of IR transmitting crystal. A similar pair of flat mirrors directs the beam from the other end of the ATR crystal to the spectrometer detector. The ATR crystal made up of ZnSe is of a trapezoid shape with its thickness suitable to produce optimum performance. To reduce variance each sample is measured several times (at least five) and the ADC rates are empirically chosen between 4000-5000 counts/sec.

7. Advances in data analysis

Unique spectral fingerprints of biological entities in the mid IR region are the manifestation of several components absorbing at different wavenumbers, with overlap. Thus, both the

quantity and type of individual components can alter the fingerprint. As shown in Figure 3, during carcinogenesis, in both colon and cervical tissues, there is a depletion of carbohydrates likely due to increased metabolism. However the disappearance of carbohydrates evident from vanishing of the triads between 900-1185 cm^{-1} in cervical tissues is slightly different than in colonic tissues. This is likely because glycogen is known to accumulate in cervical tissues, increasing in concentration from the basal to superficial layer, the absorbance associated with colonic tissues is more likely to be from glycoproteins than pure glycogen. Thus, though similar functional groups may contribute to the absorbance, they can manifest as spectral variations. This also necessitates that each tissue or cell type is investigated independently though common biomarkers are used. Such type of differences and the gradual variation at specific wave numbers due to transition of tissues or cells from one type to another requires that contribution of individual metabolites like carbohydrates, nucleic acids, proteins is clearly evaluated.

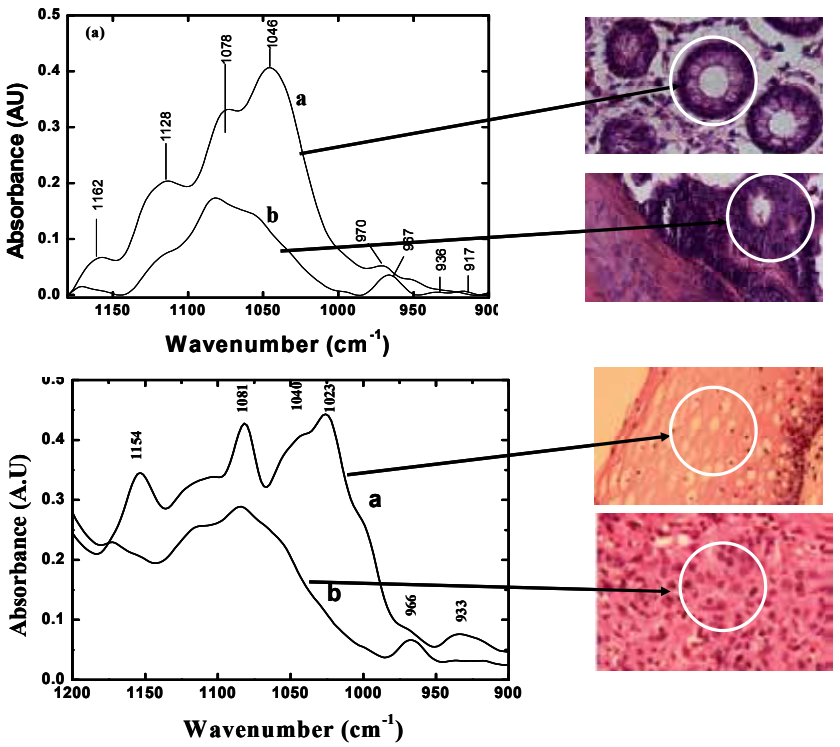

Fig. 3. Baseline corrected spectra from (top) normal and cancerous colonic tissues and (bottom) normal and cancerous cervical tissues, indicating changes in the region 900-1200 cm^{-1}. The circles in the histological sections depict the measurement sites. Note that spectra in the upper panel are further baseline corrected by using a rubber band baseline in the region 900-1200 cm^{-1} while in the lower panel the data presented are after normalization to the amide II peak (not shown). Note also the similarity in the trends in peak intensity on carcinogenesis irrespective of tissue origin.

Figure 4a shows the variation in the integrated intensity in colonic biopsies with different diagnostic features. It is noted that while both normal and hyperplastic samples show

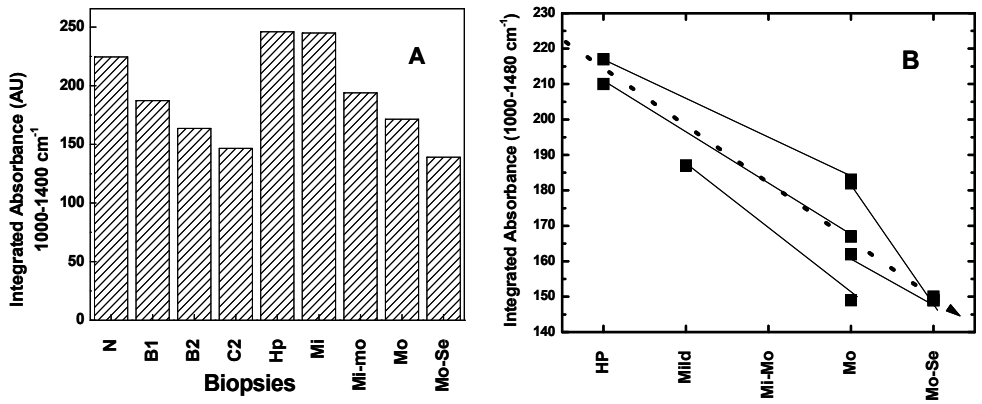

Fig. 4. (A) Variation in levels of integrated absorbance between 1000-1480 cm^{-1} of colonic biopsies with different levels of malignancy or premalignancy. (B) Variation in the parameter over time. The biopsies of the same patients are joined by solid lines. The dotted arrow points to the progression of the disease. N=normal, C1, B2, C2=Cancer grades, Hp=hyperplastic, Mi=mild, Mo=moderate, Se=severe.

similar quantitative traits, the other biopsies with varying degrees of malignancy or premalignancy display a decrease in the levels. It is also noted that the samples with worst prognosis show similar values (For example C2 grade cancer and Severe level of hyperplasia have similar value). This indicates that systems with similar spectral features pertain to a class of conditions with similar outcomes. The feature can also be used to monitor the progression of the disease over time, indicating its possible potential as a biomarker (Figure 4b).

However the two groups of tissues need separate independent analysis i,e the samples of cancerous biopsies and hyperplastic biopsies when dealing from a clinical perspective. To further be able to differentiate between these two subgroups additional biomarkers become necessary. The availability of several biomarkers, suitable for disease diagnosis can complicate the selection though they can increase the sensitivity of the technique. Therefore other than using simple ratios, cluster analysis using several biomarkers or spectral data in entire regions can be undertaken. These help to minimize the false negatives or positives. Inclusion of mathematical and computational methods to analyze suitable wavenumbers for diagnosis focused on the differences between normal and abnormal tissues can utilize artificial neural networks and set up data bases that are used as a reference. Usually a part of the study sample is used to train the system before the blind samples are analyzed. Setting up of reference data base with spectra from clearly identified histopathological systems is a primary step in setting up of a good diagnostic software.

The potential of FTIR increased several fold by the combination of computational methods can thus also be used to overcome spatial and temporal variation in samples. The setting up of such database becomes more crucial when microorganisms (that have a tendency to mutate and change rapidly) are being studied as the older database can be used to monitor such evolution by studying spectral variations. Cluster analysis where different groups are separated by the distance proportional to their heterogeneity is another way to study the evolutionary relation between species and subspecies of microorganism. However clustering may not be sensitive enough to discriminate among closely related samples. Thus,

more methods of analyses are resorted to like ANNs (Goodacre et al 1996). Artificial neural networks make it possible to examine samples over time by setting up reference data bases. These systems often work on the principal of classifying the tissue in a binary progression mode as depicted in Figure 5a. The final results are displayed as a confusion matrix where the probability of classifying a particular biopsy into one of the diagnostic group is expressed as a percentage.

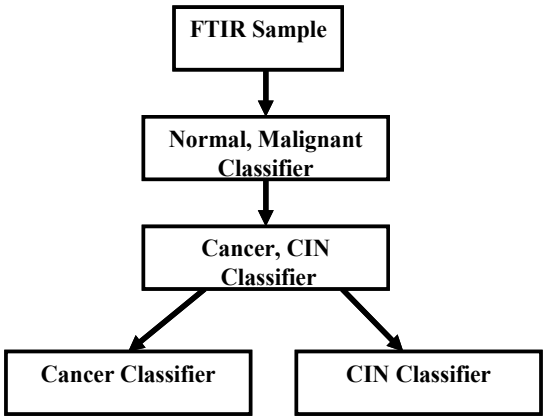

Fig. 5. A model displaying a possible methodology to classify cervical biopsies using an ANN.

Data analysis involving FTIR spectra focuses on utilization of intensities or integrated absorbance from wave number/ wave number regions or their various combinations that result in separation of the different classes of samples under study. Often diagnosis between normal and abnormal tissues is carried out by monitoring absorbance at selected wave numbers after routine mathematical manipulation of the spectra. (Sahu et al 2004, Mordechai et al 2004). Later entire regions of spectra or their derivatives were used to classify tissues or samples (supervised or unsupervised) into clusters to determine their hierarchy or their relation with one another. These types of data conventionally presented as clusters were later used in advanced methods like FPA, to organize areas with similar into pseudocolor maps to establish patterns of tissues from FTIR spectra.

Cluster analysis based on the Ward's algorithm separates samples by the distance proportional to their heterogeneity and difference spectra of colonic crypts has successfully been used their classification (Sahu et al 2004). Similarly the cluster analysis has been used for classification of microorganisms (Sahu et al 2006). Figure 5b displays a schematic diagram of how different biopsies are classified and the closely related conditions tend to group together. Cluster analysis of FEWS spectra of human skin samples using a chemical factor analysis has been shown to differentiate melanoma from basaloma (Sukuta and Bruch 1999).

The data analysis methods like DCF are more useful when classifying systems using morphological features like crypts compared to the others (Sahu et al 2010) as each of the potential biomarkers is used with its weighed contribution which helps to discriminate between normal and abnormal biopsies by representing an adequate quantitative follow up of transformations versus time. DCF can therefore used to classify biopsies using a

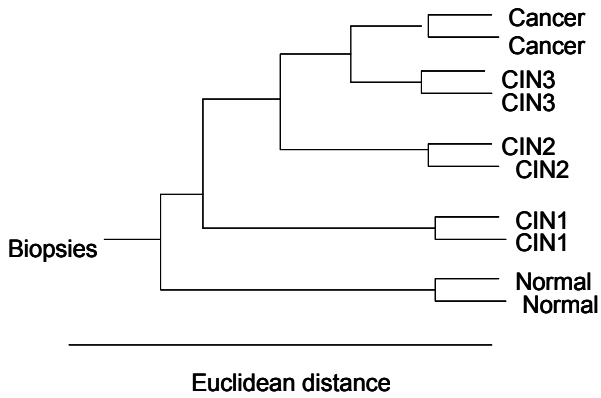

Fig. 5B. Schematic representation of a cluster analysis of cervical biopsies evaluated using hierarchal clustering to show the distance of separation between similar and dissimilar diagnosis. Not that the distance between progressively malignant groups decreases.

classification score that is a linear combination of several potential biomarkers taking advantage of the variation at several wave numbers. Usually the normal or abnormal class is given a final value of 100 and its reverse condition the value of zero by using a combination of weighted coefficients. The different intermediary stages lie within these two extreme values(Hammody et al 2007, Bogomonly et al 2009). One or more of the statistical and computational methods can be resorted to classify samples when an ambiguity is encountered.

Classification of not only the normalized spectral intensities or spectral regions but also the spectral derivatives or difference spectra may be undertaken while performing cluster analysis. Confusion matrices are obtained as a result of ANN and PNN analysis which help to classify tissues or biopsies based on their probability of falling into a particular class. The LDA and PCA techniques classify biopsies into several groups presenting them in normal graphical formats and assigning the grade. The DCF analysis improves discrimination between different stages by using a weighted value for each biomarker used and enables proper assignment during studies involving progression of changes in cells and tissues (Hammody et al 2007, Bogomonly et al 2009).

8. Recent trends and future perspectives

Though basic research has been extensively carried out including pilot scale experimentation of clinical trials in using FTIR measurements for diseases diagnosis, the potential has not been practically exploited due to inability of FTIR based diagnosis to be an independent technique for classification of diseased tissues. The role of a pathologist has been indispensable and pivotal in the preliminary process of sample selection. Advances made through development of FPA based techniques partially overcome this requirement where automated identification of diseased regions in tissues using programs like cluster analysis or ANN/PNN provide pseudocolored images depicting tissue morphology. The rapidity of the technique is however compromised in these cases. Moreover, while a pathologist could quickly look at areas of interest, the automation mandatorily examines the entire section, making it a time consuming affair. In case of complex material like melanoma

and different grades of nevi, the process still needs supporting techniques like immuno histochemistry/histology for verifications before an FTIR measurement is made. The complex dynamics of epithelial tissues that are most prone to carcinogenesis, vary from one organ to another. Thus, clear knowledge of the type of metabolic pattern variation in these tissues is a prerequisite for both acquisition and interpretation of the spectral data. This makes the technique interdisciplinary and involves people with extra specializations requiring special training. However owing to the simplicity in data acquisition and automation with most post spectral processing, these limitations may be overcome easily.

An objective and quantitative method like FTIR spectroscopy becomes crucial when metabolomics of cells and tissues are desired without requirement of different chemical analyses, as it simultaneously can monitor different metabolites. It has the ability to distinguish between microorganisms depending on their biochemical variation and this has been demonstrated in both bacteria and fungi (Sahu et al 2006b, Salman et al 2011). Similarly, minute changes can occur between the different stages of cancer or malignancy which are difficult to detect even with histochemical analyses. Under these circumstances, FTIR becomes handy as it distinguishes among different grades of premalignant and malignant tissues based on markers like carbohydrates which may not be easily stained in normal laboratory practices (Mark et al 2005). Observation of metabolite variation along tissues reflecting the dynamic nature through FTIR spectroscopy has been one of the most important findings (Chiriboga et al 1998a, Salman et al 2004, Sahu et al 2010) that has implications for cancer diagnosis. For example abnormal crypt proliferation can detect in colonic tissues to re-evaluate resection margins (Sahu et al 2010) consequently decreasing the number of surgical interventions. The technique becomes an inexpensive alternative method to follow disease progression or regression quantitatively over a period of time (Zelig et al 2011). Similarly, the growth patterns of microbes are being studied using FTIR spectroscopy. The technique has also become a method of choice to monitor drug effects on cells and tissues as it can easily monitor changes occurring due to onset of processes like apoptosis and necrosis (Zelig et al 2009).

In addition to these abilities, the availability of a qualitative evaluation along with quantization adds in determining the status of the tissues. For example, as shown in figure 6, the values of the ratio of integrated absorbance of several crypts in colonic biopsies shows two different patterns. The biopsies of patients diagnosed with polyposis show a low ratio of 1 or less for many crypts while biopsies without any polyposis have most crypts displaying a the ratio greater than 1. While conventional statistical analysis would look at values like the average for determining the probability of the biopsy being normal or abnormal, the present system allows the pathologist to examine each biopsy with the privilege of being able to designate the biopsy as abnormal based on the values of more than one crypt going with the medical practice of assigning the worst prognosis. This is an easier approach where spectral data from the biopsy cannot be analyzed using more complicated methods like DCF analysis. Thus, the spectral analysis can be tailor made to suit the availability of qualified personnel.

The fiber optic based IR probes are being increasingly examined for utilization as *in vivo* detection systems as these are non toxic. Several reports on fiber-optic based IR sensors for diagnosis of malignancies reflect the trend of incorporation of this technique in future clinical practices (Mackanos and Contag 2010). This in combination with light based

colonoscopes, colposcopes or other endosocopic tools maybe used to detect malignant or abnormal tissues in body cavities. While the optical systems could help to pin point locations , the FTIR system could provide a quantitative evaluation of the abnormal tissue in vivo , without the requirement of the pathologist and help the surgeon make real time decisions. This is especially important as histologically normal regions can be diseased when evaluated by FTIR spectroscopy (Argov et al 2004, Sahu et al 2004, 2010). For example, IR probes mounted on colposcopes may not only determine the areas of malignancy in the cervix but also possibly be able to determine the stage of the CIN. Similarly, examination of body fluids or other material for microbial infections without requiring long culture time can be rapidly done if detection systems are developed where the type of changes associated with different kinds of microbes are clearly defined and established (Bombalska et al 2011, Maquelin et al 2003). The ability of FTIR to detect biochemical changes in organs other than the one affected to possibly use these as indicator of the health status of patients has been another growing area of interest, mainly because these use materials like hairs and nails that are dispensable or blood samples that are easily obtained compared to biopsies (Lyman et al 2005, Khanmohammadi et al 2007). This type of FTIR based diagnosis would help decrease the cost through early intervention. FTIR based diagnosis of diseases, microbes, and healthy and unhealthy conditions is thus a future possibility that is less destructive and harmless compared to conventional methods (Toubas et al 2006). Similar approach can be used to diagnose microbial presence in blood samples (Maquelin et al 2003).

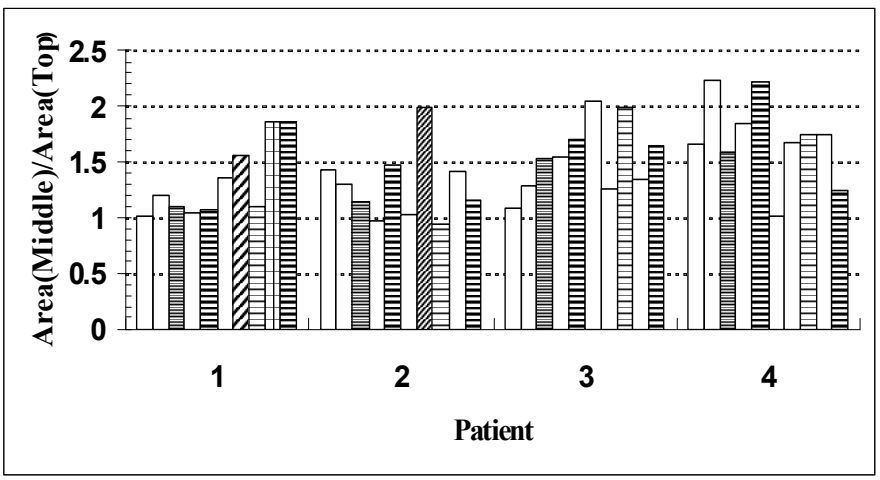

Fig. 6. Evaluation of polyposis in biopsies using the biomarkers derived from crypts. The Crypts from patients 1 and 2 had a polyposis while those of patients 3 and 4 did not. The values in the y axis are derived from the ratios of the integrated absorbance in the region 900-1185 cm^{-1} obtained at the middle and top of the crypt. The color codes are independent and used only to distinguish crypts from one another. Crypts with a value less than 1 are indicative of a propensity to have polyposis. At least 2 such abnormal crypts are required for assigning the worst prognosis.

Another clinically relevant application of FTIR spectroscopy related to the , in vivo diagnosis of diseases in human organs like colon, rectum, oesophagus, cervix, alimentary tract, nasopharynx and other areas deals with fiber optic based IR probes that can be

inserted to obtain spectra of the surface layers. Studies pertaining to these objectives have utilized fiber-optic sensors for diagnosis of malignancies (Li et al 2005, Katkuri et al 2010) and under conditions of aqueous interference (Bindig et al 2003). Presently malignant tissues are excised during colonoscopy and send for evaluation. With the development of suitable probes, it is envisoned that other than the area with the symptoms, adjoining areas can be evaluated to determine the extent of spread of disease and redefine the resection margin. Another potential use would be to differentiate diseases with similar symptoms like IBD and cancer using such probes. This would help in early intervention and prevent recurrent surgeries resulting in less patient discomfort and less expenses. Thus, the field of FTIR based disease diagnosis can be utilized in various levels such as the simple diagnosis using IR microscopes to advanced in-vivo methods using fiberoptic sensors.

9. Discussion

The diagnostic potential of FTIR spectroscopy relies upon its ability to detect and monitor changes in the biochemical fingerprint of abnormal cells, tissues and molecules as compared to the normal conditions along with its ability to monitor minute spectral differences among closely related samples. Thus, establishing reference set of spectra of every biological entity that is being studied is an integral part as with other spectroscopic methods, often the references data base built using model compounds, whose exact spectral contribution is known (Benedetti et al 1996). Biological samples are procured after many different types of procedures and thus, each type may demand different approach for spectral acquisition and analysis. In addition, the availability of the instrument set up and resources would play an important role in deciding which types of samples can be analyzed in a particular clinical set up. For example, when both FTIR microscopy and normal spectroscopy is available, blood components can be examined by the normal method while tissues and biopsies can utilize the microscopy. Similarly, the tissue architect dictates the type of measurement to be followed. While tissues like cervical epithelium where distinct zones permit the spectral acquisition at several locations within a uniform region (Figure 3) more complex tissues like melanoma and nevus make it imperative that the location is carefully selected to not exclude desired region and not include regions that do not meet the criterion of either normal or diseased conditions (Hammody et al 2005). Complicated tissues like colonic epithelium present two possibilities of data acquisition, along the cross section (Argov et al 2002,2004) or longitudinal section (Sahu et al 2004b, 2010) of the crypts and inevitably the availability of microscopic or FPA facilities. Understanding the spectral differences due to instrumentation has been undertaken with the objective of tailoring the techniques to suit set ups and also verifying the universal applicability of certain parameters compared to others (Hammody et al 2007).

The biogenesis of each cell or tissue needs to be studied before a suitable methodology is designed to obtain spectral data for the specific purpose it is intended to serve. The various protocols are also required to be suitably modified depending upon whether a sample is fresh, frozen or paraffin embedded to exclude interfering substances (Sahu et al 2005). The spectroscopy of microorganisms on the other hand may be simpler (Sahu et al 2006b).Both FTIR and Raman spectroscopy use vibrational spectroscopy and can be used independently or in combination with each other as a means of spectroscopic evaluation of biological samples(Mourant et al 2003b, Krishna et al 2005, Oust et al 2006). The prospective of

extending Fiberoptic detection systems to different organs is a future potential (Lucas et al 2005).

10. Conclusion

The technique of FTIR spectroscopy is now being used for different purposes like identification of organisms and their classification, determination of status of tissues, monitoring the effects of drugs on cell lines, monitoring treatment regimen and studying interactions between biological systems in the arena of biomedical research. Owing to its simplicity of data acquisition compared to more sophisticated methods like NMR and development of computational methods for rapid data processing, its relevance in biomedical research is bound to increase over the coming years, in spite of the initial block of having large amounts of spectra for analyses.

11. References

Ali, K.; Lu, Y.; Christensen, C.; May, T.; Hyett, C.; Griebel, R.; Fourney, D.; Meguro, K.; Resch, L. & Sharma, R.K. (2008). Fourier transform infrared spectromicroscopy and hierarchical cluster analysis of human meningiomas. Int J Mol Med. 2008 Mar;21(3):297-301.

Argov, S.; Ramesh, J.; Salman, A.; Sinelnikov, I.; Goldstein, J.; Guterman, H. & Mordechai, S. (2002). Diagnostic potential of Fourier-transform infrared microspectroscopy and advanced computational methods in colon cancer patients. *J Biomed Opt.* 2002.Apr;7(2):248-54.

Argov, S.; Sahu, R.K.; Bernshtain, E.; Salman, A.; Shohat, G.; Zelig, U. & Mordechai, S. (2004. Inflammatory bowel diseases as an intermediate stage between normal and cancer: a FTIR-microspectroscopy approach. *Biopolymers.* 2004 Dec 5;75(5):384-92.

Benedetti, E.; Bramanti, E.; Papineschi, F.; Rossi, I. & Benedetti. E. (1997). Determination of the relative amount of nucleic acids and proteins in leukemic and normal lymphocytes by means of fourier transform infrared microspectroscopy. *Appl. Spectrosc.* 1997. June; 51 (6):792–797.

Bindig, U.;Winter, H.; Wäsche, W.; Zelianeos, K. & Müller, G. (2002).Fiber-optical and microscopic detection of malignant tissue by use of infrared spectrometry. *J Biomed Opt.* 2002 Jan;7(1):100-8.

Bogomolny, E.; Huleihel, M.; Suproun, Y.; Sahu, R.K. & Mordechai S. (2007). Early spectral changes of cellular malignant transformation using Fourier transform infrared microspectroscopy. *J Biomed Opt.* 2007 Mar-Apr;12(2):024003.

Bombalska, A.; Mularczyk-Oliwa, M.; Kwaśny, M.; Włodarski, M.; Kaliszewski, M.; Kopczyński, K.; Szpakowska, M. & Trafny, E .A. (2010). Classification of the biological material with use of FTIR spectroscopy and statistical analysis. *Spectrochim Acta A Mol Biomol Spectrosc.* 2011 Apr;78(4):1221-6.

Bourassa, P.; Dubeau, S.; Maharvi, G.M.; Fauq, A.H.; Thomas, T.J. & Tajmir-Riahi, H.A. (2011). Locating the binding sites of anticancer tamoxifen and its metabolites 4-hydroxytamoxifen and endoxifen on bovine serum albumin. *Eur J Med Chem.* 2011 Sep;46(9):4344-53.

Bruun SW, Kohler A, Adt I, Sockalingum GD, Manfait M, Martens H. Correcting attenuated total reflection-Fourier transform infrared spectra for water vapor and carbon dioxide. *Appl Spectrosc.* 2006 Sep;60(9):1029-39.

Chang, J.I.; Huang, Y.B.; Wu, P.C.; Chen, C.C.; Huang, S.C. & Tsai, Y.H. (2003) Characterization of human cervical precancerous tissue through the fourier transform infrared microscopy with mapping method. *Gynecol Oncol.* 2003 Dec;91(3):577-83.

Chekhun, V.F.; Solyanik, G.I.; Kulik, G.I.; Tryndiak, V.P.; Todor, I.N.; Dovbeshko, G.I.; & Repnytska, O.P. (2002) The SEIRA spectroscopy data of nucleic acids and phospholipids from sensitive- and drug-resistant rat tumours. *J Exp Clin Cancer Res*. 2002 Dec;21(4):599-607.

Chiriboga, L.; Xie, P.; Yee, H.; Vigorita, V.; Zarou, D.; Zakim, D. & Diem, M. (1998a) Infrared spectroscopy of human tissue. I. Differentiation and maturation of epithelial cells in the human cervix. *Biospectroscopy*. 1998;4(1):47-53.

Chiriboga, L.; Xie, P.; Vigorita, V.; Zarou, D.; Zakim, D. & Diem, M. (1998b) Infrared spectroscopy of human tissue. II. A comparative study of spectra of biopsies of cervical squamous epithelium and of exfoliated cervical cells. *Biospectroscopy*. 1998;4(1):55-9.

Chiriboga, L.; Xie, P.; Yee, H.; Zarou, D.; Zakim, D. & Diem, M..(1998c).Infrared spectroscopy of human tissue. IV. Detection of dysplastic and neoplastic changes of human cervical tissue via infrared microscopy. *Cell Mol Biol.*. 1998 Feb;44(1):219-29.

Choo-Smith, L.P.; Maquelin, K.; van Vreeswijk, T.; Bruining, H.A.; Puppels, G.J.; Ngo Thi, N.A.; Kirschner, C.; Naumann, D.; Ami, D.; Villa, A.M.; Orsini, F.; Doglia, S.M.; Lamfarraj, H.; Sockalingum, G.D.; Manfait, M.; Allouch, P. & Endtz, H.P. (2001) Investigating microbial (micro)colony heterogeneity by vibrational spectroscopy. *Appl Environ Microbiol.* 2001 Apr;67(4):1461-9.

Cohenford, M.A.; Godwin, T.A.; Cahn, F.; Bhandare, P.; Caputo, T.A. & Rigas, B. (1997) Infrared spectroscopy of normal and abnormal cervical smears: evaluation by principal component analysis. *Gynecol Oncol*. 1997 Jul;66(1):59-65.

Diem, M.; Chiriboga, L. & Yee, H. (2000) Infrared spectroscopy of human cells and tissue. VIII. Strategies for analysis of infrared tissue mapping data and applications to liver tissue. *Biopolymers.* 2000;57(5):282-90.

Essendoubi, M.; Toubas, D.; Bouzaggou, M.; Pinon, J.M.; Manfait, M.& Sockalingum, G .D. (2005) Rapid identification of Candida species by FT-IR microspectroscopy. *Biochim Biophys Acta.* 2005 Aug 5;1724(3):239-47..

Fujioka, N.; Morimoto, Y.; Arai, T. & Kikuchi, M. (2004). Discrimination between normal and malignant human gastric tissues by Fourier transform infrared spectroscopy. *Cancer Detect Prev*. 2004;28(1):32-6.

Fukuyama, Y.; Yoshida, S.; Yanagisawa, S. & Shimizu, M. (1999) A study on the differences between oral squamous cell carcinomas and normal oral mucosas measured by Fourier transform infrared spectroscopy. *Biospectroscopy*. 1999;5(2):117-26.

Gao, T.; Feng, J. & Ci Y. (1999) Human breast carcinomal tissues display distinctive FTIR spectra: implication for the histological characterization of carcinomas. *Anal Cell Pathol.* 1999;18(2):87-93.

Goodacre, R.; Timmins, E.M. Rooney, P.J.; Rowland, J.J. & Kell, D.B. (1996). Rapid identification of Streptococcus and Enterococcus species using diffuse reflectance-absorbance Fourier transform infrared spectroscopy and artificial neural networks. *FEMS Microbiol Lett*. 1996 Jul 1;140(2-3):233-9.

Hammody, Z.; Sahu, R.K.; Mordechai, S.; Cagnano, E. & Argov, S. (2005). Characterization of malignant melanoma using vibrational spectroscopy. *Scientific World Journal.* 2005; 5:173-82.

Hammody, Z.; Huleihel, M.; Salman, A.; Argov, S.; Moreh, R.; Katzir, A. & Mordechai, S. (2007). Potential of 'flat' fibre evanescent wave spectroscopy to discriminate between normal and malignant cells in vitro. *J Microsc.* 2007 Nov;228(Pt 2):200-10.

Hammody, Z.; Argov, S.; Sahu, R.K.; Cagnano, E.; Moreh, R. & Mordechai S. (2008). Distinction of malignant melanoma and epidermis using IR micro-spectroscopy and statistical methods. *Analyst.* 2008 Mar;133(3):372-8.

Harvey, T.J.; Henderson, A.; Gazi, E.; Clarke, N.W.; Brown, M.; Faria, E.C.; Snook, R.D. & Gardner, P. (2007). Discrimination of prostate cancer cells by reflection mode FTIR photoacoustic spectroscopy. *Analyst.* 2007 Apr;132(4):292-5.

Katukuri, V.K.; Hargrove, J.; Miller, S.J.; Rahal, K.; Kao, J.Y.; Wolters, R.; Zimmermann, E.M.; Wang, T.D. (2010). Detection of colonic inflammation with Fourier transform infrared spectroscopy using a flexible silver halide fiber. *Biomed Opt Express.* 2010 Sep 21;1(3):1014-1025.

Khanmohammadi, M.; Nasiri, R.; Ghasemi, K.; Samani, S.; & Bagheri Garmarudi A. (2007). Diagnosis of basal cell carcinoma by infrared spectroscopy of whole blood samples applying soft independent modeling class analogy. *J Cancer Res Clin Oncol.* 2007 Dec;133(12):1001-10.

Kirschner, C.; Maquelin, K.; Pina, P.; Ngo Thi, N.A.; Choo-Smith, L.P.; Sockalingum, G.D.; Sandt, C.; Ami, D.; Orsini, F.; Doglia, S.M.; Allouch, P.; Mainfait, M.; Puppels, G.J. & Naumann D. (2001) Classification and identification of enterococci: a comparative phenotypic, genotypic, and vibrational spectroscopic study. *J Clin Microbiol.* 2001 May;39(5):1763-70.

Krafft, C.; Shapoval, L.; Sobottka, S.B.; Schackert, G. & Salzer, R. (2006). Identification of primary tumors of brain metastases by infrared spectroscopic imaging and linear discriminant analysis. *Technol Cancer Res Treat.* 2006 Jun;5(3):291-8.

Krasteva, M.& Barth, A. (2007). Structures of the Ca2+-ATPase complexes with ATP, AMPPCP and AMPPNP. An FTIR study. *Biochim Biophys Acta.* 2007 Jan;1767(1):114-23.

Krishna, C.M; Kegelaer, G.; Adt, I.; Rubin, S.; Kartha, V.B.; Manfait, M. & Sockalingum, G.D. (2005) Characterisation of uterine sarcoma cell lines exhibiting MDR phenotype by vibrational spectroscopy. *Biochim Biophys Acta.* 2005 Nov 15;1726(2):160-7.

Krishna, C.M.; Kegelaer, G.; Adt, I.; Rubin, S.; Kartha, V.B.; Manfait, M. & Sockalingum, G.D. (2006). Combined Fourier transform infrared and Raman spectroscopic approach for identification of multidrug resistance phenotype in cancer cell lines. *Biopolymers.* 2006 Aug 5;82(5):462-70.

Krishna, C.M.; Sockalingum, G.D.; Bhat, R.A.; Venteo, L.; Kushtagi, P.; Pluot, M. & Manfait, M. (2007). FTIR and Raman microspectroscopy of normal, benign, and malignant formalin-fixed ovarian tissues. *Anal Bioanal Chem*. 2007 Mar;387(5):1649-56.

Kohler, A.; Sulé-Suso, J.; Sockalingum, G.D.; Tobin, M.; Bahrami, F.; Yang, Y.; Pijanka, J.; Dumas, P.; Cotte, M.; van Pittius, D.G.; Parkes, G. & Martens, H.(2008). Estimating and correcting mie scattering in synchrotron-based microscopic fourier transform infrared spectra by extended multiplicative signal correction. *Appl Spectrosc.* 2008 Mar;62(3):259-66.

Kumar, S. & Barth, A.(2010). Phosphoenolpyruvate and Mg2+ binding to pyruvate kinase monitored by infrared spectroscopy. *Biophys J.* 2010 May 19;98(9):1931-40.

Lasch, P.; Diem, M.; Hänsch, W. & Naumann, D. (2007) Artificial neural networks as supervised techniques for FT-IR microspectroscopic imaging. *J Chemom.* 2007 Mar 28;20(5):209-220.

Lasch, P. & Naumann, D. (1998) FT-IR microspectroscopic imaging of human carcinoma thin sections based on pattern recognition techniques. *Cell Mol Biol* . 1998 Feb;44(1):189-202.

Lee, J.; Gazi, E.; Dwyer, J.; Brown, M.D.; Clarke, N.W.; Nicholson, J.M. & Gardner, P.(2007). Optical artefacts in transflection mode FTIR microspectroscopic images of single cells on a biological support: the effect of back-scattering into collection optics. *Analyst.* 2007 Aug;132(8):750-5.

Li, Q.B.; Xu, Z.; Zhang, N.W.; Zhang, L.; Wang, F.; Yang, L.M.; Wang, J.S.; Zhou, S.; Zhang, Y.F.; Zhou, X.S.; Shi, J.S. & Wu, J.G.(2005). In vivo and in situ detection of colorectal cancer using Fourier transform infrared spectroscopy. *World J Gastroenterol.* 2005 Jan 21;11(3):327-30.

Liquier, J., Taillandier, E. . In Infrared spectroscopy of biomolecules; H.H. Mantsch, D. C., Ed.; Wiley-Liss, John Wiley & Sons, INC., Publication: NY, 1996, p 131-158.

Lucas, P.; Le Coq, D.; Juncker, C.; Collier, J.; Boesewetter, D.E.; Boussard-Plédel, C.; Bureau, B. & Riley, M.R. (2005). Evaluation of toxic agent effects on lung cells by fiber evanescent wave spectroscopy. *Appl Spectrosc.* 2005 Jan;59(1):1-9.

Ly, E.; Piot, O.; Wolthuis, R.; Durlach, A.; Bernard, P. & Manfait M. (2008). Combination of FTIR spectral imaging and chemometrics for tumour detection from paraffin-embedded biopsies. *Analyst.* 2008 Feb;133(2):197-205.

Lyman, D.J. & Murray-Wijelath, J. (2005). Fourier transform infrared attenuated total reflection analysis of human hair: comparison of hair from breast cancer patients with hair from healthy subjects. *Appl Spectrosc.* 2005 Jan;59(1):26-32.

Mackanos, M.A. & Contag, C.H. (2010). Fiber-optic probes enable cancer detection with FTIR spectroscopy. *Trends Biotechnol.* 2010 Jun;28(6):317-23.

Malins, D.C.; Polissar, N.L & Gunselman, S.J.(1997). Infrared spectral models demonstrate that exposure to environmental chemicals leads to new forms of DNA. *Proc Natl Acad Sci* . 1997 Apr 15; 94(8):3611-5.

Malins, D.C.; Johnson, P.M.; Barker, E.A.; Polissar, N.L.; Wheeler, T.M. & Anderson K.M. (2003). Cancer-related changes in prostate DNA as men age and early identification of metastasis in primary prostate tumors. *Proc Natl Acad Sci*. 2003 Apr 29;100(9):5401-6.

Malins, D.C.; Gilman, N.K.; Green, V.M.; Wheeler, T.M.; Barker, E.A. & Anderson, K.M. (2005). A cancer DNA phenotype in healthy prostates, conserved in tumors and adjacent normal cells, implies a relationship to carcinogenesis. *Proc Natl Acad Sci* 2005 Dec 27;102(52):19093-6.

Malik, Z.; Dishi, M & Garini Y.(1996) Fourier transform multipixel spectroscopy and spectral imaging of protoporphyrin in single melanoma cells. *Photochem Photobiol.* 1996 May; 63(5):608-14.

Maquelin, K.; Kirschner, C.; Choo-Smith, L.P.; Ngo-Thi, N.A.; van Vreeswijk, T.; Stämmler, M.; Endtz, H.P.; Bruining, H.A.; Naumann, D. & Puppels, G.J. (2003). Prospective study of the performance of vibrational spectroscopies for rapid identification of bacterial and fungal pathogens recovered from blood cultures. *J Clin Microbiol.* 2003 Jan;41(1):324-9.

Mark, S.; Sahu, R.K.; Kantarovich, K.; Podshyvalov, A.; Guterman, H.; Goldstein, J.; Jagannathan, R.; Argov, S. & Mordechai, S.(2004) Fourier transform infrared microspectroscopy as a quantitative diagnostic tool for assignment of premalignancy grading in cervical neoplasia. *J Biomed Opt.* 2004 May-Jun;9(3):558-67.

Maziak, D.E.; Do, M.T.; Shamji, F.M.; Sundaresan, S.R.; Perkins, D.G. & Wong, P.T. (2007). Fourier-transform infrared spectroscopic study of characteristic molecular structure in cancer cells of esophagus: an exploratory study. *Cancer Detect Prev.* 2007;31(3):244-53.

Mordechai, S.; Sahu, R.K.; Hammody, Z.; Mark, S.; Kantarovich, K.; Guterman, H.; Podshyvalov, A.; Goldstein, J. & Argov S. (2004) Possible common biomarkers from FTIR microspectroscopy of cervical cancer and melanoma. *J Microsc.* 2004 Jul;215(Pt 1):86-91.

Mourant, J.R.; Gibson, R.R.; Johnson, T.M.; Carpenter, S.; Short, K.W.; Yamada, Y.R.; & Freyer, J.P.(2003b). Methods for measuring the infrared spectra of biological cells. *Phys Med Biol.* 2003 Jan 21;48(2):243-57.

Mourant, J.R.; Short, K.W.; Carpenter, S.; Kunapareddy, N.; Coburn, L.; Powers, T.M. & Freyer, J.P. (2005). Biochemical differences in tumorigenic and nontumorigenic cells measured by Raman and infrared spectroscopy. *J Biomed Opt.* 2005 May-Jun;10(3):031106.

Oust, A.; Møretrø, T.; Naterstad, K.; Sockalingum, G.D.; Adt, I.; Manfait, M. & Kohler A. (2006). Fourier transform infrared and raman spectroscopy for characterization of Listeria monocytogenes strains. *Appl Environ Microbiol.* 2006 Jan;72(1):228-32.

Parker, F.S. (1971). Application of Infrared spectroscopy in Biochemistry, Biology and Medicine. Plenum. NY.

Podshyvalov, A.; Sahu, R.K.; Mark, S.; Kantarovich, K.; Guterman, H.; Goldstein, J.; Jagannathan, R.; Argov, S. & Mordechai, S. (2005). Distinction of cervical cancer biopsies by use of infrared microspectroscopy and probabilistic neural networks. *Appl Opt.* 2005 Jun 20;44(18):3725-34.

Prathiba, J. & Malathi, R. (2008). Probing RNA-antibiotic interactions: a FTIR study. *Mol Biol Rep.* 2008 Mar;35(1):51-7.

Ramesh, J.; Salman, A.; Hammody, Z.; Cohen, B.; Gopas, J.; Grossman, N. & Mordechai, S. (2001). FTIR microscopic studies on normal and H-ras oncogene transfected cultured mouse fibroblasts. *Eur Biophys J.* 2001 Aug;30(4):250-5.

Rigas, B.; LaGuardia, K.; Qiao, L.; Bhandare, P.S.; Caputo, T & Cohenford, M .A. (2000) Infrared spectroscopic study of cervical smears in patients with HIV: implications for cervical carcinogenesis. *J Lab Clin Med*. 2000 Jan; 135(1):26-31.

Rigas, B.; Morgello, S.; Goldman, I.S. & Wong, P.T.(1990) Human colorectal cancers display abnormal Fourier-transform infrared spectra. *Proc Natl Acad Sci*. 1990 Oct;87(20):8140-4

Romeo, M.J.; Wood, B.R.; Quinn, M.A. & McNaughton, D. (2003). Removal of blood components from cervical smears: implications for cancer diagnosis using FTIR spectroscopy. *Biopolymers*. 2003;72(1):69-76.

Sahu, R.K.; Argov, S.; Bernshtain, E.; Salman, A.; Walfisch, S.; Goldstein, J. & Mordechai, S. (2004a). Detection of abnormal proliferation in histologically 'normal' colonic biopsies using FTIR-microspectroscopy. *Scand J Gastroenterol*. 2004 Jun;39(6):557-66.

Sahu, R.K.; Argov, S.; Salman, A.; Huleihel, M.; Grossman, N.; Hammody, Z.; Kapelushnik, J. & Mordechai, S. (2004b). Characteristic absorbance of nucleic acids in the Mid-IR region as possible common biomarkers for diagnosis of malignancy. *Technol Cancer Res Treat.*2004 Dec;3(6):629-38.

Sahu, R.K.; Argov, S.; Salman, A.; Zelig, U.; Huleihel, M.; Grossman, N.; Gopas, J.; Kapelushnik, J. & Mordechai, S. (2005). Can Fourier transform infrared spectroscopy at higher wavenumbers (mid IR) shed light on biomarkers for carcinogenesis in tissues? *J Biomed Opt.* 2005 Sep-Oct;10(5):054017.

Sahu, R.K.; Zelig, U.; Huleihel, M.; Brosh, N.; Talyshinsky, M.; Ben-Harosh, M.; ,Mordechai, S. & Kapelushnik, J. (2006a) Continuous monitoring of WBC (biochemistry) in an adult leukemia patient using advanced FTIR-spectroscopy. *Leuk Res.* 2006; 30(6):687-93.

Sahu, R.K.; Mordechai, S.; Pesakhov, S.; Dagan, R. & Porat, N. (2006b) Use of FTIR Spectroscopy to Distinguish between Capsular Types and Capsular Quantities in Streptococcus pneumoniae. *Biopolymers*. 2006; 83(4):434-442.

Sahu, R. K.; Mordechai,S. & Manor, E. (2008) Nucleic acids absorbance in Mid IR and its effect on diagnostic variates during cell division: a case study with lymphoblastic cells. *Biopolymers*. 2008 Nov;89(11):993-1001.

Sahu, R.K.; Argov, S.; Walfisch, S.; Bogomolny, E.; Moreh, R. & Mordechai, S. (2010). Prediction potential of IR-micro spectroscopy for colon cancer relapse. *Analyst.* 2010 Mar;135(3):538-44.

Salman, A.; Ramesh, J.; Erukhimovitch, V.; Talyshinsky, M.; Mordechai, S. & Huleihel, M. (2003). FTIR microspectroscopy of malignant fibroblasts transformed by mouse sarcoma virus. *J Biochem Biophys Methods*. 2003 Feb 28;55(2):141-53.

Salman, A.; Sahu, R.K.; Bernshtain,E.; Zelig, U.; Goldstein, J.; Walfisch,S.;, Arov, S. & Mordechai,S. (2004). Probing cell proliferation in the human colon using vibrational spectroscopy: a novel use of FTIR-Microspectroscopy. *Vib. spec*. 2004. 34:301-308.

Salman, A.; Pomerantz, A.; Tsror, L.; Lapidot, I.; Zwielly, A.; Moreh, R.; Mordechai, S. & Huleihel, M. (2011). Distinction of Fusarium oxysporum fungal isolates (strains)

using FTIR-ATR spectroscopy and advanced statistical methods. *Analyst.* 2011 Mar 7;136(5):988-95.

Sandt, C.; Sockalingum, G.D.; Aubert, D.; Lepan, H.; Lepouse, C.; Jaussaud, M.; Leon, A.; Pinon, J.M.; Manfait, M. & Toubas, D. (2003) Use of Fourier-transform infrared spectroscopy for typing of Candida albicans strains isolated in intensive care units. *J Clin Microbiol.* 2003 Mar;41(3):954-9.

Sandt, C.; Madoulet, C.; Kohler, A.; Allouch, P.; De Champs, C.; Manfait, M. & Sockalingum, G.D. (2006). FT-IR microspectroscopy for early identification of some clinically relevant pathogens. *J Appl Microbiol.* 2006 Oct;101(4):785-97.

Schultz, C.P.; Liu, K.; Johnston, J.B. & Mantsch, H .H. (1996) Study of chronic lymphocytic leukemia cells by FT-IR spectroscopy and cluster analysis. Leuk Res. 1996 Aug;20(8):649-55.

Sukuta, S. & Bruch, R. (1999) Factor analysis of cancer Fourier transform infrared evanescent wave fiberoptical (FTIR-FEW) spectra. *Lasers Surg Med.* 1999;24(5):382-8.

Toubas, D.; Essendoubi, M.; Adt, I.; Pinon, J.M.; Manfait, M. & Sockalingum, G.D. (2007). FTIR spectroscopy in medical mycology: applications to the differentiation and typing of Candida. *Anal Bioanal Chem.* 2007 Mar;387(5):1729-37.

Wang, H.P.; Wang, H.C. & Huang YJ. (1997) Microscopic FTIR studies of lung cancer cells in pleural fluid. *Sci Total Environ*. 1997 Oct 1; 204(3):283-7.

Wong, P.T.; Capes, S.E. & Mantsch, H.H.; Hydrogen bonding between anhydrous cholesterol and phosphatidylcholines: an infrared spectroscopic study. *Biochim Biophys Acta.* 1989 Mar 27;980(1):37-41.

Wood, B.R.; Quinn, M.A.; Tait, B.; Ashdown, M.; Hislop, T.; Romeo, M. & McNaughton, D. (1998). FTIR microspectroscopic study of cell types and potential confounding variables in screening for cervical malignancies. *Biospectroscopy.* 1998;4(2):75-91.

Wu, J.G.; Xu, Y.Z.; Sun, C.W.; Soloway, R.D.; Xu, D.F.; Wu, Q.G.; Sun, K.H.; Weng, S.F. & Xu, G.X.. Distinguishing malignant from normal oral tissues using FTIR fiber-optic techniques. *Biopolymers.* 2001;62(4):185-92.

Yang, D.; Castro, D.J.; el-Sayed, I.H.; el-Sayed, M.A.; Saxton, R.E & Zhang NY.(1995) A Fourier-transform infrared spectroscopic comparison of cultured human fibroblast and fibrosarcoma cells: a new method for detection of malignancies. *J Clin Laser Med Surg*. 1995 Apr;13(2):55-

Yano, K.; Ohoshima, S.; Gotou, Y.; Kumaido, K.; Moriguchi, T. & Katayama H. (2000) Direct measurement of human lung cancerous and noncancerous tissues by Fourier transform infrared microscopy: can an infrared microscope be used as a clinical tool? *Anal Biochem.* 2000 Dec 15;287(2):218-25.

Zelig, U.; Kapelushnik, J.; Moreh, R.; Mordechai, S. & Nathan, I. (2009). Diagnosis of cell death by means of infrared spectroscopy. *Biophys J.* 2009 Oct 7;97(7):2107-14.

Zelig, U.; Mordechai, S.; Shubinsky, G.; Sahu, R.K.; Huleihel, M.; Leibovitz, E.; Nathan, I. & Kapelushnik, J.(2011). Pre-screening and follow-up of childhood acute leukemia using biochemical infrared analysis of peripheral blood mononuclear cells. *Biochim Biophys Acta.* 2011 Sep;1810(9):827-35.

Zhang, L.; Small, G.W.; Haka, A.S.; Kidder, L.H. & Lewis, E.N. (2003) Classification of Fourier transform infrared microscopic imaging data of human breast cells by cluster analysis and artificial neural networks. *Appl Spectrosc*. 2003 Jan;57(1):14-22.

18

Characterization of Bone and Bone-Based Graft Materials Using FTIR Spectroscopy

M.M. Figueiredo, J.A.F. Gamelas and A.G. Martins
Chemical Engineering Department, University of Coimbra
Portugal

1. Introduction

Despite its static appearance, bone is a very dynamic living tissue that undergoes constant remodelling throughout life. After blood, bone is the second most commonly transplanted tissue in human medicine, and thus a thorough characterization of this material is of crucial importance. For instance, although it has been accepted that the whole bone strength is related to the bone mineral density (BMD), changes in this parameter often do not correlate with the probability of fracture. To improve the mechanical performance of bone, other material properties related to bone quality, and not only quantity, have to be investigated.

FTIR spectroscopy constitutes an excellent tool to characterize the bone matrix because its main components (carbonated hydroxyapatite and collagen) absorb infrared radiation at distinct, almost complementary, regions within the 500-4000 cm^{-1} range. This not only enables the study of the main contributions of each component separately, but also allows a further investigation of relevant parameters that mostly affect the structural and mechanical properties of bone, as well as its active metabolism. Furthermore, FTIR analysis, particularly when combined with microscopic technologies, enables the measurement of spatial variations in bone composition, allowing their correlation with micro-to-macro morpho-structural properties. In clinical studies, this allows the comparison between sound and diseased bone, and the analysis of therapeutic effects of drugs, among many other examples. On the other hand, FTIR spectroscopy is also commonly used to characterize bone grafts. Moreover, evidence that optimizing the osteointegration requires a fundamental knowledge of the material properties both of the bone graft and of the host bone tissue, has driven to extensive research on this subject, often supported by FTIR spectroscopy.

2. Bone composition and structure

Besides providing mechanical support, bone also plays diverse important metabolic functions. Even though bones possess various sizes and shapes, they share general chemical and structural features that, despite a static appearance on adult vertebrates, vary with and within species (Gamsjaeger et al., 2010; Mkukuma et al., 2004). In fact, among similar individuals, bone properties change with age, nutrition, hormonal equilibrium and health condition, in addition to other factors such as biomechanical environment (Aerssens et al., 1997; Fratzl et al., 2004). These variations are relatively restricted due to the constant remodelling processes that re-establish equilibrium. The bone turnover or remodelling, that consists on the resorption,

followed by the replacement of bone with little change in shape, acts as a dynamic response to multiple local and systemic factors (Robling et al., 2006). The bone metabolic functions are regulated by the combined action of two principal cell lineages: the bone forming cells (mainly osteoblasts and osteocytes) and bone resorption cells (osteoclats). Diverse enzymes and many other molecules, such as the important bone morphogenetic proteins (BMPs), participate in those dynamic cellular processes (Katz et al., 2009; Urist, 1965).

The composition of the extracellular matrix of bone, often described as a two-phase composite, consists of about 65 wt. % mineral component (carbonated hydroxyapatite) and 25 wt. % organic component (mainly type I collagen), being the remaining 10 wt. % water (Judas et al., 2005). These components have extremely different mechanical properties: the mineral is stiff and brittle while the (wet) protein is much more elastic and also much tougher than the mineral. Bone combines both the stiffness and the toughness in an unusual arrangement of material properties that result on a remarkable tensile strength and resistance against fracture (Fratzl et al., 2004; Rho et al., 1998).

The bone components are so tightly embedded that require the use of chemical procedures to obtain an effective separation of the mineral from the organic phase. The mineral component may be obtained using thermal treatment at high temperatures (calcination) to eliminate the organic component and conversely, the latter may be isolated using acid demineralization processes (Martins et al., 2008).

Mineral phase

Bone mineral is a poorly crystalline calcium-deficient apatite, with a Ca:P ratio that differs from 1.67, which is the theoretical value for pure hydroxyapatite [$Ca_{10}(PO_4)_6(OH)_2$]. The nonstoichiometric biological apatites contain several ion substitutions. For example, Na^+ and Mg^{2+} may substitute Ca^{2+} ions, HPO_4^{2-} ions may substitute phosphate ions, and Cl^- and F^- may replace OH^-. Additionally, carbonate ions, the most abundant substitutions (3-8 wt. %), may occupy either the OH^- (type A apatite) or PO_4^{3-} (type B apatite) positions in the crystal lattice. The mineral component of bone is usually closer to B-type apatite (Landi, 2003; Murugan et al., 2006).

The crystalline structure of carbonated hydroxyapatite belongs to the hexagonal system, although a portion of the bone mineral remains amorphous. In fact, the apatite crystals comprise two different environments: a non-apatitic hydrated domain, containing diverse labile and reactive ions, surrounds a relatively inert and more stable apatitic domain (Fig. 1) (Farlay et al., 2010). In the interface between these domains, labile anions (PO_4^{3-}, HPO_4^{2-} and CO_3^{2-}) and cations (Ca^{2+}, Mg^{2+}) are easily and reversibly exchangeable. During initial crystal formation, ionic exchange occurs and ions gradually incorporate into the interior unit cell. The maturation of the mineral is associated with reduction of labile non-apatitic environments while stable apatitic domains augment. Moreover, as bone mineral becomes more mature, it contains less structural defects, both the size and number of crystals increase and its composition becomes closer to the stoichiometric hydroxyapatite. For this reason, crystal maturity is often associated with crystallinity (that augments with crystal size and mineral perfection).

Organic phase

The organic matrix of bone consists of collagen and a series of non-collagenous proteins and lipids. About 85–90 wt. % of the total bone protein corresponds to Type I collagen fibers.

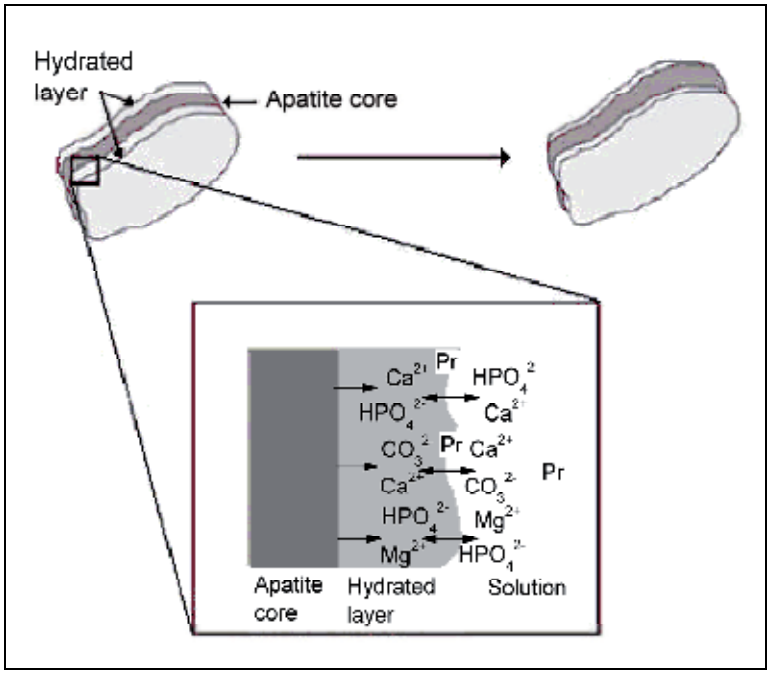

Fig. 1. Evolution of the apatite crystal and of the surrounding hydrated layer. During maturation and growth of the mineral, the apatitic domain of the crystal increases whereas the hydrated layer decreases, due to continuous ionic exchange between these domains and the solution bath. Soluble charged groups of proteins (Pr) can also participate in the ionic equilibrium of the non-apatitic domain (adapted from Farlay et al., 2010).

This principal component of the organic matrix of bone is a large fibrous protein with a highly repetitive amino acid sequence [Gly (glycine)–X–Y]n (often X is proline and Y is hydroxyproline). Other amino acids may also be found, such as alanine, lysine and hydroxylysine. These monomers are bound together by peptide bonds (between the carboxyl and amino groups of adjacent amino acids) constituting three polypeptide chains (two α1 and one α2 chains) that fold into a unique structure (Fig. 2). This consists of a single uninterrupted triple helix which represents more than 95% of the molecule (tropocollagen) and two non-helical domains (the telopeptides) containing the – COOH and – NH_2 terminals of the protein.

The integrity of the collagen molecule is attributed to the formation of intra- and inter-molecular cross-linking which contribute to the mechanical strength of the bone organic matrix (Eyre & Wu, 2005; Ottani et al., 2001; Saito & Marumo, 2009). Inter-molecular collagen cross-links can be divided into two types: lysine hydroxylase/lysyl oxidase-controlled cross-links (enzymatic cross-links) and glycation/oxidation-induced cross-links. In both cases, cross-linking sites are at specific Lys (lysine) or Hyl (hydroxylysine) residues of the collagen molecule. Concerning the first type, the enzymatic activity leads to the formation of Lys and Hyl aldehyde-derived covalent cross-links, in which a molecular fragment binds a telopeptide and a triple helix of adjacent molecules (divalent cross-link). As a consequence of chemical reactions and rearrangements, divalent cross-links may be converted into trivalent cross-links, in which a helix is bound to two telopeptides. As

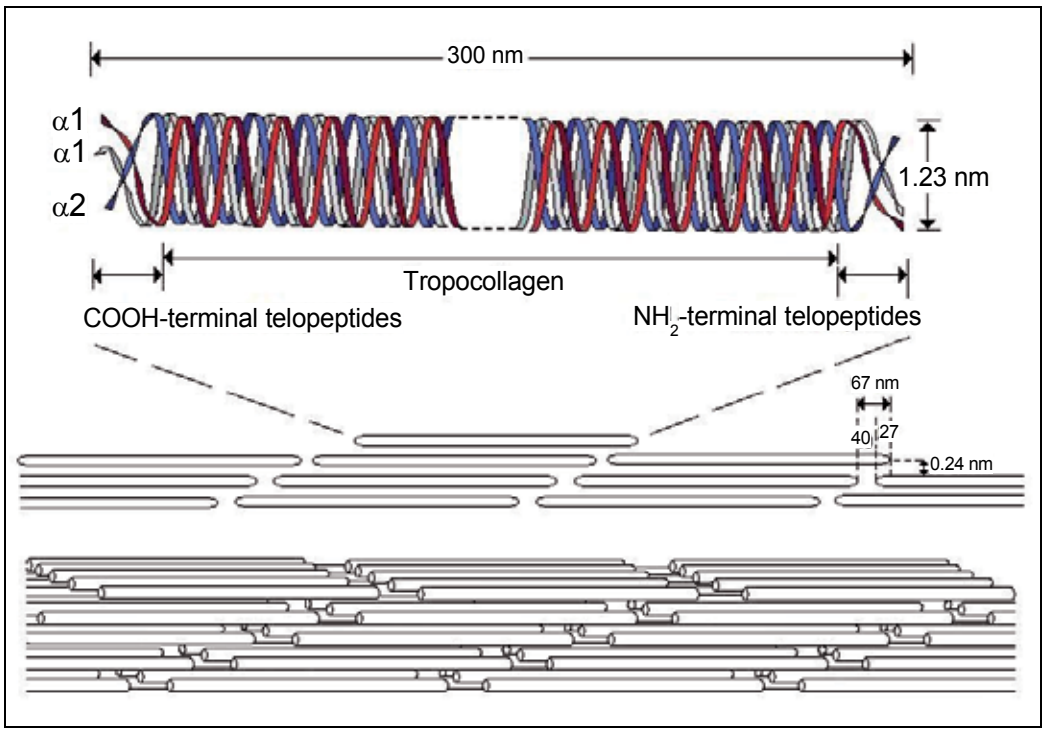

Fig. 2. Structure of the collagen molecule: three intertwined polypeptide chains (two α1 and one α2) constitute a major triple helical domain (tropocollagen) and two non-triple helical domains (telopeptides) at the –COOH and $–NH_2$ terminals of the protein. The typical staggered arrangement found in the collagen fibrils is displayed both in 2D and 3D configurations. The gap regions between the molecules are nucleation sites for hydroxyapatite.

suggested by the sequence of the mechanism of formation, divalent cross-links are classified as immature, whereas trivalent are considered as mature. These cross-links are also commonly named after their reactivity with sodium borohydride: typically, divalent cross-links are reducible fragments whereas trivalent are non-reducible. As for the second type, glycation cross-links, these are formed between collagen helices (telopeptides are not involved), being frequently associated with the ageing process that is generally deleterious to the function of the bone tissue. In fact, the extent and type of collagen cross-linking are known to change throughout life, leading to less flexible and less elastic properties. Besides the usual bone mass loss associated with age, the accumulation of glycation cross-links and of mature enzymatic cross-links in collagen is also thought to contribute to the fragility and brittleness of bone (Saito & Marumo, 2009; Viguet-Carrin et al., 2010).

Bone matrix structure

The structure of the mature bone matrix (Fig. 3) is highly organized on several hierarquical levels, starting with nanoscopic crystals of hydroxyapatite that are oriented and aligned within collagen fibrils (Fratzl et al., 2004; Olszta et al., 2007; Rho et al., 1998; Tzaphlidou, 2005; Viguet-Carrin et al., 2005). These result from the self-assembly of collagen molecules and mineral deposition, mainly in the regularly spaced gap regions of the organic structure

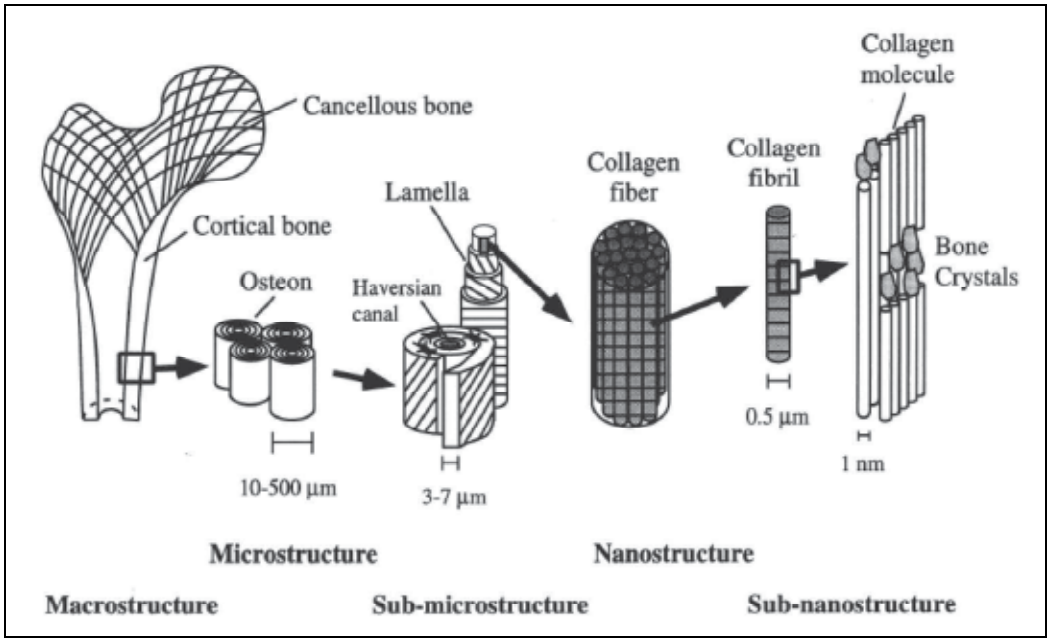

Fig. 3. Hierarquical structure of the bone matrix (from Rho et al., 1998).

(Fig. 2) (Nudelman et al., 2010). The association of the mineralized fibrils constitutes larger fibers which are layered in parallel arrangement forming lamellae with an alternate oriented "plywood" appearance (Goldman et al., 2005). Lamellar bone may be disposed concentrically around blood vessels, like rings of a tree, to form osteons (Havers Systems). This organization, from a nano to a macroscopic level, leads essentially to two distinct morphologies: compact bone, composed of densely packed osteons (Silva et al., 2005), and cancellous bone, wherein lamellae are assembled as spaced spicules (trabeculae), originating an interconnected microporous structure (Lozupone & Favia, 1990; Olszta et al., 2007). Compact bone is also called cortical because it always occupies a peripheral position relative to cancellous (or trabecular) bone.

It is interesting to perceive that each hierarchical structure of this anisotropic composite material is optimised to achieve a remarkable mechanical performance, from its basic building block (the mineralized collagen fibril wherein hydroxyapatite crystals have the long axis parallel to the longitudinal axis of the collagen molecules) to the tri-dimensional architecture of compact and cancellous bone. Moreover, each structural level may undergo minor but fundamental modifications, to better adapt and respond to various biomechanical forces (Ottani et al., 2001). As stated in a basic rule of skeletal biology known as Wolff´s law, "the bone´s morphology is a reflection of what function the bone has been built to do or adapted to perform".

3. FTIR spectroscopy applied to bone characterization

The Fourier transform infrared (FTIR) spectroscopy is based upon the absorption of IR radiation during vibrational transitions in covalently bound atoms. The frequencies and intensities of the infrared bands provide relevant information on the nature of the molecular

bonds, their environment and their relative content in the material being analysed. In some cases, some structural information regarding molecular conformations can also be obtained (Nyquist et al., 1997).

In order to obtain FTIR spectra, solid state samples in powdered form are often mixed with the infrared transparent KBr salt and prepared as pellets. Using FTIR in the transmission mode, the incident infrared radiation passes through the sample pellet and the spectrum corresponds to the transmitted fraction of the radiation. Alternatively, using the attenuated total reflection (ATR) mode, the solid samples can be analysed directly (without mixing with other substances) and the infrared spectrum corresponds mainly to the interaction up to about 2 μm depth from the surface of the sample.

In addition to the conventional FTIR spectroscopy, a microscopic analysis coupled to the vibrational spectra is also currently used to characterize bone samples, providing further insight into the correlation between structural and functional features. In fact, the introduction of the technique of infrared microspectroscopy (FTIRM) in 1988, followed by the development of the infrared imaging (FTIRI) from 1998, enabled to combine the advantages of hystomorphometry of the bone tissue with spectroscopy in the infrared range. Firstly, FTIRM allowed acquiring the sequential infrared mapping of a sampling area. Later, using focal plane array detector technologies, FTIRI enabled the simultaneous spectral acquisition in each detector pixel, representing an important progress both quantitative and qualitatively. In fact, FTIR imaging provides all the functionality of mapping but does so faster, with better spatial resolution and most importantly, with considerably better sensitivity than FTIRM. Nowadays, both techniques are regularly applied to the *in vitro* analysis of human tissues, namely bone samples (healthy, diseased and archeological bone), as well as animal models (Isaksson et al., 2010; Lebon et al., 2008; Marcott et al., 1998). Samples are usually prepared from thin cut sections that, for FTIRM/FTIRI analyses and in opposition to conventional histological analysis, do not require specific staining. However, samples may have to be fixed with appropriate solvents and embedded on a rigid support (often polymeric resins) and these procedures may cause some deviations of the infrared absorption bands relative to the direct analysis of the material (Aparicio et al., 2002; Paschalis et al., 2011). To overcome this interference, the thin sections may be analyzed in the ATR mode (that most frequently requires little or no sample preparation) but this option may cause some loss of spatial resolution due to intrinsic limitations of the technique (Agilent Technologies, 2011; Petibois et al., 2009).

3.1 FTIR spectrum of the bone matrix

The composite nature of the bone matrix becomes very clear when its FTIR spectrum is compared with those of the model compounds of its components, hydroxyapatite and collagen (Fig. 4). In fact, the spectrum of bone exhibits all the most intense bands observed in the spectrum of hydroxyapatite (at 500-700 cm^{-1} and 900-1200 cm^{-1}) and that of collagen (in the 1200-1700 cm^{-1} and 2800-3700 cm^{-1} regions), being nearly coincident with the sum of the respective profiles. Nevertheless, there are some new bands (namely at around 870 cm^{-1} and 1400-1450 cm^{-1}) originated from carbonate substitutions in the crystal lattice of hydroxyapatite.

From the detailed spectral assignments presented in Table 1, some bands must be discussed, particularly in the 500-1700 cm^{-1} region of the spectrum of bone. The most intense bands are

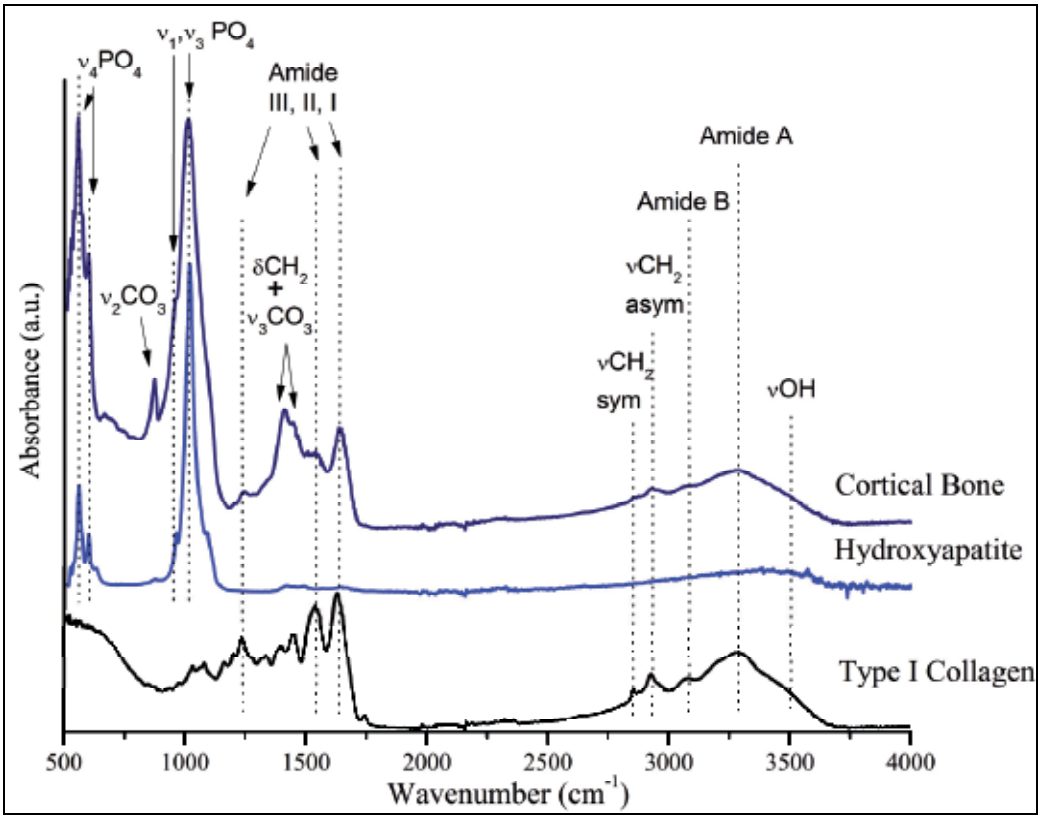

Fig. 4. Typical FTIR spectra of bone, hydroxyapatite and collagen showing the vibrational assignments of the most significant bands.

originated from the mineral phase, in accordance to its larger proportion in the composite. In particular, the bands at 557 and 600 cm^{-1} correspond mainly to ν_4 PO_4^{3-} bending vibrations, despite some minor contribution from collagen (amide bands) in that region. Moreover, the absorptions at 961 and 1012 cm^{-1} correspond to the symmetric (ν_1) and asymmetric (ν_3) stretching of phosphate, respectively. Thus, most of the absorptions from phosphate vibrations are clearly observed both in the spectra of bone and of hydroxyapatite.

It should be also mentioned that acidic phosphate (HPO_4^{2-}), a frequent anionic substitution in the crystal lattice of hydroxyapatite, usually originates a band at *ca.* 1110 cm^{-1}, which is normally overlapped with that from ν_3 PO_4^{3-} vibration.

On the other hand, the collagen moiety of bone originates the typical Amide I and Amide II bands at 1634 and 1548 cm^{-1}, respectively. Furthermore, the bands at 1410 and 1445 cm^{-1} show a different profile and higher intensity in the spectrum of bone relative to its organic model compound. These bands correspond, in fact, to absorptions from CH_2 wagging and bending vibrations superimposed with those from asymmetric stretching (ν_3) vibrations of CO_3^{2-} groups, present as ionic substitutes in the apatite crystal. Carbonate also originates a band at *ca.* 870 cm^{-1}, which is assigned to the ν_2 bending vibration. This band is characteristic of a type B apatite.

Wavenumber (cm^{-1})	Vibration modes		
	Bone	Hydroxyapatite	Collagen
557	ν_4 PO_4^{3-} bend (mineral) +Amide (organic)	ν_4 PO_4^{3-} bend	500-750 cm^{-1} Amide IV-VII
600	ν_4 PO_4^{3-} bend (mineral) +Amide (organic)	ν_4 PO_4^{3-} bend	
630	–	ν_4 PO_4^{3-} bend	
871	ν_2 CO_3^{2-} bend	–	–
961	ν_1 PO_4^{3-} sym stretch	ν_1 PO_4^{3-} sym stretch	–
1012	ν_3 PO_4^{3-} asym stretch	ν_3 PO_4^{3-} asym stretch	–
1250	Amide III		Amide III
1395	–	–	CH_2 wag
1410	ν_3 CO_3^{2-} (mineral)+ CH_2 wag (organic)	–	–
1445	CH_2 bend (organic)+ ν_3 CO_3^{2-} (mineral)	–	CH_2 bend
1548	Amide II	–	Amide II
1634	Amide I	–	Amide I
2850	CH_2 sym stretch	–	CH_2 sym stretch
2930	CH_2 asym stretch	–	CH_2 asym stretch
3072	Amide B	–	Amide B
3278	Amide A	–	Amide A
3500	ν OH	ν OH	ν OH

Table 1. Band assignments for the FTIR spectra of bone, hydroxyapatite and collagen, illustrated in Fig. 4.

As described, the infrared spectrum is a good diagnostic of the presence of phosphate (and also of carbonate) groups in the mineral component of bone, as well as the presence of amide groups in the organic fraction. In fact, these groups originate many typical absorption bands, as predicted theoretically.

Concerning the phosphate anions in tetrahedral geometry, there are four fundamental vibrations distributed as ν_1 (symmetric stretch), ν_2 (bend), ν_3 (asymmetric stretch), and ν_4 (bend) (Fig. 5) and these vibration modes (except ν_2) give rise to medium to strong bands (Nyquist et al., 1997). Typically, in hydroxyapatite, ν_1 (a non degenerate vibration mode) originates one intense band at around 960 cm^{-1}, and ν_3 and ν_4 (triply degenerate modes) originate up to three bands each in the 1000-1100 cm^{-1} and 500-650 cm^{-1} regions, respectively. Finally, the doubly degenerate mode ν_2 may be observed at less than 500 cm^{-1}.

Carbonate anions may also show up to four normal modes of vibration: symmetric stretch (ν_1), out-of-phase bending (ν_2), asymmetric stretch (ν_3) and in-plane CO_2 bending (ν_4) (Fig. 5). Whereas ν_2 is a non degenerate mode, both ν_3 and ν_4 are doubly degenerate and ν_1 is not

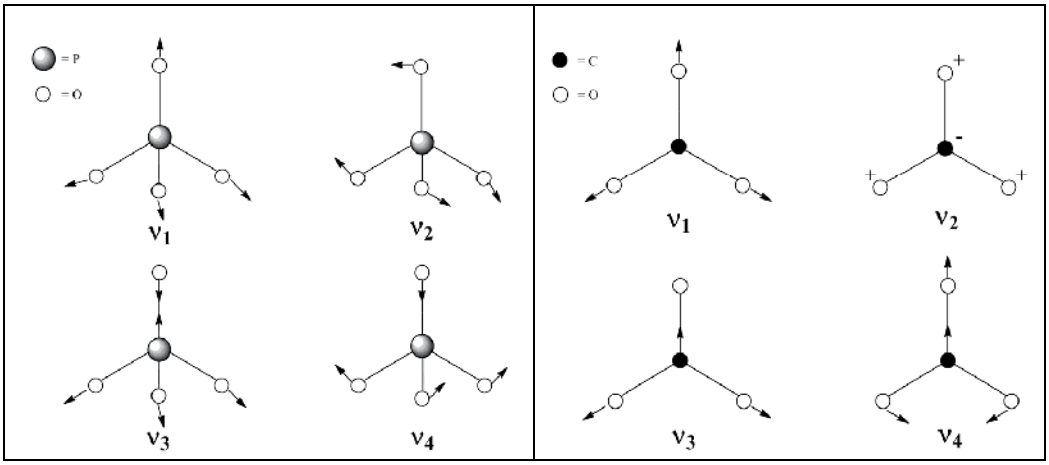

Fig. 5. Vibration modes for phosphate anions in tetrahedral symmetry and carbonate anions in D_{3h} symmetry (adapted from Nyquist et al., 1997).

an active vibration in the infrared because it does not change the dipole moment of the molecule (Nyquist et al., 1997). In carbonated apatites, the CO_3^{2-} characteristic bands appear at 870-880 cm^{-1} (ν_2, as a single band) and at 1400-1450 cm^{-1} (ν_3, usually as a double band). Depending on the type of carbonate substitution in the crystal lattice, bands may appear at slightly different wavenumbers: type *A* carbonated apatite is characterized by a ν_2 band at *ca.* 880 cm^{-1} and a ν_3 double band around 1450 and 1540 cm^{-1}, whereas type *B* configuration has these bands at about 870, 1430 and 1450 cm^{-1}, respectively (Fleet, 2009; Landi, 2003). The ν_2 band is often used to estimate the CO_3^{2-} content of the sample, by calculating the respective area underneath. Moreover, this band may also contain a component at *ca.* 865 cm^{-1}, due to the contribution of non-apatitic (labile) carbonate (Verdelis et al., 2007).

As for type I collagen, the organic component of bone, many vibrational bands are originated from the amide groups that constitute the peptide bonds of this protein. The characteristic vibrations of amide groups in collagen are usually combined modes designated as Amide I-VII, Amide A and Amide B (Chang & Tanaka, 2002; Garip & Severcan, 2010). The Amide I band, typically observed in the 1600-1700 cm^{-1} range, is the most intense absorption band in collagen. It results mainly from the C=O stretching vibration (with minor contribution from C-N stretch) and is directly related to the backbone conformation. Amide II, which originates a band at 1500-1600 cm^{-1} in collagen, is also conformationally sensitive and results mainly from an out-of-phase combination of N-H in-plane bending and C-N stretching vibrations of the peptide linkages. The Amide III band (1200-1300 cm^{-1}), just like the Amide II band, mainly arises from C–N stretch and N–H in-plane bending. The main difference between Amide II and III lies in the relative contribution of these modes for the respective mixed vibrations: whereas the N–H bending mode makes the larger contribution for the Amide II, the opposite occurs for the Amide III band. Amide IV is a C=O in-plane deformation and Amide V, VI and VII are out-of-plane motions (Roeges, 1994). The Amide A and Amide B bands, near 3300 cm^{-1} and 3100 cm^{-1} respectively, result from a Fermi resonance between the N-H stretch fundamental band and the overtone of amide II (Lee et al., 1999).

As demonstrated, the spectral contribution of the mineral and organic components to the overall FTIR spectrum of bone may be analyzed almost independently. This enables to estimate, for instance, the relative amount of mineral to organic matter and the proportion of carbonate in the bone apatite. Moreover, since high carbonate (and other ions) substitution correlates with a less mature mineral, FTIR data may also provide a measure of the crystal maturity based on the crystal stoichiometry. On the other hand, the maturity of the organic component of bone may also be evaluated through the analysis of specific amide bands from collagen.

Next section addresses the methodology usually applied to determine these and other parameters important for bone quality, demonstrating the extraordinary potential of FTIR analysis.

3.2 Assessing bone quality using FTIR

Bone quality is a broad term that encompasses factors affecting the geometric and material properties that contribute to fracture resistance. Geometric properties include the macroscopic geometry of the whole bone and the microscopic architecture of the trabeculae. On the other hand, material properties include the composition and arrangement of the primary constituents of bone tissue (collagen and mineral), as well as microdamage and microstructural discontinuities (Boskey, 2006, 2011; Paschalis et al., 1997). As mentioned earlier, the recent interest in bone quality arises from the fact that the traditional measurement of bone strength in clinical practice, namely bone densitometry, does not always reliably predict fracture risk. In fact, the bone mineral density (BMD) measurements primarily show the quantity of bone in the skeleton, overlooking more subtle aspects of bone's properties that may also contribute to its fragility. It is therefore important to understand alterations in bone that occur at the macro-, micro- and nanoscopic levels to determine what parameters affect bone quality and how they change with age or health condition.

FTIR spectroscopy, including FTIRM and FTIRI, providing information on all bone constituents at molecular level, represents an excellent tool to explore bone quality. The most frequently reported outcomes of FTIR related to bone material properties are the relative mineral and organic content, mineral maturity and crystallinity, carbonate substitution into the apatite lattice and collagen crosslinking. Because most of the bands of the bone spectrum are composed of several spectral components, deconvolution methods based on second derivative-spectroscopy and curve fitting have to be applied, being the results normally reported as a percentage of the area of specific underlying bands (Donnely 2010; Petibois et al., 2009). Hence, FTIR data are most commonly used for comparison purposes (between regions of the same sample, among samples or throughout time) rather than in absolute terms.

The proportion between the mineral and organic content in bone expresses its degree of mineralization and can be calculated from the ratio of the integrated area due to phosphate bands (usually ν_1, ν_3 in the 900-1200 cm^{-1} region) to that of a amide band (normally Amide I in the 1600-1700 cm^{-1} region). This ratio is an important indicator of the maturation or aging of bone and is linearly related to the bone mineral density (BMD) routinely measured in clinical medicine by dual energy X-ray absorptiometry. However, it should be pointed out that these parameters are not expressed in the same basis (BMD quantifies the amount of

mineral per volume whereas the ratio of the mentioned areas represents the amount of mineral per amount of collagen per volume analysed).

The mineral maturity is normally estimated based on sub-bands of the ν_1, ν_3 phosphate vibrations in the 900-1200 cm^{-1} region (Fig. 6). From deconvolution in this spectral range several individual peaks arise underneath the ν_3 band, being those at *ca.* 1020 and *ca.* 1030 cm^{-1} regarded as representative of specific chemical environments: typically, the sub-band at 1020 cm^{-1} is associated to nonstoichiometric apatites (containing HPO_4^{2-} and/or CO_3^{2-}) and that at 1030 cm^{-1}, to stoichiometric apatites. Given that the ratio of the areas of the sub-bands at 1020 and 1030 cm^{-1} has shown to decrease as mineral maturation proceeds, this ratio is often applied to evaluate the maturity of the bone apatite (Miller et al., 2001; Paschalis et al., 2011; Verdelis et al., 2007).

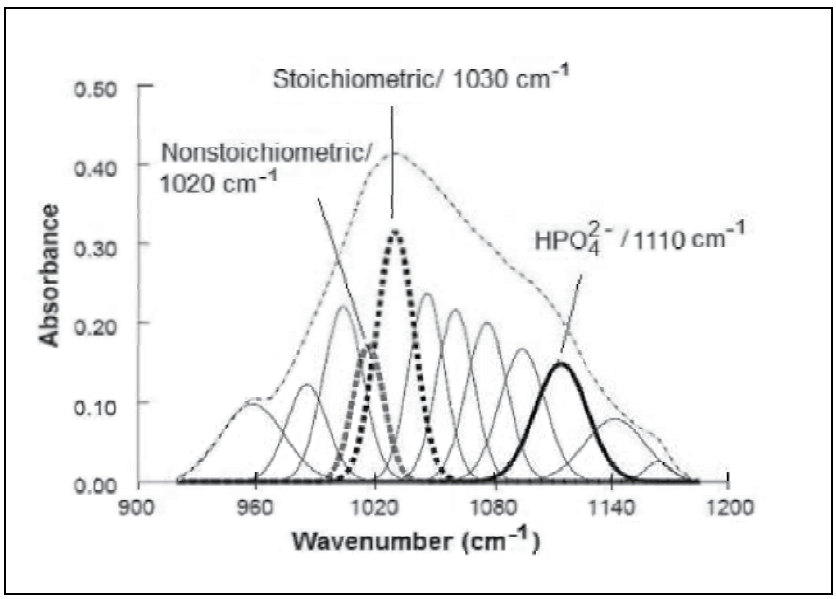

Fig. 6. Spectral region of the ν_1, ν_3 phosphate bands with underlying components revealed by curve-fitting. Sub-bands associated with the stoichiometry of the apatite (generally used for determination of mineral maturity) and the sub-band from HPO_4^{2-} (a common substitute in the apatite crystal) are highlighted (adapted from Verdelis, 2005).

It should be mentioned that since they evolve concomitantly, mineral maturity is normally associated with crystallinity. Thus, the simultaneous expression mineral maturity/ crystallinity is commonly employed, regardless these parameters do not refer to the same mineral properties (Farlay et al. 2011). Although the crystallinity of a mineral is typically calculated from X-ray diffraction, it has been suggested that in the particular case of hydroxyapatite, this parameter may also be determined from the well resolved FTIR band at *ca.* 600 cm^{-1} corresponding to a ν_4 phosphate vibration. Since the inverse of the full width at half maximum (1/FWHM) of this peak was found to be highly correlated with the state of crystallinity of the apatite (the narrower the peak, the higher the crystallinity), this ratio may be used as a crystallinity index. (Farlay et al. 2011). Moreover, it has been suggested that the ν_4 PO_4^{3-} peak at *ca.* 600 cm^{-1} is more reliable than the ν_3 PO_4^{3-} peak at *ca.* 1030 cm^{-1}, most

frequently associated with crystallinity (Shemesh, 1990). Finally, it should be emphasized that mineral maturity and crystallinity seem to be strongly correlated in synthetic apatites, but poorly correlated in human bone (especially in pathological bone). As expected in such a dynamic remodelling tissue, both parameters depend upon numerous factors including age, nutrition and health condition.

On the other hand, the maturity of the mineral phase is also related to the amount of substitutions in the crystal lattice of hydroxyapatite, being carbonate the most abundant in bone. Carbonate to phosphate ratio indicates the level of carbonate substitution and is calculated as the ratio of the carbonate band integrated area (850-890 cm^{-1}) to that of ν_1, ν_3 phosphate bands. This parameter seems a good indicator of the bone turnover and remodeling activity (Isaksson et al 2010). A combination of second derivative spectroscopy and curve fitting of the carbonate band (Fig. 7) reveals whether the carbonate has replaced hydroxide (A-type) or phosphate (B-type) in the apatite crystal, or is loosely attached to its surface (labile CO_3^{2-}). Considering that acidic phosphate is another eventual substitute in bone apatite, mineral maturity may also be estimated from the ratio between the overall ν_1, ν_3 phosphate band and the HPO_4^{2-} sub-band at *ca.* 1110 cm^{-1}.

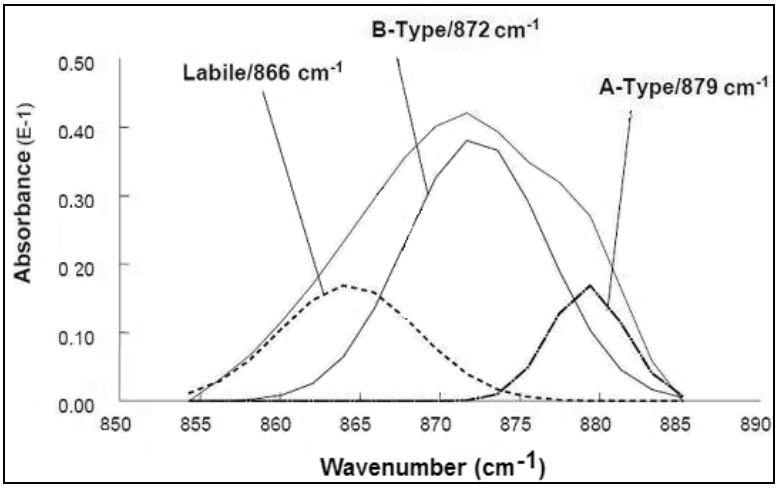

Fig. 7. Spectral region of the ν_2 carbonate band with components determined by curve-fitting, indicating the different types of carbonate substitution (adapted from Verdelis, 2005).

As previously mentioned, one of the most distinct features of type I collagen in mineralized tissues is its cross-linking chemistry. The intermolecular cross-linking provides high tensile strength and viscoelasticity to the fibrillar matrices. FTIR has been used to analyse the secondary structure of collagen, namely through the analysis of Amide I band. Information on protein structure may be obtained from the underlying bands of Amide I spectral region by resolution enhancement techniques (Fig. 8) (Paschalis et al., 2003). Of particular interest are two sub-bands: 1660 and 1690 cm^{-1}, related to the presence of non-reducible (mature) and reducible (immature) collagen cross-links, respectively. Thus, the ratio of the integrated areas of these bands (1660/1690) can be used as an indicator of the collagen maturity (Paschalis et al., 2011; Paschalis et al., 2001; Saito & Marumo, 2009).

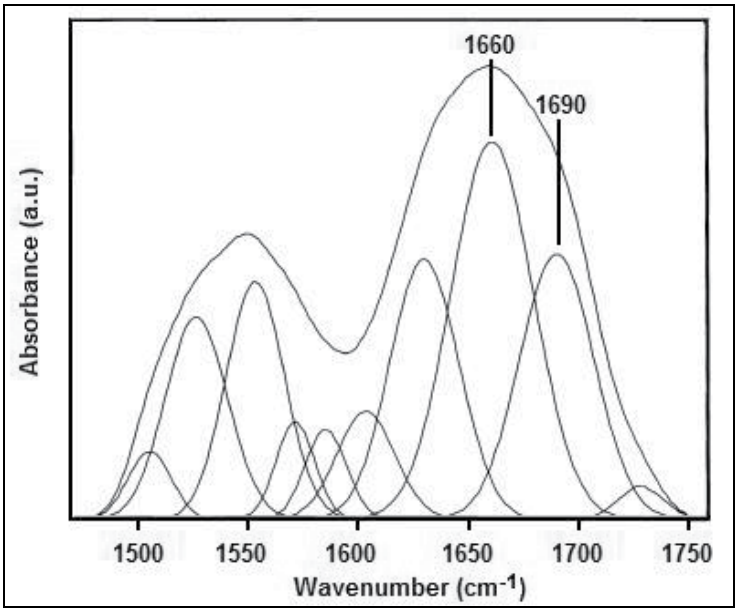

Fig. 8. Typical FTIR spectrum of collagen obtained from demineralized bovine bone in the region of Amide I and Amide II, resolved to its underlying components. Sub-bands at 1660 and 1690 cm^{-1} may be used to determine the maturity of collagen crosslinks (adapted from Paschalis et al., 2001).

Parameter	Ratio of the integrated areas or peaks intensities
Mineral/organic content	Phosphate bands (900-1200 cm^{-1})/amide I band (1600-1700 cm^{-1})
Mineral maturity	1030 cm^{-1} sub-band (stochiometric apatites)/1020 cm^{-1} sub-band (non-stochiometric)
CO_3^{2-}/PO_4^{3-} ratio	Carbonate bands (850-890 cm^{-1})/phosphate bands (900-1200 cm^{-1})
Type of CO_3^{2}substitution	Ratio of integrated area or intensity of sub-bands at *ca.* 870 cm^{-1} (B-type carbonate), 880 cm^{-1} (A-type carbonate) and 865 cm^{-1} (labile carbonate)
Collagen maturity	1660 cm^{-1} sub-band (non-reducible/mature cross-links)/1690 cm^{-1} sub-band (reducible/immature cross-links)

Table 2. Relevant bone quality parameters derived from the FTIR data.

Table 2 summarizes the most important parameters generally used to evaluate bone quality derived from FTIR spectroscopy data. In addition, Figure 9 illustrates the spatial distribution of some of these parameters in thin sections of osteoporotic bone samples, as observed by FTIRI.

4. Characterization of bone-based graft materials using FTIR spectroscopy

Bone tissue posses a remarkable capacity to self-repair microdamages. Nevertheless, when a bone defect reaches a critical size, healing usually requires the introduction of grafting materials. Ideally, these should be able to provide a porous scaffold to enable cell invasion and attachment, and the subsequent formation of new bone.

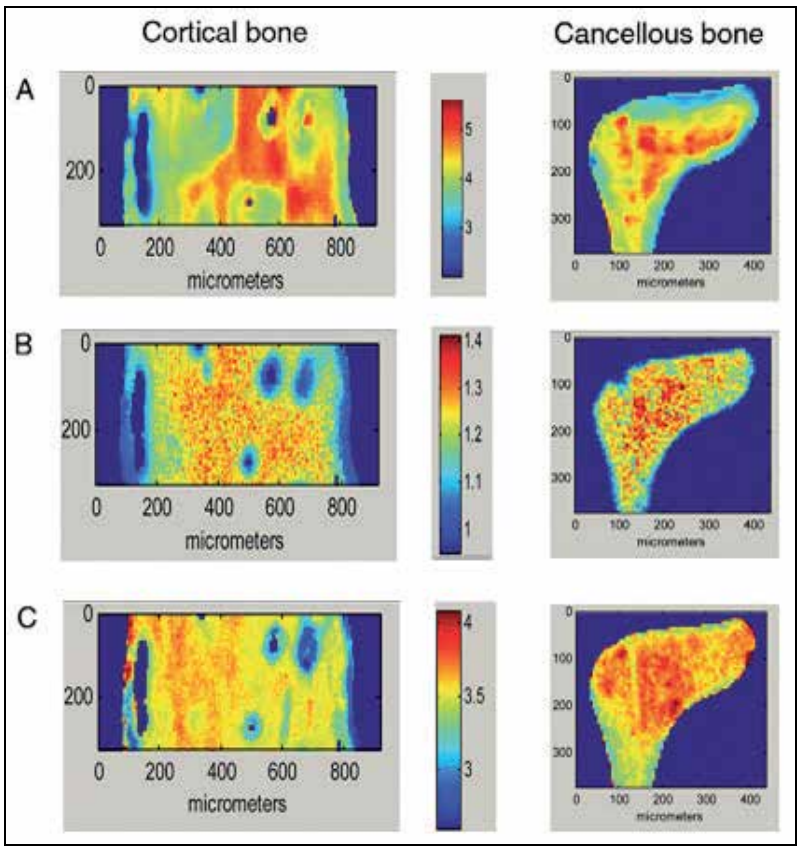

Fig. 9. Typical images obtained by FTIRI from an osteoporotic human iliac crest showing the spatial distribution of bone quality parameters in regions of cortical and cancellous bone: mineral/organic ratio (A), mineral maturity (B), and collagen maturity (C) (from Boskey, 2011).

A standard strategy applied when a bone loss occurs is using bone grafts which include autografts, allografts and xenografts (Bauer & Muschler, 2000; Torroni, 2009). An autograft consists of a tissue that is transferred from one site of the organism of an individual to a different location, an allograft represents a tissue transfer between individuals of the same species, and xenografts, between different species. Bone autografts, the "gold standard" in bone grafting procedures, have the advantage of no adverse immunological response and thus represent the best for inducing new bone formation. However, they are usually available in limited quantity (depending on donor site anatomy) and harvesting requires additional surgery, resulting in increased morbidity for the patient. Human allografts, which can be appropriately preserved in bone banks being thus available in greater abundance, represent a valuable alternative to autografts (Judas et al., 2005). Even so, the application of allografts is often limited due to uncertainty on compatibility and risk of disease transmission. Xenografts, most often of bovine or porcine origin, have no limitations regarding availability but, similarly to allogenous bone, can introduce risk of rejection and disease transmission.

Currently, the most common alternatives to bone-based grafts are synthetic biomaterials (often composites made of Ca/P ceramics and polymers) (Kikuchi et al., 2001). Although the raw materials of these composites are selected to fulfil many requirements (such as biocompatibility, osteoconductivity and non-toxicity), being often produced/modified to mimic the characteristics of natural bone, the best clinical results still derive from the application of autografts. Nonetheless, synthetic materials not only overcome most disadvantages of the natural bone grafts, but also provide more consistent and controllable properties. This is the case of diverse ceramic materials, namely hydroxyapatite, that besides being applied as components of composites, are also frequently used alone. In fact, synthetic hydroxyapatite is the most commonly used graft material mostly due to its resemblance with the bone mineral and similar osteocondutive potential. Synthetic hydroxyapatite, however, possesses some limitations including poor mechanical properties (specially when exposed to wet environments) and lack of osteoinductive properties. In addition, for the time being, synthetic apatites are not yet able to duplicate the composition and structure of the mineral component of bone, known to influence the grafts osteointegration. In fact, natural hydroxyapatite is nonstoichiometric and contains carbonate and other ions built into its structure. Although the presence of these ions is very low, they play a vital role in the biological reactions associated with bone metabolism (Barrere et al., 2006; Joschek et al., 2000). It has been shown that carbonate incorporation tends to decrease the crystallinity and to augment the solubility of hydroxyapatite, enhancing its biodegradation rate. Thus, synthetic hydroxyapatite is frequently modified chemically in order to include additional properties favorable to bone grafting.

A given type of graft can function by more than one mechanism. For instance, autografts are osteoconductive, osteoinductive and osteogenic whereas allografts and xenografts are mainly osteoconductive. Evidences that natural apatites also possess osteocondutive properties has stimulated their application as grafting materials, alone or combined with other materials. Currently, this mineral component of bone is usually obtained from calcined xenografts, being commercially available from different animal origins, under various formulations. On the other hand, in addition to osteocondutive properties, demineralized bone grafts have demonstrated to also possess osteoinductive capacities, which are mainly attributed to the exposure of bone morphogenetic proteins (BMPs) caused by the demineralization procedure. Thus, not only natural bone grafts, but also calcined and demineralized bone grafts constitute very important options that require extensive research regarding materials characterization, processing methods and application conditions, in order to help the prediction of their clinical outcome.

4.1 Bone-derived hydoxyapatite: Influence of the calcination temperature

One strategy to improve non-autograft materials while maintaining their advantages regarding their chemical and physical properties is to process natural bone, for example by heat treatment (Haberko et al., 2006; Joschek et al., 2000; Murugan et al., 2006; Ooi et al., 2007). Natural hydroxyapatite obtained in this way has the advantage of inheriting the chemical composition and structure of the raw material (Catanese et al., 1990; Etok et al., 2007; Murugan et al., 2003), being therefore an alternative solution for numerous applications based on its analogous synthetic products. As compared to allogeneic bone, hydroxyapatite derived from xenogeneic bone (usually of bovine origin) is considered a good option because it is easier to obtain at lower cost and is available in unlimited supply.

The problem that arises with heat treatment at elevated temperatures is that the biogenic composition and structure of bone mineral can change and this may affect the efficacy of this material (Etok et al., 2007; Hillera et al., 2003; Ooi et al., 2007). Although there is some controversy regarding the onset of chemical and structural changes as a consequence of heat treatment, it has been reported that changes in the mineral phase of bone are not significant until degradation and combustion of most of the more labile organic components occurs (around 500 ºC) (Etok et al., 2007; Mkukuma et al., 2004; Murugan et al., 2006; Ooi et al., 2007). Regarding sample mineralogy, it is generally accepted that heat treatment promotes the crystallinity of bone derived hydroxyapatite and increases the crystallite size (Etok et al., 2007; Hillera et al., 2003; Ooi et al., 2007).

A recent study concerning cortical bone samples of different origins (human and animal) subjected to different calcination temperatures (600, 900 and 1200 ºC) revealed that the calcination temperature highly affects the properties of the bone samples (Figueiredo et al., 2010). As expected, higher temperatures led to more pure forms of hydroxyapatite, with higher crystallinity degrees and larger crystallite sizes and a less porous structure. Furthermore, samples heated to the same temperature exhibited similar characteristics, regardless their origin.

FTIR spectra (Fig. 10) indicated that the organic constituents were no longer present in the samples calcined at 600 ºC, suggesting that this temperature is adequate to obtain protein-free samples. Moreover, these spectra have also revealed that, at this temperature, a carbonated apatite was obtained, being the carbonate removed from the mineral at higher temperatures. Furthermore, no new mineral phases were evident at higher temperatures, in good agreement with the results of thermal analysis, X-ray diffraction and additional confirmation by chemical analysis. Nevertheless, it has been reported that the apatite base

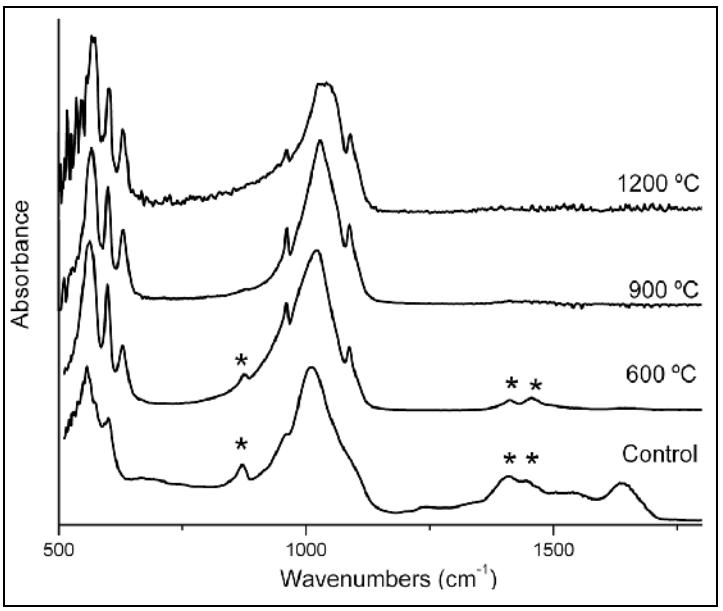

Fig. 10. FTIR spectra of human cortical bone before (control) and after calcination at 600, 900 and 1200 ºC. *Bands attributed to lattice carbonate vibrations (Figueiredo et al., 2010).

structure may be partially degraded by heating at temperatures higher than 800 ºC, originating β-tricalcium phosphate ($Ca_3(PO_4)_2$) and/or CaO. However, the presence of these products in the mineral is better detected by X-ray diffraction than by FTIR spectroscopy (Etok et al., 2007; Haberko et al., 2006; Mkukuma et al., 2004; Ooi et al., 2007; Rogers & Daniels 2002).

SEM pictures (Fig. 11) of the human bone sample calcined at various temperatures showed that the samples surfaces no longer present the characteristic concentric lamellae around the Havers Canals, due to the elimination of collagen with heat treatment. Nonetheless, the basic microstructure of cortical bone (Havers Canals and osteocyte lacunar spaces, in particular) was preserved after calcination. Additionally, it was also apparent that the size of the apatite crystals increased with temperature, resulting on increased crystalinity (as confirmed by X-ray diffraction).

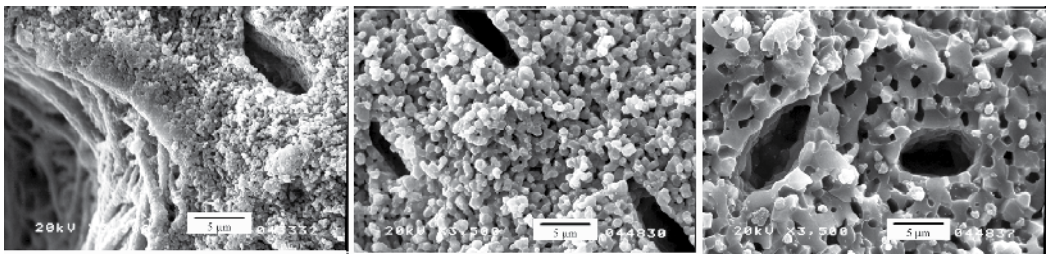

Fig. 11. Scanning Electron Microscopy images of human cortical bone calcined at 600, 900 and 1200 ºC (from left to right) showing the increase in crystal size with temperature (Figueiredo et al. 2010).

Moreover, heat treatment also resulted in different porosity characteristics. Regarding porosity and pore size distribution, assessed by mercury intrusion (Fig. 12), it was clear that samples calcined at 600 ºC exhibit the highest porosity, around 50%, which, for a compact bone, is quite relevant. However, as the heating temperature increases, the porous structure condenses, sintering at very high temperatures (1200 ºC) and originating porosity values comparable to those of the non-calcined samples.

4.2 Demineralized bone matrix: Effect of the acid concentration

Demineralized bone matrix (DBM) is often applied in orthopedics, periodontics, oral and maxillofacial surgery because of its inherent osteoconductive and osteoinductive properties, generally related, as mentioned, to bone morphogenetic proteins (BMPs) (Bauer & Muschler, 2000; Eppley et al., 2005; Katz et al., 2009). In fact, as mineral is removed, the matrix associated BMPs become available rendering DBM grafts osteoinductive (Pietrzak et al., 2009). These grafts can be used either alone (Libin et al., 1975; Morone & Boden, 1998; Pietrzak et al., 2005) or in combination with bone marrow, autogenous bone graft, or other materials (Kim et al., 2002; Kucukkolbasi et al., 2009; Nade & Burwell, 1977). Additionally, DBM exhibits elastic features, being easily shaped to fill osteochondral lesions with different shapes and sizes (Costa et al., 2001).

Despite the extensive use of DBM, conflicting results have been published in the literature regarding its bone-inducing abilities. This may be a consequence of following different

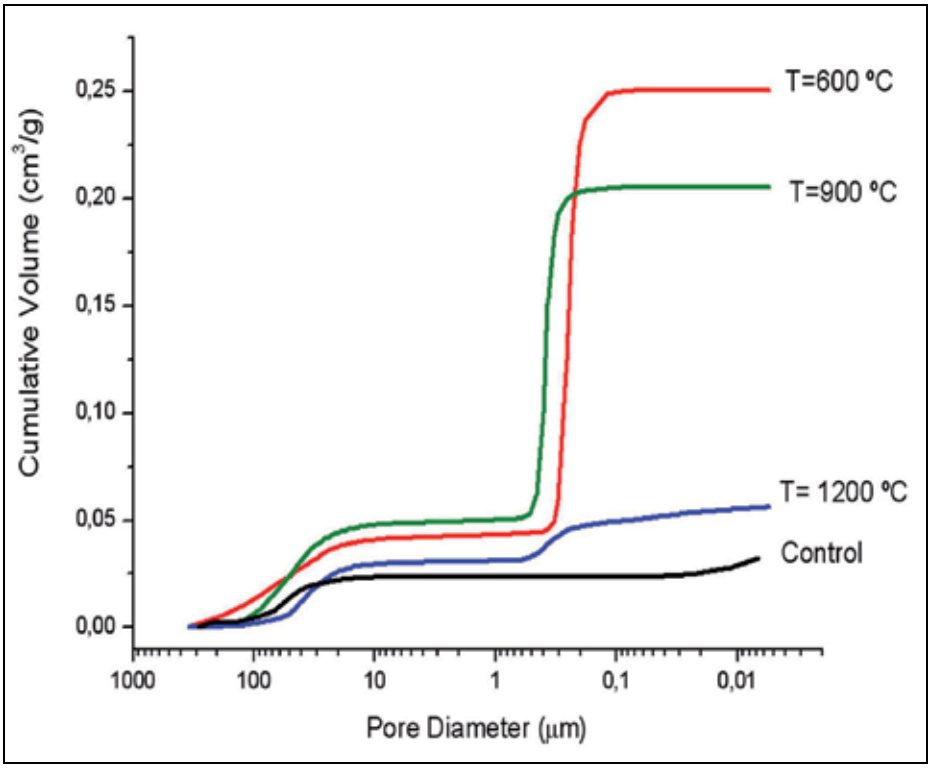

Fig. 12. Cumulative intrusion curve of human cortical bone, before (control) and after calcination at 600, 900 and 1200 ºC, measured by mercury porosimetry (Figueiredo et al., 2010).

demineralization procedures that naturally result in products with different properties (Bae et al., 2006; Eggert & Germain, 1979; Y. P. Lee et al., 2005; Lomas et al., 2001; Peterson et al., 2004). As reported in a recent study about BMPs depletion in particles of bovine cortical bone under acid exposure (0.25 and 0.5 M HCl) (Pietrzak et al., 2009), the availability of BMP-7 increases as demineralization occurs but, after reaching a maximum in the extraction bath, continuously declines. These results alert for the need to control the demineralization processing conditions. Normally, the process of bone demineralization is carried out by immersing the sample in a variety of strong and/or weak acids. In the case of using HCl (the most frequently used), the major inorganic constituent of bone (hydroxyapatite) reacts to form monocalcium phosphate and calcium chloride (Dorozhkin, 1997; Horneman et al., 2004).

FTIR has been used to monitor the bone demineralization process using HCl under different experimental conditions (acid concentrations and exposure times) (Figueiredo et al., 2011). Fig. 13 shows the FTIR spectra of bone samples (¼ of a ring of a human femoral diaphysis after being transversely cut into rings of approximately 1 cm width) submitted to demineralization with HCl 1.2 M for different periods of time. From the analysis of the FTIR spectra of the surface and of the core of the bone blocks, it was confirmed that the demineralization starts at the surface (absence of ν_1, ν_3 PO_4^{3-} bands and relative increase of the

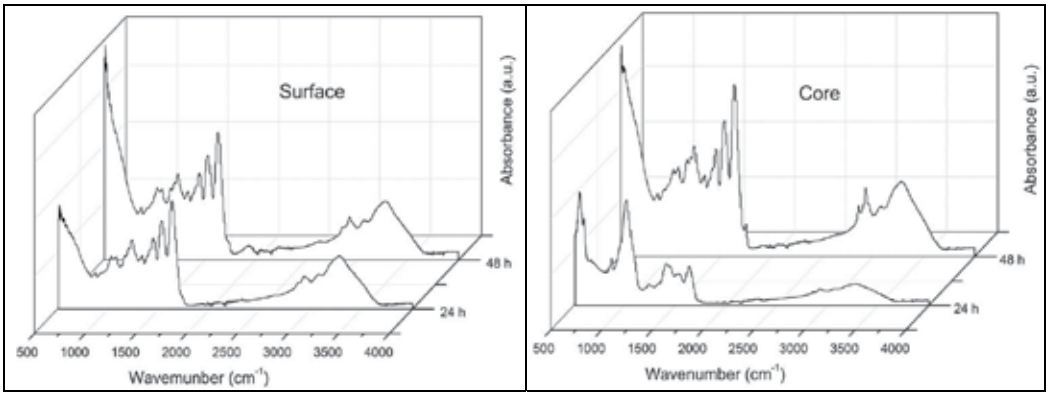

Fig. 13. FTIR spectra from the outer surface and from the core of the human bone samples after immersion in 1.2 M HCl for different time intervals. Demineralization proceeds from the surface into the core of the bone samples, as evidenced by the absence of phosphate bands and by the similarity with the spectrum of collagen.

collagen bands intensity) and progresses to the interior of the samples. These results support the concept of a diffusion model and agree with the proposed theory of the unreacted core during demineralization (Horneman et al., 2004; Lewandrowski et al., 1996, 1997).

This study was complemented with kinetic profiles and analysis of the samples´ structural modifications. As expected, increasing the acid concentration led to an increase in the demineralization rate, but not in a proportional way. In addition, microscopic observations demonstrated that despite the structural deformation resultant from demineralization, the basic bone microstructure was preserved. The loss of mineral led to a progressive reduction of mechanical strength and an increase of plastic properties (e.g. flexibility and elasticity) of the resultant material, mostly composed of collagen.

Although the deterioration of the organic component of bone was not examined in detail in this work, other studies using FTIR to analyse the effect of acids on the composition and structure of collagen during extraction from different tissues, may provide useful information on that subject. In fact, acid treatment of collagen samples was found to originate reduction of intermolecular cross-linking and hydrolysis of peptide bonds, as evidenced after curve-fitting in the spectral regions of the Amide I, II and III bands of collagen (Muyonga et al., 2004). These changes in collagen composition explained the observed loss of structural order. In addition, the amount and characteristics of the extracted fragments of collagen was related with the experimental conditions. These results agree with those from a FTIR study concerning the cross-linking of a collagen-hydroxyapatite nanocomposite with glutaraldehyde, as a model for the bone matrix (Chang & Tanaka, 2002). The spectral analysis showed that the increase of the cross-linking degree induces higher retaining of the organic content in the composite.

5. Conclusions

From the above, it is clear that FTIR spectroscopy is a sensitive and convenient tool to study the physicochemical modifications of bone composition regarding the mineral phase as well as the organic matrix. The detailed information provided by this technique is extremely

useful to study bone alterations that occur at macro-, micro- and nanoscopic levels, helping to reach a more consistent diagnostic.

Additionally, FTIR has been extensively used to characterize natural or synthetic graft materials, as well as to monitor the properties of the new bone formation. Furthermore, since the composition and the morphostructural parameters of a bone graft affect their biocompatibility, biodegradation and ultimately their osteointegration, the use of FTIR spectroscopy (including FTIRM and FTIRI) allows an interdisciplinary approach between chemists, molecular biologists and medical investigators.

6. References

Aerssens, J., Boonen, S., Joly, J., & Dequeker, J. (1997). Variations in trabecular bone composition with anatomical site and age: potential implications for bone quality assessment. *Journal of Endocrinology 155*, 411–421.

Agilent Technologies (2011). FTIR chemical imaging using focal plane array–based systems (Technical Overview ed.): Agilent Technologies, Inc.

Aparicio, S., Doty, S. B., Camacho, N. P., Paschalis, E. P., Spevak, L., Mendelsohn, R., et al. (2002). Optimal Methods for Processing Mineralized Tissues for Fourier Transform Infrared Microspectroscopy. *Calcified Tissue International 70*(5), 422-429.

Bae, H. W., Zhao, L., Kanim, L. E. A., Wong, P., Delamarter, R. B., & Dawson, E. G. (2006). Intervariability and intravariability of bone morphogenetic proteins in commercially available demineralized bone matrix products. *Spine, 31*(12), 1299–1306.

Barrere, F., van Blitterswijk, C. A., & de Groot, K. (2006). Bone regeneration: molecular and cellular interactions with calcium phosphate ceramics. *International Journal of Nanomedicine, 1*(3), 317-332.

Bauer, T. W., & Muschler, G. F. (2000). Bone graft materials. An overview of the basic science. *Clinical Orthopaedic Related Research, 371*, 10-27.

Boskey, A. (2006). Assessment of Bone Mineral and Matrix Using Backscatter Electron Imaging and FTIR Imaging. *Current Osteoporosis Reports, 4*, 71–75.

Boskey, A. (2011). Using bone quality to assess fracture risk. *American Association of Orthopaedic Surgeons Now, 5*(9).

Catanese, J., Featherstone, J. D. B., & Keaveny, T. M. (1990). Characterization of the mechanical and ultrastructural properties of heat-treated cortical bone for use as a bone substitute. *Journal of Biomedical Materials Research-Part A, 45*, 327-336.

Chang, M. C., & Tanaka, J. (2002). FT-IR study for hydroxyapatite/collagen nanocomposite cross-linked by glutaraldehyde. *Biomaterials, 23*, 4811–4818.

Costa, A., Oliveira, C., Leopizzi, N., & Amatuzzi, M. (2001). The use of demineralized bone matrix in the repair of osteochondral lesions. Experimental study in rabbits. *Acta Ortopédica Brasileira, 9*(4), 27-38.

Donnelly, E. (2010). Methods for Assessing Bone Quality: A Review. *Clinical Orthopaedics and Related Research, 469*(8), 2128-2138.

Dorozhkin, S. V. (1997). Surface Reactions of Apatite Dissolution. *Journal of Colloid Interface Science, 191*(2), 489–497.

Eggert, F. M., & Germain, J. P. (1979). Rapid Demineralization in Acidic Buffers. *Histochemistry, 59*, 215-224.

Eppley, B. L., Pietrzak, W. S., & Blanton, M. W. (2005). Allograft and alloplastic bone substitutes: a review of science and technology for the craniomaxillofacial surgeon. *Journal of Craniofacial Surgery, 16*(6), 981–989.

Etok, S. E., Valsami-Jones, E., Wess, T. J., Hiller, J. C., Maxwell, C. A., Rogers, K. D., et al. (2007). Structural and chemical changes of thermally treated bone apatite. *Journal of Materials Science, 42*(23), 9807-9816.

Eyre, D. R., & Wu, J.-J. (2005). Collagen cross-links. *Topics in Current Chemistry, 247*, 207–229.

Farlay, D., Panczer, G., Rey, C., Delmas, P. D., & Boivin, G. (2010). Mineral maturity and crystallinity index are distinct characteristics of bone mineral. *Journal of Bone and Mineral Metabolism, 28*(4), 433-445.

Figueiredo, M., Cunha, S., Martins, G., Freitas, J., Judas, F., & Figueiredo, H. (2011). Influence of hydrochloric acid concentration on the demineralization of cortical bone. *Chemical Engineering Research and Design, 89*(1), 116-124.

Figueiredo, M., Fernando, A., Martins, G., Freitas, J., Judas, F., & Figueiredo, H. (2010). Effect of the calcination temperature on the composition and microstructure of hydroxyapatite derived from human and animal bone. *Ceramics International, 36*(8), 2383-2393.

Fleet, M. E. (2009). Infrared spectra of carbonate apatites: v2-Region bands. *Biomaterials, 30*(8), 1473-1481.

Fratzl, P., Gupta, H. S., Paschalis, E. P., & Roschger, P. (2004). Structure and mechanical quality of the collagen/mineral nano-composite in bone. *Journal of Materials Chemistry, 14*(14), 2115.

Gamsjaeger, S., Masic, A., Roschger, P., Kazanci, M., Dunlop, J. W. C., Klaushofer, K., et al. (2010). Cortical bone composition and orientation as a function of animal and tissue age in mice by Raman spectroscopy. *Bone, 47*(2), 392-399.

Garip, S., & Severcan, F. (2010). Determination of simvastatin-induced changes in bone composition and structure by Fourier transform infrared spectroscopy in rat animal model. *Journal of Pharmaceutical and Biomedical Analysis, 52*(4), 580-588.

Goldman, H. M., Bromage, T. G., Thomas, C. D. L., & Clement, J. G. (2003). Preferred collagen fiber orientation in the human mid-shaft femur. *Anatomic Record Part A – Discoveries in Molecular Cellular and Evolutionary Biology, 272A*, 434-445.

Haberko, K., Bucko, M., Brzezinskamiecznik, J., Haberko, M., Mozgawa, W., Panz, T., et al. (2006). Natural hydroxyapatite—its behaviour during heat treatment. *Journal of the European Ceramic Society, 26*(4-5), 537-542.

Hillera, J. C., Thompson, T. J. U., Evison, M. P., Chamberlain, A. T., & Wess, T. J. (2003). Bone mineral change during experimental heating: an X-ray scattering investigation. *Biomaterials, 24*, 5091–5097.

Horneman, D. A., Ottens, M., Hoorneman, M., van der Wielen, L. A. M., & Tesson, M. (2004). Reaction and diffusion during demineralization of animal bone. *AIChE Journal, 50*(11), 2682-2690.

Isaksson, H., Turunen, M. J., Rieppo, L., Saarakkala, S., Tamminen, I. S., Rieppo, J., et al. (2010). Infrared Spectroscopy Indicates Altered Bone Turnover and Remodeling Activity in Renal Osteodystrophy. *Journal of Bone and Mineral Research, 25*(6), 1360-1366.

Joschek, S., Nies, B., Krotz, R., & Gopferich, A. (2000). Chemical and physicochemical characterization of porous hydroxyapatite ceramics made of natural bone. *Biomaterials, 21*, 1645-1658.

Judas, F., Teixeira, L., & Proença, A. (2005). Coimbra University Hospitals' Bone and Tissue Bank: twenty-two years of experience. *Transplantation Proceedings, 37*, 2799–2801.

Katz, J. M., Nataraj, C., Jaw, R., Deigl, E., & Bursac, P. (2009). Demineralized bone matrix as an osteoinductive biomaterial andin vitropredictors of its biological potential. *Journal of Biomedical Materials Research Part B: Applied Biomaterials, 89B*(1), 127-134.

Kikuchi, M., Itoh, S., Ichinose, S., Shinomiya, K., & Tanaka, J. (2001). Self-organization mechanism in a bone-like hydroxyapatite/collagen nanocomposite synthesized *in vitro* and its biological reaction *in vivo*. *Biomaterials 22*, 1705-1711.

Kim, S. G., Kim, W. K., Park, J. C., & Kim, H. J. (2002). A comparative study of osseointegration of Avana implants in a demineralized freezedried bone alone or with platelet-rich plasma. *Journal of Oral and Maxillofacial Surgery, 60*, 1018–1025.

Kucukkolbasi, H., Mutlu, N., Isik, K., Celik, I., & Oznurlu, Y. (2009). Histological evaluation of the effects of bioglass, hydroxyapatite, or demineralized freeze-dried bone, grafted alone or as composites, on the healing of tibial defects in rabbits. *Saudi Medical Journal, 30*(3), 329-333.

Landi, E. (2003). Carbonated hydroxyapatite as bone substitute. *Journal of the European Ceramic Society, 23*(15), 2931-2937.

Lebon, M., Reiche, I., Froehlich, F., Bahain, J. J., & Falgueres, C. (2008). Characterization of archaeological burnt bones: contribution of a new analytical protocol based on derivative FTIR spectroscopy and curve fitting of the υ_1 ν_3 PO_4 domain. *Analytical and Bioanalytical Chemistry, 392*(7-8), 1479-1488.

Lee, S.-H., Mirkin, N. G., & Krimm, S. (1999). A quantitative anharmonic analysis of the amide A band in α-helical poly(L-alanine). *Biopolymers, 49*, 195–207.

Lee, Y. P., Jo, M., Luna, M., Chien, B., Lieberman, J. R., & Wang, J. C. (2005). The efficacy of different commercially available demineralized bone matrix substances in an athymic rat model. *Journal of Spinal Disorder Technology, 18*(5), 439–444.

Lewandrowski, K. U., Tomford, W. W., Michaud, N. A., Schomacker, K. T., & Deutsch, T. F. (1997). An electron microscopic study on the process of acid demineralization of cortical bone. *Calcified Tissue International, 61*, 294–297.

Lewandrowski, K. U., Venugopalan, V., Tomford, W. W., Schomacker, K. T., Mankin, H. J., & Deutsch, T. F. (1996). Kinetics of cortical bone demineralization: controlled demineralization - a new method for modifying cortical bone allografts. *Journal of Biomedical Materials Research Part B: Applied Biomaterials, 11*(3), 365-372.

Libin, B. M., Ward, H. L., & Fishman, L. (1975). Decalcified, lyophilized bone allografts for use in human periodontal defects. *Journal of Periodontology, 46*, 51–56.

Lomas, R. J., Gillan, H. L., Matthews, J. B., Ingham, E., & Kearney, J. N. (2001). An evaluation of the capacity of differently prepared demineralized bone matrices (DBM) and toxic residuals of ethylene oxide (EtOx) to provoke an inflammatory response in vitro. *Biomaterials, 22*, 913–921.

Lozupone, E., & Favia, A. (1990). The structure of the trabeculae of cancellous bone. 2. Long bones and mastoid. *Calcified Tissue International, 46*, 367-372.

Marcott, C., Reeder, R. C., Paschalis, E. P., Tatakis, D. N., Boskey, A. L., & Mendelsohn, R. (1998). Infrared microspectroscopic imaging of biomineralized tissues using a mercury-cadmium-telluride focal-plane array detector. *Cellular and Molecular Biology, 44*(1), 109-115.

Martins, G., Freitas, J., Judas, F., Trindade, B., & Figueiredo, H. (2008). Evaluating Structural Differences in Cortical Bone Tissue After Demineralization and Calcination. *Microscopy and Microanalysis, 14*(S3), 162.

Miller, L. M., Vairavamurthy, V., Chance, M. R., Mendelsohn, R., Paschalis, E. P., Betts, F., et al. (2001). In situ analysis of mineral content and crystallinity in bone using infrared micro-spectroscopy of the ν4 PO43- vibration. *Biochimica et Biophysica Acta, 1527*(1-2), 11-19.

Mkukuma, L. D., Skakle, J. M. S., Gibson, I. R., Imrie, C. T., Aspden, R. M., & Hukins, D. W. L. (2004). Effect of the Proportion of Organic Material in Bone on Thermal Decomposition of Bone Mineral: An Investigation of a Variety of Bones from Different Species Using Thermogravimetric Analysis coupled to Mass Spectrometry, High-Temperature X-ray Diffraction, and Fourier Transform Infrared Spectroscopy. *Calcified Tissue International, 75*(4), 321-328.

Morone, M. A., & Boden, S. D. (1998). Experimental posterolateral lumbar spinal fusion with a demineralized bone matrix gel. *Spine, 23*, 159–167.

Murugan, R., Ramakrishna, S., & Rao, K. P. (2006). Nanoporous hydroxy-carbonate apatite scaffold made of natural bone. *Materials Letters, 60*, 2844–2847.

Murugan, R., Rao, K. P., & Kumar, T. S. S. (2003). Heat-deproteinated xenogeneic bone from slaughterhouse waste: physico-chemical properties. *Bulletin of Materials Science, 26*(5), 523–528.

Muyonga, J. H., Cole, C. G. B., & Duodu, K. G. (2004). Fourier transform infrared (FTIR) spectroscopic study of acid soluble collagen and gelatin from skins and bones of young and adult Nile perch (Lates niloticus). *Food Chemistry, 86*(3), 325-333

Nade, S., & Burwell, R. G. (1977). Decalcified bone as a substrate for osteogenesis: an appraisal of the interrelation of bone and marrow in combined grafts. *Journal of Bone Joint Surgery, 59-B*(2), 189–196.

Nudelman, F., Pieterse, K., George, A., Bomans, P. H. H., Friedrich, H., Brylka, L. J., et al. (2010). The role of collagen in bone apatite formation in the presence of hydroxyapatite nucleation inhibitors. *Nature Materials, 9*, 1004-1009.

Nyquist, R. A., Putzig, C. L., & Leugers, M. A. (1997). *The Handbook of Infrared and Raman Spectra of Inorganic Compounds and Organic Salts* (Vol. 1 and 4). San Diego, USA: Academic Press.

Olszta, M. J., Cheng, X., Jee, S. S., Kumar, R., Kim, Y. Y., Kaufman, M. J., et al. (2007). Bone structure and formation: A new perspective. *Materials Science and Engineering R 58*, 77-116.

Ooi, C., Hamdi, M., & Ramesh, S. (2007). Properties of hydroxyapatite produced by annealing of bovine bone. *Ceramics International, 33*(7), 1171-1177.

Ottani, V., Raspanti, M., & Ruggeri, A. (2001). Collagen structure and functional implications. *Micron, 32*, 251-260.

Paschalis, E. P., Betts, F., DiCarlo, E., Mendelsohn, R., & Boskey, A. L. (1997). FTIR microspectroscopic analysis of normal human cortical and trabecular bone. *Calcified Tissue International 61*, 480-486.

Paschalis, E. P., Mendelsohn, R., & Boskey, A. L. (2011). Infrared assessment of bone quality: a review. *Clinical Orthopaedics and Related Research, 469*(8), 2170-2178.

Paschalis, E. P., Recker, R., Di Carlo, E., Doty, S. B., Atti, E., & Boskey, A. L. (2003). Distribution of collagen cross-links in normal human trabecular bone. *Journal of Bone and Mineral Research, 18*(11).

Paschalis, E. P., Verdelis, K., Doty, S. B., Boskey, A. L., Mendelsohn, R., & Yamauchi, M. (2001). Spectroscopic characterization of collagen cross-links in bone. *Journal of Bone and Mineral Research, 16*(10).

Peterson, B., Whang, P. G., Iglesias, R., Wang, J. C., & Lieberman, R. J. (2004). Osteoinductivity of commercially available demineralized bone matrix. Preparations in a spine fusion model. *Journal of Bone Joint Surgery, 86*, 2243–2250.

Petibois, C., Wehbe, K., Belbachir, K., Noreen, R., & Déléris, G. (2009). Current Trends in the Development of FTIR Imaging for the Quantitative Analysis of Biological Samples. *Acta Physica Polonica A, 115*(2).

Pietrzak, W., Perns, S. V., Keyes, J., Woodell-May, J., & McDonald, N. (2005). Demineralized bone matrix graft: a scientific and clinical case study assessment. *Journal of Foot and Ankle Surgery, 44*, 345-353.

Pietrzak, W. S., Ali, S. N., Chitturi, D., Jacob, M., & Woodell-May, J. E. (2009). BMP depletion occurs during prolonged acid demineralization of bone: characterization and implications for graft preparation. *Cell and Tissue Banking, 12*(2), 81-88.

Rho, J.-Y., Kuhn-Spearing, L., & Zioupos, P. (1998). Mechanical properties and the hierarchical structure of bone. *Medical Engineering & Physics 20*, 92–102.

Robling, A. G., Castillo, A. B., & Turner, C. H. (2006). Biomechanical and Molecular Regulation of Bone Remodelling. *Annual Review of Biomedical Engineering, 8*, 455–498.

Roeges, N. P. G. (1994). *A guide to the complete interpretation of infrared spectra of organic structures*. Chichester, England: Wiley & Sons.

Rogers, K. D., & Daniels, P. (2002). An X-ray diffraction study of the effects of heat treatment on bone mineral microstructure. *Biomaterials, 23*, 2577–2585.

Saito, M., & Marumo, K. (2009). Collagen cross-links as a determinant of bone quality: a possible explanation for bone fragility in aging, osteoporosis, and diabetes mellitus. *Osteoporosis International, 21*(2), 195-214.

Shemesh, A. (1990). Crystallinity and diagenesis of sedimentary apatites. *Geochimica Et Cosmochimica Acta, 54*(9), 2433-2438.

Silva, L. d. M. S., Ebacher, V., Liu, D., McKay, H., Oxland, T. R., & Wang, R. (2005). Elasticity and Viscoelasticity of Human Tibial Cortical Bone Measured by Nanoindentation. *Materials Research Society Symposium Proceedings, 874*, L 5.8.1-L 5.8.6.

Torroni, A. (2009). Engineered Bone Grafts and Bone Flaps for Maxillofacial Defects: State of the Art. *Journal of Oral and Maxillofacial Surgery, 67*(5), 1121-1127.

Tzaphlidou, M. (2005). The role of collagen in bone structure: An image processing approach. *Micron, 36*(7-8), 593-601.

Urist, M. R. (1965). Bone formation by autoinduction. *Science, 150*, 893–899.

Verdelis, K. (2005). *Study of mineral and matrix maturation in dentin*. Ph.D. Dissertation, Faculty of North Carolina, Chapel Hill, USA.

Verdelis, K., Lukashova, L., Wright, J. T., Mendelsohn, R., Peterson, M. G. E., Doty, S., et al. (2007). Maturational changes in dentin mineral properties. *Bone, 40*(5), 1399-1407.

Viguet-Carrin, S., Follet, H., Gineyts, E., Roux, J. P., Munoz, F., Chapurlat, R., et al. (2010). Association between collagen cross-links and trabecular microarchitecture properties of human vertebral bone. *Bone, 46*(2), 342-347.

Viguet-Carrin, S., Garnero, P., & Delmas, P. D. (2005). The role of collagen in bone strength. *Osteoporosis International, 17*(3), 319-336.

19

Brain-Computer Interface Using Near-Infrared Spectroscopy for Rehabilitation

Kazuki Yanagisawa, Hitoshi Tsunashima and Kaoru Sakatani
Nihon University
Japan

1. Introduction

Currently, the Brain Computer Interface (BCI) is being studied vigorously. BCI extracts thoughts in the human brain as cranial nerve information and uses the information as inputs to control machinery and equipment. Fig. 1 describes schematic BCI system. If this system enables operating machinery and equipment directly from cranial nerve information without the subject moving his or her hands and feet, it can be applied to care-taking robots and rehabilitation for physically handicapped individuals.

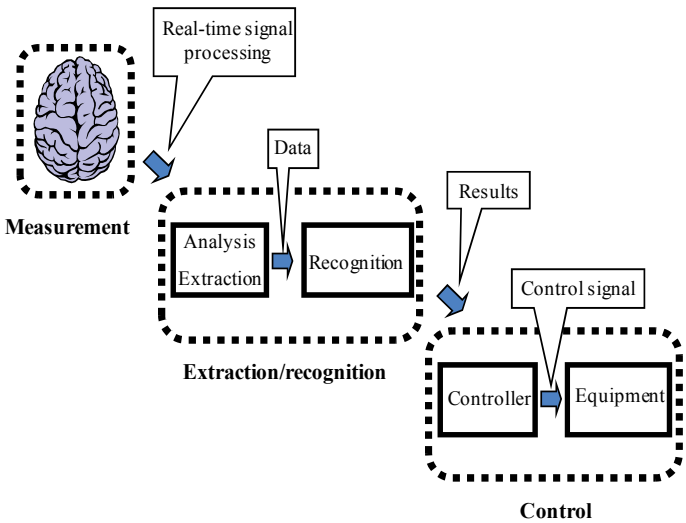

Fig. 1. Schematic of BCI system

BCI systems can be divided into two forms. The invasive form reads cranial nerve information using electrodes embedded directly into the brain. The non-invasive form reads cranial nerve activity from the surface of the head using near infrared spectroscopy (NIRS) or electroencephalography (EEG). as an example of invasive form, Donoghue LR. et al. extracted nerve activity of primary motor area and controlled a robot hand and mouse cursor (Hochberg LR et. Al, 2006). Though the invasive form has high signal accuracy, it imposes a heavy load on the user (e.g., surgery and infections after surgery).

Therefore, the non-invasive form has a wider applicable range. In a study on the non-invasive form, Pfurtscheller have developed BCI that physically handicapped individuals can control a character of the virtual reality (Pfurtscheller G. et. Al, 2006), electricaldriven hand (Pfurtscheller G. et. al, 2000) and functional electrical stimulation (FES) (Pfurtscheller G., 2003). Vaughan TM et al. have developed in prototype systems for everyday use in people's homes for locked-in patients (Vaughan TM, 2006). Many other studies of BCI have used EEG. However, EEG has low spatial resolution and it is vulnerable to electrical noise. In contrast, NIRS imposes fewer restrictions on body movement than EEG does and is more resistant to electric noise, so the load imposed on the user is less and electronic devices have no influence. And, NIRS has high space resolution. Therefore, the present study focuses on BCI that uses NIRS.

In an earlier study, Nagaoka et al. developed a NIRS-BCI rehabilitation system (Nagaoka T, 2010). In their study, electric stimuli corresponding to cranial nerve information are applied to the user's biceps brachii muscle by setting a threshold on signals measured from NIRS, in order to cause the elbow joint to move. But, Signals measured by NIRS are unstable because they include signals components that are irrelevant to the subject (e.g., noise of measuring instruments, heartbeat, and respiration). Moreover, a processing method for NIRS signals has not yet been established. For these reasons, it is difficult obtain a high identification rate by merely setting a simple threshold on NIRS signals. And this BCI system lacks versatility, because it is large system using multi-channel NIRS equipment.

In this study, we propose a new detection method that uses oxy-Hb and its differential as indexes for application to the NIRS-BCI rehabilitation system, detecting brain activity from the data measured using NIRS. First, we develop a BCI system to control robot arm using NIRS, and confirm that NIRS-BCI system can control machine and device. Next, we apply NIRS-BCI system developed for rehabilitation.

2. Near-infrared spectroscopy (NIRS)

Using near-infrared rays, NIRS non-invasively measures changes in cerebral blood flow. The principle of measurement was developed by Jöbsis (1977) , based on the measurement of hemoglobin oxygenation in the cerebral blood flow.

In uniformly distributed tissue, incident light is attenuated by absorption and scattering. The following expression, a modified Lambert-Beer law, was therefore used:

$$Abs = -\log(I_{out} / I_{in}) = \varepsilon \bar{l} C + S \,. \tag{1}$$

Here, I_{in} is the irradiated quantity of light; I_{out} is the detected quantity of light; ε is the absorption coefficient; C is the concentration; $\bar{l}$ is the averaged path length; and S is the scattering term.

If it is assumed that no scattering changes in brain tissue occur during activation of the brain, the change in absorption across the activation can be expressed by the following expression:

$$\Delta Abs = -\log(\Delta I_{out} / \Delta I_{in}) = \varepsilon \bar{l} \Delta C(\Delta X_{oxy}, \Delta X_{deoxy}) \,. \tag{2}$$

Furthermore, if the change in concentration (ΔC) is assumed to be proportional to the changes in oxygenated hemoglobin (ΔX_{oxy}) and deoxygenated hemoglobin (ΔX_{deoxy}), the following relational expression can be obtained:

$$\Delta Abs(\lambda_i) = \overline{l}[\varepsilon_{oxy}(\lambda_i)\Delta X_{oxy} + \varepsilon_{deoxy}(\lambda_i)\Delta X_{deoxy}]. \quad (3)$$

The absorption coefficients of oxygenated hemoglobin and deoxygenated hemoglobin at each wavelength, $\varepsilon_{oxy}(\lambda_i)$ and $\varepsilon_{deoxy}(\lambda_i)$, are known. As a result, $\overline{l}\Delta X_{oxy}$ and $\overline{l}\Delta X_{deoxy}$ can be obtained by performing measurements with near-infrared rays of two different wavelengths and solving simultaneous equations for Equation 3. However, the physical quantity obtained here is the product of the change in concentration and the averaged path length. In general, this averaged path length $\overline{l}$ varies greatly from one individual to another, and from one part of the brain to another. Caution must therefore be exercised in evaluating the results.

In general, changes in oxygenated hemoglobin and deoxygenated hemoglobin when the brain is activated and restored to the original state exhibit the trend illustrated in Figure 2 (Huettel, 2004).

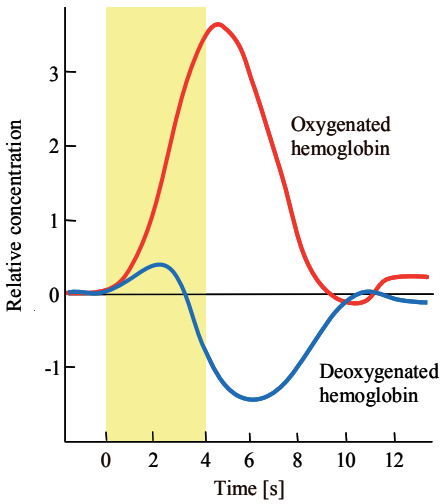

Fig. 2. Schematic of changes in hemoglobin concentration due to neural activity

3. Brain-computer interface using NIRS

Figure 3 depicts a robot control system that uses NIRS-BCI. This system is composed of a cerebral function measurement section, a feature extraction and recognition section, and a device control section. In the cerebral function measurement section, the subject's oxy-Hb is measured using a multichannel NIRS instrument, OMM-3000, made by Shimadzu Corporation, Japan. The system operated at three different wavelengths of 780,805,830nm. In the feature extraction and recognition section, the threshold is obtained by analyzing the original signal of oxy-Hb that was measured. When oxy-Hb after analysis exceeds the threshold obtained in the feature extraction and recognition section, the on signal is sent to the device control section in order to enable rotation of the joint of the robot arm (MR-999; Elekit, Japan).

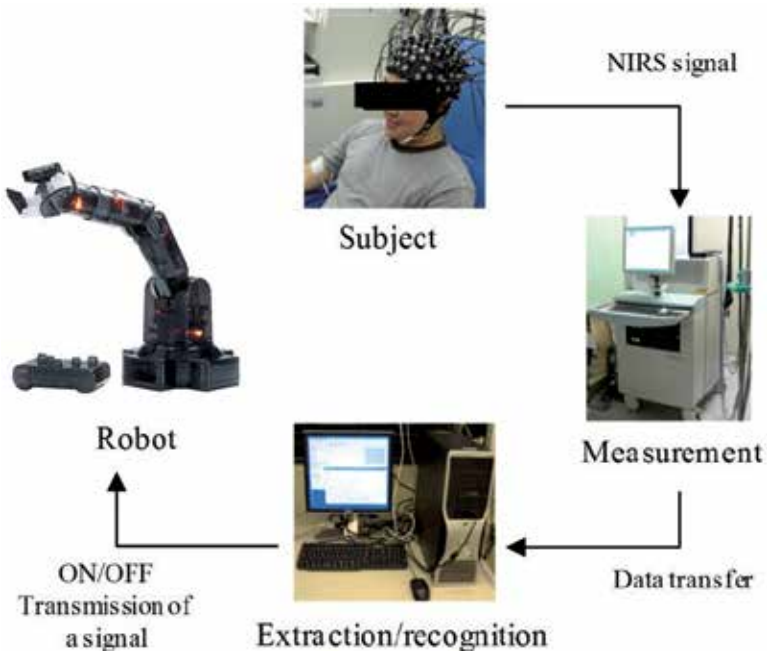

Fig. 3. BCI robot control system

Subjects were conducted using the robot arm control system depicted in Fig. 1. Five trials were carried out, with each trial consisting of 10sec of pre-task rest, 30sec of task, and 10sec of post-task rest. The first two trials were defined as the learning stage, where the feature extraction and recognition section learned the fluctuation pattern of the subject's oxy-Hb without moving the robot. In the third and subsequent trials, the robot's arm was rotated according to the learned pattern corresponding with oxy-Hb. The subject was instructed to perform grasping during tasks and instructed to rest during the rest time. The motor area was selected as the measurement site.

Optical fibers were arranged in 4×4 matrices on the right and left sides to perform measurement, with a total of 48 channels (Fig.4). The subjects were two healthy male

volunteers in their twenties. Prior informed consent was obtained from all subjects, in an effort to ensure full consideration of their safety and protection of their human rights.

In the detection method that used a simple threshold, the moving average was obtained. The threshold was set to 20% of the maximum oxy-Hb during the first two trials; detection was made in the third and subsequent trials, and an on state was judged when oxy-Hb exceeded the threshold.

Changes in concentration of oxy-Hb and the detection results for grasping tasks are depicted in Fig.5. ON detections were made in tasks from the first to second trials. OFF decisions in rest were wrong. ON and OFF detections alternated within a short time, indicating instability.

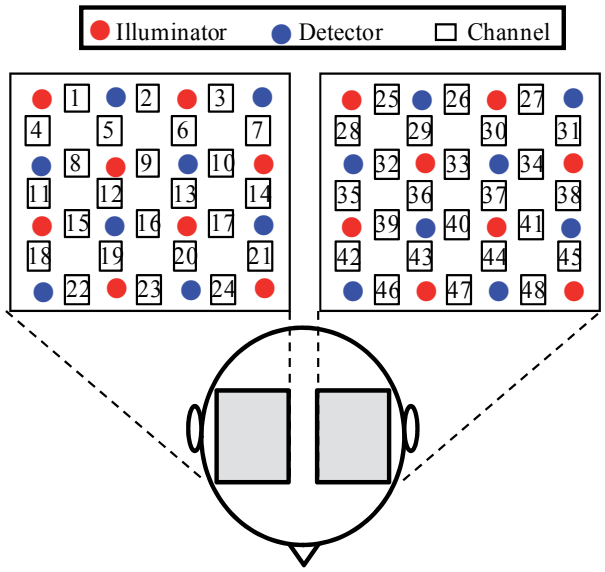

Fig. 4. Position of optical fibers and channels for recording NIRS signals (grasping tasks: matrix, 48 channels)

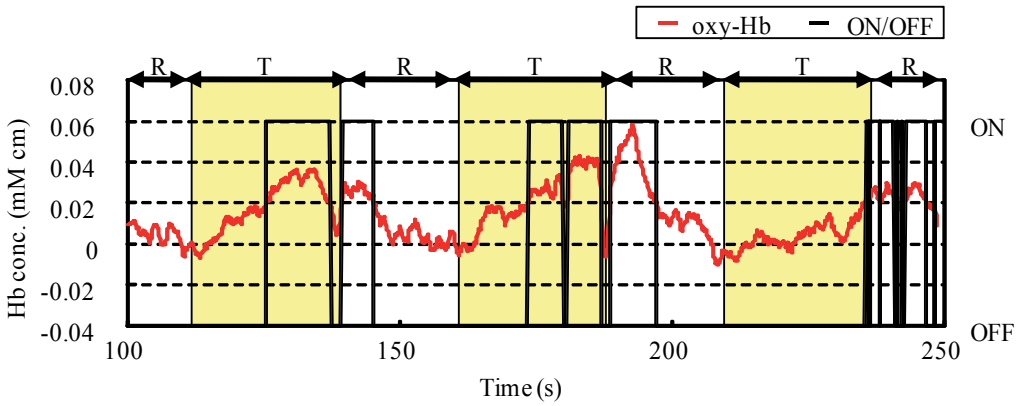

Fig. 5. Result of ON/OFF decision using conventional method

4. Signal processing method for NIRS-BCI

4.1 Detection method of brain activity

NIRS signals also include signals that are not related to brain activity (e.g., measuring device noise, influences of respiration, and fluctuations of blood pressure). Therefore, to evaluate brain activity in detail, it is necessary to remove these extraneous signals. For this purpose, we selected the channels that have a good S/N ratio and exhibit remarkable task-related fluctuations (44 channels (contralateral motor cortex) in this case), and subjected the NIRS signals obtained from them to magnetic resonance angiogram analysis (MRA) (Kojima et. al, 2006, Yanagisawa et. al, 2009, Tsunashima et. al, 2009) through discrete wavelet transformation to decompose and reconfigure the signals.

Figure 6 presents the MRA results for oxy-Hb in the 44 channels, where task-related changes were remarkable. The components of the very short frequency bands of d_1 and d_2 correspond to the measurement noises. The components of d_3 and d_4 which contains the signal period from 3 to 4 seconds correspond to the breathing. The components of d_5 and d_6 include changes of blood pressure (Elwell C.E et al. ,1999). The trend of the whole experiment was extracted on the approximated component (a_{10}). Because the interval of repetition of tasks and rests was 50sec, the d_8 component was the central component of task-related changes. Therefore, signals were reconstructed by adding the d_7 , d_8 , d_9 and d_{10} components.

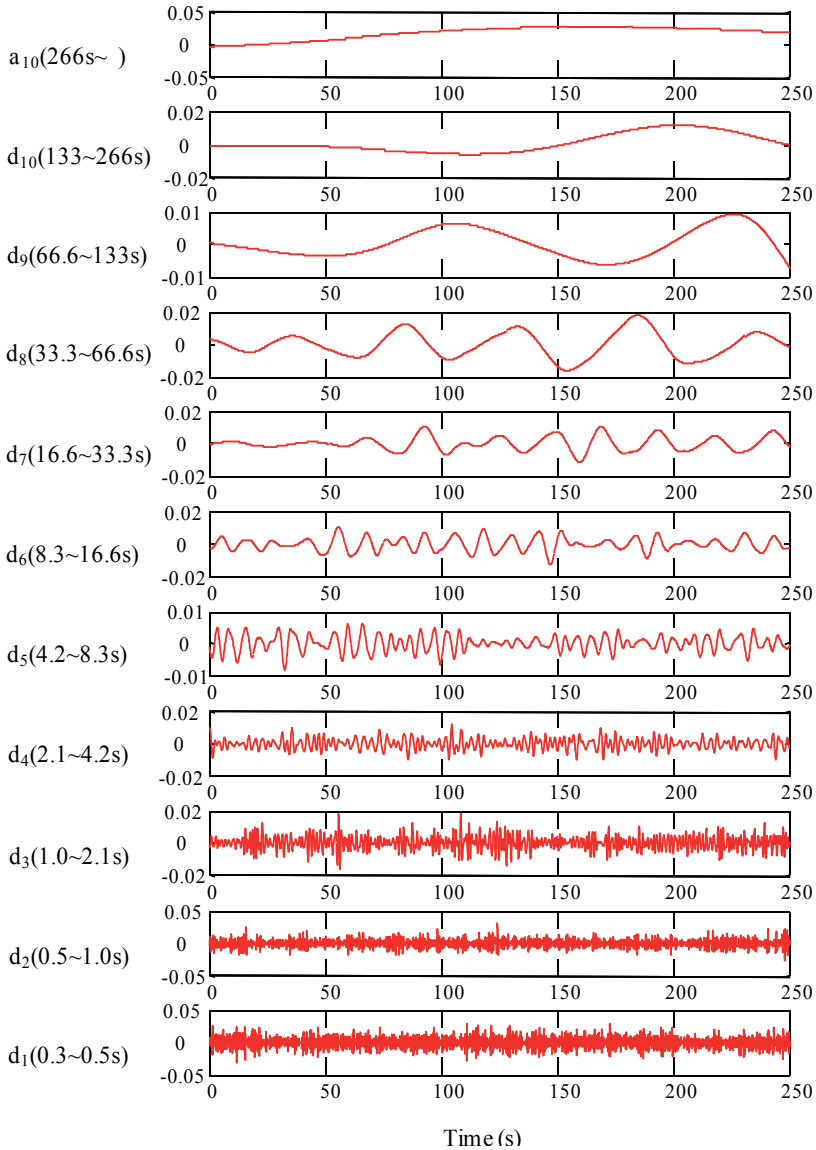

Fig. 6. Decomposition of NIRS signal (channel 44)

Reconstructed signals from channel 44 are illustrated in Figure 7. Results revealed that oxygenated hemoglobin increased and the brain was activated during grasping tasks.

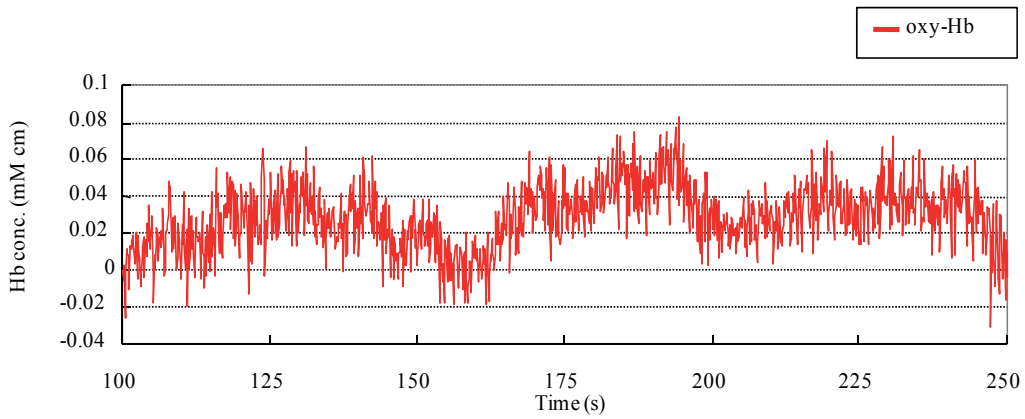

a. Original signal

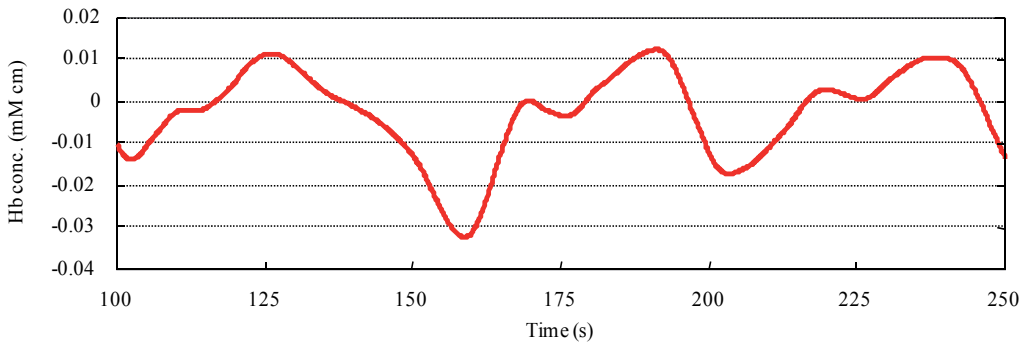

b. Reconstructed NIRS signal

Fig. 7. Comparison of original signal and reconstructed signal (channel44)

We propose the detection method of brain activity. NIRS can measure changes in concentrations of oxy-Hb and deoxy-Hb, as well as the total-Hb signal (the sum of these two values). In this study, we focus on the oxy-Hb signal because changes in concentration of oxy-Hb are highly correlated with the regional cerebral blood flow (rCBF) (Sakatani et, al, 2007), and an increase in rCBF reflects an increase in neural activity (Jueptner, et. al, 1195) Furthermore, we evaluate brain activity using two indexes, oxy-Hb and its differential, because the differential of oxy-Hb is correlated with the workload of the task (Shimizu T. et. al, 2009).

Common fluctuations of oxy-Hb and its differential are depicted in Fig. 8 (a). As the detection method, we propose that oxy-Hb be taken on the horizontal axis and the differential of oxy-Hb on the vertical axis, and detection be made from the area of its trajectory. The trajectory of the activity in Fig. 8(a) is depicted in Fig. 8(b). When the trajectory passes through the red zone in Fig. 8(b), it can be assumed that brain activity is occurring.

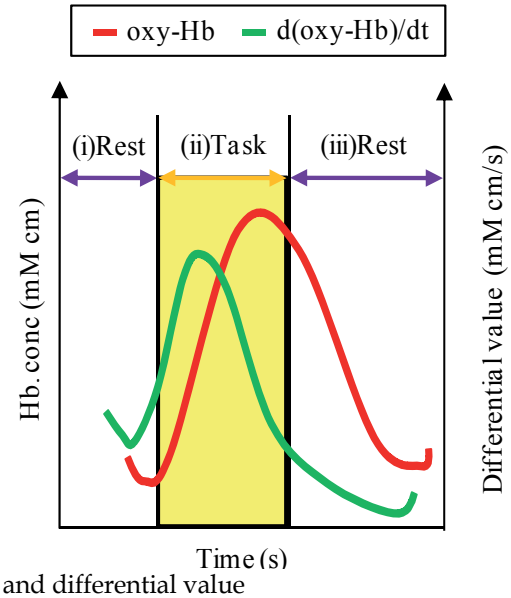

a. Change of oxy-Hb and differential value

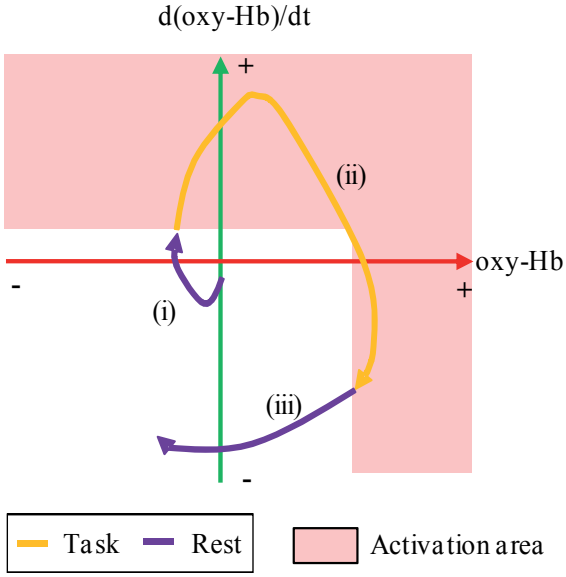

b. Trajectory of oxy-Hb and d(oxy-Hb)/dt

Fig. 8. Relations between oxy-Hb and differential

About grasping tasks, we selected the channels that have a good S/N ratio and exhibit remarkable task-related fluctuations (44 channels (contralateral motor cortex) in this case), and subjected the NIRS signals obtained from them to MRA through discrete wavelet transformation to decompose and reconfigure the signals.

Figure 9 depicts the trajectory with oxy-Hb on the horizontal axis and the differential of oxy-Hb on the vertical axis using the signals from grasping tasks as reconfigured. As with the

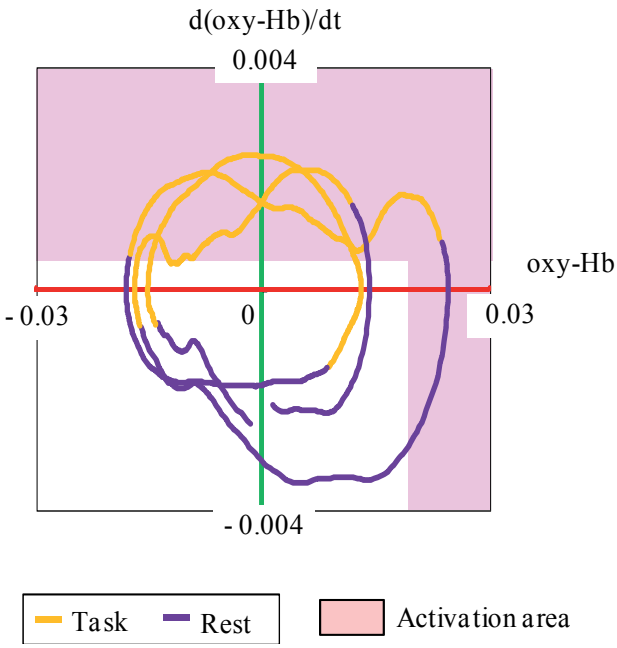

Fig. 9. Trajectory of oxy-Hb and differential value (grasping task)

trajectory depicted in Fig. 8 (b), the trajectory passes through the red zone, where brain activity is assumed to be occurring during the task.

The area where both oxy-Hb and its differential increase (first quadrant) is assumed to be the area where brain activity is occurring. When the differential of oxy-Hb is large, it can be assumed that brain activity is occurring even if the value of oxy-Hb is small. When the activity level is low, such as during rest time, the trajectory tends to draw a circle of the area of activity around the datum point. To avoid judging the trajectory of the signals that pass through the area around the datum point as a sign of activity, a threshold will be set on the differential of oxy-Hb. However, the differential of oxy-Hb does not always continue to increase when activity is occurring, so we assume that activity is also occurring when oxy-Hb is above a threshold level. Furthermore, when the trajectory does not stay in the area for more than a specified period (2.0s), we assume that it is an influence of artifact and that no activity is occurring.

4.2 Detection result

Figure 10 presents the detection results with the proposed detection method applied. Comparison with the results of the conventional detection method presented in Fig. 35confirmed the ON detection during all tasks. Furthermore, the threshold was set on the value of oxy-Hb alone in the conventional detection method, so it was impossible to make the ON detection during the first half of a task with a low level of oxy-Hb, and the detection result was delayed even if relevant brain activity could be confirmed. The proposed detection method, however, reduced the delay due to using the differential of oxy-Hb.The proposed detection method did enable highly accurate detection of many subjects, compared with the conventional detection method.

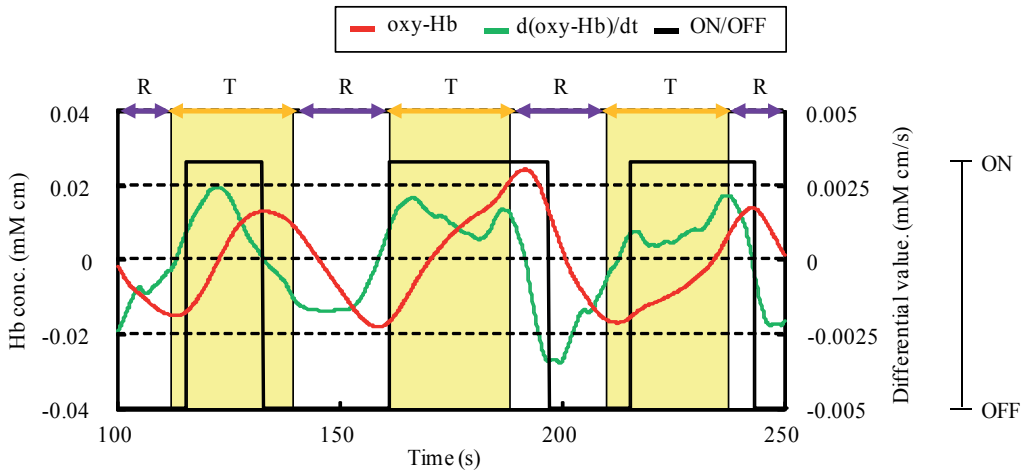

Fig. 10. Result of ON/OFF decision using proposed method (grasping task)

On the same condition, the subject was instructed to imagine grasping without moving the hand during the tasks. The detection of brain activity during imagined grasping tasks using the proposed detection method is presented in Fig. 11. Also during imagined grasping tasks, as in actual grasping tasks in Fig. 10, the ON detection was confirmed during all tasks. Furthermore, a correct detection could be made with little time delay, due to using the differential of oxy-Hb. These results confirm that the proposed detection method is valid for imagined grasping tasks as well.

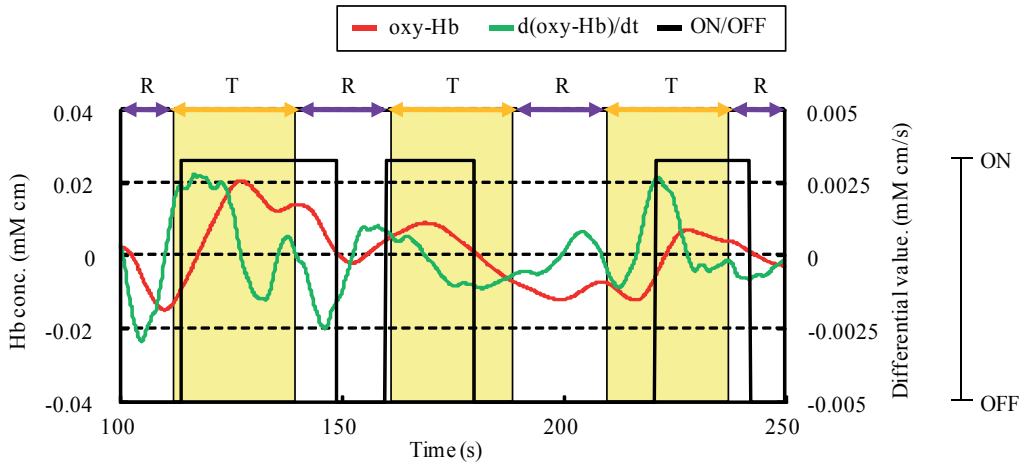

Fig. 11. Result of ON/OFF decision using proposed method (imagined grasping tasks)

5. IRS-BCI system for rehabilitation

5.1 BCI-rehabilitation system

In the NIRS-BCI rehabilitation system (Fig.12), the signals measured with NIRS are transferred to the analysis workstation in real time. A threshold is set based on oxy-Hb

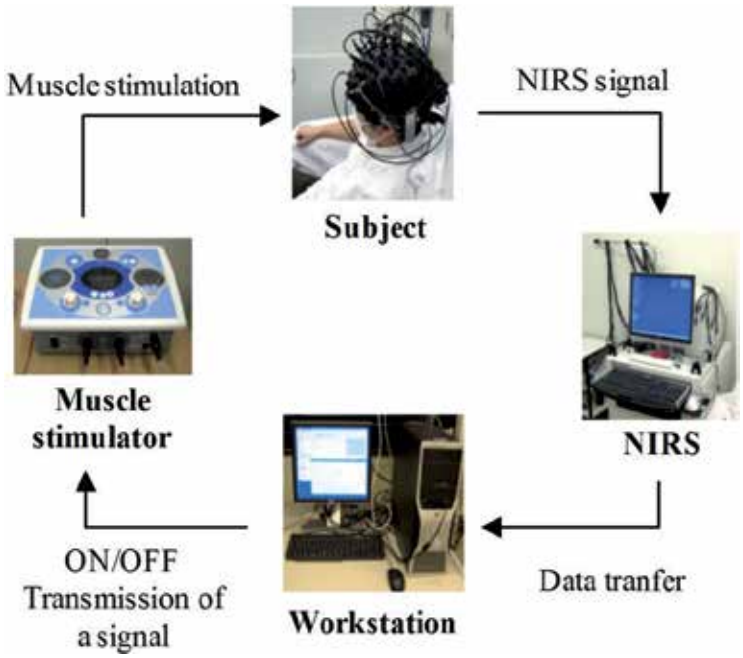

Fig. 12. NIRS-BCI rehabilitation system

signals that are transferred; when the signals exceed the threshold, the percutaneous electrical stimulator gives percutaneous electrical stimulation to the biceps brachii muscle to induce an elbow joint refraction movement. Therefore, even those who cannot move their arms can actually participate in rehabilitation.

5.2 Detection of brain activity

We conducted experiments using the NIRS-BCI rehabilitation system depicted in Fig. 12. In the experiment, five cycles are performed: each cycle consists of 10sec of pre-task rest, 30sec of task, and 10sec of post-task rest. The threshold is set during the first two cycles, and muscle stimulation is applied when oxy-Hb has exceeded the threshold during the third and succeeding cycles.

Two kinds of tasks were set: one to perform actual grasping and the other to imagine grasping. The subject was instructed to perform grasping with right hand during actual grasping tasks, and to imagine grasping without moving the hand during the imagined grasping tasks. The biceps brachii muscles of the left arm were stimulated. In either task, the subject was instructed to rest during rest time.

To consider application of this system for rehabilitating patients with hemiplegia, muscles must be stimulated by detecting brain activity during imagined grasping tasks instead of during actual grasping tasks. However, large differences exist between individuals' brain activity during imagined grasping tasks. Therefore, in this study, we confirm the validity of the proposed detection method by conducting grasping tasks associated with significant brain activity appears remarkably. Furthermore, we will apply the proposed detection method to brain activity during imagined grasping tasks.

Brain activity in the motor area was measured using NIRS. The measurement device was a near-infrared device made by Shimadzu Corporation (multichannel NIRS instrument, OMM-2001, Shimadzu Corporation, Japan). Figure 13 depicts a scene of the experiment. With 4×4 probes arranged on the left and right sides, measurement was performed with a total of 48 channels (Fig. 4). Seven healthy males in their twenties were selected as subjects, and informed consent was obtained from them before conducting the experiment after explanation of the experiment purpose.

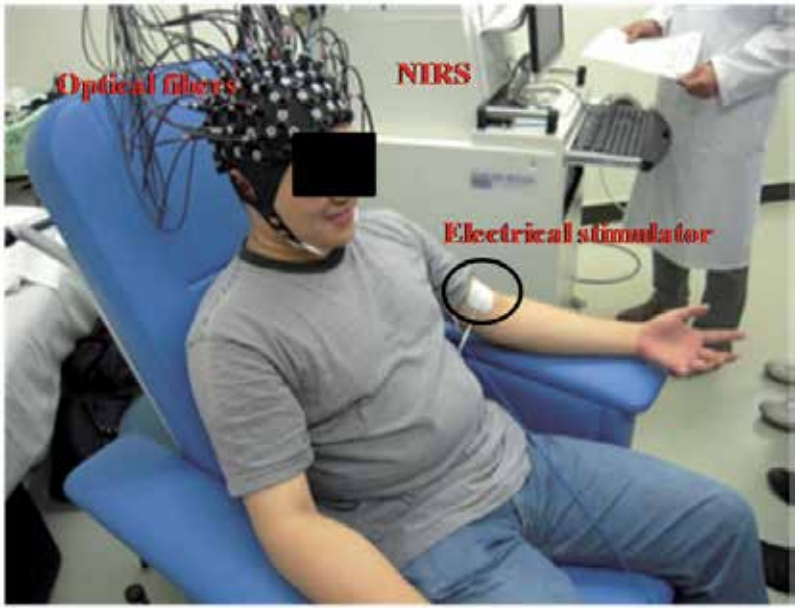

Fig. 13. Scene of the experiment

In the conventional detection method, the z-score was established from the mean value of the first two cycles of the signals measured by NIRS, and the standard deviation and the moving average were obtained. The threshold was set to 20% of the maximum oxy-Hb value obtained during the first two cycles; detection was made on the third and succeeding cycles, where the values of oxy-Hb that exceeded the threshold were judged as ON.

Changes in concentration of oxy-Hb during grasping tasks and the detection results are presented in Fig. 14 ON detection was observed during the first task; however, it was confirmed that no ON detection was made during the succeeding tasks, even though some changes in oxy-Hb concentration of were detected.

Figure 15 presents the detection results with the proposed detection method applied. Comparison with the results of the conventional detection method presented in Fig. 14 confirmed the ON detection not only during the first task but during all tasks. Furthermore, the threshold was set on the value of oxy-Hb alone in the conventional detection method, so it was impossible to make the ON detection during the first half of a task with a low level of oxy-Hb, and the detection result was delayed even if relevant brain activity could be confirmed. The proposed detection method, however, reduced the delay due to using the differential of oxy-Hb.

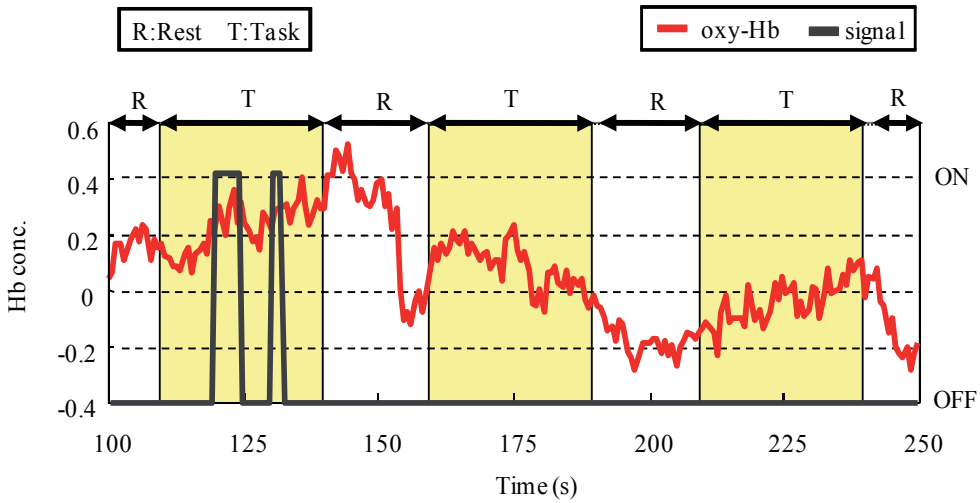

Fig. 14. Result of ON/OFF decision using conventional method

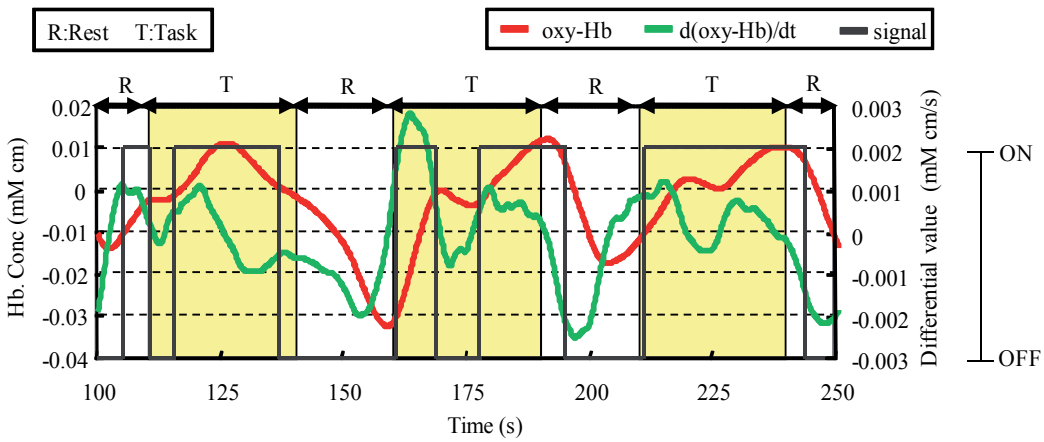

Fig. 15. Result of ON/OFF decision using proposed method (grasping task)

Some problems exist in the proposed detection method. For example, the ON detection was made during the rest time before starting the task because the differential had increased, and the OFF detection was made during the second task because the differential of oxy-Hb decreased during the rest time between tasks. However, the proposed detection method did enable highly accurate detection of many subjects, compared with the conventional detection method.

The detection of brain activity during imagined grasping tasks using the proposed detection method is presented in Fig. 16. Also during imagined grasping tasks, as in actual grasping tasks in Fig. 15, the ON detection was confirmed during all tasks. Furthermore, a correct detection could be made with little time delay, due to using the differential of oxy-Hb. These results confirm that the proposed detection method is valid for imagined grasping tasks as well.

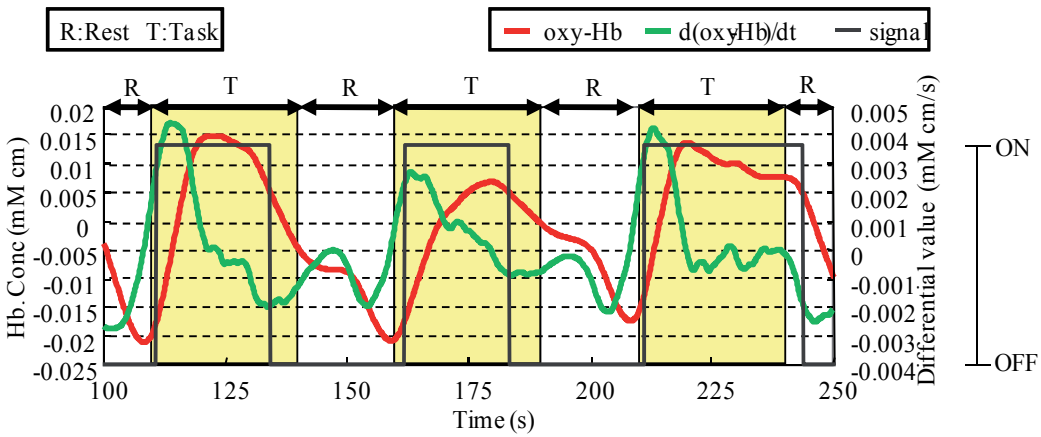

Fig. 16. Result of ON/OFF decision using proposed method (imagined grasping tasks)

6. Summary

In this study we proposed a new detection method that uses oxy-Hb and its differential as indexes for application to the NIRS-BCI rehabilitation system, detecting brain activity from the data measured using NIRS. First, we developed a BCI system to control robot arm using NIRS, and confirmed that NIRS-BCI system can control machine and device. When a detection method with a simple threshold is employed, no stable operation was made during the tasks. This study proposes a method by which oxy-Hb is plotted on the horizontal axis and the differential of oxy-Hb on the vertical axis, and brain activity is judged from the area of the plotted trajectory. As a result, we confirmed that the proposed detection method enables highly accurate detection with little time delay compared with the conventional detection method, during both grasping tasks and imagined grasping tasks.

Next, we applied NIRS-BCI system developed for rehabilitation. We also confirmed that the proposed detection method enables highly accurate detection compared with the detection method with a simple threshold during both grasping tasks and imagined grasping tasks. These results confirm the validity of the proposed detection method for the NIRS-BC rehabilitation system. We gathered experiment data from healthy men in the present study, but in future studies, we will develop portable NIRS-BCI rehabilitation system, and conduct experiments on patients with hemiplegia to put this system into practical use.

Furthermore, the detection method proposed in this study uses the oxy-Hb level and its differential alone as indexes, so it is applicable to the brain activity of the prefrontal area while the brain is performing cognition tasks, where deoxy-Hb exhibits various fluctuation patterns (Toichi M. et. al, 2004). Therefore, BCI can be expected to be applied to measure other than the motor area (e.g., the field of entertainment).

7. Acknowledgment

This work was supported by the Nihon University Multidisciplinary Research Grant in 2010 and 2011.

8. References

Hochberg LR., Serruya MD., Friehs GM., Mukand JA., Seleh M., Caplan AH, Branner A., Chen D., Penn RD, Donoghue JP. (2006), "Neuronal ensemble control of prosthetic devices by a human with tetraplegia", Nature Vol.442 (7099), pp.164 -171

Pfurtscheller G., Leeb, R., Keinrath C., Friedman D., Neuper, C. (2006)"Walking from thought", Brain Res Vol.1071 (1), pp.145-152

Pfurtscheller G., Guger C., Müller G., Krausz G., Neuper C. (2000), "Brain oscillations control hand orthosis in a tetraplegic", Neurosci Lett Vol.292 (3), pp.211-214

Pfurtscheller G., Müller GR., Pfurtscheller J., Gerner HJ., Rupp R. (2003), "'Thought' - control of functional electrical stimulation to restore hand grasp in a patient with tetraplegia", Neurosci Lett 351, pp.33-36

Vaughan TM, McFarland DJ, Schalk G, Sarnacki WA, Krusienski DJ, Sellers EW, Wolpaw JR. (2006), "The Wadsworth BCI Research and Development Program: at home with BCI", IEEE Trans Neural Syst Eng Vol.14 (2), pp.229 -233

Nagaoka T., Sakatani K, Awano T., Yokose N., Hoshino T., Murata Y., Katayama Y., Ishikawa A., Eda H. (2010), "Development of a new rehabilitation system based on brain-computer interface using near infrared spectroscopy," *Advances in Experimental Medicine and Biology*, Vol. 662, pp. 497-503

Jöbsis, F.F. (1977), "Non-invasive infrared monitoring of cerebral and myocardial oxygen sufficiency and circulatory parameters", Science, Vol. 198, pp. 1264-1267

Huettel, S. A. (2004). *Functional Magnetic Resonance Imaging,* Sinauer Associate, Inc., ISBN 978-0878932887, USA

Kojima T., Tsunashima H., Shiozawa T., Takada H., Sakai T. (2006), "Measurement of Train Driver's Brain Activity by Functional Near-Infrared Spectroscopy (fNIRS)," Computers in Railways X: Computer System Design and Operation in the Railway and Other Transit Systems, pp. 245-254

Yanagisawa K., Tsunashima H., Marumo Y., Hirose S., Shimizu T., Taira M., Haji T. (2009), "Measurement and evaluation of higher brain function by using functional near-infrared spectroscopy (fNIRS)", Journal of Human Interface Society, Vol. 11(2) , pp. 183-191 (in Japanese)

Tsunashima H., Yanagisawa K. (2009), "Measurement of brain function of car driver using functional near-infrared spectroscopy (fNIRS)," Computational Intelligence and Neuroscience, Vol.2009

Elwell C.E., Springett R., Hillman E., Delpy D.T. (1999), "Oscillations in Cerebral Haemodynamics, Implications for Functional Activation Studies", Advances in Experimental Medicine and Biology, Vol. 471, pp. 57-65

Sakatani K., Murata Y., Fujiwara N., Hoshino T., Nakamura S., Kano T., Katayama Y. (2007), "Comparison of blood-oxygen-level-dependent functional magnetic resonance imaging and near-infrared spectroscopy recording during functional brain activation in patients with stroke and brain tumors," Journal of Biomedical Optics, Vol. 12 (6), p. 062110

Jueptner, M., Willer,C. (1995), "Dose measurement of regogional cerebral blood flow reflects synaptic activity?- implications for PET and fMRI," Neuroimage, Vol. 2, pp.148-156

Shimizu T., Hirose S., Obara H., Yanagisawa K., Tsunashima H., Marumo Y., Haji T., Taira M. (2009), "Measurement of frontal cortex brain activity attributable to the driving

workload and increased attention," SAE International Journal of Passenger Cars - Mechanical Systems, Vol. 2 (1), pp.736-744

Toichi M., Findling RL., Kubota Y., Calabrese JR., Wiznitzer M., McNamara NK., Yamamoto K. (2004), "Hemodynamic differences in the activation of the prefrontal cortex: attention vs. higher cognitive processing," *Neuropsychologia*, Vol. 42 (5), pp. 698-706

20

Biopolymer Modifications for Biomedical Applications

M.S. Mohy Eldin[1,*], E.A. Soliman[1], A.I. Hashem[2] and T.M. Tamer[1]
[1]*Polymer Materials Research Department, Advanced Technologies and New Materials Research Institute (ATNMRI), Mubarak City for Scientific Research and Technology Applications (MUCSAT), New Borg El-Arab City, Alexandria*
[2]*Organic Chemistry Department, Faculty of Science, Ain-Shams University, Cairo*
Egypt

1. Introduction

Chitosan is typically obtained by deacetylation of chitin under alkaline conditions, which is one of the most abundant organic materials, being second only to cellulose in the amount produced annually by biosynthesis. Chitosan is a linear polysaccharide, composed of glucosamine and *N*-acetyl glucosamine units linked by (1–4) glycoside bonds. The content of glucosamine is called the degree of deacetylation (DD). In fact, in a general way, it is considered that when the DD of chitin is higher than about 50%(depending on the origin of the polymer and on the distribution of acetyl groups along the chains), it becomes soluble in an aqueous acidic medium, and in these conditions, it is named chitosan. The DD also affects the biodegradability of this polymer, and for DD above 69% a significant decrease of *in vivo* degradation has been found (1). Chitosan displays interesting properties such as biocompatibility, biodegradability (3, 4) and its degradation products are non-toxic, non-immunogenic and non-carcinogenic (5, 6). Therefore, chitosan has prospective applications in many fields such as biomedicine, waste water treatment, functional membranes and flocculation. However, chitosan is only soluble in few dilute acid solutions, which limits its applications.

Recently, there has been a growing interest in the chemical modification of chitosan in order to improve its solubility and widen its applications (7–9). Derivatization by introducing small functional groups to the chitosan structure, such as alkyl or carboxymethyl groups (10, 11) can drastically increase the solubility of chitosan at neutral and alkaline pH values without affecting its cationic character.

Substitution with moieties bearing carboxylic groups can yield polymers with polyampholytic properties (12). The antimicrobial activity of chitosan increases with decreasing pH (13-17). This is due to the fact that the amino groups of chitosan become

* Corresponding Author

ionized at pH below 6 and carry a positive charge. Unmodified chitosan is not antimicrobially active at pH 7, since it does not dissolve and also since it does not contain any positive charge on the amino groups (18, 19). The antimicrobial activity of chitosan also increases with increasing degree of deacetylation, due to the increasing number of ionisable amino groups (19). Several approaches were done to increase the antimicrobial activity of chitosan by introduce amino groups, on the primary amino groups of the back bone of chitosan polymer chains but it was failed (20). The obtained results were explained based on the remote position of the new introduced amino groups.

In this work, we aim to increase both the solubility and antimicrobial activity of chitosan via increase the amino groups on the polymer back bone by attaching amino groups directly on the hydroxyl groups of polysaccharide to wide its applications.

A new technique has been used to avoid the consumption of the original amino groups of the chitosan as sites of grafting, so chitin was first grafted with amino groups in separate step then it was de-acetylated to have the aminated chitosan. Aminated chitosan was tested as antimicrobial agent and aminated chitosan membranes were prepared, characterized and evaluated for wound dressing applications.

2. Modified chitosan membranes

Modified chitosan was prepared through introducing extra amino groups to its structure. A new chemical route was used to graft selectively the extra amino groups on the hydroxyl groups of chitosan rather than its amine ones. To achieve this goal, chitin has been activated first with PBQ then amino groups were grafted using ethylene diamine as source of amino groups. The obtained aminated chitin was finally de-acetylated (21-22) to have modified chitosan with extra amino groups as shown in the following schema (figure 1). Different concentrations of PBQ were used to have modified chitosan with different amine content (table1). From the table it is clear that increasing PBQ concentration increased the nitrogen content in an obvious manner. This increment starts in linear way then turns to level off.

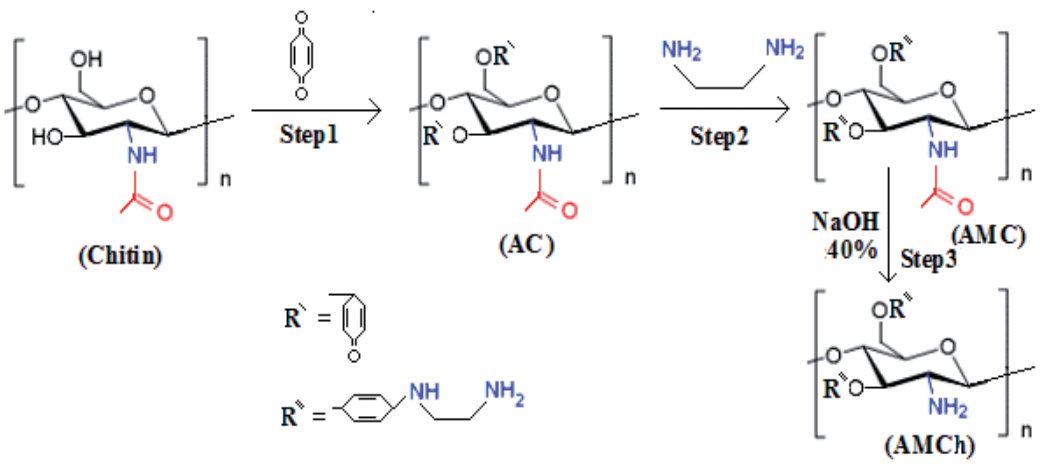

Fig. 1. Schematic diagram for synthesis of aminated chitosan.

PBQ :chitin ratio	N %
Chitosan control	7.42
0.0935	7.50
0.187	7.56
0.374	8.73
0.545	9.60
0.747	9.62

Table 1. Effect of PBQ concentration on the nitrogen content of modified chitosan

2.1 Characterization of modified chitosan membranes

In the characterization of modified chitosan membranes, different characters were monitored to show the effect of modification process on their properties. The occurrence of amination process was verified through examination of the chemical structure changes using FT-IR, TGA analysis and solubility test.

The FTIR spectrum of the modified chitosan and intermediates to verify structure changes was obtained using FTIR-8400S SHIMDZU. Japan. As shown in figure 2, the major difference are the wide peaks at 3431 cm^{-1}, (I) corresponding to the stretching vibration of $-NH_2$ and OH groups became more sharp at modified chitosan as result of alternation of –OH groups with $-NH_2$ groups. Absorption band intensity at 1560, 1649 cm^{-1} (II) corresponding to carbonyl bands have been increased in (AC), curve (b), via introduce further carbonyl groups of PBQ as illustrated in schema1, then return to normal at aminated chitin, curve (c). Finally, peaks will reduced after deacetylation as a result of removal the acetyl groups in modified chitosan. This observation confirmed the occurrence of the modification process with different steps indicated in figure 1.

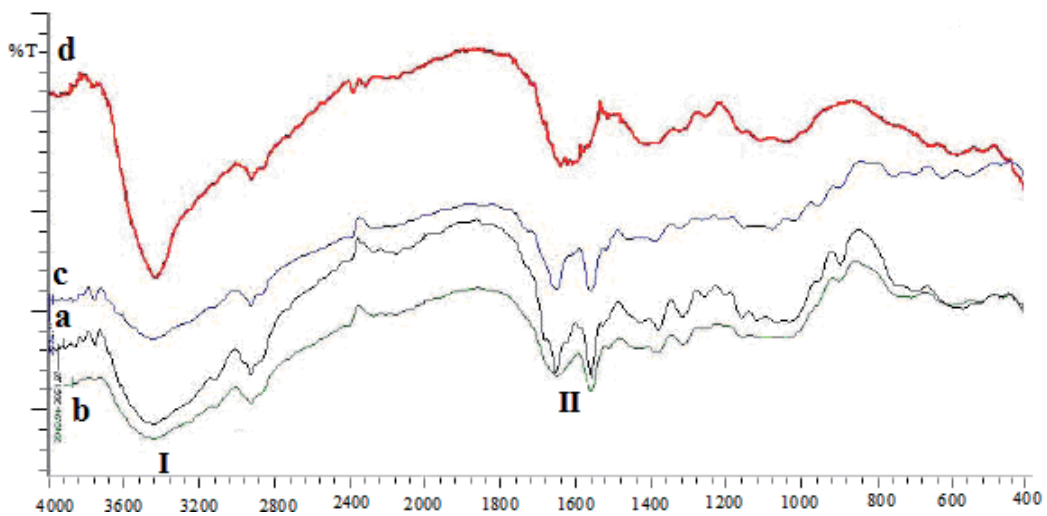

Fig. 2. FTIR spectra of chitin (a), activated chitin (AC) (b), aminated chitin (c) and modified chitosan (d).

Changes in the structure of modified chitosan via introducing extra hydrophilic amine groups were expected to influence its solubility. The solubility of chitosan and the modified chitosan in different pH was measured as in table 2. The improving of the solubility of modified chitosan over chitosan itself was attributed to grafted amino groups. The aminated chitosan solubility at pH range from 5.0 to 6.0 was almost double of its unmodified chitosan counter part. These results, along with the obtained data from FT-IR analysis, confirmed the occurrence of amination process.

pH	Chitosan solubility (%)	Modified chitosan solubility (%)
4	97.2	99
5	41.7	81.1
6	17.9	29.6
7	0	3.9
8	0	0

Table 2. Solubility percent of chitosan and modified chitosan in different pH

Thermal graph metric analysis of chitosan and aminated chitosan membranes with different content of glycerol was done; figures 3. The data of the TGA was summarized in table (3). From the table a number of informations were abstracted. First notice is the increase of weight loss in the temperature range 0 – 118^{o}C which refers to loss of water. The water loss

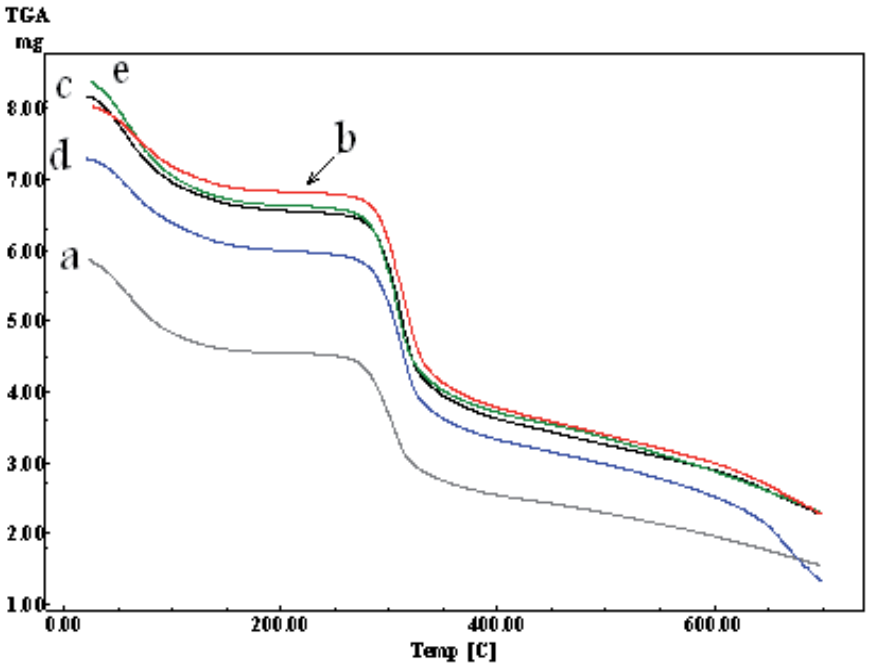

Fig. 3. Thermal graph metric diagrams of chitosan membrane (a), chitosan modified membrane (b), chitosan modified membrane (glycerol 2%)(c), chitosan modified membrane (glycerol 4%)(d), and chitosan modified membrane (glycerol 6%)(e).

Sample	T50	Weight loss at	
		$T_{(0-118)}$	$T_{(240-380)}$
Chitosan	351.6	12.28 %	42.9 %
Aminated chitosan (0% glycerol)	325.89	19.638 %	42.47 %
Aminated chitosan (2% glycerol)	333.06	16.523 %	43 %
Aminated chitosan (4% glycerol)	346.72	14.415 %	42.68 %
Aminated chitosan (6% glycerol)	335.86	17.741 %	42.57 %

Table 3. Thermo-gravimetric data of chitosan and aminated chitosan membranes with different percent of glycerol

increases by about 50% upon amination. This observation confirms the modification of membranes hydrophilicty as a result of the amination process. The second notice is the shift of T50, temperature needed to lose 50% of sample weight, to lower temperature which came as a result of chemical structure modification and as a result its hydophilicity improvement. The last notice is the insignificant changes of the characteristic thermo-gram of pristine chitosan in the temperature range 240 -380^{o}C, which indicates the absence of crosslinking role of the glycerol content between aminated chitosan chains.

The membrane was prepared as the following 1 gm of chitosan or aminated chitosan was dissolved in 50 ml 2% acetic acid. Glycerol was added to the solution as a plasticizer. The solution was strained through cheesecloth to remove any un-dissolved particulates. The solution was then casting in a clean Petri dish and left at room temperature for 48 hours to ensure complete solvent evaporation. The humidity of the room was not controlled. Once the membrane was dried and separated from the Petri dish it was rinsed with 500 ml of 1 M of NaOH. The rinsing of the membrane in a caustic solution gives the films water-resistance by neutralizing and removing any acetic acid anions present in the membrane then the membrane was washed with distilled water to remove the traces of alkali and neutralized it.

Finally, the wet membranes were spread out and attached to the clean glass support with clamps and allowed to dray for 24 hours at room temperature. The resulting membranes were transparent and flexible.

Physico-chemical properties like water uptake, tensile strength, elongation (23), surface roughness, SEM and finally water vapor permeability have been conducted for the casted membranes. The obtained results show the impact of modification process on the properties of chitosan membranes through evaluation of their bio-characters such as; antimicrobial activity (24-25), hemocompatibility (26), cytotoxicity (27), and biodegradability (28).

Water up-take

The introduction of biomaterials surface in blood creates a new interface between cellular and fluid components of blood and material. This results in a thermodynamic driving force that acts to reduce the solid-liquid interfacial free energy at this interface. Ignoring interactions with blood cellular components, the blood plasma-biomaterial interfacial free energy is a thermodynamic quantity that incorporates the surface free energy contributions of both solid and liquid phases and provides a measure of the driving force for the adsorption of blood components on solid surfaces. The configuration of the initially

adsorbed proteins on the solid surface may be determined by the magnitude of the blood plasma-biomaterial interfacial free energy (29). Andrade proposed the minimum interfacial free energy hypothesis of biocompatibility (30). Water plays an important role in determining the biocompatibility of synthetic materials. Ratner et al. (31) have recognized that high water levels within the surface of materials will help provide a low interfacial free energy with blood and will reduce both protein adsorption and cell adhesion on the polymeric surface. Therefore, a surface with a hydrated polymer (hydrogel) coating would be expected to be more compatible with body fluids than a non-polar or less hydrated type of surface. The water up take of chitosan and aminated chitosan membranes with 0, 2, 4 and 6 % glycerol content was recorded in table (4).

Sample	Water uptake %
Chitosan	183.14
Aminated chitosan (glycerol 0%)	197.83
Aminated chitosan (glycerol 2%)	208.94
Aminated chitosan (glycerol 4%)	220.62
Aminated chitosan (glycerol 6%)	255.59

Table 4. Water uptake of chitosan and aminated chitosan membranes with different percent of glycerol

The water sorption of the chitosan was attributed to the hydrophilic groups of the polysaccharide chains; hydroxyl and amino groups. From the table, it is clear that increase of the water sorption of aminated chitosan over the chitosan it self. This was explained by increase the hydrophilic groups on the chitosan via grafted with amine groups. In the other hand, the increase of the water sorption of the aminated chitosan as increase the plasticizer percent was attributed to the hydrophilic power of the glycerol as polyols and also results from the effect of the plasticizer on the limitation of crystallinty of the membrane. The obtained results are in accordance with published results by other authors in which they added poly propylene glycol as a plasticizer to chitosan (32).

Mechanical properties

The tensile properties of chitosan and aminated chitosan membranes with different percent of plasticizer were measured and recorded in table (5). It was determined from the critical breaking point of the stretching test pieces. The maximum stress σ_{max} (Nm^{-2}) was evaluated as the ratio of the stretching force divided by the cross-sectional area of broken membrane piece. The maximum strain λ_{max} was measured as the elongation ratio of the initial length of the test piece.

The effect of the stress on the elongation of the membranes was found more clear for aminated chitosan higher than chitosan. The change of elastic intensity suggested that the number of the functional groups significantly affected the network elasticity of chitosan. This was reflected on increase the maximum stress and decreases the maximum strain.

By added the glycerol, the elongation of the aminated chitosan was increased with increase the percent of glycerol in polymer. Glycerol is miscible easily with chitosan, so the introduction of glycerol moisture resulting in drastic chain flexibility which reduced the

Sample	Max force N	Max strain λ_{max} %	Max stress σ_{max} N/mm2
Chitosan	19.80 N	24.36	37.72
Aminated chitosan (0% glycerol)	20.60 N	31.85 %	43.32
Aminated chitosan (2% glycerol)	26.88 N	28.60 %	46.66
Aminated chitosan (4% glycerol)	25.78 N	29.30 %	36.83
Aminated chitosan (6% glycerol)	28.75 N	34.33 %	42.91

Table 5. The maximum stress and strain of chitosan and aminated chitosan membranes with different percent of glycerol

rigidity of native chitosan. Other authors used poly propylene glycol as a plasticizer and obtained similar results. They claimed the obtained results to the fact that propylene glycol is containing several OH groups, which can form intermolecular bonds with the excess of NH_3^+ groups in the chitosan polymer (32).

Surface roughness

It is known that biomaterials have to fulfill many conditions. However, the surface quality is one of the most important properties of biomaterial, which limits its applications. It is so important because most of biological reactions occur on the surface and at interface. Among other things the hydrophilicty, chemical structure, topography and roughness of surface create the response of the host tissue to presence of implant. The adhesion and proliferation of cells is also determined by the surface properties. They play a significant role in biocompatibility as well as for tissue engineering.

The surface roughness of chitosan and aminated chitosan membranes was evaluated (table 6). It was found that the roughness of aminated chitosan membranes is less than chitosan. Also the table shows a decrease in the film roughness with increase of glycerol concentration. This behavior could be referred to the changes in chemical structure, hydrophilicty and as well as the surface energy which separately or in combination affect the arrangement of the macromolecules and hence its surface roughness. It can be seen the role of glycerol in improving the surface smoothness. In natural skin, the dense skin layer has a surface roughness of 20 to 165 nm. This means that increase of the glycerol

Sample	Surface roughness μm		
	Front face	Behind face	average
Chitosan	3.853	3.57	3.7133
Aminated chitosan (0% glycerol)	2.34	2.28	2.31
Aminated chitosan (2% glycerol)	1.92	1.3	1.611
Aminated chitosan (4% glycerol)	1.73	1.25	1.49
Aminated chitosan (6% glycerol)	1.4	1.28	1.35

Table 6. Surface roughness of chitosan and aminated chitosan membranes with different percent of glycerol

concentration in the membrane caste solution, brings the membrane roughness close to that of skin which increases the contact area and hence preventing frictions and simultaneously reduces the healing time.

Scanning electron microscope

The surface of chitosan membrane and aminated chitosan membranes with different percent of plasticizer was scanned using scan electron microscope (SEM) (figure 4). The surface became smoother with amination and furthermore with glycerol addition. This observation is in agreement with roughness test obtained data in table 6.

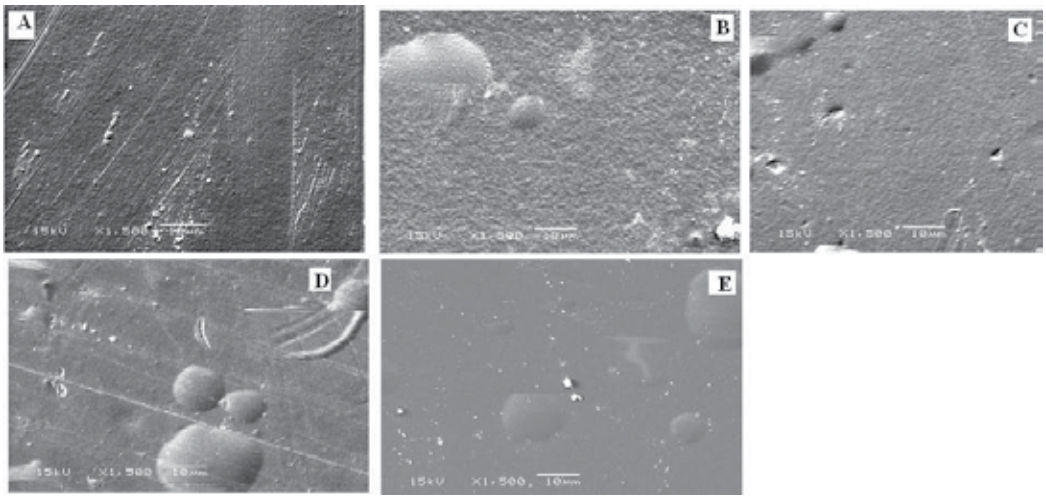

Fig. 4. Surface scan electron microscope photo of chitosan membrane (a), aminated chitosan membrane (b), aminated chitosan membrane with 2% glycerol (c), aaminated chitosan membrane 12 with 4% glycerol (d), and aminated chitosan membrane with 6% glycerol (e).

Water vapour permeability

One of the main functions of wound dressing membrane is maintains a moist environment at the wound/ dressing interface. This characteristic was measured for chitosan and modified chitosan membranes, with different glycerol content, through measuring of its water vapor permeability (table 7).

Sample	Permeability gm – mil / m2-day
Chitosan	3.843057
Aminated chitosan (glycerol 0%)	3.372898
Aminated chitosan (glycerol 2%)	2.476318
Aminated chitosan (glycerol 4%)	1.178036
Aminated chitosan (glycerol 6%)	0.586429

Table 7. Water permeability of chitosan and aminated chitosan membranes with different percent of glycerol

The decrease of the membrane permeability as exposed to water vapor was attributed to two factors. First, the swelling of polymer chains which decreases the pores diameter of the membrane and second is the reduction of the pore volume due to the presence of bulk PBQ benzene ring in the structure. The decrease of the aminated chitosan membranes permeability proved the changes in the chemical structure which in consequence affects the hydrophilicity of the membranes. In the same way, the addition of glycerol decreases the permeability of membranes gradually with its content. These results are in accordance with the water uptake percentage measurements. This future enables us to control the water vapor permeability.

2.2 Bio-evaluation of modified chitosan

For application as wound dressing, modified chitosan membranes have been evaluated from Bio-point of view. Properties such as cytotoxicity, Hemocompatability and Biodegradability have been evaluated.

Antimicrobial activity

Chitosan derivatives present interesting properties for biomedical applications, because such materials can exhibit enhanced bacteriostatic activity with respect to pure chitosan. Ethylene diamine tetraacetic acid (EDTA) grafted onto chitosan increases the antibacterial activity of chitosan by complexing magnesium that under normal circumstances stabilizes the outer membrane of gram-negative bacteria (33). The increase in chitosan antimicrobial activity is also observed with carboxymethyl chitosan, which makes essential transition metal ions unavailable for bacteria (34) or binds to the negatively charged bacterial surface to disturb the cell membrane (35). Therefore, these materials are used in wound healing systems, such as carboxymethyl chitosan for the reduction of periodontal pockets in dentistry (34) and chitosan-grafted with EDTA as a constituent of hydro-alcoholic gels for topical use (33). Chitosan and chitooligosaccharide-grafted membranes showed antibacterial activity against *Escherichia coli*, *Pseudomonas aeruginosa*, methicilin-resistant *Staphylococcus aureus* (MRSA), and *S. aureus* (36). Also, it was observed that the antimicrobial activity of chitosan and graft copolymers against *Candida albicans*, *Trichophyton rubrum*, and *Trichophyton violaceum* depends largely on the amount and type of grafted chains, as well as on the changes of pH (37).

Table 8 shows the effect of chitosan amination degree variation on its antimicrobial activity. It was found that antimicrobial activity of the aminated chitosan increased as a result of increase grafted amine groups due to selective grafting of this external amine groups on the hydroxyl groups of chitosan. This leads consequently to increase the positive charges on the polymer backbone. The antibacterial activity was improved against two gram negative bacteria, *Escherichia coli* and *pseudomonas aeruginosa*, by 50% and 40%, respectively. At the same time, it was improved against two gram positive bacteria, *Bacillus cereus* and *Staphylococcus aureus*, by 114% and 45%, respectively. In microbial profile, the powerful effect of modified chitosan on the gram negative rather than the gram positive bacterium was explained by the difference on the pathological composition of the cell wall. Gram negative bacteria have thick layer of phospholipids rather than the peptidoglycan comparing to the gram positive which has thick layer of peptidoglycan. The negative charges of the phospholipids enhance the adhesion power of poly cationic polymer such as

PBQ :chitin ratio	N content (relative percentage)	Maximum inhibition (%)			
		E.coli	*Bacillus*	*Pseudomonas*	*Stapylococcus*
Chitosan control	100	62.6298	35.689	68.73178	67.047076
0.0935	101	77.4394	46.2014	80.53936	69.258203
0.187	102	79.8616	57.3322	86.22449	73.18117
0.374	117.7	83.1834	58.2155	87.17201	85.805991
0.545	129.3	88.7889	62.3675	92.34694	94.293866
0.747	129.6	90.7958	76.7668	96.13703	97.360913

Table 8. Effect of the degree of amination on the antimicrobial activity of modified chitosan against different microorganisms

chitosan on the cell wall. Increasing the cell inhibition capability of modified aminated chitosan affects directly on the time needed for wound healing and almost eliminates the possibility of bacterial infections. This idea was the base for preparation and synthesis of different quaternary chitosan derivatives (38). Improvement of the antibacterial activity has been achieved by other authors by adding silver to chitosane polyphosphate membranes (39). However, the cytotoxicity of this derivative was found very high.

The effect of adding glycerol as plasticizer to aminated chitosan on the antimicrobial activity was studied. Four samples with different percent of glycerol 0, 2, 4 and 6 % were tested. It was found that the antibacterial activity is nearly constant and does not affect with increase of the glycerol content in the membranes.

Hemocompatability

Hemolysis is regarded as an especially significant screening test, once it provides quantification of small levels of plasma hemoglobin, which may not be measurable under in vivo conditions. As reported in literature (ISO 10993–4 (1999)), it is not possible to define a universal level of acceptable or unacceptable amounts of hemolysis. Although by definition a blood-compatible material should be non-hemolytic, in practice several medical devices cause hemolysis. This means that when such hemolytic effect takes place, it is important to make sure that clinical benefits overcome the risks and that the values of hemolysis are within acceptable limits. It has been shown that chitosan derivatives have great potential to be used in other biomedical applications. As a result of the biocompatible properties such as good blood compatibility and cell growth efficiency, grafted chitosan materials have potential to be used in cardio-vascular applications (40-41).

According to ASTM F 756-00 (2000) materials can be classified in three different categories according to their hemolytic index (hemolysis %). Materials with percentages of hemolysis over 5% are considered hemolytic; while the ones with hemolytic index between 5% and 2% are classified as slightly hemolytic. Finally, when the material presents a hemolysis percentage below 2% it is considered as a non-hemolytic material. Table 9 represents the values of hemolysis obtained for all membranes. The obtained results indicate that the chitosan and chitosan derivatives are non hemolytic compounds and compatible with human body. Addition of glycerol with any percent of studied range reduced the

Sample	Hemolytic percent
Chitosan	1.933816
Aminated chitosan (glycerol 0%)	2.109617
Aminated chitosan (glycerol 2%)	1.447777
Aminated chitosan (glycerol 4%)	1.168563
Aminated chitosan (glycerol 6%)	1.013444

Table 9. Hemolytic percent of chitosan and aminated chitosan membranes with different percent of glycerol

heamolysis to less than 2%, so the presence of glycerol is beneficial from this point of view. Best results obtained with 6% sample; 1.01 hemolytic percent. The effect of glycerol addition may be explained according to reduce the surface roughness and accordingly the contact area between the blood vessels and the membranes surface. It is worthy to mention here that the reduction of hemolytic effect is directly proportional with surface roughness mentioned in table (6). Reduction of surface roughness by 50% relative to chitosan has been obtained with aminated chitosan with 2% glycerol. This reduction was aligned with reduction in hemolytic percentage by about 25%. Critical value of surface roughness obtained with aminated chitosane with 2% glycerol, 1.61, which beyond the hemolytic percent reduced linearly and with higher rate. Addition of glycerol as plastizer may also contribute in increasing of the porous structure.

Cytotoxicity

Several searches were tested and measured the cytotoxicity of Chitosan (39, 42). Cytotoxicity of Chitosan and aminated Chitosan was measured using mouse fibroblasts with the direct connect method and the data are shown in table 10. According to the tabulated results, the viability of the live cell decreased by increase the amine group substitution.

sample	Live cells X 10^5	Dead cell X 10^5	Total cells X 10^5	viability %
Control	6.75	1.2	7.95	89.9
Chitosan	5.35	0.8	6.15	86.9
aminated Chitosan	5	1.5	6.5	76.9
aminated Chitosan with plasticizer glycerol (4%)	4.3	1.6	5.9	72.9

Table 10. Cytotoxicity of chitosan and modified chitosan (0.6 x 10^5 cells incubated for five days)

Several authors have discussed the role of amine substitute on polymers in influencing toxicity. Dekie et al. (43) noted that the presence of primary amines in poly(L-glutamic acid) (PGA) derivatives has a significant toxic effect on red blood cells. Based on studies with modified poly(L-lysin) (PLL), Ferruti et al, (44) conclude that polymers with tertiary amine groups exhibit a lower toxicity than those with primary and secondary residues. They have also synthesized tertiary amine group containing poly (amidoamine)s (PAAS); these substitutes polymers have good biocompatibility and can form complexes with heparin

(45-47). Fischer et al (48) confirmed these observations for PLL and PEI, but argued that cationized human serum albumin and starburst dendimer, which also contain primary amino groups, showed only moderate cytotoxic effects. They conclude that not only the type of amino function but also the charge density and arrangement is an important factor for determining cytotoxicity and hence biocompatibility (48). This may be explains the moderate increment of cytotoxicity of modified chitosan, table 10, in which the cell viability % decreases by about 10%, although the nitrogen content increases by about 30%. Only part of this increment is referred to primary amino groups and the other part is referred to secondary amino groups (figure 1), which is less toxic.

Biodegradability

The biodegradability of chitosan and aminated chitosan was measured as produced reduced sugar results from the cellulase enzyme action on the chitosan. Table 11 represents the OD of the total reduced sugar produced from chitosan and aminated chitosan hydrolysis with cellulase enzyme for 30 minutes at 50°C. It was observed that the degradation in the case of chitosan is higher than the aminated chitosan. This may be attributed to the steric effect result from increase the amine content and presence of benzene ring of PBQ on the polymer chains which consequently reduced the accessibility of the aminated chitosan to enzyme hydrolytic activity.

Polymer	OD
Chitosan	0.747
Aminated chitosan	0.643

Table 11. Biodegradability effect of cellulase enzyme on the chitosan and aminated chitosan (30 minute, at 50°C and pH 7)

3. Conclusion

Modified chitosan with antibacterial potentials superior to native chitosan was prepared. To achieve this goal, new route of chemical modification to graft extra amine groups onto native chitosan has been presented. As a result of modification, the nitrogen content of modified chitosan increased by about 30%.

FT-IR, TGA analysis and solubility test confirmed the occurrence of amination process. The solubility near neutral media, pH 6.0, increases by about 65%. Using glycerol as plasticizer improved the surface roughness, water uptake, and the mechanical properties of aminated chitosan membranes while its water vapor permeability was reduced.

The modified chitosan membranes were evaluated as wound dressing biomaterial and show high profile. Its bacterial cell inhibition capability against gram negative and gram positive was improved in the range of 40 – 100%. Moreover, no hemolytic effect was observed. In addition, its biodegradability was not affected significantly. However, the cytotoxicity was increased, not in a dramatic way, and the water vapor permeability also reduced which limit the application of modified chitosane membranes as wound dressing. In the meanwhile, further investigations are conduction in this direction to overcome these drawbacks through quaterinization process.

In conclusion the new route of modification was found successful and is recommended for preparation of novel chitosan biomaterials.

4. References

[1] Tomihata, K. Ikada, Y. Biomaterials 1997, 18, 567.
[2] Cho, Y.W. Cho, Y.N. Chung, S.H. Yoo, G. Ko, S.W. Biomaterials 1999, 20,2139.
[3] Kumar, R. Muzzarelli, M.N.V. Muzzarelli, R.A.A. Sashiwa, C.H. Domb, A.J. Chem. Rev 2004, 104, 6017.
[4] Sanford, P.A. in: G. Skjak-Braek, T. Anthonsen, P.A. Sanford (Eds.), Chitin and Chitosan-sources, Chemistry, Biochemistry, Physical Properties and Applications, Elsevier, London, 1989, pp. 51–70.
[5] Muzzarelli, R.A.A. Cell Mol. Life Sci 1997, 53,131.
[6] Bersch, P.C. Nies, B. Liebendorfer, A. J.Mater. Sci. Mater. Med. 1995, 6, 231.
[7] Kurita, K. Kojima, T. Munakata, T. Akao, H. Mori, T. Nishiyama, Y. Chem. Lett. 1998, 27, 317.
[8] Sashiwa, H. Shigemasa, Y. Carbohydr. Polym. 1999, 39, 127.
[9] Heras, A. Rodriguez, N.M. Ramos, V.M. Carbohydr. Polym. 2001, 44, 1.
[10] Jayakumar, R. Reis, R.L. Mano, J.F. Mater. Sci. Forum 2006, 514–516, 1015.
[11] Lu, G. Kong, L. Sheng, B. Wang, G. Gong, Y. Zhang, X. Eur. Polym. J. 2007, 43, 3807.
[12] Muzzarelli, R.A.A. Emmanueli, M. Mariotti, S. Carbohydr. Res. 1982, 107, 199.
[13] Roller, S. Covill, N. Int. J. Food Microbiol. 1999, 47, 67.
[14] Tsai, G.J. Su, W.H. Journal of Food Protection 1999, 62, 239.
[15] Jeon, Y. J. Park, P. J. Kim, S. K. Carbohydrate Polymers 2001, 44, 71.
[16] Wang, G. H. Journal of Food Protection 1992, 55, 916.
[17] Yang, T. C. Chou, C. C. Li, C. F. International Journal of Food Microbiology 2005, 97,237.
[18] Chung, Y. C. Kuo, C. L. Chen, C. C. Bioresource Technology 2005, 96,1473.
[19] Liu, H. Du, Y. Yang, J. Zhu, H. Carbohydrate Polymers 2004, 55,291.
[20] Jukka, H. Martha, H. Mar, M. Ogmundur, R. Tomas, A. Pasi, S. Carbohydrate Polymers 2006, 65, 114.
[21] Rigby, G.W. U.S.Patent 2,040,879 (1936).
[22] Wolf.Rom, M.L. Maher, G.G. Chney, A. J. Org. Chem. 1958, 23, 1990.
[23] American Society for Testing and Materials .ASTM. (1995). (pp. 159–167). Philadelphia, PA, USA:
[24] Muhannad, J. Franz, H. Furkert, B. Miiller, W. Eur. J. Pharm. Biopharm. 2002, 53,115.
[25] Jeon, Y.J. Kim, S.K. Carbohydr. Polym. 2000, 41,133.
[26] American Society for Testing and Materials, ASTM (2000). ASTM F 756-00: Standard Practices for Assessment of Haemolytic Properties of Materials, Philadelphia.
[27] Pielka, S. fibres and textiles in Eastern Europe 2003, 11, 41.
[28] MILLER, G.L. Anal. Chem. 1959, 31, 426.
[29] Ruckenstein, E. Gourisankar, S. V. Biomaterials 1986, 7, 403.
[30] Andrade, J. D. med. Instrum. 1973, 7, 110.
[31] Ratner, B. D. Hoffman, A. S. Hanson, S. R. Harker, L. A. Whiffen, J. D. J. Polym. Sci. Polym. Symp 1979, 66, 363.
[32] Wittaya-areekul, S. Prahsarn, C. Int. J. of Pharmac. 2006, 313,123.
[33] Valanta, C. Christen, B. Bernkop-Schnurch, A. J. Pharm. Pharmacol. 1998, 50, 445.

[34] Muzzarelli, R.A.A. Skjak-Braek, G. Anthonsen, T. Sandford, P. Appl. Polym. Sci. (1989) 87–99 (Elsevier, London).
[35] Liu, X.F. Guan, Y.L. Yang, D.Z. Li, Z. Yao, K.D. J. Appl. Polym. Sci. 2001,79, 1324.
[36] Hu, S.G. Jou, C.H. Yang, M.C. J. Appl. Polym. Sci. 2003, 88, 2797.
[37] Jung, B.O. Kim, C.H. Choi, K.S. Lee, Y.M. Kim, J.J. J. Appl. Polym. Sci. 1999,72, 713.
[38] Kenawy, E. Worley, S. Broughton, R. Biomacromolecules 2007, 8 , 1359.
[39] Ong, S.Y. Wu, j. Moochhala, S. M. Tan, M.H. Lu, J. Biomaterials 2008, 29, 4323.
[40] Mao, C. Zhao, W.B. Zhu, A.P. Shen, J. Lin, S.C. Process. Biochem. 2004, 39, 1151.
[41] Chung, T.W. Lu, Y.F. Wang, S.S. Lin, Y.S. Chu, S.H. Biomaterials 2002, 23, 4803.
[42] Zhang, X. Yang, D. Nie, J. International Journal of Biological Macromolecules , 2008, 43, 456.
[43] Dekie, L. Toncheva, V. Dubruel, P. Schacht, E. H. Barrett, L. Seymour, L. W. J. Cont. Rel. 2000, 65, 187.
[44] Ferruti, P. Knobloch, S. Ranucci, E. Gianasi, E. Duncan, R. Proc. Int. Sump. Control. Rel. Bioact. Mater. 1997, 24, 45.
[45] Ferruti, P. Ranucci, E. sartore, L. bingnotti, F. Marchito, M. A. Bianciardi, P. Veronese, F. M. Biomaterials. 1994, 15, 1235.
[46] Lin, W. Garnett, C. Davies, M. C. Bignotti, F. Ferruti, P. Davies, S. S. Illum, L. Biomaterials 1997, 18, 559.
[47] Ferruti, P. Marchisio, M. A. Barbucci, R. Polymer 1985, 26, 1336.
[48] Fischer, D. Li, Y. Ahlemeyer, B. Krieglsein, J. Kissel, T. Biomaterials 2003, 24, 1121.

Edited by Theophile Theophanides

This informative and state-of-the art book on Infrared Spectroscopy in Life sciences designed for researchers, academics as well as for those working in industry, agriculture and in pharmaceutical companies features 20 chapters of applications of MIRS and NIRS in brain activity and clinical research. It shows excellent FT-IR spectra of breast tissues, atheromatic plaques, human bones and projects assessment of haemodynamic activation in the cerebral cortex, brain oxygenation studies and many interesting insights from a medical perspective.

ISBN 978-953-51-4298-0

Photo by Kd5uno / iStock

IntechOpen